RHYOLITE VOLCANISM AT ÖRÆFAJÖKULL VOLCANO, S.E. ICELAND – A WINDOW ON QUATERNARY CLIMATE CHANGE

A thesis submitted to the University of Manchester for the degree of

Doctor of Philosophy

in the Faculty of Engineering and Physical Sciences

2011

ANGELA JANE WALKER

SCHOOL OF EARTH, ATMOSPHERIC AND ENVIRONMENTAL SCIENCES

List of contents

Final word count: 52996

List of figures

Chapter 1

Chapter 2

Chapter 3

Chapter 4

Chapter 5

Chapter 6

Chapter 7

List of tables

Chapter 3

Chapter 4

Chapter 5

Chapter 6

List of abbreviations

BP	Before present
Ma	Millions of years ago
ka	Thousands of years ago
Ga	Billions of years (absolute)
My	Millions of years (absolute)
k	Thousands of years (absolute)
mm	Millimetre
cm	Centimetre
m	Metre
km	Kilometre
mg	milligram
g	Gram
MIS	Marine interval stage
m.a.s.l	Metres above sea level
STP	Standard temperature and pressure
kbar	Kilobars
Ar	Argon
40Ar*	Radiogenic argon
$39Ar_K$	Neucleogenically produced ^{39}Ar
ACs	Alder Creek sanidine
GW	Goðafjall West
GE	Goðafjall East
HVG	Hvalvörðugil

Abstract

Öræfajökull is an ice-capped stratovolcano situated in the south east of Iceland which has developed throughout the mid to late Quaternary. It has erupted basaltic and rhyolitic lavas during interglacial and glacial periods, many of which display strong physical evidence of volcano-ice interaction. This makes Öræfajökull an ideal location to reconstruct terrestrial palaeo-environments.

The area of Goðafjall and Hrútsfjall is one of a small number of rhyolitic depositional centres situated on the south west flanks of the volcano and is the first rhyolitic area of Öræfajökull to be mapped in detail.

The relatively high K content of the rhyolitic units make them good candidates for $^{40}Ar/^{39}Ar$ dating, yielding eruption ages that provide a temporal constraint on the development of the stratovolcano.

$^{40}Ar/^{39}Ar$ dating of young rocks (<1 My) is challenging and many of the samples were found to contain both excess and atmospheric argon. A small number exhibited a fractionated argon source with a sub-atmospheric $^{40}Ar/^{36}Ar$ ratio that could not be explained by a single episode of mass fractionation. Soret thermal diffusion has been suggested as a possible mechanism for fractionation, although further investigation is required.

Two dominant rhyolite eruptions have been identified by detailed field mapping supported by the geochemical application of chemostratigraphy.

The stratigraphically lower group of lavas outcrop between 100 to 380 m.a.s.l. and were erupted subaerially into a relatively ice-free environment at the base of the edifice. A $^{40}Ar/^{39}Ar$ age of 202 ± 9 ka implies that eruption occurred during the interglacial MIS 7.

Conversely the upper group of lavas show strong evidence of volcano-ice interaction, suggesting that they were erupted subglacially and confined by ice with a minimum ice surface elevation of at least 800 m.a.s.l. These lavas yield a $^{40}Ar/^{39}Ar$ age of 116 ± 14 ka, which implies that eruption occurred during the transitional period between the MIS5e interglacial and colder sub-stages prior to MIS 4.

At least two further glacial advances have occurred since the emplacement of the subglacial rhyolite unit.

In addition, an ice confined trachydacite flow from the Vatnafjall ridge situated 20 km north east of Goðafjall has also been dated yielding a $^{40}Ar/^{39}Ar$ age of 95 ± 7 k. This lava was emplaced at an elevation of over 700 m in the presence of an adjacent valley fill glacier was at least 700 m thick.

Ice thickness has varied dramatically throughout the evolution of Öræfajökull and glacial erosion has played an important role in its topographic development.

Declaration

The author declares that no portion of the work referred to in the thesis has been submitted in support of an application for another degree or qualification of this ot any other university or other instituate of learning.

Copyright statement

i. The author of this thesis (including any appendixces and/or schedules to this thesis)owns certain copyright or related rights in it (the "copyright") and she has given The University of Manchester certain rights to use such copy right, including for administrative purposes

ii. Copies of this thesis, either in full or in extracts and whether in hard or electronic copy, may be made only in accordance with the copyright, Designs and Patents Act 1988 (as amended) and regulations issued under it or, where appropriate, in accordance with licensing agreements which the University has from time to time. This page must form part of any such copies made.

iii. The ownership of certain copyright, patents, designs, trade marks and other intellectual property (the "Intellectual Property") and any reproductions ofcopyright works in the the thesis, for example graphs and tables ("Reproductions"), which may be described in this thesis, may not be owned by the auther and may be owned by third parties. Such Intellectual Property and Reproductions cannot and must not be made available for use without the prior written permission of the owner(s) of the relevant Intellectual Property and/or Reproductions.

iv. Further information on the conditions under which disclosure, publication and commercialisation of this thesis, the copyright and any Intellectual Property and/or Reproductions described in it may take place is available in the University IP policy (see http://www.campus.manchester.ac.uk/media library/policies/intellectualproperty.pdf), in any relevant Thesis restriction declarations deposited in the University Library, The University Library's regulations (see http://www.manchester.ac.uk/library/aboutus/regulations) and in the University's policy on presentation of thesis.

In memory of Rory Milne (1940 – 2011)

a great friend and field companion

Acknowledgements

A very big thank you to my main supervisor Ray Burgess for his endless patience, unfailing support and ability to keep calm, even after being asked the same question 14 times. Thank you to my field supervisor Dave McGarvie for coming up with this great project, sharing his passion for and knowledge of Iceland and the wonders of subglacial rhyolites; for introducing me to pylsur, Beanfeast and for his endless supply of really bad jokes. Thanks also to my two co-supervisors John Smellie and Jennie Gilbert for their invaluable help and expertise both in the field and the UK.

Many thanks to my two field assistants, Julia Cartwright and Bridget Weston for their good company, patience and their ability to carry very heavy bags of rocks over long distances without complaining.

In Iceland thanks are due to Magnus Gudmundsson at the University of Iceland, Regina, Klaus and all the staff at Skaftafell National Park for providing me with help and accommodation way beyond the standard of most field geologists. Also thanks to the staff of Umhverfisstofnun and Iceland Conservation Volunteers for lots of moral and logistical support and to Beggi at Holdur for providing reliable hire cars.

For technical assistance, thanks to Bev Clementson and Dave Blagburn for helping to keep the old MS1 running for at least two out of the last four years, to Paul Lythgoe and Alastair Bewsher for help with XRF and to Steve Stockley for thin sections; also thanks to Torsten Henkel for his proof-reading skills and to Ruth Carter for admin help and always providing a friendly ear.

On a personal level, thanks to all the Staff at Birkbeck College and Dean Podolsky for setting me off on this path and convincing me that I could do this.

Thanks for ongoing support from my friends over the past four years, especially Shiv, Jo and Paul, Rach and Rob, Saf, Frankie and to Gregg who's pep talk in Landmannalaugar helped me to turn this project around. Thanks also to Leeds St. Christopher's Cycling Club and to my MCR cycling girls – especially Em and Ange for helping to keep me sane over the last few months of writing-up.

And finally, huge thanks go to my Dad and Aunty Joan who probably thought I was bonkers for giving up a good job in London to poke about with rocks, but who supported me anyway and always made sure I had somewhere to go home to.

Chapter 1
Introduction

1.1. Aims and objectives

The main aim of this research project is to provide an insight into the temporal and physical evolution of Öræfajökull stratovolcano situated in the south east of Iceland by compiling a detailed, multi-disciplinary analysis of the Goðafjall and Hrútsfjall region which is situated on the exposed southern flanks of the volcano. Aside from two historical eruptions in 1362 and 1727 relatively little is known about the eruptive history of Iceland's largest stratovolcano.

The Goðafjall and Hrútsfjall area was chosen for its exceptionally well-preserved silicic exposures which display strong phyiscal evidence of volcano-ice interaction. The relatively high K content of the silicic units make them good candidates for $^{40}Ar/^{39}Ar$ dating, thereby providing eruption ages which can be evaluated in conjunction with detailed field observations in order to provide an absolute time constraint for the evolution of Öræfajökull.

The secondary aim of this reseach project is the reconstruction of local terrestrial palaeoenvironments throughout the evolution of Öræfajökull.

Iceland is an ideal location to study the effects of terrestrial climate change throughout the quaternary as it has the most complete terrestrial record of glaciations in the Northern Hemisphere due to the preservation of palaeo-glacial horizons that have been overlain and protected by later volcanic products.

Placing constraints on the eruption ages of the lava flows that show good evidence for interaction with and / or confinement by ice provides information on the extent, variability and thickness of palaeo-glaciers. Correlation of this data with the

marine oxygen isotope record allows us to determine whether changes in marine temperatures were mirrored by land-based glacial advance and retreat. This information is valuable in providing parameters for present day climate modelling and ice sheet dynamics, enabling a better understanding of how glaciers respond to changes in global climate.

In order to achieve these aims the project is sub-divided into three main categories of study, the results of which have been synthesised in order to compile an evolutionary timeline for the southern flanks of Öræfajökull. The three main areas are field observation, geochemistry and geochronology:

1: Detailed field observation

A supplementary 1:10 000 geological map of the Goðafjall and Hrútsfjall area has been produced in order to provide information on the stratigraphic development of Goðafjall and Hrútsfjall. Detailed field observations and evidence of interaction with ice / snow / meltwater have been compiled and samples have been collected for geochemical and geochonological determination.

2: Geochemistry

Major and trace element geochemistry has been used as an aid to identifiy the main eruptive units within the field area with the application of 'chemostratigraphy' in order to both support and supplement the field observations provided by conventional mapping techniques.

3: $^{40}Ar/^{39}Ar$ dating of silicic units

The Goðafjall and Hrútsfjall area is dominated by silicic volcanics, which makes them ideal candidates for the $^{40}Ar/^{39}Ar$ dating method. Providing dates for the eruption ages of the silicic units has enabled a temporal framework in which to discuss the evolution of the Goðafjall and Hrútsfjall area and the wider palaeoclimatic implications for the Öræfi region of south east Iceland throughout the phyiscal evolution of Öræfajökull.

1.2. Thesis structure

This thesis is divided into seven chapters:

Chapter 1 introduces the main aims of this research and the thesis structure. This is followed by a geological history of Iceland, an introduction to Öræfajökull stratovolcano and a review of the work undertaken by previous authors.

Chapter 2 provides a synopsis of the relatively new research area of glaciovolcanism and discusses other examples of subglacial volcanism both in Iceland and elsewhere.

Chapter 3 presents the major and trace element geochemistry of all of the rock types located within the Goðafjall and Hrútsfjall area.

Chapter 4 provides detailed field observations of all of the rock types present within the Goðafjall and Hrútsfjall area. A full description of each lithofacies is followed by an interpretation.

Chapter 5 introduces the $^{40}Ar/^{39}Ar$ dating technique and discusses the methodology and the difficulties surrounding the application of this dating technique to young Icelandic rhyolites.

Chapter 6 provides a temporal and phyiscal evolutionary history of the Goðafjall and Hrútsfjall area by synthesising the main findings of chapters 3, 4 and 5. The findings are discussed within the wider context of palaeoclimatic variability throughout the development of Öræfajökull statovolcano.

Chapter 7 summarises the main conclusions of this body of reserach and outlines recommendations for future areas of work.

1.3. Geological setting of Iceland

Situated in the north Atlantic Ocean on the boundary between the North American Plate and the Eurasian Plate, Iceland owes its existence to the Mid-Atlantic Spreading Ridge (MAR) and the Icelandic Hotspot (Allen et al., 2002, Prestvik, 1979, Prestvik, 1982, Prestvik, 1985, Thorarinsson, 1958, Bjarnason and Schmeling, 2009), which is generally accepted to be a mantle plume, although alternative theories have been proposed (e.g. Foulger, 2002).

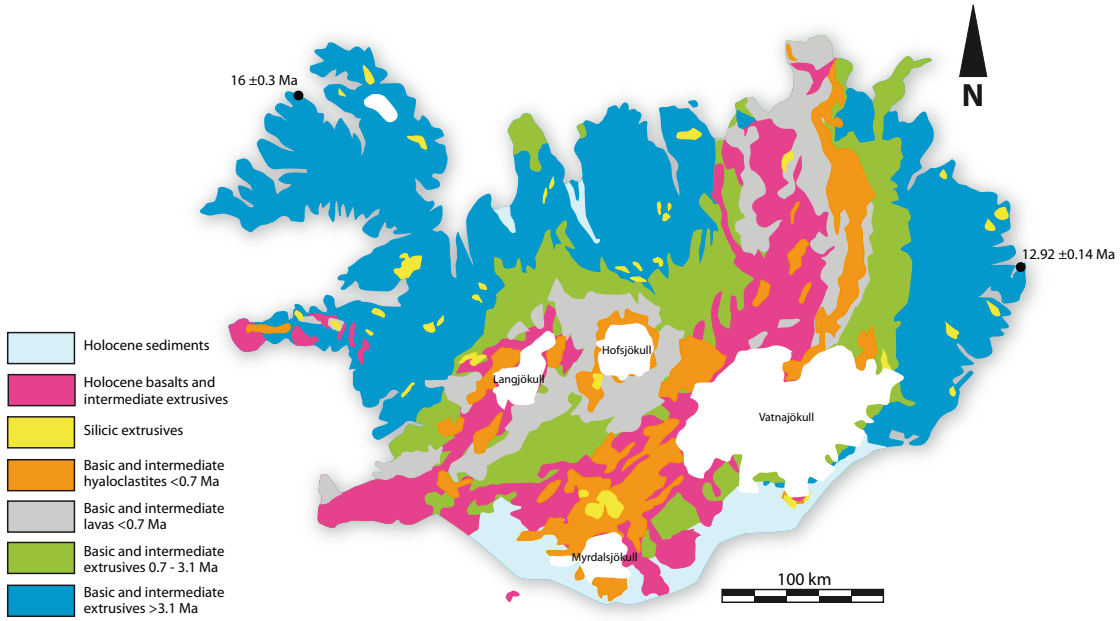

Fig. 1.1. Simplified geological map of Iceland with location and ages of Icelands oldest rock formations (adapted from Johannesson &Sæmundsson, 1998; Thordarsson & Hoskuldsson; Foulger, 2006).

Although the plume itself may have been active since the late Palaeocene (Holbrook et al., 2001, Helgason and Duncan, 2001), the spreading ridge and the hotspot conjoined approximately 27 million years ago in the early Miocene and have continued to realign together since then (Oskarsson et al., 1985). The ridge spreading axis has realigned itself with the hotspot throughout the geological history of Iceland by migrating 'eastward' in a series of 'rift jumps' (Hardarson et al., 1997, Mittelstaedt et al., 2011).

The combined activity of the spreading ridge and the mantle plume has led to an anomalous excess of magma production, generating a topographic highpoint along the ridge which eventually emerged from the Atlantic to form the subaerial island (White, 1997, Allen et al., 2002, Mihalffy et al., 2008).

The subaerial landmass is situated at the intersection between the MAR and the Greenland-Iceland-Faroes Ridge and represents just 30 per cent of the Iceland Basalt Plateau which is a much larger, mainly submarine, landmass. The plateau rises over 3000 m from the Atlantic seafloor to the top of Hvannadalshnúkur, Iceland's highest point and covers an area of around 350,000 km^2 (Thordarsson & Hoskuldsson, 2002). The Icelandic crust ranges in thickness from 15 to 46 km, and is anomalously thick when compared to adjacent sections of the MAR with a thickness of 9

– 11 km, and is 4 - 5 times thicker than the average oceanic crust (6 km) (Allen et al., 2002).

The North American and Eurasian plates in central Iceland (64.5°N, 18°W), are currently spreading away from each other at a rate of 18.3 mm/yr, in the divergence direction of N105°E (according to the NUVEL-1A model: DeMets et al., 1994). The variation in spreading rate across Iceland, due to different distances from the pole of rotation, is less than 2 mm/yr (Sigmundsson et al., 2008). While diverging, both plates are also simultaneously drifting toward the northwest, while the mantle-plume itself is stationary, thus explaining the apparent 'eastward' migration of the active spreading rift over time (Torsvik et al., 2001).

Iceland's oldest exposed rocks are Miocene basalts (fig. 1.1) , located away from the spreading ridge axis at opposite ends of the Island. In the west the oldest are dated at 16 ± 0.3 Ma, while in the east they have been dated at 12.92 ± 0.14 Ma (Foulger (2006) and references therein). Generally, with the exception of off-rift volcanic systems, the rocks become progressively younger towards the centre of the island as they approach the active spreading ridge (fig. 1.1).

Volcanic activity on Iceland can be split into two types: rift zone volcanism and flank zone volcanism (fig. 1.2). Rift zone volcanism can be defined as the subaerial expression of the active spreading ridge at axial rift zones. The axial rift zones are linked to each other and the MAR by transform faults. Rift zone volcanism is influenced by the rift's extensional tectonic forces and is characterised by fissure swarm eruptions, leading from a central volcanic system, running parallel to the rift. This prevents the volcanic structures from developing edifices to a great height. Geochemically, rift zone volcanoes tend to be tholeiitic.

The Reykyanes Ridge (RR) segment of the MAR surfaces at the Reykyanes Peninsula in the south west of the island and is known as the Reykjanes Rift Zone (RRZ). Further north the RRZ joins the Western Rift Zone (WRZ) which bends toward the centre of the island to join the Nothern Rift Zone (NRZ). Due to its oblique positioning, the easternmost section of the WRZ is often defined as a separate zone, the Central Volcanic Zone (CVZ), despite its geochemical similarity to the rest of the WRZ, and has been described as a leaky transform fault system (Oskarsson et al., 1985, Martin and Sigmarsson, 2010). The NRZ extends from the north

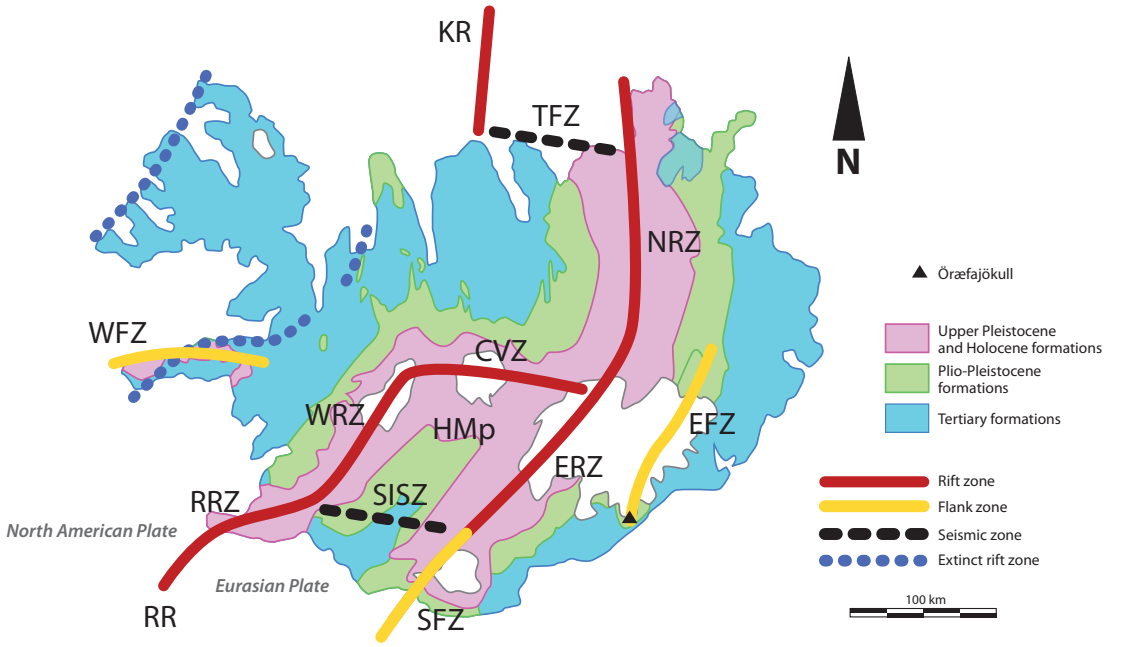

Fig. 1.2. Simplified map of Iceland's neovolcanic and seismic zones (adapted from Johannesson & Sæmundsson, 1998; Martin & Sigmarsson, 2010). Solid red lines indicate zones of rifting: RR – Reykjanes Ridge; RRZ – Reykjanes Rift Zone; WRZ – Western Rift Zone; CVZ – Central Volcanic Zone; ERZ – Eastern Rift Zone; NRZ – Northern Rift Zone; KR – Kolbeinsey Ridge. Solid Yellow lines indicate flank zones: WFZ – Western Flank Zone; SFZ – Southern Flank Zone; EFZ – Eastern Flank Zone. Dotted blue lines indicate lation of extinct rift zones. Dashed black line indicate non-volcanic seismic zones: SISZ – South Iceland Seismic Zone; TFZ – Tjornes fracture zone; HMp – Hrappar microplate.

coast, where it links to the submarine continuation of the MAR by a non-magmatic transform fault, the Tjornes Fracture Zone (TFZ). The Eastern Rift Zone (ERZ) propagates from the southern section of the NRZ in centre of the island, to the south and is currently the most active rift zone, responsible for numerous historical eruptions including Laki (1783) and the more recent subglacial Grimsvötn eruptions (e.g. 1996, 2004, 2011).

Flank zone volcanism occurs off-rift and is less affected by spreading tectonics, therefore the volcanoes in flank zones are able to build up much larger, more competent, stratovolcanic edifices. Geochemically the eruptive products of flank zone volcanoes tend to be more alkaline, produced from smaller degrees of partial melting (Jonasson, 2007), and they generally erupt a higher proportion of silicic rocks than rift zone central volcanoes.

There are three active flank zones: The Western Flank Zone (WFZ), also known as the Snæfellsnes Volcanic Zone (SnVZ), is situated on the western peninsula of Iceland. The SnVZ overlies the extinct Snæfellsnes Rift Zone (Moorbath et al.,

1968) and has been described as the continuation of a leaky transform fault (Martin and Sigmarsson, 2010). The Southern Flank Zone (SFZ or SIVZ) features many historically active volcanoes including Hekla, Katla and Eyjafjallajökull and also Torfajökull, Iceland's largest silicic depositional centre. It is the most active of the flank zones and is influenced by the southward propagation of the ERZ (Martin and Sigmarsson, 2010), although geochemically it retains an alkaline signature. The Eastern Flank Zone (EFZ or EVZ) is also known as the Öræfi Volcanic Belt (ÖVB) and runs from Snæfell in the North to Öræfajökull in the South. Öræfajökull, the focus of this research, is currently the only active volcano in the zone which has led to the suggestion that the EFZ is dormant and the classification of Öræfajökull as a separate isolated volcanic centre (Prestvik, 1985). Due to its current proximity to the mantle plume, the EFZ has been described as both a failed rift jump (Hards et al., 2000) and a nascent rift zone (Martin and Sigmarsson, 2010).

Icelandic lavas are strongly bimodal and the majority of outcropping rocks in Iceland are basaltic (85 per cent) (fig. 1.1) (Gunnarsson et al., 1998). Exposures of intermediate composition are minimal, and in most cases have been formed by magma mixing and hybridisation rather than 'true' intermediate rocks such as andesites. An estimated 10 - 12 per cent of the outcropping rocks in Iceland are silicic (Walker, 1966; Jonasson, 2006), with rhyolites being the most widespread. Seventy per cent are lavas and intrusions; the rest is pyroclastic material, although this estimate may be underestimated due to erosion (Lacasse and Garbe-Schönberg, 2001). This amount of silicic rock is anomalously conspicuous and not observed to the same degree in any other ocean island setting (i.e. Hawaii / Galapagos).

Icelandic rhyolite generation is of great interest to geologists, however it is still not well-understood. Due to their relatively high abundance within an ocean island-type setting and the absence of true intermediate rocks, Icelandic rhyolite generation is considered to be important as a possible key to understanding the formation of the first continental crust (e.g. Martin et al., 2008).

Sr and Nd isotopic similarity between the rhyolites and associated basalts at central volcanoes rules out the possibility of formation due to the remelting of remnant continental crust (Gunnarsson et al., 1998). Two end-member models of rhyolite generation have been proposed; the first model favours near-liquidus, fractional

crystallisation of a primitive, possibly enriched, basalt source (Hards et al., 2000, Prestvik et al., 2001, Carmichael, 1964), while the second model favours sub-solidus partial melting of pre-existing crust (Gunnarsson et al., 1998, Jonasson, 2007, Marsh et al., 1991), although many authors favour a combination of fractionation, crustal anatexis and magma mixing (Gunnarsson et al., 1998, McGarvie, 1984, MacDonald, 1990, McGarvie et al., 1990).

Jonasson (2007) argues that although rhyolite melts may collect in high-level holding reservoirs prior to eruption, they do not differentiate prior to this within a long-lived magma chamber and are instead produced by deformation-induced melting of intrusive rocks beneath central volcanoes.

However it is likely that different conditions prevail in the two neovolcanic zones, resulting in two contrasting mechanisms of rhyolite generation. This is corroborated by Nd isotope studies which verify the presence of rift zone and flank zone signatures (Martin and Sigmarsson, 2010). The 'rift-zone source' is dominated by sub-solidus processes, while the 'flank-zone source' is dominated by fractional crystallisation.

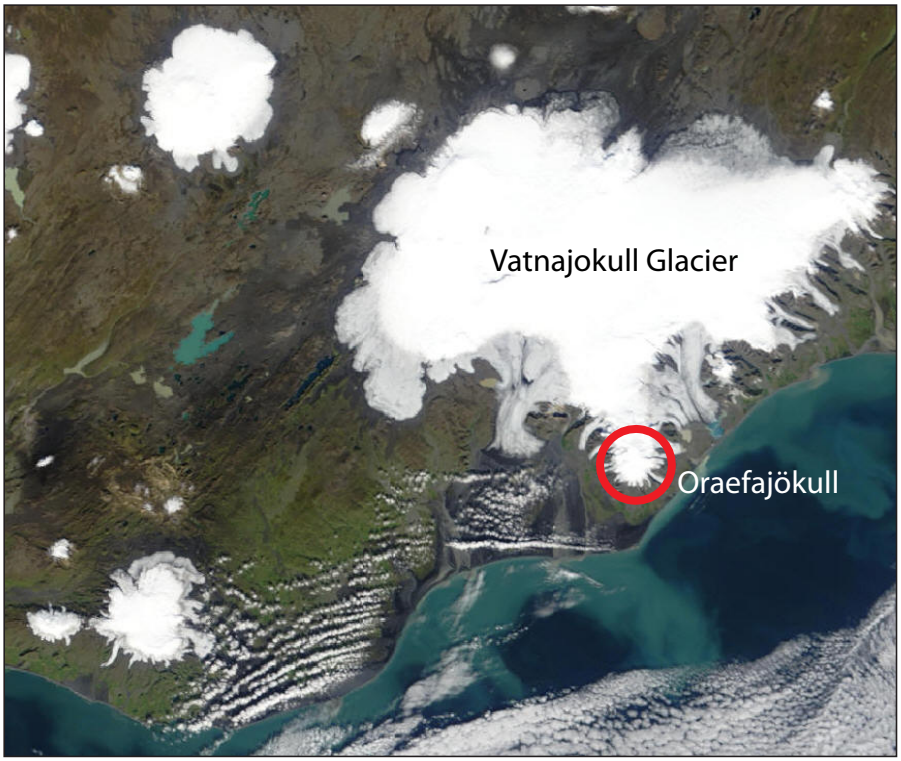

Fig. 1.3. Google Earth image of S.E. Iceland indicating Vatnajökull glacier and Öræfajökull.

1.4. Öræfajökull – geological setting and historical eruptive history

Fig. 1.4. The ice-capped summit of Öræfajökull Volcano, looking north east toward Svinafellsjökull glacier. (Image courtesy of D. McGarvie)

Situated in the south east of Iceland on the south eastern edge of the Vatnajökull Icecap, Öræfajökull Volcano is Iceland's largest active stratovolcano in both height and volume (fig. 1.3).

The summit, Hvannadalshnúkur, is situated on the north western rim and reaches a height of 2110 m. At least two thirds of the edifice is currently covered by an ice cap which flows down from the upper slopes, forming deep glacier valleys (fig. 1.4) that radiate from the ice-filled summit crater, dissecting its south-east to south-western flanks. The crater itself is 5 km in diameter and has an area of 14 km^2 (Bjornsson and Einarsson, 1990).

Öræfajökull is an-off rift central volcano and is tectonically isolated from Iceland's other neovolcanic zones (fig. 1.2). It is often classified as the southernmost expression of the otherwise dormant Eastern Flank Zone, which runs northward up to Snæfell Volcano (Prestvik, 1985, Prestvik et al., 2001, Hards et al., 2000).

The volcano sits unconformably on the remains of two glacially eroded, older volcanoes (Prestvik, 1985) and K-Ar dating of interbedded lavas and lacustrine

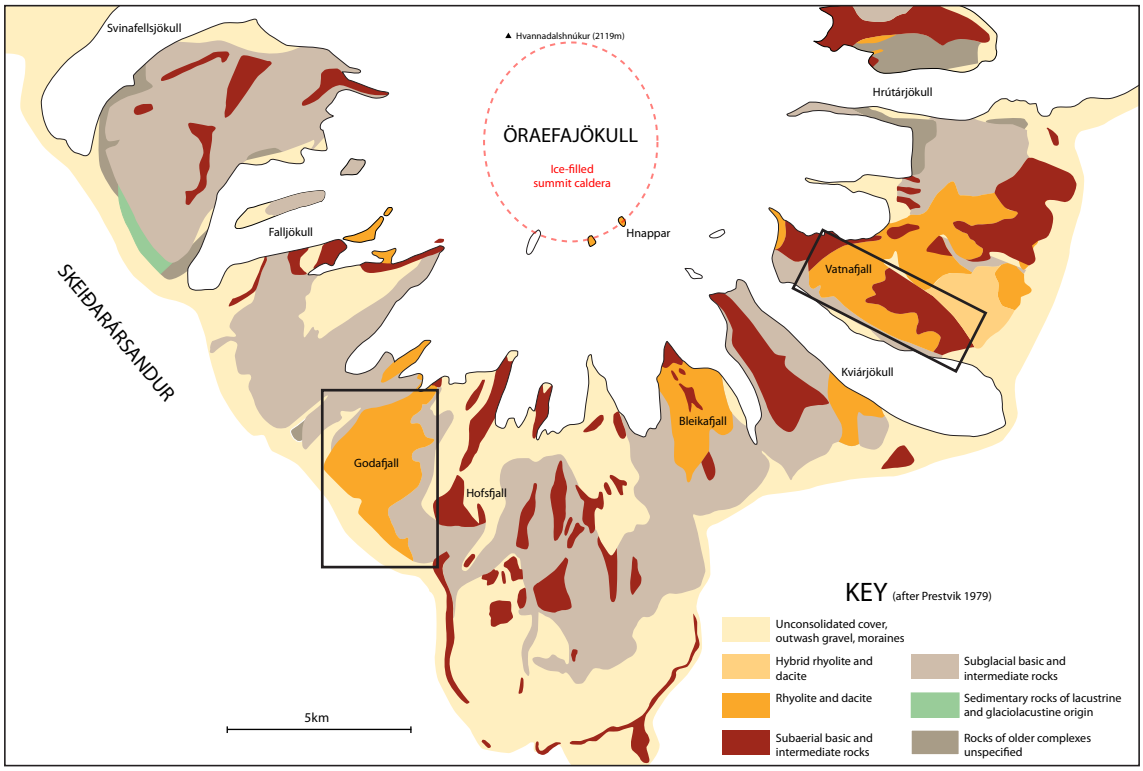

Fig. 1.5. Geological map of Öræfajökull (after Prestvik, 1979). Black outlined boxes define the field area of Goðafjall and Hrútsfjall mapped as part of this study and also Vatnafjall ridge mapped by Stevenson (2004).

sediments near the base of the edifice at Svinafellsfjall yield an age of 600,000 to 890,000 years (Albertsson, 1976). The majority of outcropping rocks are normally magnetised, which suggests that the bulk of the edifice has developed since the Brunhes magnetic reversal, further constraining its age to less than 780,000 years. One of the main aims of this study is to use the $^{40}Ar/^{39}Ar$ dating method to constrain the age of individual lava flows.

Öræfajökull is a compositionally bimodal volcano, producing both basaltic and rhyolitic lavas and associated eruptive products, although a small number of exposures with intermediate compositions have also been identified (Stevenson et al., 2006 and this study).

A full range of volcanic products are exposed on the south western to south eastern flanks, comprising mainly of subglacially and subaerially erupted mafic deposits including pillow lavas, palagonatised hyaloclastite breccia and tuff, and lava flows which are interbedded with glaciofluvial sediments and tillites. A small number of isolated silicic outcrops are also present on the exposed flanks and as isolated nunataks near the ice covered crater summit (Thorarinsson, 1958, Stevenson et al., 2006).

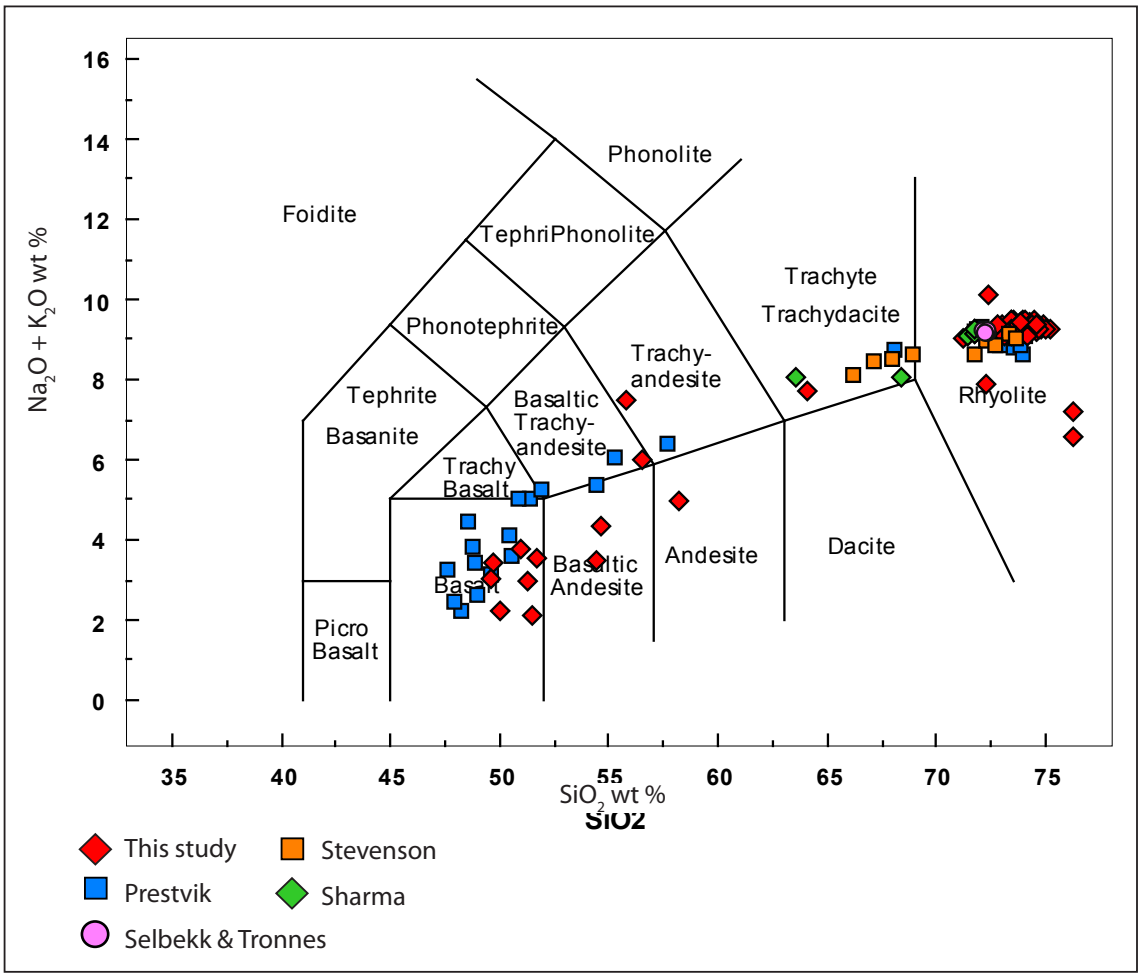

Fig. 1.6. TAS (total alkali v silica) diagram comparing all published Öræfajökull major element data to date.

The most extensive geological map (fig.1.5) to date was compiled by Prestvik (1979).

Öræfajökull has erupted twice since recorded history began (circa 900 AD), with the most recent basaltic eruption occurring in 1727. However the 1362 phreatoplinian eruption, producing 6 x 10^9 m^3 of rhyolitic tephra, with a dense rock equivalent of 2 km^3, is now believed to be Iceland's most explosive eruption to date. The eruption and its associated jölkulhaups (glacial outbust floods) caused widespread damage to the local agricultural community, destroying over 30 farms and leaving the area uninhabited for half a decade. Thorarinsson (1958) provides a detailed description of the 1362 eruption based upon recorded historical accounts and tephra studies. The 1727 eruption also caused jökulhlaups and localised destruction but on a smaller scale.

Compared to many other Icelandic volcanoes, the evolution of Öræfajökull is less well known. Prior to this research, a number of studies have been carried out at Öræfajökull but have largely been confined to geochemical analyses or studies of

the 1362 eruption (Thorarinsson, 1958; Prestvik, 1979; 1980; 1982; 1985; Prestvik et. al, 2001; Stevenson et al., 2006; Selbekk & Trønnes, 2007; Sharma et al., 2007).

Geochemically, Prestvik (1980) describes the Öræfajökull suite as essentially tholeiitic but with a transitional character toward alkaline rocks, with the full compositional suite ranging from basalt, through hawaiite, mugearite, benmoreite and trachyte to rhyolite (fig. 1.6).

Rhyolite generation at Öræfajökull is most likely due to a combination of crustal anatexis and fractional crystallisation processes. Based on major element modelling, Prestvik (1985) initially concluded that some of the more evolved intermediate rocks are derived by fractional crystallization, but that the majority of rhyolites have been formed by partial melting of older crustal rocks. However, Prestvik et al. (2001) later argued that the consistent O–Sr–Nd–Pb isotopic composition of the entire rock suite supports rhyolite production by fractional crystallization of an enriched basaltic parental magma. The magma is characteristic of an EM2-type mantle and its origin may be linked to the proximity of the hotspot plume which has been imaged beneath the neighbouring Vatnajökull glacier. A further description of the petrography and geochemistry of the samples collected in this study is given in chapter 3.

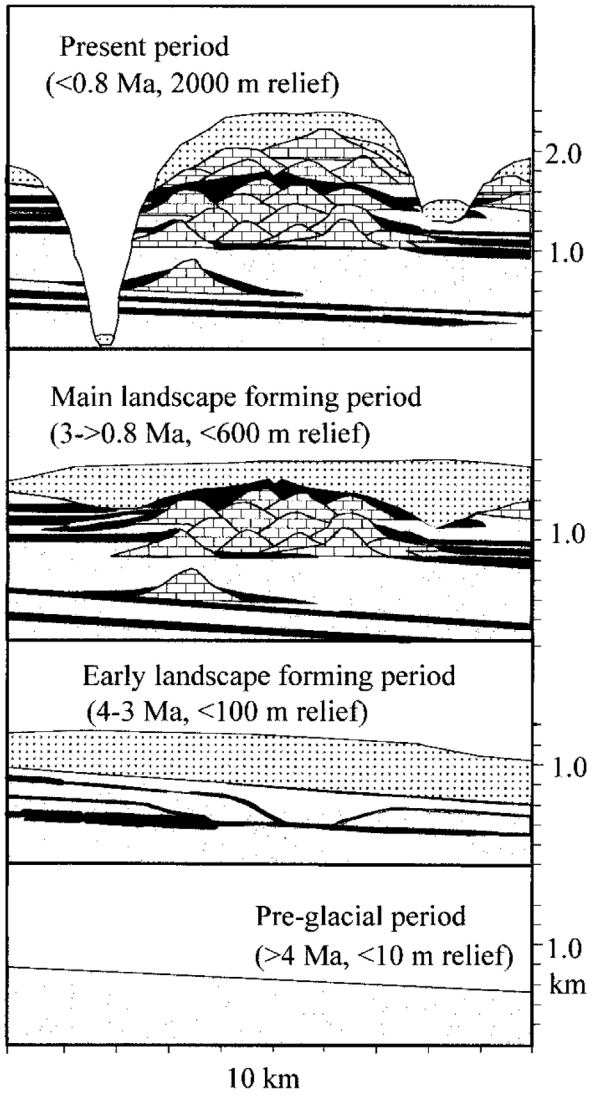

Fig. 1.7. (After Helgason & Duncan, 2001) Local topographic relief has been amplified over past 5 My in the area of Skaftafell on the south western flank, as subglacially erupted ridges and deepening valleys developed under thickening ice.

The overall topography of the current volcanic edifice has been greatly influenced throughout its

evolution by the presence of glacial ice. This is corroborated by work carried out by Helgason and Duncan (2001) at Skaftafell, located 18 km to the west of Goðafjall and Hrútsfjall, which suggests that the region has been under permanent but varying levels of ice cover throughout the last million years. They present a model for the topographic evolution of Skaftafell in which the build-up of topographic relief was formed by predominantly basaltic subglacial eruptions producing hyaloclastite ridges, with present-day valley locations initially formed by an absence of hyaloclastite rather than by glacial erosion, although thick valley glaciers later contributed to the increase in topographic relief (fig. 1.7).

The first detailed field-based study of physical volcanology and eruptive environment at Öræfajökull was carried out by Stevenson (2004), concentrating on Vatnafjall, a rhyolite ridge exposed on the south-eastern flanks located 10 km to the east of Goðafjall and Hrútsfjall (fig. 1.5). Samples collected by Stevenson (2004) have been dated using the $^{40}Ar/^{39}Ar$ method as part of this study in order to establish an eruption age for the ridge and provide a temporal framework for Stevenson's et al. (2006) interpretation. The Vatnafjall samples also provide a direct comparison of silicic rocks erupted in a similar environment to the rocks found in the Goðafjall and Hrútsfjall area.

With the exception of the study by Prestvik (1980) on the hybrid intermediate and silicic rocks, this is the first major study to focus solely on the Quaternary silicic rocks of the Öræfajökull suite and the first to focus on the Goðafjall and Hrútsfjall area. Prior to this study, only one silicic sample had been analysed from the Goðafjall area by Prestvik (1980, 1982). The Goðafjall and Hrútsfjall field area will be described in further detail in chapter 4.

Chapter 2
Glaciovolcanism

2.1. What is glaciovolcanism?

The term glaciovolcanism can be defined as volcano-ice interaction, and refers to the processes and products that occur when a volcanic eruption encounters and interacts with ice, snow and meltwater. This interaction may occur under ice (subglacial), above ice (supraglacial) and/or proximal to ice (ice-confined or ice-contact).

The study of glaciovolcanism is a relatively new area of volcanological research compared to its subaerial and submarine counterparts. The roots of glaciovolcanic research were laid down in the early to mid 20th century by pioneering workers such as Kjartansson (1943) and Matthews (1947), who both described glaciovolcanic successions in the field, working independently of one another on two separate continents. Throughout the late 20th and early 21st centuries, interest in glaciovolcanism has grown exponentially due to the current global concern over climate change and deglaciation. This interest has led to the publication of a number of detailed studies covering a wide range of glaciovolcanic processes and landforms, both past and present (Guðmundsson et al., 2002, Smellie and Hole, 1997, Smellie, 2001a, Jones, 1969, Allen, 1980, Kelman, 2002, Stevenson et al., 2006, Tuffen et al., 2001, Smellie and Skilling, 1994, McGarvie, 2007, McGarvie, 2009, Edwards et al., 2009 amongst others).

2.2. Contemporary glaciovolcanism

Present day volcano-ice interaction is most likely to occur in areas of high latitude including Alaska, British Columbia, Antarctica and Iceland, with the most recent examples being the 2009 Mount Redoubt, eruption, Alaska, the 2010 Eyjafjal-

Fig. 2.1. Aerial view of eruption column from 2011 Grimsvötn eruption. Image courtesy of Magnus Guðmundsson.

lajökull and 2011 Grimsvötn eruptions, Iceland (fig. 2.1). It can also occur in high altitude temperate zones, at snow-capped stratovolcanoes, including the Andean Cordillera, the North American Cascades, the Kamchatka Peninsula and New Zealand. Hazards such as the potential generation of large volumes of meltwater leading to the formation of jökulhlaups and lahars (mudflows), have been documented from the early 20th century (Nielsen, 1937). In Iceland, the 1996 Gjálp eruption, under the Vatnajökull glacier, triggered Iceland's largest jökulhlaup in recent times, when over 3.5km^3 of meltwater drained from Grimsvötn subglacial lake, destroying roads bridges and power lines (Gudmundsson et al., 1997). In Alaska, meltwater lahars of up to 0.6km^3 were generated by the 2009 Redoubt eruption (Waythomas, 2010), and during the 2007 Mount. Ruapehu eruption, New Zealand, primary ice-slurry lahars flowed into a commercial ski field (Kilgour et al., 2010).

In terms of human loss, the most catastrophic glaciovolcanic hazard in historical times occurred at Nevado del Ruiz, Colombia in 1985, when meltwater lahars swept into the village of Armero, killing over 25,000 (Lowe et al., 1986, Voight, 1990).

The study of glaciovolcanism has allowed scientists to gain a better understanding of these hazards, which has in turn led to improvements in risk communication and mitigation, especially in Iceland, the U.S.A and New Zealand (Keys, 2007).

2.3. Prehistoric glaciovolcanism

In the past, ice cover has been far more widespread across the globe than it is today. Studies of oxygen isotopes in marine sediment cores (fig. 2.2) have shown that cyclical temperature fluctuations, known as glacials and interglacials, have occurred throughout the Quaternary (Lisiecki and Raymo, 2005). As many as 52 glacial cycles have been recognised over the past 2.6 My (Gibbard, 2008), yet compared to marine records, terrestrial representation of glacial cycles prior to the last glacial maximum (LGM), circa 21-18 ka, is very poor. Glacial deposits, such as tills and moraines, are often poorly consolidated and have poor preservation potential as advancing glaciers strip away any evidence of preceding glacial cycles. Glaciovolcanic depositional environments have a far greater preservation potential because volcanic rocks have a much greater resistance to erosion and form a protective layer over the underlying strata.

The mapping of prehistoric glaciovolcanic landforms can be used to help reconstruct the advance and retreat of paleo-ice sheets in the northern hemisphere and Antarctica in order to understand terrestrial palaeoclimates, which may in turn lead to a better understanding of contemporary ice sheet behaviour in response to current global climate change.

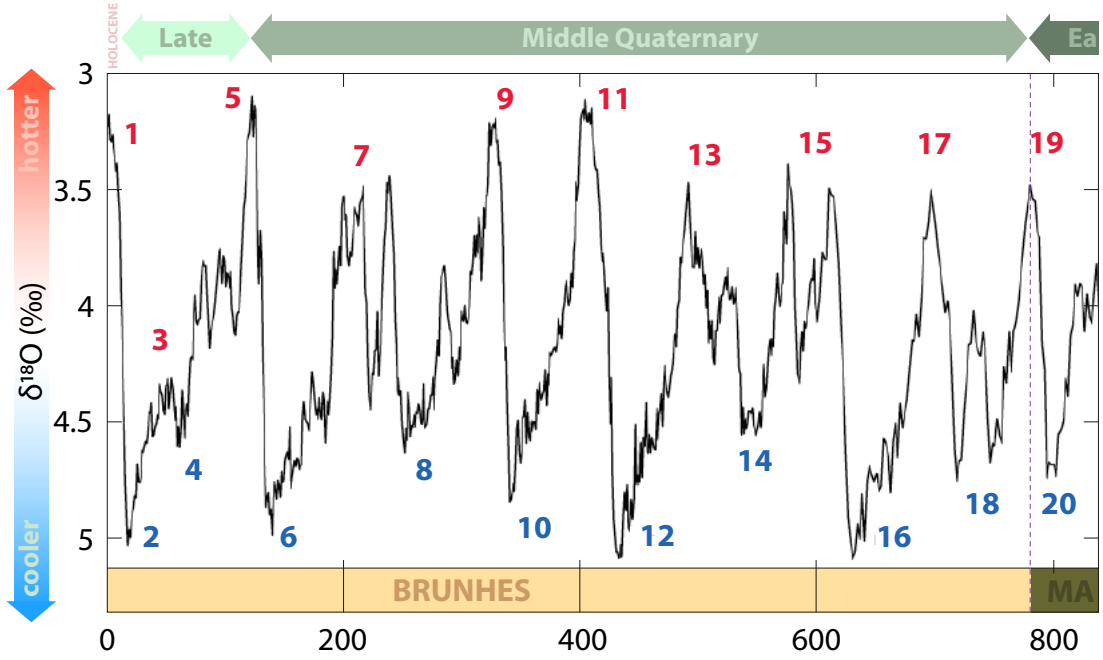

Fig. 2.2. Stacked benthic oxygen isotope record throughout the mid to late Quaternary. Adapted from Lisiecki, L.E. and Raymo, M.E. (2005).

Another factor to consider is the possible link between deglaciation and enhanced volcanic activity (Maclennan et al., 2002, Hall, 1982, Carrivick et al., 2009). It has been suggested that in Iceland, towards the end of the LGM, basaltic volcanism increased by a factor of 30 (Maclennan et al., 2002) as the removal of ice led to relaxation of the mantle which triggered an increase in mantle melting. However, there is only one known example of deglaciation-linked silicic volcanism in the early Holocene (Sigvadsson, 2002). There may be evidence to suggest that the reverse may be true of silicic eruptions in Iceland, as most silicic depositional centres contain volcanic landforms that are indicative of subglacial or ice marginal environments. The increase in pressure from the overburden of ice may lead to prolonged magma chamber storage times, leading to the build-up of more evolved magmas.

2.4. Glaciovolcanic Landforms

2.4.1. Basaltic glaciovolcanic successions

Basaltic glaciovolcanic landforms have exceptional preservation potential due to the formation of palagonite. Palagonitisation is a post-depositional hydrothermal alteration process that occurs in subglacial (and subaqueous) environments, which effectively cements glassy basalt tephras and / or fragmental deposits together in order to form lithified tuffs and breccias (Fisher, 1984). Any large or small-scale depositional features, such as cross-bedding or lamination, are preserved within the rock.

Fig. 2.3. Tuya Butte, British Columbia, Canada. The subglacial edifice first described by Matthews (1947). Photo courtesy of Ben Edwards.

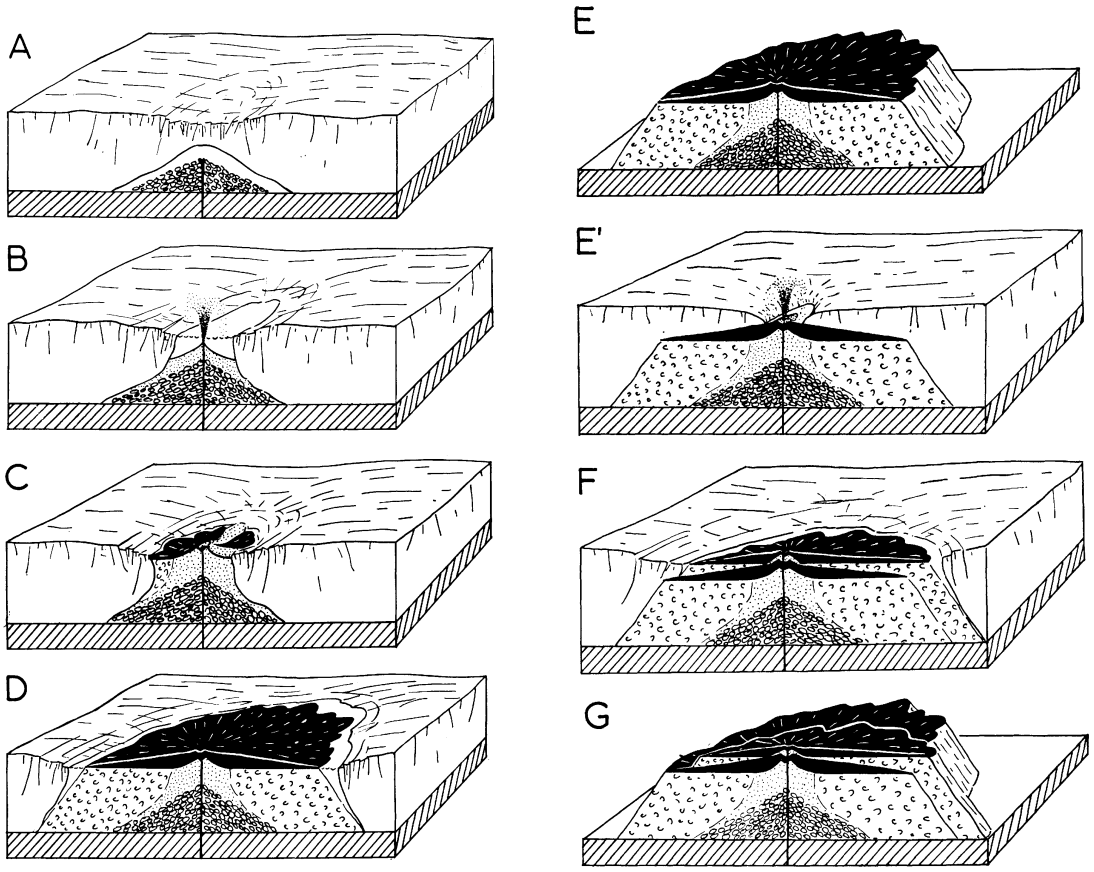

Fig. 2.4. Jones' (1969) model of basaltic tuya formation. A: Aquatic effusive phase. Magmatic heat causes melting of ice sheet above eruptive fissure forming melt-water vault. Within this vault erupting lava builds a steepsided pillow lava pile. B: As pile mounts roof of vault collapses forming intraglacial lake. Effusion gives way to explosive phase of emergence and resulting tuff accumulates between walls of ice on top of pillow lava pile. C: Emergent explosive phase gives way to aerial effusive phase. Lava issues from vent and pushes out into melt-water lake on deltas of flow-foot breccia. D: Advanced stage of aerial effusive phase. Products of earlier eruptive phases overwhelmed and buried by flow-foot breccia. E: Withdrawal of ice sheet exposes eruptive pile in characteristic form of tuya. E'/ F: Alternatively, with temporary cessation of volcanism progressively thickening ice sheet overwhelms tuya. Subsequent eruptive phase results in partial mantling of earlier sheet lava flow-foot breccia unit by another such unit. G: Withdrawal of ice sheet exposes tuya of compound structure expressed in benched morphology.

The first glaciovolcanic landforms to be identified and recognised as such, in the field were steep-sided, flat-topped basaltic volcanic mountains, known as tuyas (Matthews, 1947), and ridges, known as tindars (Jones, 1969). The largest constituent of both edifices is hyaloclastite – fragmented basaltic glass formed by the interaction of magma with water, the process of quench fragmentation. Tuyas represent eruptions from a central vent, while tindars form from eruptions along fissures. Both landforms are a common feature of Quaternary basalt morphology in Iceland, where they were first documented in the early 20th Century.

Matthews (1947) coined the phrase 'tuya' for a flat-topped edifice formed by a subglacial basaltic eruption after his work on Tuya Butte in British Columbia (fig.

2.3), and Matthews' model for the construction of a tuya emerging through an ice-confined lake is still generally accepted today. The idealised model of tuya formation can be summarised as follows: a pillow basalt base, formed by effusive lavas into ponded meltwater, followed by an explosive hyaloclastite-producing phase in the mid-section, topped with an effusive subaerial lava cap which forms above the level of ponded water (fig. 2.4).

Tindars were first described by Jones (1969) in his detailed study of the Laugarvatn intraglacial volcanoes, Iceland (1969). He described tindars as steep-sided linear ridges or mounds. Jones (1969) noted that the edifice Kalfstindar displayed similar subaqueous effusive, emergent explosive and subaerial effusive lithofacies to Matthew's Tuya model, however he also noted that some tindars had much simpler structures composed purely of hyaloclastite tuff and lacking either (or both) pillow base and lava top. Jones (1969) compared the tuyas and tindars at Laugarvatn to field descriptions of the subaerial to subaqueous transition sequences of the Columbia River flood basalts (Fuller, 1931). Fuller (1931) likened the flow-foot breccias and overlying subaerial lavas to a sedimentary course-grained alluvial deltaic succession, marking the point where subaerial lavas had entered a body of water, and forming lava fed deltas. Jones (1969) recognised that in a subglacial environment, this succession marked the point where the subaqueous lava pile had built up above the ponded meltwater level to become emergent. Jones coined the term 'passage zone' to describe this zone of transition between inclined beds of hyaloclastite and overlying sheet lavas.

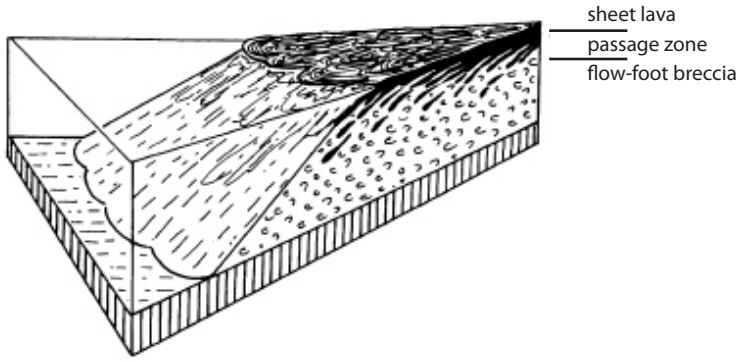

Fig. 2.5. Jones' (1969) passage zone sequence between inclidened hyaloclastite and overlying lava sheets.

The original models of Matthews (1947) and Jones (1969) (fig. 2.4) were built upon by a number of workers, producing both detailed observational studies and theoretical models of basaltic glaciovolcanic sequences in Iceland (Jones 1970), British Columbia (Allen 1980; Allen et al., 1982) and Antarctica (Smellie et al 1993,

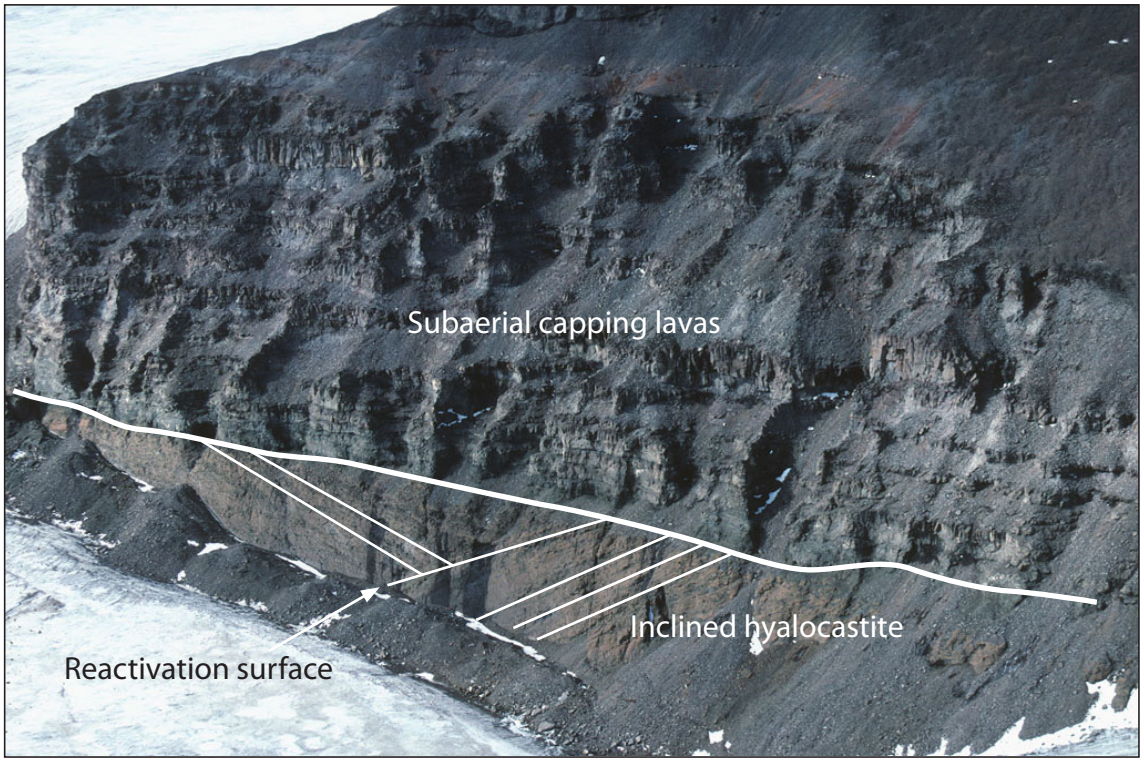

Fig. 2.6. The Lachman Passage Zone, Antarctica. The section through a basaltic lava-fed delta shows an unusually thick subaerial lava capping unit over orange coloured hyaloclastite foreset beds. The latter also show a prominent reactivation surface near centre. Image courtesy of John Smellie.

Smellie & Skilling 1994, Smellie & Hole, 1997).

A number of passage zones (fig. 2.6) were recognised in lithofacies sequences in Antarctica by Smellie et al. (1994) whilst compiling detailed facies analysis of well-exposed volcanic sequences in a number of locations (Skilling, 1994, Smellie and Skilling, 1994, Skilling, 2002). Stacked lava-fed deltas displayed a succession of passage zones with variable elevations. Smellie et al. (1994) interpreted this as a record of the relative change in the palaeo-meltwater level which could be used to infer changes in palaeo-ice sheet thickness.

The most commonly observed lava-fed deltas are produced by pahoehoe lavas, however mafic aa-aa lava fed deltas have recently been described by Smellie et al. (2011) in the Hallett Volcanic Province, Victorialand, Antarctica. Aa-aa lava fed deltas have essentially the same upper subaerial lava sheet units and lower subaqueous inclined hyaloclastite units but the subaqueous hyaloclastites contain a higher proportion of intercalated lava sheets and the inclination is less steep – around 25° compared to 30-40° for pahoehoe deltas (Fig. 2.7).

Further insights into the formation of basaltic glaciovolcanic edifices were revealed during the 1996 Gjálp subglacial eruption, Iceland (figs. 2.8 - 2.11). For the

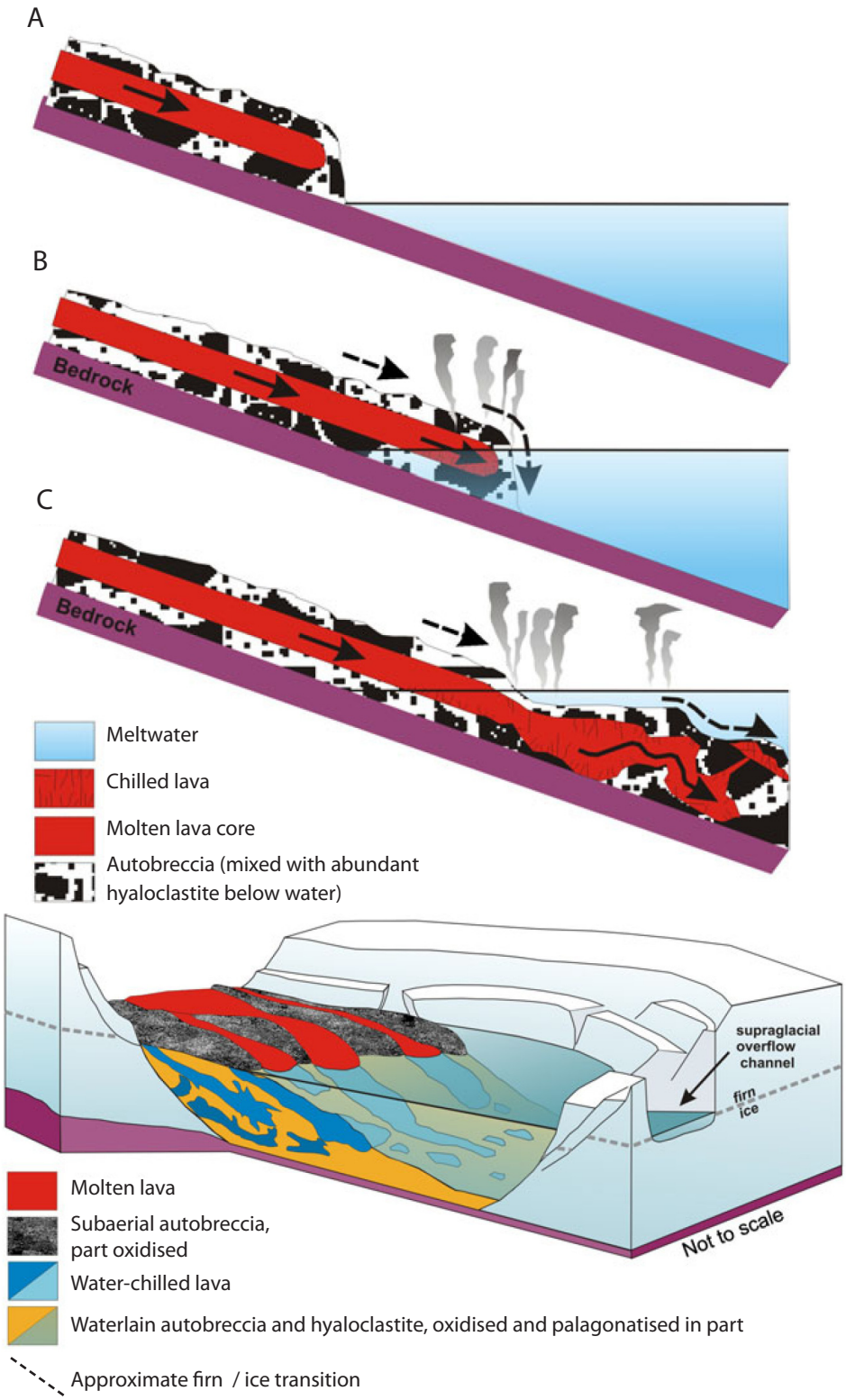

Fig. 2.7. (After Smellie et al. 2011) Schematic diagram illustrating aa-aa lava flowing into water.
A: The subaerially chilled autobreccia carapace is advected passively on the lava surface and becomes overridden at the lava flow front, ending up emplaced beneath the massive (originally molten) flow interior.
B: The coarse, highly permeable autobreccia permits vigorous interaction of the molten lava interior with overlying(melt) water, resulting in distinctive cooling fractures in the lava caused by rapid water-chilling and the generation of abundant hyaloclastite detritus, which is able to mingle with the slower-cooled subaerial autobreccia debris.
C: Relationships between massive lava and breccia become complicated and chaotic further below the waterline and lobe-hyaloclastite is produced.

first time, researchers were able to observe a subglacial eruption and tindar formation in real time, and collect data using modern volcanological and geophysical techniques (Guðmundsson et al. 1997). This led to the understanding that geophysical parameters can also exert control over the style of eruptive products, as it was demonstrated that a very high heat flux between the volcano and surrounding ice led to the formation of explosively generated fragmental deposits, resulting in the formation of a hyaloclastite ridge, rather than pillow lavas.

Observation of the Gjálp eruption also highlighted the limitations of the use of lithofacies associations at prehistorical sites for determining palaeo-ice thicknesses accurately. It was noted during the eruption that the base of the cauldron that formed in the surface of the ice above the vent was as much as 150 m below the glacier surface (fig. 2.9) (Guðmundsson et al., 2002), therefore demonstrating that lithofacies sequences could only be used to infer minimum palaeo-ice thicknesses.

The hypothesis that glaciovolcanic lithofacies sequences could be used as a proxy for palaeo-ice thicknesses, and that differing lithological associations could represent

Fig. 2.8. Day 1 of 1996 Gjálp eruption - fully subglacial.

Fig. 2.9. Day 3 of 1996 Gjálp eruption.

Fig. 2.10. Day 12 of 1996 Gjálp eruption. Ice cauldron width is 3 km with a depth of 150-200 m where the initial ice thickness was 600-750 m.

Fig. 2.11. Gjálp ridge, April1997, six months after eruption. Ridge was reburied by ice by late 1997.
Images courtesy of Magnus Guðmundsson.

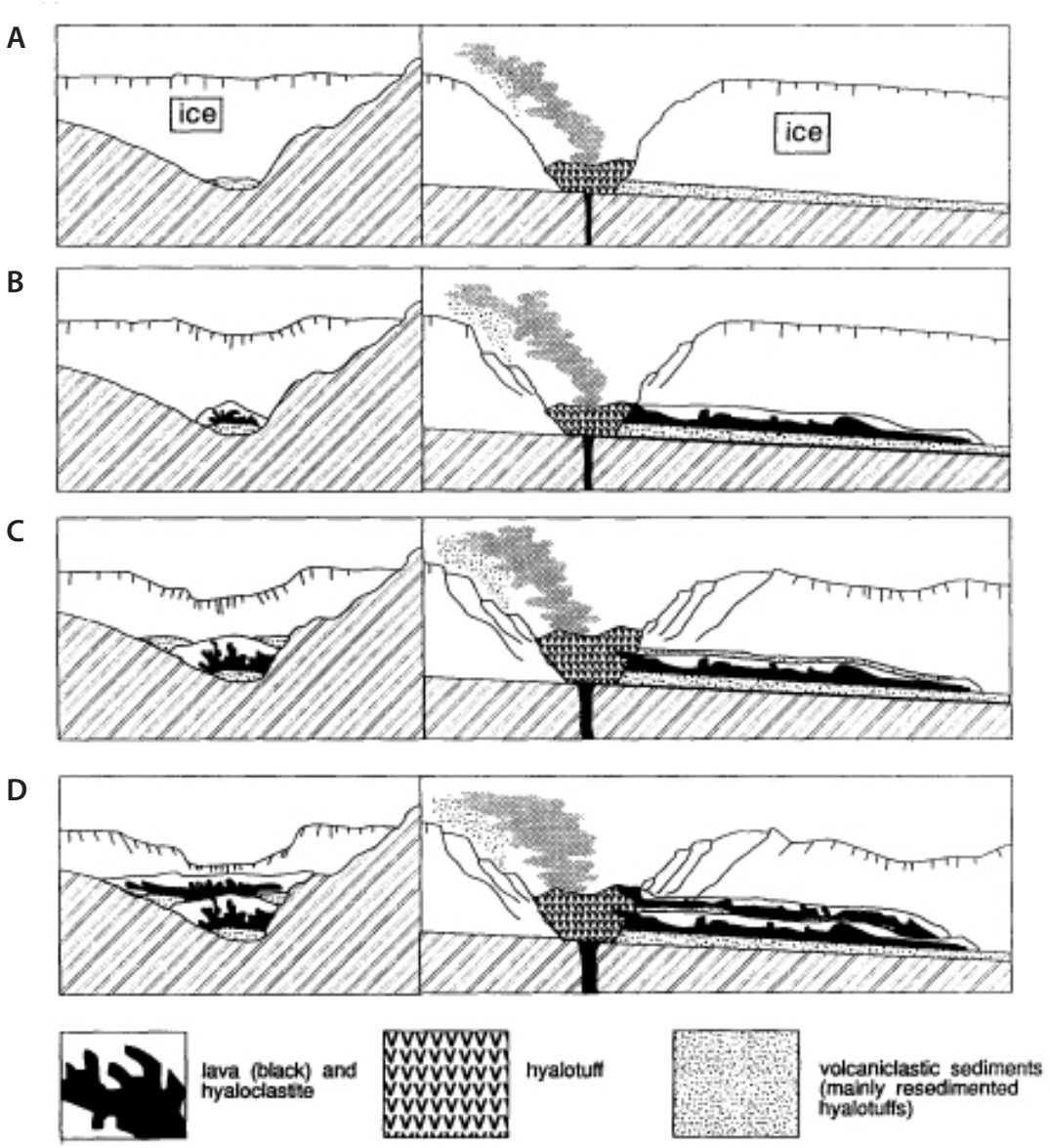

Fig. 2.12. A to D: (Smellie & Skilling, 1994) Series of cartoons illustrating possible events leading to the formation of the sequence of lithofacies preserved at Mount Pinafore, Antarctica. Left and right views represent transverse (cross-valley) and longitudinal (down-valley) sections, respectively (not to scale). A: Phreatomagmatic subglacial eruption geberates large volumes of volcanically heated meltwater that flushes abundant vitric tephra down-valley beneath a capping glacier. B:effusive lava phase follows. C & D: pattern repeats.

different emplacement environments, led to the initial development of two emplacement models based upon ice thickness (reviewed in Smellie & Chapman, 2002): The thick ice model occurring under impermeable ice sheets, over a kilometre thick, and the thin ice model occurring at locations with permeable ice less than 150 m thick, including valley-confined alpine glaciers and thinning ice sheet margins.

Eruptions under thin ice (<150-200 m) produce a unique set of lithofacies (Smellie and Skilling, 1994), known as thin-ice sheet sequences, or 'Mount Pinafore type' (fig. 2.12), that form under flowing water conditions due to good meltwater

drainage. Because the ice is much thinner and permeable, the meltwater is unlikely to pond at the vent, therefore pillow basalts are unable to form. Instead, the initially explosive phreatomagmatic interaction of magma and meltwater leads to the formation of a hyalotuff cone, while reworked tephra is carried along by the meltwater through drainage tunnels, forming esker-like fragmental deposits. As the cone grows, the meltwater – magma interaction decreases and phreatomagmatic activity begins to wane, replaced by a more effusive eruption style leading to the deposition of lavas over the fragmental deposits. The lavas often display entablature columnar jointing. Ribbon-like 'thin ice' sequences are a relatively common feature in Antarctica and Iceland (Loughlin, 2002; Smellie et al., 2006). The volcanic sequences are separated by a glacial unconformity, usually represented by a sharp contact overlain by tillite and also bedded sequences of sandstones and / or conglomerates containing faceted and / or striated clasts.

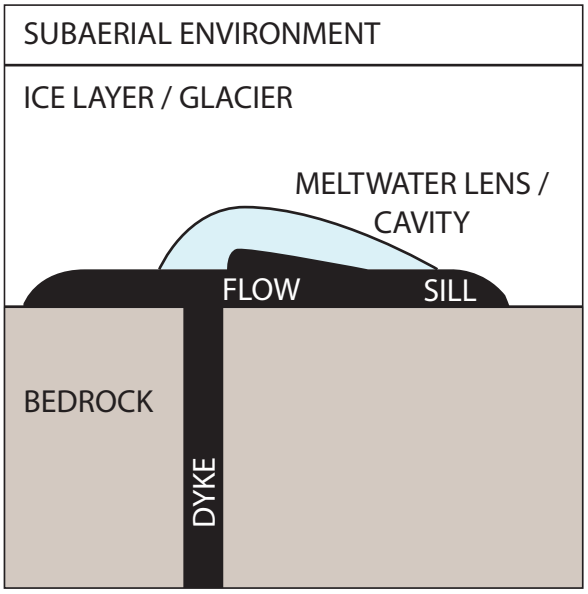

Fig. 2.13. After Wilson & Head, 2002; The formation of a subglacial sill at the glacier - bedrock interface under thick ice.

Basaltic eruptions under thick ice had traditionally been represented by the basaltic tuya and tindar models previously described due to the presence of ponded meltwater around the vent. More recently, another thick-ice emplacement model has been proposed (Smellie, 2008), known as 'thick ice sheet-like' sequences, or the 'Dalsheidi' type'. Lithologically, thick ice sheet-like sequences are very similar to thin sheet-like sequences. Both consist of the same four basic components of diamict, hyalotuff, hyaloclastite and lava, however the lithofacies sequence differs from the thin ice sequence in a number of ways. A diamict is a poorly sorted conglomerate with a mud matrix and within this sequence it is glacially derived (diamictite: lithified; diamicton: unlithified).

Thick ice sheet-like sequences are typically much thicker vertically (>100s m) and cover a much wider lateral extent than their thin-ice counterparts, often forming a

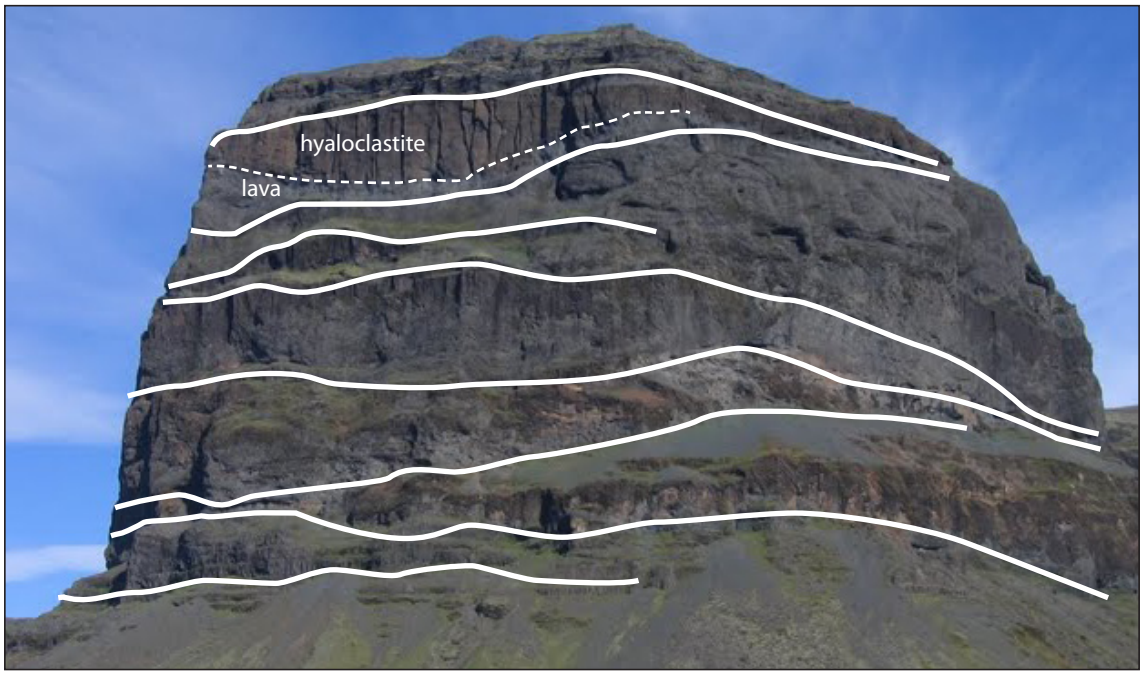

Fig. 2.14. Thick ice sequence succession at Lomagnúpúr cliffs, southern Iceland. Each sequence has an upper hyaloclastite underlain by a basal lava which often intrudes into the layer above (see upper sequence annotation). Each sequence is bound unconformably by a glacial diamict. Solid white lines represent sequence boundaries.

'layer cake' stratigraphy, dominated by a massive hyaloclastite layer which is often 100s of metres thick, over distances of up to 20km. The much larger dimensions are often too great to be accommodated in tunnels under thin ice, therefore Smellie (2008) proposed a wholly subglacial depositional environment.

Thick ice sheet-like sequences occur when magma is injected as a sill at the interface between the bedrock and the glacier base. The idea that magma sills could form at the base of thick ice sheets was first proposed as a theoretical hypothesis before any terrestrial examples had been discovered (Wilson and Head, 2002) (fig. 2.13).

A typical depositional sequence begins when eruption commences and magma melts the ice at the bedrock-ice interface, producing large amounts of meltwater that temporarily lifts the ice from its base. The resulting volcaniclastic products are deposited unconformably onto a glacially-derived diamict, usually tills and conglomerates with faceted and striated clasts. Magma-meltwater interaction leads to the production and emplacement of massive, fine-grained, hyaloclastite sheets formed in turbulent, hyperconcentrated flows. The subsequently erupting magma is then injected into the bedrock-hyaloclastite interface, intruding the hyaloclastite base and leading to the development of a lava base unit with flame-like apophyses pushing up into the hyaloclastite above. As meltwater production subsides and hyperconcen-

trated flow dynamics are replaced by steadier stream flow, the hyaloclastite beds are sometimes capped with a finely laminated layer of mudstone, although this layer is not always present.

Lava-hyaloclastite pairs with erosive sequence boundaries are a common feature – each pair the product of a single eruptive episode. A good example of stacked thick-ice sequences can be seen at Lomagnúpúr, Iceland (fig.2.14), where at least eight lava-hyaloclastite pairs are stacked unconformably, separated by a diamict horizon.

At present thick ice sheet-like sequences have only been documented in Iceland, although similar trachyte and phonolite sheet-like flows have been described at Hoodoo Mountain, British Columbia (Edwards & Russell, 2002).

2.4.2. Intermediate glaciovolcanic successions

The majority of well-doumented field examples of intermediate glaciovolcanism are in British Columbia and the U.S Cascades range (Kelman, 2002, Edwards et al., 2002, Lescinsky and Sisson, 1998), although examples of intermediate glaciovolcanism have also been documented in Chile (Mee et al., 2006), Antarctica (LeMasurier, 2002) and Iceland (Stevenson et al., 2009).

The first field observations of intermediate glaciovolcanism were carried out on The Table, an andesitic tuya in British Columbia (Matthews, 1951), which was described as 'a steep-walled mass of lava, made up of a core of thick flat-flying layers, partly surrounded by thin, nearly-vertical sheets'. Field descriptions of The Table

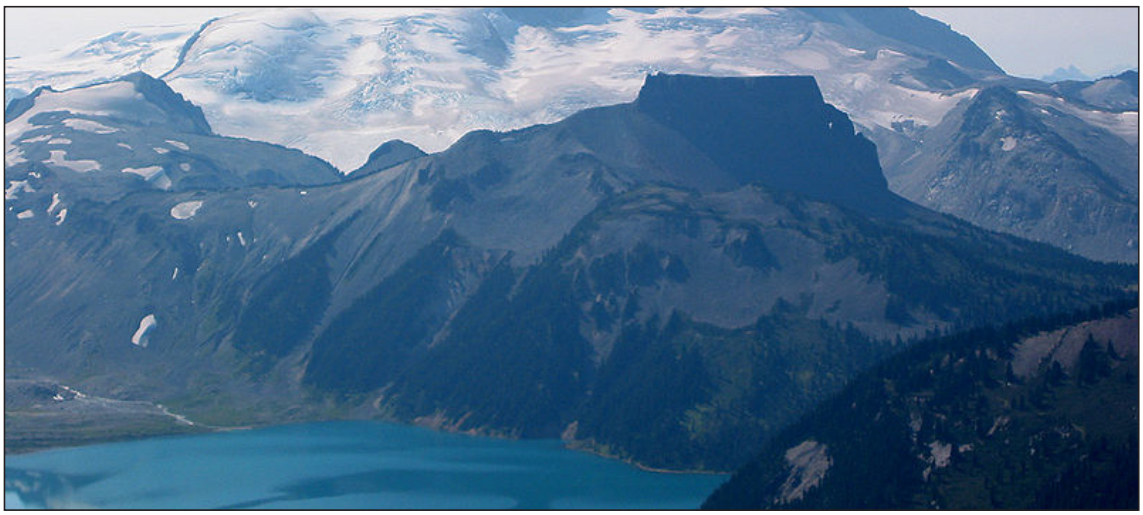

Fig. 2.15. The Table, British Columbia, Canada; the first andesitic tuya to be described in the field by Matthews (1951).

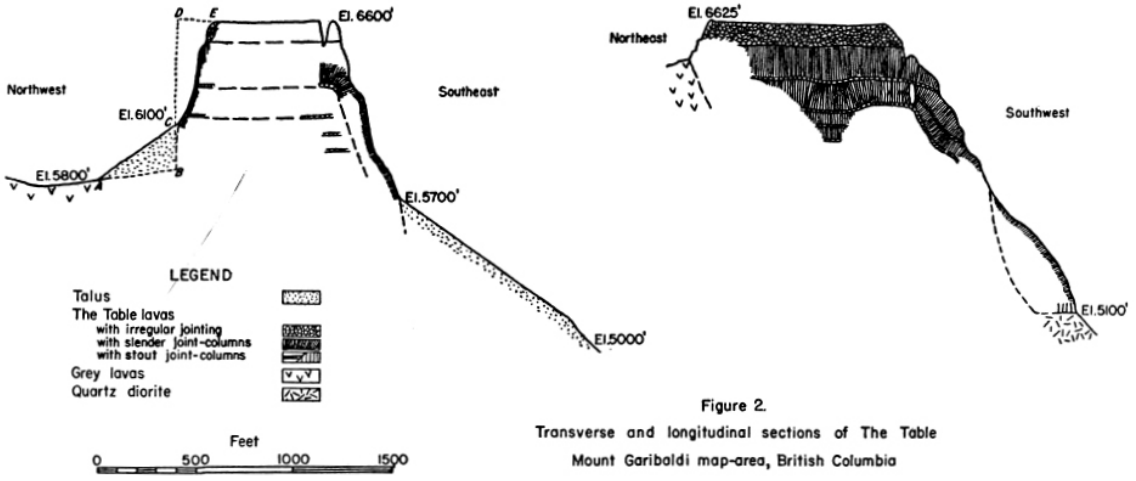

Fig. 2.16. After Matthews (1951); Cross section of the andesitic tuya, The Table, with continously columnar jointed lavas on upper surface.

differed in a number of ways from Matthews' (1947) earlier basaltic tuya model. The base of the structure was obscured by locally-produced scree; therefore basal pillows were not present. The majority of the edifice was built up of alternating lava layers of large and smaller columnar joints. Matthews noted that the joint orientation at the edge of the lava layers changed from vertical in the central portion of the layer to steeply dipping at the sides (fig. 2.16). He attributed this change in orientation to the lava cooling against the sides of a well-drained ice cavity, as columnar joints form perpendicular to the cooling surface.

The occurrence of intermediate glaciovolcanism is not only limited to the emplacement of monogenetic edifices such as tuyas and tindars. Andesitic to dacitic volcanism is often associated with stratovolcanoes, many of which have ice-capped summits and ice-filled craters, and are associated with relatively thin permeable glaciers (<150 m). Their flanks are often steep sided, which aids the drainage of meltwater and lowers the risk of catastrophic flooding. These features combine to produce a distinct set of glaciovolcanic lithofacies, present at many intermediate glaciovolcanic domains, where ice-contact and ice-confining facies are more dominant.

Matthews' (1951) initial observation that glassy flow margins and columnar joint orientation could be used to infer the presence of ice, was later corroborated by the mapping of ridge-forming lava flows at Mount Ranier volcano, Washington state (Lescinsky and Sisson, 1998; Lescinsky and Fink, 2000). These studies proposed that the elongate, steep-sided lava flows that sat upon ridges above valleys or

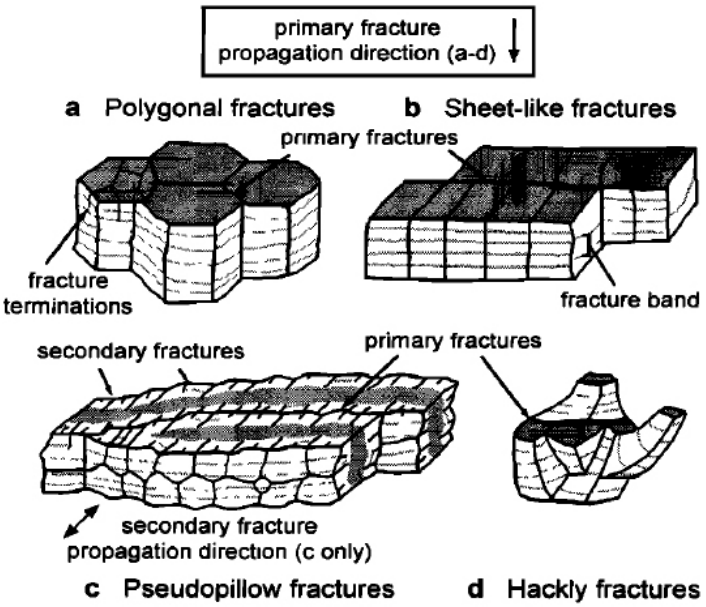

Fig. 2.17a. After Lescinsky and Fink (2000); Sketches showing range of fracture morphologies. A: polygonal fractures, B: sheet-like fractures, C: pseudopillow fractures, D: hackly fractures.

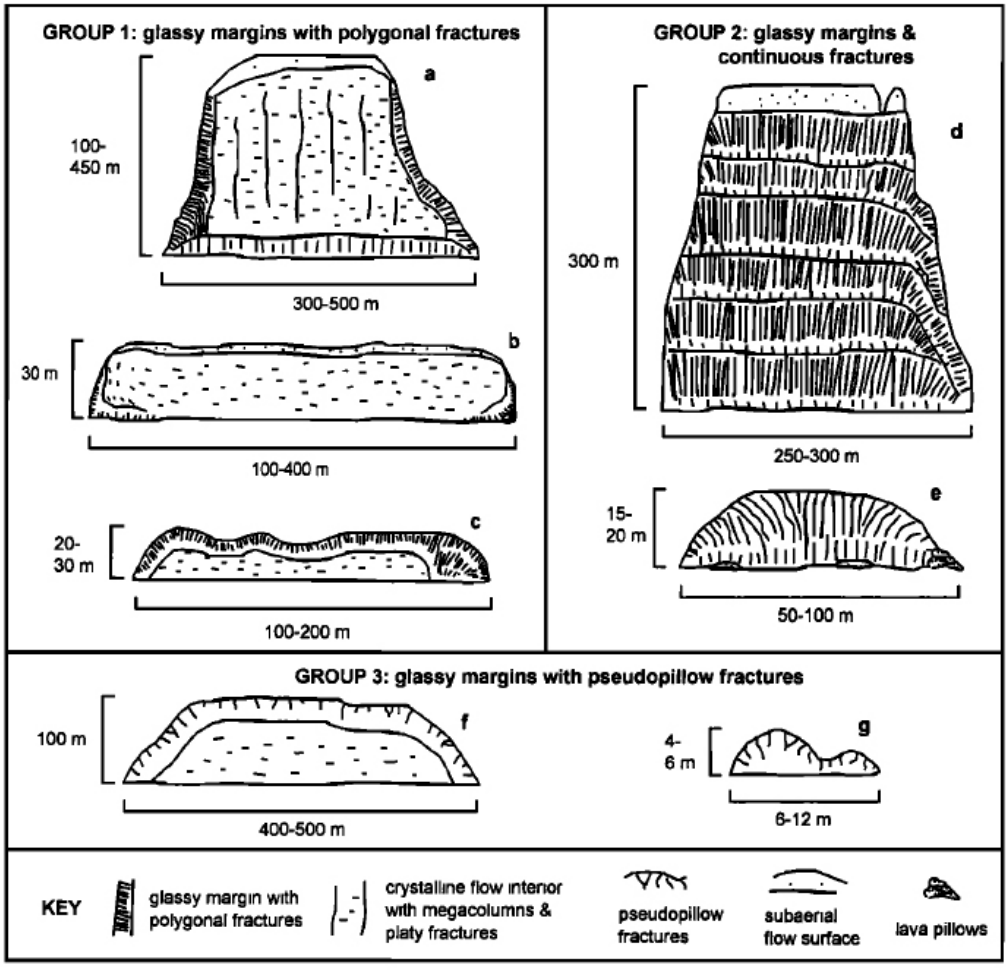

Fig. 2.17b. After Lescinsky and Fink (2000); Sketches showing the cross sections of landforms and fracture distribution. Group1, A: ridge-forming flow; B: smaller flow; C: polygonal columnar jointed subglacial dome. Group 2, D: tuya (after Matthews (1951)); E: esker-like flow. Group 3, F: subglacial dome with pseudopillow fractures; G: pillow lobe.

perched high on the flanks of steep-sided valley slopes had been confined and / or deflected by glaciers infilling the valleys during the time of eruption. The confined flows and lobes were formed of massive crystalline interiors with glassy margins displaying a range of fracture types with gradational contacts, from hackly jointed to sub-horizontal columnar joints (fig. 2.17a-b). The lavas were confined by but not completely encased within ice, therefore the top surfaces of the lava flows were believed to have been emplaced subaerially, however any evidence of subaerial emplacement had been stripped away by successive glaciations. Other smaller lobate and esker-like structures displayed outer carapaces with radiating columnar joints suggesting flow into ice tunnels created pre or syn-eruptively by meltwater at the valley wall-glacier interface (bergshrund).

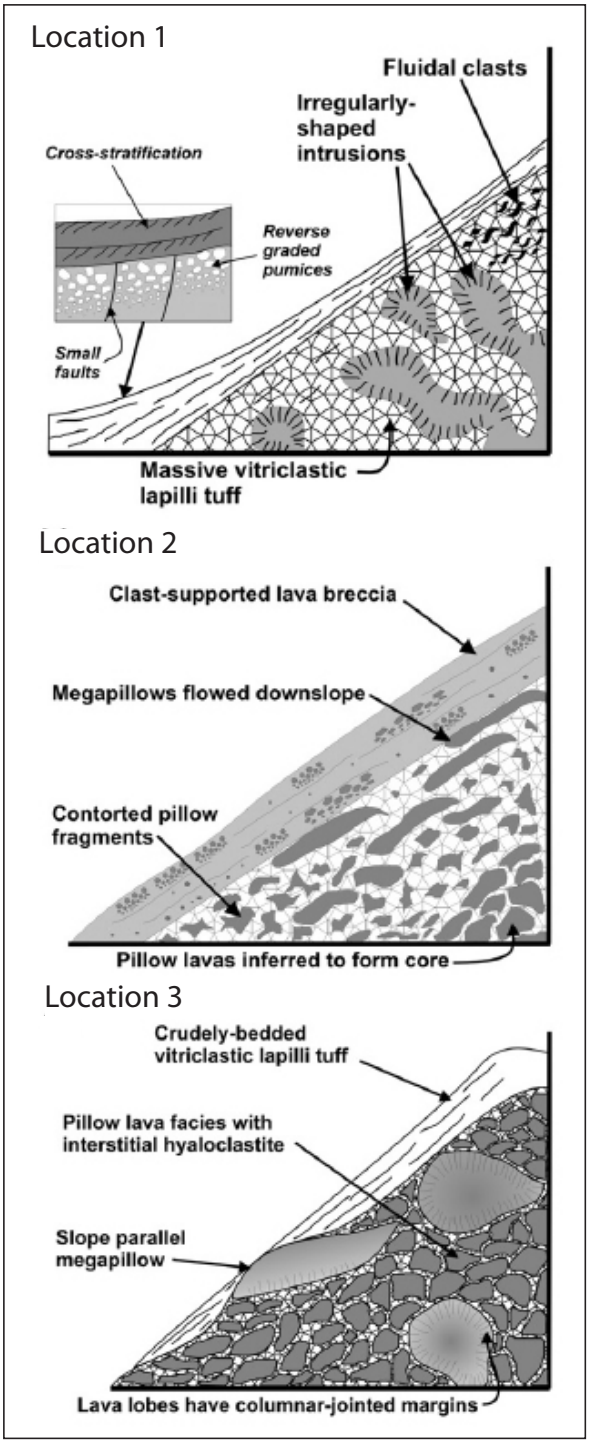

Fig. 2.18. After Stevenson et al. (2009); three different lithofacies associations at intermediate tuyas in Kerlingarfjöll.

Similar edifices have been recognised at Hoodoo Mountain, B.C. where ice confined phonolite lavas produced vertical cliffs up to 200 m in height, displaying sub-horizontal columnar jointed margins (Edwards et al., 2002).

The only known example of intermediate glaciovolcanism into thick ice in the presence of ponded water has recently been documented by Stevenson et al. (2009) at Kerlingarfjöll, Iceland. Three lithofacies sequences have been recognised (fig. 2.18); two andesitic sequences and one dacitic sequence, which are now overlain by

younger subglacial rhyolite edifices. The two andesite sequences include massive lapilli tuffs intruded by lava lobes with highly irregular morphologies, pillow breccias and stratified lapilli tuffs. The dacite sequence consists of pillow lavas with interstitial hyaloclastite and slope draping megapillow intrusions, overlain by crudely bedded lapilli tuff. All of the lithofacies strongly suggest emplacement within a fully subaqueous environment and are interpreted as small-scale fissure eruptions of low-viscosity magmas into thick ice. Stevenson et al. (2009) speculated that the low-viscosity magmas were hot enough to generate large volumes of water, and that it is the combination of large volumes of water and thick overlying ice that enabled the water to be confined at the vent.

2.4.3. Silicic glaciovolcanic successions

Silicic glaciovolcanic landforms are more easliy eroded than their palagonatised basaltic counterparts. Rhyolite lava bodies often form plates and/or columns that are easily fractured, as is evident by the large amount of locally-derived scree that often dominates the slopes of rhyolitic depositional centres. Poorly consolidated tephras that may give insight into the initial stages of eruption are highly susceptible to erosion and are often only well-exposed in gullies and topographic lows or where protected by capping lavas.

Although there are instances of silicic subglacial exposures in Antarctica (Smellie et al. 2011), the majority of silicic glaciovolcanic rocks outcrop in Iceland. Compared to the comprehensive body of published work on basaltic glaciovolcanism, there have been relatively fewer studies of silicic glaciovolcanism. However, in recent years a number of studies have produced detailed field observations and theoretical models of silicic glaciovolcanism in Iceland (Stevenson, 2004; Tuffen et al., 2001; Tuffen et al., 2002a-b; Stevenson et al., 2011; McGarvie, 2007), a review of which can be found in McGarvie (2009).

Towards the end of the 20th century, fieldworkers had identified the presence of a number of Quaternary silicic subglacial exposures in Iceland by making comparisons of their overall morphology to that of the basaltic tuyas (Fridleifsson, 1973; Grönvold, 1972; Saemundsson, 1972). The first major study to concentrate solely on the formation of silicic glaciovolcanic deposits was carried out by Furnes et al.

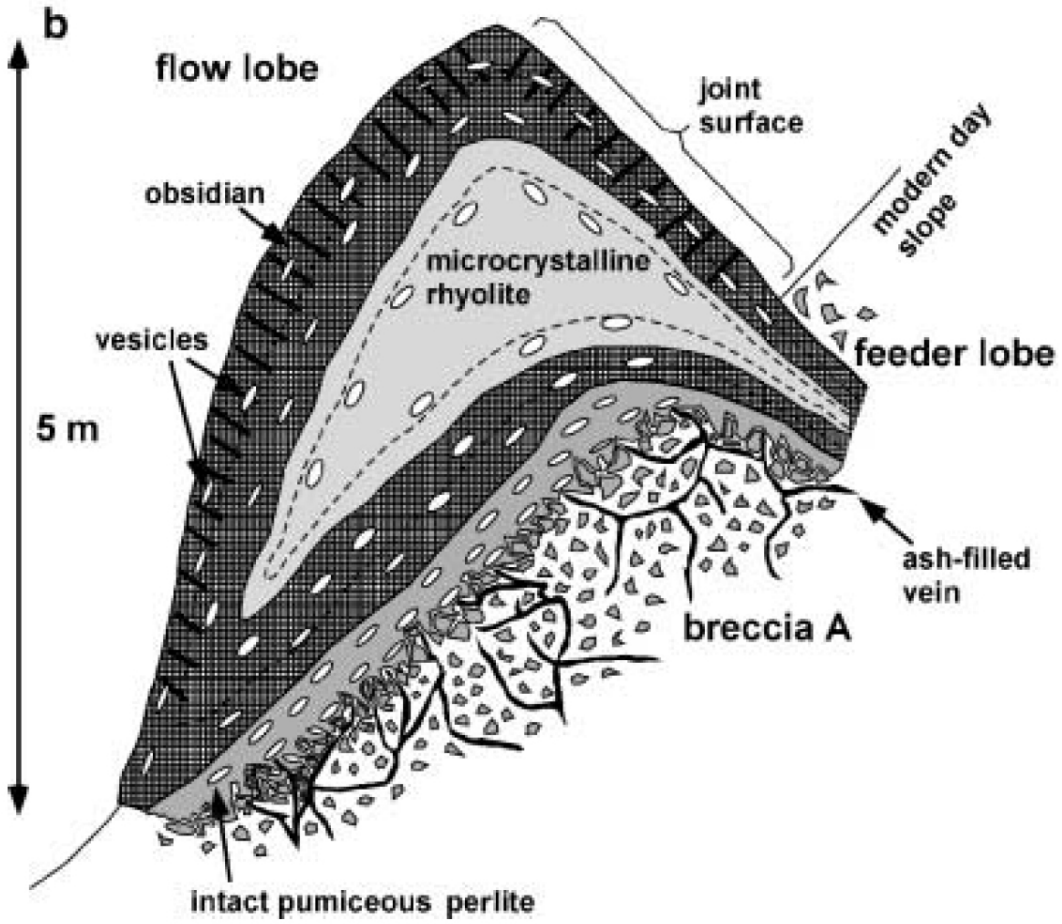

Fig. 2.19. After Tuffen et al. (2001); idealised internal structure of a rhyolitic lava lobe.

(1980), who noted that subglacial silicic hyaloclastite sequences displayed more complex lithologies than basaltic subglacial hyaloclastites.

Furnes et al. (1980) conducted detailed field studies in Torfajökull volcanic complex, Iceland's largest silicic depositional centre featuring both subaerially and subglacially erupted rhyolites. Torfajökull is an elongate plateau covering an area of 450 km^2, containing the largest concentration of rhyolite tuyas in Iceland (McGarvie, 2009).

Working at Bláhnúkur, a subglacial rhyolite edifice, Furnes et al. (1980) described two types of hyaloclastite and associated lava lobes with obsidian rims grading into a microcrystalline core. The pumice-rich 'type one' hyaloclastite was interpreted to be explosively generated by an alternating subplinian / surtseyan type eruption, while the obsidian-rich 'type two' hyaloclastite, which was intimately associated with the lava lobes, was interpreted as a direct product of lobe construction and disintegration as the magma intruded into the 'type one' hyaloclastite.

More than 20 years later Tuffen et al. (2001) built upon the initial work of Furnes er al. (1980) and developed a revised interpretation of Bláhnúkur.

The lava lobes and 'hyaloclastite' deposits at Bláhnúkur are the products of a relatively small-scale subglacial eruption that blanket an older edifice, up to 50 m thick in places.

Tuffen et al. (2001) dissected the lobe structure, from the outer ash matrix at the lobe base to the inner microcrystalline core, into six concentric textural zones (fig. 2.19). The lobes themselves displayed many of the jointing and fracturing patterns that had previously been described by Lescinsky and Sisson (1998) at Mount Ranier, indicating that the lobes had quickly cooled against a cold surface. A layer of perlite, formed by the hydration of obsidian, was present at the base of most lobe structures, suggesting that the magma had intruded into a wet environment.

Tuffen et al. (2001) suggested that lobe formation occurred by the intrusion of magma into conical ice cavities up to 5 m in height. The cavities were proposed to have formed at the base of the overlying glacier as a result of hot gases escaping immediately prior to eruption. This proposed formation mechanism led to the random distribution pattern of lobes over the edifice surface (fig. 2.20). Tuffen et al. (2001)

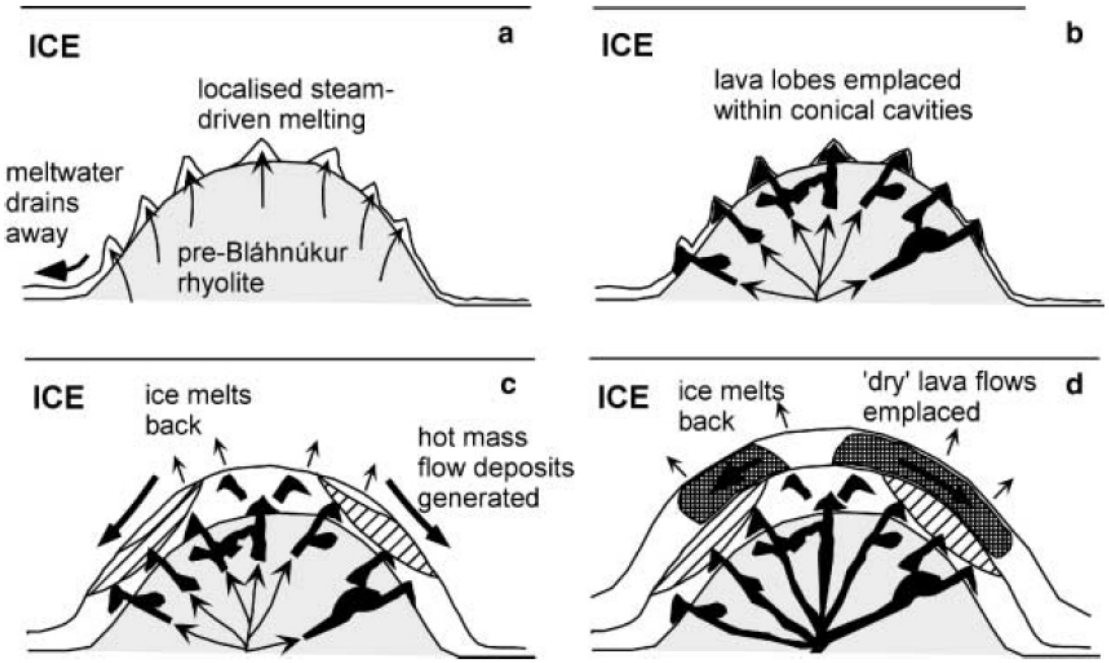

Fig. 2.20. After Tuffen et al. (2001); Sequence of events at Bláhnúkur. A: early eruptive products are reworked by meltwater in subglacial tunnels. Steam released from cooling lavas generates cavities in the glacier base; B: Lava lobes and breccia A (see fig.2.19) are emplaced within conical cavities in the ice; C: Hot avalanche deposits are generated as the ice melts back from lava lobes and breccia; D: 'Dry' lava flows are emplaced within drained subglacial tunnels.

argued that Furnes' 'type one' hyaloclastite was in fact an ash-grade matrix produced by quench fragmentation rather than volatile-driven explosivity. The fine-grained ash shards displayed a blocky morphology with low vesicularity and pitted surfaces due to magma-meltwater interaction (Heiken and Wohletz, 1985), with only very minor signs of volatile release. However, Tuffen et al. (2001) broadly agreed that Furnes' 'type two' hyaloclastite had formed as a result of lobe formation intruding into 'type one', with additional breccias forming due to lobe collapse.

An absence of any subaerial features at Bláhnúkur, such as platy lavas or pumiceous flow tops, suggested that the eruption had occurred subglacially under a minimum ice thickness of 400 m, marked by the current height of the edifice.

Tuffen et al. also examined a number of other rhyolite edifices in the Torfajökull complex – Rauðufossafjöll (Tuffen et al., 2002b) and Dalakvísl (Tuffen et al., 2008) and recognised similar gradational sequences as those first described in detail at Bláhnúkur, however there were also notable differences which led to the formation of different environmental emplacement models.

At Rauðufossafjöll, the flanks of the edifice are composed of massive unwelded, poorly-consolidated ash up to 300m thick and capped by multiple lava flows. Lower level lava bodies similar to those at Bláhnúkur, are also present. The base of the ash pile consists of phreatomagmatically-produced ash with blocky shards and low vesicularity; however Tuffen et al. (2002b) noted an increase in pumiceous clasts as elevation increased. The capping lavas are non-vesicular with some subaerial features, such as platy fracturing.

These differences led to the formation of an emplacement model for a phreatomagmatically-produced subglacial-to-emergent rhyolite tuya. Initially emplaced into a well-drained ice cavern, the eruption eventually broke through the surface of the ice cauldron to deposit subaerial capping lavas. Tuffen et al. (2002b) speculated on the formation of an ice cauldron above the eruption site. As the cauldron would have been lower than the surrounding ice surface, the 350 m ice thickness presented represents a minimum level of ice thickness.

In contrast, the Dalakvísl formation displays strong evidence to suggest an explosive eruption, driven by volatile degassing, into thin ice (150 m) followed by an intrusive phase, producing lava lobes similar to those at Bláhnúkur. Tuffen et al.

Fig. 2.21. Rhyolitic tuyas at Kerlingarfjoll's eastern cluster, Left to right: Lodmundur, Snaekollur and Fannbjorg.

(2008) noted the presence of a wide range of ash morphologies and vesicularities, including tube pumices which are indicative of magmatically-driven vesiculation. Well-bedded units of primary and reworked material are also present at the base of the structure. The beds display a range of bedforms and lithologies that suggest the presence of both flowing and ponded water. This suggests that the present-day stream that cross-cuts the Dalakvísl formation pre-dates the eruption and demonstrates how pre-existing topography can exert controls on meltwater drainage (Tuffen et al., 2008).

Dalakvísl is currently the only rhyolitic glaciovolcanic edifice to show strong evidence of interaction with ponded water. Meltwater drainage appears to be a common central theme in the formation of rhyolitic glaciovolcanic edifices regardless of whether the eruption is explosively or effusively driven. This may be due to the fact that basaltic eruptions are capable of generating much greater amounts of heat than rhyolite eruptions. A seminal paper by Höskuldsson and Sparks (1997), considering the thermodynamics of effusive subglacial eruptions (summarised in Tuffen et al. 2002a), showed that meltwater accumulation at the vent during rhyolite eruptions is less likely to occur, as relatively lower eruption temperatures (800-900˚C compared to 1100-1200˚C in basalts) have a much lower melting potential, leading to positive pressure changes in the ice cavity which will promote meltwater drainage.

Unlike their basaltic counterparts, meltwater interaction also appears to play a far lesser role in the explosive-effusive transition of subglacial rhyolite eruptions. As discussed previously, explosivity and fragmentation at basaltic subglacial eruptions are governed by water – magma interaction (phreatomagmatism). Recent studies of

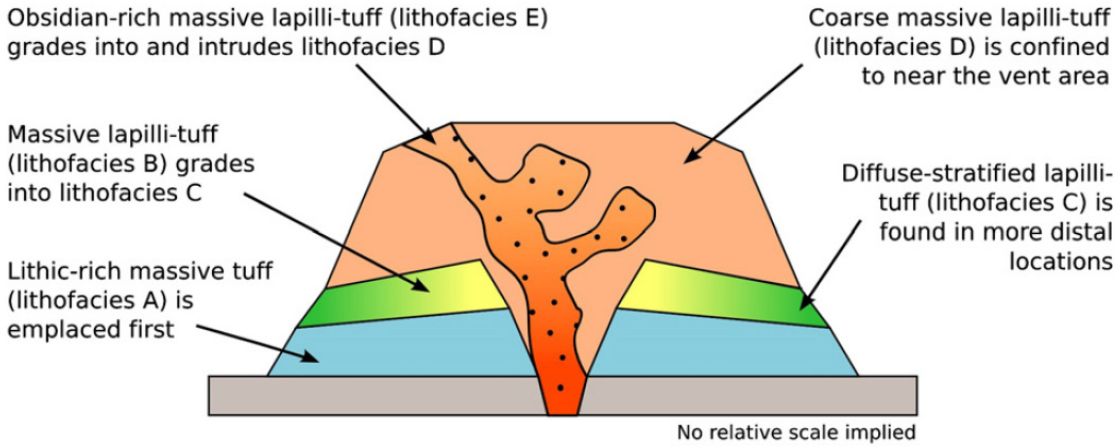

Fig. 2.22. After Stevenson et al., 2011; Schematic cross section through South Ögmundur tuya indicating distribution and relationships between the five lithofacies A to E generated during explosive phase of eruption. Lithofacies A is a massive lithic-rich tuff with blocky ash grins produced by phreatomagmatic fragmentation. Lithofacies B is a massive lapilli-tuff with bimodal grain size showing increasing signs of magmatic volatile fragmentation. Lithofacies C is diffusely stratified and found in more distal locations. Lithofacies D is a vent-proximal course-grained massive lapilli tuff that grades into Lithofacies E, an obsidian-rich massive lapilli tuff with tube pumices. None of the lithofacies were deposited in subaqueous conditions and there is an upward trend of decreasing magma / water interaction.

rhyolite tuyas at Kerlingarfjöll by Stevenson et al. (2011), suggest that during rhyolitic subglacial eruptions, although meltwater plays a role in the initial stages of the eruption, explosivity appears to be driven by the same factors that drive explosivity in subaerial rhyolitic eruptions, namely magma chamber overpressure caused by magma ascent rate and volatile release.

Kerlingarfjöll is Iceland's second largest Quaternary rhyolite glaciovolcanic complex, accounting for approximately 20% of the outcropping rocks and comprising at least 21 distinct silicic eruptions (Flude et al., 2010). All of the volcanic products at Kerlingarfjöll are believed to be glaciovolcanic in origin and the skyline is dominated by steep-sided rhyolite tuyas, which can be split into Eastern and Western clusters (fig. 2.21).

Detailed field studies compiled by Stevenson (2004) concentrated on four edifices constructed mainly of partially-consolidated tephras with capping lavas in the central area of the Western Cluster. Five pyroclastic lithofacies

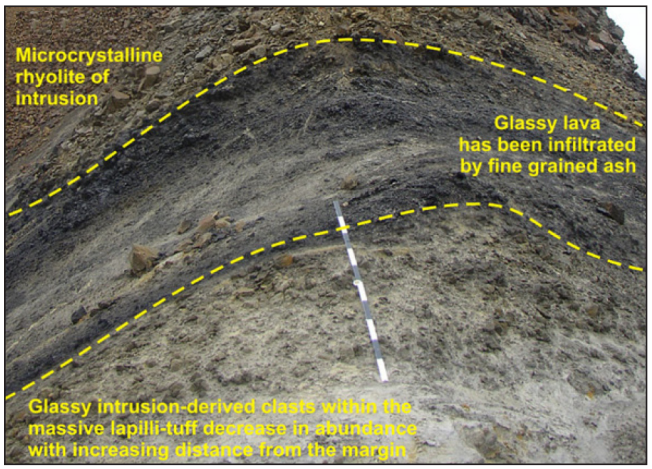

Fig. 2.23. After Stevenson et al., 2011; Transition zone highlighting gradational contact between massive lapilli tuff and overlying lavas.

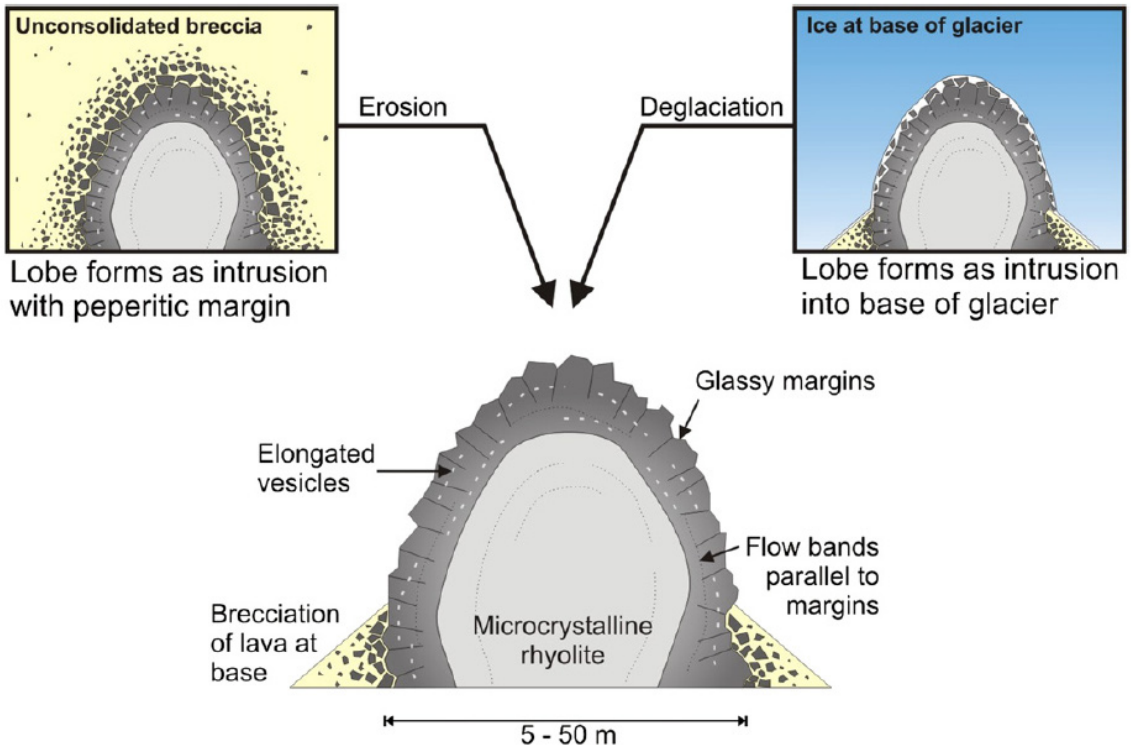

Fig. 2.24. After Stevenson et al., 2011; Two scenarios for lava lobe formation with glassy and columnar-jointed margins. Lobes can either form by intrusion into host breccia with a pepperitic margin or by emplacement into a cavity at the base of a glacier. Both scenarios leave behind similar edifices once erosion and deglaciation has occured.

were identified (fig. 2.22), each demonstrating increasing levels of vesicularity with increasing elevation. A final effusive stage was represented by degassed lava flows and lobes.

The identification of these lithofacies led to the development of a new model for explosive rhyolite tuya formation. Stevenson's et al. (2011) model proposes that initial fragmentation is produced phreatomagmatically by vent proximal magma-meltwater interaction, but as the eruption progresses meltwater plays a less influential role, either due to continued drainage or dissociation of the vent by the increasing tephra pile. This leads to a change in the style of fragmentation, which is now driven by volatile exsolution, resulting in the deposition of massive, poorly-sorted, lapilli tuffs, similar to subaerial pyroclastic density currents (PDC). The lateral spread of the PDC is prevented due to the confining nature of the ice, instead leading to the formation of poorly-consolidated massive tuffs with high aspect ratios. As the eruption continues, explosivity declines due to magma degassing, and initiates explosive-effusive transition. The transition zone is represented by a gradational sequence: from obsidian-rich massive lapilli tuff containing tube pumices; peperitic margin; brecciated obsidian to microcrystalline rhyolite (fig. 2.23). The sequence broadly

resembles that described by Tuffen et al. (2001, 2002) for lava lobe formation at Bláhnúkur, Rauðufossafjöll and Dalakvísl.

Stevenson et al. (2011) also outlines two contrasting methods of lobe formation – either by intrusion into an unconsolidated tephra pile, or by intrusion into an ice cavity at the glacier base – but points out that once deglaciation and subsequent erosion have occurred, differentiation between the two styles of emplacement may become difficult (fig. 2.24).

2.5. Glaciovolcanism at Stratovolcanoes

Unlike tuyas and tindars, which are often the products of one eruptive event, stratovolcanoes – alternatively known as composite volcanoes – are formed over far longer periods of geological time from the build up of numerous volcanic eruptions.

At long-lived volcanic sites that have evolved throughout the Quaternary it is likely that eruptions will have occurred during glacial and interglacial periods, therefore stratovolcanoes can display a wide and complex variety of lithofacies resulting from varying thicknesses, and at times, complete absence of ice at lower elevations.

Stratovolcanoes with a glaciovolcanic history provide an ideal environment to study the effects of long-term palaeo-environmental variablility. As previously discussed, the presence of ice during the build up of a volcanic edifice can play a highly influential role in shaping volcano morphology, and many stratovolcanoes that have been formed in glacial regions, or areas of high-altitude with snow-covered summit regions, have a more complicated structure than those with the standard composite structure of alternating lava and ash layers often found in more temperate regions. During periods of volcanic activity glacial ice offers protection to deposits that may otherwise be buried by the products of successive eruptions. Conversely, fragile glacial deposits may be preserved underneath more robust lava flows, which can be subsequently revealed by glacial erosion, providing information about the evolution of the volcano and the eruptive palaeo-environment.

Mount Hoodoo, a phonolitic volcano in British Columbia, is a notable example of a stratovolcano that has been active throughout the Quaternary (Edwards et al.,

2002, Edwards and Russell, 2002), where the identification of distinct glaciovolcanic lithofacies sequences have enabled a reconstruction of eruptive environments and variability in ice thickness over the past 85 Ka. Six episodes of volcanism have been documented at Mount Hoodoo, of which three show evidence of glaciovolcanism. The three lithofacies sequences record the presence of thick ice, thin ice and valley glaciers at different times throughout the volcano's evolution. Edwards et al. (2002) speculate that thick ice has been present at Hoodoo Mountain on at least two occasions; the first episode between 85 – 80 ka with a minimum height of 1400 m above sea level, followed by a period of relatively thin ice (<1300 m) between 80 – 54 ka, building back up to over 2000 m above sea level and completely blanketing the edifice between 54 – 40 ka.

To further complicate matters, some stratovolcanoes have a bimodal geochemistry, erupting a range of lavas from basalts through to rhyolites. This also has implications for palaeo-environmental reconstruction, adding a further dimension to the interpretation of lithofacies sequences. Stratovolcanoes in Iceland are recognised for their ability to erupt bimodally (Lacasse et al., 2007, Martin and Sigmarsson, 2007, Hards et al., 2000). Öræfajökull, the subject of this research, has erupted basalts, rhyolites and sparse intermediate lavas throughout its evolution.

2.6. Recent developments in glaciovolcanic research

The traditional field-based approach to glaciovolcanic research has been enhanced in recent years by combining field observations with other areas of geological research in order to apply further constraints to palaeo-environmental models. Two of the more successful techniques, FTIR analysis and $^{40}Ar/^{39}Ar$ dating are briefly reviewed here.

Fourier transform infrared spectroscopy (FTIR) analysis

FTIR analysis can be used to measure the dissolved volatile content trapped within subglacially erupted glasses. As the solubility of magmatic volatile species (H_2O, CO_2, S, F and Cl) is pressure dependent, the measured volatile content can be used to infer the thickness of the overlying ice (or water); however the calculation

assumes that quenching occurred under equilibrium degassing conditions.

Dixon et al. (2002) were the first to use FTIR to measure volatile contents in order to estimate ice thicknesses at Tanzilla Mountain, an alkali basalt subglacial ridge in British Columbia. Dixon et al. (2002) measured H_2O, S and Cl concentrations in the quenched glassy rinds of the tholeiitic pillow basalt base and the overlying alkali basalt lavas and demonstrated that while the pillow basalt had not significantly degassed, the overlying lavas had significantly. Estimations of pressure solubilities for basaltic magma were compared with the measured volatile concentrations, enabling Dixon et al. to estimate an overlying ice thickness of 300-900 m during the eruption.

At Kverkfjöll, Central Iceland, water contents of 0.85 to 1.04 wt % were measured in Pleistocene pillow basalts (Höskuldsson et al. 2006) yielding an estimated overlying ice thickness of 1240-1880 m. Ice of this thickness is possible in central Iceland, where ice sheets are likely to reach thicknesses up to 2 km during glacial maxima (Hubbard et al., 2006).

Whereas Dixon et al. (2002) found a relationship between sample height and water content, a number of other analyses of basaltic edifices have proved less conclusive (Schopka et al., 2006; Edwards et al., 2009), however rapid meltwater drainage and subsequent pressure release have been cited as a possible cause for decoupling.

The only intermediate study to date focussed on andesite and dacite glasses from Kerlingarfjöll, Iceland (Stevenson et al., 2009). Three glass samples from two different locations were analysed and two of the samples, although produced in different eruptions, yielded the same water content of 0.67 wt % producing an estimated minimum ice thickness of 550 m.

Examples of silicic subglacial sample analysis include Prestahnúkur, Iceland (McGarvie et al., 2007) where the dissolved water content was measured in two obsidian samples taken from different elevations. The overall low water content increased slightly with elevation from 0.10 to 0.14 wt %.

Denton et al. (2009) analysed silicic glasses from Torfajökull and Krafla, Iceland and reported high levels of heterogeneity in the water content due to post-emplacement alteration. Tuffen et al. (2010) also reported extreme volatile heterogeneity in flowbands from samples taken at different elevations from Bláhnúkur, Torfajökull. Variations within the flowbanding of the same sample indicates that spatial hetero-

geneity of volatiles is far more common in rhyolites than in basalts, where the glass composition is more uniform.

Many issues still surround the use of this technique, including sample heterogeneity, the relationship between volatile content and sample elevation, styles of degassing (equilibrium and non-equilibrium) and post-emplacement hydration. Taking all these outstanding issues into consideration, FTIR analysis of volatile degassing alone is not, as yet, a reliable indicator of palaeo-ice thickness, however used in conjunction with reliable field observations, it may allow a secondary constraint to be applied.

$^{40}Ar/^{39}Ar$ Dating

The ability to add age constraints to glaciovolcanic deposits enables the reconstruction of palaeoenviroments, allowing estimations to be made on the thickness and extent of previous ice sheets for glacial periods other than MIS 1.

As tuyas are generally formed during one sustained eruption, obtaining an eruption age for the tuya provides us with information about the minimum syn-eruptive ice thickness throughout a single glacial period.

Rhyolitic tuyas are more suitable than basalts for $^{40}Ar/^{39}Ar$ dating due to their higher K content.

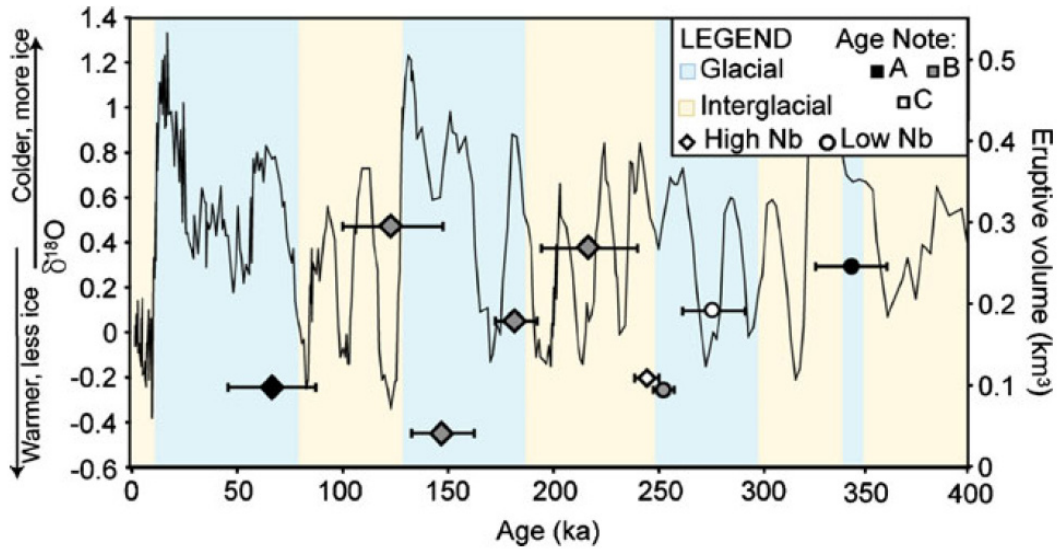

Fig. 2.25. After Flude et al., 2010: The ages and eruptive volume of the Kerlingarfjöll rhyolites superimposed onto the oxygen isotope curve from the Vostok Ice Core. Eruptions occured during glacial and interglacial periods suggesting that Kerlingarfjöll has experienced almost continual ice cover for the past 300,000 years.

Despite the challenges of dating young Icelandic rhyolites (see section 5.4) a number of rhyolitic tuyas in Iceland have been successfully dated using the $^{40}Ar/^{39}Ar$ method. Three tuyas at Torfajökull were the first Quaternary Icelandic rhyolites to be dated (McGarvie et al., 2006, 2007) producing ages of 67±9 k, 72±7 k, and 278±18 k).

$^{40}Ar/^{39}Ar$ dating of the Prestahnúkur tuya produced an age of 89±24 k (McGarvie et al., 2007) and despite yielding higher errors than the Torfajökull rhyolites, this age falls within MIS stage 5 (substages 5d–5b). By combining this age with detailed field observation, McGarvie et al. (2007) concluded that the Prestahnúkur tuya formed completely subglacially within a syn-eruptive ice sheet at least 700 m in thickness. The eruption dates and field evidence support climate models that suggest that the transitional sub-stages of MIS 5 were characterised by rapid temperature fluctuations and rapid build-up of land based ice.

Flude et al., (2010) dated a number of silicic subglacial edifices at Kerlingarfjöll, including those mapped previously by Stevenson et al (2009; 2011), yielding eruption dates spanning 300, 000 years from 68 - 350 k. The eruptions occurred during both glacial and interglacial periods (Fig. 2.25) indicating that the area of Kerlingarfjöll has spent most of its eruptive history covered in ice except during sustained periods of exceptional warmth (as in the present-day climate).

$^{40}Ar/^{39}Ar$ dating of the rocks in the Goðafjall area of Öræfajökull is one of the primary objectives of this study and is covered comprehensively in chapter 5.

Chapter 3
Major and trace element geochemistry

3.1. Introduction

Establishing an eruptive stratigraphy at stratovolcanoes that have experienced fluctuations in ice cover can be a challenging task. This is because the products of a single lava eruption can be widely dispersed due to prevailing topography in combination with the irregular influence of ice on lava pathways. Over time, these lavas become variably eroded by rejuvenated glaciers. For example, two lava flows channelled along divergent paths from the same vent require only a modest amount of erosion to remove any physical links between the lavas, thereby creating separated outcrops with no physical evidence that these were once products of the same eruption (Lescinsky & Sisson 1998, Lescinsky & Fink, 2000).

Where physical evidence proves inconclusive, geochemical evidence can be used to enable correlation between physically separated products from individual eruptive events.

Chemostratigraphy is an application of geochemistry that utilises the similar geochemical compositions of coevally erupted material to correlate volcanic units that are products of the same eruption but, because of the glaciovolcanic eruptive environment and subsequent erosion, are now physically unconnected. Chemostratigraphy has proven to be a particularly powerful tool for correlating Icelandic rhyolites as it has been firmly established that individual eruptive events have 'geochemical fingerprints' reflected in an eruption-specific range of trace element concentrations (Macdonald et al., 1990; McGarvie et al., 1990).

Rather than focusing on magma chamber processes and petrogenesis, the main purpose of carrying out geochemical analysis on the rock suite of the Goðafjall area is as an aid to identification of individually erupted units and to support

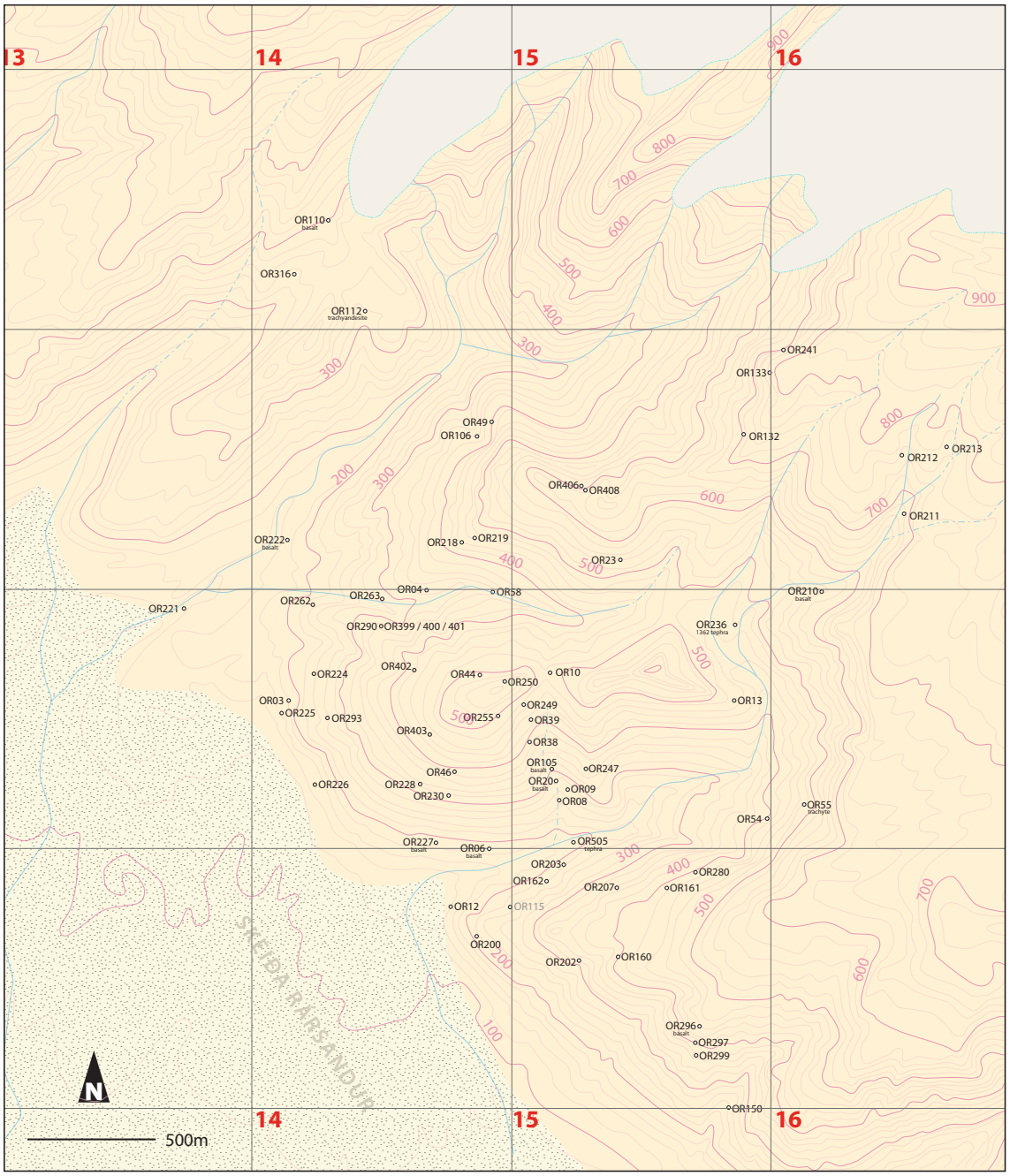

Fig. 3.1: Location map of all samples collected within Goðafjall area for geochemical analysis. All samples are rhyolite unless marked otherwise.

observations made in the field.

In order to set the scene for later discussions of the evolution of the study area (the rhyolite-dominated southern flanks of Öræfajökull), geochemical data are evaluated using chemostratigraphy in order to confirm and establish an eruption stratigraphy prior to discussing physical volcanology and field relationships.

Finally, to enable evaluation of whether silicic rocks forming domes and lava flows at nearby field locations are contemporaneous with those in the field area, six rocks from these nearby locations were analysed.

3.2. XRF Sample preparation

Over 300 rock and tephra samples (appendix 1) were collected from the main research area and also neighbouring sites that contain silicic rocks. A total of 77 samples were analysed for major and trace element abundances, of which 71 make up the Goðafjall / Hrútsfell suite (table 3.1; fig. 3.1).

Major and trace element XRF analysis and LOI were carried out at the University of Manchester Geochemical Analysis Unit. Both major oxide (wt%) and trace element (ppm) abundances were analysed with an Axios Sequential X-ray Fluorescence Spectrometer running Panalytical's IQ+ and Pro-Trace software packages respectively. To ensure correct calibration, two USGS analytical standards - BHVO-2 and AVO plus four previously analysed silicic samples (Stevenson, 2005) were analysed alongside the new samples.

Prior to analysis the samples were examined in order to remove as much surface weathering and alteration as possible, then crushed into granules, and finally milled into powders using tungsten carbide mills. The powders were then mixed with a wax binder inside an agate mill and pressed into 15 g pellets (12 g sample + 3 g wax). As tungsten carbide mills are known to cause contamination of W and Co, these elements have not been considered further in any discussion. There is also evidence to suggest that tungsten carbide mills may cause contamination of Nb and Ta. In order to test for contamination, pellets of samples JS202 and JS244

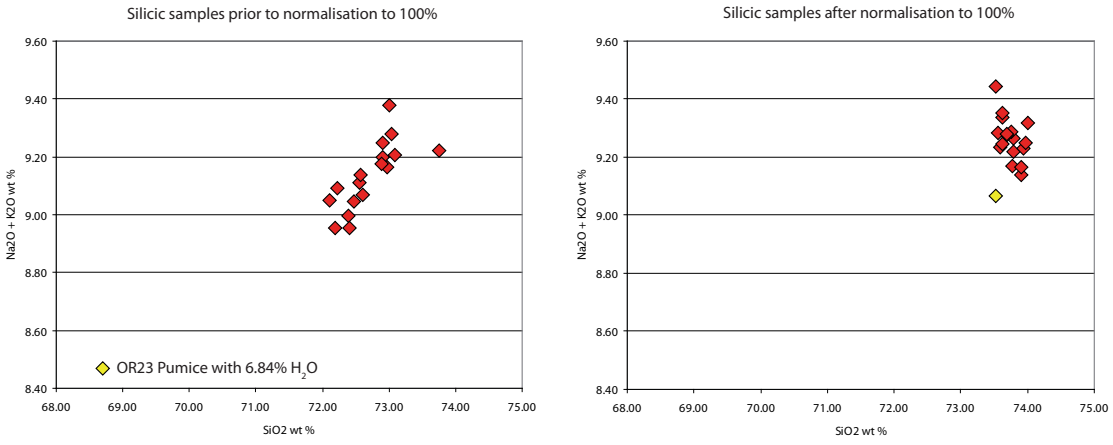

Fig. 3.2: Comparison of pre and post normalisation of major element data. Red diamonds represent microcrystalline lavas with low water content. Yellow diamond represents pumice sample OR23 with 6.84% water content.

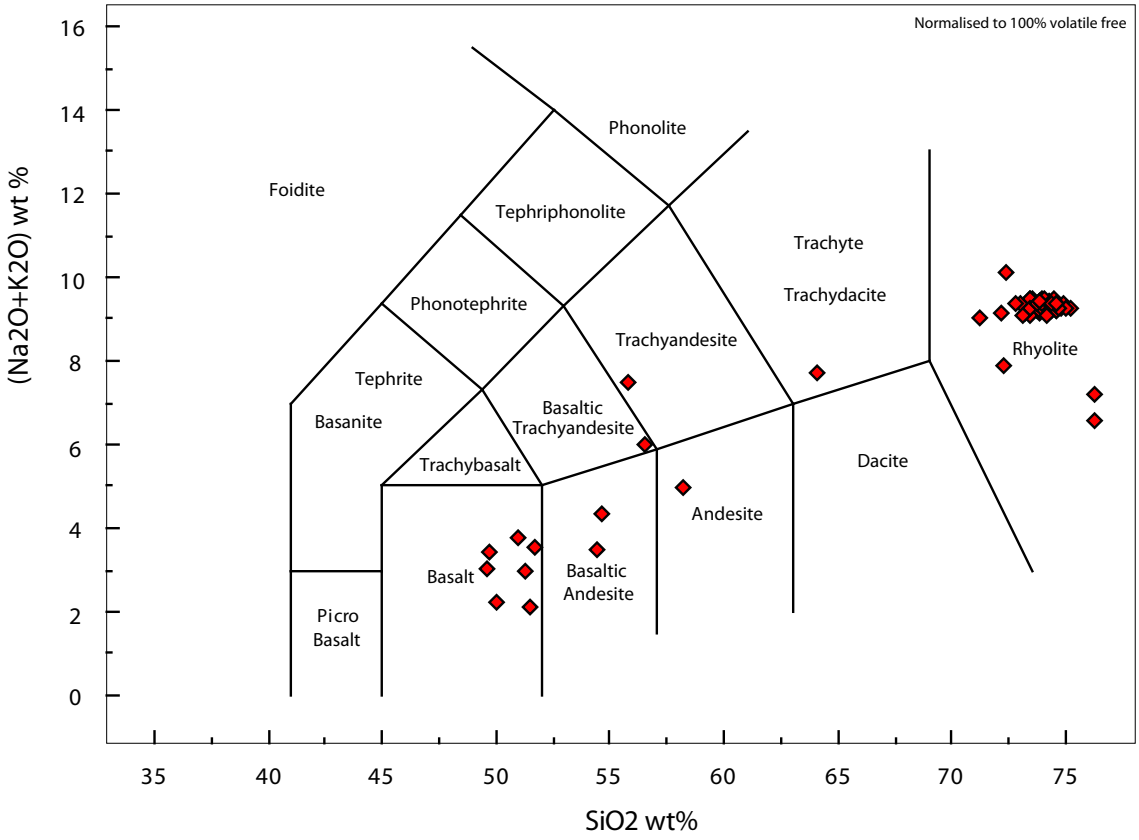

Fig. 3.3: Total Alkalis versus Silica (wt %) of all Öræfajökull samples.

pressed from powders milled at Manchester, were compared to those pressed from powders milled in an agate barreled TEMA mill at the Open University (Stevenson, 2004). The samples showed strong evidence of Co and W contamination but no evidence of Nb and Ta contamination (appendix 2). This finding is corroborated by empirical tests on pure vein quartz (Johnson et al., 1999) which show only minor contamination, which is typically of the same order of magnitude as the precision of the XRF method itself. As the whole suite was prepared with the same set of mills, it is likely that any potential milling contamination will be uniform throughout the suite and therefore only needs to be taken into consideration when comparing to datasets compiled by other workers.

Volatile contents (CO_2 and H_2O) were calculated by recording loss on ignition (LOI) with two consecutive heating steps of 100°C and 1000°C. After normalisation, the majority of high LOI samples do not plot significantly away from those with low LOI and have therefore been included in the following results in order to attempt to match-up explosive eruptive phases of eruptions with their effusive counterparts (fig. 3.2).

3.3 Major element characteristics

Major element data for the 77 analysed samples have been normalised to 100% on a volatile-free basis (Table 3.1). Appendix 2 contains the pre-normalised and LOI data. The samples range from basalts (47.81 wt% SiO_2) to rhyolites (76.35 wt% SiO_2), with a small silica gap between 58.7 and 64.12 wt% SiO_2(fig. 3.3) Although a distinct bimodality to the data set is due in part to this study's strong focus on rhyolitic compositions, nevertheless this bimodality has been reported by previous workers (e.g. Prestvik 1979; 1980; 1982; 1985 Prestvik et. al, 2001) (fig. 3.4).

In this chapter the samples are grouped into the following classifications: basaltic (45-52 wt% SiO_2), intermediate (52-69 wt% SiO_2) and rhyolitic (69-77 wt% SiO_2).

There are seven basaltic samples ranging from 47.81 to 51.54 wt% SiO_2, six intermediate samples ranging from 54.50 to 64.12 wt% SiO_2 and 58 rhyolitic rocks ranging from 71.23 to 76.35 wt% SiO_2 (fig.3.3). Errors and reproducibility are discussed further in appendix 3.

The rhyolitic samples vary considerably in texture, and include glassy obsidian, microcrystalline obsidian, variably devitrified and spherulitic obsidian,

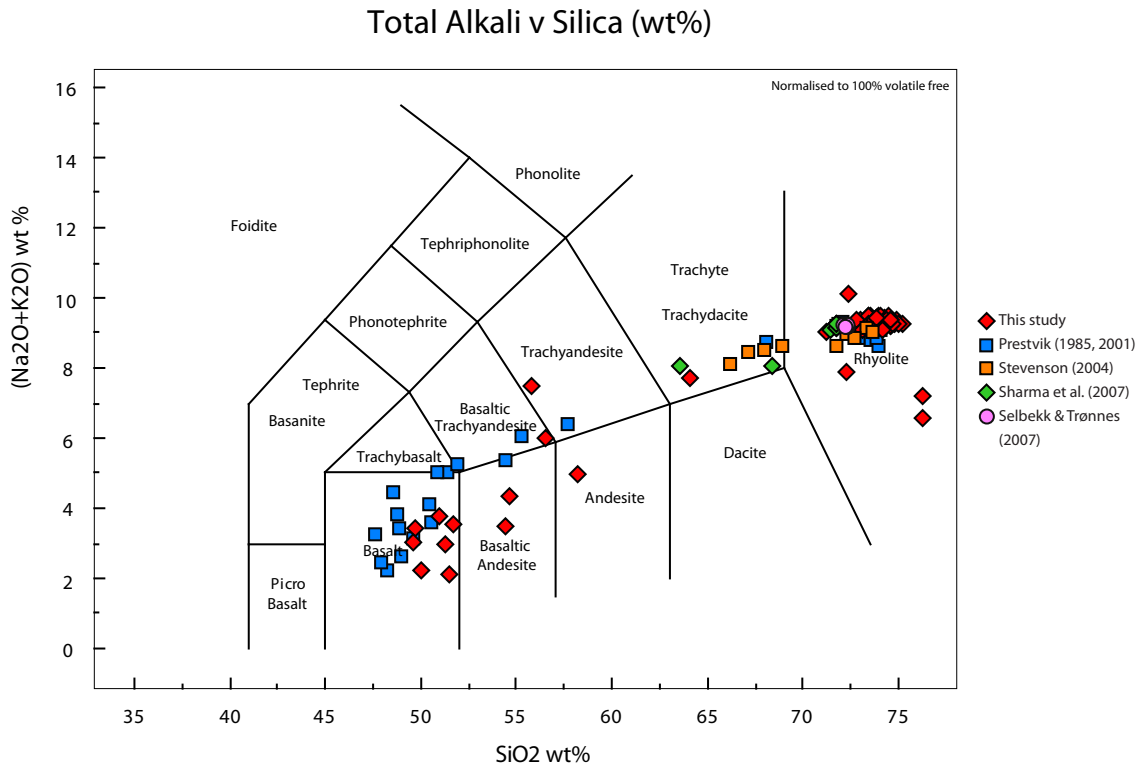

Fig. 3.4: Comparison of previously reported data with this study.

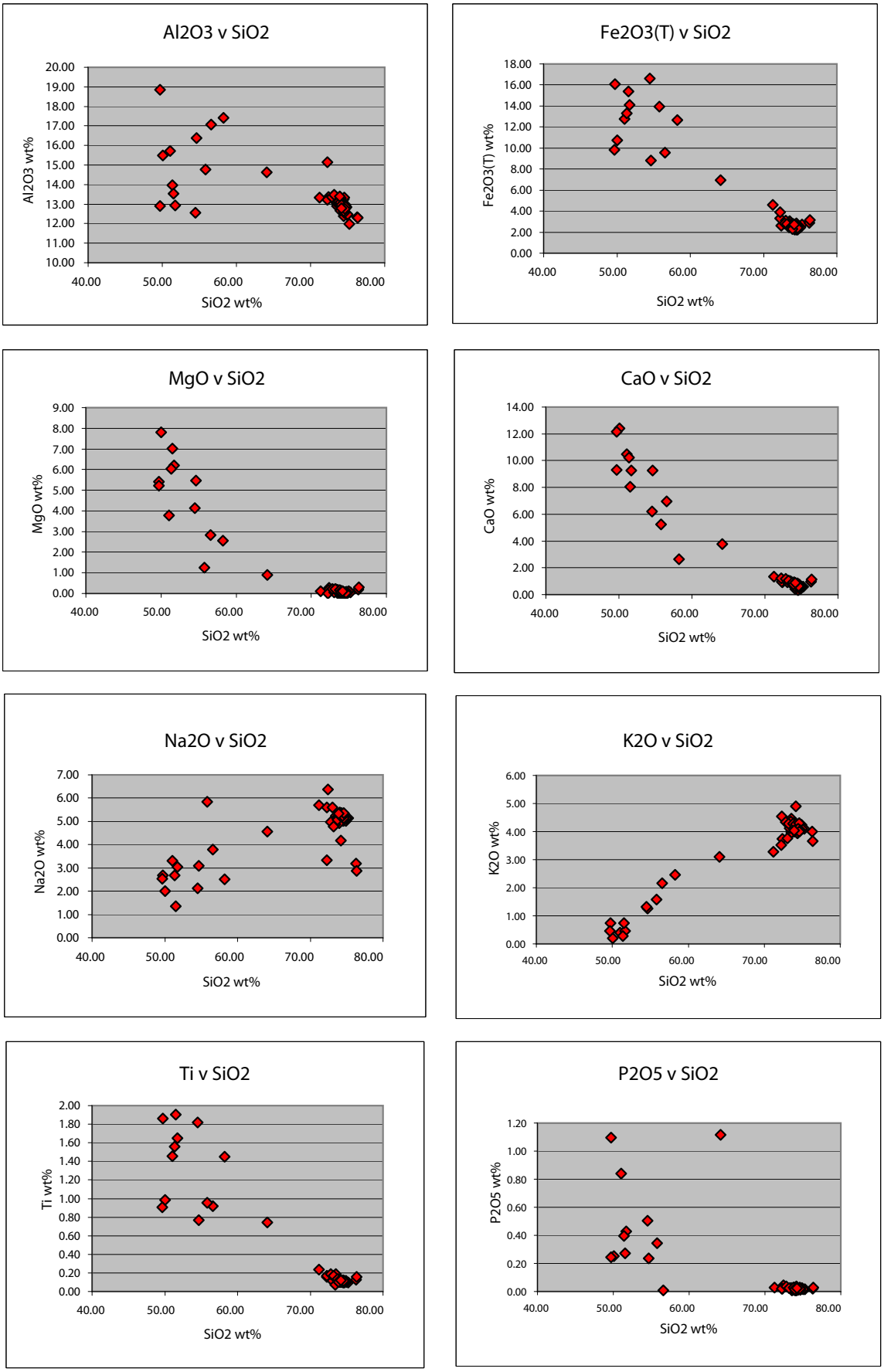

Fig. 3.5: Variation diagrams of major elements plotted against Silica (weight %).

Sample no.	or06	or20	or105	or227	or222	or210	or296	or110	tuff01	OR408	OR505
location	Basement 0414894/ 7089991	Basement 0415166/ 7090260	God w - basement 0415147/ 7090312	God w 0414718/ 7090070	God w river 0414050/ 7091187	HVG top - young 0416192/ 7090992	Hof 0415726/ 7089298	slaga 0414295/ 7092406	tuff cone	orange/brown fined grained rock	red ash 15241/ 90094
Majors (wt%)											
SiO2	51.04	51.71	50.05	51.38	49.73	56.57	54.64	49.68	51.54	54.50	58.24
Al2O3	15.71	12.92	15.48	13.95	12.90	17.07	16.37	18.85	13.54	12.57	17.42
Fe2O3	12.78	14.13	10.74	13.31	16.07	9.56	8.80	9.81	15.39	16.59	12.65
MgO	3.79	6.21	7.80	6.05	5.40	2.83	5.46	5.23	7.02	4.13	2.55
CaO	10.50	9.28	12.39	10.22	9.32	6.98	9.28	12.16	8.03	6.20	2.62
Na2O	3.32	3.03	2.00	2.69	2.68	3.79	3.09	2.54	1.34	2.13	2.50
K2O	0.40	0.47	0.20	0.28	0.75	2.15	1.25	0.47	0.75	1.32	2.45
P2O5	0.84	0.43	0.25	0.40	1.10	0.01	0.24	0.24	0.27	0.50	-0.06
Ti	1.45	1.65	0.98	1.56	1.86	0.92	0.77	0.91	1.90	1.82	1.45
Mn	0.16	0.18	0.12	0.16	0.21	0.12	0.11	0.11	0.21	0.24	0.16
Volatile free Total	100.00	100.00	100.00	100.00	100.00	100.00	100.00	100.00	100.00	100.00	100.00
total alkalis:	3.72	3.50	2.20	2.97	3.42	5.94	4.34	3.01	2.09	3.45	4.96
LOI total	0.50	0.73	1.71	1.50	2.05	0.43	0.28	0.57	11.37	4.23	5.00
Traces (ppm)											
Sc	27	29	26	29	22	13	17	18	65	49	63
V	362	394	268	383	221	142	186	250	238	153	213
Ni	36	36	64	40	17	302	51	31	22	7	24
Zn	123	144	87	128	151	91	87	82	140	186	170
Ga	21	22	18	21	22	21	20	22	22	23	27
Rb	3	4	BDL	5	26	52	31	8	BDL	16	58
Sr	262	252	238	243	358	253	286	401	291	246	59
Y	40	48	25	42	58	44	36	26	51	75	84
Zr	168	223	98	179	261	382	277	122	194	401	381
Nb	13	19	7	14	34	33	23	12	43	54	58
Mo	BDL	BDL	0	BDL	0	6	BDL	0	BDL	BDL	BDL
Ba	90	117	65	83	197	388	266	141	396	885	605
Th	2	3	2	4	5	9	6	4	8	10	11
U	BDL	1	BDL	BDL	0	0	BDL	BDL	BDL	3	2
Pb	BDL	BDL	0	3	0	2	2	0	1	2	5
Cr	31	14	158	29	36	1050	160	52	BDL	BDL	BDL
Cu	124	210	105	149	68	76	80	111	21	6	94
Nb/Y	0.33	0.39	0.27	0.33	0.58	0.75	0.63	0.48	0.84	0.73	0.69

Table . 3.1: Major and trace element data for all samples (Normalised to 100%). BDL: below detection limit.

Sample no.	or112	or55	OR03	OR12	OR38	OR150	OR200	OR202	OR221	OR228	OR230
location	Slaga int. 0414433/ 7092062	int lobes HVG 0416169/ 7090313	0414119/ 7090551	0414722/ 7089834	0415068/ 7090428	0415836/ 7088905	0414855/ 7089690	0415260/ 7089580	0413728/ 7090958	0114648/ 7090208	0414762/ 709021
Majors (wt%)											
SiO2	55.80	64.12	74.25	74.36	74.28	73.91	74.13	73.79	73.58	74.04	73.95
Al2O3	14.78	14.63	13.14	13.03	13.12	13.02	12.89	13.11	12.89	13.03	13.05
Fe2O3	13.92	6.95	2.26	2.49	2.55	2.71	2.71	2.73	3.02	2.56	2.66
MgO	1.26	0.91	0.09	0.05	0.04	0.01	0.01	0.06	0.01	BDL	0.01
CaO	5.24	3.75	0.72	0.70	0.53	0.82	0.74	0.82	0.84	0.71	0.75
Na2O	5.85	4.56	5.36	5.25	5.34	5.18	5.15	5.14	4.98	5.38	5.27
K2O	1.58	3.11	4.00	3.94	3.95	4.15	4.19	4.15	4.45	4.10	4.12
P2O5	0.34	1.12	0.01	0.01	0.01	0.01	0.01	0.01	0.01	0.01	0.01
Ti	0.95	0.74	0.10	0.11	0.11	0.12	0.11	0.12	0.13	0.10	0.11
Mn	0.27	0.11	0.07	0.07	0.06	0.07	0.07	0.07	0.08	0.07	0.07
Volatile free Total	100.00	100.00	100.00	100.00	100.00	100.00	100.00	100.00	100.00	100.00	100.00
total alkalis:	7.43	7.67	9.36	9.19	9.29	9.33	9.34	9.29	9.44	9.48	9.39
LOI total	0.83	0.48	0.75	0.66	0.81	0.00	0.72	0.67	0.27	0.30	0.36
Traces (ppm)											
Sc	15	8	BDL	BDL	BDL	0	BDL	BDL	0	1	BDL
V	0	69	BDL	BDL	2	0	0	0	0	0	0
Ni	BDL	5	0	1	1	2	1	0	1	4	0
Zn	195	97	87	107	90	116	117	116	118	118	117
Ga	28	22	27	27	27	26	26	26	26	26	26
Rb	34	80	92	91	91	97	96	97	99	97	98
Sr	309	191	38	36	39	39	35	40	38	37	37
Y	86	55	99	98	105	97	99	97	99	98	98
Zr	501	543	456	482	470	472	479	472	477	473	476
Nb	48	45	74	79	77	76	78	77	79	78	79
Mo	1	1	BDL	1	2	2	3	2	2	2	2
Ba	437	577	829	797	804	789	784	793	780	816	804
Th	8	12	14	13	13	14	14	15	14	14	14
U	0	2	2	3	1	4	3	4	4	4	10
Pb	1	1	0	6	7	7	7	7	7	6	6
Cr	0	5	1	BDL	BDL	8	2	0	3	12	BDL
Cu	6	27	4	BDL	3	3	3	3	3	0	2
Nb/Y	0.55	0.81	0.75	0.81	0.74	0.79	0.80	0.79	0.79	0.79	0.80

Sample no.	OR255	OR263	OR280	OR293	or224	or226	or250	or160	or207	or297	or161
location	0414943/ 7090519										
Majors (wt%)											
SiO2	73.88	74.66	74.49	74.43	74.92	74.49	74.52	74.56	74.87	74.12	74.29
Al2O3	13.04	12.50	12.38	12.68	12.44	13.25	13.34	12.79	12.84	13.31	12.90
Fe2O3	2.71	2.69	2.80	2.59	2.53	2.25	2.35	2.50	2.42	2.53	2.48
MgO	0.01	0.02	0.05	0.02	0.09	0.03	0.05	0.05	0.03	0.06	0.07
CaO	0.81	0.77	0.82	0.74	0.51	0.39	0.35	0.58	0.44	0.41	0.71
Na2O	5.16	5.05	5.02	5.23	5.09	5.25	5.03	5.13	5.01	5.09	5.16
K2O	4.18	4.10	4.21	4.08	4.25	4.18	4.17	4.21	4.20	4.27	4.21
P2O5	0.01	0.02	0.02	0.02	0.02	0.02	0.02	0.03	0.03	0.04	0.02
Ti	0.12	0.12	0.12	0.12	0.11	0.10	0.10	0.10	0.12	0.11	0.10
Mn	0.07	0.07	0.07	0.08	0.05	0.05	0.05	0.05	0.05	0.05	0.05
Volatile free Total	100.00	100.00	100.00	100.00	100.00	100.00	100.00	100.00	100.00	100.00	100.00
total alkalis:	9.34	9.15	9.23	9.31	9.34	9.43	9.21	9.34	9.21	9.36	9.37
LOI total	0.64	0.41	0.53	0.51	0.33	0.41	0.70	0.28	0.57	0.57	0.21
Traces (ppm)											
Sc	0	BDL	1	1	BDL	0	BDL	BDL	1	1	1
V	0	BDL	BDL	BDL	BDL	BDL	BDL	8	8	17	BDL
Ni	0	BDL	BDL	0	BDL	BDL	BDL	BDL	BDL	BDL	BDL
Zn	117	118	117	119	240	73	113	74	62	49	80
Ga	26	26	26	26	26	27	28	27	26	26	26
Rb	97	97	97	97	94	96	110	93	93	94	94
Sr	38	39	40	38	38	38	37	40	40	40	40
Y	98	97	96	97	95	53	54	81	71	113	88
Zr	473	475	472	473	476	478	477	473	472	477	462
Nb	78	76	75	76	78	78	81	76	77	77	76
Mo	2	2	2	3	3	3	BDL	3	1	3	3
Ba	794	800	792	801	797	807	791	804	778	796	788
Th	14	13	14	14	14	14	15	14	14	14	14
U	3	5	6	4	3	3	3	3	4	4	4
Pb	7	6	7	6	9	5	35	5	8	10	6
Cr	3	0	2	2	11	13	13	18	10	19	18
Cu	3	1	1	1	0	BDL	11	BDL	0	0	0
Nb/Y	0.80	0.78	0.78	0.78	0.82	1.48	1.51	0.94	1.08	0.68	0.86

Sample no.	0r203	or262	or08	or09	or10	or13	or44	or49	or54	or106	or132
location			0415166/ 7090260	0415166/ 7090260	0415156/ 7090712	0415826/ 7090585	0414877/ 7090666	0414914/ 7091661	0415952/ 7090190	0414863/ 7091616	0415881/ 7091602
Majors (wt%)											
SiO2	75.24	75.01	73.77	73.79	73.58	73.94	73.79	73.75	73.69	73.62	73.52
Al203	11.98	12.46	13.22	13.14	13.13	13.15	13.29	13.18	13.28	13.07	13.07
Fe203	2.75	2.46	2.63	2.65	2.75	2.55	2.54	2.59	2.61	2.79	2.77
MgO	0.05	0.10	0.12	0.08	0.16	0.07	0.07	0.09	0.12	0.07	0.08
CaO	0.58	0.57	0.86	0.89	0.91	0.86	0.84	0.88	0.82	0.89	0.90
Na2O	5.14	5.12	5.11	5.17	5.21	5.22	5.25	5.26	5.22	5.13	5.17
K2O	4.10	4.10	4.06	4.05	4.02	4.01	4.02	4.03	4.06	4.21	4.28
P205	0.01	0.02	0.03	0.02	0.02	0.02	0.02	0.02	0.02	0.02	0.02
Ti	0.10	0.10	0.13	0.13	0.14	0.12	0.12	0.12	0.12	0.12	0.13
Mn	0.05	0.05	0.07	0.07	0.07	0.06	0.06	0.06	0.07	0.07	0.07
Volatile free Total	100.00	100.00	100.00	100.00	100.00	100.00	100.00	100.00	100.00	100.00	100.00
total alkalis:	9.24	9.22	9.17	9.22	9.23	9.23	9.27	9.29	9.28	9.34	9.44
LOI total	1.56	0.35	1.30	1.17	1.26	1.34	1.17	1.15	1.18	0.57	0.36
Traces (ppm)											
Sc	0	1	1	BDL	1	0	1	BDL	1	BDL	0
V	BDL	BDL	BDL	BDL	1	BDL	BDL	BDL	BDL	0	BDL
Ni	0	0	2	1	2	1	0	1	5	0	BDL
Zn	127	88	109	109	114	116	107	111	112	107	105
Ga	27	27	26	25	26	26	26	26	26	25	26
Rb	95	93	95	98	97	104	99	98	98	99	99
Sr	31	38	46	46	46	46	45	46	45	46	46
Y	99	72	88	91	92	95	92	91	92	91	91
Zr	464	469	474	475	475	476	478	477	475	476	478
Nb	81	77	72	72	72	72	72	72	72	71	72
Mo	3	3	2	2	2	2	2	2	2	2	2
Ba	761	804	804	791	829	823	804	792	824	769	776
Th	14	14	14	14	14	14	14	14	14	14	15
U	3	3	1	2	1	1	2	2	2	4	4
Pb	7	4	3	4	BDL	2	3	6	4	7	7
Cr	12	13	1	BDL	0	BDL	0	0	1	BDL	1
Cu	1	BDL	BDL	1	BDL	BDL	BDL	2	BDL	4	5
Nb/Y	0.82	1.07	0.81	0.79	0.78	0.76	0.79	0.79	0.78	0.78	0.79

Sample no.	or133	or211	or212	or219	or247	OR301a	or23	or213d	or241	OR400	or399
location	0415997/ 7091846	0416399/ 7091204	0416455/ 7091398	0414858/ 7091200	0415279/ 7090302		0415399/ 7091161				
Majors (wt%)											
SiO2	73.62	73.55	73.91	73.68	73.62	73.91	73.53	74.01	73.97	74.01	74.13
Al2O3	13.17	13.12	13.21	13.13	13.07	13.04	13.22	12.68	13.18	13.07	12.97
Fe2O3	2.60	2.76	2.63	2.74	2.86	2.69	2.99	2.75	2.49	2.58	2.54
MgO	0.10	0.08	0.01	0.10	0.08	0.10	0.03	0.11	0.13	0.05	0.11
CaO	0.93	0.94	0.89	0.87	0.90	0.87	0.96	0.93	0.76	0.74	0.59
Na2O	5.05	5.00	5.00	5.09	4.95	5.02	5.11	4.99	4.93	5.31	5.23
K2O	4.30	4.29	4.14	4.19	4.30	4.14	3.96	4.32	4.32	4.03	4.26
P2O5	0.02	0.01	0.02	0.02	0.02	0.02	0.01	0.02	0.03	0.02	0.02
Ti	0.14	0.19	0.12	0.13	0.13	0.13	0.12	0.13	0.13	0.12	0.10
Mn	0.06	0.07	0.06	0.06	0.07	0.07	0.09	0.05	0.05	0.07	0.05
Volatile free Total	100.00	100.00	100.00	100.00	100.00	100.00	100.00	100.00	100.00	100.00	100.00
total alkalis:	9.35	9.28	9.14	9.28	9.25	9.17	9.07	9.32	9.25	9.34	9.48
LOI total	0.35	0.58	1.74	0.43	0.56	0.74	6.84	1.13	0.27	0.06	0.33
Traces (ppm)											
Sc	0	BDL	0	BDL	1	0	1	BDL	1	0	0
V	BDL	0	BDL	0	0	BDL	BDL	BDL	BDL	BDL	BDL
Ni	2	0	BDL	BDL	BDL	0	2	BDL	BDL	1	BDL
Zn	96	105	105	109	110	111	101	104	68	138	111
Ga	25	25	25	25	25	25	23	24	25	26	26
Rb	103	99	97	97	98	99	95	98	100	95	100
Sr	49	47	48	47	45	46	45	47	51	39	38
Y	86	90	87	91	91	92	86	91	66	112	90
Zr	479	479	473	480	475	477	448	476	497	475	477
Nb	69	72	71	72	72	72	67	72	70	76	79
Mo	3	2	2	2	2	2	2	3	3	3	3
Ba	767	776	771	775	767	794	734	760	777	819	799
Th	14	14	14	14	13	14	12	14	14	14	14
U	4	5	3	3	4	5	2	4	3	2	4
Pb	7	7	9	8	7	5	6	7	4	4	6
Cr	7	1	BDL	0	BDL	BDL	2	15	18	BDL	13
Cu	6	5	6	4	6	1	0	1	0	0	1
Nb/Y	0.79	0.80	0.81	0.79	0.80	0.78	0.78	0.79	1.05	0.68	0.87

Sample no.	or290	or401	OR402	OR403	OR218	or46	or304	or306	or308	OR04 dyke	OR406
location						0414759/ 7090437				0414707/7091056	0415277/709140C
Majors (wt%)											
SiO2	74.70	74.57	74.66	74.45	74.63	73.91	76.28	76.35	74.19	72.41	72.29
Al2O3	12.78	12.57	12.89	12.64	12.75	13.40	12.32	12.29	12.78	13.37	15.15
Fe2O3	2.48	2.58	2.27	2.60	2.41	2.31	2.86	3.14	2.74	2.64	3.32
MgO	0.09	0.07	0.03	0.03	0.04	0.09	0.19	0.29	0.12	0.26	0.16
CaO	0.54	0.59	0.61	0.74	0.64	0.74	0.96	1.13	0.89	0.94	0.94
Na2O	5.22	5.15	5.31	5.24	5.35	5.34	3.19	2.87	4.18	6.36	3.32
K2O	4.03	4.29	4.06	4.11	4.01	4.03	3.99	3.67	4.90	3.74	4.54
P2O5	0.01	0.02	0.02	0.02	0.02	0.02	0.02	0.03	0.02	0.04	0.02
Ti	0.10	0.10	0.10	0.11	0.11	0.10	0.13	0.16	0.12	0.16	0.16
Mn	0.05	0.05	0.06	0.07	0.05	0.06	0.06	0.06	0.05	0.06	0.08
Volatile free Total	100.00	100.00	100.00	100.00	100.00	100.00	100.00	100.00	100.00	100.00	100.00
total alkalis:	9.25	9.44	9.37	9.34	9.35	9.37	7.18	6.54	9.08	10.11	7.87
LOI total	0.38	0.36	0.24	0.27	0.44	0.37	8.26	7.80	0.57	2.83	4.78
Traces (ppm)											
Sc	2	BDL	BDL	BDL	BDL	BDL	1	1	0	BDL	2
V	BDL	BDL	BDL	BDL	BDL	BDL	BDL	1	BDL	2	BDL
Ni	BDL	0	BDL	BDL	BDL	2	BDL	0	BDL	1	BDL
Zn	99	122	86	119	107	81	100	104	108	99	111
Ga	26	27	26	26	26	27	23	23	25	24	25
Rb	92	98	95	97	94	97	95	106	99	99	92
Sr	37	37	39	39	39	38	45	67	46	50	45
Y	74	92	84	84	84	82	85	86	92	86	102
Zr	474	478	438	473	469	441	431	430	479	468	480
Nb	77	78	76	75	75	74	67	67	73	67	72
Mo	3	3	BDL	BDL	BDL	1	3	3	2	2	BDL
Ba	782	801	808	799	800	804	716	708	780	764	758
Th	14	14	14	13	14	13	13	12	14	14	14
U	3	3	3	3	3	2	3	4	4	3	5
Pb	6	7	4	8	5	3	6	18	7	6	7
Cr	15	17	2	1	0	4	18	23	18	0	BDL
Cu	BDL	1	1	1	1	3	0	23	2	BDL	3
Nb/Y	1.04	0.85	0.90	0.90	0.90	0.90	0.79	0.78	0.79	0.78	0.71

Sample no.	OR115 tephra	OR162	OR236 tephra	OR151 kotar	OR154	OR164	OR165	OR166	OR146	OR139	OR316
location	0414989/7089780	0415117/7089866	0415862/7090883	0415836/7088905	Kristinartindar	0414623/ 7094977	0414623/7094977	0414623/ 7094977	Stadharfjall	kvisker	Slaga
Majors (wt%)											
SiO2	73.31	74.67	71.23	72.26	73.05	73.52	73.47	73.83	72.84	73.20	73.76
Al2O3	13.37	12.95	13.33	13.23	13.30	13.32	13.15	13.07	13.35	13.47	13.14
Fe2O3	2.85	2.51	4.61	3.88	3.12	2.44	2.78	2.73	2.83	2.75	2.50
MgO	0.19	0.01	0.12	0.01	0.07	0.09	0.16	0.11	0.22	0.21	0.15
CaO	0.94	0.59	1.34	1.22	0.91	0.96	1.02	0.75	1.16	1.05	0.90
Na2O	4.99	5.10	5.70	5.60	5.60	5.24	4.89	5.22	4.97	4.79	5.08
K2O	4.13	4.05	3.28	3.51	3.76	4.21	4.37	4.11	4.35	4.27	4.27
P2O5	0.02	0.00	0.03	0.02	0.00	0.02	0.02	0.00	0.04	0.03	0.03
Ti	0.13	0.10	0.24	0.17	0.11	0.14	0.07	0.11	0.18	0.17	0.13
Mn	0.07	0.03	0.11	0.10	0.09	0.05	0.07	0.07	0.06	0.07	0.05
Volatile free Total	100.00	100.00	100.00	100.00	100.00	100.00	100.00	100.00	100.00	100.00	100.00
total alkalis:	9.12	9.15	8.99	9.11	9.35	9.45	9.25	9.33	9.31	9.06	9.35
LOI total	3.61	0.95	2.21	0.13	1.68	0.13	0.35	0.49	1.04	0.48	0.55
Traces (ppm)											
Sc	BDL	BDL	BDL	BDL	BDL	1	0	0	BDL	4	BDL
V	BDL	0	10	0	0	1	BDL	0	2	3	BDL
Ni	BDL	2	1	BDL	1	0	1	0	0	5	0
Zn	112	120	175	113	152	75	92	119	88	95	95
Ga	25	27	29	27	28	24	23	27	23	25	24
Rb	92	88	73	81	81	101	100	96	105	103	103
Sr	44	31	75	83	50	53	50	36	61	53	46
Y	93	129	112	96	102	79	82	99	79	85	86
Zr	454	470	837	793	552	469	464	477	502	482	478
Nb	73	82	76	67	85	66	65	78	64	69	68
Mo	2	2	2	BDL	2	2	2	2	2	2	3
Ba	759	789	702	706	838	769	742	797	741	786	769
Th	13	14	12	12	12	14	14	14	14	14	14
U	4	4	2	2	2	4	4	4	5	4	3
Pb	7	7	7	3	11	6	7	6	7	4	5
Cr	BDL	6	BDL	BDL	1	1	2	0	2	BDL	16
Cu	5	1	5	3	0	5	5	2	9	1	2
Nb/Y	0.79	0.64	0.67	0.70	0.83	0.84	0.79	0.80	0.81	0.81	0.79

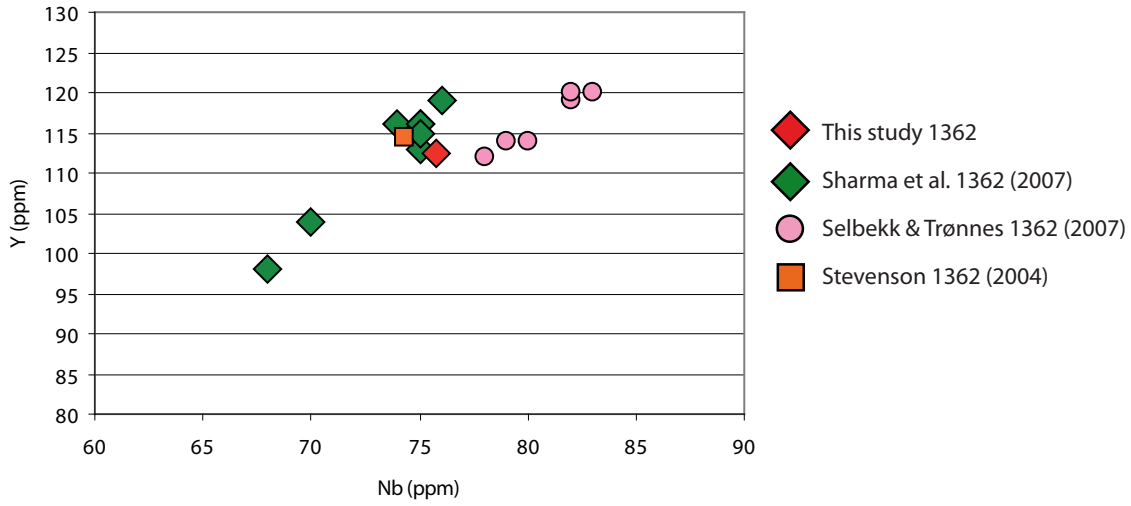

Fig. 3.6: Comparison of previously reported trace element abundances of 1362 tephra samples with this study.

microcrystalline rhyolite, pumice, various breccias, plus unconsolidated tephra piles comprising inflated to microvesicular pumice and ash. Associated tephras have also been sampled in order to establish their relationship to the rhyolites, if any. Samples from the unconsolidated tephra piles have LOIs of up to 8.26%, which contrasts with the low LOI of lavas and intrusive samples ranging from 0 to 1.74 wt % .

Due to the sampling bias towards silicic rocks, the variation diagrams of major element abundances have been plotted against SiO_2 wt% (fig. 3.5). The diagrams display some scatter but coherent trends are evident. Fe_2O_3(total), MgO and CaO decrease with increasing SiO_2, with rhyolites (> 69 wt%) all displaying very low amounts of MgO (<0.26 wt%) and CaO (<1.34 wt%) while the Fe_2O_3(total)content is relatively high (2.26 to 3.88 wt%). Al2O_3 shows an initial increase within the mafic samples followed by a decrease. TiO_2 and P_2O_5 also decrease with increasing SiO_2, whilst K_2O increases with increasing SiO_2. Although there is considerable scatter, Na_2O does show a general increase with increasing SiO_2.

This dataset broadly agrees with the results of previous workers (Prestvik 1979, 1980, 1982, 1985; Prestvik et. al, 2001; Selbekk & Trønnes, 2007; Sharma et al., 2008; Stevenson, 2004) (fig. 3.4), however there are some exceptions. Prestvik (1980, 1982) describes the Öræfajökull suite as essentially tholeiitic but with a transitional character toward alkaline rocks. However, the majority of basaltic and intermediate rocks presented in this dataset, while being close to the upper limit for a tholeiitic suite, still plot in the range of basalt, basaltic andesite and andesite as opposed

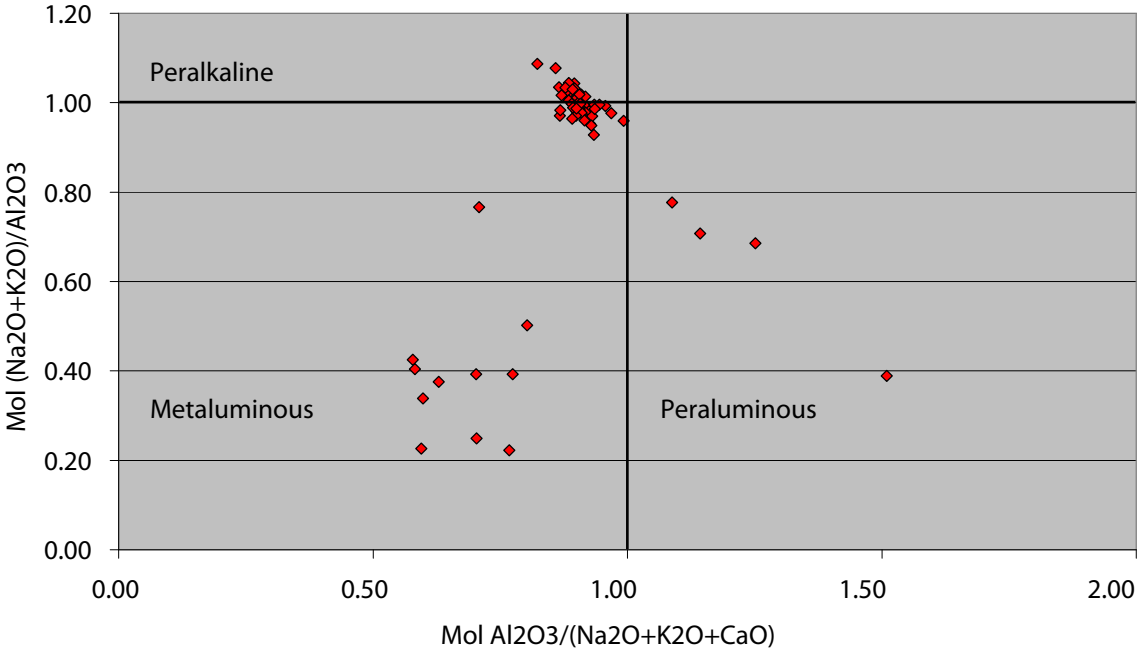

Fig. 3.7: Alumina saturation index. The majority of the rhyolites plot in the metaluminous / peralkaline transition area.

to the more alkaline hawaiite, mugearite and benmoreite. This may be due to the limited number of mafic rocks presented in this data set, as only mafic rocks that have a direct field relationship to the silicic rocks of the Goðafjall area have been analysed, therefore the whole range of mafic rocks within the Öræfajökull suite may not be fully represented here. The suite displays a predominantly bimodal distribution of basalts, basaltic andesites and rhyolites with only two samples plotting in the andesite / trachyandesite range and one trachydacite. The lack of intermediate samples is in accordance with the 'Daly gap' and is a common feature in Icelandic volcanic suites (Carmichael, 1964; Macdonald et al., 1990; McGarvie et al., 1990; Hards et al., 2000, Jonasson, 2007).

The dataset is less evolved than other Icelandic flank zone suites such as Snæfellsjökull and Ljosufjoll in the Western flank zone which have a higher proportion of trachyte lavas (Flude et al. 2008) and also the neighbouring Snæfell which has a slightly more alkalic signature (Hards et al., 2000).

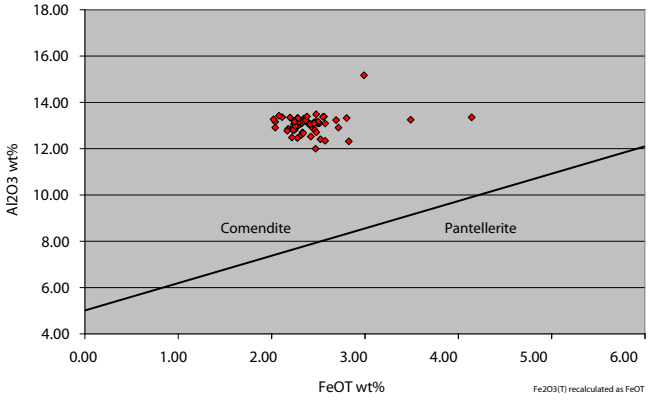

Fig. 3.8: The peralkaline rhyolites are comenditic.

Although internal consistency

within this dataset is the primary focus of this study, in order to check for consistency with other Öræfajökull datasets, a known sample of 1362 pumice was analysed and the trace element concentrations plotted against the datasets from other 1362 analyses (fig. 3.6)

The mafic and intermediate samples are metaluminous (fig. 3.7), while the rhyolites are metaluminous to mildly peralkaline (mol. $Al_2O_3 > CaO + Na_2O + K_2O$) and comenditic (fig. 3.8), which reflects the transitional tholeiitic / alkaline nature of the suite. All of the basalts contain low abundances of MgO (Goðafjall <7.8wt %) and can therefore be classed as evolved tholeiites (Prestvik et al., 2001). Some of the major elements show a range of scatter across the suite. Scattered trends on variation diagrams can be an indicator of element mobility. The very low abundance of MgO in the silicic samples (<0.1 wt %) is characteristic of the Öræfajökull suite and has previously been used to distinguish Öræfajökull tephras from those of other silicic volcanoes (Larsen et al., 1999, 2008).

The mafic rocks of the Goðafjall area can be split into two groups – an older Neogene group consisting of four samples of subaerially erupted basalt sheets which lie unconformably below the silicic rocks and a younger Pleistocene / Holocene group consisting of subglacially and subaerially erupted basalts and basaltic andesites. It is likely that the pre-Quaternary basalts will have been subjected to complete burial by ice during each progressive glacial cycle, with repeated exposure to glacial meltwater in a subglacial environment. Mobile major element concentrations such as Na_2O and K_2O can be affected by post-emplacement hydrous alteration and this may account for some of the scatter seen in the Na_2O variation diagram. Some alteration is visible in the basalt samples OR06 and OR227 in hand specimen and thin section, where pyroxene in the groundmass has been replaced by orange-brown

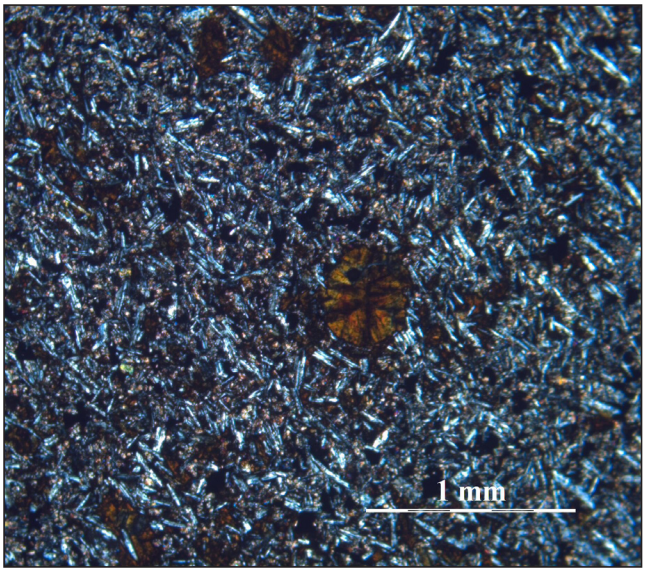

Fig. 3.9: OR227 basalt thin section displaying secondary alteration of glassy groundmass and Fe-rich olivine.

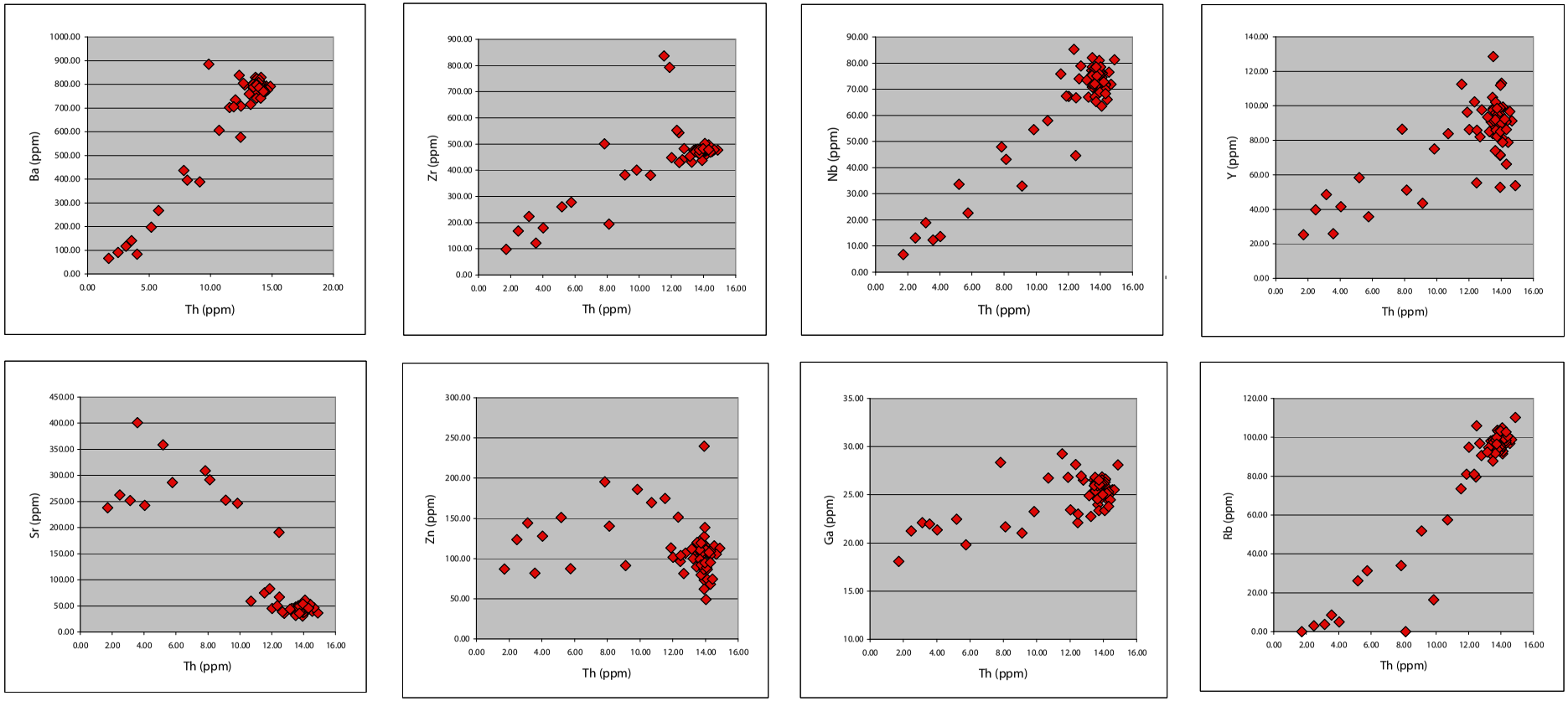

Fig. 3.10: Selected trace element variation diagrams plotted against Th (ppm) for all samples.

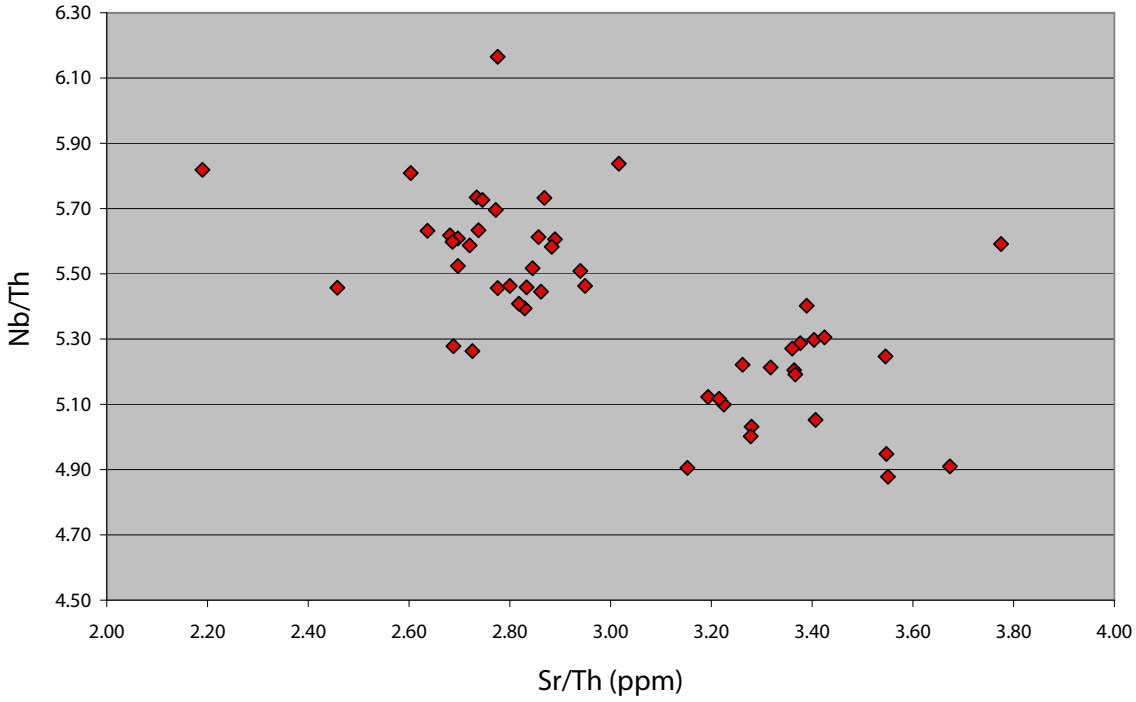

Fig. 3.11: Trace element plot of Sr/Th against Nb/Th shows a strong division within the more evolved samples in the dataset.

clay minerals. (fig.3.9). Macdonald (1974) has shown that obsidians can undergo a loss of Na_2O during post-eruptive cooling and crystallisation compared to the other major elements and this may further contribute to the scatter across the silicic samples in the Na_2O variation diagram (fig. 3.5).

The low CaO and high FeO (total) abundances displayed in the rhyolite samples are a common characteristic of Icelandic silicic rocks and have been attributed to low pressure formation and low water pressure in the source which increases the stability of plagioclase relative to pyroxene (Jonasson, 2007).

3.4. Trace element characteristics

Variation diagrams of the trace element concentrations have been plotted against Th (fig. 3.9). Thorium has been used for the differentiation index as it is known to be highly incompatible in both basaltic and silicic rocks (Rollinson, 1993). It is also resistant to alteration and also present in a consistent concentration range of 12-15 ppm throughout the silicic samples.

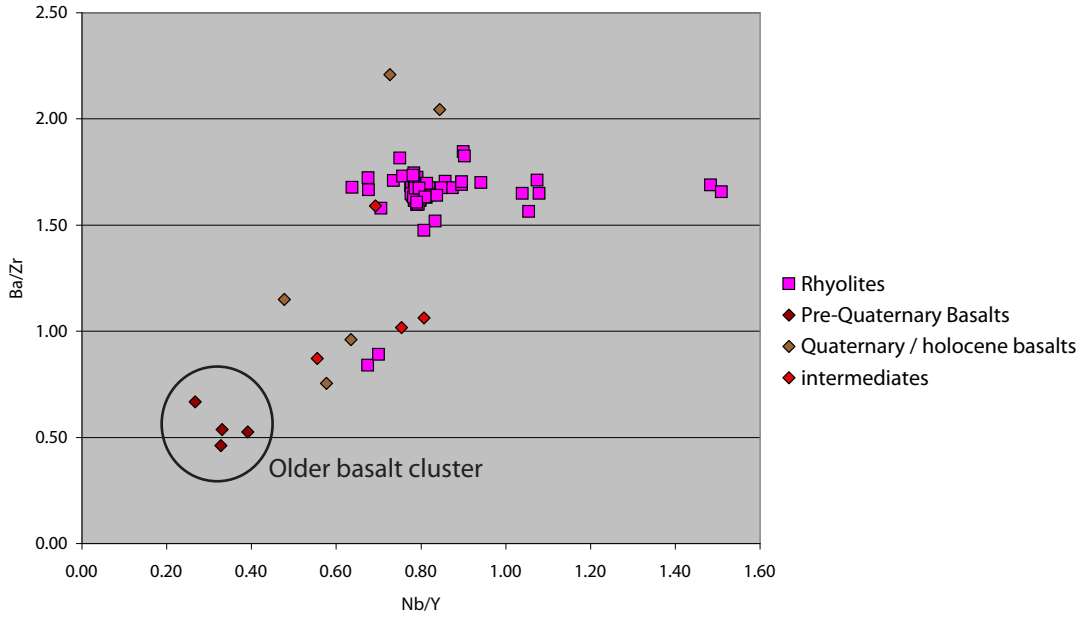

Fig. 3.12: Incompatible trace element plot of mafic, intermediate and silicic samples. Pre -Quaternary basalts form separate cluster.

Scandium, V, Ni, Co and Cu (see table 1) have their highest concentrations in the basaltic samples and all show a negative correlation with Th, while in the rhyolitic samples these element concentrations are so low that they are below XRF detection limits. These trace elements are behaving compatibly with minerals in the basalts.

Across the whole suite, Ba, Zr, Nb and Rb display a strong positive correlation with Th while Y shows a weaker positive correlation. Zn and Ga both correlate poorly while Sr displays a negative correlation (fig. 3.10).

Closer inspection of the more evolved sample clusters reveals that Ba, Rb and Zr form clusters over a very limited range, while Y displays a much wider continuous range. Sr and Nb concentrations form two distinct clusters which become more pronounced when Sr/Th ratios are plotted against Nb/Th (fig. 3.11).

Overall, the trace element variation diagrams display similar trends to those of other Icelandic central volcanoes with substantial silicic deposits (Jonasson, 2007; Martin & Sigmarsson, 2010) and Th concentrations in the silicic samples are similar to those of other central flank volcanoes, Snæfellsjökull and Ljosufjoll (Jonasson, 2007).

Although the primary focus of the geochemical analysis presented in this study is not petrogenetic, it can be noted that the incompatible trace element ratios Nb/Y plotted against Ba/Zr (fig. 3.12) show that the samples identified in the

Trace element variation diagrams of group 1 and group 2 rhyolite

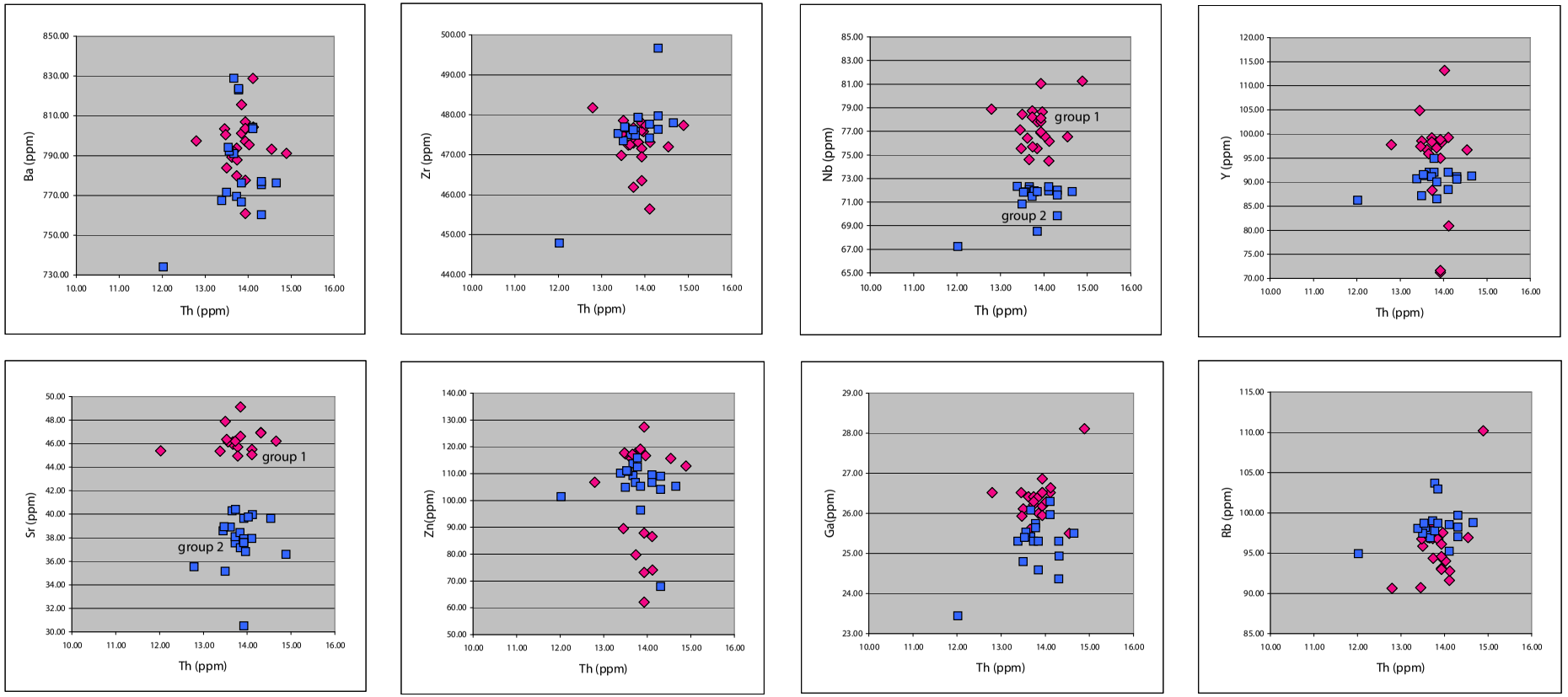

Fig. 3.13: Two main rhyolite gropups displayed in terms of trace element distribution on selected trace element variation diagrams plotted against Th (ppm).

field as Tertiary basalts form a separate cluster away from the younger basalts and more evolved rocks. Ratios of highly incompatible trace elements should remain constant throughout the suite if the rocks are related to one another by fractional crystallisation; this suggests different source magma for the Tertiary basalts and the younger ones. The rhyolites however do cluster together, suggesting that they are all related to a single magma batch. The presence of silicic rocks with relatively high concentrations of highly incompatible elements, such as Th, suggests that fractional crystallisation has played a role in their production even though other mechanisms may be involved (Martin & Sigmarsson, 2010).

3.5. Chemostratigraphy

The primary role of geochemical analysis in this study is the identification of subtle differences in lava compositions. Individual Icelandic rhyolitic eruptions have been shown to have a unique geochemical 'fingerprint' (Macdonald, 1990; McGarvie, 1990, Flude et al, 2008) which is most easily identified through trace element abundances and ratios.

Chemostratigraphy combines geochemistry with detailed field observation in order to match up outcrops that are products of the same eruption but have been physically separated from one another, either during emplacement or by post-emplacement erosion.

All of the silicic units outcropping at Goðafjall have been influenced by glacial erosion. Most outcrops are isolated knolls and buttresses rather than continuous flows and a build up of scree has formed a skirt around the unit bases often obscuring any contacts or evidence of glacial unconformities.

The outcrops range in size from less than a few cubic metres to much larger buttresses and ridges up to 500 m in length. Two dominant types of rhyolite lava can be identified in the field, a devitrified aphyric lava with a brown / grey patina and platy habit, which will further be referred to as 'Group One' rhyolite, and a mildly porphyritic obsidian with a waxy lustre and well-developed pale grey flow banding, which will be referred to as 'Group Two'. Both rock types display a range

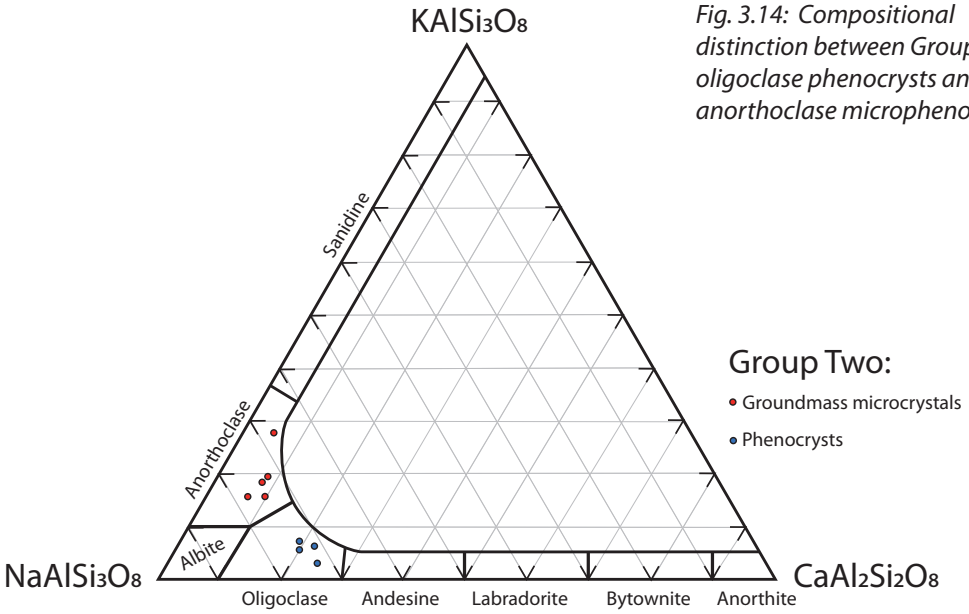

Fig. 3.14: Compositional distinction between Group Two oligoclase phenocrysts and anorthoclase microphenocrysts.

of crossover textures, such as platy zones, glassy obsidian-rich zones and pumice-rich zones and this can often lead to problems with identification in the field. A more comprehensive description of these rock types and their relationships in the field will be covered in chapter 4.

The geochemical dataset represents a range of isolated rhyolitic units located across the field area (fig. 3.1). When the two dominant rhyolite lava types identified in the field are distinguished from each other on the variation diagrams, the trace element data supports the presence of two subtle but distinct groups (fig. 3.13).

A clear distinction between the two rhyolite groups can be seen in concentrations of Nb and Sr, where two separate clusters form for each group, with Group One displaying relatively higher concentrations of both elements than Group Two. Group One concentrations of Nb range from 75.53 - 81.24 ppm compared to 67.23 - 72.32 ppm in Group Two, while Sr ranges from 30.50 - 40.39 ppm in Group One and 43.12 - 50.82 ppm in Group Two. The Group Two rhyolites also form a tight concentration of Y and Rb, while the spread across Group One is wider and displays some overlap with Group Two (fig.3.13). There is no distinction between the two groups in concentrations of Ga, Zn and Zr, although Group One has a much narrower range of Ga while Group Two has a much narrower range of Zn and Zr. It is not possible to distinguish the two groups in concentrations of Ba.

Group Two is more phenocryst-rich than Group One (see section 3.6) and this

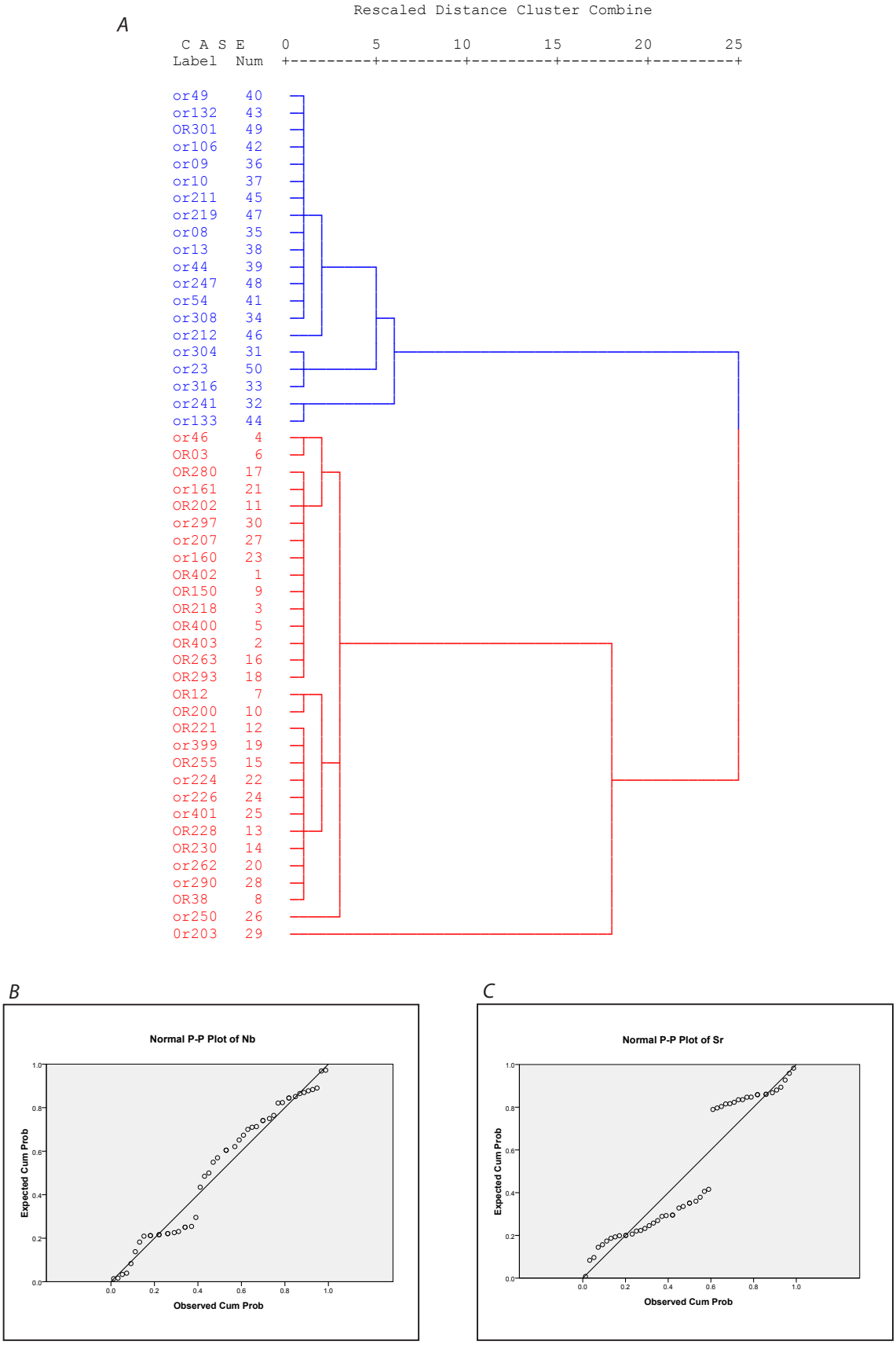

Fig. 3.15: A: Statistical dendgrogram based on division determined by Sr and Nb concentrations; B: P-P plot of Nb concentrations; C: P-P plot of Sr concentrations, showing clear division between the two groups.

may have some influence on trace element distribution. The lower concentrations of Sr in Group Two may be attributed to the substitution of Ca and Na in the crystallisation of plagioclase (Cherniak and Watson, 1994) and K in K-feldspar (Cherniak, 2010); however other trace elements that substitute for K such as Rb and Ba do not show a similar trend in Group Two.

Probe analysis (appendix 5) of Group Two samples reveals that the majority of feldspar phenocrysts are oligoclase plagioclase with > 8 wt % Na_2O (fig. 3.14). Anorthoclase microphenocrysts are only present in the groundmass with 2 - 3 wt% K_2O, therefore it is likely that the lower concentrations of Sr are a result of substitution for Na within the oligoclase plagioclases.

In order to test the robustness of the two dominant geochemical groups identified in this study, the trace element data were analysed with the SPSS statistical package (IBM's SPSS 16.0 for Windows). Hierarchical cluster analysis dendrograms were constructed for Group One and Two samples for all of the trace elements that are present in detectable concentrations (appendix 4). The dendrograms are a graphic representation of the recognised cluster groups, with the sample name listed on the vertical axis and the distance between the grouped clusters on the horizontal axis. The robustness of a cluster is represented by the length of the gap between each group along the horizontal axis. The results support the groupings that were identified in the trace element diagrams, with two dominant clusters identified from Nb and Sr concentrations (fig. 3.15 A). P-P plots show measured distribution of Nb (fig. 3.15 B) and Sr (fig. 3.15C) against what would be expected against a normal distribution; the 45-degree line indicates where the data should plot if it corresponds perfectly to a normal distribution. Figure 3.15 C shows a distinct separation forming two groups away from the 45-degree line. Further statistical analysis of data of other trace elements can be found in appendix 4.

3.6. Rhyolite petrography

Subdivision into two rhyolite groups based upon the trace element concentrations is also mirrored in the petrography and examples of the subtle differences are evident in thin section photomicrographs.

Group One rhyolites

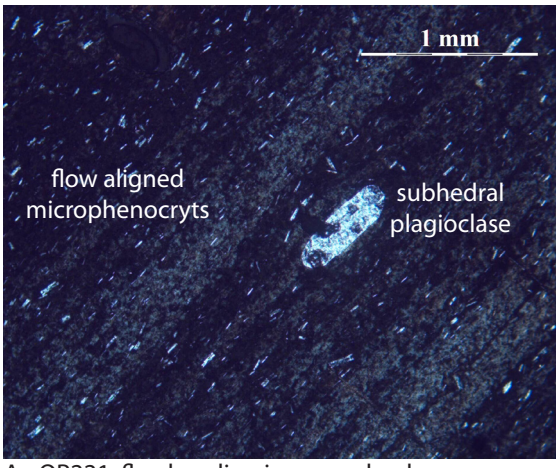

A - OR221: flowbanding in crossed polars

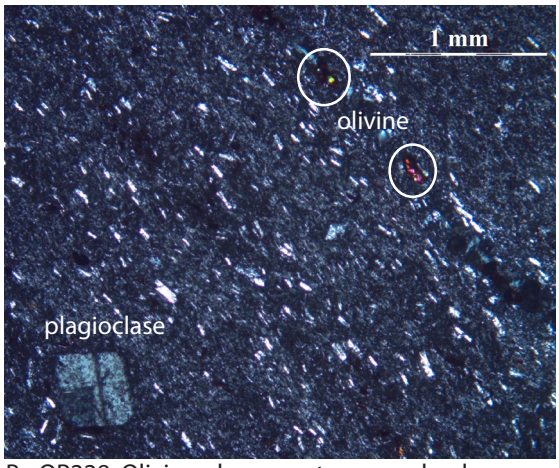

B - OR228: Olivine phenocrysts, crossed polars

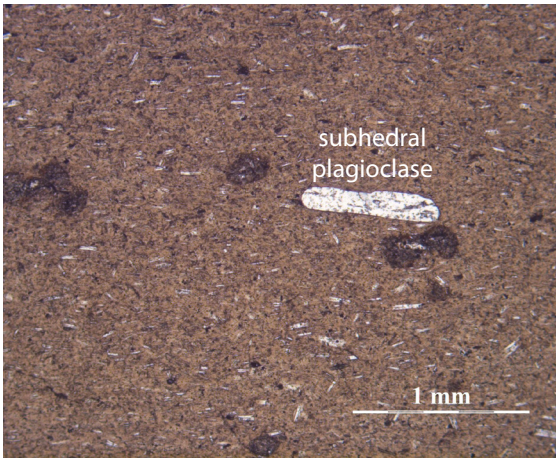

C - OR230: flow aligned microphenocrysts in plain polars

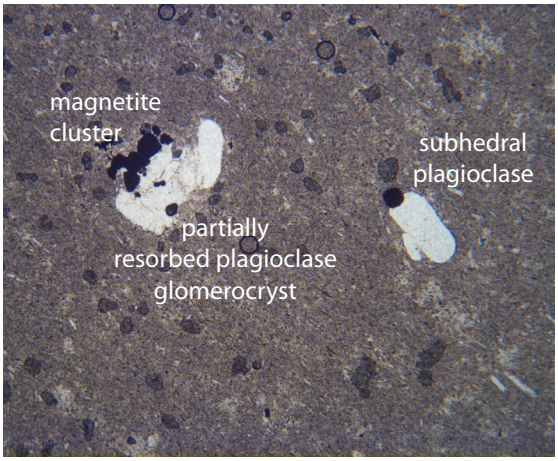

D - OR38: magnetite and plagioclase, plain polars

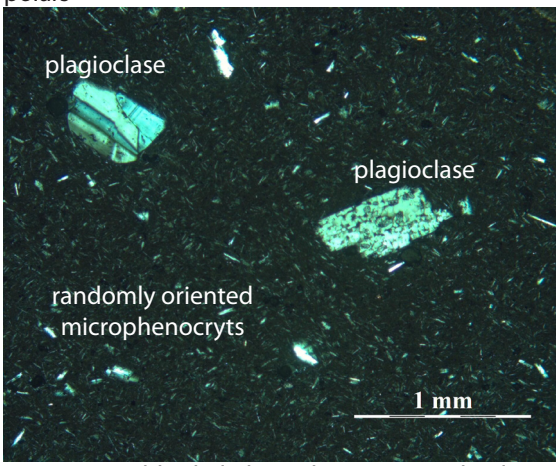

E - OR255: subhedral plagioclase in crossed polars

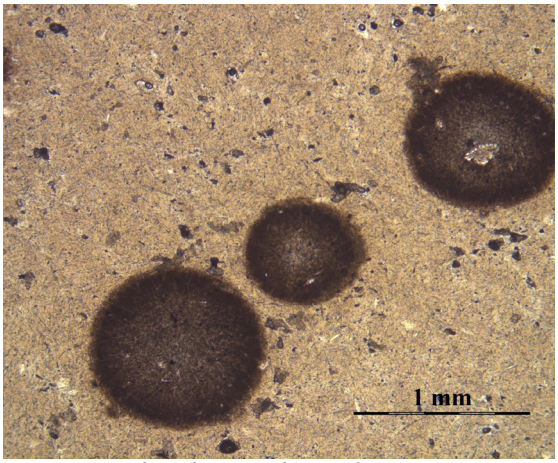

F - OR255: spherulites in plain polars

Figs. 3.16 A to F: A selection of photomicrographs of Group One rhyolites demonstrating the group's typical phenocryst assemblage and petrological similarities between samples. A to D feature a glassy groundmass with abundant flow aligned microphenocrysts, while E and F display a less-common randomly oriented groundmass. Spherulites (fig. F) are often found in zones within otherwise aphyric lavas.

Group Two rhyolites

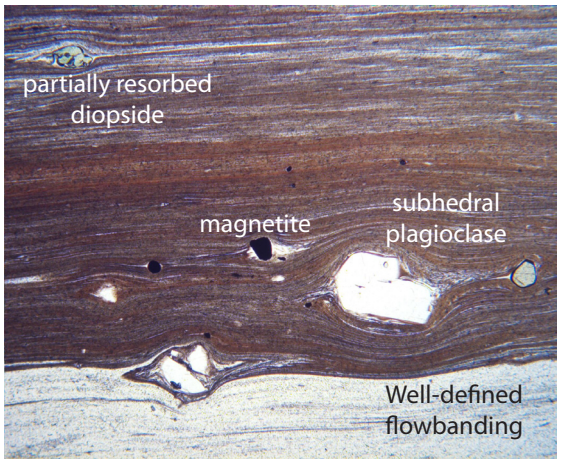

A - OR10: flowbanding in plain polars

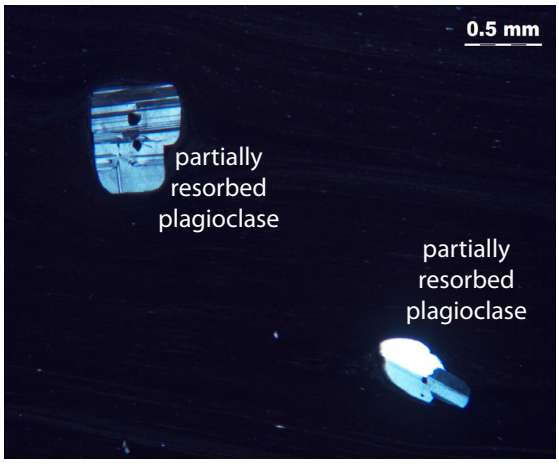

B - OR10: crossed polars

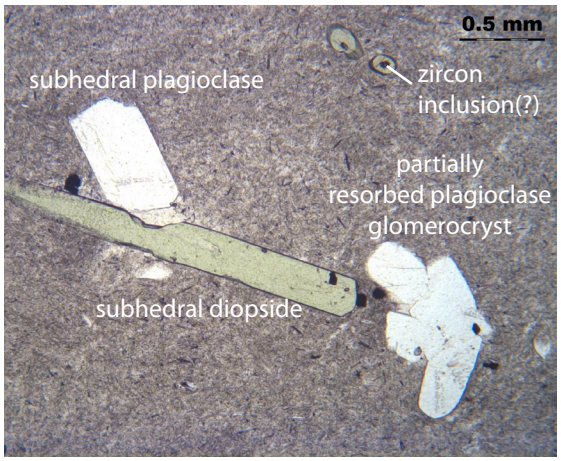

C - OR54: Plagioglase and diopside in plain polars with zircon inclusions

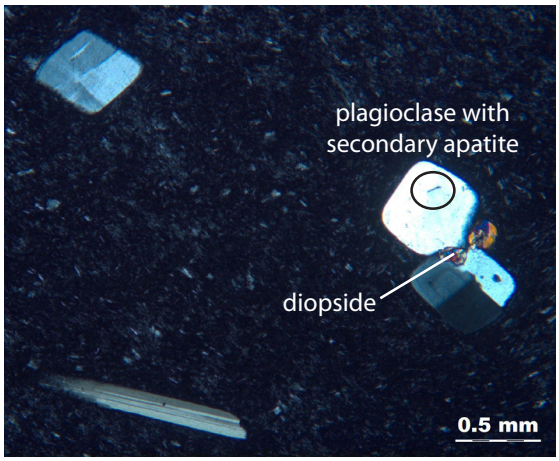

D - OR54: Apatite needle within plagioglase, crossed polars

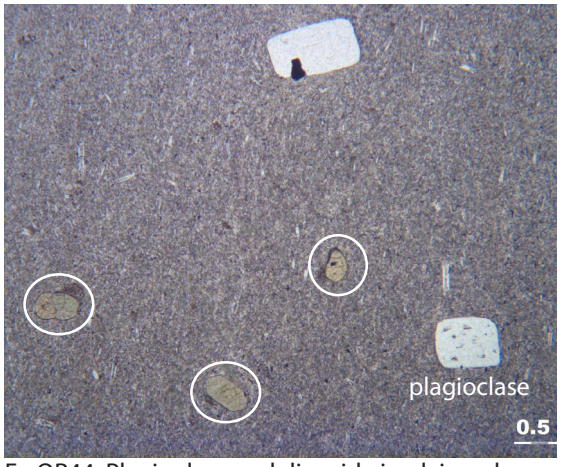

E - OR44: Plagioglase and diopside in plain polars

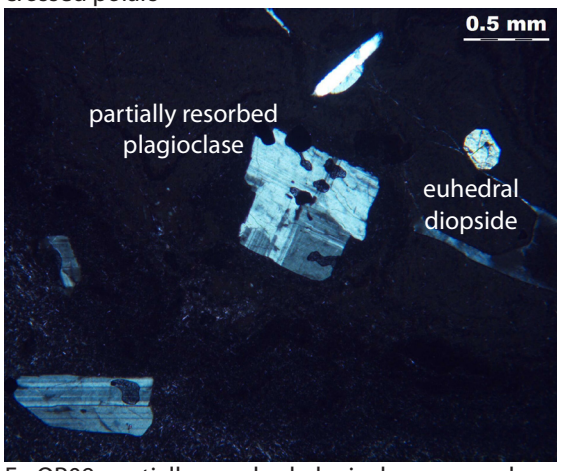

F - OR09: partially resorbed plagioclase, crossed polars

Figs. 3.17 A to F: A selection of photomicrographs of Group Two rhyolites demonstrating the group's typical phenocryst assemblage and petrological similarities between samples. Well-defined flow banding (fig A) flows around the plagioclase and pyroxene phenocrysts. The majority of phenocrysts in Group Two lavas are subhedral and display resorption features such as partial intergrowths and scalloped edges (fig. F)

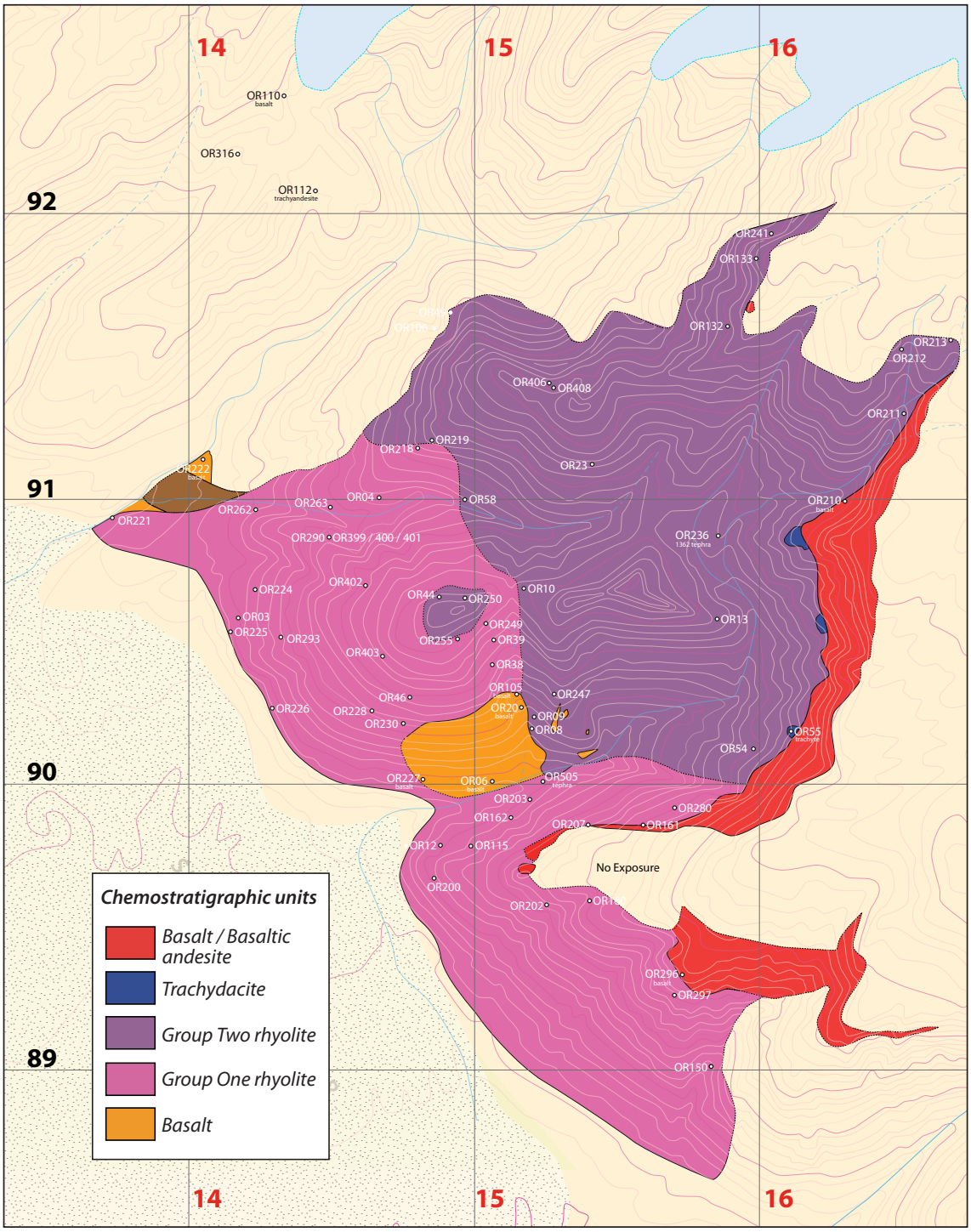

Fig. 3.18: Map indicating extent of chemostratigraphic groups within the Goðafjall and Hrútsfjall area highlighting two main rhyolite groups along with basement basalts, trachydacites and Quaternary basalts .

Group One

The Group One rhyolite lavas (figs. 3.16: A to F) are typically fine-grained with 1 to 2% phenocrysts and a glassy groundmass with abundant microphenocrysts. The typical Group One assemblage is plagioclase (oligoclase) + magnetite +

olivine + anorthoclase + quartz. Plagioclase phenocrysts are between 0.5 and 1mm in diameter and display either simple or multiple twinning. The majority of phenocrysts are subhedral to sub-rounded, although occasional euhedral phenocrysts are present.

Many of the plagioclases are embayed and display sieve textures and secondary internal crystal growth (fig. 3.16E). Sparse olivine phenocrysts up to 0.2 mm in diameter are also present. Anorthoclase and quartz are only present as microphenocrysts within the groundmass. The microphenocrysts consist of small needles which are usually flow aligned (fig. 3.16: A to E) although some Group One samples display a more randomly oriented groundmass (fig. 3.16: D).

Group Two

The Group Two rhyolite lavas (figs. 3.17: A to F) are more phenocryst-rich with 2 to 5% phenocrysts within a glassy groundmass. The typical Group Two assemblage is plagioclase (oligoclase) + augite + magnetite + zircon (?) + apatite (?) + anorthoclase. The plagioclase phenocrysts are up to 1 mm in diameter, subhedral to sub-rounded and some contain glass inclusions and secondary crystal growth (fig.3.17F). Augite phenocrysts are euhedral to sub-rounded and range between 0.2 to 1.5 mm in diameter (fig. 3.17C). Glomerocrysts of plagioclase, augite and magnetite are also occasionally present. Small, high-relief inclusions occasionally present within the augite and plagioclase may be zircon (fig.3.17C), along with occasional small low-relief acicular phenocrysts present within the plagioclase which may be apatite (fig. 3.16D). Anorthoclase is only present as acicular microphenocrysts within the groundmass. The glassy groundmass ranges from samples displaying very pronounced flowbanding with strongly defined dark and light zones (fig. 3.17A), to samples with randomly-oriented microphenocrysts (fig. 3.17D).

3.7. Summary

This chapter has demonstrated the application of chemostratigraphy as an aid to the identification of physically-separated, contemporaneously-erupted units.

Two dominant rhyolite groups within the Goðafjall area (fig. 3.17) have been identified with the aid of this application, which has enabled the production of a chemostratigraphic map marking the extent and coverage of the individual units across the field area.

The geomorphology and emplacement evironment of the two dominant units, alongside other smaller units, will be discussed further in chapter four.

Chapter 4
Lithology and field relationships of the Goðafjall and Hrútsfjall area, S.W. Öræfajökull

4.1. Introduction

This chapter describes the volcanic geology of the south-western flank of Öræfajökull, a region where topography has been heavily influenced by glacial erosion (Helgason and Duncan, 2001). The field area covers approximately 10 km^2 and contains one of the most prominent rhyolitic exposures on the otherwise basalt-dominated flanks of Öræfajökull (Prestvik, 1985). In addition to the rhyolitic rocks, there are extensive exposures of mafic and intermediate rocks.

The field area is dominated by Goðafjall and Hrútsfjall (fig. 4.1), which are two adjacent and parallel rhyolite ridges aligned south-west to north-east. The ridges are separated by an un-named v-shaped valley which will be referred to by the informal name of the Hrútsfjall stream valley (fig. 4.2). The two ridge crests rise to a maximum elevation of 653 m.a.s.l. from the sandur plain at around 100 m.a.s.l.

Both ridges have been constructed by multiple rhyolite eruptions, which overlie mafic sheet flows and volcaniclastic deposits. The rhyolitic outcrops that form the summit crests of both ridges have been heavily eroded causing the lower slopes to be dominated by locally-derived talus, through which isolated outcrops protrude.

As previously discussed in chapter 3, chemostratigraphy has been used to identify contemporaneously erupted but physically separated units, which has resulted in three major geochemically distinct silicic units (two rhyolitic and one intermediate) being identified. Generally, this division is corroborated by field observations, however a complication of the glaciovolcanic eruptive environment is that one eruptive unit can produce a wide variety of lithofacies that display a range of morphologies and textures. There are some instances where geochemical distinctions are not corroborated by field relationships; therefore it is important to document the character-

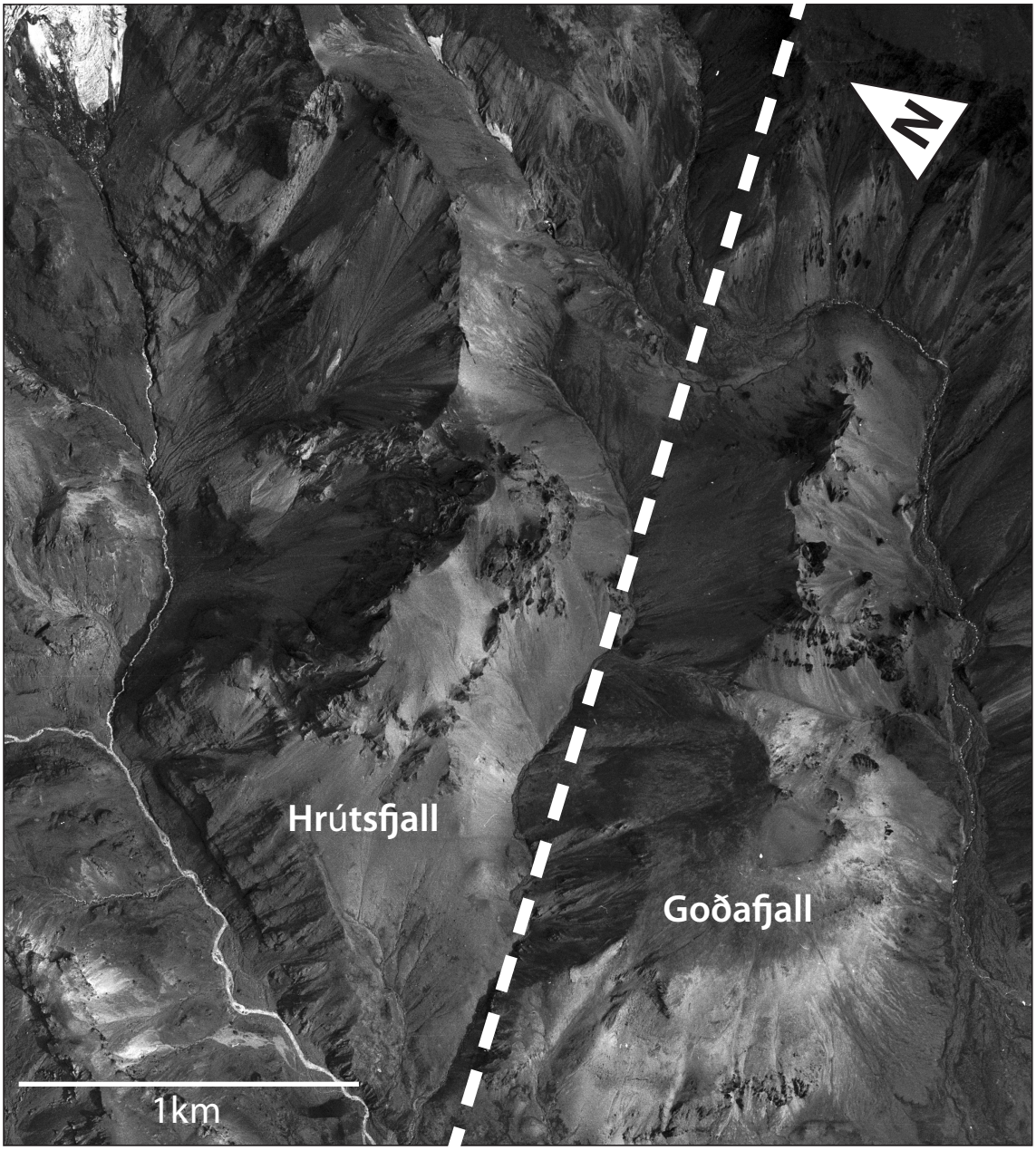

Fig. 4.1. Aerial photograph of Hrútsfjall (left) and Goðafjall ridges.

istics of the lithologies present in the field area.

Table 4.1 gives a summary of each lithology present, listing its corresponding geochemical unit and its distribution across the field area. As the focus of this research centres on rhyolite volcanism, emphasis has been placed on the description and interpretation of rhyolitic lithofacies within the field area. Mafic and intermediate lithofacies that have a direct field relationship with the rhyolite lithofacies are also discussed in order to help reconstruct a more complete palaeoenvironmental history of the area, but are not covered in the same detail.

As part of this study, the research area was mapped at 1:10 000 scale with the aid

Table 4.1 # Lithofacies present at Goðafjall and Hrútsfjall

Geochemical unit	Lithofacies	Distribution	Description	Interpretation
Mafic	A	Basal unit of Goðafjall and Entrance to HVG valley; basal unit of Slaga formation	Stacked lava sequences gently dipping towards north west	Stacked subaerial lava sheets
Mafic / mixed	B	North West facing lower wall of Kotá river valley	Stacked lava sequences, tuff breccia, polymict diamict	Successive subaerial lavas/ subglacial hyaloclastites
Mafic	BA	Mid-section of North West facing lower wall of Kotá river valley; Slaga	Laminated tuff	Glacio-lacustrine, ice marginal sediments
Silicic - Lower rhyolite	C	RHS of valley entrance to HVG	Columnar jointed lava lobe	water-saturated rhyolite
	D	Comprises majority of Goðafjall edifice; lower elevations of Hrútsfjall and lower HVG valley, south-facing slopes of HVG plateau	Microcrystalline 'platy' rhyolite with glassy obsidian and spherulitic and pumiceous zones	Subaerial rhyolite flows / domes
	E	Mid to upper south-facing slopes of Goðafjall; Mid to upper slopes of south-facing HVG Plateau	Clast-supported rhyolite breccia	Subaerial rhyolite flows
	F	West-facing slope of Goðafjall West	Slope-draping platy rhyolite with brecciated base	Subaerial rhyolite flows
Silicic - Upper rhyolite	G (mLT)	NW facing slope on RHS of valley entrance to HVG	Pumice ash breccia tuff	Ice confined rhyolite tephra
	H (mLT)	NW and SE facing slopes of upper Hrútsfjall; NW and SE facing slopes of col between Goðafjall West and East; Cirque; Upper HGV valley	Massive, poorly sorted pumice obsidian breccia	Ice confined rhyolite tephra
	I (dsLT)	Mid section of South East facing slope of Hrútsfjall	Diffusely stratified lapilli tuff	Ice confined rhyolite tephra
	J	Mid to upper section of North west facing slope of Hrútsfjall	Massive poorly sorted pumice breccia	Ice confined rhyolite tephra
	K	South East facing slope of Hrútsfjall	Vesicular rhyolite dyke	Feeder dyke for lithofacies L
	L	Comprises majority of Goðafjall East, Cirque and Upper HVG valley; summit of Goðafjall West; Upper elevations of Hrútsfjall;	Columnar jointed, flow banded microcrystalline rhyolite with zones of obsidian and spherulite	Subglacial / ice confined rhyolite flows and domes
Sedimentary	M	Mid section of southwest facing slope of cirque	Stratified pumice rich sandstione with cross-stratification	Epiclastic - reworked rhyolite volcaniclastic sediments
Intermediate	N	Upper elevations of North west facing slope of HVG valley; upper elevations of south west facing slope of cirque	Glassy columnar jointed lobes with slope draping orientation	Subglacial 'sill'
Mafic	O	Upper Hrútsfjall; upper HVG Valley; upper HVG plateau	Sub-horizontal lava sheets,	Subaerial / ice marginal flows
Mafic	P	Eastern wall HVG; HVG Plateau	Granular fragmental basalt and lava intrusions	Volcaniclastic sediments
Sedimentary	Q	Eastern wall HVG; HVG Plateau	Diamict	Glacial sediments
Mafic	R	Eastern wall HVG; HVG Plateau	Slope draping tuff	Tuff cone deposits

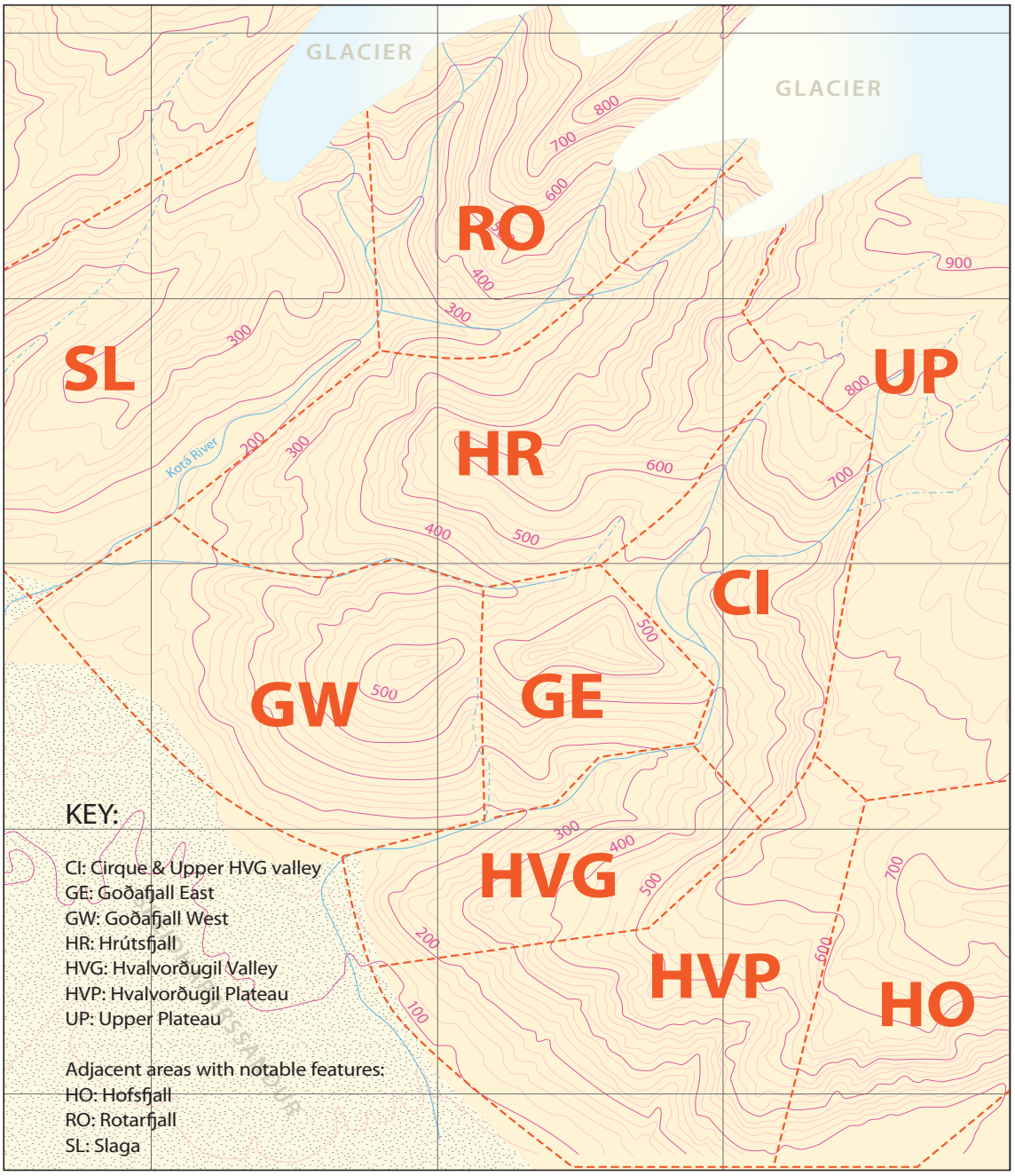

Fig. 4.3. Area zones

of enlarged 1:50 000 topographic maps. The lithologies described in this chapter relate to corresponding units on the map (supplementary map). The lithofacies are listed in order of age, from the oldest to the youngest, each will be described in detail and the field characteristics will then be used to interpret the emplacement style and eruptive environment.

In order to aid discussion and interpretation, the field area has been sub-divided into seven smaller areas (fig. 4.3), as follows, from upper elevation (> 800 m) to lower elevation (100 m): Upper Öræfajökull Plateau (UP); Cirque & Upper Hval-

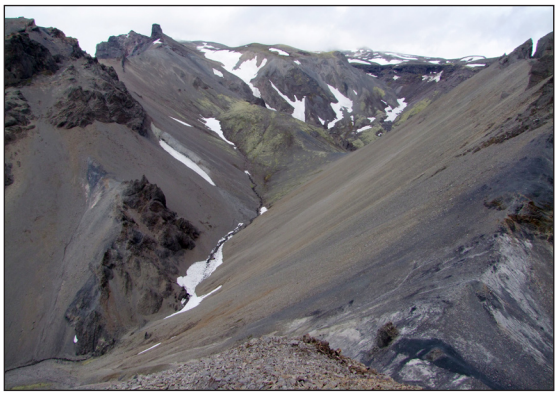

Fig. 4.2. Hrútsfjall stream, separating Hrútsfjall ridge (left) from Goðafjall ridge, looking north east.

Fig. 4.4. Cirque located to the north east of Goðafjall ridge (left), looking south west.

vorðugil valley (CI); Hrútsfjall (HR); Goðafjall West (GW); Goðafjall East (GE); Hvalvorðugil Valley (HVG); Hvalvorðugil Plateau (HVP). Three adjoining areas which exhibit notable features have also been included: Hofsfell (HO); Rotarfjall (RO); and Slaga (SL).

Before each lithofacies is described in detail, a brief overview of the seven main areas and the features of each are presented below and shown in figure 4.3.

4.1.1. Upper Öræfajökull Plateau (UP) overview

The gently sloping upper plateau is exposed below the glacier summer snowline, which is currently above an elevation of 880m. The plateau is dominated by hummocky blankets of till, Pleistocene and Holocene lava flows (Lithofacies O and P), and tephra deposits from the 1362 rhyolitic eruption which are concentrated in topographic depressions. The plateau is incised by a number of glacial streams, some of which converge to form the streams that flow through the Hrútsfjall and Hvalvorðugil valleys. The upper surfaces of a number of the lava flows are smoothed and striated by glacial activity. Silicic lavas do not outcrop on the plateau.

4.1.2. Upper Hvalvorðugil Valley and Cirque (CI) overview

The upper Hvalvorðugil stream and the upper Hrútsfjall stream, along with a number of small tributaries, flow down from the plateau, incising the till-covered upper slopes of Öræfajökull and converging at the base of a large (>50 m) rhyolitic

dome composed of lobes of columnar jointed rhyolite (Lithofacies L) .Where the streams converge, a glacially-carved cirque (fig. 4.4) has been formed at the eastern terminus of the current day Goðafjall ridge at an elevation of 438 m. Within the cirque, further downstream the two streams diverge again, forming the incised stream valleys that separate Hrútsfjall ridge, Goðafjall ridge and the Hvalvorðugil plateau on the lower flanks of the volcano.

The large, columnar-jointed outcrop dominates the northern section of the cirque, while the remaining scree-covered slopes that make up the surrounding walls of the cirque are punctuated by smaller lobes and angular knolls of columnar jointed rhyolite (Lithofacies L). To the east of the large columnar jointed outcrop, separated by the Hvalvorðugil stream, the rhyolite-dominated north-western facing slopes of the upper Hvalvorðugil valley are capped with subaerial basalt lava flows (Lithofacies O, P). These slopes form the south-eastern walls of the cirque and curve around to the south west to form the south western facing flank of the Hvalvorðugil valley, which curves again further downstream toward the west. The slopes are punctuated with angular knolls of columnar jointed lobes (Lithofacies L), a group of which are crosscut by two mafic dykes. The dykes can be traced across the Hvalvorðugil stream to the North West facing slopes of Goðafjall East.

4.1.3. Hrútsfjall (HR) overview

Hrútsfjall ridge is the most northerly (fig. 4.3) of the two ridges featured in the mapping area. The north facing slopes of the ridge form the glacially-carved Kotá river valley, adjacent to Slaga – a smaller, predominantly mafic, ridge situated to the North East of Hrútsfjall (fig. 4.2). The lower northern flanks of Hrútsfjall comprise sheer-sided cliffs, predominantly made up of polymict conglomerate (glacial till deposits), basalt lavas and fragmental deposits. Access to the lower north facing slopes of Hrútsfjall is limited due to a fast-flowing, deep water stream originating from the current day glacier tongue which is situated at the head of the valley.

The upper northern slopes of Hrútsfjall (fig. 4.5) are capped by a large columnar jointed rhyolite exposure (Lithofacies L) comprising composite lobes, the base of which sits unconformably upon basalt at an elevation of 426 m (Map grid Ref:

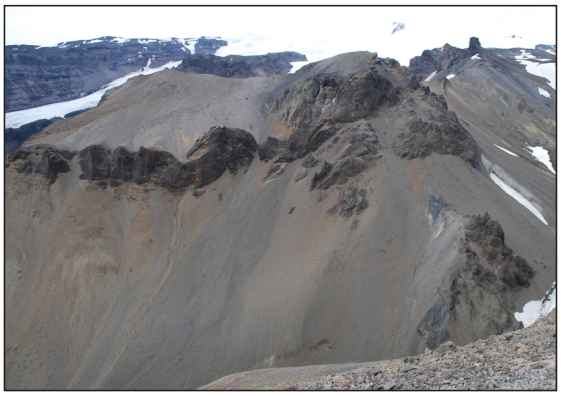

Fig. 4.5. Hrutsfjall Ridge looking north from Goðafjall Ridge West.

Fig. 4.6. Goðafjall Ridge West, looking north west from Hvalvorðugil Valley.

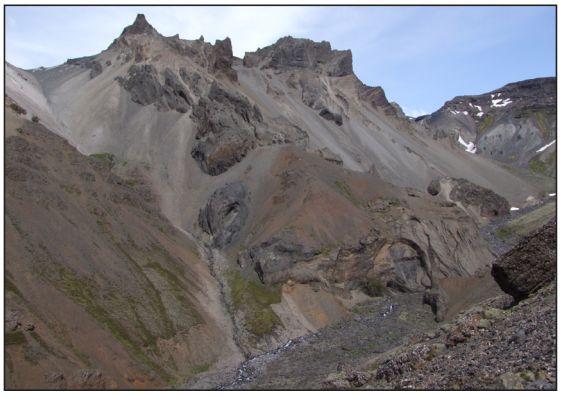

Fig. 4.7. Goðafjall Ridge East, looking north from Hvalvorðugil Valley.

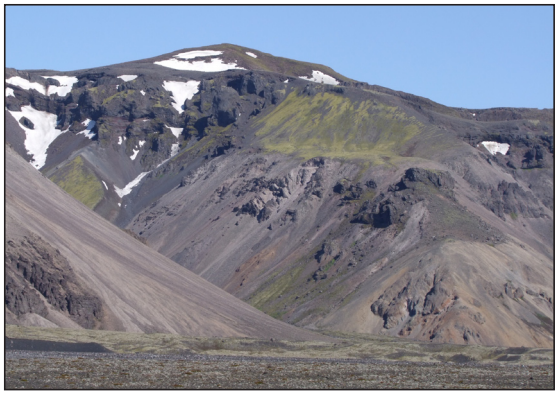

Fig. 4.8. Hvalvorðugil Valley and plateau, looking north east from the sandur, with Hofsfjall tuff cone in the background.

0414863/7091616). The unit forms a discontinuous capping ridge, approximately 600 m along the summit of Hrútsfjall. At a higher elevation on the upper south facing slopes, a poorly consolidated, massive pumice rich tuff (Lithofacies J is exposed below the columnar jointed lobes.

The south facing slopes, opposite Goðafjall, are predominantly scree-covered with isolated outcrops of platy rhyolite (Lithofacies D) occurring at lower elevations. The platy rhyolites have been dissected by the course of an unnamed tributary stream that flows into the river, from hereon referred to as the Hrútsfjall stream, and match up with similar units at the base of Goðafjall West. The lower south-facing slopes are crosscut by a vesicular rhyolite dyke (Lithofacies K). Further upstream in the Hrútsfjall valley, slope parallel columnar-jointed lobes (Lithofacies L) sit upon the south facing flank and appear to be aligned with columnar jointed units at the base of the adjacent north-facing slopes of Goðafjall East (Lithofacies L). An isolated outcrop of diffusely bedded, poorly consolidated tuff (Lithofacies I) is exposed in a gully adjacent to the slope-parallel lobes.

4.1.4. Goðafjall West (GW) overview

Goðafjall West (fig. 4.6) has a height of 560 m and a conical shaped aspect. On its south facing flank, from stream level to an elevation of 315 m, the base of the structure comprises layered units of block jointed basalt lavas (Lithofacies B), dipping into slope to the North, between 20 to 30°. The exposed faces are stained brown (presumably due to oxidisation) and the rock itself is very fissile probably as a result of prolonged weathering exploiting the pervasive joint system.

The basalt lavas are unconformably overlain by a number of discontinuous rhyolite outcrops with a platy habit (Lithofacies D). The outcrops have been subject to much erosion and are now surrounded by locally eroded, loose scree which drapes the flanks of Goðafjall West. In areas, the platy nature of the rhyolite is interrupted by lenses of obsidian, which is often spherulitic. A number of south west-facing outcrops are brecciated and comprise orange micro-vesicular rhyolite (Lithofacies E) interbedded with flow-banded obsidian and spherulitic obsidian.

Unlike the lower units, the outcropping unit at the summit of Goðafjall West is sparsely porphyritic (Lithofacies J). This difference is corroborated by geochemical analysis which indicates that the summit outcrop has a different chemistry (geochemical Group Two) to that of the lower units (geochemical Group One (see chapter 3). Due to a blanket of locally derived scree, any contact between the two geochemically distinct rhyolite types is not identifiable in the field, but can be inferred to be present above an elevation of 458 m.

4.1.5. Goðafjall East (GE) overview

Goðafjall East has a height of 614 m and is separated from Goðafjall West by NE-SW facing gullies which bisect the Goðafjall ridge, creating a col, at a height of 483 m (fig. 4.7). A tributary stream of the HVG river breaks through the gully mid-slope. The col is dominated by a poorly consolidated obsidian-rich pumice ash breccia (Lithofacies H), which grades into very well-preserved, large exposures of glassy, columnar jointed, porphyritic, flow banded rhyolite (Lithofacies J), which form both the capping ridge to Goðafjall East, and also slope-parallel lobes with

radially oriented columnar joints that outcrop on the south facing flank (fig. 4.6). At a lower elevation, the lobes sit unconformably upon block jointed, aphyric microcrystalline basalt lavas (Lithofacies A). The north facing flank of Goðafjall east is a relatively featureless scree covered slope, with minor lobes of columnar joined rhyolite outcropping at stream level (Lithofacies L).

4.1.6. Hvalvorðugil valley (HVG) overview

Hvalvorðugil valley (fig. 4.8) cuts through the columnar jointed rhyolites from the cirque down to the sandur plain, separating Goðafjall ridge from the Hvalvorðugil plateau. The upper north-west facing flanks of the valley wall are dominated by isolated outcrops of columnar jointed flow banded rhyolite (Lithofacies L) which are unconformably overlain by a number of slope-parallel columnar jointed intermediate lobes (Lithofacies N). Downstream the lower north-west facing flanks are dominated by platy rhyolites (Lithofacies D) that are crosscut by NE-SW trending mafic dykes which may be a continuation of the dykes that crosscut the cirque and Goðafjall East.

The rhyolites and intermediate lavas on the eastern HVG valley wall are capped by two extrusive sequences (Lithofacies O and P) comprising a stratigraphically lower sequence of sub-horizontal mafic lavas and a younger sequence of breccias and lava lobes. The uneven exposed surface of the lava sequence is largely obscured by alluvium containinng faceted cobbles and boulders that are assumed to be glacial in derivation. Where the lava surface is exposed, it is glacially smoothed and striated.

The entrance to the valley from stream level to an elevation of 345 m is dominated by an outcrop of columnar jointed, composite rhyolite lobes (Lithofacies C). The lobes are overlain by mafic units which are a continuation of lithofacies O and P.

4.1.7. Hvalvorðugil plateau (HVP) overview

Hvalvorðugil plateau (fig. 4.8) is a gently sloping, undulating, plateau sitting above steep-sided scree-covered slopes that rise up from the sandur. The slopes are punctuated by discontinuous angular knolls and buttresses of silicic platy lavas which

continue from the north-west facing slopes of Hvalvorðugil valley, along the south facing plateau slopes, to a gully behind the village of Litla Hof, which marks the eastern lateral extent of the rhyolite exposures. The plateau itself is dominated by basalt lavas and fragmental deposits (Lithofacies O, P), alongside glacial diamictites and epiclastic deposits (lithofacies M).

Situated to the east of the plateau, approximately 1.8 km east of the entrance to Hvalvorðugil valley, is the tuff cone Hofsfjall – outcropping at 750 m.a.s.l. Well-stratified tuff cone deposits dominate the southern extent of the plateau. Distal deposits displaying evidence of re-working (Lithofacies Q) partially drape the capping lavas of HVG toward the entrance to the valley.

4.2. Lithofacies Descriptions

Apart from a small number of exceptions, most of the lithofacies described are present across more than one of the seven areas previously described. Key textural features of each lithofacies are described in terms of their location within one of the seven areas. The accompanying geological map (separate map) shows the extent of each lithofacies.

4.2.1. Lithofacies A: Mafic sheet lavas

Description

This lithofacies (figs. 4A1 - A4) outcrops along the base of the south-facing flanks of Goðafjall West and East and is exposed from stream level in the HVG valley (100 m elevation), up to an elevation of 317 m. Similar outcrops are also present at the base of the south-facing flank of Slaga Plateau. Lithofacies A comprises a succession of stacked mafic units ranging from 400 mm to over 4 m in thickness (fig. 4. A1).

At stream level the outcrop exposure is irregular but higher up in the sequence at least 10 laterally continuous stacked units are exposed on the north-facing slope of Goðafjall (fig. 4.A2). Lateral continuation can be traced over distances ranging from less than 10 m to over 100 m. The unit contacts are not directly exposed, however

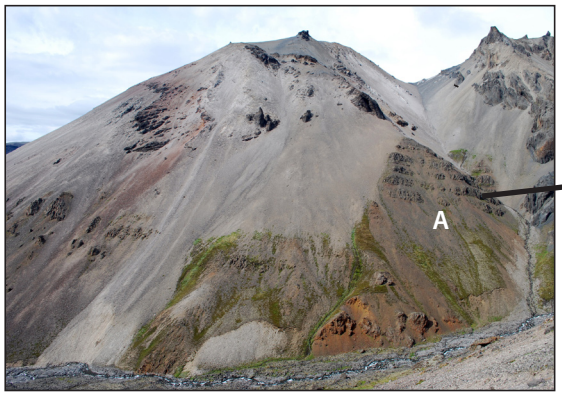

Fig. 4. A1. Lithofacies A basalts at Goðafjall Ridge West, looking north west from Hvalvorðugil Valley.

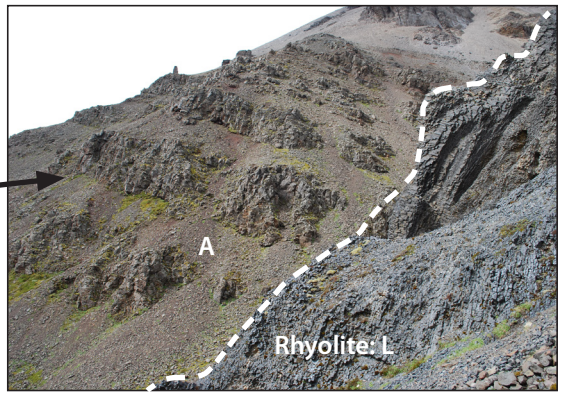

Fig. 4. A2. Continuous units of Lithofacies A, looking south from Goðafjall East.

Fig. 4. A3. Vesicles and amygdales in lower units of lithofacies A. Lens cap is 70 mm in diameter

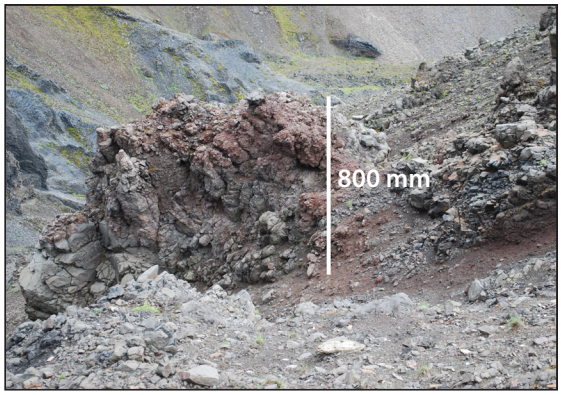

Fig. 4. A4. Red brecciated upper surface of uppermost basalt unit in Lithofacies A.

their position can be inferred by sloping ramps filled with rubbly talus between each lava sheet.

The stacked units dip uniformly at an angle between 10 and 20˚ to the north west into the north-facing slope of Goðafjall West (Fig. 4. A1). The basalt is weathered and oxidised orange with the exposed faces highly fractured especially at lower elevations (fig. 4. A2), in contrast fresh surfaces are mid to dark reddish grey. At lower elevations the units are porphyritic, displaying white weathered feldspar phenocrysts up to 3 mm but these appear to be less abundant in successive sheets. XRF analysis confirms the lava composition as tholeiitic basalt (chapter 3: sample OR06 and OR20).

Some of the units are massive while others exhibit fine sub-horizontal, planar foliations approximately 30-50 mm in thickness (fig. 4. A2). The units toward the top of the succession have an oxidised, brecciated upper surface (Fig. 4. A4).

Zones of vesiculation are present in some units, which often become more pronounced towards the top of the unit. The vesicles are spherical in some areas with

a diameters ranging from < 1 mm to 7 mm, and elongated in others, ranging from approximately 1 mm to 80 mm in length. There are also occasional zeolites within the vesicle cavities (Fig. 4. A3).

Lithofacies A: Interpretation

The stacked units are the product of repeated episodes of subaerial basalt volcanism, as indicated by the presence of irregular, oxidised, brecciated upper surfaces on the units at higher elevations within the succession and also by the presence of brecciated material between each sheet at lower elevations.

The laterally continuous nature of the units suggests that they were emplaced as sheet lava flows that were laid down in succession, perhaps over long periods of time. Planar foliations present in some of the units are indicators of flow orientation.

The presence of zeolites within the units at lower elevations indicate very low grade metamorphism associated with compaction and shallow burial at the base of a thickening lava pile (Walker, 1960).

The uniform angle of dip suggests that the succession was most likely emplaced horizontally, but later deformed by subsequent burial and uplift due to glacial loading and post-glacial rebound, resulting in the present-day gentle dip toward the north west. This local dip direction is similar to the overall regional dip toward the west which is seen throughout other pre-Quaternary basalt sequences in the East of Iceland (Sigmundsson, 1991).

Although palaeomagnetic studies of lithofacies A have not been carried out, field evidence and radiometric dating (chapter 5) suggest that it pre-dates the main, normally magnetized, edifice of Öræfajökull and may be part of a much older Tertiary basement sequence. Prestvik (1979) describes slightly altered aphyric basalt lavas in the south western section of neighbouring Slaga with reversed magnetic polarity and similar stacked sheet flows displaying reverse magnetization commonly outcrop at lower elevations of the southern and south eastern flanks of Öræfajökull, including Skaftafell, where stacked sequences at Hafrafell have been dated to 3.94 Ma (Helgason, 2007).

4.2.2. Lithofacies B: Basalt lavas, fragmental deposits and polymict conglomerates

Description

Lithofacies B collectively covers all outcropping rocks comprising the eastern Kotá river valley wall that forms the north-west boundary of Hrútsfjall ridge (fig. 4.B1). It is approximately 300 m in height and the very steep slopes make the exposure inaccessible from river level to the base of Lithofacies K at an elevation of 430 m.a.s.l. Due to the lack of direct access, mapping of this exposure was mostly carried-out from the adjacent valley slopes at Slaga using binoculars and therefore represents a broad overview of the main features in order to construct an interpretation of possible palaeoenvironmental setting.

The steep sides of the valley have been stripped away to reveal a stacked succession of eroded, laterally discontinuous units of subhorizontal basalt lavas, well bedded, crudely bedded and massive fragmental deposits, and polymict conglomerates. The layer cake stratigraphy has been partially overlain by a fragmental volcaniclastic drape with a pervasive orange fabric containing irregular lenses of columnar jointed lava.

The conglomerates have previously been mapped by Prestvik (1979) as tillite horizons, assuming a glacial depositional environment. Two prominent horizons are accessible at the base of the succession and towards the top. The lower horizon is exposed in discontinuous lenses at river level and overlain by fragmental volcaniclastic deposits, while the upper conglomerate is exposed toward the top of the succession (fig. 4. B2)

Some of the discontinuous subhorizontal lava sheets are interbedded with bright red horizons, while other subhorizontal units include massive tuffs. A thin, partially exposed layer of very well-bedded breccia can be traced at an elevation of around 300 m and has been described separately as sub-lithofacies BA. Large sections of the subhorizontal layered succession are overlain by steeply draping fragmental volcaniclastic deposits that appear to be 'adhered' to the sides of the slopes at an angle steeper than repose (fig. 4. B1). Occasional lenses of columnar joined lava with curved columnar joints are dispersed throughout the fragmental deposit.

Lithofacies B: Interpretation

Collectively lithofacies B (fig. 4.B1) is interpreted as a combination of subhorizontal sheet lavas and lapilli tuffs with lava intrusions, interlayered with polymict conglomerates which were originally identified by Prestvik (1978) which have built up successively over time and have been revealed in a layer cake stratigraphy as a result of glacial erosion. The succession records changes within the depositional environment, featuring both subaerially and subglacially emplaced lavas interbedded with what may be red paleosol horizons and fragmental deposits, along with at least two polymict conglomerates at the base and top of the succession.

The interpretation of polymict conglomerates in Iceland can be problematic due to the similarity of units from different depositional environments, and the similarities in the volcanic source rock (Loughlin, 2000). However the presence of cobble sized faceted clasts within the visible upper (fig. 4. B2) and lower conglomerated beds corroborate Prestvik's (1978) initial interpretation of tillite horizons.

The subhorizontal stacking lavas have been later draped by massive lapilli tuffs and breccias which are interpreted as reworked hyaloclastites. The very steep angle of repose suggests that the tuffs formed by fragmental deposits flowing down into the interface between the valley glacier and the valley walls. The hot volcaniclastic deposits would further melt the ice at the bedrock-ice interface to allow the hyaloclastite to be cooled in place against a very steep slope (fig. 4 B1). The pervasive orange colouring is indicative of palagonatisation which has cemented the draped unit on to the face of the underlying rocks. The occasional columnar jointed lenses within the fragmental deposits are interpreted as coeval lava intrusions.

4.2.3. Sub-lithofacies BA: Ice marginal glaciolacustrine sediments

Description

Sub-lithofacies BA (figs. 4. BA1 - BA6) is exposed at an elevation of around 300 m.a.s.l on the mid section of the slopes of the eastern wall of the Kotá river valley (fig. 4. BA1) that have been collectively described above as lithofacies B. Due to its distinct appearance sub-lithofacies BA has been described and interpreted separately

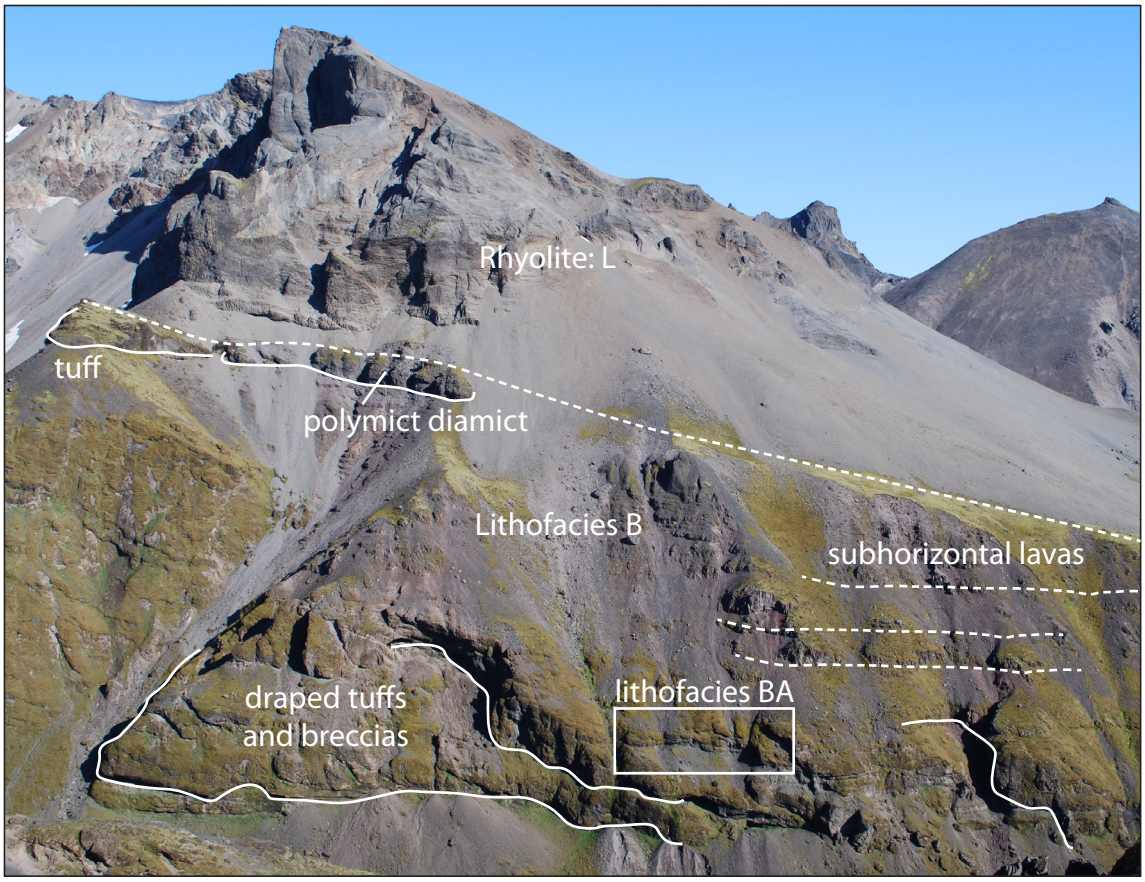

Fig. 4. B1: Well bedded, continuous stratified tuff layers sit unconformably on thin diamict layer and volcaniclastic sediments (access limited to lower beds).

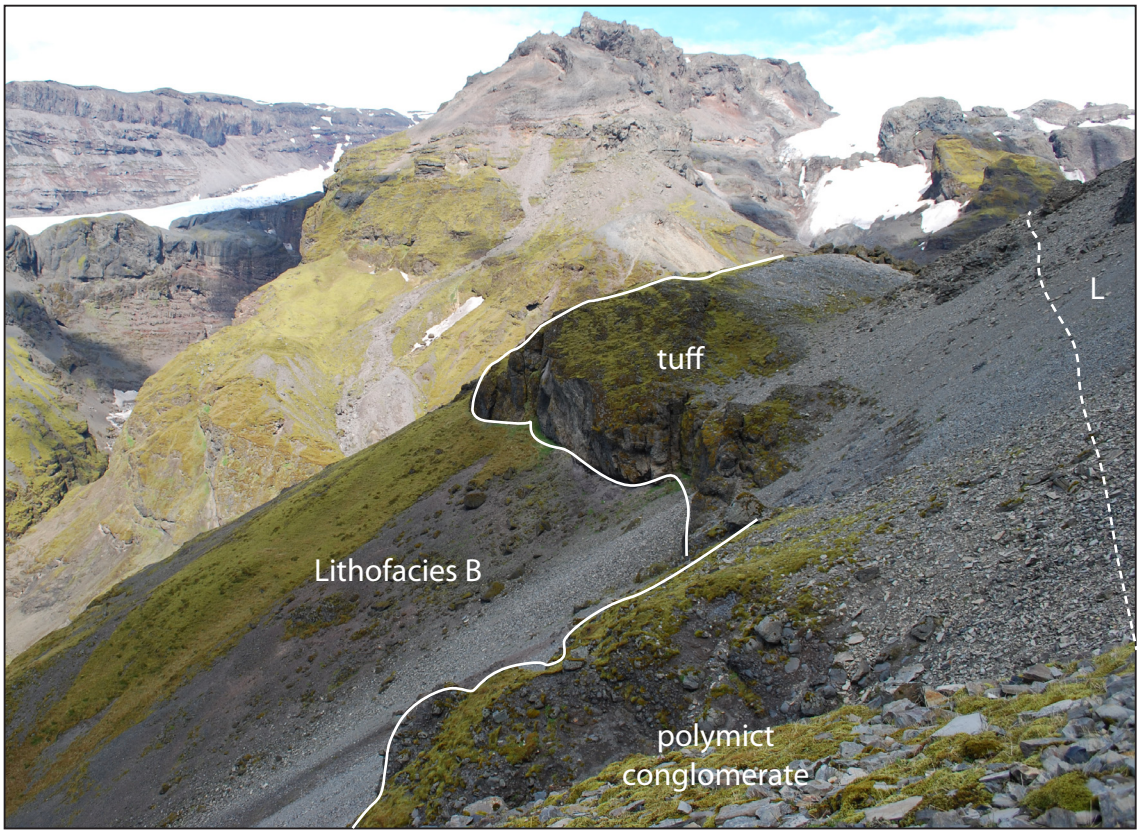

Fig. 4. B2: Massive palagonatised lapilli tuff overlain by polymict conglomerate containing faceted clasts below base od large rhyolite outcrop.

from the other collective outcrops in Lithofacies B.

Sub-lithofacies BA outcrops as discontinuous exposures of very well-bedded, laminated sedimentary units which can be matched up to corresponding units at a similar elevation on the western slopes of the Kotá river valley at Slaga (figs. 4. BA2 - BA6). As the units at Hrútsfjall are not accessible on foot, the exposure at Slaga will be described as the type locality for this lithofacies.

At this location lithofacies BA is approximately 15 m in height and outcrops at an elevation of 330 m.a.s.l. The base of the unit is a matrix supported polymict breccia with large faceted cobbles and boulders up to 1 m in width within a very fine-grained pale pink matrix (figs. 4. BA3). This grades abruptly into finer grained, laminated horizontal light and dark bands of volcaniclastic sands and granules within a pale pink, very fine sand to silt grade matrix. The pale bands range from 200 to 300 mm while the darker bands are thinner (80 to 140 mm).

The light bands are comprised primarily of very fine-grained sands and silts, while the darker bands have a higher percentage of courser grained sands and gravels with clasts ranging in size from 3 to 25 mm (fig. 4. BA4). The majority of clasts are mafic porphyritic volcanic rocks, displaying a range of vesicularities; some scoreaceous clasts are also present. Unlike the large clasts at the base of the unit, these clasts are more angular.

Larger 'dropstones' up to a metre in length are present throughout the unit (figs. 4.BA4 - BA6) cutting through a number of bands. Some of the dropstones are angular while others are faceted. The bands themselves are undisturbed by the presence of the stones and sagging structures in the underlying beds are absent.

On the eastern wall of the Kotá river the outcrops are partially obscured by fragmental deposits which are interpreted as reworked hyaloclastite tuffs (lithofacies B) (fig. 4. B1).

Sub-lithofacies BA: Interpretation

Lithofacies BA outcrops at similar elevations (330 m.a.s.l.) on both sides of the Kotá Valley. The basal conglomerate is not visible on the exposure on the Eastern wall, however the large proportion of faceted clasts suggests glacial emplacement.

The repetitive nature of the lighter and darker layers resemble turbidite deposits

Fig 4. BA1: Well bedded sediments exposed on East wall of Kotá Valley below Hrutsfjall ridge.

Fig 4. BA2: Corresponding outcrop on West Wall of Kotá Valley at Slaga

Fig 4. BA3: Base of corresponding outcrop on West Wall of Kotá Valley at Slaga featuring sub-angular faceted clasts.

Fig 4. BA4: Lithofacies BA is around 10 m in height with more than 25 pairs of dark / pale bands

Fig 4. BA5: Clasts in upper layers are more angular. Note-book is 190 mm in length.

Fig 4. BA6: Dropstones range in size from <30 cm to > 500 mm

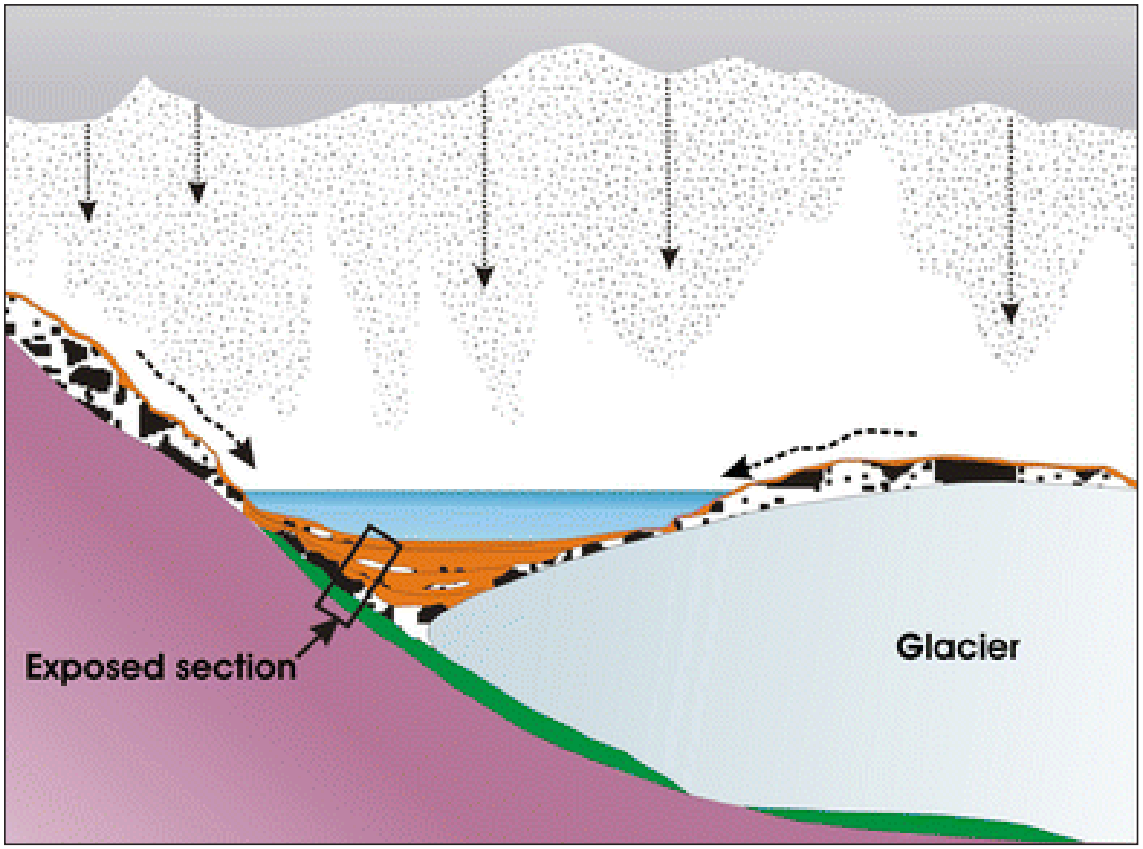

Fig. 4. BA7. After Smellie et al., 2011: Cartoon depicting an ice-marginal depositional environment located in Victoria Land, Antarctica. Lithofacies BA may have been deposited by a similar process to the above at the glacier margins of the Kotá valley.

and probably represent ice marginal glaciolacustrine sediments (Fig. 4.BA7), similar to varve sediments, consisting of reworked locally erupted volcaniclastic material deposited locally on ice marginal slopes.

The angular nature of the clasts within the sediment layers suggests that the clasts have not been transported far from source. The presence of large dropstones and lack of bedding disturbance within the underlying layers suggests that these may have been transported supraglacially, suspended in ice that later melted away, depositing the stones on the underlying bedding without causing disturbance to the underlying sediments.

Comparisons can be made between sub-lithofacies BA and similar units located in Victoria Land, Antarctica (Smellie et al., 2011) (Fig. 4. BA7). The Herschel Tuffaceous Moraine also features well-stratified volcanic sandstones featuring drop stones and lenses of till. These deposits have been interpreted as reworked phreatomagmatic tuffs and tephras redeposited as ash tubidites in an ice marginal lacustrine environment.

4.2.4. Lithofacies C: Composite columnar-jointed rhyolite lobes

Description

Lithofacies C outcrops at the entrance to the HVG valley, on the lower north-facing slope at elevations between 100 and 280 m.a.s.l., forming a composite collection of columnar jointed lobes of pale grey /golden weathered rhyolite with occasional glassy zones (Figs. 4.C1 - C3). The lobes have undergone a substantial amount of erosion; however the lobate structure of individual units can still be traced.

The columnar joints are both straight and curved (fig. 4. C2), often changing orientation on less than a metre scale, leading to the formation of fluidal arcuate and fanning patterns. In some areas differently-oriented joints converge to form platy and hackly jointing and then form back into joints again (fig. 4. C3). Some joint surfaces have developed a scratchy cross-hatched 'rind' up to 20 mm thick in places.

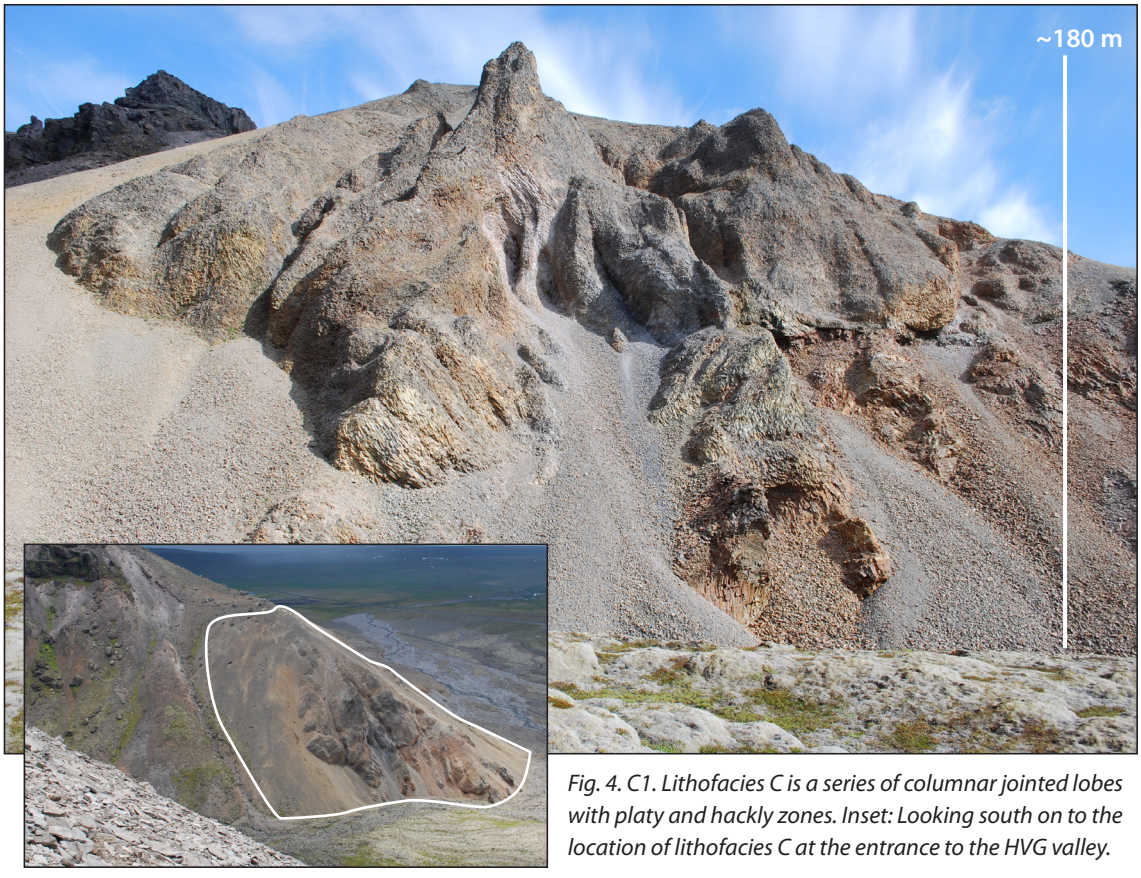

Fig. 4. C1. Lithofacies C is a series of columnar jointed lobes with platy and hackly zones. Inset: Looking south on to the location of lithofacies C at the entrance to the HVG valley.

Fig. 4. C2. Change in orientation of columns within lithofacies C occurs on a sub-metre scale. Column diameter ranges between 80 - 100 mm.

Fig. 4. C3. Differently oriented columns converge to form platy and hackly zones

Lithofacies C: Interpretation

Geochemically Lithofacies C falls into the Group One rhyolite. However it is markedly different in appearance to the other rhyolite lithofacies within this group. This change in appearance may represent a change in the emplacement environment. The fluidal, arcuate and roseate columnar jointing patterns suggest that water may have been present when this unit was emplaced. Similar fluidal jointing patterns have been reported in rhyolite lavas at Rauðufossafjöll (Tuffen, 2001). At this location the lavas are adjacent to a waterfall and have been interpreted to have formed by rapid quenching due to the flow of water over the upper surface of the lava.

The lobes are also very similar in shape and distribution to those reported in submarine dacite lava dome formations in Japan (Goto et al., 2004).

This lithofacies C's relationship to the other lavas of the same geochemical group that outcrop at the same elevation is unclear. The outcrop is located at the base of the entrance of a glacial valley, therefore it is probable that the lavas may have erupted in the presence of water, possibly within a fluvial environment.

4.2.5. Lithofacies D: Platy rhyolite lavas

Description: overview

Lithofacies D (figs. 4. D1-D14) is the most laterally extensive silicic rock type in the field area (fig. 4. D1), forming a number of discontinuous outcrops at a range of elevations from 100-350 m.a.s.l that punctuate the slopes of Goðafjall West (Figs. 4. D2), the lower to mid slopes of the HVG valley and south facing slopes of HVG

plateau. It is also present at river level in the Kotá valley and the lower south-facing slopes of Hrútsfjall.

It is an aphyric microcrystalline rhyolite lava comprising glassy, obsidian-rich and pumiceous zones, forming isolated outcrops that range in size and shape from < 1 m^2 to cliffs and buttresses over hundreds of metres in length. It can be broadly subdivided into four main textural zones (Figs. 4.D4-D14) as follows:

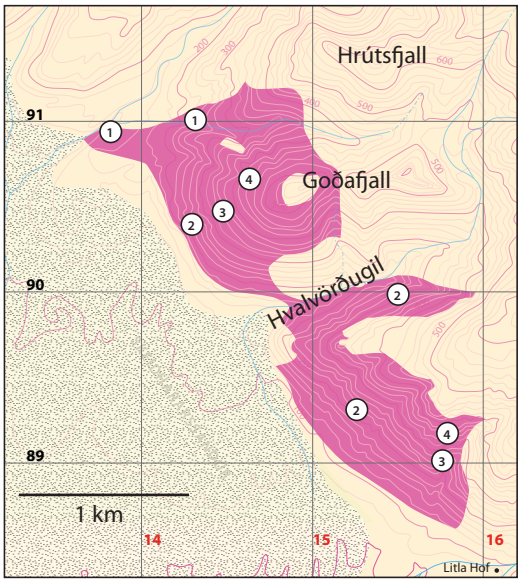

Fig. 4. D1. Extent of lithofacies D across field area. Numbers indicate best examples of lithofacies textural zones 1 to 4.

Zone 1 – basal breccia

Zone 2 – massive microcrystalline rhyolite with platy habit

Zone 3 – highly folded, interlayered rhyolite and obsidian

Zone 4 – highly folded interlayered rhyolite and microvesicular pumice.

Some outcrops only display one textural variety while others display various combinations of two or more. Generally the microcrystalline rhyolite displays a platy habit while the obsidian is more massive.

Textural variations occur over sub-metre scale and are too small to be represented on the geological map, therefore the primary textural variations are described in further detail below.

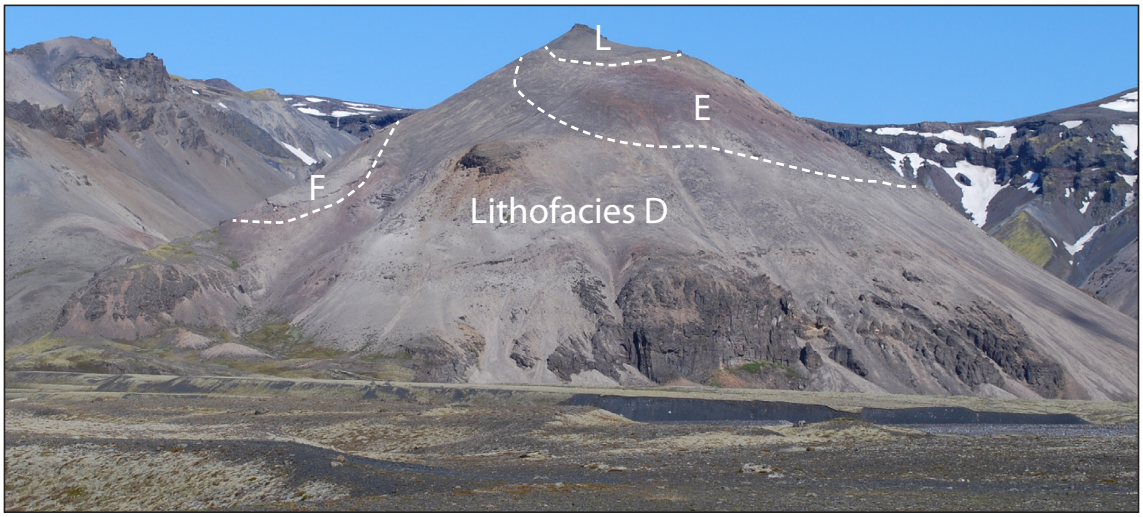

Fig. 4. D2. Lithofacies D dominates the lower to mid west to south west facing slopes of Goðafjall. View is approximately 1 km across

Fig. 4. D3-5. Lithofaces D, Zone 1 basal breccia. Hammer is 279 mm in length.

Zone 1: Basal Breccia

The majority of outcrops have their bases obscured by scree aprons; therefore basal zones are not well represented. However two exposures do occur (fig. 4.D1) at the base of the large buttress at the entrance to Hrútsfjall stream valley and also in the lower section of a distal exposure present along the banks of the Kotá river valley which will be discussed at the end of this section.

The base of the Zone 1 sequence is represented by a complex zone of deformed, folded platy rhyolite layers interspersed with obsidian layers (Fig. 4. D4). Plate orientations range from sub-horizontal to vertical over metre scales.

Brecciation occurs in irregular lenses and also with the fold axes. The breccias consist of angular, jigsaw-fit clasts of rhyolite varying in size from < 10 mm to 150 mm within a matrix of pale pink / orange comminuted, rewelded rhyolite (fig. 4. D3). In some areas the clasts have been rotated, while in others the original orientation has been preserved and flow banding can be matched between the separate clasts.

In some areas the platy rhyolite grades into discontinuous massive obsidian layers over a metre in thickness. The obsidian layers contain brecciated lenses of angular black obsidian jigsaw-fit fragments set within a fine orange matrix of comminuted rhyolite (fig. 4. D5). The obsidian features red flow banding and in some areas spherulites have developed along flow bands. Some of the larger clasts of obsidian have shattered in situ and the cracks have been penetrated by fingers of orange matrix material (fig. 4. D3).

At all locations, folded platy rhyolite breccias grade into more massive obsidian layers of varying thickness (110 mm to 450mm). Zone 1 grades into textural Zone 2, forming more regularly aligned, sub-horizontal rhyolite plates.

Zone 2: Massive devitrified platy rhyolite

The largest continuous outcrops of Lithofacies D are dominated by textural Zone 2 which is characterised by devitrified, microcrystalline red-brown (and occasional pale grey and pale golden brown) rhyolite, with a distinctive platy habit. The plates vary in thickness from <5 to 12 mm and develop along the horizontal plane (fig. 4. D7). Fine flow banding is also visible in the same orientation as plate formation. In the lower to mid sections of outcrops the plates are sub-horizontal, but in the upper sections plate inclination gradually increases and can be almost vertical in some areas.

One of the best examples of textural Zone 2 is situated at the base of the western to south-western flank of Goðafjall West (fig. 4. D6-D9), where it forms a steep-sided cliff face that protrudes from the base of the slope with a height of 269m.a.s.l. and a length of approximately 350 m (fig. 4. D9). No basal zone is visible as the base of the edifice is surrounded by apron of locally derived talus.

The majority of the cliff face comprises horizontal to sub-horizontal plates of

Fig. 4. D6-9: Examples of lithofacies D, Zone 2 platy rhyolite. Cliffs (D6) are approximately 130 - 150 m in height.

microcrystalline red-brown rhyolite (fig. 4. D7). At the western end of the outcrop plate orientation is predominantly sub-horizontal, occasionally displaying folds with a low amplitude wavelength, but no intense folding is visible, however toward the eastern end, large-scale folding, with amplitudes over 10s of metres, becomes much greater (fig 4. D8). Toward the top of the cliff face the plate orientation becomes much more steeply inclined as they begin to ramp up and dip into the flank of Goðafjall West at angles between 70-75˚. Large scale vertical joints (fig. 4. D6), over a metre wide, are present throughout the whole structure and are a common feature in all of the larger outcrops of lithofacies D. The top of the cliff stands proud from the remainder of the upper scree-covered slopes of Goðafjall; here Zone 2 grades into textural zone 3.

Zone 2 is also dominant across the north to northwest facing lower eastern wall of the HVG valley (fig. 4. D1) and the south facing roadside slopes of the HVG plateau.

Zone 3: Irregular, folded, interlayered devitrified rhyolite and obsidian

Zone 3 is characterised by folded, discontinuous platy layers of rhyolite, grey-black, and occasionally dark red, lustrous obsidian and glassy black obsidian (fig. 4. D10). Spherulites are often present in the obsidian bands, or at the interface between rhyolite and obsidian bands (fig. 4. D11), but occur less frequently within the rhyolite bands. They nucleate along the same plane as the flow banding indicating a relationship between flow banding and spherulite location. Occasionally the flow banding appears to flow around the spherulites, suggesting that some spherulites began to nucleate while the lava was still flowing (i.e. prior to glass transition temperatures). In many areas, the outcrops are broken-up into disarticulated blocks so that they appear as if they are not 'in-situ', but many are present at a similar elevation along strike across the upper north to north west facing eastern wall of HVG valley and in the gully behind Litla Hof on the south facing slopes of HVG plateau.

Zone 3 also caps the upper surface of the large cliff at the base of Goðafjall West. Here the distribution of Zone 3 is irregular with disarticulated blocks of platy brown rhyolite interlayered with massive bands of dark grey, lustrous obsidian and black, glassy obsidian. In some areas, along the same plane as the plates, red and grey spherulites have developed within the layers between the platy rhyolite and the glassy obsidian bands and some disarticulated blocks of black obsidian display fine red flow banding.

Fig. 4.D10. Lithofacies D, Zone 3: Interlayered rhyolite and obsdian outcropping on the HVG plateau slopes.

Fig. 4.D11. Lithofacies D, Zone 3: Close-up of spherulite development.

Fig. 4. D12: Lithofacies D, zone 4: Interlayered platy rhyolite and microvesicular pumice.

Fig. 4. D13: Lithofacies D, zone 4: Brecciated blocks of microvesicular pumice.

Zone 4: Highly folded interlayered rhyolite and finely vesicular pumice

Textural Zone 4 is characterised by alternating layers of rhyolite and dense microvesicular pumice with a frothy, lumpy texture and blocky, brecciated zones (figs. 4. D12-D13). The layers form along the same horizontal plane as the platy joints although the layering tends to be much more irregular. Both the pumice and rhyolite layers can range in thickness from sub mm to 10's of cm, although the layer thickness is irregular and discontinuous, often displaying multiple folded and refolded folds. Complex structural relationships occur between the two rheologies; pumiceous layers pinch out, while others form boudins within the rhyolite. The pumiceous layers also display elongated cavities or vesicles and brittle deformation, while the devitrified rhyolite layers are non-vesicular, suggesting that pumiceous layers cooled more quickly than the rhyolite layers and that the flow was still under stress after cooling had occurred.

Smaller isolated outcrops of textural Zone 4 punctuate the scree covered slopes above the cliffs on Goðafjall West, above an elevation of 350 m. The outcrops are all very weathered but the orientation and dip of the plates can still be determined at most outcrops. The majority of the upper outcrops exhibit plates dipping back into the slope at an angle of 65-80°, all forming at a steeper angle to the much larger continuous outcrops at lower elevations.

Distal outcrops

At distal locations the four zones are represented over a smaller scale and, in some cases, are absent from the sequence. This is demonstrated at the western lateral extent of lithofacies D on the eastern bank of the Kotá river (fig. 4. D14),

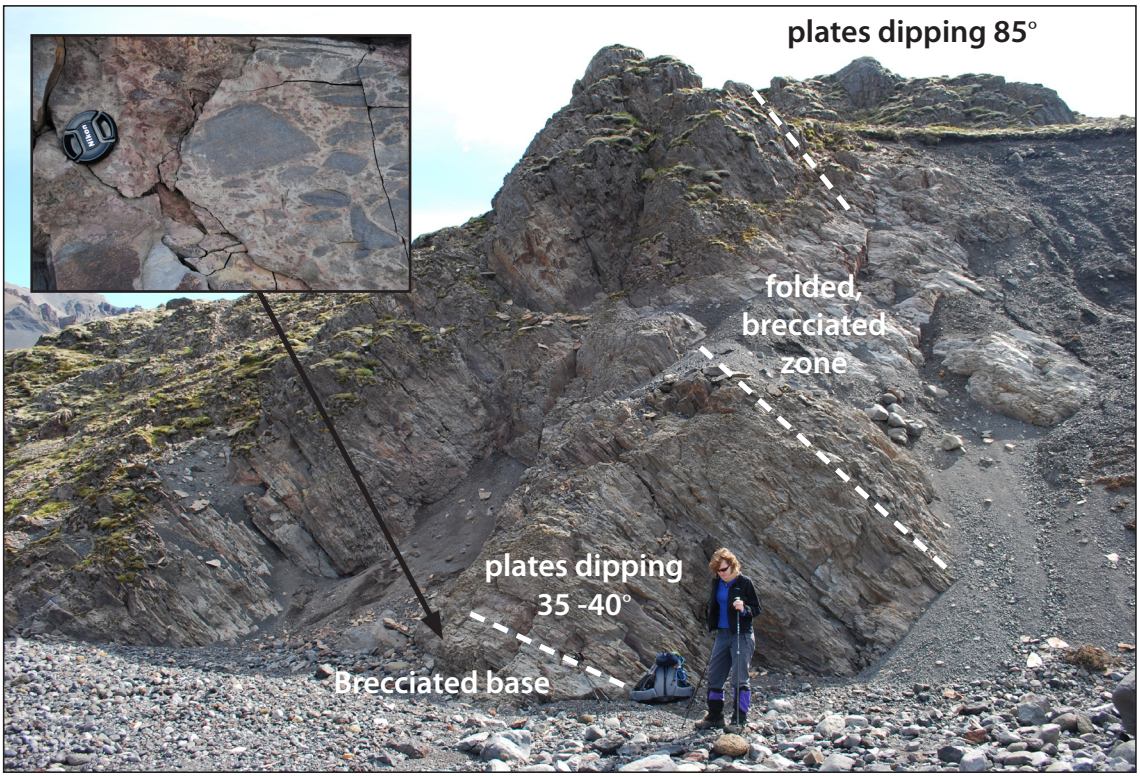

Fig. 4.D14: Distal outcrop of Lithofacies D at western extent of unit. Zones 1 , 2 and 3 occur. 'Ramping up' of platy fabric is evident from base (30° dip) to top (85° dip) of exposure. Height of exposure is 15 m.

which is 15 m in height, where the whole sequence occurs over a metre scale. Over the lower two to three metres, Zones 1 and 2 grade into each other. The dominant platy fabric of Zone 2 is punctuated by folded zones, often with brecciation present within the fold axes. At lower elevations (< 3 m) the plates ramp up at an angle between 35 to 40°, dipping toward the bulk of the outcrop, which is south east in this instance, but the dip direction is governed by the outcrop morphology. The dip of the parallel plates increases gradually throughout the outcrop as elevation increases, although occasional folding does occur. The plates in the uppermost section of this sequence are not folded but have steepened or 'ramped up' to almost vertical with a dip of approximately 80-85°. Zone 4 is absent from this sequence, although as the upper section of this sequence is very weathered and smoothed, therefore Zone 4 may have been removed by erosion.

Lithofacies D: interpretation

A lack of associated, early stage pyroclastic deposits suggests that Lithofacies D was emplaced effusively rather than explosively, although their absence may also be

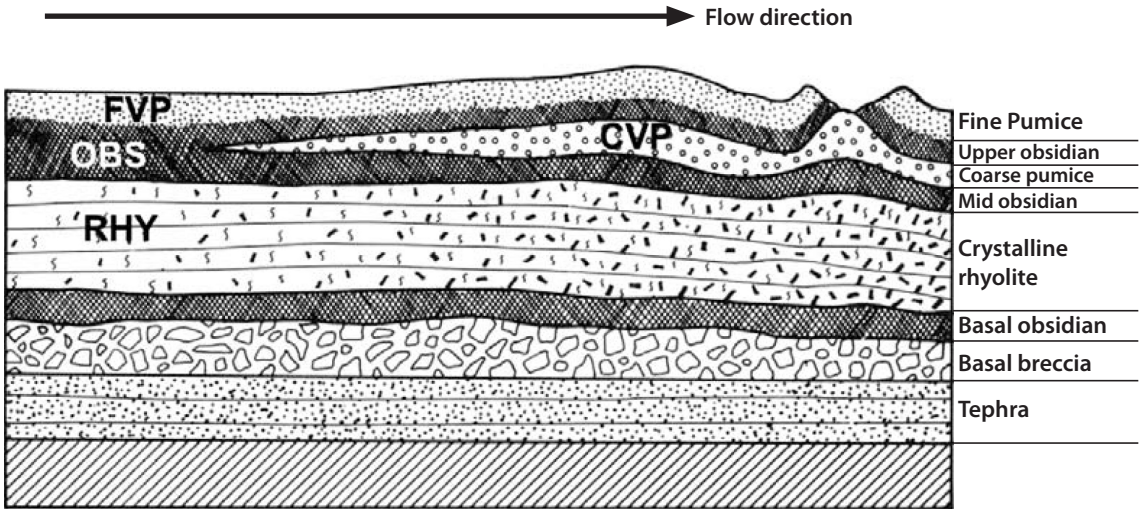

Fig. 4. D15: After Fink & Manley (1987), schematic diagram of the internal structure of a silicic lava dome based on drill cores from the Inyo Domes, California, USA.

due to poor preservation potential in an area which has undergone multiple stages of extensive glacial erosion. Geochemistry shows that lithofacies D is a metaluminous to peralkaline rhyolite with relatively low silica and high alkalis. LOI analysis (chapter 3) reveals a low volatile content (H_2O typically < 1 wt %) and crystal mineral assemblage shows typically anhydrous minerals (pyroxene and plagioclase), therefore it is possible that lithofacies D had a relatively high eruption temperature compared to a typical rhyolite and subsequently lower viscosity which may have resulted in an effusive rather than explosive eruption style. This hypothesis is supported by the presence of disequilibrium textures including partially resorbed and sieve textured feldspar phenocrysts (chapter 3).

The four textural zones described in lithofacies D broadly represent the textural variations that are commonly found in subaerial, dry (< 1 wt % H_2O) rhyolite lava flows (Fink, 1983). The internal textural stratigraphy of a subaerial rhyolite flow was revealed by research drilling in California and New Mexico, USA (Fink & Manley, 1987; Manley and Fink, 1987). Manley and Fink demonstrated that large-scale subaerial rhyolite flows can be sub-divided into five main textural zones: 'basal breccia', 'lower obsidian', 'crystalline rhyolite centre', 'upper obsidian', 'coarsely vesicular pumice' and 'finely vesicular pumice' (microvesicular) (fig. 4. D15). Studies of a number of different flows revealed that the relative thicknesses of the textural zones can differ greatly between flows and that some zones may be omitted completely from flow stratigraphy (Manley and Fink, 1987). In this study, Zone 1 represents

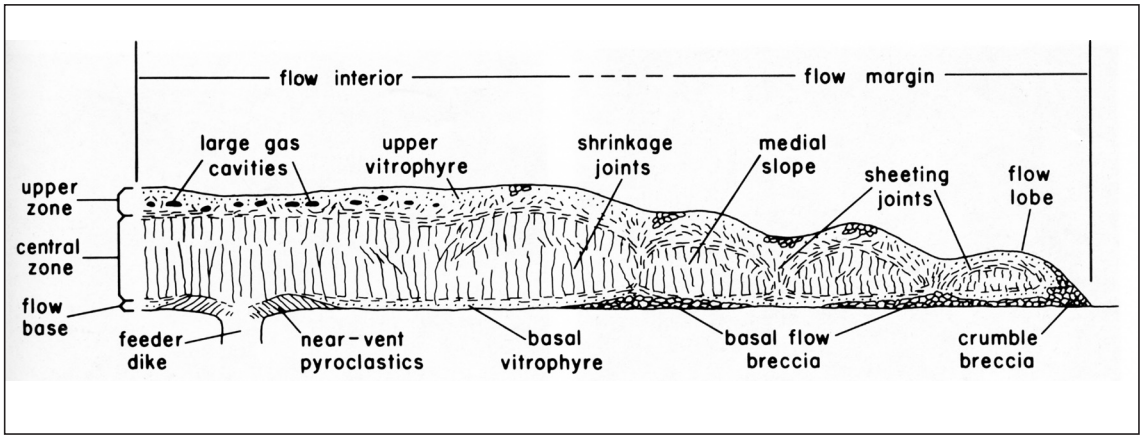

Fig. 4. D16: After Bonnischen and Kauffman (1987). Schematic diagram of idealized longditudinal section of large volume subaerial lava flows of the Snake River Plain, Idaho, USA. Many of the textural features seen in these flows are also present within lithofacies D.

Manley and Fink's basal breccia and lower obsidian, Zone 2 represents crystalline rhyolite centre, Zone 3 represents upper obsidian and Zone 4 represents finely vesicular pumice.

Lithofacies D also displays many textural similarities to the large volume, high-temperature effusive rhyolite flows described by Bonnischen and Kauffman (1987) at Snake River Plain Volcanic Province, Idaho (fig. 4.D16). Bonnischen and Kauffman describe zones of autobrecciation similar to the breccias observed in the basal breccias of lithofacies D. Brecciation occurring within fold hinges and flow margins suggests that the flow cooled sufficiently and/or was under enough stress for brittle deformation to take place while the flow was advancing. It is also possible for breccias to form in ductile zones when strain rates are high and then to reweld once the strain rate is reduced. Alternatively, the flow may have been rapidly cooled and fragmented by interaction with steam or water. The black and orange breccias located at the lateral extent of the unit are very similar to 'fumarolic-type' breccias described by Bonnischen and Kauffman (1987), who suggest that this type of breccia is generated by the explosive release of steam produced by superheated water flowing down fractures penetrating the hot flow. Only small volumes of water are required to produce this type of localised brecciation and in this location it is likely that even during interglacial periods some snow cover or meltwater runoff may have been present.

Glassy obsidians with red micro- and macroscopic streaks have been identified in other subaerial rhyolite flows and formation of red streaks within glassy black obsidians is attributed to oxidisation of re-fused glass domains which are drawn into

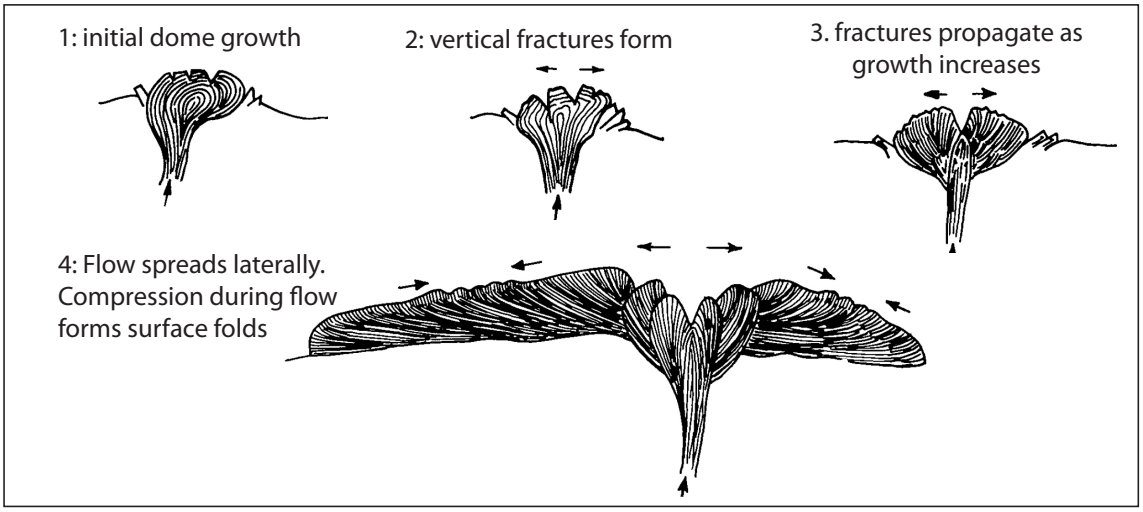

Fig. 4. D17: After Fink (1983), schematic diagram of the structure and emplacement of a rhyolite obsidian flow. Platy, fractured surface develops as flow spreads laterally, leading to the development of 'ramping up' structures from the base to the upper flow surface.

streaks by subsequent deformation (Manley, 1996).

The sub-parallel platy habit within the central zones of Lithofacies D is also a common feature of subaerial rhyolite flow interiors, where the pervasive stress regime throughout the flow is initiated by basal shear and propagates upwards (Fink and Anderson, 2000). The ramping up of plates has also been documented in the flow margins and upper zones of the Snake River flows and also at Little Glass Mountain (Fink, 1983, Fink et al., 1992). Kinematic studies have shown that fold structures and orientation of folds in rhyolite flows are governed by gravity spreading (Smith and Houston, 1994), and also by differences in viscosity between the flow interior and the yield strength of the outer carapace (Fink and Anderson, 2000). As the flow spreads away from the vent it is pushed laterally leading to plate development that fans outward (fig. 4. D17). Plate strike orientations and dip measurements collected across a number of outcrops across Goðafjall West suggest that flow movement and growth occurred radially in a SSE to SSW direction (see map), however this does not take into account any pre-existing topography which will have also exerted some control on flow emplacement.

Vesicularity is variable within the pumiceous upper layers of the Lithofacies D, however it does not appear to display evidence of Manley and Fink's (1987) 'coarsely vesicular pumiceous zone', although the highly eroded nature of the individual outcrops that represent the upper section of the flow make this difficult to establish. Textural Zone 4 has many similarities to 'interlayered flow upper flow surfaces'

documented at Little Glass Mountain lava flow, USA (Fink and Manley, 1987).

Texturally complex pumiceous zones in the upper regions of effusive silicic lava flows and domes form in response to vesiculation driven by post-emplacement redistribution of volatiles during surface flow (Fink et al., 1992). The complex structural relationships, such as refolded folds, buckle folding and pinching out between the rhyolite layers and pumiceous layers, in textural zone 4 occur due to difference in viscosity between the bubble-rich pumice layers and bubble-free rhyolite / obsidian layers (Castro and Cashman, 1999).

In summary lithofacies D is a small-volume, subaerially emplaced lava flow with a 1.5 km flow front which shows evidence for minor interaction with water / steam where the base is visible. No obvious vent structures are preserved and much of the upper surface is heavily eroded. The rhyolite plates on the south west facing slopes of Goðafjall West and HVG plateau dip generally to the north east which suggests that the flow spread laterally outward from this direction. The lithofacies is limited to the lower 350 m of elevation and does not outcrop beyond the mouth of the Kotá river valley and no more than 500 m upstream in the HVG valley, which suggests that lithofacies D is the most likley the product of a flank eruption.

4.2.6. Lithofacies E: Rhyolite breccia

Description

Lithofacies E outcrops on the upper slopes of Goðafjall West (Grid Ref: 0414799/ 7090276, between 416 to 441 m elevation) across a distance of around 200 m and comprises a collection of discontinuous, texturally heterogeneous outcrops ranging from 2 to 5 m in height (Figs. 4. E1-E4). Some of the outcrops have brecciated bases of angular clasts of material from the upper zone of lithofacies D consisting of interlayered devitrified rhyolite and finely vesicular pumice (textural zones 3 and 4). The breccias grade into massive glassy layers with complex interlaying of red/brown platy rhyolite interspersed with glassy black obsidian with orange streaky flow banding and lenses of orange finely vesicular rhyolite. The upper sections of some of the outcrops grade into platy, devitrified rhyolite with plates that increase in dip back towards the slope; the outcrops at the highest elevation have

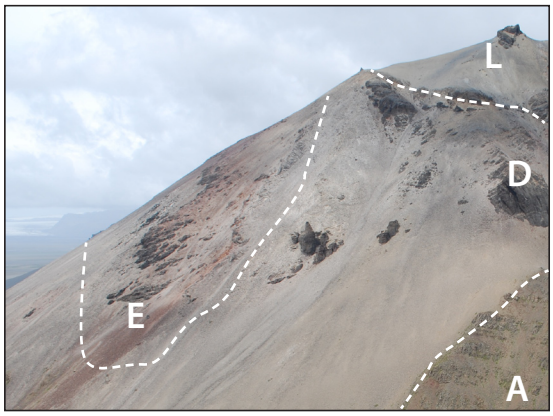

Fig. 4. E1. Extent of lithofacies E on south facing slope of Goðafjall West.

Fig. 4. E2. Largest continuous outcrop of lithofacies E

Fig. 4. E3. Lithofacies E is a poorly sorted clast supported breccia with a fine grained matrix.

Fig. 4. E4. Lithofacies E is a series of disarticbackground.

steeply inclined plates, dipping north to north west at 72 - 80°). The outcrops are surrounded by blocks of disarticulated orange scree containing pieces of glassy black obsidian with red flow banding.

The largest continuous outcrop is an orange finely vesicular and non-vesicular breccia which stretches approximately 50 m downslope and between 2 to 5 m in width with a variable height between <1 to 5 m.

The breccia is made up of bright orange clasts ranging in size from 30 to 350 mm in diameter, the clasts do not display a jigsaw-fit and are rotated within a paler orange matrix – some areas are matrix supported while others are clast supported with very little matrix. At the same elevation, toward the east and west, the unit is juxtaposed with small-scale isolated outcrops of platy rhyolite. However the presence of blocks of orange vesicular material in the surrounding scree down slope (fig. 4. E1) suggests that this outcrop may have covered a larger area when initially emplaced and has subsequently been reduced by erosion. In some sections plates have formed above the breccias, while in others only fragmental material is present.

Lithofacies E: Interpretation

Geochemically, Lithofacies E matches the Group One rhyolite, and has some similarities to textural Zones 3 and 4 of Lithofacies D; however it also differs from Lithofacies D in colour, vesicularity and lack of fine grained matrix within the breccia lenses. The pervasive orange colour occurs as a result of oxidisation, which suggests that the breccias were emplaced subaerially.

Flow banding orientation is slope-parallel in many of the massive glassy sections of the outcrops, suggesting that the present-day slope existed prior to emplacement.

Repeated pulses of lava during a sustained eruption may lead to the development of small-scale flow lobes that, over time, become successively stacked. The abundance of breccias across the mid to upper south facing slopes of Goðafjall West may be formed by the collapse of each successive lobe flow front as it encounters an oversteepened slope.

The lack of a fine grained matrix within the clast supported breccia suggests that no water or steam interaction occurred at this stage of flow advance. Patchy coverage of an upper zone of platy rhyolite suggests that a relatively large amount of material has been stripped away by erosion.

4.2.7. Lithofacies F: Slope-draping rhyolite with brecciated base

Description

Lithofacies F (fig. 4. F1-F4) is an isolated outcrop on the west facing slope of Goðafjall West (Map grid ref: 0414422/7090895). The unit drapes over the current slope and is situated upslope of an extensive outcrop of platy, devitrified Lithofacies D which skirts the lower to mid elevation of the west and north west facing slopes of Goðafjall West, adjacent to Hrútsfjall, although no direct contact between the two units is exposed. Lithofacies F is approximately 200 m in length and the downslope section of the unit varies in thickness from 1.5 to 2 m. Fresh surfaces are mid to dark grey in colour but exposed surfaces have a patina of dark brown / red. Texturally it has many similarities to the upper sections of Lithofacies D and E but does not contain glassy layers.

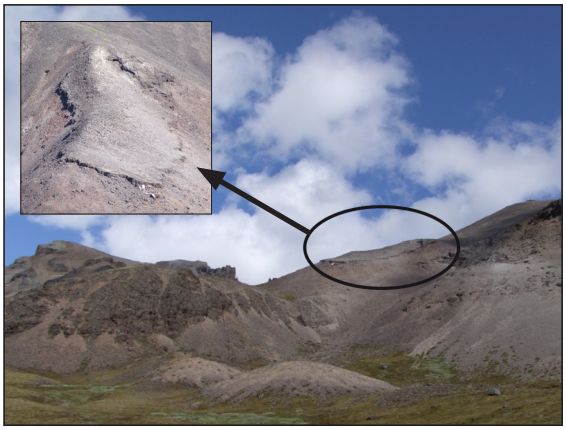

Fig. 4. F1 . Lithofacies F location and extent on west facing slopes of Goðafjall West, looking east from base.

Fig. 4. F3. Platy fabric of lithofacies F has been emplaced slope-parallel.

Fig. 4. F2. Cavities up to 1 m in width are present in the base of the unit.

Fig. 4. F4. Brecciated base has a 'ripped up' texture which suggests partial rewelding occurred during brecciation.

The upper section of the outcrop is approximately 1 to 1.2 m thick (fig. 4. F3) and comprises aphyric rhyolite with a platy habit. The plates are 10-15 mm in thickness, some of which are folded, with the fold axis facing in a downslope direction. It is a devitrified aphyric microcrystalline rhyolite with very faint flow banding present throughout. The complete top section is spherulitic, with spherulites ranging from mm scale to >2 cm in diameter. In many areas the spherulite walls are touching, inhibiting further radial growth, causing deformation to the outer structure and creating an effect similar to that of hexagonal close packing. The spherulites appear to develop along the planes of flow banding and on the surface of the plates; although in some areas the flow banding is deflected around the spherulites. Upslope, texturally the upper layers of Lithofacies F resemble the mid to upper section of lithofacies D (textural Zones 3 and 4), with interlayered microvesicular pumice layers that have been eroded to give a 'sugar-coated' appearance.

The base of the outcrop is a breccia ~600 mm thick (but this varies laterally) containing red/orange angular rotated clasts ranging from mm scale to 170 mm in

diameter. In some areas there are cavities in the base which contain loose blocks of breccia that have fallen from the cavity roof (fig. 4. F2). Some domains are matrix-supported with a slightly vesicular matrix, but in other areas the matrix is absent and there are voids between the clasts. In places the clasts have a 'torn' appearance where they have re-welded and been ripped apart again, suggesting that the flow was still hot enough to reweld while brecciating (fig. 4. F4).

Lithofacies F: Interpretation

In comparison with the geochemistry of other silicic units analysed in this study, the major and trace element concentration of Lithofacies F is slightly more variable across different sampled sections of the outcrop (four analyses), but overall the geochemical variability is not great enough for it to be classified as heterogeneous. The analyses are within the range of Group One rhyolite and it has therefore been included in that group.

With a thickness of less than 2 m and a low aspect ratio (ratio of width to height), it is a very thinly-draped deposit compared to texturally similar outcrops of lithofacies D and E and is also lacking in glassy zones, however in many other respects Lithofacies F is texturally identical to the smaller isolated lobes of Lithofacies D. It is ikely that a considerable amount of the upper section of this outcrop has been removed by subsequent erosion; therefore its current aspect ratio may bear little resemblance to the outcrop when it was initially emplaced.

The slope-parallel plate formation and downslope orientation of fold axes suggests emplacement on a pre-existing slope, possibly as a later stage lobe of a relatively long-lived silicic eruption on top of earlier erupted units. Although the unit was most likely emplaced subaerially, cavities present in the base may be caused by interaction with minor amounts of surficial water or snow.

4.2.8. Lithofacies G: Massive pumice-rich lapilli tuff (mLT)

Description

Lithofacies G (Figs. 4.G1-G2) is a very limited, isolated outcrop approximately 15 m^2 which is poorly exposed on the south eastern flank of the lower HVG valley. It comprises massive, pale grey / light beige, partially consolidated pumice-rich tephra with sparse obsidian clasts in a fine ash-grade matrix. The pumice lapilli make up approximately 50 % and vary in size from 20 mm to 200 mm. The sparse (10 %), angular obsidian clasts are less than 10 mm in diameter.

The unit is unconformably overlain by mafic lavas, tuffs and conglomerates (Lithofacies O and P), while any underlying strata and basal contacts have been completely obscured by scree. To the left it is flanked by scree slopes punctuated by isolated outcrops of lithofacies D and to the right by scree punctuated by columnar jointed rhyolite lobes of lithofacies C.

Lithofacies G: Interpretation

Geochemically, pumices entrained within the tuff match Group Two rhyolite, however there is insufficient exposure to be able to confidently identify the emplacement mechanism. The relatively high abundance of pumice suggests that the tuff was explosively generated rather than phreatomagmatically driven, while the massive structure and poorly-sorted nature suggests either close proximity to the vent or disruption during transport/deposition.

Fig. 4. G1. Location of lithofacies G on north east facing slope of HVG valley.

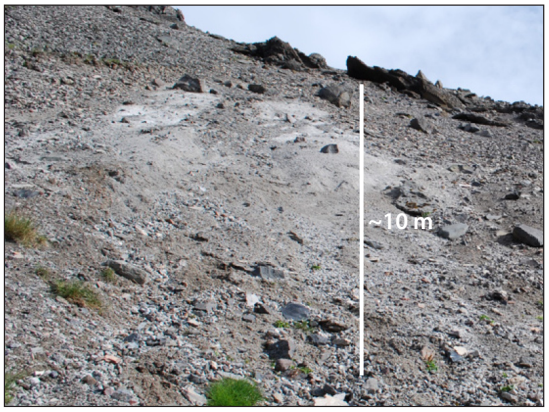

Fig. 4. E2. Lithofacies G; exposure is approximately 10 m in length.

4.2.9. Lithofacies H: Massive obsidian-rich pumice lapilli tuff (mLT)

Description

Lithofacies H (Fig. 4. H1-H7) is a massive, poorly sorted, poorly consolidated obsidian-rich pumice lapilli tuff that outcrops at the col separating Goðafjall West from Goðafjall East on the east and west facing flanks of the upper elevation of Goðafjall (460-483 m.a.s.l.).

It consists of partially-consolidated pale grey, fine-grade ash matrix with a range of grain sizes from a few microns to over 200 microns (Fig. 4. H6-7). The tuff contains up to 30% angular glassy obsidian shards (Fig. 4. H2), clasts and larger blocks ranging in size from 3 mm to 150 mm diameter, 10% pale grey moderately vesicular pumice blocks (up to 230 mm diameter) and, more rarely, blocks of more dense, microvesicular dark grey pumice (up to 90 mm diameter). Occasional sub-rounded, oxidised mafic lithics are also present (up to 70 mm diameter) (Fig. 4. H4) .

SEM images of the ash matrix reveal that the grains are sub-angular and display a range of vesicularities (Fig. 4. H6-7). The vesicles have moderately thick bubble walls (up to 5 microns) whilst bubble coalescence is also visible. Very fine ash (1 - 2 microns) adheres to the surface of some larger grains. Tube pumices are also present within the matrix (fig. 4. H6).

A number of irregular obsidian bodies are dispersed throughout the upper 15 m of the deposit ranging in size from 120 mm to 3.6 m in diameter (fig. 4. H2-5). Many of the larger obsidian bodies stand proud from the unconsolidated tuff surface due to their more robust nature, similar to small lobe formations, while other smaller bodies are grouped together in clusters (Fig. 4. H4) The abundance of obsidian bodies increases with increasing proximity to the margins of the capping lava lobes.

The body interiors consist of porphyritic, glassy obsidian grading into a rim of microvesicular dark grey pumice which varies in thickness from body to body – some pods have sharp boundaries with the surrounding ash. The rims are less well-defined in areas where the clusters of bodies are densely grouped together. Some of the obsidians have shattered cores which feature very fine, pale gray ash within

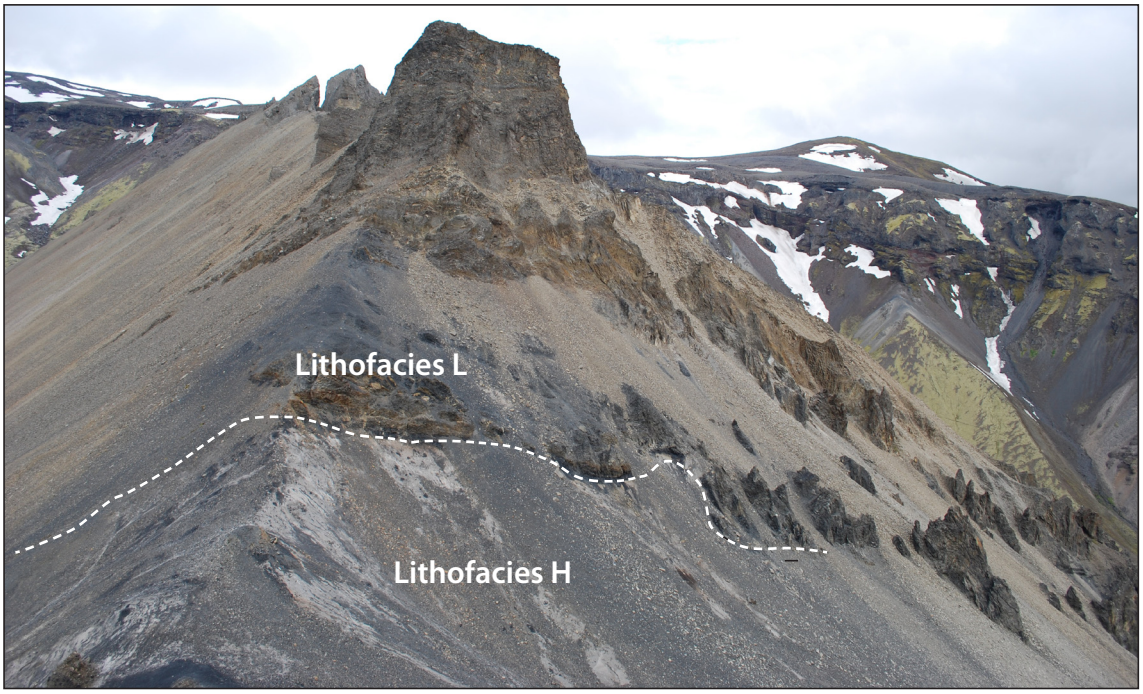

Fig. 4. H1. Location of lithofacies H at col between Goðafjall West and East, looking toward Goðafjall East.

Fig. 4. H2. Fine ash matrix with obsidian shards and larger pumices.

Fig. 4. H3. Largest irregular obsidian body is over 3 m in length (ruler is 1 m).

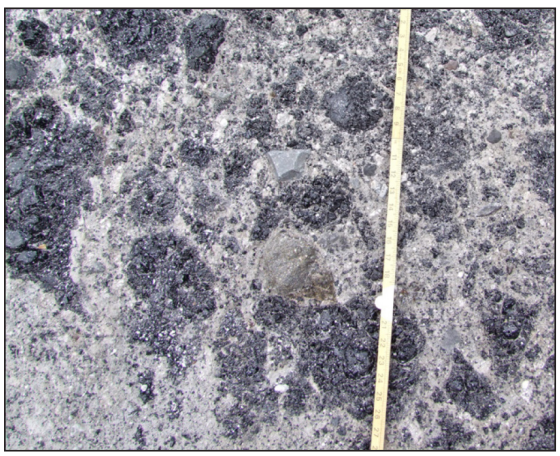

Fig. 4. H4. Occasional lithic clasts are present.

Fig. 4. H5. Lithofacies H obsidian bodies.

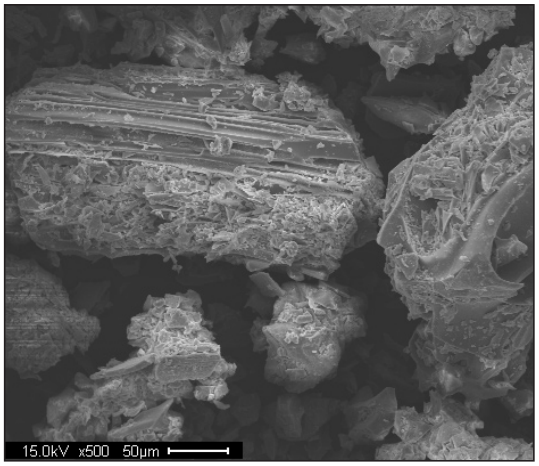

Fig. 4. H6. SEM images of lithofacies H displays a range of grain sizes from 50 to 200 microns. Tube pumices are also present (left).

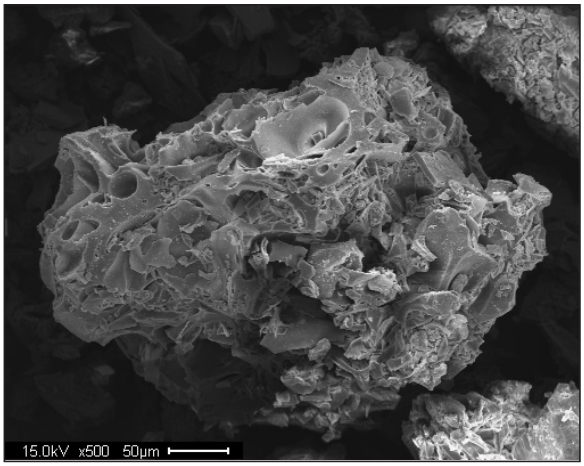

Fig. 4. H7. SEM images of lithofacies H: Some grains are more blocky with thick bubble walls.

the cracks. Similar exposures with obsidian pods are also located on the south facing slopes of Hrútsfjall (fig. 4. H8) but are very poorly exposed and draped by granular obsidian scree.

Lithofacies H: Interpretation

Lithofacies H is poorly sorted with a wide range of grain sizes and vesicularities and displays no internal structure. The variety of grain morphologies and sizes present within the unit do not give any conclusive indication of either a subaerial or subaqueous depositional style, however the overall features of lithofacies H suggest deposition as a dense mass flow.

In a subaerial environment, massive, poorly sorted pyroclastic flows with high clast concentrations are dominated by fluid escape rather than by the turbulence-driven traction currents that develop stratification. (Branney and Kokelaar, 2002); however, an eruption into a confined space such as a subglacial cavity, would be prevented from sorting or transport due to the limited space available within the cavity. The inability to infer a depositional style from the grain size of lithofacies H may be due to confinement, making comparisons with conventional subaerial pyroclastic deposits impossible.

Fig. 4. H8. Irregular obsidian pods also outcrop to the north on the south facing slope of Hrútsfjall.

The range of vesicularities present within both the ash and pumice lapilli suggest that fragmentation was due in part to magmatic volatile release, however the adhesion of very fine grained particles of ash upon larger ash grains is characteristic of interaction with water (Heiken and Wohletz, 1985), suggesting a combination of volatile release driven fragmentation and quench fragmentation. It is unlikely that ponded water was present in great amounts as this would have been reflected in the sorting and structure of the deposit, however lack of space within an ice cavity may still prevent sorting even in the presence of water (Stevenson et al., 2011). Any water produced by the melting of ice most likely drained away via pre-exisiting channels in the ice/bedrock interface or as a result of pre-existing topographic relief.

The presence of tube pumice often implies that a deposit is vent proximal; however no nearby vent structures are evident in the field. Tube pumices are produced by shear fragmentation which occurs high-up within the volcanic conduit just prior to eruption, when magma undergoes ductile-brittle transition, due to stresses exceeding the magma's tensile strength (Marti et al., 1999). Similarly highly mixed, poorly sorted, unconsolidated deposits have been described at Kerlingarfjöll (Stevenson et al., 2011), where a high number of clast types and vesicularities were attributed to repeated explosions and slumping.

In a confined setting, such as an ice cavity, larger degrees of mixing may occur while transport may be prohibited, leading to a range of grain sizes and morphologies not usually seen together in conventional tephra deposits. This may explain why vent proximal tube pumices are found alongside both blocky and vesicular ash shards within lithofacies H.

The obsidian bodies randomly distributed throughout the upper section of the deposit are interpreted to be caused by the intrusion of lava (lithofacies L) into the unconsolidated host. Many of the obsidian clasts have radial fractures around the edges which suggest that they were warm when emplaced. Repeated injection of lava may lead to the further break-up of larger obsidian bodies, forming clusters of smaller groups forming a peperitic margin.

Obsidian bodies associated with tube pumices within unconsolidated host tephras have been documented at South Ogmundur, Kerlingarfjöll (Stevenson, 2005, 2011) where their formation is attributed to extremely vent-proximal conditions at

the explosive-effusive boundary. Irregularly shaped obsidian bodies have also been documented at Dalakvísl in Torfajökull (Tuffen et al., 2008), where they are described as obsidian sheets or 'Stringers'. formed by the collapse of partly fragmented foam, marking the transition from an explosive to an intrusive, effusive eruption.

Geochemically, both the pumices from the tuff and the obsidian lava bodies match the Group Two rhyolite (see chapter 3). This suggests that the two lithofacies were cogenetic and may represent the initial explosive and later effusive stages of the same eruption.

4.2.10. Lithofacies I: Diffusely-stratified lapilli tuff (dsLT)

Description

Lithofacies I (log 4.1 and figs. 4. I1 - 4) is a diffusely stratified fragmental deposit exposed in a gully on the east-facing slope of Hrútsfjall from an elevation of approximately 452 to 535 m.a.s.l. It ranges in width from 2-5 m and continues downslope for over 50 m (fig. 4. I1). A similar deposit with very diffuse bedding is located 200 m west on the same slope but is very poorly exposed. The lower extent of the exposure is not clear as the lower section of the gully is covered with talus.

The lithofacies can be sub-divided into four sub-parallel packages (log 4.1) and are described below from the base upwards:

Package A (height: 2 m) displays the coarsest grain size and is dominated by large obsidian clasts up to sizes of 230 x 180 mm, oxidised and sub-rounded lithics up to 300 x 180mm and very large pumices up to 400 x 250 mm in diameter. In areas it is almost clast supported with minor interstitial, non-vesicular ash.

Package B (height: 15.5 m) is more massive, with a pale brown vesicular ash matrix containing sparse pumice lapilli, obsidian fragments and very occasional lithic clasts. The matrix is obsidian-poor compared to the other packages, as the obsidian granular lapilli, up to 10 mm diameter, are concentrated in irregular, anastamosing zones, or 'pipes' which have formed parallel to the bed boundary above. The pipes also contain pumice lapilli up to 15 mm in diameter.

Package C (height: 7.2 m): This package is relatively well bedded, with alternating obsidian and lithic-rich layers, pumice-rich layers and ash-dominated sub-hori-

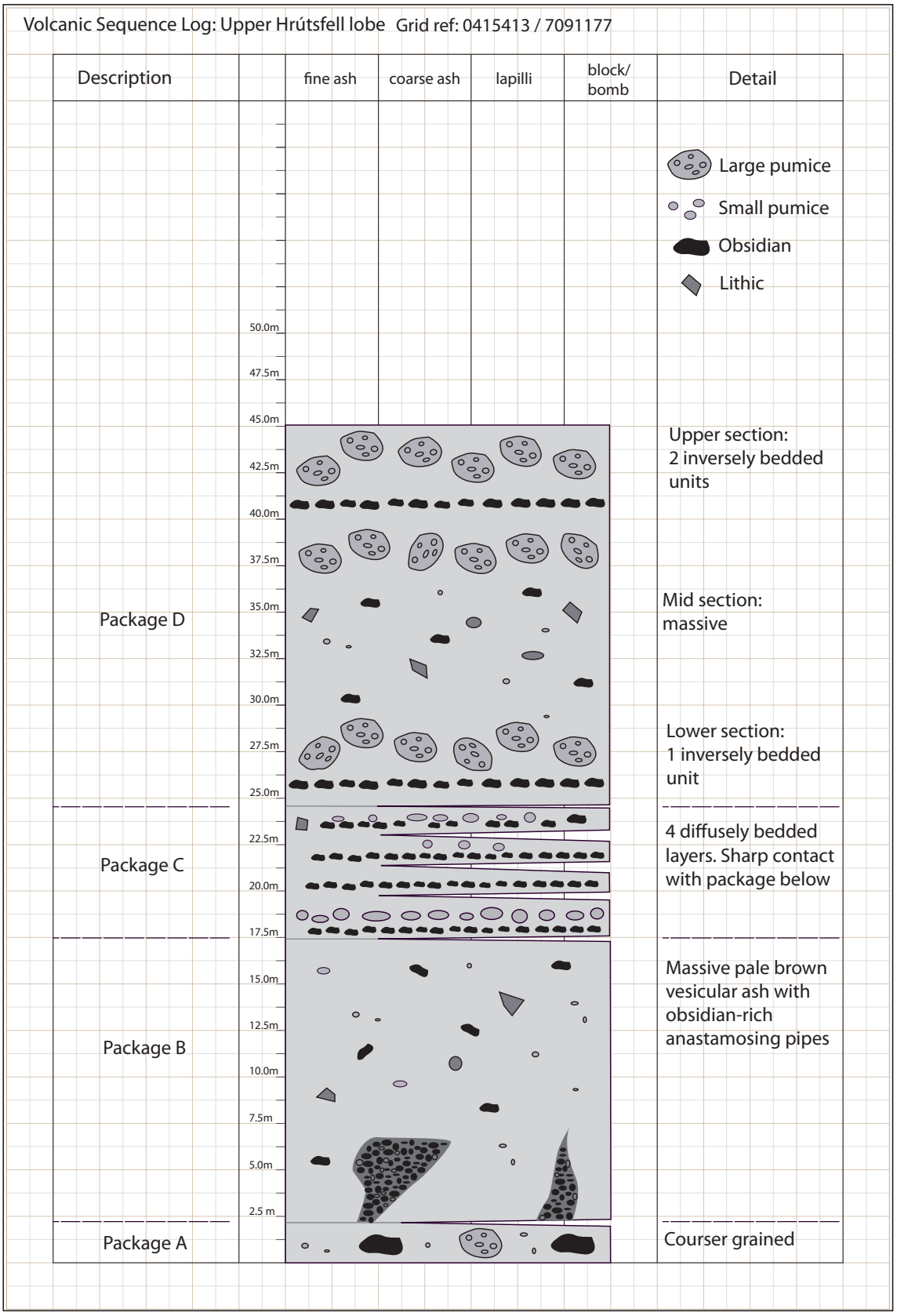
Volcanic Sequence Log: Upper Hrútsfell lobe Grid ref: 0415413 / 7091177
Description
fine ash
coarse ash
lapilli
block/ bomb
Detail
Large pumice
Small pumice
Obsidian
Lithic
50.0m
47.5m
45.0m
42.5m
40.0m
37.5m
35.0m
32.5m
30.0m
27.5m
25.0m
22.5m
20.0m
17.5m
15.0m
12.5m
10.0m
7.5m
5.0m
2.5 m
Package D
Upper section: 2 inversely bedded units
Mid section: massive
Lower section: 1 inversely bedded unit
Package C
4 diffusely bedded layers. Sharp contact with package below
Package B
Massive pale brown vesicular ash with obsidian-rich anastamosing pipes
Package A
Courser grained

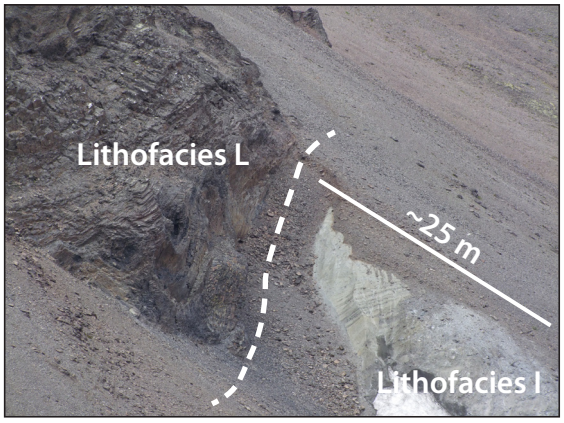

Fig. 4. I1. Lithofacies I exposed in gully beneath outcrop of lithofacies L on south facing slope of Hrútsfjall.

Fig. 4. I2.Lithofacies I, package C.

Fig. 4. I3. Package D pumices (pencil is 14 cm).

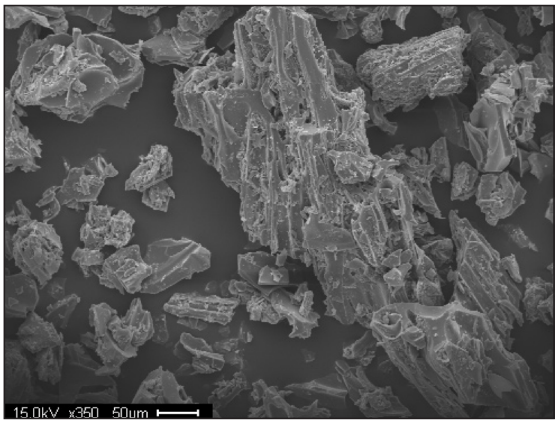

Fig. 4. I4. SEM image of ash matrix from package D.

zontal layers (dipping north-west into the slope at 22°) ranging in thickness from 20 cm to 1.25 m – the boundaries between each layer are often diffuse, although the bottom layer of this package has a sharp contact with the ash rich layer below. Some soft sediment deformation ('s' shape folding) has occurred.

Package D (height: 20 m): Overall the package is relatively poorly sorted with a pale brown / grey ash matrix; however some structure is visible at the top and base. The upper section of package D has two inversely bedded units of around 1-1.5 m each. Both units contain a number of large, fibrous pumices (>250 mm diam.) (fig. 4. I3) towards the top, and a narrow band of angular obsidian shards (1-3 mm) at the base. The mid section of the package is massive and poorly sorted. The bottom 2 m is also inversely graded with large sub-rounded pumices at the top and a narrow obsidian-rich layer at the base. Occasional larger obsidian clasts and sparse mafic and rhyolitic lithic clasts tend to be associated with the obsidian-rich layers.

SEM images of ash shards within the matrix of package D (OR303) (fig. 4.I4), package C (OR306) and package B (OR309) show a range of grain sizes from a few

microns up to 200 microns (Figs. I6-I11). Large blocky grains display vesicles up to 20 microns in diameter with thick bubble walls. Some of the larger grains have smaller grains aggregated to their surface. Angular grains with cuspate bubble walls and tube pumices are also present.

Lithofacies I: Interpretation

Although some sorting is visible in between the diffuse pumice and obsidian layers of Lithofacies I, it is unlikely that the tuff was deposited in a subaqueous environment as deposition within water would have led to more developed stratification and sorting, however this does not completely exclude interaction with meltwater or steam.

The ash grains present in the matrix of all four packages cover a broad range of sizes and vesicularities, ranging from fine ash up to large vesicular grains, blocky grains, cuspate shards and tube pumices (Figs. I6-I11). This variation suggests that more than one mechanism of fragmentation may have occurred. Grains with equant bubbles and thick bubble walls suggest that some vesiculation occurred prior to fragmentation, while the presence of tube pumice suggests near-vent activity. The variety of grain morphologies and sizes may be due to deposition within a confined space, causing grains that would ordinarily be sorted by transport processes to become mixed together.

The adhesion of very fine grained particles of ash upon larger ash grains suggests interaction with water (Heiken and Wohletz, 1985). The presence of matrix vesicles in the matrix of package D is also indicative of magma - water interaction but only a small amount of water vapour is required, which may have been caused by the melting of surrounding ice rather than ponded water (Stevenson et al. 2006). In comparison, package A matrix is non-vesicular and more coarse-grained, which may indicate less interaction with steam/meltwater.

The inversely graded pumice layers of package D and the segregated layers of package C are most likely formed by a mildly fluidised pyroclastic flow deposit. Concentrated zones of pumice and lithics are segregated by fluidisation due to increasing gas flow (Wilson, 1980). Unlike fluid-escape dominated Lithofacies H, diffusely-stratified flows are most likely produced by a small degree of turbulence-

induced traction, but not enough turbulence to cause a higher degree of stratification. This is corroborated by the presence of the anastamosing, obsidian-rich pipe like structures, which are likely to be gas elutriation pipes. The pipes are created post-depositionally, in situ as a result of gas escape. Gas and fine ash are expelled upwards as a result of settling and compaction and become laden with lithics or vesicular fragments (Branney and Kokelaar, 2002).

The shallow angle of dip back into the slope may be due to post-depositional rotational slumping due to the overlying burden of capping lavas and/or ice which have subsequently been removed.

Geochemically, pumice and obsidian clasts extracted from the tuff match the Group Two rhyolite (chapter 3), which indicates a close association with lithofacies H and the overlying lavas of lithofacies L.

Similar diffusely stratified ash-rich tuffs and breccias have been interpreted to have been emplaced within a subglacial setting have been documented at rhyolitic tuyas in Kerlingarfjöll (Stevenson et al., 2011).

4.2.11. Lithofacies J: Massive pumice & lithic-rich breccia tuff (mLT)

Description

Lithofacies J is a semi-consolidated, massive matrix-supported, ash-rich, pumice and lithic-rich breccia exposed at upper elevations, from approximately 427 to 653 m.a.s.l., on the north-west facing slopes of Hrútsfjall (figs. J 1-J7). The unit sits unconformably upon the basaltic hyaloclastite breccias and diamictite of lithofacies B, on the steep-sided slopes of the Kotá river valley. It is the largest continuous exposure of silicic pyroclastic deposits in the field area, however due to difficult access and slope instability; only the lower 50m of the unit is accessible. The upper sections of the deposit have not been examined closely and binoculars were used to describe many of the details, therefore the following description should be viewed in that context.

Lithofacies J comprises massive, poorly sorted, pale grey / light beige, partially consolidated pumice-rich tephra containing large lithic blocks of platy rhyolite >1m

Fig. 4. J1. Lithofacies J exposed on the north facing slopes of Hrútsfjall below the capping lavas of lithofacies L.

Fig. 4. J2. Lower section of Lithofacies J is more pumice-rich.

Fig. 4. J3. Localised hydrothermal alteration.

Fig. 4. J4. Close-up of surface texture.

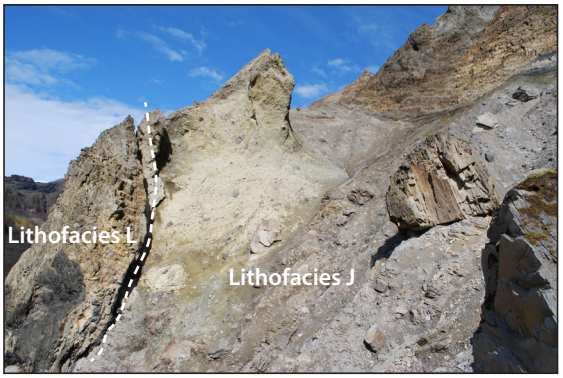

Fig. 4. J5. Upper section of lithofacies J is more lithic-rich.

Fig. 4. J6. Close-up of dense grey pumice.

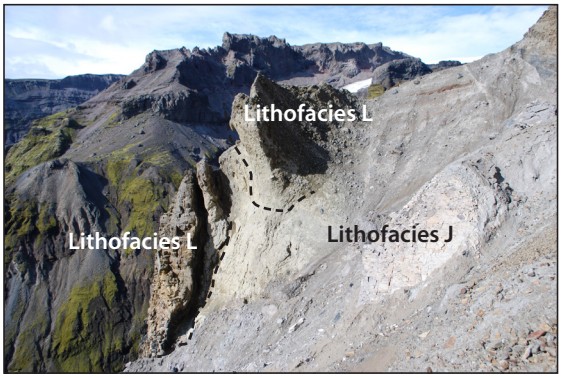

Fig. 4. J7. Sub-vertical sheets of lithofacies L overlay lithofacies J.

in diameter in places. The upper section of the unit is more chaotic, containing a larger amount of angular rhyolite blocks (fig. 4. J5). The lower 100 m of the unit is more pumice-rich (fig. 4. J2), with poorly-vesicular pumice lapilli and blocks varying in size from 20 mm to 0.5 m in diameter. Sparse angular obsidian lapilli and blocks up to 30 mm in diameter are also present within a fine grained matrix. The lower slopes also feature brightly coloured sections, with green zones and dark yellow ochre zones (fig. 4. J3). The colouring is pervasive throughout the zones, colouring the matrix and pumices within.

Lithofacies J is overlain by series of lava lobes of Lithofacies L (fig. 4. J1). In places along the slopes of lithofacies J the overlying lavas of Lithofacies L have flowed downslope away from the main overlying outcrop and the remains of lobes with vertical glassy chilled margins are present (fig. 4. J5-J7), some developing into irregular platy and columnar jointed knolls. The knolls outcrop at a similar elevation along strike (SW-NE) and help to preserve the underlying breccia up-slope by providing a barrier against gravitational instability (fig. 4. J7). The lobes will be further discussed within Lithofacies L (section 4. 2. 14).

Lithofacies J: Interpretation

The lower, massive, poorly-sorted, pumice rich-section of the unit does not show much evidence of interaction with water, although SEM images of the ash matrix shows very small particles of smaller ash grains adhering to larger grains, which is a common feature of phreatomagmatic eruptions (Butter et al, 1999; Stevenson et al 2006).

If these early pyroclastic products were confined within an ice cavity, as the relationship with the overlying lavas suggest, it is likely that some meltwater / steam was generated in the early stages of the eruption. A thick valley glacier filling the adjacent Kotá valley would most likely have been present at the time of eruption, confining the inital pyroclastic products to the north. The steep palaeovalley walls at the ice-bedrock interface would have ensured good drainage of any meltwater produced during the eruption, which may explain why there is very little evidence of water interaction. The irregular, brecciated nature of the upper section of lithofacies J, with large angular, and what appear to be monogenetic, angular blocks of rhyolite, obsid-

ian and pumice appears to be typical of a block and ash flow caused by the gravitational collapse of a lava flow or dome (Cas & Wright, 1987). This collapse maybe due to oversteepening of a confined flow during ice melt or retreat, however access to this section of the unit is limited making a thorough interpretation difficult.

A more comprehensive description of the role of ice confinement on the north west facing slope of Hrútsfjall is described within Lithofacies L (section 4.2.14).

The pervasive yellow ochre and green zones present across the mid-slope are attributed to hydrothermal alteration.

Geochemically, pumices removed from the slope match the Group Two rhyolite, therefore lithofacies J is a product of the same eruption as lithofacies H, I and L.

4.2.12. Lithofacies K: Vesicular rhyolite dyke

Description

Fig. 4. K1. Lithofacies J rhyolite dyke cuts across lower slopes of Hrútsfjall.

Fig. 4. K2.Contact with lithofacies D.

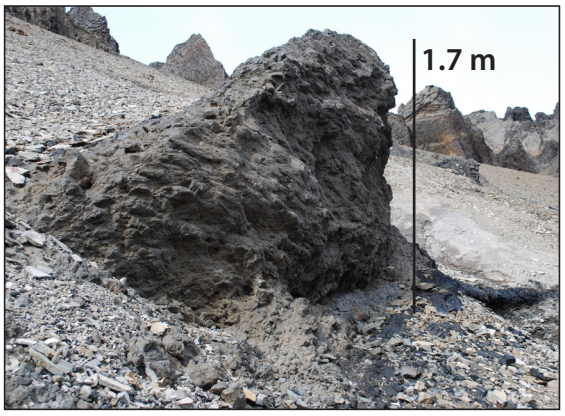

Fig. 4. K3. Glassy chilled margin of dyke (lower right).

A 3-4 m wide sinuous, vesicular, porphyritic rhyolite dyke crosscuts the lower south facing slopes of Hrútsfjall, trending at approximately 230°, from stream level at 327 m.a.s.l. to an elevation of 396 m.a.s.l. It crosscuts exposures of lithofacies C present at stream level for a length of 5 m and then stands proud of the talus-covered slope for the remainder of its visible length. The dyke has a grey interior and a black glassy margin. In places the dyke bifurcates. The dyke is vesicular throughout and the vesicles are elongated, measuring up to 70 mm in length and are oriented along the length of the dyke (fig. K1). Feldspar phenocrysts up to 8 mm in length are also present throughout.

Lithofacies K: Interpretation

A cross-cutting relationship is observed with lithofacies C; however the dyke is not traceable above an elevation of 396 m.a.s.l. and does not show any evidence of a cross-cutting relationship with the ridge capping lavas of lithofacies L. Although the dyke is porphyritic and displays a greater vesicularity than the capping lavas, geochemically, the dyke matches lithofacies L and may therefore may be a feeder dyke for the overlying ridge lavas.

4.2.13. Lithofacies L: Columnar jointed, flow banded rhyolite lavas

Description overview

Volumetrically, Lithofacies L is the largest unit in the mapping area (fig. 4. L1), outcropping as a series of lobes and flows covering the majority of Goðafjall East (fig. 4. L2), Hrútsfjall, the cirque and the upper Hvalvorðugil valley. It sits unconformably above lithofacies A at the base of Goðafjall East and has a gradational relationship with lithofacies H at the col between Goðafjall West and East and also with lithofacies I and J on the north west and south east facing slopes of Hrútsfjall. It also forms the isolated summit outcrop on Goðafjall West where it sits unconformably upon lithofacies D.

Lithofacies L outcrops as a series of columnar-jointed isolated and compound lobes and flows (fig. 4. L2) . The outcrops range in size and morphology from small

lobes less than a metre in diameter to large ridges and compound lobe flows over 100 m in height with lengths of up to 0.5 km.

It is a mildly porphyritic, lustrous to glassy microcrystalline rhyolite, containing sparse phenocrysts of sodium-rich feldspar approximately 1-3 mm in length. Thin section photomicrographs and microprobe analysis reveal that lithofacies L also contains sparse sub-rounded diopside phenocrysts, fayalite microphenocrysts and a microlite-rich groundmass of quartz and plagioclase (chapter 3). Flow banding is also present throughout, however the strength and colour of the flow banding varies between outcrops from microscopic to mesoscopic scale (fig. 4. L3).

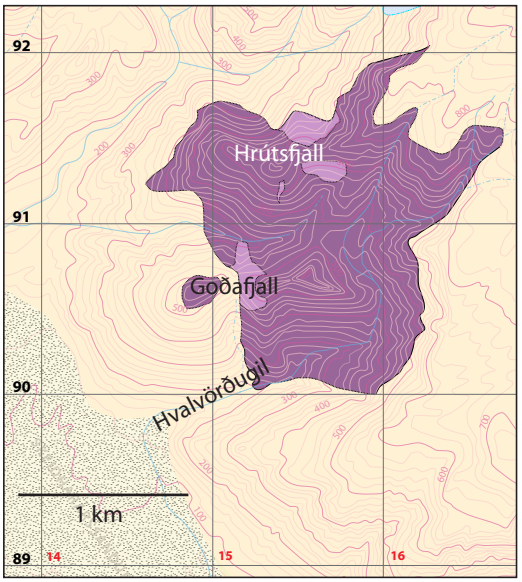

Fig. 4. L1. Extent of lithofacies L across field area. Pale purple areas indicate location of associated pyroclastic units (lithofacies H, I, J).

A high degree of textural and geomorphological variation is present across the outcropping rocks of lithofacies L, however microprobe analysis of groundmass glass taken from a number of samples across the field area reveals that lithofacies L is geochemically homogenous (chapter 3), therefore textural variations occur as a result of syn- and post-emplacement processes rather than as a result of compositional variation.

Each individual flow lobe has an internal structure which can be represented by an idealised set of five zones A to E, from base to inner core (fig. 4. L4):

Zone A: Gradational contact with underlying partially consolidated ash-rich tuffs. Lithofacies G obsidian-rich tuff grades into dark brown of fine sand-grade obsidian.

Zone B: Shattered obsidian breccia. Highly fractured, clast-supported, jigsaw-fit obsidian set within a matrix of dark brown fine sand-grade obsidian. Matrix becomes less prominent towards zone C.

Zone C: Massive, irregularly fractured, banded glassy obsidian and vitreous grey rhyolite with spherulitic layers (not present in all cases).

Zone D: Platy-jointed rhyolite with glassy zones.

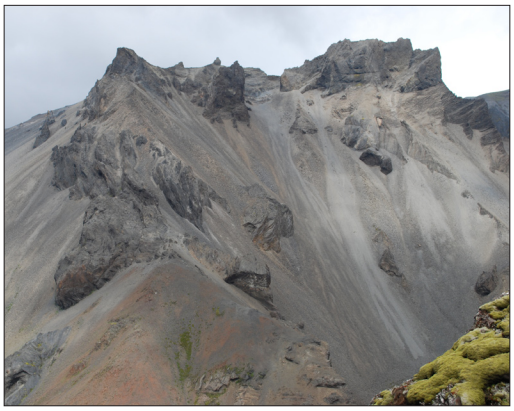

Fig. 4. L2. Lithofacies L lobes at Godafjall East.

Fig. 4. L3. Typical flow banding and columnar jointing . Column diameter ranges between 80-100 mm.

Zone E: Columnar-jointed rhyolite.

The width and complexity of each zone differs from outcrop to outcrop and where compound lobes have formed, zones A and B are omitted.

More detailed descriptions of examples of textural and geomorphological variations from specific localities of outcropping Lithofacies L are presented below.

Goðafjall East: Capping lavas

A discontinuous spine of lava outcrops along the crest of Goðafjall East (fig. 4. L2). At the col between Goðafjall East and West, a very well preserved contact is visible between lithofacies L and lithofacies H, at the base of the lowermost outcrops with well-defined textural zones A to E (fig.4. L4). At the ridge crest, columnar joints are oriented vertically and flow banding is folded but subhorizontal. Away from the summit apex the outcrops display zones of intense platy fracturing and large vertical fractures have developed with pseudopillow fractures. The northwest facing slopes, facing into the cirque, have been sheared away by glacial erosion to leave a shear-sided steep buttress. Isolated, angular columnar jointed units have been preserved on the lower slopes within the cirque. Here the columns are subhorizontal and flowbanding is orthogonal to column orientation (fig. 4. L3).

Goðafjall East: 'The onions'

Located on the south east facing slope of Goðafjall East, these outcrops form large lobate structures comprising radially-distributed sets of columnar joints. The best-preserved examples have been informally named 'Big Onion and Little Onion' (Grid Ref: 0415146/7090253) (fig 4. L5), due to the prominent sub-circular surfaces

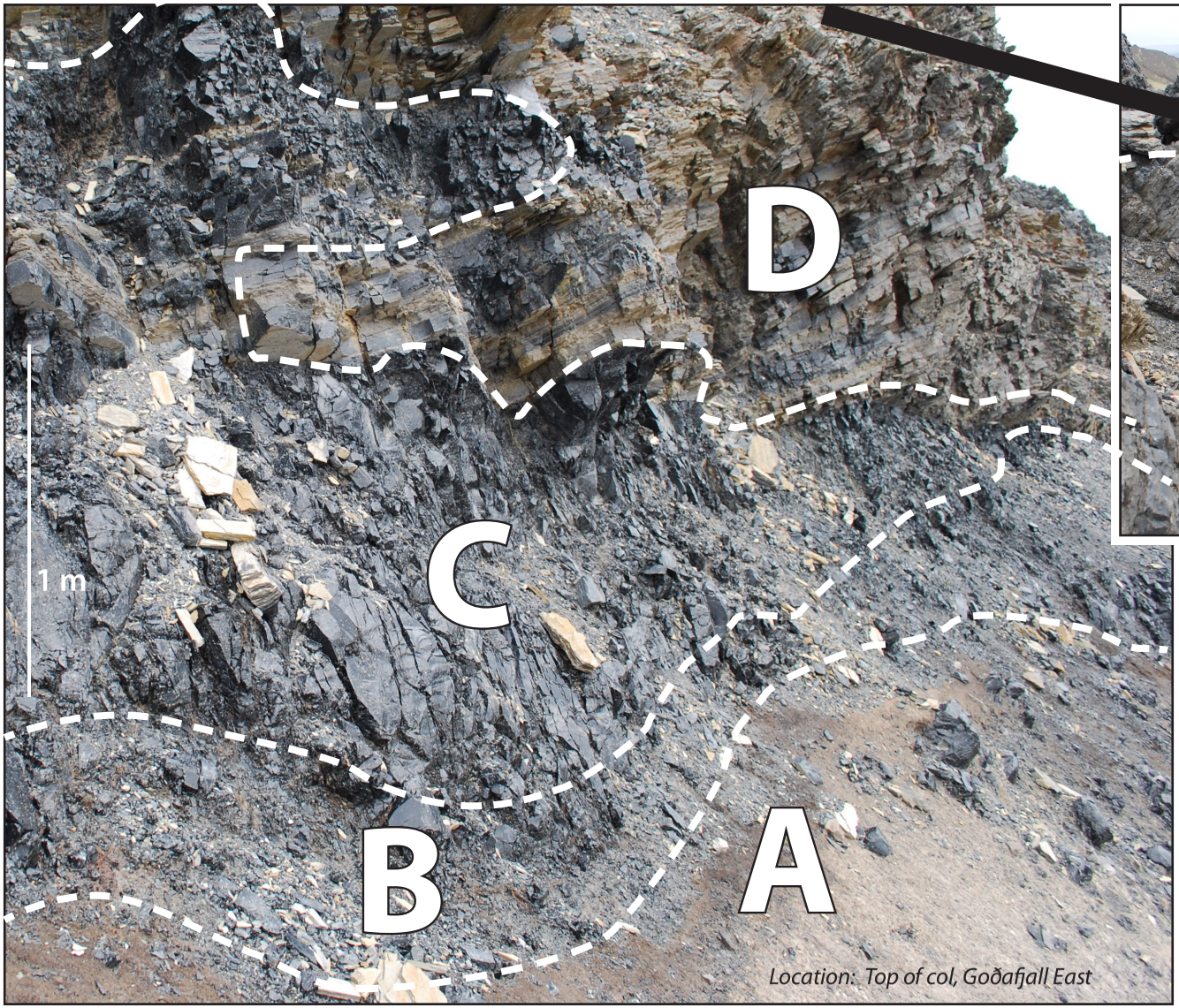

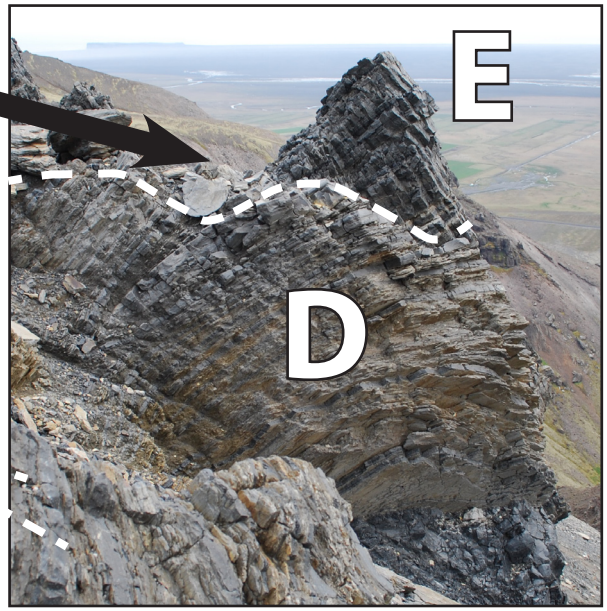

Fig. 4.L4. LITHOFACIES L – Lobe Zones A to E:

Zone E: Columnar-jointed rhyolite

Zone D: Platy-jointed rhyolite with obsidian zones

Zone C: Massive, chaotically-fractured, banded obsidian / rhyolite with spherulitic layers

Zone B: Shattered obsidian within fine grained brown obsidian matrix

Zone A: Gradational contact with underlying partially consolidated ash-rich tuffs.

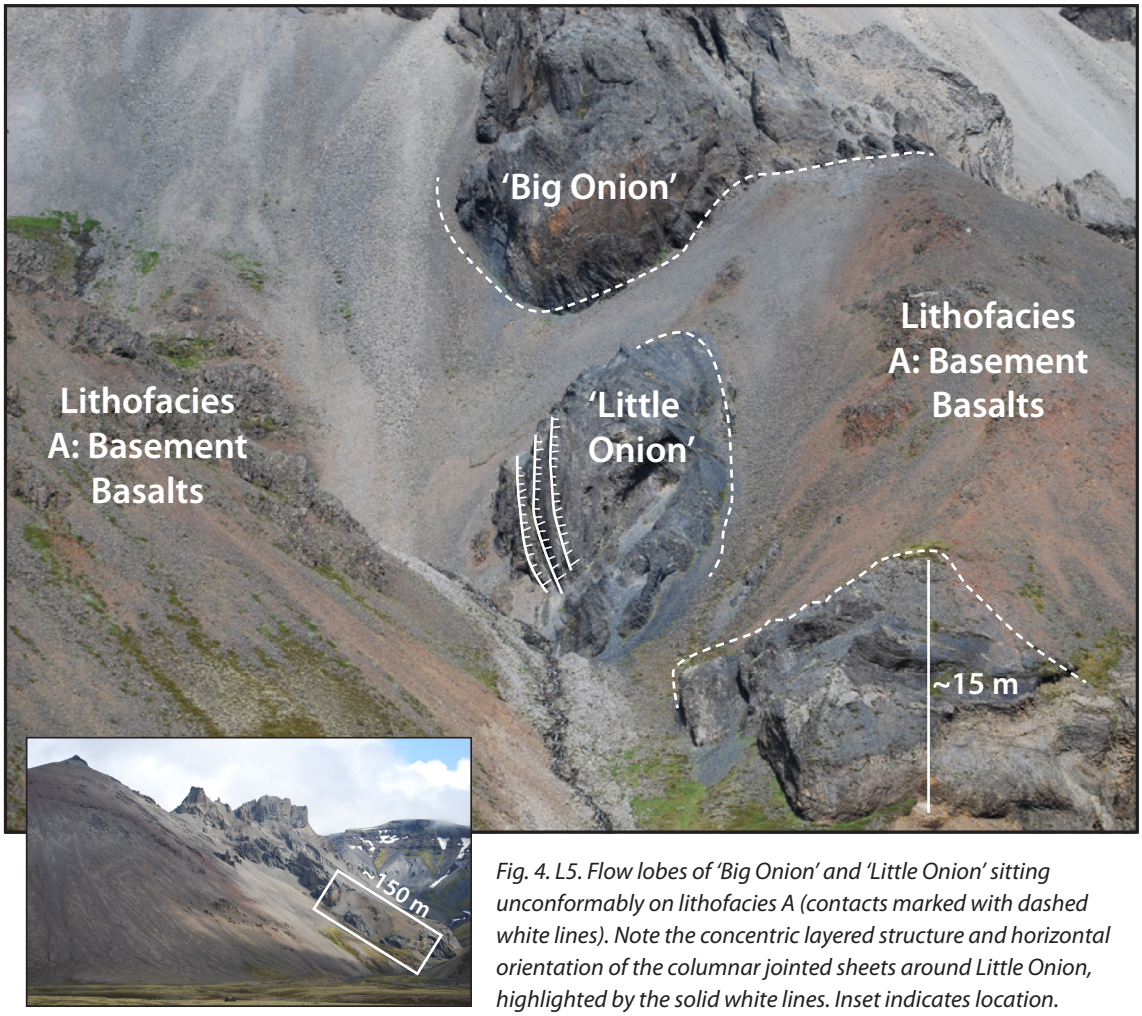

Fig. 4. L5. Flow lobes of 'Big Onion' and 'Little Onion' sitting unconformably on lithofacies A (contacts marked with dashed white lines). Note the concentric layered structure and horizontal orientation of the columnar jointed sheets around Little Onion, highlighted by the solid white lines. Inset indicates location.

exposed within the lobes. The lobes are part of a chain of discontinuous, slope-parallel outcrops that appear to originate from the large lava unit forming the summit of Goðafjall East, although the lobes are discontinuous. At lower elevations the lobes sit directly upon lithofacies A, no unconsolidated tephra is present.

The columnar joints are very well defined at this location (fig. 4. L6). The polygonal cross-sections form irregular pentagons and tetragons. Hexagonal cross-sections were not observed, so may be rare or absent. Cross-section diameters range from 50 mm up to 142 mm, with the majority being around 100 mm. Where the long axis of the column is visible, most are over 1 m in length, although many columns are fractured and in many cases the fracture propagates across more than one column.

The long axis surfaces of the columns display regularly spaced 'chisel marks' or step-wise advance cracks, oriented at 90° to the joint at intervals of 6 to 10 mm. Each advance crack can be sub-divided into a smooth section and a rough section. Some advance cracks are very strongly developed at the joint surface but fade to-

ward the centre of the column and do not appear to propagate completely. In other instances, the cracks bend towards adjacent cracks as they propagate through the column.

Flow banding is usually perpendicular to jointing, but is also visible at angles between 90° and 45°. The flowbanding cuts across the columns and in some areas the flow banding remains vertical, but the columns themselves change orientation. The columns are distributed radially and 3-dimensionally but the downslope facing front sections of the lobes have now eroded away. Bases of the lobes are obscured by locally-derived scree which has fallen away from the downslope front sections of the lobes (most likely due to gravitational instability once support is removed).

At the edges of the lobes, near to the contact with basalt lithofacies A, the lobes

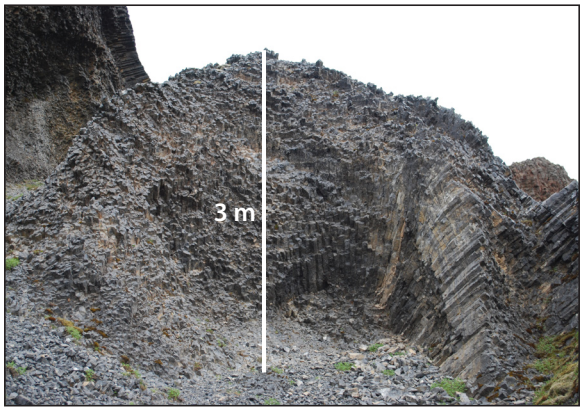

Fig. 4. L6. internal, radially columnar jointed structure of Little Onion.

Fig. 4. L7. Chilled, glassy 'rinds' form within concentric layers of columnar joints.

Fig. 4. L8. Large outcrop at base of Goðafjall East featuring 'mega columns' over 5 m in length.

have a very glassy rind or chilled margin, with some zones displaying arcuate fractures similar to perlitic fractures, suggesting interaction with water or steam (fig. 4. L7).

Adjacent to the 'onion' lobes, within the HVG valley, toward the north east, a larger columnar jointed lobe sits at the base of the Goðafjall East slope, approximately 20 m in length and 15 m high. The upstream section of the lobe has been eroded away, revealing the internal structure. It comprises between 10 to 15 concentric 'sheets' of columnar joints. Each sheet displays an almost uniform set of columns of similar length and diameter which drape over the preceding sheet. Column orientation changes gradually from the top of the lobe where columns are sub-vertical, to the base of the lobe, where they are sub-horizontal.

Another larger, neighbouring lobe structure outcropping at stream level (Fig. 4. L8) comprises columnar jointed, sandy-gold to dark brown coloured rhyolite with very faint flow banding. The most important factor that distinguishes this from the lobes downstream is the formation of well-defined 'mega-columns' 350-500 mm in diameter and over 5m long, although the columns have fractured into smaller sub-sections between 600 and 900 mm in length . The unit is around 15 m in height but other smaller outcrops are situated adjacent and above, although these are not as well preserved. At the base of the exposure, at stream level, the columns are almost horizontal, plunging 10° NE. Moving up through the unit, the columns gradually change orientation, so that at the top of the exposure the columns are plunging 16° SW. Above this exposure, in some areas within the scree, frost shattering has caused the columns to fracture along the perpendicular stepwise advance cracks, producing thin 'sheets' where the columns have split apart.

Goðafjall West Summit:

An isolated unit of Lithofacies L outcrops at the summit of Goðafjall West (Fig. 4. L8-L9)(grid ref: 0414848/7090653). The outcrop is approximately 3 m high and 5 m in diameter with a glassy base that develops into plates higher up – no columnar jointing is present, although a weak vertical linear alignment is visible in some upper sections (fig. 4. L9). Striking mainly to the north, the plates change dip angle (varies from 28°W to 72°E) on a sub-metre scale and in some areas groups of plates

Fig. 4. L9. Goðafjall West summit.

Fig. 4. L10.Goðafjall West summit outcrop close-up

oriented at slightly different angles come together and are beginning to fracture into needle-like joints. The Goðafjall West summit unit is the only isolated occurrence of lithofacies L that does not display columnar jointing on its upper outer margins.

Hrútsfjall Ridge

The Hrútsfjall ridge crest (fig. 4. L11-L14). is 1.3 km long oriented north east - south west and outcrops at an elevation of 827 m.a.s.l. at its north east margin and 653 m.a.s.l. at its western tip. It can be divided into three sections: the western ridge tip; the lava lobe dominated mid section; and the north eastern scree-covered ridge.

The south western tip of the ridge has a rounded, scree-covered summit draped with patches of slope-parallel deposits. The summit is surrounded by a continuous ring of columnar jointed rhyolite lavas that form a buttress around the western end of the ridge. On the North West facing slopes the flow base is visible (fig. 4. L11-L13) where it sits unconformably on basalt breccias and a diamictite horizon (litho-facies B).

The flow base comprises a glassy, fractured obsidian margin approx 1.3 m thick displaying hackly jointing at the base (fig. 4. L13) . The obsidian margin grades into a vitreous grey-brown sub-horizontal platy layer approximately 10 mm thick. There is a strong sense of vertical lineation throughout this section, eventually developing into fully-formed columnar joints. The flow base broadly represents textural zones C to E of the idealised lobe formation sequence (fig. 4. L4). The main body of the lava flow appears to be formed of multiple, 'compound' columnar jointed lobes, which display arcuate and radial jointing patterns throughout.

The mid section of the ridge summit comprises a collction of smaller lobes

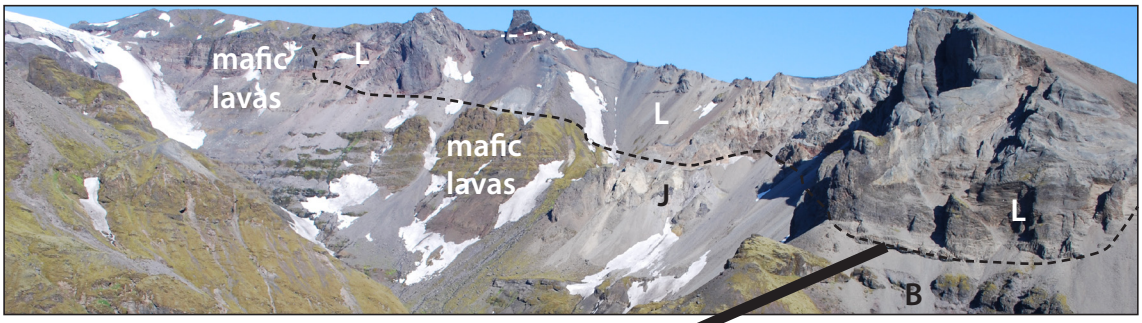

Fig. 4. L11. North facing slope of Hrútsfjall

Fig. 4. L12. Glassy flow base of Hrútsfjall lava lobes.

Fig. 4. L13. Close-up of glassy flow base (ruler is 1 m).

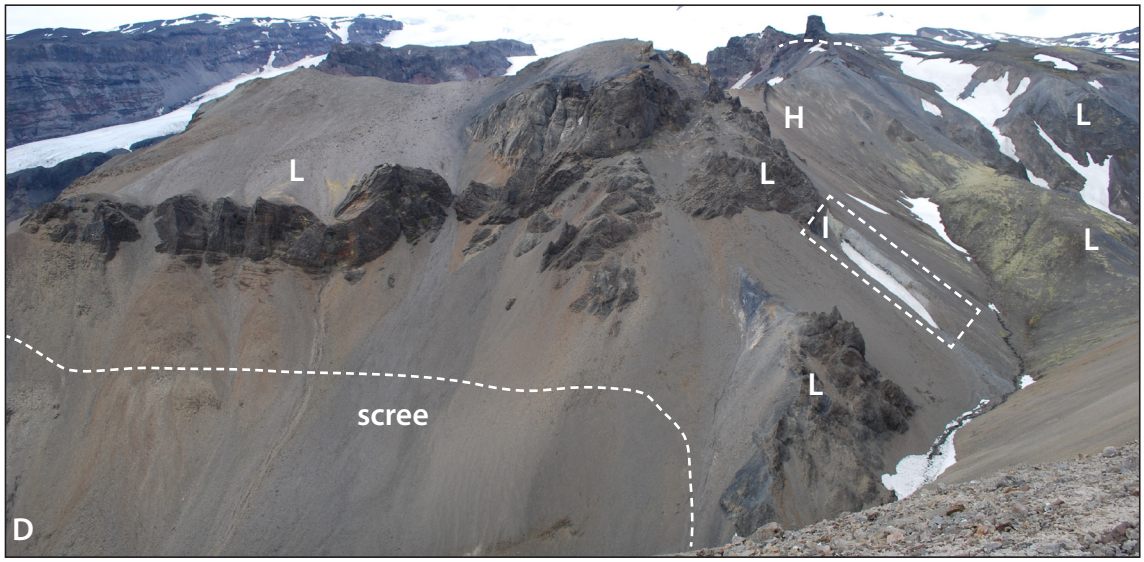

Fig. 4. L14. South facing slope of Hrútsfjall indicating lithofacies associations.

with heights of up to 5 m and remains of lobate structures that have been partially eroded to reveal their inner structure (Fig. 4. L15a-b). Many of the lobes have columnar jointed outer surfaces and their inner structure can be sub-divided into a sequence of textural zones, broadly similar to the idealised lobe formation sequence seen at the col, but with some notable differences, which is represented in a log (Fig. 4. L15b). Zones A and B are present but have a much more irregular relationship with the overlying lobe. Zone B grades into a new zone of pale brown-grey devitrified rhyolite with flow aligned, angular and elongated obsidian clasts. The majority

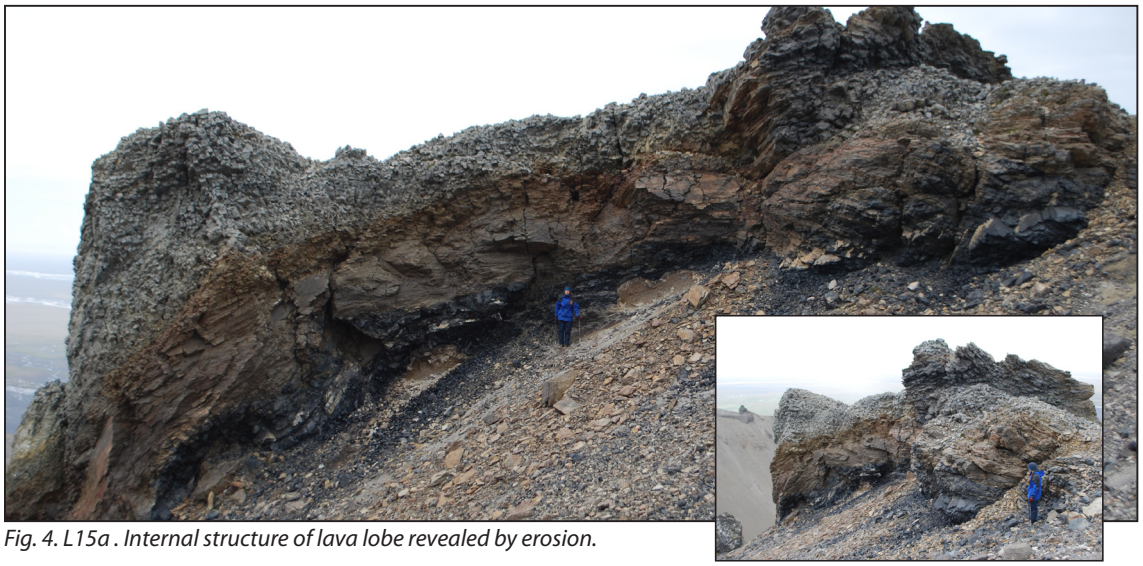

Fig. 4. L15a . Internal structure of lava lobe revealed by erosion.

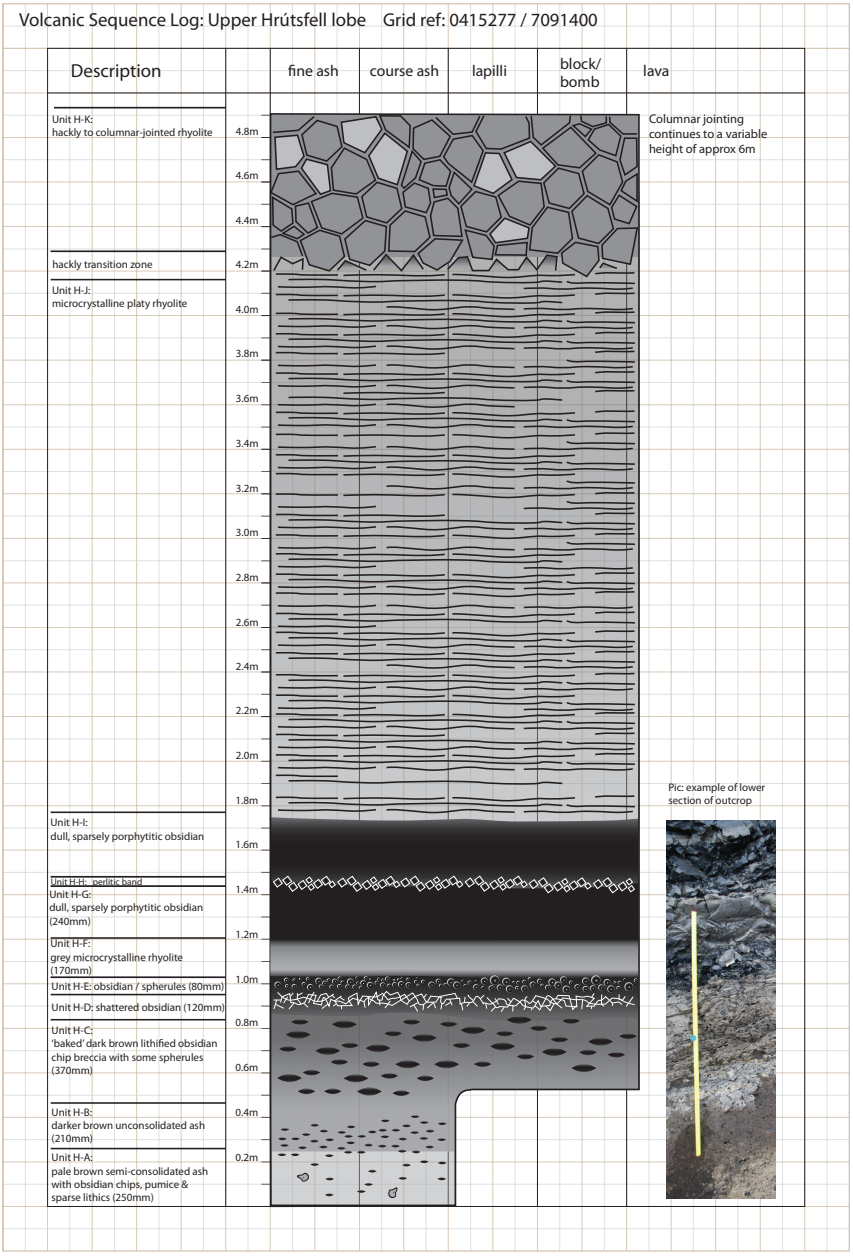

Fig. 4. L15b . Log of internal structure of lava lobe.

Fig. 4. L16. Arcuate lava spines with a sub-vertical platy habit

of clasts are between 5 to 10 mm in length and 1 to 6 mm wide, but there are also occasional larger clasts up to 30 mm in diameter. The smaller flow oriented clasts flow around the larger clasts (fig. 4. L15b). This zone shares some similarities with autobrecciated zones observed in the flow base margins of lithofacies D and may be a result of a greater interaction with water / steam. Above this zone is a zone of more regular fractured rhyolite. This zone is folded and in places has flowed around and over irregular rounded pods of material from zone A. Alongside the lobes are arcuate lava spines (fig. 4. L16) which display a sub-vertical platy habit. These sub-vertical spines differ from the ones present around the walls of the 'Little Onion' at Godafjall East as they are not columnar jointed and appear to represent an 'inner' rather than outer portion of these lobes.

The layers comprise devitrified rhyolite separated by fractured, flowbanded obsidian. Some of the spines are over 5 m in height. They appear to be similar to crease structures found on the surface of subaerial rhyolite domes and coulees (Anderson and Fink, 1992), however crease structures usually develop as a result of lateral spreading and in this location flow confinement due to ice is more likely. The spines may represent the inner vertical walls of tightly compressed flow lobes.

The uppermost section of the ridge comprises a narrow arête punctuated by angular spine-like vertical walls of layered rhyolite and obsidian with granular obsidian scree-covered slopes falling away to the North West to the Slaga Valley and to the South East, obscuring a poorly exposed underlying pumice-rich tuff (Lithofacies H).

On the North West facing slopes of Upper Hrútsfjall, the capping lava lobes of Hrútsfjall ridge flow down the upper sections of both flanks of the ridge. On the North West facing slopes of the mid to upper section they overlie the tuff breccias of Lithofacies J.

Along the slope, at elevations around 450 m.a.s.l. a number of isolated vertical lava walls (fig. 4. L17a) are positioned along the same elevation parallel to the ridge alignment. The lava walls have a variable thickness of 1.5-2 m with an inner and outer chilled obsidian margin 100 mm thick followed by a 0.5 m sub-vertical platy zone. An inner zone of sub-horizontal columnar joints (fig.4. L17b) is sandwiched between the two outer zones. Flow banding throughout the exposure is perpendicular to column orientation and parallel to plate orientation. Asymmetric fold pairs present within the flow banding act as flow direction indicators (fig. 4. L17c).

The innermost margin is chilled against the semi-consolidated tuffs of lithofacies J which stand proud from the slope as it has been protected from erosion by the lava wall (fig. 4. L17a - b).

The chilled margin grades from the tuff (zone A) to a brown fine grained obsidian layer (zone B) to a highly fractured obsidian layer (zone C). The first 80 mm of this layer is highly shattered into elongate shards with the long axis in alignment with flow banding.

Hrútsfjall Lobe with shattered obsidian breccia carapaces

An isolated, discontinuous lobate lava body (fig. 4. L14) is perched on the south western facing slopes of Hrútsfjall where is it exposed down to stream level and is adjacent to a similar but less well-exposed lava body on the opposite side of the stream at the base of Goðafjall East. Where the lobe contact with the underlying lithofacies H (partially consolidated tuff) is visible it has a gradational contact with a margin that displays textural zones A to E. The lobe does not appear to have been linked to the upper lobes at the ridge crest.

Fig. 4. L17a -c. Double-chilled margin of sub-vertical spines on mid north-facing slopes of Hrutsfjall overlaying lithofacies J (mLT). Asymetric fold-pairs indicate flow direction of lava (c).

Upper HVG Valley columnar jointed rhyolite dome

A large rhyolite dome (fig. 4.L18) is situated within the cirque at the head of the upper HVG valley, adjacent to Hrútsfjall Ridge. The top of the dome at 835 m.a.s.l. marks the highest occurrence of rhyolite within lithofacies L.

It comprises columnar jointed pale gray and dark grey flowbanded rhyolite and obsidian. The dome is bound to the north west and south east by the Hvalvorðugil stream which flows in eroded gullies and crosscuts the dome at its margins. The dome forms the link between the lithofacies L lavas situated on Hrútsfjall ridge and

Fig. 4. L18. Columnar jointed rhyolite dome at the head of the HVG valley. Dome is approximately 350 m in height.

those situated on the flanks of the eastern wall of the HVG valley.

The dome is columnar joined throughout and on its accessible south east facing side within the upper HVG valley the columnar joints are uniformly plunging to the north (357˚) between 20˚ to 60˚. The prominent grey and black flowbanding is very irregular, displaying contorted folds and folded fold patterns. No obvious kinematic indicators are visible. The dome had been subjected to erosion which has led to the development of spiny vertical rows of joints on its western to southern sides.

Lithofacies L: Interpretation

Lithofacies L lavas display a wide variety of textures and morphologies at different locations throughout the field area. Geochemistry reveals that it is identical to and therefore closely associated with the underlying partially consolidated tuff deposits of lithofacies H, I and J.

The lava lobes present on the lower south facing slopes of Goðafjall East are columnar jointed throughout, while the internal marginal structure of the larger summit outcrop, where visible, follows the gradational pattern represented by zones A to E (fig. 4. L14). At the summit, columnar jointing is vertical and flow banding

is folded and horizontal. Away from the summit apex the columnar joints and flow banding change orientation to produce lobe structures with often sub-vertical to vertical flow banding and radially fanning and sub-horizontal columnar joint orientations. The unit is columnar jointed throughout which suggests enhanced cooling, with water and/or ice being the likely coolant. Basal breccias typical of subaerial rhyolite flows are not present anywhere on Goðafjall East. Instead, the lobe bases, where visible, have chilled fractured obsidian margins and a gradational contact with the underlying tuffs of lithofacies H (which is represented by zone A). It is therefore suggested that the Goðafjall East lavas were emplaced into the ice- confined pumice rich lapilli tuff of lithofacies H leading to the development of a peperitic margin between the two lithofacies (fig. 4.H2-H5).

Prolonged eruption built up a spine of columnar-jointed lobes that chilled quickly against the confining ice. Further downslope, the elongate, esker-like, slope-parallel morphology of the 'Onion' lobes and the relationship of the contact with the underlying lithofacies A suggest that the confined lava may have exploited pre-existing cracks and voids within the ice at the interface between the base of the glacier and the pre-existing bedrock. This hypothesis is supported by the radial, fanning orientation of the columnar jointing which suggests cooling against a cold, cylindrical confining surface such as an ice tunnel wall.

The development of concentric, stacking layers of columns is most likely formed by the incremental penetration of water vapour. As the lava chills quickly against the cold ice surface, water vapour is generated, this pervades the outer skin of the lava causing it to behave in a brittle manner, while the inner lobe is still hot, ductile and flowing downslope. This leads to the development of a plane of separation between the outer cooled lava and the inner ductile lava as it travels forward. Water vapour is now able to exploit the fractures within the outer brittle layer in order to propagate and chill a further inner layer of the still ductile lava. This cycle of internal cooling and fracturing continues incrementally while the ductile lava core travels downslope, forming concentric 'sheets' of radially oriented columnar joints on separate planes (Fig. 4. L1).

The lack of associated pyroclastic material at the contact between the lobes and basalt lithofacies A suggests that the tunnels were well-drained and free of any un-

consolidated fine material when the lava was emplaced. Meltwater drainage and the resulting transport of tephra may have been enhanced by the pre-existing bedrock topography.

Some of the concentric sheet column formations on the slopes of Goðafjall East are detached from their adjacent lobe forming freestanding 'spines' with sub-horizonal columnar jointing. This suggests that many of these isolated lobes may be all that is left of the 'cores' of several much larger, continuously columnar jointed lobes, or even one large continuous lava flow that has experienced large amounts of glacial erosion.

The summit of Goðafjall West is contemporaneous with the summit outcrops of Goðafjall East and has been isolated the by subsequent glacial erosion of the partially consolidated tuffs of lithofacies H within the col area.

On the neighbouring Hrútsfjall summit where no underlying unconsolidated tephras are exposed – for example at the exposed flow base at the western tip of the Hrútsfjall compound lobes (fig. 4. L11-14) – the prominent chilled obsidian base displays hackly jointing in the lower 15cm which is indicative of quench fragmentation (McGarvie, 2009) .

On the Hrútsfjall summit ridge, the lava lobe segments and arcuate spines display a complex distribution pattern and range of flow banding orientations. Lobes featuring bases with sub-horizontal or slope parallel plate formation and flow banding are closely associated with, or adjacent to, arcuate lava spines that display sub-vertical plate formation and flow banding that are absent of columns. These outcrops are interpreted as the highly eroded segments of intensely folded lavas that have been unable to flow freely away from the vent due to restriction or confinement by ice (fig. 4. L16).

The visible gradational contacts with lithofacies H have a thin zone of highly shattered obsidian and / or devitrified rhyolite with a strong linear fabric and flow aligned obsidian shards. This zone is formed as a result of the combination of basal shearing and rapid chilling due to quench fragmentation and may record the point of ductile-brittle transition in the cooling lavas.

The double-chilled vertical walls that outcrop at a similar elevation along strike on the mid north-facing mid slopes of Hrútsfjall is interpreted as a lava flow that

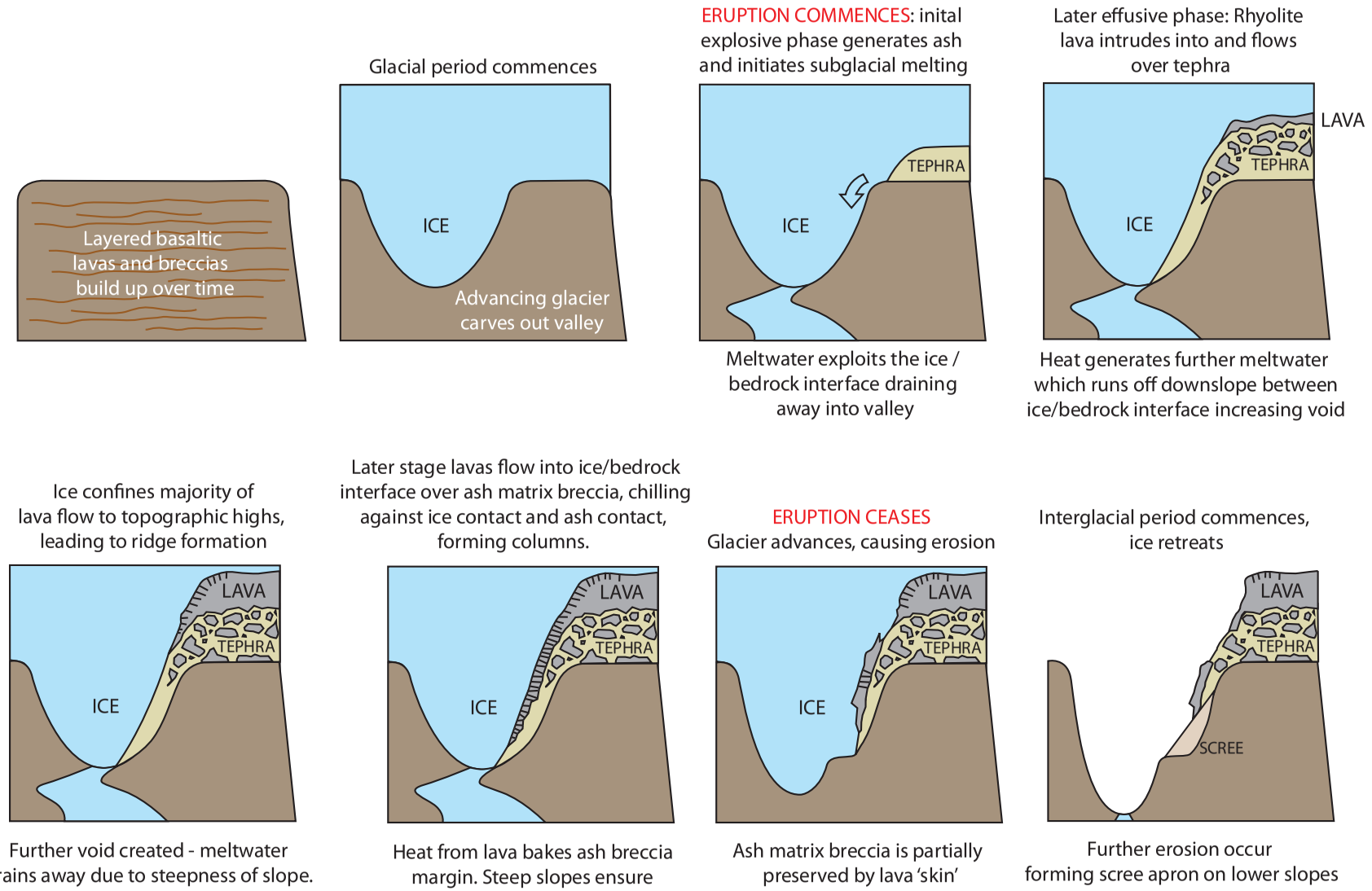

Fig. 4. L19. Schematic diagram of development of double-chilled vertical walls on north-facing slope of Hrútsfjall.

has exploited the thick valley-fill glacier margin. The lava flows over the tuff forming a protective layer and as it reaches the glacier margin it exploits the near-vertical glacier / tephra interface. Chilled margins form against both the tuff and the ice. Any meltwater generated immediately flows away due to the steepness of the valley sides. Figure 4. L19 is schematic representation of how the sub-vertical walls were formed.

Two types of lobe architectures – intrusive and extrusive – appear to occur within lithofacies L (Stevenson et al., 2011) (fig. 4. L20). The first type occurs where lavas have intruded into unconsolidated host tephras and is typified by the multiple lobe structures at the summit of Hrútsfjall. The second type occurs where lobes have formed flows and travelled downslope or some distance away from the point of eruption, typified by the lobe structures on the south facing slopes of Goðafjall East and in the HVG valley.

Subglacial rhyolite lobe architecture has previously been attributed to two contrasting styles of emplacement at other sites in Iceland including Torfajökull and Kerlingarfjöll (Stevenson et al., 2011)

Apart from the dyke on the southfacing slope of Hrutsfjall (lithofacies K), no

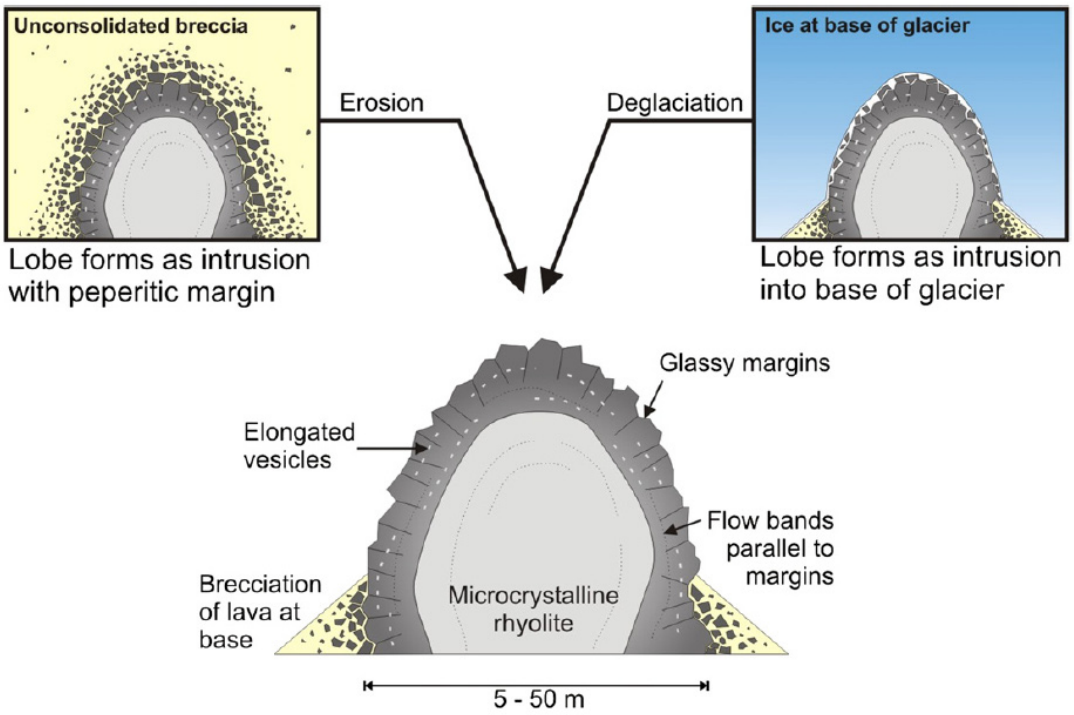

Fig. 4. L19. After Stevenson et al, 2011: Intrusive and extrusive lava lobe formation.

other obvious feeder dykes or vent structures have been identified on the summit of either ridge or on the large dome at the head of the upper HVG valley, therefore it is assumed that the source vent or vents for lithofacies L have been subsequently removed by erosion and/or overlain by younger units at higher elevations.

4.2.14. Lithofacies M: Cross-bedded sandstone – breccia

Description

Lithofacies M (fig. 4.M1-M4) outcrops in the cirque, on the mid-slope of the south west facing valley wall. It sits unconformably on rhyolite lithofacies L, although no contact is visible, and is overlain by lithofacies N, a columnar jointed, glassy intermediate lobe. It is the only example of its kind in the field area.

Cross-bedded fine to medium grained golden sands with both pumice-rich and gravel-rich lenses of variable thickness that pinch out are observed. Wavy bedding surfaces, truncated beds and ripple laminations are evident throughout the exposure. Many of the beds have sharp, irregular, scoured bases.

Fig. 4 M1: Ripple lamination, pumice-rich lenses, cross bedding and sharp, irregular bases

Fig. 4. M2: Obsidian and lithic lenses within medium sandstones

Fig. 4. M3: Large (110 x 90 mm) obsidian clast entrained .

Fig. 4. M4: Obsidian rich layers .

Reverse graded pumice-rich beds are a prominent feature with larger sub-rounded pumice clasts within a matrix of golden brown medium to coarse- grained sand. The pumice clasts are relatively well sorted, ranging between 8 to 25 mm in diameter with the occasional outsize clast up to 80 mm in diameter. Lithic and obsidian-rich lenses are also present but are less common.

Lithofacies M: Interpretation

Lithofacies M comprises mainly of reworked rhyolitic volcaniclastic material. The beds displays sedimentary features that are indicative of a fluvial environment with migrating bedforms, channels and irregular erosive scoured bases all suggesting fluvial transportation similar to the bedforms produced within a migrating stream system. Lithofacies M may represent the remains of a palaeo-cirque valley floor exposed by subsequent glacial erosion, although other exposures within the cirque have not been identified. The current stream system within the cirque valley floor is situated approximately 15 m below lithofacies M exposure. A large clast of obsidian within the unit (fig. 4. M3) was analysed geochemically and matches the Group Two rhyolites, of which the underlying lithofacies L is a member.

4.2.15 Lithofacies N: Trachydacite lava lobes

Description

Lithofacies N outcrops as a series of three lava lobes located on the east facing wall of HVG valley. The three lobes are isolated and are situated between 15 and 20 m away from one another, outcropping at around the same elevation at the interface between the lower lithofacies L rhyolites and

Fig. 4. N1. Radially columnar jointed trachydacite lobe.

the sub-horizontal lavas of lithofacies N. Direct contacts are obscured by talus but lobe morphology and orientation indicate that the lobes have been emplaced on the current angle of the slope (Fig. 4. N1). The lobes are glassy and display hackly to columnar jointing and the columns are oriented radially around the shape of the lobes. No flow banding is visible but some sections of the lobe display zones of elongate vesicles. The joints themselves are coated with a very fine ash-grade material.

Lithofacies N: Interpretation

Major element analysis (chapter 3) shows that the lobes are trachydacite in composition and are the only examples of intermediate lavas in the field area.

The pervasive radial columnar joint orientation is similar to many of the rhyolite lobes distributed throughout the field area and may suggest emplacement into a subglacial environment and rapid chilling within an ice cavity.

As the lobes appear to have been deposited onto the pre-existing slope, the underlying rhyolite must have undergone erosion prior to emplacement, suggesting the occurrence of least one glacial cycle between the emplacements of the two units.

The three lobes outcrop in only three locations at the interface between columnar jointed rhyolite and sub-horizontal mafic sheet lavas and show no evidence of having been conjoined. This suggests that the lobes were emplaced as sills that exploited the interface between the two units and may therefore be younger than the overlying sheets.

The lobes provide evidence to suggest that at the time of emplacement, the cirque and HVG valley was filled with ice up to an elevation of at least 541 m.a.s.l.

The most northerly lobe (fig. 4. N1) has the remnants of the base of a smaller lobe adjacent to it. Alternatively this may be an eroded section of the larger lobe that has since undergone erosion and become disconnected to the main body of the lobe. Columnar jointed lobe structures in other locations in Iceland have been shown to display 'onion skin' weathering (Stevenson et al, 2011). This type of erosion makes interpretation difficult between intrusive dyke-like bodies or lavas that have flowed into and cooled against ice cavities.

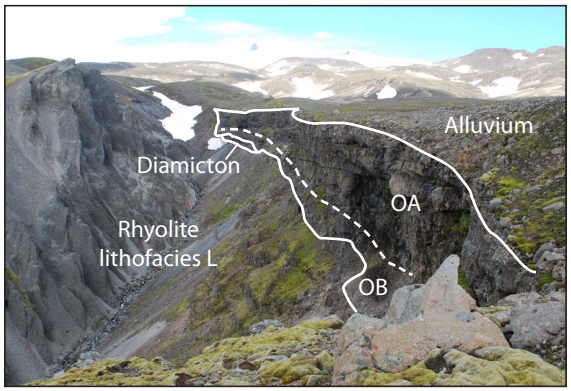

Fig. 4. O1: Eastern Wall of HVG Valley, viewed from the south west. Sub-lithofacies OB sit unconformably on diamicton at head of valley. Dashed line marks transition from sub-lithofacies OB to OA.

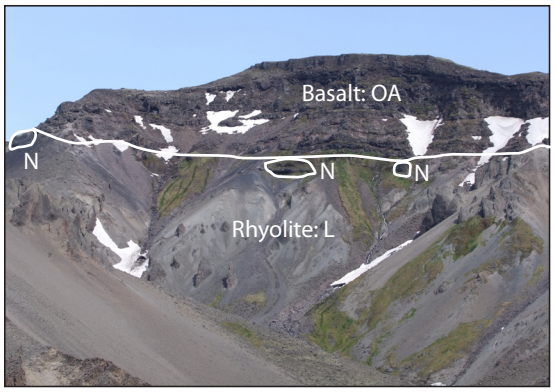

Fig. 4. O2: Eastern Wall of HVG Valley. Sub-lithofacies OA, continuous subhorizontal mafic units sit unconformably on rhyolites and isolated trachydacite lobes of lithofacies N (white ovals).

Fig. 4. O3: Close-up of vesicles (Camera lens is 70 mm in diameter).

Fig. 4. O4: Sub-lithofacies OA, blocky breciated upper surface of subhorizontal flows at upper HVG valley.

4.2.16. Lithofacies O: Basaltic lavas

Description

The uppermost section of the high cliffs on the eastern wall of the HVG Valley is formed of a series of subhorizontal lava flows which are collectively described as lithofacies O (fig. 4.O1-O4). Lithofacies O is sub-divided into two types, upper OA and lower OB.

Sub-lithofacies OA forms the uppermost layers at the head of the HVG valley and is characterised by fractured and blocky lavas. Many have autobrecciated upper surfaces in which clasts are partly welded, massive central zones, and autobrecciated lower surfaces. The lavas are variably vesicular, with coarse, spherical and elongated vesicles up to 50 mm in diameter (fig. 4. O3). They form continuous sheets that are exposed for at least 300 m in a vertical cliff along the eastern crest of HVG valley. The lavas dip gently to the SW and they form the upper 30 m of the lower of the

two sequences present. The upper lavas in the section are relatively coarse grained, blocky in places and coarsely jointed with prominent vesicular tops. Tracing the exposure south, around the eastern wall of the cirque, the number of sheet lavas increases and their individual thicknesses increase to around 5 m (fig. 4. O2). The lavas mantle the gentle topography of the underlying rhyolite (L). Traced down-dip to the south, the lavas display bright red oxidised surfaces.

Following the outcrop futher south, the lavas become more uneven and laterally discontinuous where they overlie a steeper palaeosurface upon the underlying ryolite. At this location the lavas are are now ovelain by what appears to be a thin layer of volcaniclastic sediments and diamictite (Fig. 4. R1), however direct access is not possible and this section of the cliff can only be examined from a distance of several metres with the aid of binoculars.

The OA lavas are porphyritic with feldspar phenocrysts ranging in size from 2 to 10 mm in diameter. XRF analysis (chapter 3) indicates that the individual lava units range from basalt to basaltic andesite in composition.

By contrast sub-lithofacies OB form the lowermost section of the lava sequence in the upper HVG valley (fig. 4. O1). It increases in thickness toward the south from 10 m to 35 m further downslope and is composed of fine-grained, non-vesicular cube jointed lava layers that are individually ≤ 5 m thick.

At the head of the valley OB is 10 m thick and displays hackly jointing and a prominent glassy chilled lower margin. The base of that lava also has a sharp, blocky peperitic contact with an underlying layer of soft clay-like partially consolidated sediment (likely diamicton), which separates the lava from the underlying rhyolites. Occasional fingers of diamicton penetrate the joints of the overlying lavas by up to 3 m. The basal diamicton layer is up to 7m in thickness. It overlies columnar jointed rhyolite in which the tops of the columns are fractured and broken.

Lithofacies O: Interpretation

The relatively coarse grain size, coarse jointing and presence of coarsely vesicular, partly welded and reddened (oxidised) autobreccia in Sub-lithofacies OA suggest effusion of basaltic lavas in a dry subaerial setting in an absence of surface water and/or snow and ice. By contrast, the presence of glassy and locally peperitic margins to

lavas of Lithofacies OB, together with their finer grain size and closer-spaced, often blocky jointing are indicative of strong chilling in the presence of some water (e.g. Lescinsky and Fink, 2000).

The absence of hyaloclastite and lava pillows suggests that the volume of water was minor and may have been a product of contact with snow. A broadly glacial setting is implied by the presence of underlying partially consolidated diamict. The diamict must have been unconsolidated at the time of extrusion in order to be back-injected up into the basal lava and react with the lava to form peperite. However, there is no evidence that the glacial ice that deposited the diamict was still present at the time of extrusion, since the presence of overlying glacier ice would have led to the formation of either a sheet-like glaciovolcanic sequence or a lava-fed delta (Smellie et al., 1993; Smellie, 2008). Therefore it is assumed that these lavas were deposited in the waning stages of a glacial period or very early post glacial.

4.2.17. Lithofacies P: Basaltic breccia with lava lobes

Description

The lava sequence formed by Lithofacies O above HVG Valley thins out to the south and is draped across an uneven surface by apparoximately 50 m of breccia (figs. 4. P1-P3). Due to the steepness of the upper slopes of HVG, access to Lithofacies P was very restricted. The basal 10 m of the breccia is massive but it becomes crudely bedded above (Fig. 4. P1). It is clast-supported and monomict, consisting predominantly of coarse grained, poorly vesicular to non-vesicular often glassy or aphanitic basalt granules interspersed with amoeboid cube-jointed lava lobes and pillow-like masses up to 1 m in diameter featuring 'tiny normal joints' around the edges. Irregular cavities with jointed rims up to 50 cm in diameter are also present within the breccia.

The breccia matrix has a strong yellow colour (fig. 4. P2). Very occasional accidental clasts of angular to sub-rounded pebble to cobble-sized clasts are randomly dispersed throughout the breccias, including rare clasts of platy rhyolite, obsidian and pumice. The contact between the underlying rhyolite and the breccia is sharp and erosive (fig. 4. P3). Large columnar and hackly jointed porphyritic lava lobes up

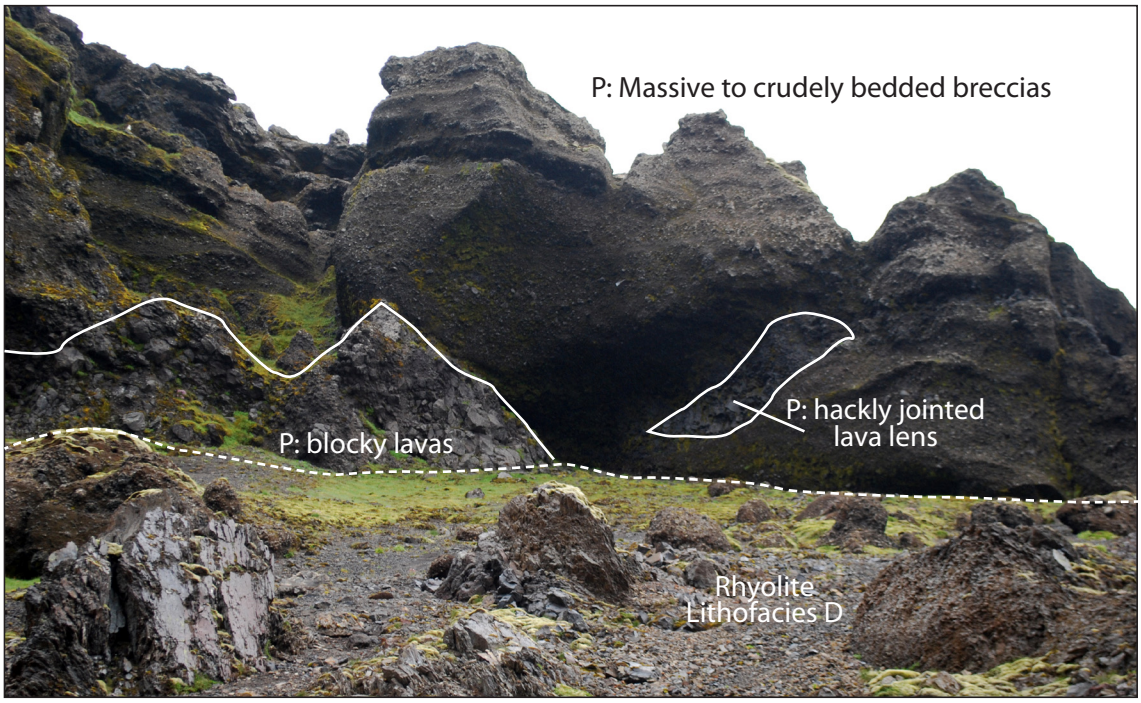

Fig. 4. P1: Breccias and jointed lava lobes of lithofacies P which cap the eastern wall of the HVG valley (above dashed line). Beds are more massive at base but develop crude bedding higher in the sequence. Lava lenses and pillows with chilled margins are present throughout the breccia. Lithofacies P is approximately 10 m in height at this location.

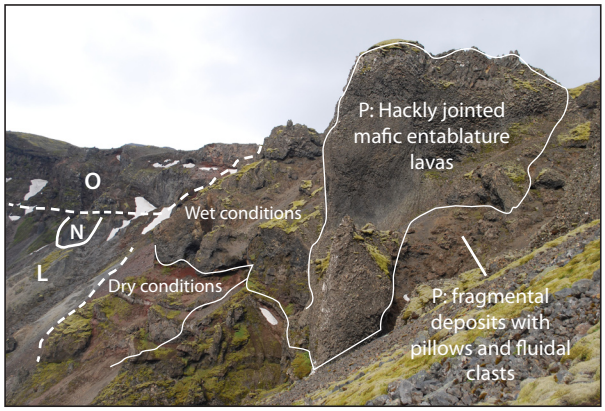

Fig. 4.P2: Breccias and jointed lava lobes sitting above subhorizontal lavas with red soil horizons. Hackly jointed lava lobes within breccia have steepened, flattened fronts.

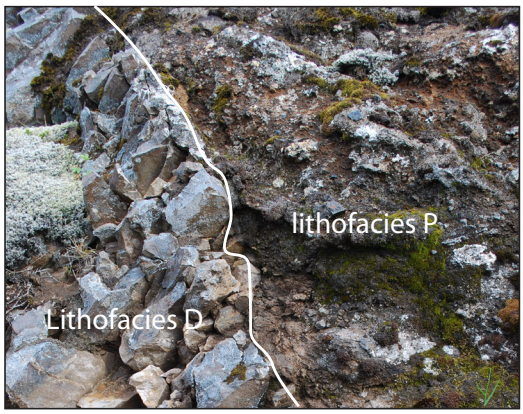

Fig. 4.P3: Contact between rhyolite and mafic breccia on eastern wall of HVG valley. Image shows section approximately 600 mm in length.

to 15 m thick are prominent in the top 15 m of the breccias (fig. 4. P2) and display curved and fanning columnar joints resembling entablature. No corresponding colonnade is observed. Some of the larger lava lobes thicken downslope and may have flattened snouts.

Lithofacies P: Interpretation

The presence of crude bedding suggests that Lithofacies P was deposited in multiple stages rather than en-masse as, for example, a debris avalanche, but it is not known if those emplacement stages relate to different eruptive pulses. The overall

monomict composition, dominance of unabraded clasts and absence of any clear internal erosional unconformities suggest that the lithofacies is related to a single eruptive episode.

The abundance of angular glassy and aphanitic lava granules displaying a strong yellow colouring is indicative of palagonite alteration and suggests a water-saturated eruptive setting, as is the presence of numerous water-chilled lava lobes showing entablature jointing and lava pillows. Unlike sub-lithofacies OB, however, considerably more water was involved in the formation of Lithofacies P, leading to the far greater degree of brecciation and widespread chilling to glass. It is regarded as a hyaloclastite breccia but, because of the limited access, it is unclear exactly how the lithofacies formed. However, the presence of distinctive and unusual joint-rimmed cavities in the breccias is attributed to melting of former ice blocks incorporated within the advancing sediment, suggesting a possible glacial environment. The scarce rhyolite, obsidian and pumice clasts may be erratics derived from melting a coeval ice mass, or otherwise may be entrained within the breccia during transport over the underlying rhyolite.

Similar coarse-grained hyaloclastite br eccias with intercalated lavas have been described in other subglacial volcanic environments in Iceland and Antarctica (Loughlin, 2002; Smellie et al., 2006, 2011; Smellie, 2008). Most of those deposits are associated with a thin glacial cover (<150-200 m) and some show signs of transport within flowing water. Those associated with lava-fed deltas (e.g. the lobe-hyaloclastite described by Smellie et al., 2011) seem a less likely analogy as Lithofacies P does not seem to have a coeval capping unit of subaerial feeding lavas.

4.2.18. Lithofacies Q: Diamict

Description

Lithofacies Q is a thin bed of pale grey diamict that sits between between volcaniclastic sediments that are associated with Lithofacies P, and Lithofacies R (stratified lapilli tuff), situaated at the top of the mid to lower eastern wall of HVG valley around an elevation of 500 m.a.s.l. Access to the deposit is poor (cliff face; fig. 4. R1) Because of difficult access, the surface on which the bed rests could not be

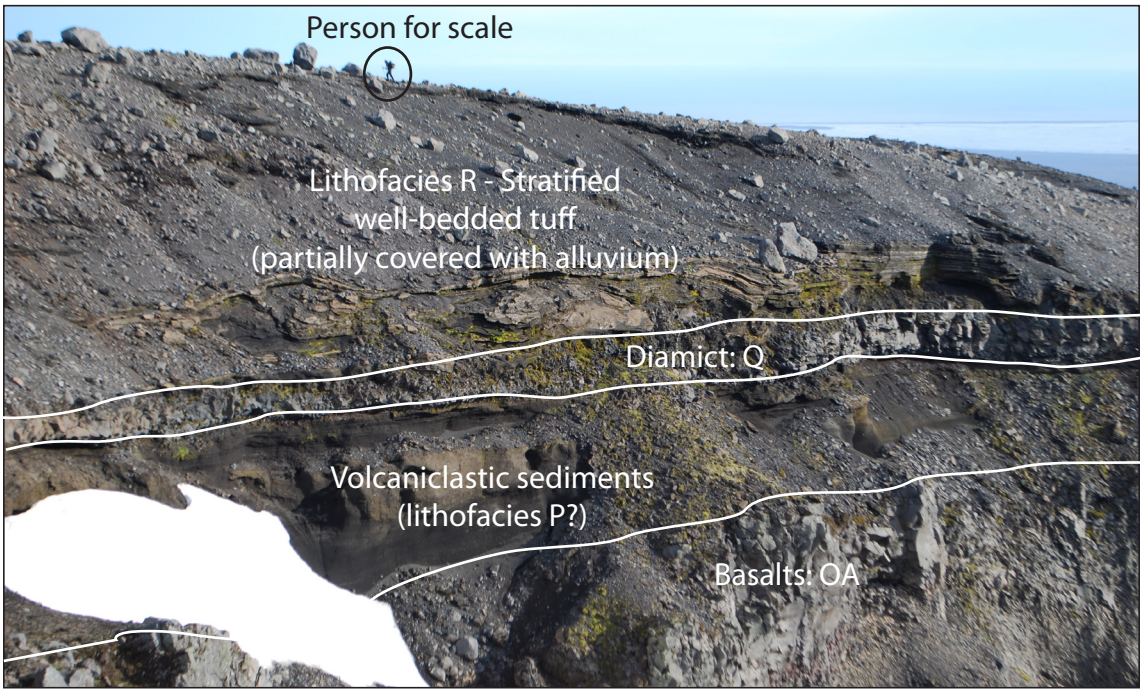

Fig. 4. R1. Well bedded, continuous stratified tuff layers sit unconformably on thin diamict layer and volcaniclastic sediments (access limited to lower beds).

examined and the deposit was only viewed from a distance of several metres. Binoculars were used for many of the details and the following description should be viewed in that context.

The diamict is 0.5-1 m thick and contains polymict angular to rounded pebble to cobble-sized clasts of rhyolite and basalt dispersed in a fine sandy to silty matrix that shows faint laminations. Some of the clasts are polished and facetted but no striations are visible. Lithofacies Q seems to cover a limited lateral range of approximately 20 m as it has not been identified further upslope towards the head of the valley above the subaerial basalt sequence (Lithofacies OA).

Lithofacies Q: Interpretation

The presence of polymict abraded clasts with polished and facetted surfaces within a mainly massive fine-grained bed suggests that it is a glacial deposit probably formed in-situ from basal ice, either as lodgement till or by meltout processes. The faint laminations seen in the fine sandy-silty matrix might be evidence for local reworking of the matrix by flowing water. The clast abrasion and evidence for water suggest that the ice was wet based.

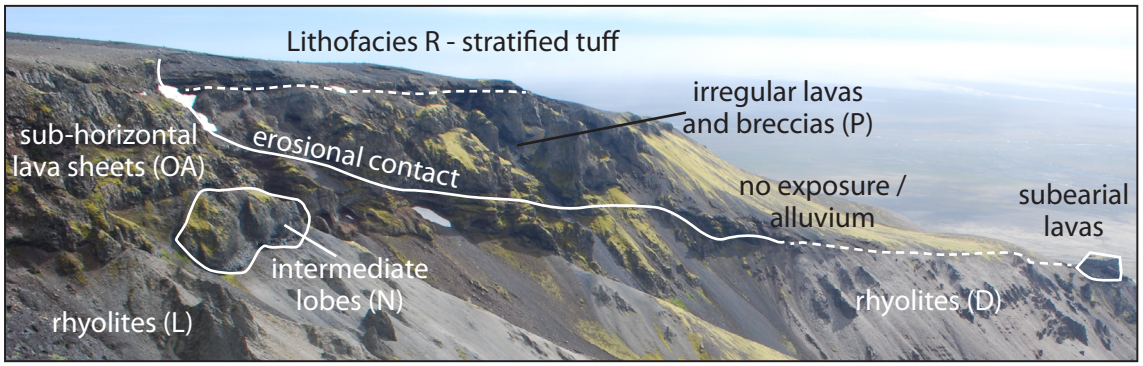

Fig. 4. R2: mid to lower Eastern Wall of HVG Valley. Continuous subhorizontal lithofacies OA become more irregular and is overlain by breccias and jointed lava lobes of lithofacies P toward the south. Lithofacies R caps the lower breccias and lava lobes.

4.2.19. Lithofacies R: Wavy to planar bedded stratified lapilli tuff

Description

Lithofacies R is a stratified lapilli tuff (fig. 4. R1-R2) that forms the upper surface of the eastern wall of the HVG valley and extends across the HVG plateau east towards the Hofsfjall tuff cone which is situated ~1.8 km to the East of the HVG valley, but does not extend north-west and therefore does not directly overlie the subaerial lavas of Lithofacies OA. It is approximately 15 m in maximum thickness and thins downslope to the south, with a minimum thickness of 25 cm present at the HVG cliff face. Downslope towards the south the upper planar surface of the deposit is often obscured by a drape of alluvium .

Lithofacies R is well-bedded and monogenetic, formed of relatively well-sorted coarse-grained glassy sand to fine gravel-grade clasts that contain rounded lava lapilli. The glass grains are blocky and angular, poorly to non-vesicular and variably affected by palagonite alteration, mainly as thick yellow clay rims and replacing any fine tuff matrix. Some of the lapilli have a fine ash coating. Thin, granular lenses are also present and there are dispersed pebble to cobble-sized vesicular basalt clasts with chilled margins. Some of the basalt clasts are fluidal in shape and feature tiny normal joints around their outer surface. The bedding is also wavy locally and there are lenses of cross-bedding that truncate sub-horizontal layers. Impact structures are present beneath several cobble-size blocks with trajectories that broadly suggest a source in the Hofsfjall tuff cone.

Lithofacies R: Interpretation

The lithofacies is monogenetic and well stratified, formed of abundant glassy poorly vesicular partly palagonite altered grains and larger vesicular lava clasts, some with prominent chilled margins, and lapilli with ash coatings. These are characteristics of explosively generated tephra formed in phreatomagmatic eruptions (Cas & Wright, 1987). The stratification locally shows impact structures caused by ballistically emplaced lava blocks (bomb sags) that appear to have been sourced from the east in the direction of the Hofsfjall tuff cone. However, the beds are well sorted and contain a proportion of rounded lapilli, the stratification is commonly wavy and includes sandy-gravelly lenses, and erosive-based steep-faced cross stratification is present, which are features more characteristic of fluvial deposits.

The presence of other lapilli lacking ash coatings also implies that any original ash coating was removed during transport, and the extent of palagonite alteration is greater than in pyroclastic tuffs of the nearby Hofsfjall tuff cone, suggesting a very wet environment.

The origin of the lithofacies R is therefore uncertain. It appears to be sourced in an active tuff cone (Hofsfjall) but shows additional evidence for fluvial reworking. It also overlies glacial diamict (Lithofacies Q) which might imply a glacial setting.

In glacial environments, during basaltic eruptions, sediment-laden meltwater drainage away from the vent occurs under the surrounding ice sheet and leads to the formation of thin sheet flows (Smellie and Skilling, 1994; Smellie, 2008).

An explosive basaltic eruption through ice leading to the formation of the tuff cone is a likely scenario. Meltwater generated during the eruption is likely to have simultaneously flushed downslope away from the tuff cone while transporting and depositing the tephra (Smellie et al., 1993; Smellie and Skilling; Smellie, 2008). In order to account for the presence of impact structures, the surrounding ice cover must have been locally melted through, so some of the deposit may be primary but, in general, much of Lithofacies R was probably fluvially deposited.

4.3. Summary

At present, during this interglacial period, permanent ice cover within the field area is restricted to the head of the Kotá valley at an elevation of 650 m.a.s.l. and the snow line on Öræfajökull plateau is around 880-900 m.a.s.l. during the summer months. During the winter months however, the cirque, HVG valley and Hrútsfjall stream valley may have snow and ice cover up to 3 m in thickness down to an elevation of less than 200 m.a.s.l.

In contrast, during glacial maxima, this area of southern Iceland has been covered in thick ice. There is extensive offshore evidence around the coast of Iceland to suggest that the ice sheet during the last glacial maximum (LGM: 21-18 ka) extended out beyond the current shoreline by up to 150 km (Boulton et al., 1988, Andrews et al., 2000). LGM Ice sheet modelling estimates an ice sheet surface elevation of around 2000m with a mean ice thickness of 940 m, with the sheet extending in the south and east of Iceland to 30km beyond the current day shoreline. (Hubbard et al., 2007). Consequently, ice thickness during the evolution of Öræfajökull may have varied dramatically between current conditions and ice up to 2000 m thick during each glacial cycle.

The field evidence presented in this chapter shows abundant evidence of volcanic interaction with ice, snow and meltwater. Conversely there is also evidence to suggest periods of relatively dry, ice-free conditions throughout the evolution of Öræfajökull which suggests that ice cover may have varied dramatically throughout the Quaternary. This hypothesis is corroborated by studies of nearby areas such as Skaftafell (Helgason & Duncan, 2001) and Vatnafjall (Stevenson et al, 2006).

Stratovolcanoes often display highly variable ice thicknesses around their flanks, with thinner ice toward higher elevations and much thicker ice present within glacial valleys. Stevenson et al. (2006) demonstrated that ice thicknesses on the lower flanks of Öræfajökull have been highly variable throughout the Quaternary.

The rhyolite dominated ridges of Goðafjall and Hrútsfjall, and the immediate surrounding area of the exposed south west flank of Öræfajökull, are composed of successive mafic and silicic eruptive units that have all been influenced by the pres-

Development of Goðafjall and Hvalvörðugil Valley Lithology			
LITHOFACIES	CHEMOSTRAT GROUP	ROCK TYPE DESCRIPTION	PALAEOENVIRONMENT
Q	mafic	hyolaoclastite tuff	subaqueous / glacial
GLACIAL UNCONFORMITY (Diamict)			
N	trachydacite	columnar jointed lavas: sill	subglacial
GLACIAL UNCONFORMITY (Diamict)			
P	mafic	channel fill hyaloclastite	subaerial – ice-marginal / water interaction
OA	mafic	oxidised lavas	subaerial
M		cross-bedded sandstone	subaerial fluvial
OB	mafic	lavas with diamict apopheses	ice-marginal / snow contact
GLACIAL UNCONFORMITY (Diamicton)			
L	'Group Two' rhyolite	columnar jointed lavas	subglacial
K		dyke	
J		lapilli tuffs and breccias	evidence of both phreatomagmatic and volatile-driven explosivity – subglacially confined
I			
H			
G			
GAP IN STRATIGRAPHY (?)			
F	'Group One' rhyolite	platy rhyolite lobes and breccias	subaerial – dry with minor water interaction
E			
D			
C			subaerial – possible fluvial
GAP IN STRATIGRAPHY – onset of large scale glaciation circa. 2.75 Ma (Kleiven et al., 2002)			
A	basalt	basement basalt complex	subaerial interglacial

Table 4.2. Summary of development of the Goðafjall & Hrútsfjall area. Blue areas highlight lithofacies that show evidence of emplacement within a subglacial enviroment, while red areas highlight those that show evidence of a subaerial emplacement environment.

ence of ice. Older units at the base of edifice show evidence of one or more episodes of post-emplacement glacial modification, while units higher up in the stratigraphy show evidence of both syn-eruptive interaction with ice, snow or meltwater, and post-emplacement glacial modification.

Table 4.2 provides a summary of each lithofacies and its corresponding eruptive environment which is derived from each lithofacies interpretation. Evidence of lacial horizons is also inlcuded in the sequence.

Snow and ice contact features described within many of the lithofacies cannot exclusivley be attributed to emplacement during glacial periods. For example, the predominantly subaerially-emplaced lavas of lithofacies D display the occasional localised red and black breccias at its base, which suggest interaction with minor amounts of water or steam which may have been provided by snow cover and/or

meltwater runoff present during an interglacial period.

At least four glacial horizons have been identified within the field area. The lowest is situated at the base of Hrútsfjall ridge in the Kotá river valley at an elevation of 230 m.a.s.l and is overlain by a succession of mafic lavas and fragmental deposits.

The second horizon is situated at an elevation of 430 m.a.s.l within the same succession and below the lithofacies L rhyolite unit that dominates Hrútsfjall ridge.

The third horizon occurs at an elevation of 741 m.a.s.l at the head of the upper HVG valley between rhyolite lithofacies L and basalt lithofacies OB, while a fourth horizon is indicated by the occasionally striated and polished upper surface of lithofacies OA (> 800 m) and a discontinuous outcrop of diamict (Lithofacies Q), and may represent the last major episode of glaciation in the area.

In order to construct a more complete evolutionary history of Öræfajökull, the field evidence presented in this chapter must be evaluated in the context of an absolute timescale. To acheive this aim, the depositional environmental information from this chapter is combined with the $^{40}Ar/^{39}Ar$ dating results (chapter 5) of the key silicic units within the field area and presented in chapter 6.

Chapter 5
^{40}Ar / ^{39}Ar dating

5.1. Introduction

The ability to model contemporary climate patterns with accuracy relies greatly on our understanding of climate patterns of the past. At present, much of our understanding of climate trends comes from the analysis of temperature-dependent oxygen isotope ratios in sea floor sediments (Bradley, 1999; Lisiecki and Raymo, 2005) and although this method provides a comprehensive record of global sea level temperatures throughout the Quaternary period, it yields little direct information on corresponding terrestrial conditions. Ice core analysis offers a greater insight into terrestrial environments, however cores from the North Greenland ice sheet only provide an isotope record for the northern hemisphere up to the late Quaternary period (Svensson et al., 2005).

Due to their unconsolidated nature, terrestrial preservation of glacial deposits is generally very poor; however subglacial volcanism in Iceland has helped to preserve a unique record of terrestrial environmental conditions, including the presence and fluctuation of ice, throughout the Quaternary. The ability to accurately determine a chronological timescale for the occurrence and duration of subglacial volcanic activity in Iceland would therefore be a major step toward the understanding of palaeo-ice sheet behaviour throughout glacial/interglacial cycles of the Quaternary period.

Dating Icelandic volcanic rocks from the mid to late Quaternary is a challenging task and until recently, terrestrial geochronological studies in Iceland have been limited to the dating of either older, pre-glacial Tertiary basalts using the K/Ar or $^{40}Ar/^{39}Ar$ dating techniques (McDougall et al., 1977, McDougall and Harrison, 1999, Merrihue and Turner, 1966, Saemundsson et al., 1980), or younger post-glacial sedi-

ments using the ^{14}C and ^{210}Pb techniques (Doner, 2003, Gathorne-Hardy et al., 2009, Geirsdóttir et al., 2009).

In recent years, due to improvements in the accuracy of dating minerals used as age standards for Quaternary rocks (Nomade et al., 2005), there has been some limited success dating young (<1Ma) basaltic and silicic subglacial rocks using the K/Ar and $^{40}Ar/^{39}Ar$ techniques, (McGarvie et al., 2007, Flude et al., 2008, Flude et al., 2010, Guillou et al., 2010), however the errors associated with these dates are still too large to accurately constrain individual volcanic eruptions to one particular glacial or interglacial cycle.

This chapter presents an overview of the $^{40}Ar/^{39}Ar$ dating technique and reviews the outstanding problems associated with the $^{40}Ar/^{39}Ar$ dating of young and relatively K-poor, glass-rich volcanic rocks. It goes on to describe the methods and techniques used in this study along with problems encountered during analysis. Finally, new $^{40}Ar/^{39}Ar$ ages for a number of outcropping units at the Goðafjall and Vatnafjall areas of Öræfajökull are presented and discussed.

The significance of the calculated eruption ages for each unit and the implications for Icelandic paleoenviromental reconstruction during the eruptive history of Öræfajökull will be discussed further in chapter 6.

5.2. Background to the $^{40}Ar/^{39}Ar$ dating technique

Since its development in the mid 1960s (Merrihue and Turner, 1966), the $^{40}Ar/^{39}Ar$ method has proven to be a useful geochronometer for both terrestrial and extraterrestrial minerals and rocks. The $^{40}Ar/^{39}Ar$ dating method is a derivative of the K/Ar dating method, which is based upon the radioactive decay of the parent ^{40}K isotope to the daughter ^{40}Ar isotope, and is calculated using the age equation that forms the basis of all geochronology:

$$t = \frac{1}{\lambda} \ln\left(1 + \frac{D}{N}\right)$$

Eq. 5.1

Where *t* is the time lapsed since the system became closed – in this case since the eruption occurred – λ is the radioactive isotope decay constant, D is the number of atoms of the daughter nuclide and N is the number of atoms of the radioactive parent nuclide that remain after time t.

In nature, potassium occurs as three isotopes, ^{39}K (93.1%), ^{40}K (0.0118%), and ^{41}K (6.9%). The most abundant of these, ^{39}K and ^{41}K, are non-radioactive. However, the radioactive isotope ^{40}K has a half-life of 1.248 Ga (1.248 x 10^9 yrs). The decay scheme of ^{40}K is branched to ^{40}Ca and ^{40}Ar, with the majority (89.5%) converting to ^{40}Ca via electron emission (beta decay), and the remaining 10.5% converting to ^{40}Ar via positron emission (inverse beta decay, electron capture) (fig. 5.1).

In magmatic systems, argon behaves as a highly incompatible trace element, strongly partitioning into melts, and from melts into gas bubbles (Kelley, 2002). Prior to a volcanic eruption, while the magma is still in a molten state, any argon that it contains, including radiogenic ^{40}Ar (^{40}Ar*), will equilibrate with the gas phase and be released through magma degassing. Ideally, if complete equilibration is achieved then any trace of pre-existing ^{40}Ar* within the melt would effectively be removed

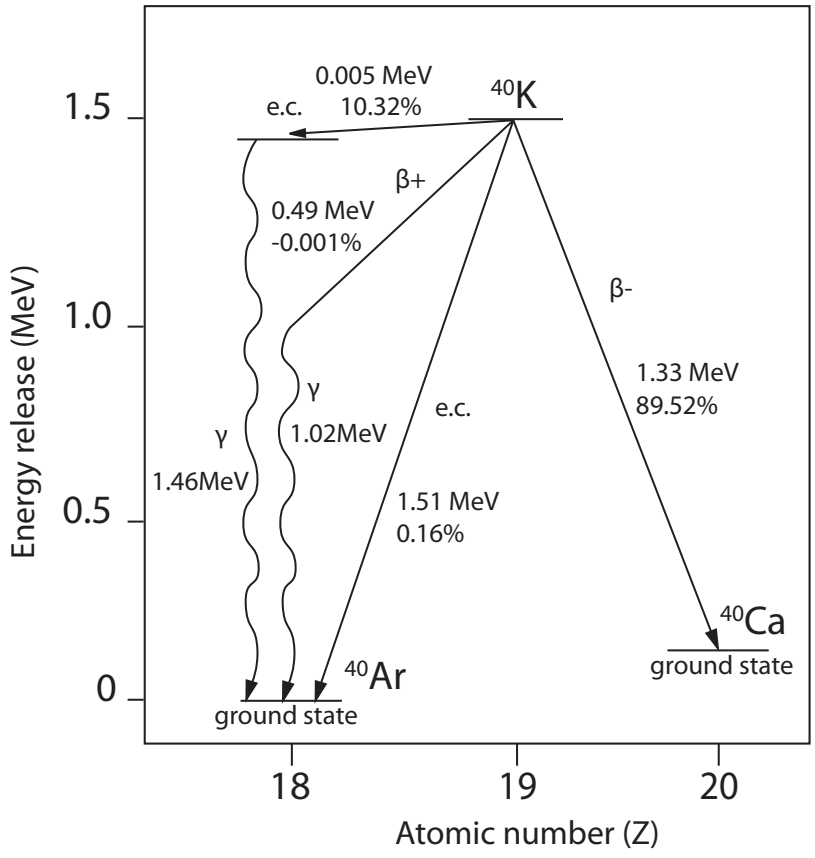

Fig. 5.1. After McDougall and Harrison, 1999; Decay scheme for ^{40}K including dual decay to ^{40}Ca.

from the lava, leaving the melt '^{40}Ar*-free' at the time of eruption.

Once the lava, and minerals within, have cooled below their argon blocking temperature, any new ^{40}Ar* produced by the in-situ decay of ^{40}K then becomes trapped within the crystal mineral lattice of the solid phase.

The K/Ar, and therefore the ^{40}Ar/^{39}Ar, age of a sample can only be calculated accurately if a number of basic assumptions are met prior to analysis (McDougall and Harrison, 1999):

1. The decay rate of ^{40}K is constant and is not affected by changes in pressure or temperature.
2. The isotopic ratio of ^{40}K/^{39}K is constant in nature at any given time (^{40}K /^{39}K: 0.000125).
3. Prior to eruption, the sample was completely degassed and free from ^{40}Ar*.
4. All ^{40}Ar* present in the sample was produced only by the in-situ decay of ^{40}K since time of eruption. The system must have remained closed since the time of the eruption, ensuring no loss or gain to both ^{40}K and ^{40}Ar* except by the in-situ decay of ^{40}K, which has since remained undisturbed.
5. Any non-radiogenic ^{40}Ar present within the sample is of atmospheric origin and can be corrected for, using ^{36}Ar present in the sample and the known isotopic abundance of ^{40}Ar/^{36}Ar = 295.5 as recommended by Steiger & Jäger (1977) based on values determined by Nier (1950). A new isotopic ratio value for ^{40}Ar/^{36}Ar of 298.56 ± 0.31 has since been measured (Lee et al., 2006), however it is not yet widely used by the scientific community, therefore the value of 295.5 will be used throughout this research project.

The continual decay of ^{40}K over time leads to an increase in the abundance of ^{40}Ar* that can be quantitatively measured by mass spectrometry. In order to measure the abundance of trapped argon, the rock samples are heated to melting point in an ultra-high vacuum. The gas is then released into a mass spectrometer, determining the ratio of ^{40}K to ^{40}Ar present in the sample. These measurements can then be substituted into equation 5.1 in order to calculate time lapse since eruption (Eq. 5.2):

$$t = \frac{1}{\lambda} \ln\left(1 + \frac{\lambda}{\lambda_e + \lambda_{e'}} \frac{^{40}Ar^*}{^{40}K}\right)$$

Eq. 5.2

Isotope Produced	Calcium	Potassium	Argon	Chlorine
36Ar	^{40}Ca			
37Ar	^{40}Ca	^{39}K	^{36}Ar	
38Ar	^{42}Ca	^{39}K ^{41}K	^{40}Ar	^{37}Cl
39Ar	^{42}Ca ^{43}Ca	^{39}K ^{40}K	^{38}Ar ^{40}Ar	
40Ar	^{43}Ca ^{44}Ca	^{40}K ^{41}K		

Beneficial reactions Insignificant reactions Interfering reactions

Table 5.1. After McDougall and Harrison, 1999; Nucleogenically produced argon isotopes.

During the K/Ar dating method, the potassium and argon are measured using two separate methods of analysis. ^{40}K is determined by flame photometry while ^{40}Ar is determined by isotope dilution mass spectrometry, and as each individual process is destructive, this opens up the possibility of error due to imhomogenieties that may occur between the two sample aliquots.

The advantage of the $^{40}Ar/^{39}Ar$ dating method over the K/Ar dating method is that the analysis can be carried-out in a single procedure, therefore removing the possibility of error from the need for multiple sample aliquots. The K/Ar technique has however recently been used successfully to date young Icelandic basalts (Guillou et al., 2009), yielding dates within error of previously calculated $^{40}Ar/^{39}Ar$ ages, but with greater accuracy, as K/Ar errors are not affected by the larger analytical uncertainty caused by excess ^{40}Ar in $^{40}Ar/^{39}Ar$ dating. K/Ar has the advantage that large sample masses (≥1g) can be analysed to improve the $^{40}Ar^*$ determination in young geological samples. Such large sample sizes are not feasible for $^{40}Ar/^{39}Ar$ technique which requires nuclear irradiation.

In the $^{40}Ar/^{39}Ar$ dating method, the total amount of ^{40}Ar present in the sample is measured directly, while ^{39}Ar is used as a proxy for the determination of ^{39}K. The ^{39}Ar isotope does not occur naturally and is produced by the irradiation of ^{39}K with fast neutrons in a nuclear reactor prior to isotopic analysis, via the reaction $^{39}K(n,p)^{39}Ar$.

During irradiation it is possible for other isotopes of argon to be produced due to interfering reactions with Ca, K, Ar and Cl (table 5.1).

When a sample is analysed the mass spectrometer will quantify all naturally-occurring and reactor-induced argon isotopes: ^{36}Ar, ^{37}Ar, ^{38}Ar, ^{39}Ar and ^{40}Ar and interference corrections must be made to account for the reactor-produced isotopes in order to accurately calculate a sample age.

In order to make the neutron interference corrections, K- and Ca-bearing salts are irradiated alongside the sample. Cadmium shielding during irradiation cuts out thermal neutrons and so reduces the $^{40}Ca(n,n\alpha)^{36}Ar$ reaction. The production of ^{38}Ar from ^{37}Cl is seen as a beneficial reaction as it allows determination of the amount of chlorine present in the sample.

Calcium fluoride (CaF_2) is used to determine the $^{36}Ar/^{37}Ar$ and $^{39}Ar/^{37}Ar$ correction factors. The beneficial production of ^{37}Ar from ^{40}Ca allows determination of how much ^{36}Ar and ^{39}Ar to correct for, as well as the K/Ca ratio of the sample. A further explanation of all interfering reactions can be found in MacDougall and Harrison (1999).

During isotopic analysis, the amount of ^{39}Ar released from a given sample (^{39}Ar K) is proportional to the amount of ^{40}K, as in nature the $^{40}K/^{39}K$ ratio is assumed to be constant at 0.000125. Therefore the $^{40}Ar^*/^{39}Ar$ value determined following irradiation is proportional to the $^{40}Ar^*/^{40}K$ ratio in the sample, and therefore proportional to age (McDougall and Harrison, 1999).

The ^{39}Ar generated by irradiation of ^{39}K ($^{39}Ar_K$) is dependant upon the amount of ^{39}K present in the sample, the sample age and neutron fluence. As neither the sample age, nor the exact neutron flux that each sample receives during irradiation can be accurately quantified, a sample of known K/Ar age, a 'fluence monitor standard', is irradiated with the samples. The sample ages can be derived by comparison of the $^{40}Ar^*/^{39}Ar$ generated by irradiation of ^{39}K with that of the fluence monitor standard.

A dimensionless irradiation parameter, known as the 'J' parameter (Mitchell, 1968) is calculated from the fluence monitor standard. The J parameter is defined using the following equation (Eq. 5.3):

$$J = \frac{(\exp \lambda t) - 1}{{}^{40}Ar^{*}/\,{}^{39}Ar_{K}}$$

Eq. 5.3

where $^{40}Ar^{*}/^{39}Ar_{K}$ is determined for the monitor standard, λ is the radioactive isotope decay constant (5.543 x 10^{-10} yr -1 for ^{40}K) and t is the known age of the monitor standard. As both *t* and *λ* are known values, only the denominator in eq.5.3 varies with the neutron flux and is required for calculation of the J parameter.

Once the J parameter has been calculated for each standard, it can then be substituted into the age equation (eq. 5.1) in order to calculate the ages of the samples irradiated alongside it (eq. 5.4):

$$t = \frac{1}{\lambda} \ln \left(1 + J \, \frac{{}^{40}Ar^{*}}{{}^{39}Ar_{K}} \right)$$

Eq. 5.4

Accurate calculation of the J parameter is essential in order to determine accurate ages for the samples under investigation, as it is a measurement of the total fast neutron flux required for the $^{39}K(n,p)\,^{39}Ar$ to occur during the irradiation. The optimum neutron flux needs to be large enough to produce a sufficient amount of ^{39}Ar from ^{39}K, but also small enough to minimise interferences from the production of ^{40}K from the $^{40}K(n,p)\,^{40}Ar$ reaction, or ^{36}Ar from the $^{40}Ca(n,n\alpha)\,^{36}Ar$ reaction (McDougall and Harrison, 1999).

Guidelines for the optimisation of the J parameter were established by Turner (1971), who devised a graph in order to calculate the optimum irradiation parameters for any given sample according to sample age and K/Ca ratio (Fig. 5.2). Turner devised the graph specifically for the Herald reactor in Aldermaston, UK but it can be used as a guide to estimate the required neutron flux at other reactors.

The samples analysed in this research project were irradiated at the Oregon State University TRIGA reactor for fast-neutron irradiation in the cadmium-lined in-core irradiation tube (CLICIT). This reactor has a slow/fast neutron flux of ~5 and a J/h value of 2.6 x 10^{-4}.

All of the rocks analysed in this research project, with the exception of the base-

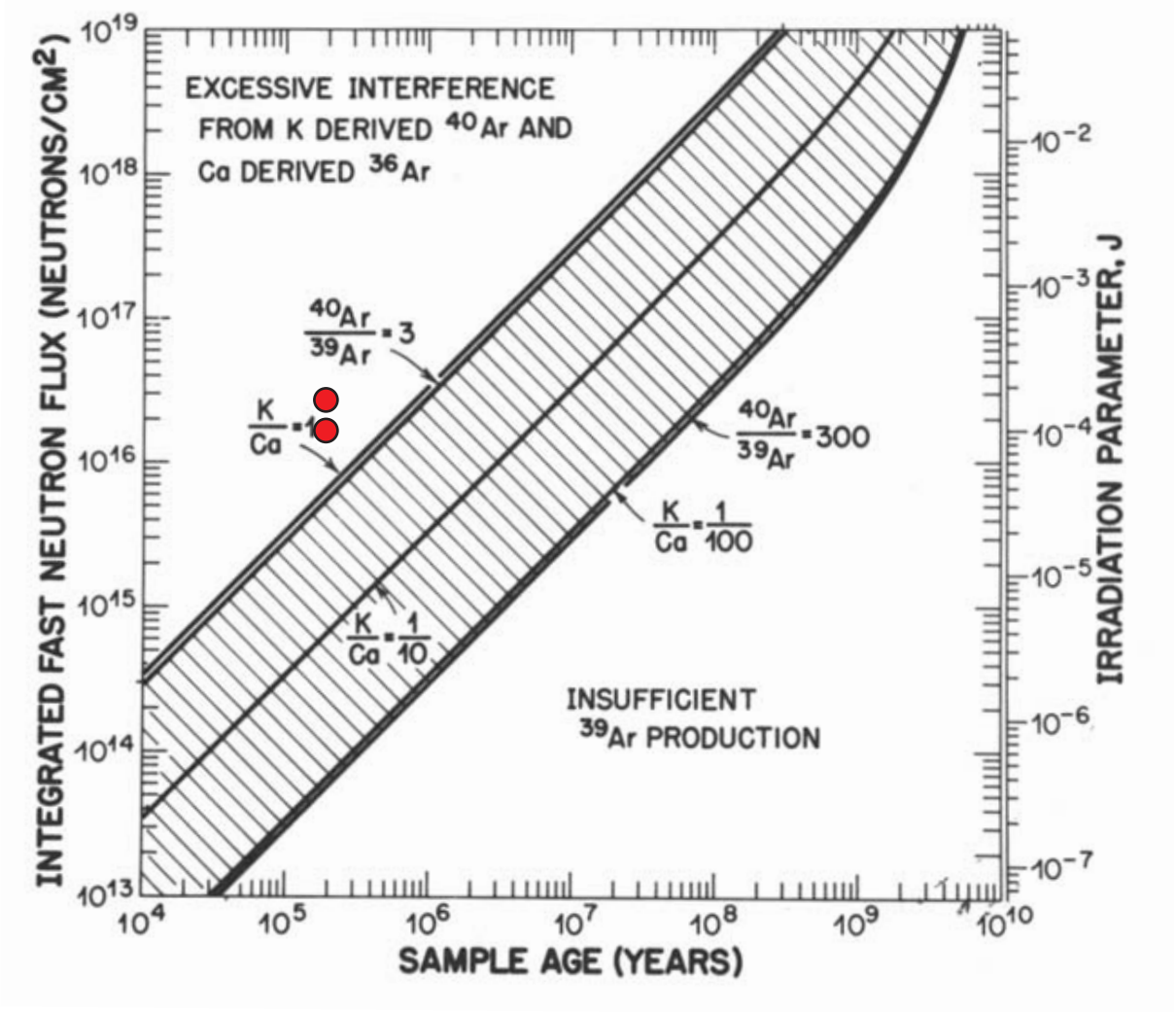

Fig. 5.2. After Turner, 1971; Diagram highlighting irradiation parameters for optimum production of ^{39}Ar from ^{39}K (lined area) for samples of varying ages and K/Ca ratios. Irradiations plotting to the left of the lined area can result in excessive interference from reactions on Ca, K and Cl, while those plotting to the right result in insufficient production of ^{39}ArK. Irradiation batches from this study are represented by red circles.

ment basalts are expected to be less than 780,000 years old, however a fluence monitor standard with a similar age to the samples is not available. Alder Creek sanidine (ACs), with an age of 1.193±0.001 Ma (Nomade et al., 2005) was chosen as the fluence monitor standard as it is presently the youngest commonly-used standard available. An age of 1.194±0.012 Ma was initially calculated for ACs by Renne et al. (1998), re-calculated by Turrin et al. (1994) as 1.186±0.006 Ma, and subsequently by Nomade et al. (2005) as 1.193±0.001 Ma (ACs-2).

Neutron flux has a vertical gradient in the reactor, therefore in order to calculate the J parameter accurately for each irradiation batch, prior to irradiation, aliquots of the monitor standard are placed at regular intervals (two or three to each sample tube) between the aliquots of the sample under investigation.

Based on figure 5.2 the fast neutron fluence received by the two irradiation batches for the samples analysed in this research project was 1.372 x 10^{16} n/cm^2 for the first batch and 1.124 x 10^{16} n/cm^2 for the second.

J values of 7.3 ± 0.3 x 10^{-5} x and 5.98 ± 0.4 x 10^{-5} for the two irradiation batches were determined by single crystal laser fusion. The percentage errors on the J values were propagated through into all of the sample ages that were derived by an age spectrum diagram plateau (see below for definition of plateau).

The incremental heating technique

The incremental, or 'step' heating technique progressively extracts argon from the sample by a number of increasing temperature steps. The technique was developed by Merrihue and Turner (1966) in order to recognise and correct against the effects of atmospheric argon contamination and argon loss, as each individual heating step yields an apparent age.

Both $^{40}Ar^*$ and $^{39}Ar_K$ are derived from potassium, therefore ideally, in a closed system where all $^{40}Ar^*$ has been retained since crystallisation, the $^{40}Ar^*$ and the $^{39}Ar_K$ should reside within similar sites in the crystal lattice. During each incremental heating steps, the $^{40}Ar^*/^{39}Ar_K$ ratio of each gas fraction should be constant, as the two isotopes will be released in proportion because of their similar transport behaviour. In an undisturbed sample, the apparent $^{40}Ar^*/^{39}Ar_K$ age generated from each gas fraction release should be constant (McDougall and Harrison, 1999)

The apparent $^{40}Ar^*/^{39}Ar_K$ age is plotted against the cumulative release of $^{39}Ar_K$ in order to create an age spectrum diagram. This should ideally yield a series of uniform flat steps, known as a plateau, indicating that the system has remained closed since crystallisation. In practise the majority of analysed samples do not conform to an ideal release pattern as many contain excess argon or have undergone $^{40}Ar^*$ loss. The majority of volcanic rocks that have been erupted into a terrestrial atmosphere will, to some extent, be contaminated by atmospheric argon.

The presence of any ^{40}Ar of atmospheric origin is determined by the measurement of ^{36}Ar released from each sample. As the $^{40}Ar/^{36}Ar$ ratio of the atmosphere is constant at 295.5, the amount of $^{40}Ar^*$ released from a sample is usually calculated by correcting for atmospheric argon with the following equation (eq.5.5):

$$^{40}Ar^{*} = {}^{40}Ar_{\text{interference corrected}} - \left[295.5 \times {}^{36}Ar_{\text{interference corrected}}\right]$$

Eq. 5.5

The step heating technique allows for these phenomena to be recognised within the age spectrum diagram.

Heating is initiated at temperatures much lower than that of the melting point of the sample. At low temperatures, the initial heating steps are often used as clean-up steps in order to remove any atmospheric argon contamination that may be adhered to grain surfaces or located within more easily penetrable sites such as those adjacent to grain boundaries. As temperatures increase the gas will be released from more retentive sites, which are more likely to contain $^{40}Ar^{*}$.

In order for an age spectrum plateau to be interpreted as a valid sample age, the plateau must be formed of adjacent steps that together account for a minimum of 60% of the total ^{39}Ar release and at least three contiguous steps must be within error of one another (parameters set by Isoplot software: Ludwig, 2003). All of the age spectrum diagrams presented in this research are given with 2σ uncertainty.

Data from heating steps can also be plotted onto an isochron diagram, a plot of $^{40}Ar/^{36}Ar$ against $^{39}Ar/^{36}Ar$ (or $^{36}Ar/^{40}Ar$ against $^{39}Ar/^{40}Ar$: inverse isochron). For a well-behaved system, the age of the sample is proportional to the slope of the correlation line and the intercept on the $^{40}Ar/^{36}Ar$ axis should represent the value of atmospheric or trapped argon. For each sample, the age calculated from an age spectrum diagram should be in agreement with that of the corresponding isochron.

Isochrons and inverse isochrons are generally accepted as a more robust age calculation method as they do not require an assumption of the initial $^{40}Ar/^{36}Ar$ ratio in order to calculate an age. However, isochron production in glassy samples is often prohibited as the uniform composition of glass is lacking in crystallographic defects where the atmospheric argon may collect. This produces heating steps with a constant $^{40}Ar/^{39}Ar$ ratio and and an insufficient spread of data points with which to construct an isochron.

Isotope correlation diagrams, or inverse isochrons (fig 5.3), enable the identification of non-atmospheric excess argon within a sample. $^{36}Ar/^{40}Ar$ is plotted against $^{39}Ar/^{40}Ar$ and the ideal isochron produced represents a mixing line between at-

Argon type	Description
3 Isotopes	Two primordial: ^{36}Ar (0.34%) ^{38}Ar (0.06%) One decay product of ^{40}K: ^{40}Ar (96.9%)
Radiogenic	^{40}Ar formed by in-situ decay of ^{40}K
Atmospheric	$^{40}Ar/^{36}Ar = 295.5$ $^{38}Ar/^{36}Ar = 0.188$ A ubiquitous nuisance component
Mantle	$^{40}Ar/^{36}Ar = 1000\text{-}40{,}000$ $^{38}Ar/^{36}Ar = 0.188$ Inherited from mantle source
Extraneous or excess	Extra ^{40}Ar that cannot be accounted for by any of the above forms of Ar (i.e. inherited from xenocrysts)
Fractionated	Sub-atmospheric $^{40}Ar/^{36}Ar = < 295.5$ (See section 5.10)

Table. 5.2. All forms of Argon that may be present within a sample.

mospheric and radiogenic argon (fig. 5.3a). The x-intercept represents the sample age and ideally the y-intercept should represent atmospheric argon (0.0033). Any deviation of the Y-intercept value suggests the incorporation of a non-atmospheric excess argon component (Kelley, 2002).

5.3. Sources of Argon

Alongside atmospheric argon and radiogenic argon, there are a number of other sources of argon that can find their way into the sample and cause contamination, which may lead to erroneous age calculation. Table 5.2 lists all of the possible sources of argon that may be present in a sample and are discussed in greater detail below.

High levels of atmospheric argon contamination within Icelandic rocks has been previously documented (Gale et al., 1966; Udagawa et al., 1999; Flude et al, 2005; Clay, 2010) and although a number of sources have been proposed (Flude et al.,

2005; Clay, 2010) the most likely scenario is addition upon eruption. It is possible that the contamination mechanism may differ between subaerially and subglacially erupted samples as subglacial samples come into contact with glacial meltwater. Ballantine and Barford (2000) demonstated that air-like noble gas signatures in subglacial basalts cannot be accounted for by partitioning of noble gases between glacial meltwater and basaltic melt. The solubility of argon in rhyolites however, is over an order of magnitude higher than basalt therefore it may be possible that glacial meltwater acts as a viable source of atmospheric contamination in subglacial rhyolites (Clay, 2010).

Mantle-derived argon produces a $^{40}Ar/^{36}Ar$ signature with ratios much greater than that of 295.5. A mantle argon source has been attributed to subglacial Icelandic basalts with $^{40}Ar/^{36}Ar$ ratios of up to 6500 (Burnard and Harrison, 2005). It may be possible that basaltic magmas with mantle-derived argon signatures become mixed with silicic magmas at bimodal volcanoes such as Öræfajökull, which is also close to the current 'hotspot' location; however, subglacially erupted basalts in the Öræfajökull area display predominantly atmosphere-like $^{40}Ar/^{36}Ar$ signatures (Pers comm. Weston, B., 2010).

Extraneous argon refers to inherited $^{40}Ar^*$ within volcanic rocks attributed to the incorporation of xenolithic material, including the incorporation of older xenocrysts into the magma prior to eruption either through interaction with a plutonic source or within crystal mush collected on the edges of the magma chamber walls (Charlier et al., 2005). This form of extraneous $^{40}Ar^*$ in Icelandic volcanic rocks has been documented by Flude (2005) who encountered contamination of a silicic lava flow at Ljosufjoll via incorporated degassed xenocrysts from a syenite xenolith, which resulted in a higher than apparent age for the lava flow.

Care can be taken to avoid inherited $^{40}Ar^*$ by the hand picking of samples and avoidance of any samples that include crystals with resporbtion and regrowth features.

Fractionated argon has a sub-atmospheric $^{40}Ar/^{36}Ar$ ratio. Ratios lower than 295.5 have been reported in a number of lavas (Kaneoka, 1980; Krummenacher, 1970; Matsumoto and Kobayashi, 1995; Ozawa et al., 2006). However the majority of reported ratios are within the range producible by a single stage of kinetic mass

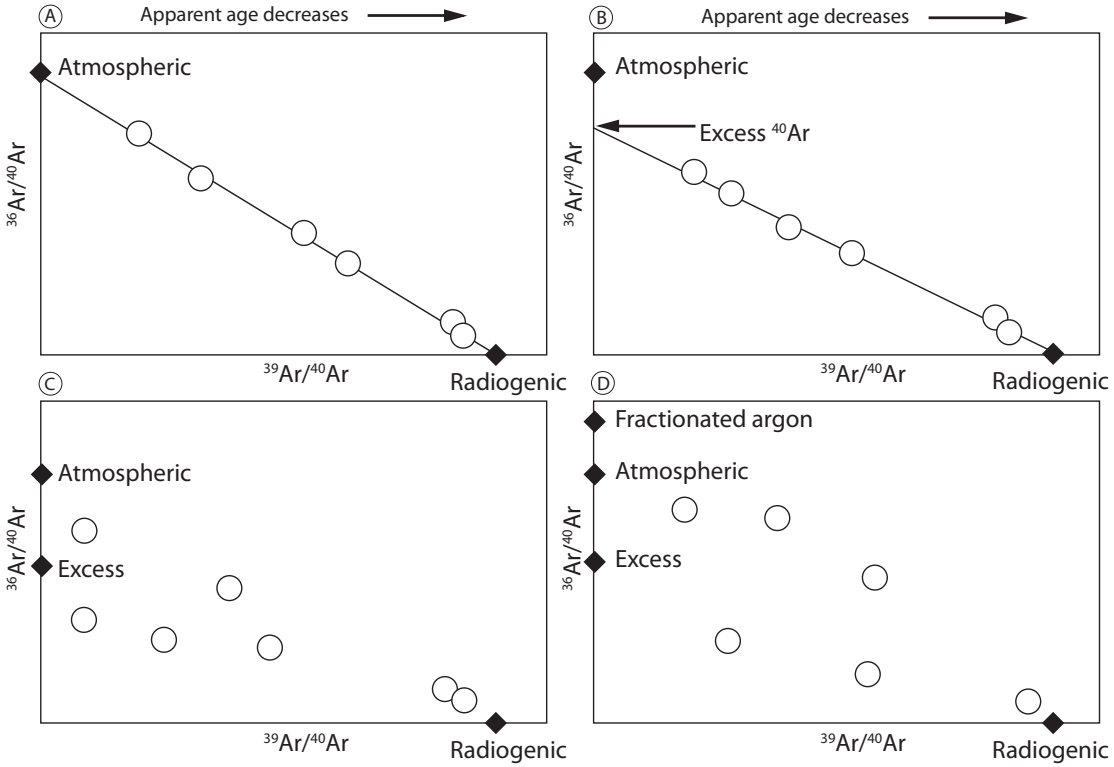

Fig. 5.3. Effects of differing argon sources on isotope correlation diagrams. Fig A shows the ideal mixing line between the two components of atmospheric argon and radiogenic argon. B shows the effect on a two component isochron by an excess with 40Ar/36Ar > 295.5. C and D show effects of three components or four components leading to scattered correlations.

fractionation. Fractionated argon is present within samples from the Öræfajökull suite and will be covered in greater detail in section 5.10.

Problems with the identification of an excess ^{40}Ar source from the total ^{40}Ar released from a sample arise when more than two components of ^{40}Ar are present. Figure 5.3 a-d illustrates how different sources of ^{40}Ar are represented on an isotope correlation diagram. As mentioned in section 5.2, the ideal isotope correlation diagram comprises a mixing line of two components (fig.5.3 a & c). However when a third (fig. 5.3 c) or fourth (fig. 5.3d) component are added it becomes increasingly difficult to construct an isochron or yield a reliable apparent age. A more comprehensive guide to excess argon in a variety of geological settings can be found in Kelley (2002).

5.4. Issues surrounding the Ar-Ar dating of young volcanic rocks

As the Ar-Ar dating method is based upon the accumulation of radiogenic argon over time, measurement becomes increasingly easier with age. Technically there is no upper age limit for $^{40}Ar/^{39}Ar$ dating, but young samples (< 1my) will only contain minimal amounts of radiogenic argon ($^{40}Ar^*$) from the decay of ^{40}K. Problems arise relating to the detection of such small amounts of $^{40}Ar^*$ from a much larger amount of background atmospheric argon within the total ^{40}Ar released from the sample. As the proportion of radiogenic to total ^{40}Ar decreases, the error in its measurement increases exponentially. A greater magnitude of error becomes more likely when the proportion of radiogenic ^{40}Ar is less than 10% of the total ^{40}Ar released from the sample (McDougall and Harrison, 1999), therefore precise age determination of young rocks relies heavily upon the ability to accurately measure the $^{40}Ar/^{36}Ar$ ratio of the sample.

In young samples that only contain a small proportion of $^{40}Ar^*$, application of the ^{36}Ar atmospheric argon correction can lead to an increase in the error of the calculated apparent age, often over an order of magnitude, leading to errors that are much greater than the age itself and therefore rendering the ages meaningless.

To complicate matters further, there may be other sources of ^{40}Ar within the sample, alongside the $^{40}Ar^*$ and the atmospheric Ar, that are also indistinguishable within the total ^{40}Ar (table 5.2).

The three phases that have been shown to yield successful reproducible results using the $^{40}Ar/^{39}Ar$ dating technique are the mineral phase, including feldspars and biotites, volcanic glass and obsidian, and groundmass. All three will be discussed below with reference to young Icelandic volcanic rocks.

Most subaerially and subglacially erupted rhyolites contain trapped atmospheric argon. The amount of atmospheric argon varies greatly in sample types but empirical data suggest that alkali feldspar and fresh, young, coarsely crushed volcanic rocks have an order of magnitude less atmospheric contamination than other K-bearing rocks (McDougall & Harrison 1999).

Sanidine is the most successful mineral from which to derive ages from young

volcanic rocks (Hora et al., 2010) due to its relatively low atmospheric argon content and high K abundance. Renne et al. (1997) used a series of total fusion analyses on sandines from the historic 79 AD eruption of Mt Vesuvius to yield an age of 1.93±0.094 k, which is within error of the date recorded by Pliny the Younger. More recently Lanphere et al. (2007) further refined the $^{40}Ar/^{39}Ar$ age of the sanidine to the actual year of eruption (1921±66 years in AD 2000) using the incremental heating technique. However, sanidine is a rare phenocryst phase in Icelandic rhyolites and has not been recorded at all in the Öraefajokull rhyolites. Microprobe data reveal that the majority of feldspar phenocrysts in the sample rocks are anorthoclase and sodium-rich plagioglase (Prestvik ,1985 and chapter 3). Plagioclase are generally unsuitable for $^{40}Ar/^{39}Ar$ dating of rocks younger than 1Ma due to their very low K content and consequently low $^{40}Ar^*$ production.

Feldspar separates can also be a source of inherited argon contamination as xenocrysts that have not nucleated from within the melt may become incorporated in the host magma prior to eruption, either from interaction with a plutonic source or magma chamber walls. The xenocrysts may also experience partial degassing depending on length of residence time within the host magma and the host magma temperature (Flude et al. 2008).

Melt inclusions within both plagioclase and anorthoclase phenocrysts of zero age have also been shown to contain excess argon, which has been attributed to rapid crystallisation processes (Esser et al., 1997; Sumino et al., 2008).

The phenocryst phases are usually hand-separated from the whole rock sample and it is often impossible to distinguish phenocrysts from one another while hand-picking under a binocular microscope. It is possible that feldspar separates collected from Icelandic rhyolites may therefore comprise a mixture of juvenile anorthoclase, K-poor plagioclase and unrelated feldspar xenocrysts in one sample aliquot, leading to an over-estimation of sample age. These problems may be avoided by single crystal analysis, but this technique is not appropriate for young rocks because relatively large sample sizes are required in order to release a measurable amount of $^{40}Ar^*$. Anorthoclase crystal separates have been successfully used to date Rauðfossafjöll Tuya, Torfajökull, with an age of 67±9 k (McGarvie et al.,0 2006).

Rapidly chilled volcanic glasses and obsidians have also proven to be a successful

dating medium, however samples must be fresh and unhydrated. Post emplacement hydration and devitrification can lead to a number of problems relating to the retention of $^{40}Ar^*$ and alkali (K+) ions, leading to both the under and over estimation of eruption ages.

The diffusional loss of $^{40}Ar^*$ attributed to hydration has been reported in fine-grained basaltic glasses from Antarctica (Foland et al., 1993), resulting in a spread of ages of over 90 million years.

Obsidian has proven to be more reliable than its basaltic counterpart and has been used to date a number of young Icelandic silicic lava flows and tuyas including Prestahnúkúr (McGarvie et al., 2007; Clay, 2010), Kerlingarfjöll (Flude et al., 2010) and Torfajökull (McGarvie et al., 2006; Clay 2010).

Problems still arise from hydration-related $^{40}Ar^*$ loss, as demonstrated by Kaneoka (1972), who compared the effects of hydration upon the K/Ar ages of samples of subaerial lava, submarine basaltic glass and obsidian. Of the three, obsidian was the most notably affected, with only a 0.5 to 1% increase in H_2O+ content required in order to cause lower than apparent ages. However Clay (2010) has demonstrated that fresh Icelandic obsidian samples have consistently low concentrations of H_2O, and other volatile species in general (CO_2, F, Cl, S), which agrees with the findings of this project (low LOI: chapter 3), suggesting that effusive Icelandic rhyolites are completely degassed prior to eruption.

As volcanic glass is metastable, the devitrification process commences shortly after emplacement, so care must be taken to ensure that only fresh obsidians are selected in order to avoid alteration products. Cerling et al (1985) documented the remobilization of Na+ and K+ ions in silicic glasses as a result of low temperature hydration. During the hydration process, H+ and H_3O+ diffuse into the glass and replace the K+ ions, however the Ar atoms are less mobile than K+ atoms, resulting in a net loss of K, which in turn leads to higher than apparent ages.

K-rich, rhyolite groundmass can also be used for $^{40}Ar/^{39}Ar$ dating. The Öræfajökull rhyolites are either aphyric or sparsely porphyritic with a microcrystalline groundmass suggesting that a small amount of crystalline order and structure was able to form prior to cooling. The rhyolites have a slightly waxy lustre which is attributed to microcrystal formation rather than devitrification. Flude et al. (2010)

examined textural differences in a number of rhyolites from Kerlingarfjöll in order to observe devitrification effects on the apparent ages obtained, however the results were inconclusive.

A greater number of steps in the heating process may be utilized in order to try to eliminate the effects of atmospheric argon contamination. The accuracy of age data derived from groundmass samples is dependent upon the complete outgassing of any pre-existing radiogenic argon at the time of emplacement. Fresh, unaltered lavas are most likely to yield good results, as alteration can lead to argon loss, but this can be taken into account, where possible, during sample collection. However, Clay (2010) reported high excess argon concentrations in pristine, degassed obsidians from Tenerife and concluded that that freshness is not always a pre-cursor to accurate age determination.

5.5. The MS1 Mass Spectrometer

The MS1 mass spectrometer (fig. 5.4), at the Isotope Geochemistry Laboratory, SEAES, University of Manchester, was used to determine ages for the rocks analysed during this research project.

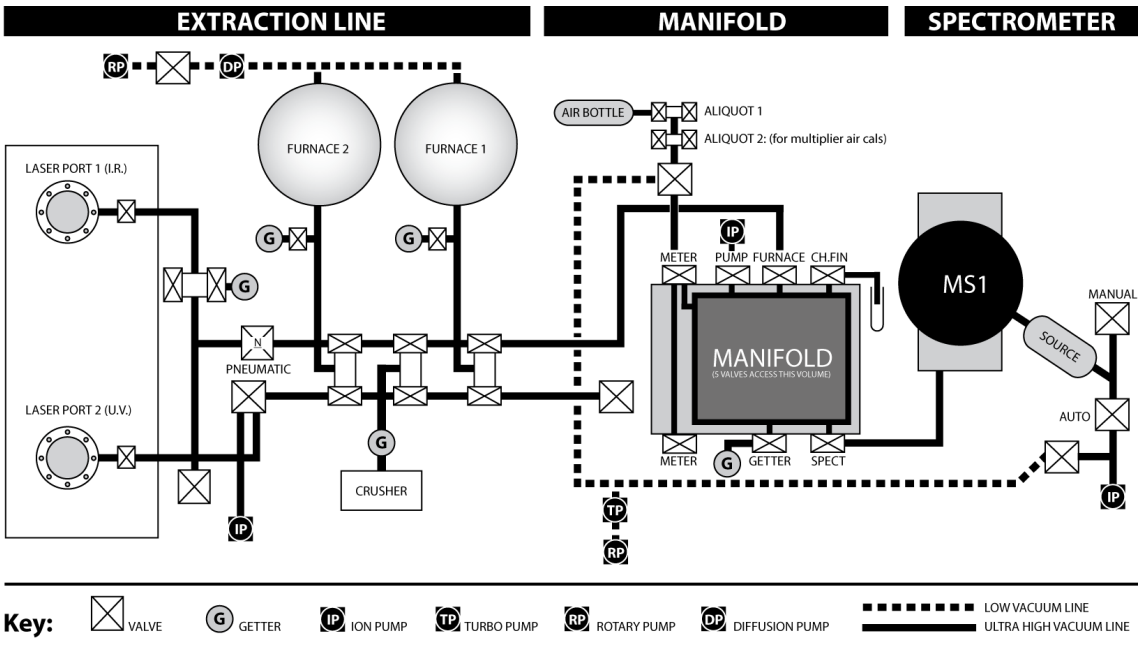

Fig. 5.4. Schematic diagram of the MS1 mass spectrometer.

The MS1 is a single focusing magnetic sector mass spectrometer with a Baur-Signer MKII electron bombardment source, 90° magnetic sector and 15 cm radius flight tube with a magnetic dispersal of 23.56 cm. The electromagnet and mass focusing are digitally controlled from a linked computer running the SPEC computer programme, which also controls the measurement of the peak intensities via a digital voltmeter (Solartron 7061 systems voltmeter). The MS1 is equipped with both Faraday cup and channel electron multiplier detectors (De Tech 2125-EIC-SL)

The MS1 can be separated into three distinct sections (fig. 5.4): the extraction line, where the gas is released from the sample using one of three techniques; the manifold, where the gas is concentrated before it enters the spectrometer, and the spectrometer itself.

The three methods of gas release available in the extraction line are: 1: Heating via two UHV tantalum resistance furnaces (F1 & F2); 2: Laser ablation and laser heating via a Spectrum Laser Systems SL902T CW (continuous wave) 130w Nd/YAG 1064nm laser with a maximum power output of 16w in TEMoo mode; 3: In vacuo crushing. Gettering devices (SAES NP10 Zr-Al and SAES ST1072 Zr-Al-V alloy getters) are present in all three sections in order to ensure that the gas is free from any reactive gases (H_2, CO_2, N_2) and other unwanted impurities prior to isotopic analysis. All three sections are maintained under an ultra high vacuum and each section is pumped by an ion pump. The spectrometer vacuum is kept at below $<7 \times 10^{-9}$ torr and the extraction line and manifold vacuum at $<10^{-8}$ torr.

Mass spectrometers do not generate absolute abundances and therefore need to be calibrated and corrections applied to the values measured during analysis. The MS1 is set up to measure the ^{40}Ar peak with the most sensitivity and therefore discriminates preferentially towards ^{40}Ar compared to other isotopes. Calibrations are carried-out regularly, by measuring the $^{40}Ar/^{36}Ar$ ratio of an aliquot of air stored in a bottle at known pressure in order to check mass discrimination and equipment sensitivity. The measured $^{40}Ar/^{36}Ar$ value is compared to that of atmosphere (295.5) in order to calculate the mass discrimination correction. The correction is then applied to the measured isotopes, upon the assumption that it is linear with mass.

5.6. Sample selection and preparation

Seventeen samples from Öræfajökull were chosen for $^{40}Ar/^{39}Ar$ dating, including one basalt, one trachydacite and 11 rhyolites from Goðafjall and also two rhyolites from Vatnafjall ridge located 20 km to the north east and collected by Stevenson (2004). The silicic samples are microcrystalline rhyolites and obsidians and the majority were chosen due to their lack of any obvious weathering or post-emplacement alteration visible in hand specimen. Where post-emplacement alteration was evident (sample OR12), care was taken to remove it by hand prior to irradiation.

As discussed in chapter 3, the Goðafjall rhyolites are subdivided into two geochemical groups; Group One, an aphyric microcrystalline rhyolite with obsidian domains, and Group Two, a sparsely porphyritic vitreous rhyolite with obsidian domains. Feldspar crystals were handpicked from the Group Two rhyolites for separate analysis. The group One rhyolites and obsidians are either aphyric or do not contain feldspar phenocrysts of a size which is suitable for manual separation, therefore analysis has been carried out on handpicked groundmass fragments in order to ensure freshness.

The samples were manually crushed and sieved to a size of 250 microns. 100 mg of each sample were selected by hand under a binocular microscope in order to remove any phenocrysts and alteration products. The samples were then placed in an ultrasonic bath and washed in acetone for five minutes, and were then rinsed in de-ionised water and dried under an infra red heat lamp. Once dry, the samples were wrapped in aluminium foil and packed into evacuated silica glass tubes and sent for irradiation.

5.7. Analytical procedures

The $^{40}Ar/^{39}Ar$ analysis was carried out using the laser step-heating technique. The 100 mg aliquots of irradiated sample were divided into smaller aliquots of ~10 mg and loaded into nine individual sample holes with a diameter and depth of 5 mm drilled in a disk-shaped aluminium sample holder. The sample holder was loaded into the laser port and covered with a glass cover slip in order to prevent ablated

material obscuring the zero-length, flanged kodial glass viewport.

Once loaded, the sample aliquots were heated with an external infrared heating lamp for ~48 hours at 100°C in an ultra-high vacuum system in order to remove adsorped atmospheric argon from the sample surfaces.

The aliquots were then subjected to a number of monotonically-increased heating steps with a continuous-wave (1064 nm wavelength) Nd:YAG laser for a duration of 10 seconds per step with a beam focused to a spot width of 5mm. The laser beam position is controlled remotely by an X-Y stage which is viewed with a video camera positioned within the laser chamber. The laser power output for each heating step ranged from 0.51 W to 13.3 W. The number of laser heating steps obtained for each aliquot is varied, depending on the amount of gas released in the previous steps, in order to release sufficient Ar gas for isotopic analysis. Samples were heated until either total fusion occurred or ^{39}Ar gas release was exhausted.

Reactive gases (H_2, CO_2, N_2) were removed in the laser port by exposure to a SAES NP10 Zr-Al alloy getter at 450°C, and in the mass spectrometer by exposure to a SAES ST1072 Zr-Al-V alloy getter at 250°C.

The gas released from each heating step was purified using getters before being admitted to the MS1 mass spectrometer for isotopic analysis using the channel electron multiplier detector.

System blanks were interspersed between every incremental heating step in order to check that blanks were stable (once the blank was deemed stable they would then be interspersed after every other heat step at higher temperature stages). This is especially important when analysing samples of a young age as the amount of ^{40}Ar* and ^{36}Ar will be relatively small and for optimum age determination the blanks need to be low and reproducible in order to accurately resolve the ^{40}Ar* from the background level. If the measured system blank is too high then analysis is postponed and further blanks are repeated until a consistently low value is achieved. Typical blank measurements for ^{36}Ar range from 2 to 5 x 10^{-13}cm^3 STP and 1 to 3 x 10^{-11}cm^3 STP for ^{40}Ar.

The measured ^{40}Ar/^{39}Ar ratios were then corrected for background levels (system blanks), mass discrimination (based upon air calibrations) and interfering neutron reactions from K. ^{37}Ar decay corrections were not applied for calcium as the sam-

ples were analysed after a time period longer than the half-life of ^{37}Ar had passed. With the exception of basalt sample OR06, the ^{36}Ar correction (see section 5.3) for atmospheric argon was not applied. Application of the correction leads to high errors in samples that contain only small quantities of $^{40}Ar^*$. The correction assumes that the initial $^{40}Ar/^{36}Ar$ of any sample is 295.5 and that any ^{36}Ar released from the sample is of atmospheric origin. As step heating increases, many of samples release very low or zero amounts of ^{36}Ar at higher temperatures, while a number of other samples release fractionated Ar with a $^{40}Ar/^{36}Ar$ ratio less than 295.5. Application of the correction in these instances can lead to an over-correction of ^{40}Ar.

Table 5.3 provides a comparison of ^{36}Ar corrected data and non-corrected data (assuming atmospheric Ar) for sample OR280. The comparison demonstrates the effects of unacceptably high errors on heating steps that release detectable amounts of $^{40}Ar^*$. For example, OR280-1-03 (table 5.3) yields a $^{40}Ar/^{36}Ar$ ratio of 327, releasing only 9% $^{40}Ar^*$. Application of the ^{36}Ar correction produces an age of 0.19 ± 3.39 Ma. Therefore, although the apparent age is within the acceptable limits for this unit, the very large error renders the age meaningless. It is therefore accepted that, with the exception of OR06, the sample ages presented in this chapter represent an upper age limit.

Further discussion of samples with $^{40}Ar/^{36}Ar$ ratios lower than 295.5 can be found in section 5.10.

			Calculated without 36Ar correction				Calculated with 36Ar correction				
	40Ar/36Ar	*± 40Ar/36Ar*	*40Ar/39Ar*	*± error*	*Age (Ma)*	*± error(Ma)*	*40Ar*/39Ar*	*± error*	*Age (Ma)*	*± error(Ma)*	*%rad 40Ar*
OR280-1-01	286	45	32.92	1.50	3.55	0.162	-1.06	121.70	-0.11	13.13	0
OR280-1-02	229	80	10.92	0.76	1.18	0.082	-3.17	15.09	-0.34	1.63	0
OR280-1-03	327	85	18.96	0.57	2.04	0.061	1.80	31.46	0.19	3.39	9
OR280-1-04	290	57	10.15	0.30	1.09	0.032	-0.20	75.75	-0.02	8.17	0
OR280-1-05	283	26	30.70	0.77	3.31	0.083	-1.35	46.87	-0.15	5.06	0
OR280-1-06	305	10	25.15	0.58	2.71	0.063	0.77	23.10	0.08	2.49	3
OR280-1-07	296	8	20.31	0.50	2.19	0.054	0.06	214.16	0.01	23.10	0
OR280-1-08	289	12	16.96	0.32	1.83	0.035	-0.37	38.01	-0.04	4.10	0
OR280-1-09	296	11	65.73	2.29	7.08	0.246	0.02	6077.50	0.00	655.66	0

Table 5.3. OR280, comparison of uncorrected and corrected data for atmospheric argon based on the ^{36}Ar release.

5.8. Analytical developments

Prior to the laser step heating method described above, an initial batch of sample aliquots of 50 mg were analysed using furnace heating following the total fusion method of Flude et al. (2008). The 50 mg samples were heated in the furnace to a temperature of 400° C which was used as an initial 'clean-up' step. The samples were then heated further to a temperature of 1200° C for the main gas release step and finally heated to a temperature of 1500° C to ensure that all of the argon had been extracted from the sample.

This method proved to be unsuccessful as the blank levels of ^{36}Ar were too high to resolve any radiogenic $^{40}Ar^*$ (the results of these analyses have not been included in this study).

Adopting the laser step heating approach enabled smaller aliquots, and thereby multiple repeats of a single sample, to be analysed with lower blanks (>100 times lower). Aliquots of OR10, OR39 and OR44 were used as test samples in various combinations of numbers of steps and laser output power in order to establish the most effective protocol of analysing glassy rhyolite samples in this study (see section 5.6).

The first approach used an initial medium-strength laser output setting, as a 'clean-up' step in an attempt to remove any atmospheric argon from grain surfaces and boundaries. This was followed by a high temperature step, during which most of the gas should be released, and finally one to two further high temperature steps in order to completely degas the aliquot. While partially successful, for many samples relatively large amounts of ^{36}Ar were released during all steps.

The second approach incorporated more lower temperature steps in order to preferentially remove any atmospheric argon adsorbed onto grain surfaces. This technique proved to be successful for sample OR44 and was adopted for all of the glassy samples.

OR39 is a non-glassy aphyric rhyolite and was initially analysed using only low and high temperature heating steps with two initial low power clean-up steps with a laser power density of 0.26×10^5 Wm^{-2} and 0.66×10^5 Wm^{-2}, proceeded by two

heating steps on a maximum power density of 6.77 x 10^5 Wm^{-2}, however very large amounts of ^{36}Ar were released at all steps.

In order to try to remove the ^{36}Ar contaminant (discussed later in section 5.10), the second approach utilised up to four steps at the same laser output which were repeated until the ^{36}Ar reduced to near-background levels. This gas was pumped away and step-heating resumed. This technique proved to be successful and was used to analyse the only other non-glassy sample, OR12. During these initial low temperature heating steps only minimal amounts (less than 10%) of ^{39}Ar were released and would probably not have been included in an age plateau calculation, therefore the apparent plateau age calculated for OR12 is still valid even though some ^{39}Ar release is not accounted for.

5.9. Results

Data from the 17 analysed samples are presented in their geochemical groups in table 5.4. The majority of Group One and all Group Two samples chosen for analysis are degassed (<1wt% H_20) and display little evidence of post-emplacement alteration, therefore no loss of ^{40}K or ^{40}Ar via diffusion due to post emplacement alteration is expected.

Age spectrum diagrams have been produced for all of the samples irrespective of whether a plateau age has been calculated. As discussed previously, the presence of any ^{40}Ar of atmospheric origin is determined by the measurement of ^{36}Ar released from each sample. The amount of ^{36}Ar released during stepped heating of each aliquot is displayed in graph form alongside the samples' appropriate age spectrum diagram. If an initial sample aliquot was found to contain high levels of ^{36}Ar then no further aliquots of this sample were analysed .

Five samples released either very low or undetectable amounts of ^{36}Ar and it is therefore assumed that these five samples do not contain detectable amounts of atmospheric argon and that any ^{40}Ar released from the sample is of radiogenic origin. Plots depicting the release of ^{40}Ar versus ^{39}Ar have been produced to calculate an apparent age instead, therefore all of the following age spectrum diagrams presented, unless otherwise stated, represent apparent ages.

Sample	Geochemical group	description	No. of aliquots	excess ^{36}Ar	$^{40}Ar/^{36}Ar$ range
0R06 (A)	n/a	basalt	3	Y	n/a
OR12 (D)	One	aphyric rhyolite	8	2 aliquots only	140-386
OR39 (D)	One	aphyric rhyolite	4	Y	–
OR150 (D)	One	obsidian	1	Y	228-485
OR202 (D)	One	obsidian	1	Y	255-336
OR221 (D)	One	rhyolite	1	Y	241-326
OR255 (D)	One	rhyolite	2	N	–
OR280 (D)	One	obsidian	3	Y	229-327
OR293 (D)	One	obsidian	3	N	–
OR10 (H)	Two	obsidian	3	Y	261-453
OR44 (L)	Two	obsidian	7	initial steps only	210
OR49 (L)	Two	obsidian	6	Y	69-656
OR54 (L)	Two	obsidian	6	N	–
OR55 (N)	n/a	porphyritic trachydacite	3	Y	151-297
OR55 (N)	n/a	feldspar separates	3	Y	195->1000 but errors are large
JS203	Vatnafjall	obsidian	3	N	–
JS226	Vatnafjall	obsidian	3	N	–

Table 5.4. Summary of samples analysed and excess argon contents. Lithofacies are indicated in brackets.

Seven samples released detectable quantities of ^{36}Ar. Diagrams depicting the $^{40}Ar/^{36}Ar$ ratio of each heating step of these seven samples are also displayed and, as the majority of the ratios are within error of 295.5, it is assumed that the non-radiogenic ^{40}Ar present within these samples is of atmospheric origin and that very little $^{40}Ar^*$ is present. Isochrons were not constructed for any of the samples containing atmospheric ^{36}Ar.

Three samples (OR49 and OR55 and, to a lesser extent, OR12) displayed $^{40}Ar/^{36}Ar$ ratios < 295.5, suggesting incorporation of a fractionated ^{36}Ar source. These samples were also not corrected for atmospheric argon as the correction assumes a $^{40}Ar/^{36}Ar$ ratios of 295.5 which would lead to an over-correction of ^{40}Ar if the ratio of the sample was lower. Further discussion of the fractionated ^{36}Ar source is discussed in section 5.10.

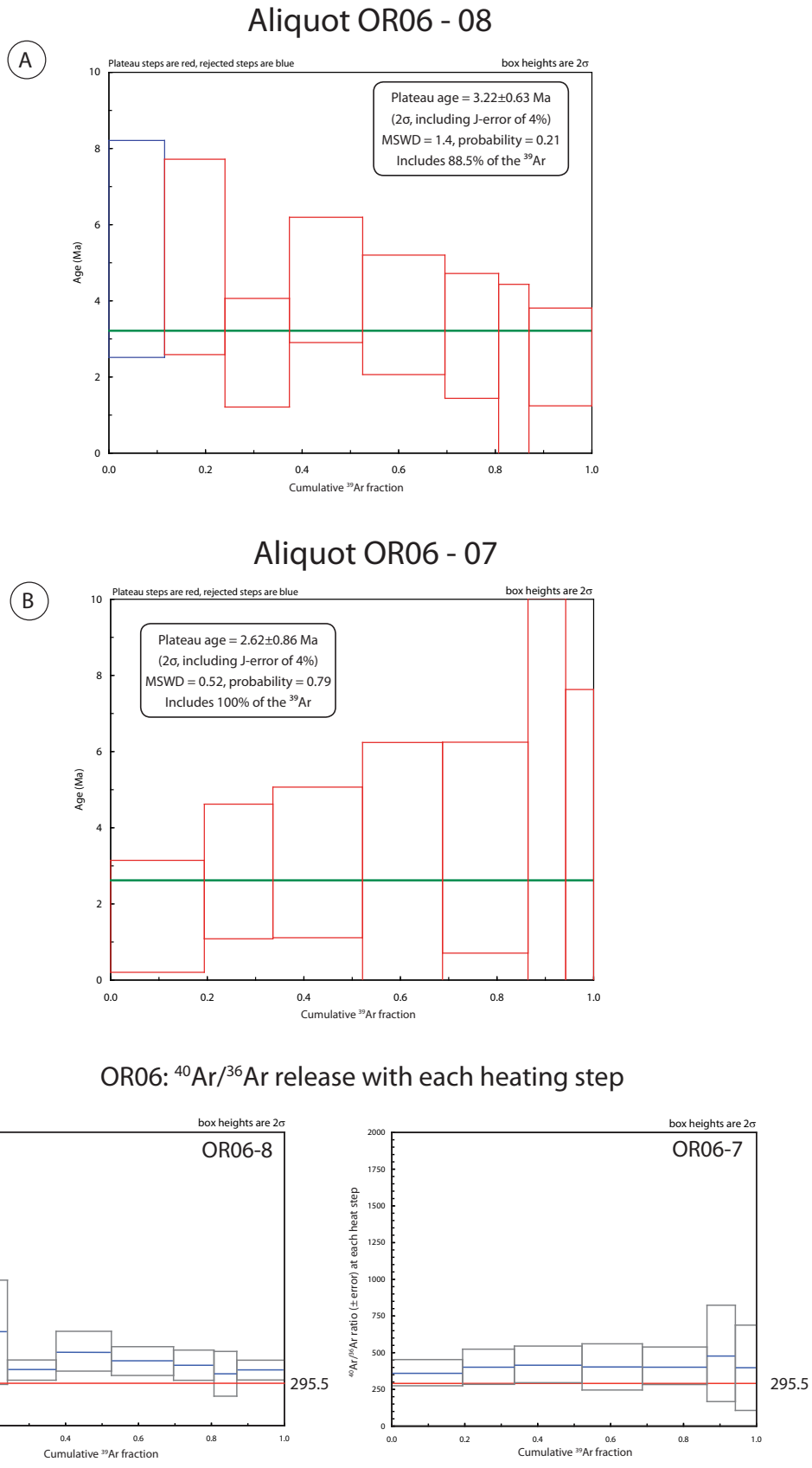

Fig. 5.5 a-c: Age spectrum diagrams for basalt aliquots OR06-8 (a) and OR06-9 (b) and $^{40}Ar/^{36}Ar$ release for both aliquots.

OR06 Basalt (fig.5.5): This sample was taken from the 'basement' basalts, the lowest stratigraphic unit in the field area. Three aliquots were analysed using the step heating method with the number of steps ranging from five to nine . As expected for an older sample, OR06 released a far greater abundance of $^{40}Ar^*$ in comparison to the younger rhyolites, allowing the atmospheric ^{36}Ar correction to be applied. Two aliquots produced age spectrum plateaus (fig. 5.5), yielding apparent ages of 3.22 ± 0.60 Ma and 2.62 ± 0.86 Ma (errors are 2σ) with a weighted mean of 3.02 ± ± 0.49 Ma.

Type One rhyolites:

OR39 (lithofacies D): OR39 was initially analysed using only two low and two high temperature heating steps however the results were unsuccessful as large amounts of ^{36}Ar was released at all steps. This initial technique was swapped for the revised incremental step heating approach for the final aliquot analysis, OR39-4 where a number of low temperature steps with very high ^{36}Ar release and minor ^{39}Ar release were pumped away rather than being released into the mass spectrometer (see section 5.8). This technique produced a more consistent gas release at higher temperatures, with atmospheric argon released during the first two lower temperature heating steps, and two higher temperature steps releasing a very small proportion of $^{40}Ar^*$. The two higher temperature steps yielded atmospheric-Ar corrected ages of 0.3±0.30 Ma Ma and 0.2 ± 0.20 Ma. Both ages produced very high errors (100%), thereby rendering the ages meaningless.

OR12 (lithofacies D) (fig. 5.6 – 5.8): This groundmass sample of aphyric rhyolite showed some signs of post-emplacement alteration in thin section but care was taken to remove this during hand picking.

A total of five aliquots were analysed, each aliquot receiving between five and seven heat steps. Four initial heating steps were repeated at a very low laser output (0.51W) in order to remove as much excess and/or atmospheric argon as possible (see section 5.8)

After the initial clean-up steps, two of the five aliquots – OR12-2 and OR12-3 –

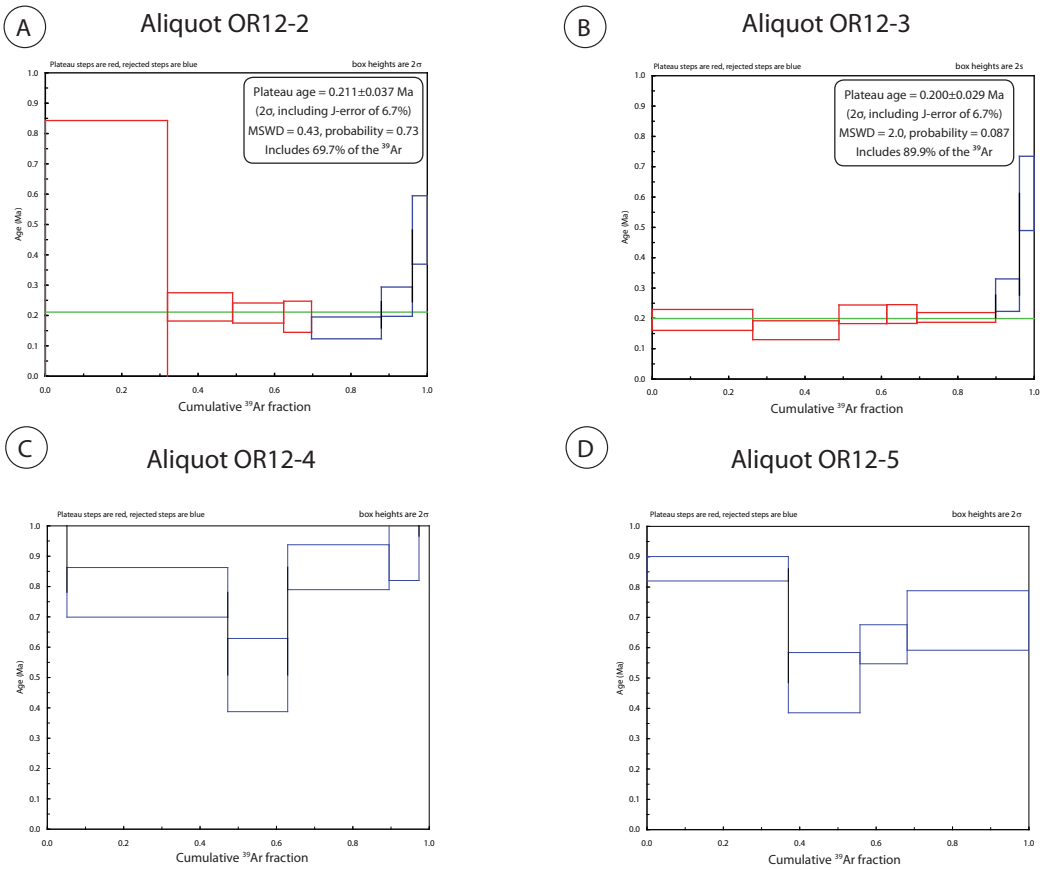

Fig. 5.6 a-d: Age spectrum diagrams for OR12 aliquots. Only OR12-2 (a) and OR12-3 (b) produce a 'plateau' age (represented by green line).

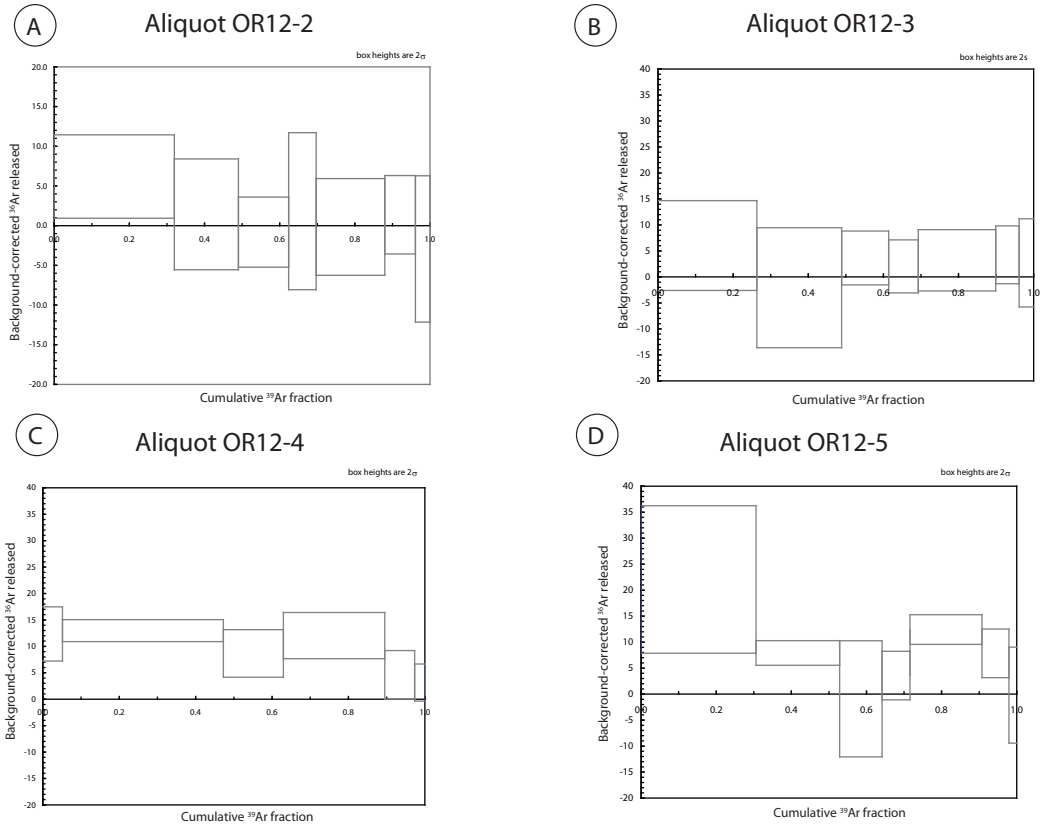

Fig. 5.8a-d. Excess ^{36}Ar release for OR12 aliquots. OR12-2 (a) and OR12-3 (b) do not release any excess ^{36}Ar.

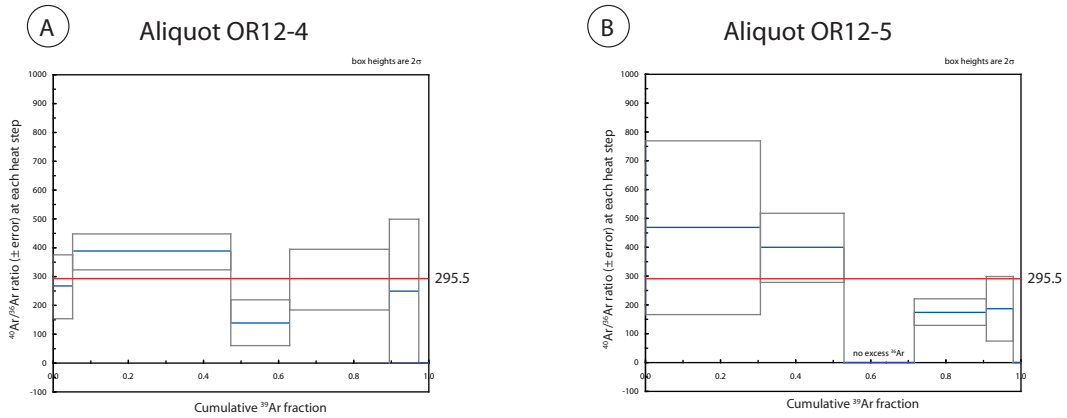

Fig. 5.8 a-b. $^{40}Ar/^{36}Ar$ ratios of aliquots containing excess ^{36}Ar. OR12-4 (a) and OR12-5 (b) both released excess ^{36}Ar and both display $^{40}Ar/^{36}Ar$ ratios significantly lower than atmospheric 295.5.

did not release any detectable ^{36}Ar above background levels, therefore it is assumed that all of the ^{40}Ar released is of radiogenic origin. Both of these aliquots produced an age spectrum plateau, yielding an age of 0.211±0.04 Ma and 0.200±0.03 Ma respectively.

The three remaining aliquots (OR12-6 is not shown) all contained excess argon during one or more heating steps, with $^{40}Ar/^{36}Ar$ ratios ranging from 140 – 476 (fig.5.8). Sub-atmospheric $^{40}Ar/^{36}Ar$ ratios suggest incorporation of an excess and a fractionated agron source or a contaminant at m/z 36 released from the sample (discussed further in section 5.10). As a result of this, aliquots OR12-4 to 5 (fig.5.6) both display a range of both higher and lower than apparent ages (non-atmospheric argon corrected).

The two OR12 aliquots that did not release any excess ^{36}Ar, OR12-2 and OR12-3 (fig. 5.6a-b) yield plateau ages that are within error of one another (0.211±0.04 Ma and 0.200±0.03 Ma respectively). The weighted average age of these two aliquots gives an eruption age of 0.204±0.02 Ma.

OR150 (lithofacies D) (fig. 5.9a-c): One aliquot of this sample yielded 14 steps, all containing atmospheric argon and an ^{36}Ar uncorrected age between 7 Ma and 1.5Ma, which is unlikely as due to normal magnetisation the sample age is constrained to < 0.78 Ma (Prestvik, 1985).

Three low temperature steps (OR150-1-04 to 06) were repeated at the same laser power output (fig. 5.9b), and a further two steps at a slightly higher output, in order

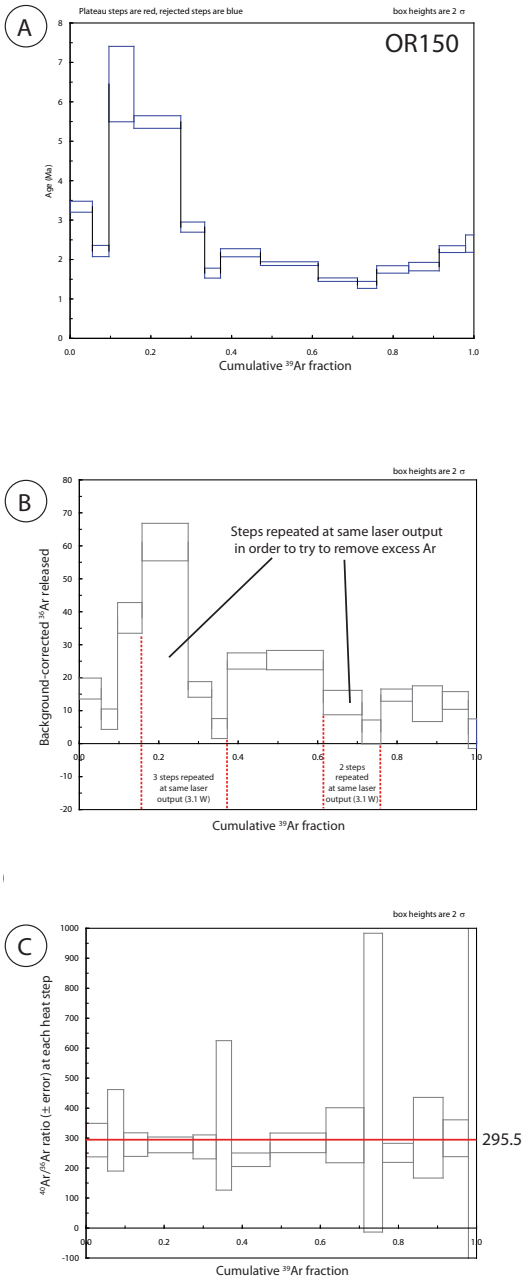

Fig. 5.9 a-c : OR150 age spectrum diagram (a); OR150 36Ar release at each heating step (b); ^{40}Ar/^{36}Ar ratio of each heating step (c).

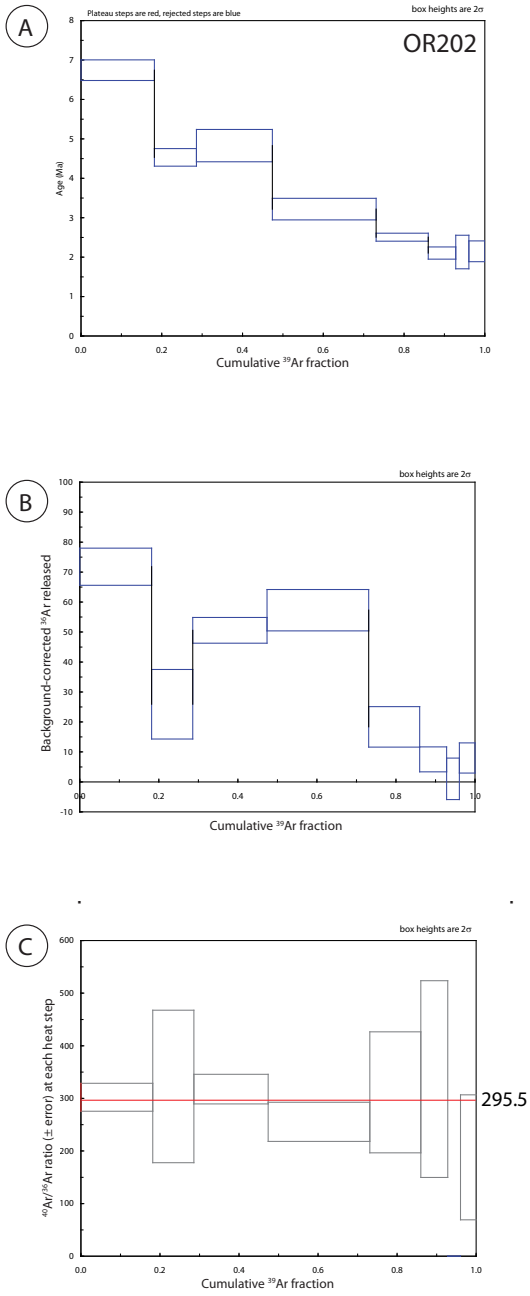

Fig. 5.10 a-c : OR202 age spectrum diagram (a); OR202 36Ar release at each heating step (b); ^{40}Ar/^{36}Ar ratio of each heating step (c).

to attempt to clean up the sample, but this technique was unsuccessful. ^{40}Ar/^{36}Ar ratios are within error of 295.5 except for one step (OR150-1-07) with a ^{40}Ar/^{36}Ar ratio of 228±12, however as all of the other heating steps release atmospheric argon this anomalous step may be due to instrument error. The two heating steps yielding the largest amount of total ^{40}Ar also released the most ^{36}Ar, suggesting that the sample is dominated by atmospheric argon. Further aliquots were not analysed.

OR202 (**(lithofacies D)** fig. 5.10a-c): One aliquot yielded eight steps with decreasing apparent ages with temperature (Fig. 5.11). All except one heating step contain high amounts of ^{36}Ar with $^{40}Ar/^{36}Ar$ ratios within error of 295.5, suggesting that the sample is dominated by atmospheric Ar and contains only minor amounts of radiogenic Ar. Further aliquots were not analysed as the apparent sample age decreased from 7 Ma to 2 Ma.

OR221 (lithofacies D) (fig. 5.11): One aliquot yielded 11 steps, all containing excess argon and producing ^{36}Ar-uncorrected ages above 1.93 Ma. The highest total ^{40}Ar release also produced the highest ^{36}Ar release with a $^{40}Ar/^{36}Ar$ ratio within error of 295.5. Only two heating steps released detectable $^{40}Ar^*$ (OR221-1-07 and OR221-1-11), producing ^{36}Ar-corrected ages with large errors 0.25±0.25 Ma and 0.26±0.26 Ma,. Further aliquots were not analysed as the apparent sample age increased from 2 Ma to 6.5 Ma.

OR255 (lithofacies D) (fig. 5.12): One aliquot produced 7 heating steps with a saddle shaped age spectrum diagram. Two heating steps (OR255-1-04 and 05) did not yield detectable ^{36}Ar and produced uncorrected ages of 0.23 ± 0.01 Ma and 0.32 ± 0.02 Ma respectively. The remaining heating steps have a $^{40}Ar/^{36}Ar$ ratio within error of 295.5. Further aliquots of this sample were not analysed, however an estimated age of 0.2 to 0.3 Ma may be inferred from the two heating steps that released zero ^{36}Ar.

OR280 (lithofacies D) (fig. 5.13): One aliquot yielded nine heating steps and did not produce an age spectrum diagram with a plateau. All of the heating steps released ^{36}Ar and all the $^{40}Ar/^{36}Ar$ ratios are within error of 295.5, suggesting that the sample is dominated by atmospheric argon, and only two heating steps (OR280-1-03 and OR280-1-06) was shown to release a detectable amount of $^{40}Ar^*$ at 9% and 3% respectively. Table 5.6 in section 5.11 highlights both the atmospheric corrected and uncorrected ages for this sample. Apparent ^{36}Ar-uncorrected ages range from 1 Ma to 7.5 Ma, however the ^{36}Ar-corrected age for the heating step that released the most detectable $^{40}Ar^*$ is 0.19±3.39 Ma. The error renders this age unacceptable.

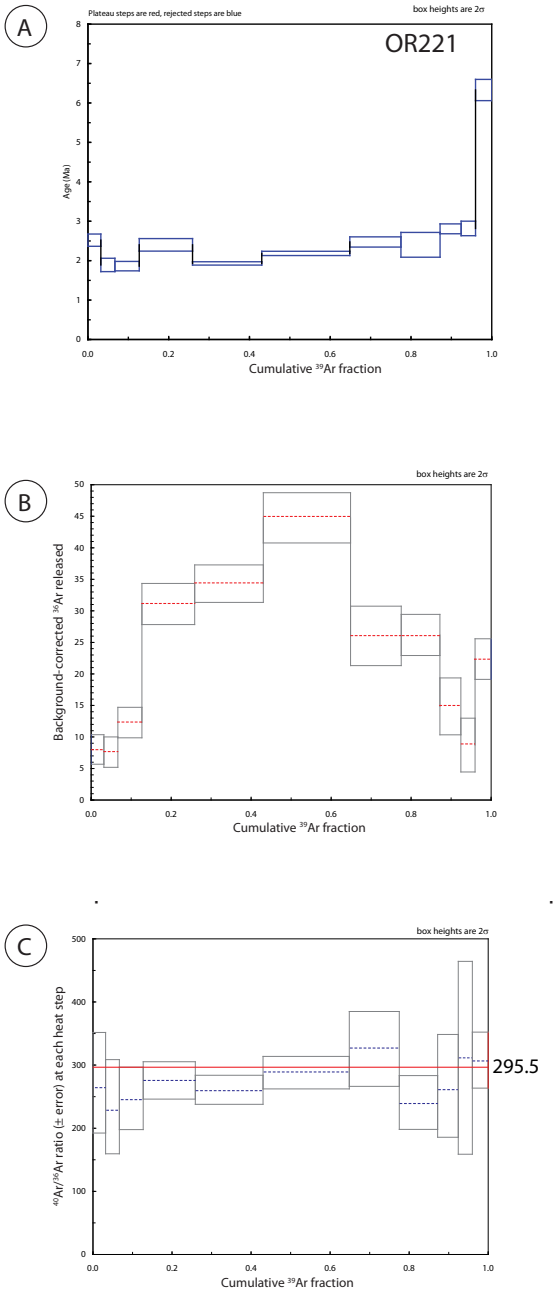

Fig. 5.11a-c. OR221 age spectrum diagram (a); OR221 ^{36}Ar release at each heating step (b); ^{40}Ar/^{36}Ar ratio of each heating step (c).

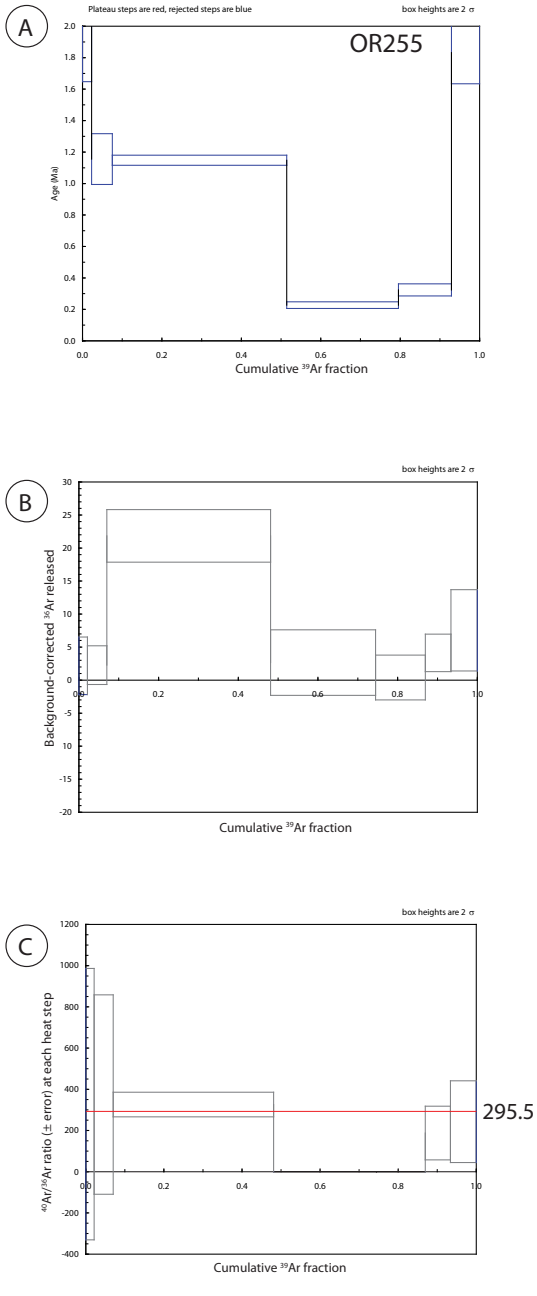

Fig. 5.12a-c. OR255age spectrum diagram (a); OR255 ^{36}Ar release at each heating step (b); ^{40}Ar/^{36}Ar ratio of each heating step (c).

OR293 (lithofacies D) (fig. 5.14-15): Three aliquots were analysed; OR293-1 consisted of nine heating steps producing a decreasing age spectrum diagram with an apparent plateau age of 0.108 ± 0.02 Ma (fig. 5.14a). The remaining two aliquots consisted of 10 heating steps each and did not produce a plateau age. OR293-2 produced a decreasing age spectrum containing a number of steps within the error of this age, but not enough to meet the criteria needed to produce a plateau, how-

ever the gas release is consistent with the age of 0.11 Ma produced by aliquot one. Detectable amounts of ^{36}Ar were released from the initial low temperature steps of aliquot 2 (fig. 5.14d) but is not present in the higher temperature steps. An eruption age of 0.11 Ma is suggested for OR293.

An age of 0.11 Ma for OR293 is problematic as this sample is geochemically classified as a Group One rhyolite and was collected from lithofacies D (fig. 3.17) but is producing an age that is lower than those of the stratigraphically younger Group Two rhyolites. The reasons for this relativley young age are unclear as the sample shows no evidence of post-emplacement alteration, only releases excess ^{36}Ar during the initial low temperature heating and produces a reproducible age over both aliquots.

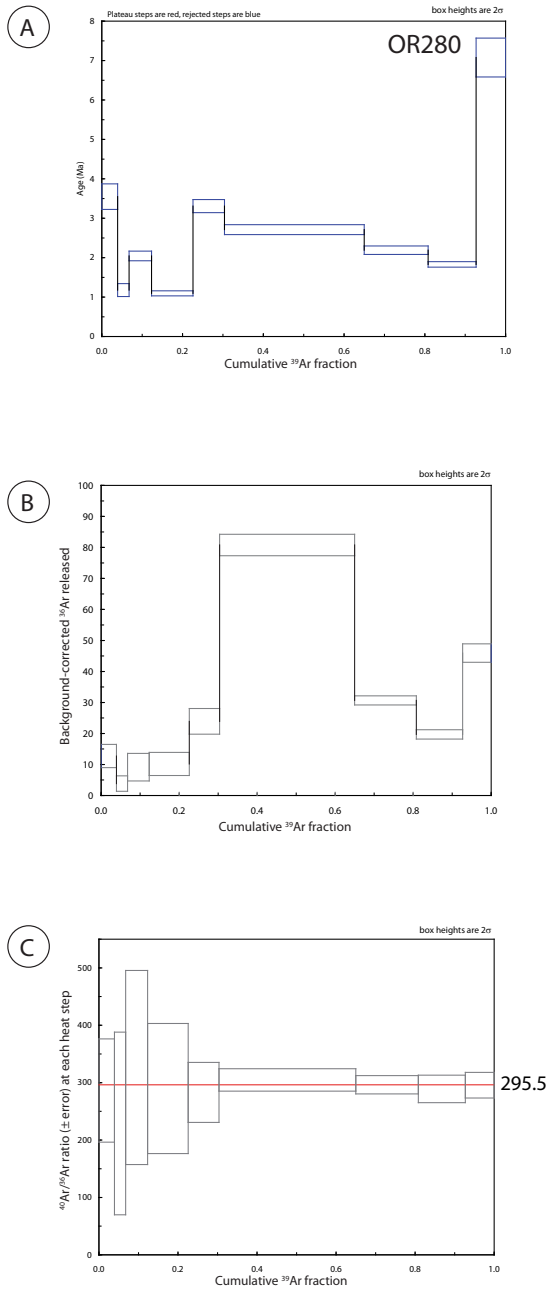

Fig. 5.13 a-c : OR280age spectrum diagram (a); OR280 ^{36}Ar release at each heating step (b); $^{40}Ar/^{36}Ar$ ratio of each heating step (c).

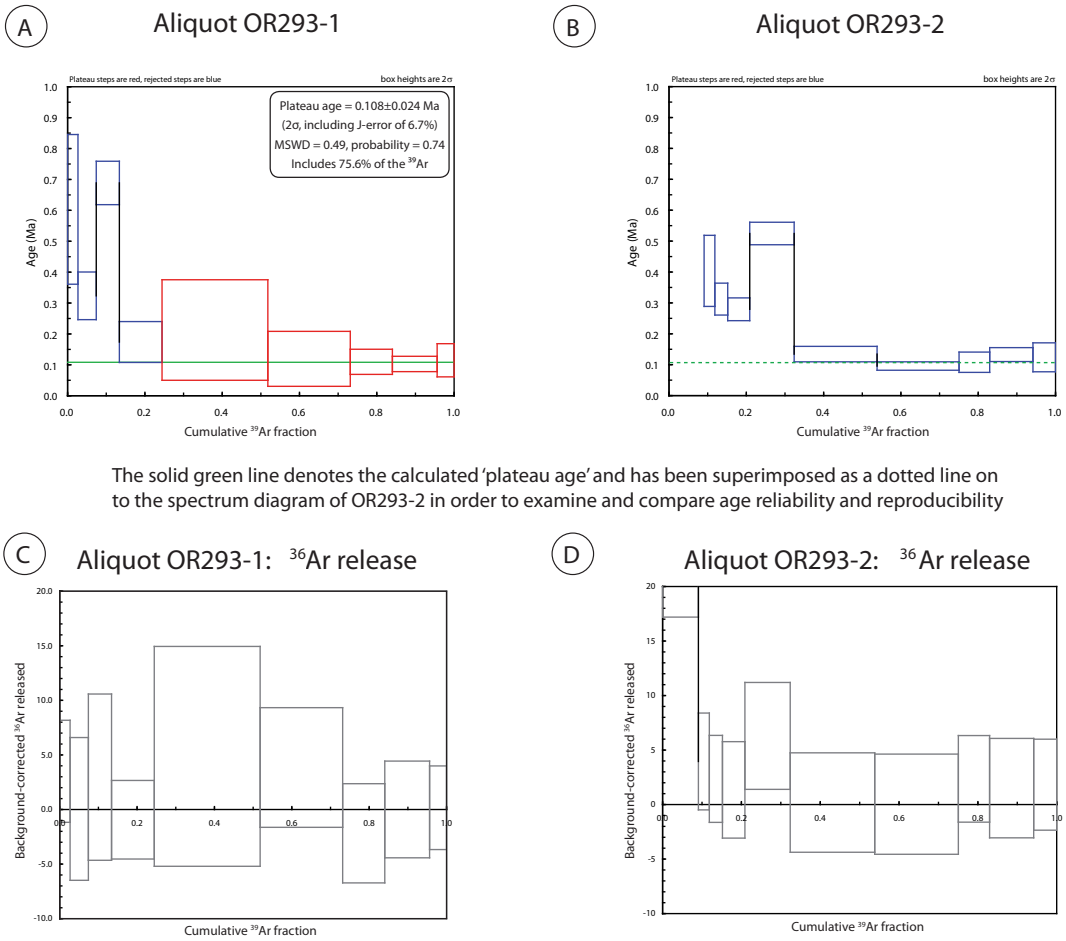

The solid green line denotes the calculated 'plateau age' and has been superimposed as a dotted line on to the spectrum diagram of OR293-2 in order to examine and compare age reliability and reproducibility

Fig. 5.14 a-d. OR293 age spectrum diagrams (a & b) producing decreasing age spectrums; OR293 ^{36}Ar release at each heating step - only the initial low temperature steps release ^{36}Ar (c & d)

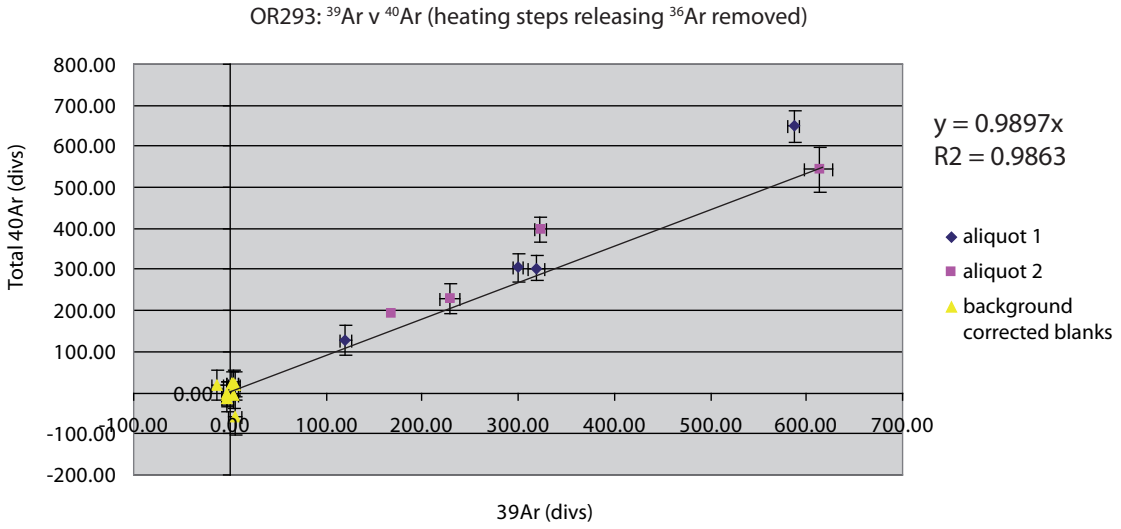

Slope indicates a lower age limit for sample OR293, which is broadly in agreement with the calculated plateau age

Fig. 5.15. OR293 ^{39}Ar release plotted against total ^{40}Ar release for all the steps that do not release ^{36}Ar, producing a slope age which is broadly in agreement with the calculated plateau age. Yellow triangles denote backgroung corrected blanks.

Type Two rhyolites:

OR10 (lithofacies H) (fig. 5.16): As discussed previously in section 5.8, three aliquots of OR10 were used as test samples in order to establish the most effective protocol of analysing glassy rhyolites, The first aliquot was abandoned due to problems adjusting the laser output setting. The remaining two aliquots were analysed over six heating steps. Gas release was inconsistent and did not produce a plateau on the age spectrum diagrams. With the exception of one, all steps released detectable amounts of Ar with a $^{40}Ar/^{36}Ar$ ratio within error of 295.5, therefore OR10 is assumed to be contaminated by atmospheric argon. No reliable age was calculated for this sample with apparent ages ranging from 0.4 to 1.6 Ma

OR44 (lithofacies L) (fig.5.17 – 5.18): Three initial aliquots of OR44 were used as test samples in order to establish the most effective laser power output for the glassy rhyolite samples in this study (see section 5.8), however large amounts of ^{36}Ar were released during these initial experiments.

This initial approach was abandoned in favour of more heating steps initiated at lower temperatures in order to try to remove more atmospheric argon prior to $^{40}Ar^*$ release.

A further three aliquots of OR44 were analysed using the revised increased step heating approach. Aliquots OR44-4 to OR44-6 were analysed over 8 to 10 steps. A detectable level of ^{36}Ar was only released during the initial low temperature heating steps and as the steps increase in temperature the ^{36}Ar becomes indistinguishable from the mass spectrometer background level, therefore it is assumed that all of the ^{40}Ar released during these heating steps is of radiogenic origin.

OR44-4 and OR44-5 produced decreasing apparent age spectrums, while OR44-6 produced a saddle-shaped spectrum. OR44-4 produced a plateau age of 0.156 Ma $\pm$ 0.02 while OR44-5 produced a number of steps within the error of 0.15 Ma even though a plateau was not produced. An age of 0.15 Ma is also consistent with the highest temperature heating steps yielded from two of the initial test aliquots.

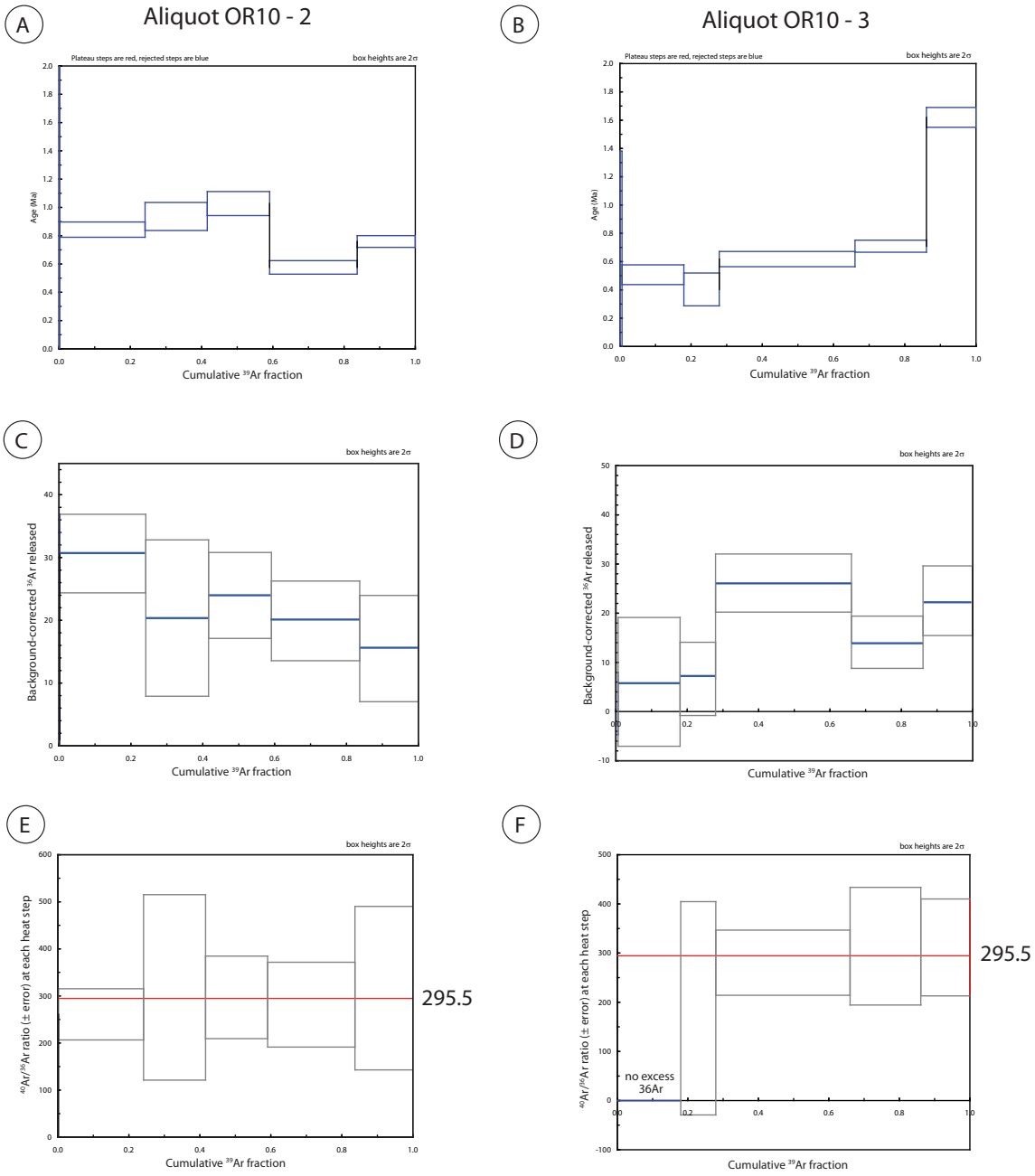

Fig. 5.16 a-f. OR10 age spectrum diagrams for aliquots OR10-2(a) and OR10-3(b); OR10 ^{36}Ar release at each heating step (c & d); ^{40}Ar/^{36}Ar ratio of each heating step (e & f).

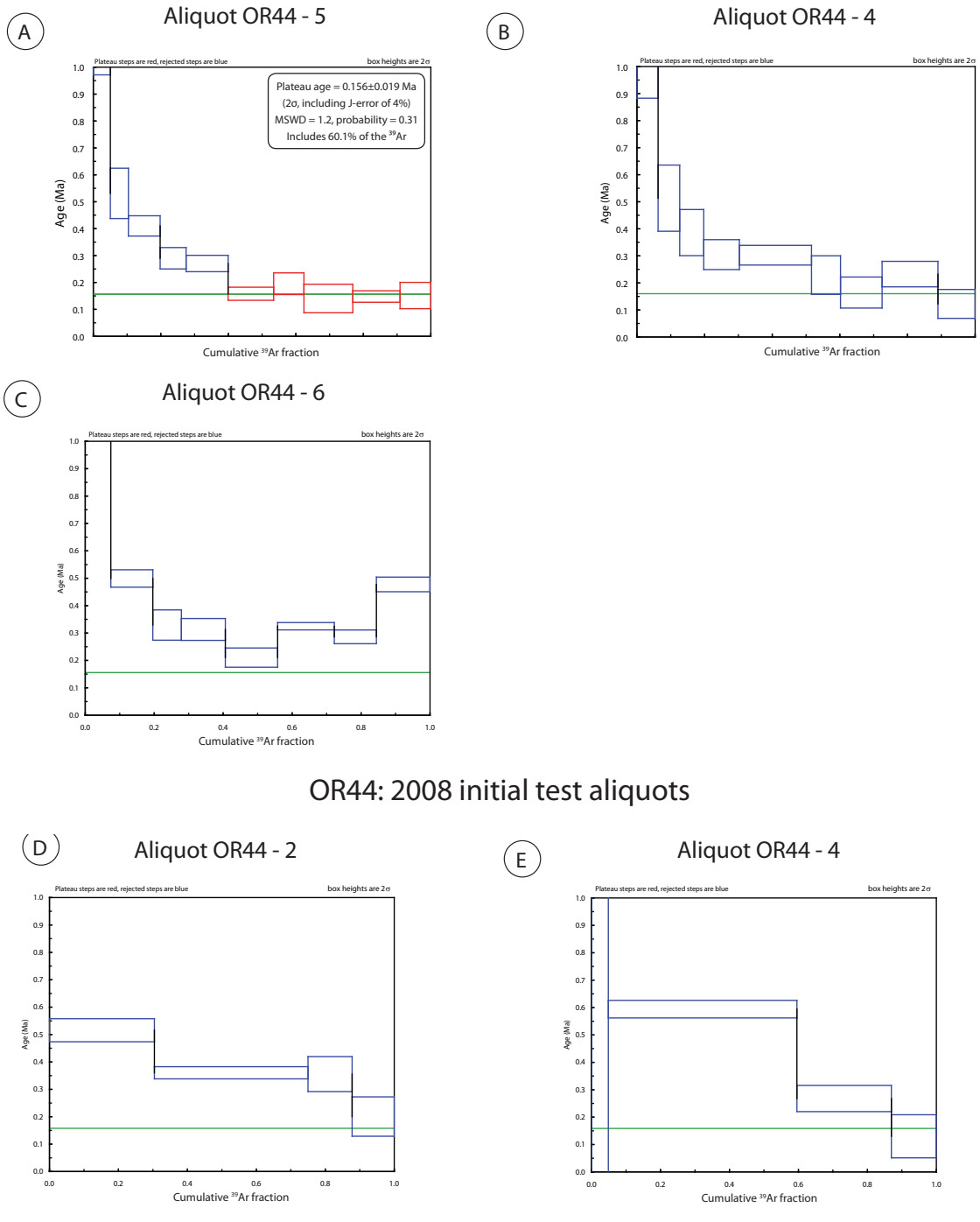

Fig. 5.17 a-e : OR44 age spectrum diagrams for aliquots OR44-5(a), OR44-4(b) and OR44-6 (c); OR44 initial 2008 test aliquots. Green line denotes calculated plateau age from OR44-5 which has been superimposed on to the other spectrum diagrams.

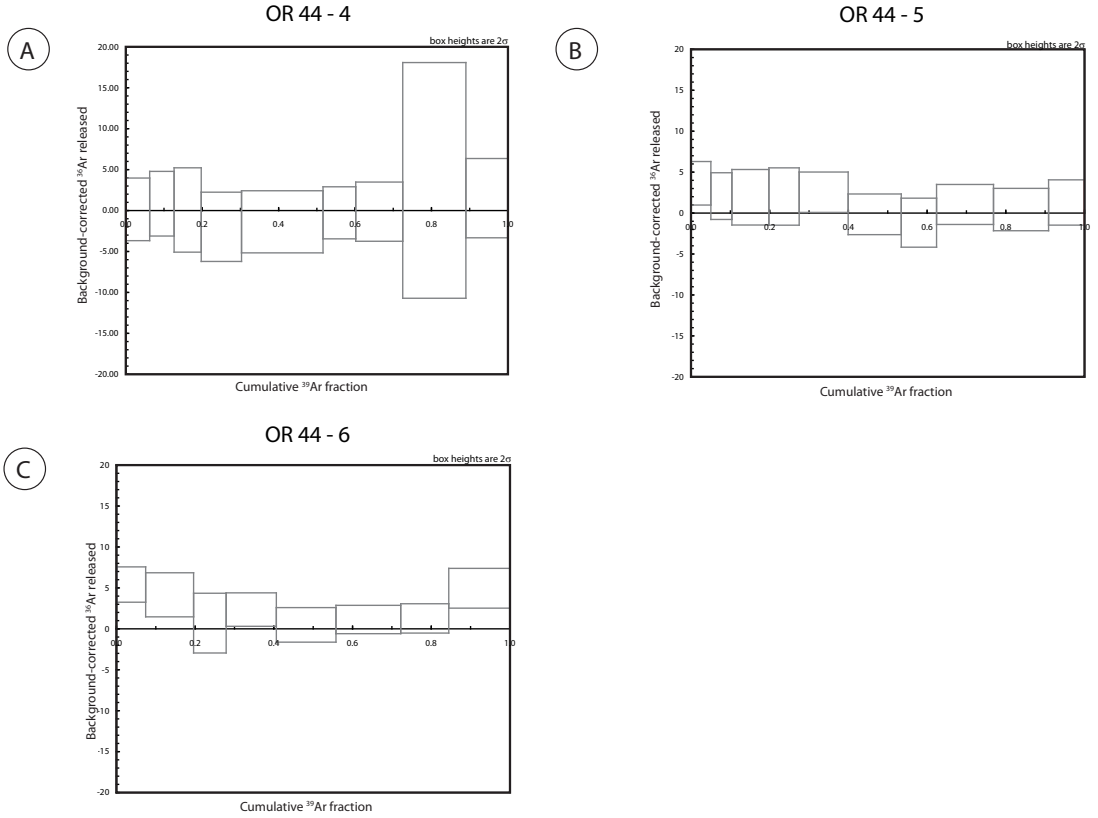

Fig. 5.18 a-c : OR44 ^{36}Ar release for aliquots OR44-4 (a), OR44-5 (b) and OR44-6 (c). None of the aliquots release detectable ^{36}Ar.

OR49 (lithofacies L) (fig. 5.19 – 5.21): Six aliquots of OR49 were analysed, each consisting of 10 heating steps. Only one aliquot, OR49-4, produced an apparent plateau age of 0.200 ± 0.03 Ma , although four out of 10 steps released a small detectable amount of ^{36}Ar therefore 0.2 Ma represents an upper age limit for this sample. ^{36}Ar release is inconsistent across the six aliquots , with OR49-1, 3 and 4 releasing very low or undetectable amounts over the range of heating steps, while OR49-2, 5 and 6 release relatively larger quantities of ^{36}Ar, even during high temperature steps (fig.5.21). ^{40}Ar/^{36}Ar ratios are also widely variable with some heating steps displaying values far lower than the atmospheric 295.5, some as low as 67 ± 23.

Consistently low ^{40}Ar/^{36}Ar ratios are also seen in sample OR55 and will be discussed further in section 5.10.

OR54 (lithofacies L) (fig. 5.22 – 5.24): Three aliquots were analysed, each consisting of nine heating steps. Two aliquots produced plateau age spectrum diagrams,

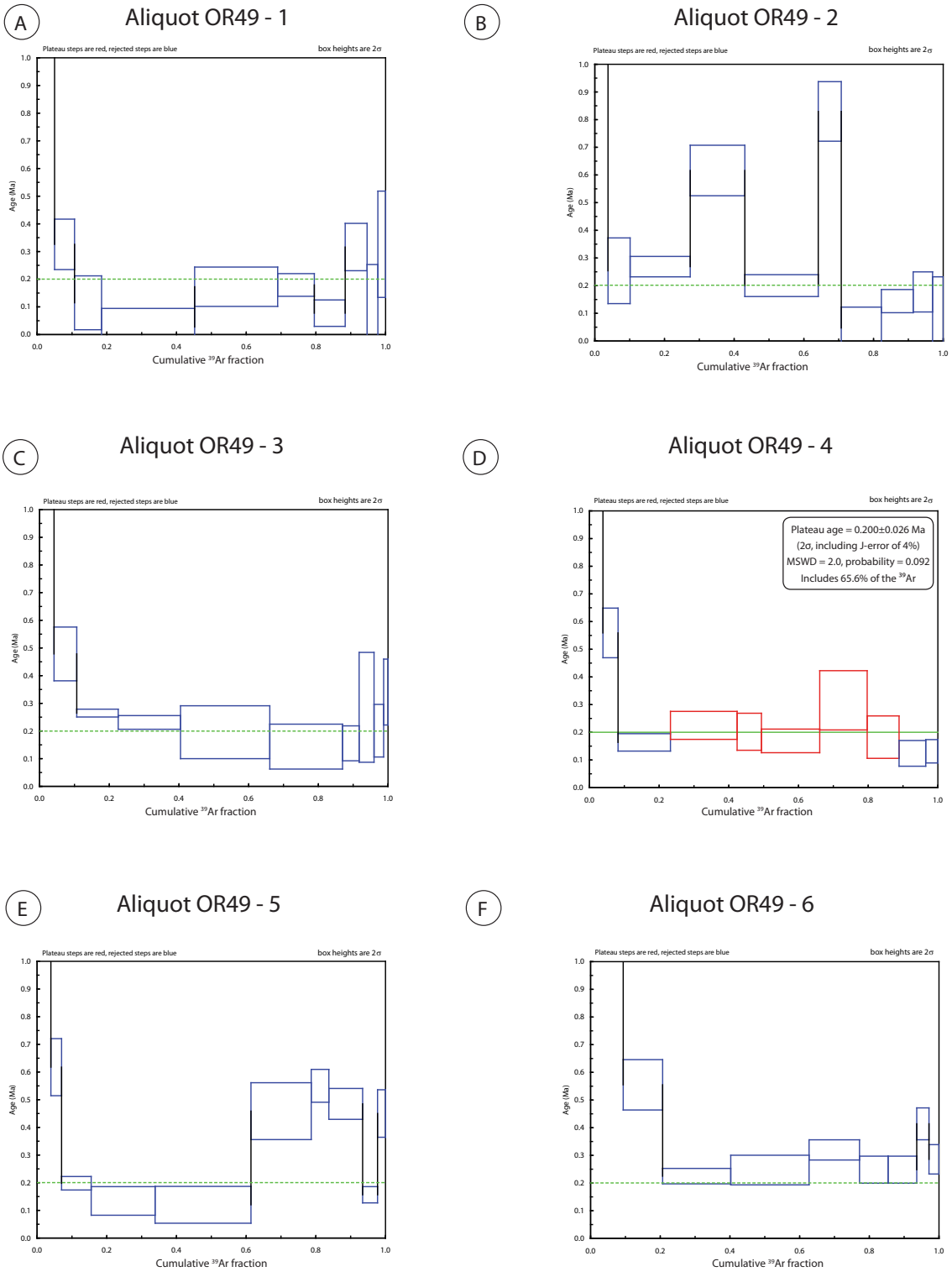

Fig. 5.19 a-f : OR49 age spectrum diagrams (a to f). Dashed green line represents calculated plateau age from OR49-4 (d) superimposed onto remaining aliquots.

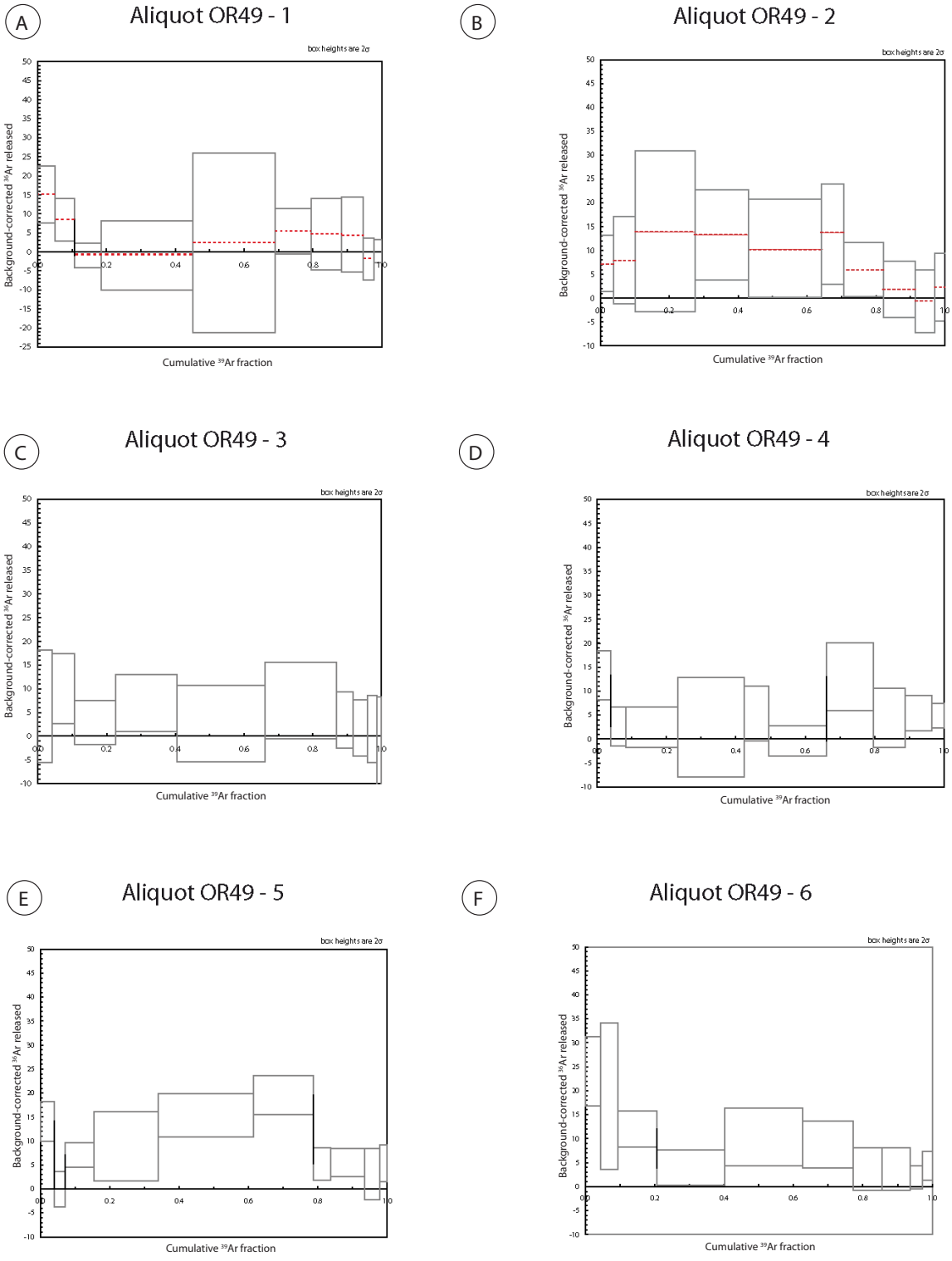

Fig. 5.20 a-f: OR49 ^{36}Ar released from each heating step for aliquots 1 to 6. The majority of boxes representing the amount of ^{36}Ar release ± error do not pass through the 'zero' line , indicating that all of the aliquots of OR49 contain excess ^{36}Ar. The graphs demonstrate that there is no relationship between the presence of excess ^{36}Ar and the amount of ^{39}Ar released in each step. (1 instrument division = 2.29 x 10^{-14} cm^3 STP)

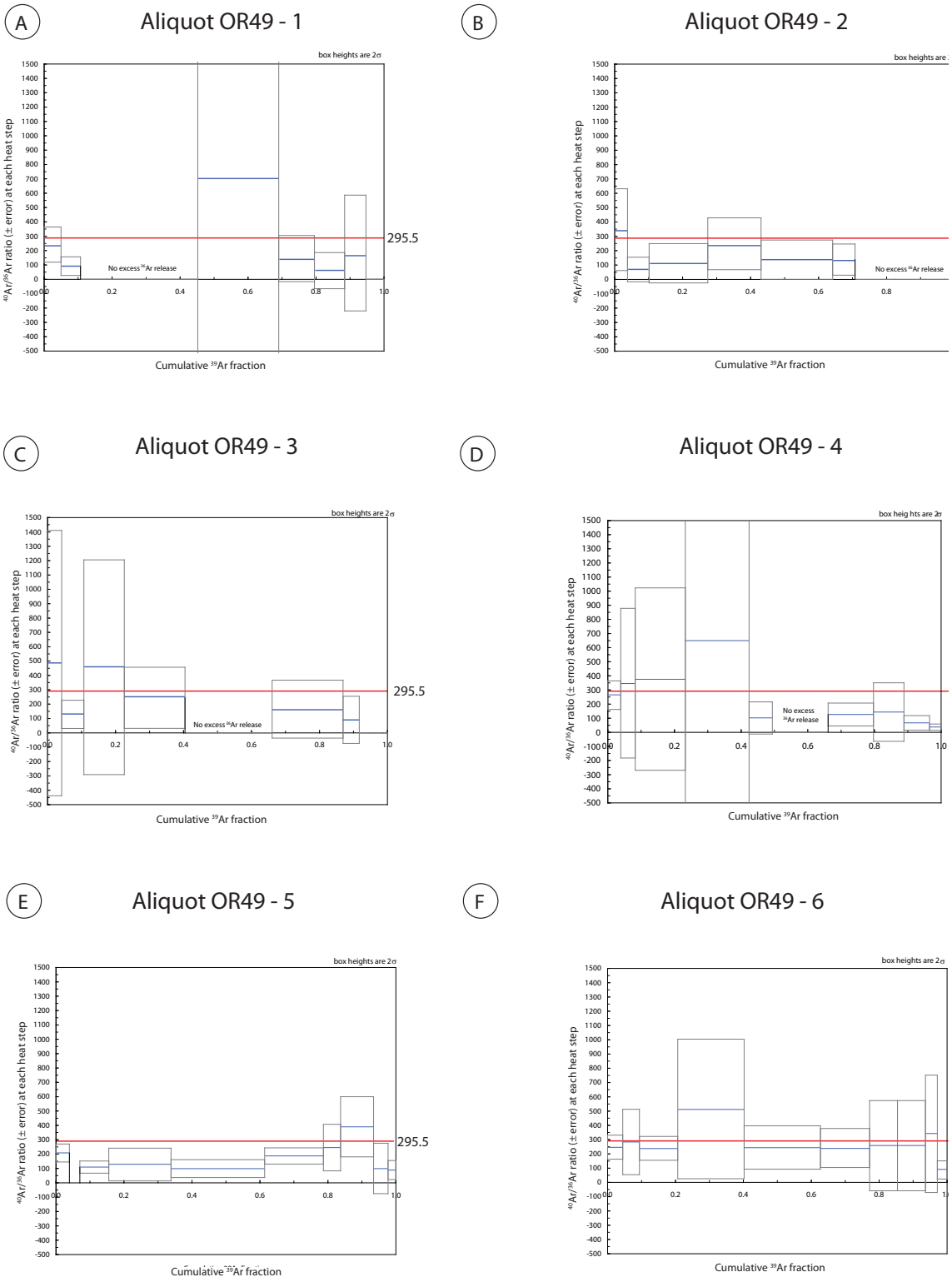

Fig. 5.21 a-f : OR49 $^{40}Ar/^{36}Ar$ ratios from each step containing excess ^{36}Ar. Heating steps that do not release excess Ar are omitted from the diagram (as indicated)

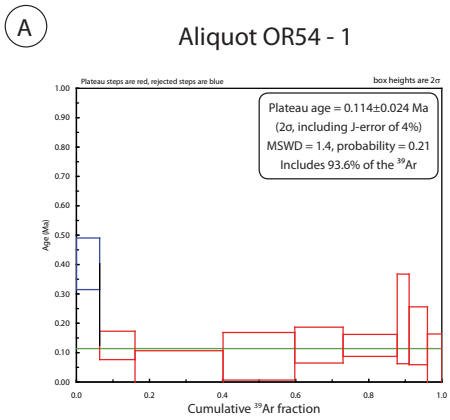

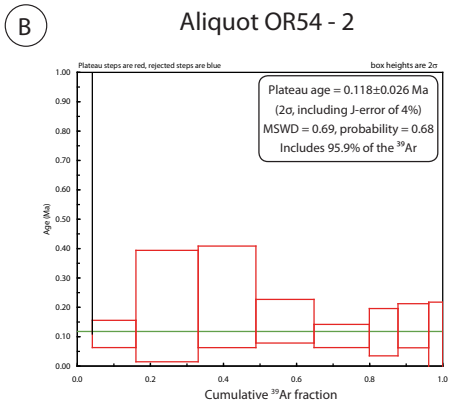

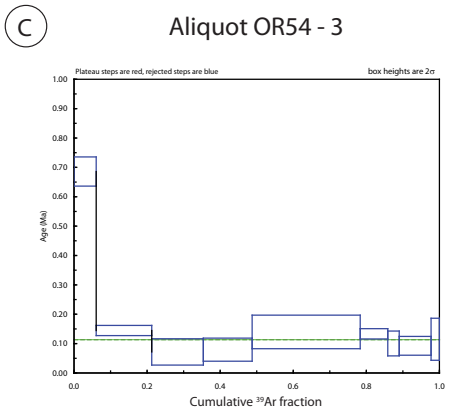

Fig. 5.22 a-c : OR54 age spectrum diagrams. Two aliquots OR54-1 (a) and OR54-2(b) produce plateau ages within error of one another, while the third OR54-3 (c) doesn't produce a plateau but is within the range of the plateau ages (age of 0.114 ± 0.02 Ma is indicated by green line)

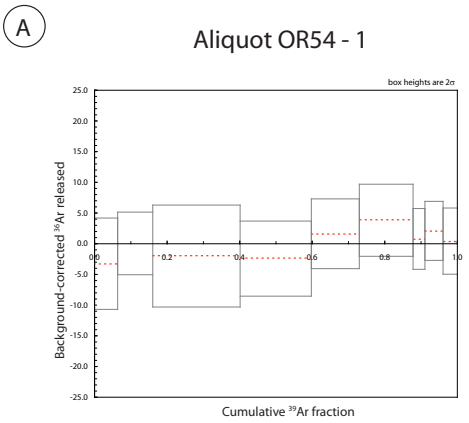

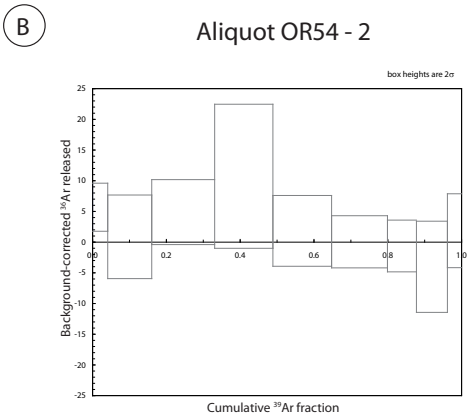

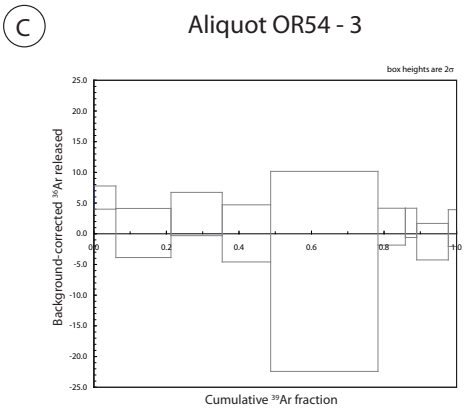

Fig. 5.23 a-c : OR54 ^{36}Ar release at each heating step. With the exception of the first heating step of aliquots 2 (b) and 3 (c), OR54 does not release excess ^{36}Ar.

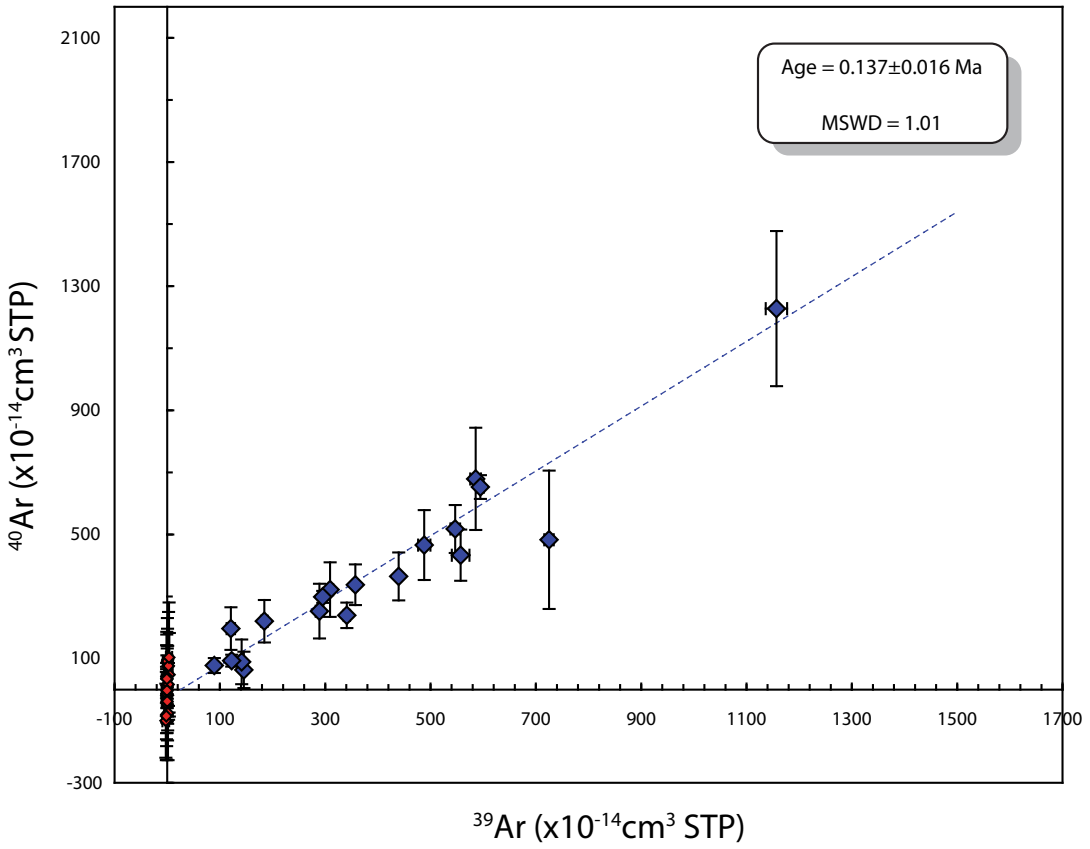

Fig. 5.24: Diagram of ^{39}Ar released at each heating step plotted against total ^{40}Ar release from all three aliquots of OR54 (blue diamonds). Red diamonds represent background-corrected blank data. Background blanks are run in between every heating step.

with plateau ages of 0.114 ± 0.02 Ma and 0.118 ± 0.03 Ma. The third aliquot produced a number of steps within the error of this age. None of the heating steps released a detectable amount of ^{36}Ar, therefore it is assumed that all of the gas released from this sample is of radiogenic origin.

A composite plot of total ^{40}Ar release against ^{39}Ar release was also constructed for OR54 (fig. 5.24), yielding an 'isochron' age of 0.137 ± 0.02 Ma which is within error of the plateau age of OR54-2.

The weighted average age of OR54-1 and OR54-2 gives an eruption age of 0.116±0.018 Ma.

Intermediate - trachydacite:

OR55 groundmass **(lithofacies N)** (fig. 5.25 a-e): This trachydacite sample (SiO2: 64 wt%) is relatively phenocryst-rich compared to the rhyolite samples. Care was taken during hand selection to ensure that any phenocrysts were removed from

A

Aliquot OR55 - 8

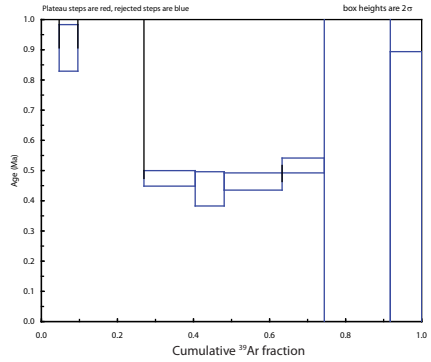

B

Aliquot OR55 - 9

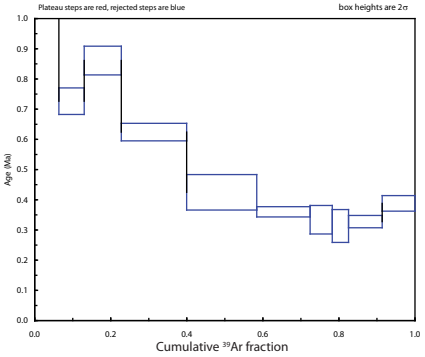

C

OR55-9: irradiated sample ^{36}Ar release

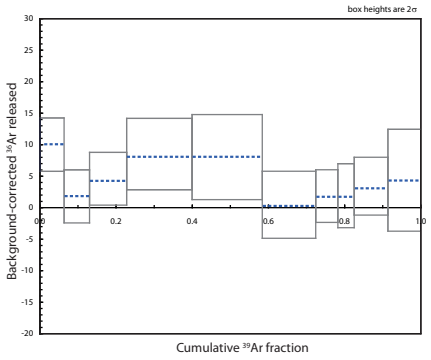

D

OR55: unirradiated sample ^{36}Ar release

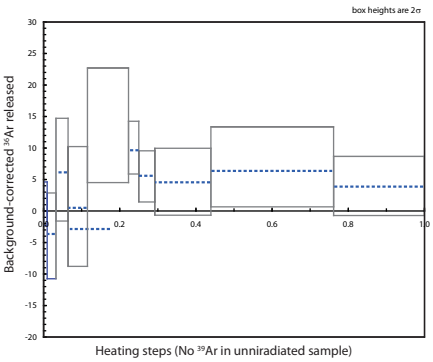

E OR55: unirradiated sample ^{40}Ar/^{36}Ar release

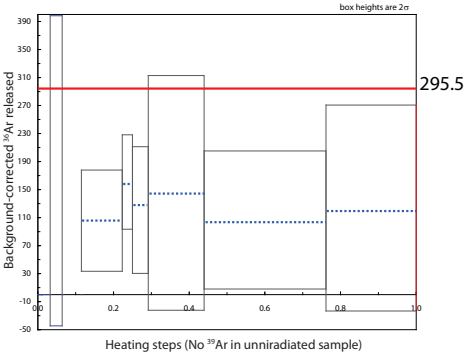

Fig. 5.25: OR55 Groundmass aliquots (a - e). Age spectrum diagrams (a - b) produced anomalously high ages and released excess ^{36}Ar (c). Unirradiated samples of OR55 also released excess ^{36}Ar (d) and yielded very low ^{40}Ar/^{36}Ar ratios.
OR55 feldspar separates (f - g) yielded anomalously high ages (f) and released excess ^{36}Ar (g).

F

OR55 Feldspars

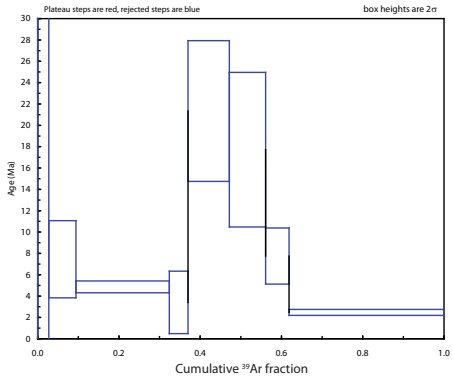

G

OR55 Feldspars ^{36}Ar release

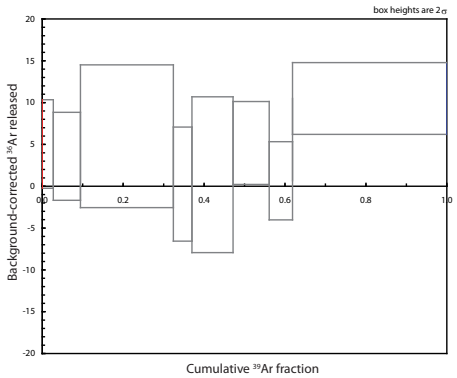

the groundmass prior to irradiation.

Two aliquots of OR55 were analysed over 10 heating steps each (fig.5.25 a - b). OR55-08 released higher amounts of ^{36}Ar, with the exception of heating steps 2 and 5 (fig.5.25 c), producing an age range between 0.5 to 1 Ma. OR55-09 (fig. 5.25b) produced a decreasing age spectrum with ages ranging from 1 to 0.35 Ma. ^{36}Ar release from OR55-09 was minor in the majority of heating steps and 50% of the steps had errors as large or larger than the amount released. In OR55-08 all but one of the steps produced gas with a $^{40}Ar/^{36}Ar$ ratio far less than the atmospheric value (ranging from 298- 82).

In an attempt to isolate the contamination source of ^{36}Ar in OR55 an unirradiated sample was analysed in order to check whether the excess ^{36}Ar was a by-product of irradiation (fig.5.25d). The unirradiated aliquot also displayed very low $^{40}Ar/^{36}Ar$ ratios in the steps that produced excess Ar. Possible causes for the observed low $^{40}Ar/^{36}Ar$ ratios will be discussed further in section 5.10.

OR55 feldspar separates (fig. 5.25 f-g) were also initially analysed, but these produced anomalously high ages. Probe data later revealed that the feldspar phenocrysts were predominantly plagioclase, however a number of heating steps released large quantities of ^{40}Ar with corresponding high $^{40}Ar/^{36}Ar$ ratios (>600), therefore it is likely that the sample contained an inherited ^{40}Ar source from older xenocryst feldspars incorporated into the lava. An upper age of 0.35 Ma is estimated for OR55.

Vatnafjall samples:

These samples were collected from Vatnafjall Ridge, another rhyolitic depositional centre within Öræfajökull, approximately 20km to the east of Goðafjall, by John Stevenson as part of a previous study on the evolution of a subglacial rhyolite ridge (Stevenson , 2005). Samples from the ridge have not yet been dated and analysis will help to constrain emplacement ages for a trachydacite flow (unit E) that caps the upper section of the ridge (Stevenson et al., 2005).

JS203 (fig. 5.26 – 5.27): Three aliquots were analysed with 6-7 heating steps in each analysis. Two of the aliquots, JS203-2 and JS203-3, produced age spectrum

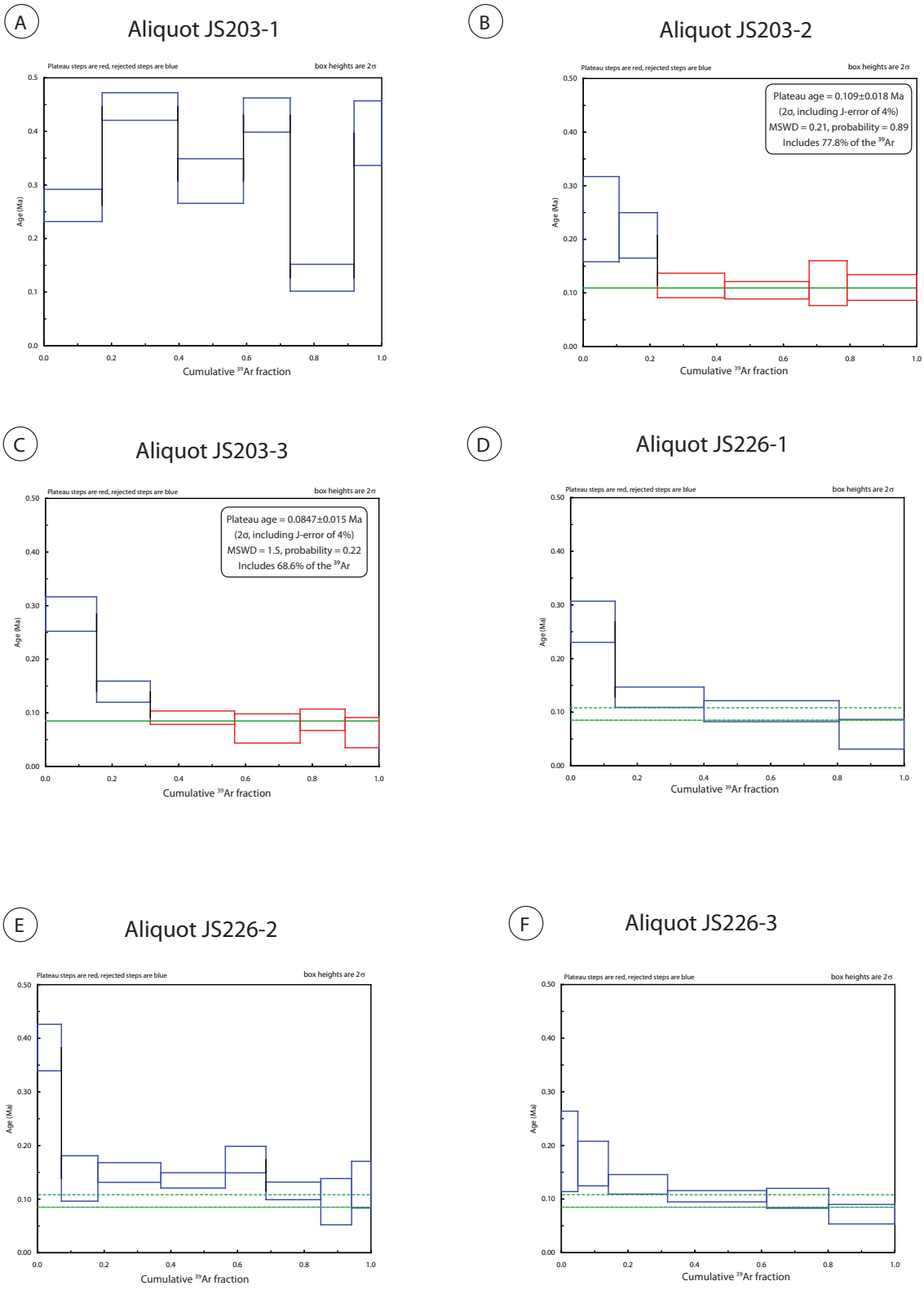

Fig. 5.26: Age spectrum diagrams for the Vatnafjall samples JS203 and JS226. Two aliquots, JS203-2 (b) and JS203-3 (c), produced plateau ages while the other remaing aliquots produced decreasing age spectra. Green dashed lines reperesent calculated ages from aliquots 203-2 and 3 and have been superimposed on the remaining spectra.

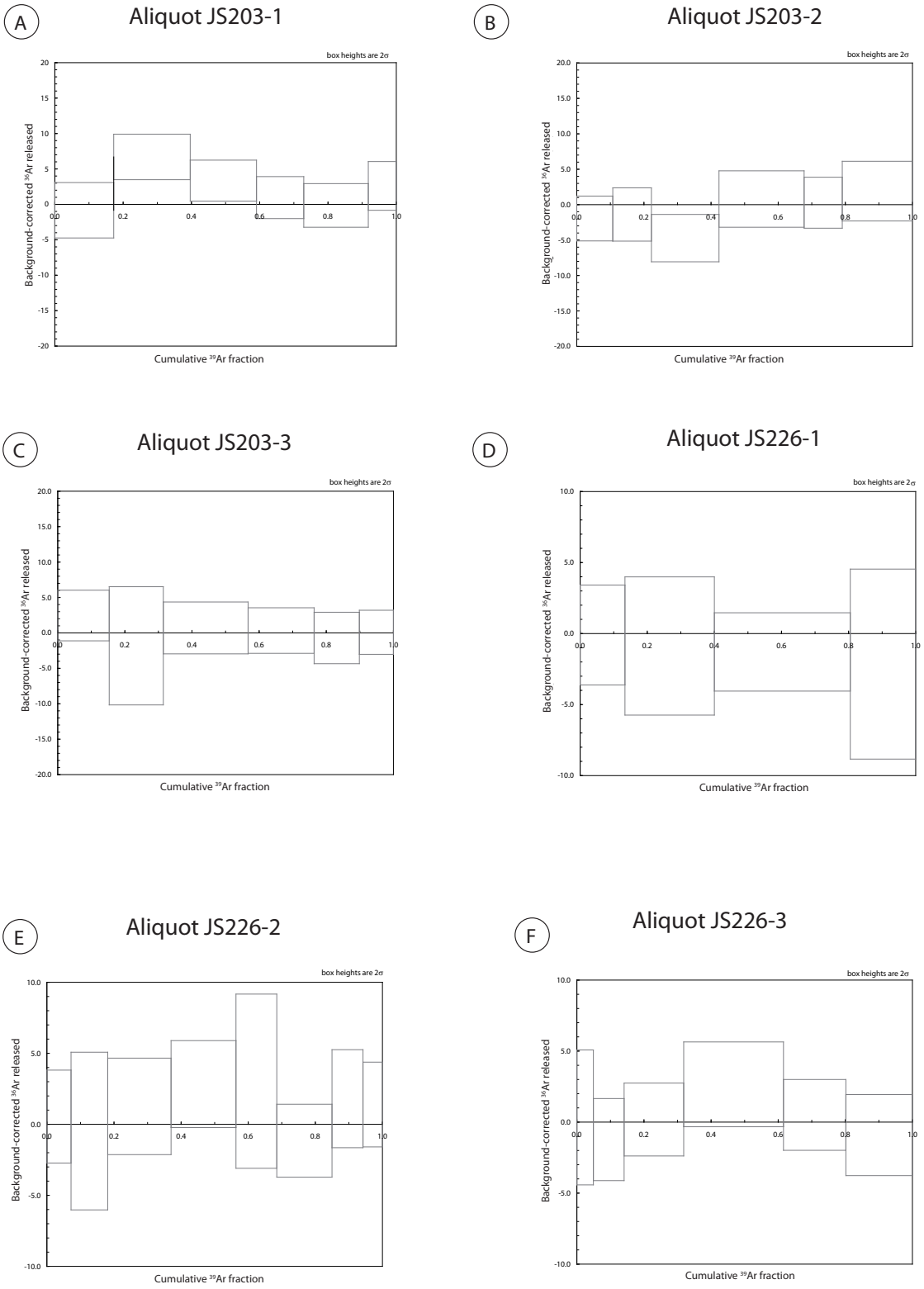

Fig. 5.27: Vatnafjall samples JS203 and JS226 ^{36}Ar release at each heating step. Only JS203-1(a) released a detectable amount of ^{36}Ar.

diagram plateaus yielding ages of 0.109± 0.02 Ma and 0.085± 0.02 Ma respectively. JS203-2 and JS203-3 did not release a detectable amount of ^{36}Ar, however JS203-1 (fig. 5.27a) released a small but detectable amount of ^{36}Ar on two heating steps and both steps produced $^{40}Ar/^{36}Ar$ ratio values slightly lower than 295.5. Based upon the weighted average age of the two plateau calculated ages, the estimated eruption age of JS203 is 0.095±0.01 Ma.

JS226 (fig. 5.26 – 5.27): Three aliquots were analysed with 4-8 heating steps in each analysis. All three produced decreasing age spectra with the higher temperature steps yielding ages within error of the age range produced by JS203. None of the heating steps released a detectable amount of ^{36}Ar, therefore it is assumed that all of the gas released from the sample is of radiogenic origin.

Based upon the weighted average age of JS203, the estimated eruption age of JS203 is 0.095±0.01 Ma.

5.10. Sources of isotopically fractionated $^{40}Ar/^{36}Ar$ ratios

Two samples in this study – OR49 and OR55 – produce isotopically fractionated $^{40}Ar/^{36}Ar$ ratios (<295.5) in the majority of heating steps.

Sub-atmospheric $^{40}Ar/^{36}Ar$ values produced by kinetic mass fractionation in lavas are not uncommon and have been reported by numerous authors (e.g., Kaneoka, 1980; Krummenacher, 1970; Matsumoto and Kobayashi, 1995; Ozawa et al., 2006). However, the values reported in this study are too low to be explained by a single stage of kinetic mass fractionation (fig. 5.28) which would produce a $^{40}Ar/^{36}Ar$ ratio of 280 from an unfractionated atmospheric argon source (Kaneoka, 1994), therefore alternative methods of preferential ^{36}Ar production or contamination have been investigated below.

Neucleogenically produced ^{36}Ar:

As previously discussed in section 5.2, sample irradiation can lead to the formation of reactor-produced Ar isotopes, including ^{36}Ar. The ^{37}Ar correction is applied in order to correct for nucleogenic production, however these samples were analysed over a time period longer than the half-life of ^{37}Ar therefore the correction could not be applied becuase the ^{37}Ar had decayed prior to measurement.

In order to determine whether the very low $^{40}Ar/^{36}Ar$ ratios seen in samples OR49 and OR55 are a naturally occurring phenomena, rather than as a result of nucleogenic ^{36}Ar produced from ^{40}Ca, unirradiated aliquots of both samples were analysed using the same experimental methods as the irradiated samples. The unirradiated samples were also analysed in order to examine whether the $^{38}Ar/^{36}Ar$ ratio values were equally fractionated. ^{38}Ar and ^{36}Ar are naturally occurring isotopes with an atmospheric ratio of 0.188. Similar $^{40}Ar/^{36}Ar$ ratios are seen in the unirradiated samples, ranging from 106±31 to 177±111 in OR55 (fig. 5.25e) and 29±16 in OR49 (fig. 5.20). However, it was not possible to calculate $^{38}Ar/^{36}Ar$ ratios on the unirradiated aliquots, as ^{38}Ar is the least abundant argon isotope and therefore difficult to measure with accuracy in sample sizes as small as 10mg. Only three heating steps were carried out in order to maximize ^{38}Ar release, but it was not possible to distin-

guish any ^{38}Ar release from the background level.

Mass 36 contamination:

Having confirmed that excess ^{36}Ar is not an artefact related to the irradiation, samples were further investigated to determine if they contain a contaminant at m/z 36. Potential contaminants include hydrocarbons derived from organic material adhered to the sample of HCl. In order to rule out any contamination, unirradiated aliquots of both samples were analysed with a quadrapole spectrometer to check for any contamination of the mass 36 peak.

Background level scans were performed prior to analysis in order to identify any peak anomalies present between masses 30 to 100 and also 30 to 42.

The samples were subject to three increasing heating steps at 1.3 W, 3.95 W and 7.6 W while the quadrapole scanned over the range of mass 30 to 100. Each heating step cycle was carried out for the same duration as a standard irradiated sample step of 10 minutes. The gas release was monitored throughout and screen grabs were taken at 1 minute, 4 minutes, 7 minutes and 10 minutes (fig. 5.29).

Initially the 36 mass peak (denoted by red triangle) is high, but as the gas is puri-

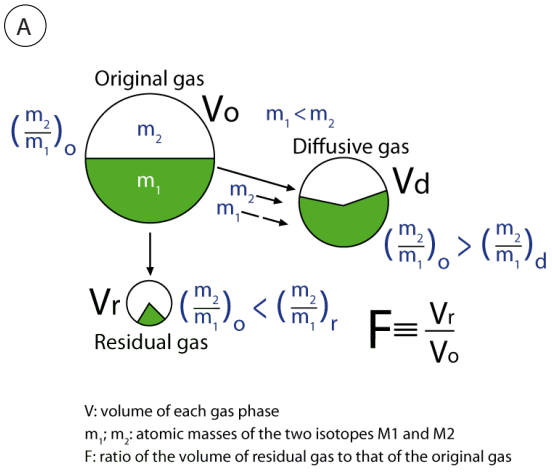

Fig. 5.28a. (After Kaneoka, 1994) Shematic model of kinetic mass fractionation of isotopes during gas transport. Original gas contains two isotopes M1 (^{36}Ar) and M2 (^{40}Ar). Part of gas is lost from original reservoir causing mass fractionation and diffusive gas is kept in another phase. Diffusive gas is enriched in lighter isotopes compared to original and residual gas.

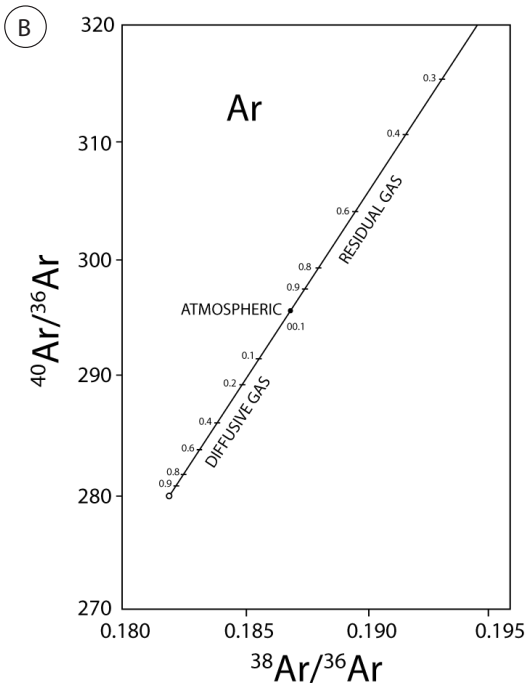

Fig. 5.28b. (After Kaneoka, 1994) Mass fractionation line of Argon during single mass fractionation process starting from Atmospheric Ar. Numerical figures on fractionation line refer to 'F' in figure 5.28a.

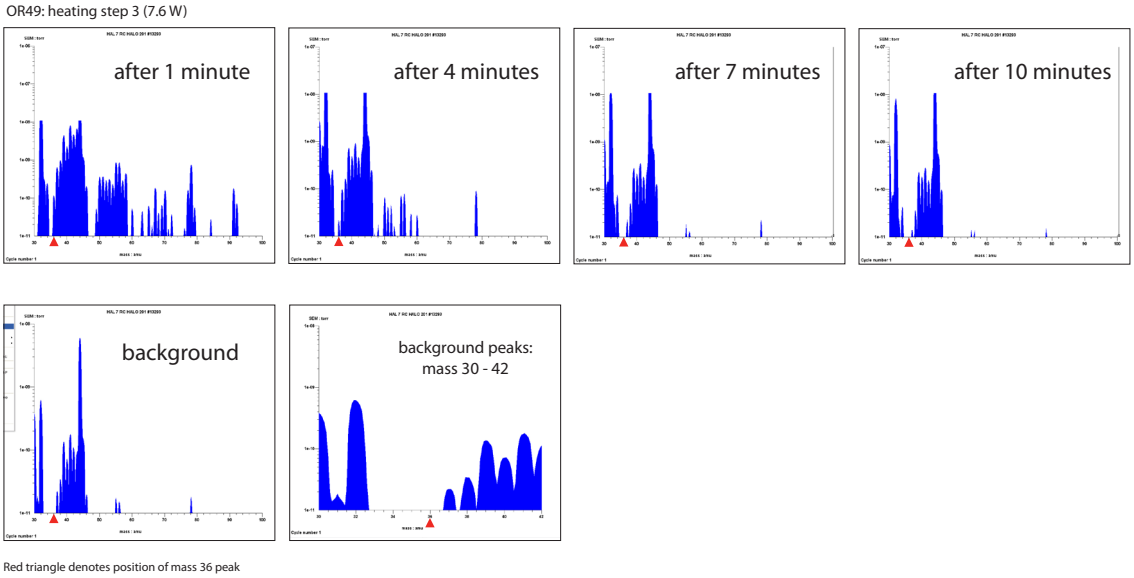

Fig. 5.29. Quadrapole analysis of gas release of unirradiated aliquot of sample OR49. Red triangle denotes position of 36 peak, after 10 minutes of gettering no anomalous peaks are observed.

fied by getters throughout the 10 minute process, the peaks decrease in height. After 10 minutes – the point where the gas would usually be released into MS1 for analysis – no 36 peak anomalies are observed.

The results above suggest that the observed fractionated $^{40}Ar/^{36}Ar$ ratios of trapped argon released from samples OR49 and OR55 are naturally occurring phenomena. Further investigation is required to suggest a process leading to the natural production of argon with a $^{40}Ar/^{36}Ar$ ratio lower than that of 295.5.

Both of the samples in this study are recognised in the field as 'subglacial' samples, however low $^{40}Ar/^{36}Ar$ ratios are also occasionally present in sample OR12 which has been identified as a subaerial sample (Fig. 5.19).

Other incidences of $^{40}Ar/^{36}Ar$ ratios as low as 153 ± 15 have also been reported in subaerial obsidians from Ethiopia (Morgan et al., 2009, Brown et al., 2009, Vogel et al., 2006). Brown et al. (2009) suggest Soret thermal diffusion as a possible mechanism for argon fractionation within an obsidian flow, by 'in-diffusion' of an already fractionated source of argon.

The Soret effect is thermal diffusion caused by a temperature gradient, where light isotopes are driven toward a hotter area and heavier isotopes toward a colder area.

Experiments carried out on argon fractionation and separation in thermal diffusion columns (Yamamoto et al., 1986, Yamamoto et al., 1987, Kobayashi et al., 1996)

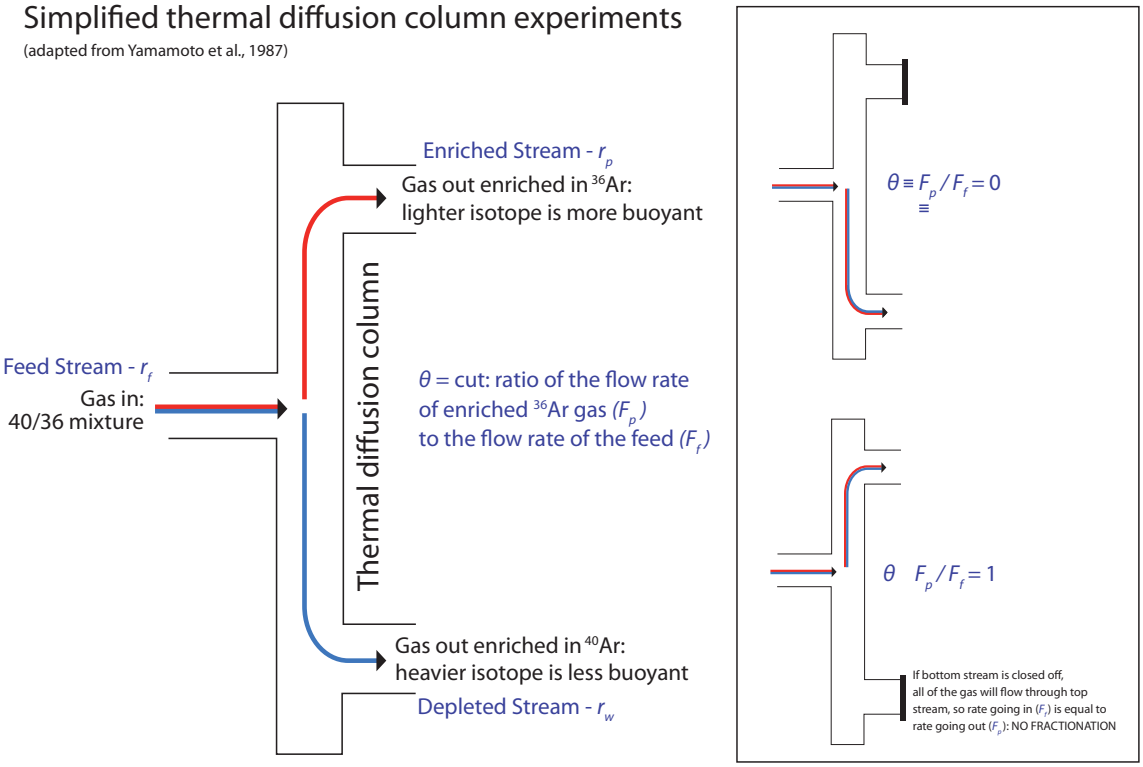

Fig. 5.30. After Yamamoto, 1987. Argon isotope diffusion column experiments.

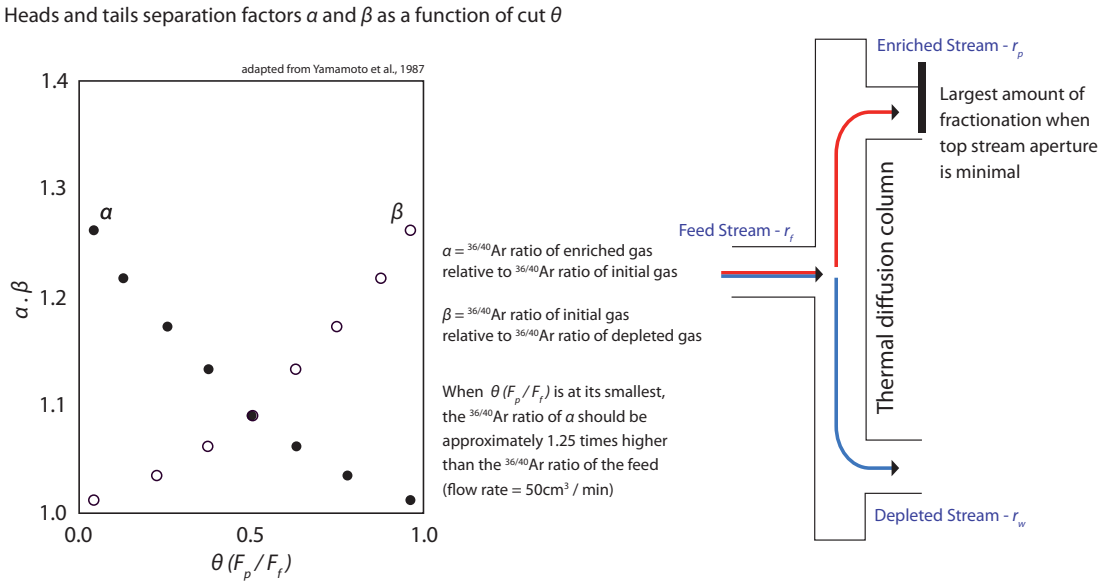

Fig. 5.31. After Yamamoto, 1987. Diffusion column experiments show that the largest amount of $^{40}Ar/^{36}Ar$ fractionation occurs when the feed flow rate is low and the 'cut' is at its smallest. Based on a feed stream with a $^{40}Ar/^{36}Ar$ ratio of 295.5, the $^{40}Ar/^{36}Ar$ ratio of $R_p = 236.4$

(figs. 5.30 and 5.31) show that at a constant temperature, $^{40}Ar/^{36}Ar$ fractionation is dependent upon two factors: the gas flow rate through the 'feed' into the diffusion column and the 'cut' control. The cut represents the ratio of the flow rate of the gas enriched in ^{36}Ar that has risen to the top of the diffusion column, to the flow rate of the initial gas through the feed (fig. 5.30). Fractionation is also influenced by flow feed rate as Yamamoto (1987) shows that fractionation decreases as flow rate increases.

The largest amount of $^{40}Ar/^{36}Ar$ fractionation (enrichment of ^{36}Ar), at a fixed temperature, occurs with a low feed flow rate when the cut is at its smallest (fig. 5.31). Calculations show that at a temperature of 650° C, an initial gas feed stream with $^{40}Ar/^{36}Ar$ ratio of 295.5, would fractionate to an enriched $^{40}Ar/^{36}Ar$ ratio (Rp) of 236.4 when the cut is at its smallest value.

It may be possible to apply the principle of thermal diffusion to an obsidian lava flow. As an obsidian flow cools and contracts, propagating cooling cracks develop into columnar joints. As the crack propagates through the cooling lava, the two parallel joint walls will be hotter than the void between the columns, which is being filled with air as the crack propagates (fig.5.32). A temperature gradient will develop along the width of the crack and as air circulates, the lighter isotopes (^{36}Ar) will preferentially move toward the hotter column walls while the heavier isotopes (^{40}Ar) will stay in the cooler, central void. The circulation of air throughout the crack is in constant flux resulting in the loss of both ^{40}Ar and ^{36}Ar, but some amount of ^{36}Ar diffuses into and is retained within the hot joint surface, thereby leading to the 'in-diffusion' of trapped argon with a lower $^{40}Ar/^{36}Ar$ ratio than that of the atmosphere.

Columnar joint formation and crack propagation in a cooling lava flow is a much more dynamic environment than that of a highly controlled thermal gradient column, and the flow rate of air around a propagating crack, and the temperature gradient within it, would be more difficult to estimate. Brown et al. (2009) suggests the implementation of the 'Grashof Number' to estimate the temperature gradient within a propagating crack. The Grashof Number is a dimensionless number which approximates the ratio of the temperature-induced convective buoyant forces to the viscous forces in a fluid (Kettleborough, 1972). The larger the number, the greater

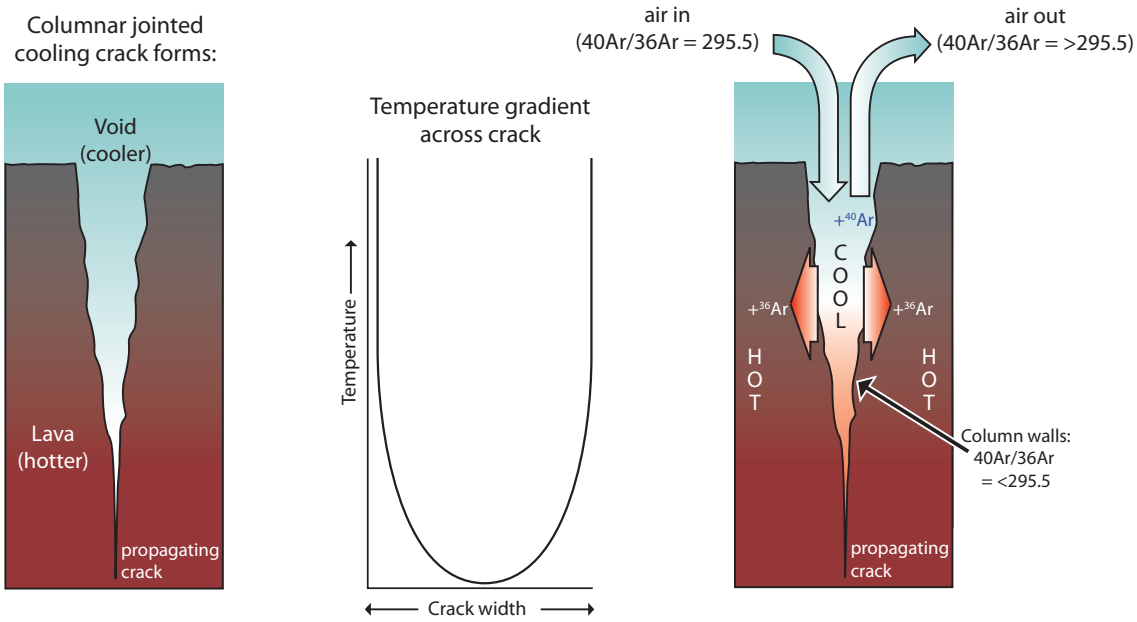

Fig. 5.32. Possible scenario for argon fractionation based on Soret diffusion. As an obsidian flow cools and contracts, propagating cooling cracks develop. As the crack propagates through the cooling lava, the two parallel joint walls will be hotter than the void between the columns, which is being filled with air. A temperature gradient will develop along the width of the crack and as air circulates, the lighter isotopes (^{36}Ar) will preferentially move toward the hotter crack walls while the heavier isotopes (^{40}Ar) will stay in the cooler, central void. The circulation of air throughout the crack is in constant flux resulting in the loss of both ^{40}Ar and ^{36}Ar, but some amount of ^{36}Ar diffuses into and is retained within the hot crack surface, thereby leading to the 'in-diffusion' of trapped argon with a lower $^{40}Ar/^{36}Ar$ ratio than that of the atmosphere. The process may be repeated many times as the lava cools.

the temperature gradient, therefore if the gas within the crack is heated up quickly it becomes more buoyant and is drawn out of the crack more quickly. However, based upon the calculations in Yamamoto's (1987) experiments, one episode of crack propagation and diffusion would not be sufficient to achieve $^{40}Ar/^{36}Ar$ ratios as low as those seen in samples OR49 and OR55. A multi-step process would be required.

One possible method to further lower the $^{40}Ar/^{36}Ar$ ratio may the process of repeated fracturing and healing (RFH) (Tuffen et al., 2003). The RFH process has been cited as a possible mechanism for non-explosive magma degassing in rhyolite melts, leading to the formation of degassed, non-vesicular obsidian (Cabrera et al., 2011, Gonnermann and Manga, 2003). The RFH process occurs prior to eruption at shallow depths within the volcano conduit, with fracture faulting and healing occurring over relatively short timescales (minutes). Cabrera et al., 2011 showed that the fractures provide a low pressure permeable pathway for H_2O that has diffused from the glass and that the fault trace itself is sensitive to post-healing diffusion. It is therefore possible that if the fractures provide a mechanism for volatile diffusion

then the same mechanism may apply to argon diffusion. Single stage kinetic fractionation in this case may occur each time a crack is fractured and healed, thereby creating a process where the single process is repeated over multiple stages, lowering the $^{40}Ar/^{36}Ar$ ratio successively each time.

The above suggestions serve only as a discussion of the possible mechanisms for achieving lower than atmospheric ratios within trapped argon. Further investigation of the low $^{40}Ar/^{36}Ar$ ratios within these samples needs to be undertaken.

Argon isotope fractionation has also been observed in gas trapped within pumices from plinian eruptions (Ruzié and Moreira, 2010). $^{38}Ar/^{36}Ar$ ratios as low as 0.182 have been attributed to kinetic magma degassing prior to fragmentation. The corresponding $^{40}Ar/^{36}Ar$ ratios display unfractionated atmospheric values, but any mass fractionation of $^{40}Ar/^{36}Ar$ may be obscured by the presence of radiogenic ^{40}Ar.

5.11. Summary

$^{40}Ar/^{39}Ar$ analysis of the Oraefajokull rocks produced a range of eruption ages from 0.08 Ma to over 3.02 Ma for the basement basalt complex.

The most reliable ages are produced by samples that release either very small or zero amounts of ^{36}Ar. For the Group One rhyolites, OR12 yielded the most reliable eruption age of 0.2±0.02 Ma, while OR293 produced a much lower age of 0.1± 0.02 Ma. As OR293 is a lithofacies D sample (fig. 3.17), field and geochemical evidence suggest that this age is anomalously low for a Group One sample, therefore the eruption age produced by OR12 will be used as the definitive age for this unit.

The Group Two rhyolites yielded two reliable and reproducible results two samples: OR44 with an age of 0.15±0.02 Ma and OR54 with an age of 0.116±0.02 Ma. OR44 released ^{36}Ar in the initial two to three heat steps producing a decreasing age spectrum, whereas OR54 only released ^{36}Ar in the initial heat step, therefore 0.116±0.02 Ma will be used as the definitive age for the Goup Two rhyolites.

Reproducible ages were also produced by the two Vatnajall samples JS203 and J226 which both yielded an eruption age of 0.095±0.01 Ma.

A summary of the rhyolite groups and ages is located in table 5.6.

A high proportion of the samples presented in this study released variable lev-

Sample	Geochemical group	description	no. of aliquots	excess ^{36}Ar	$^{40}Ar/^{36}Ar$ range	$^{40}Ar/^{39}Age$ (Ma)
0R06	n/a	basalt	3	Y	n/a	3.024 ± 0.5
OR12	One	aphyric rhyolite	8	2 aliquots only	140-386	0.204 ± 0.23
OR39	One	aphyric rhyolite	4	Y	-	no age
OR150	One	obsidian	1	Y	228-485	no age
OR202	One	obsidian	1	Y	255-336	no age
OR221	One	rhyolite	1	Y	241-326	no age
OR255	One	rhyolite	2	N	-	no age
OR280	One	obsidian	3	Y	229-327	no age
OR293	One	obsidian	3	N	-	0.108 ± 0.02
OR10	Two	obsidian	3	Y	261-453	no age
OR44	Two	obsidian	7	initial steps only	210	0.156 ± 0.02
OR49	Two	obsidian	6	Y	69-656	0.200 ± 0.03
OR54	Two	obsidian	6	N	-	0.116 ± 0.02
OR55	n/a	porphyritic trachydacite	3	Y	151-297	no age
OR55	n/a	feldspar separates	3	Y	195->1000 but errors are large	no age
JS203	Vatnafjall	obsidian	3	N	-	0.095 ± 0.01
JS226	Vatnafjall	obsidian	3	N	-	0.095 ± 0.01

Table 5.6. Summary of sample ages

els of excess ^{36}Ar. ^{36}Ar release was greater from the Group One rhyolites, where amounts reached 1.02 x $10^{-12}cm^3$ STP (OR221-1) with the majority of $^{40}Ar/^{36}Ar$ ratios around atmospheric values (295.5), which implies that only small amounts of $^{40}Ar^*$ were released from Group One rhyolites. In most cases, this dominant atmospheric signature led to the production of large errors on calculated ages or completely prohibited age calculation.

Group Two rhyolites generally released lower amounts of ^{36}Ar, with three samples producing zero. Samples from this group have yielded the most reproducible results and provided more consistent age spectrums. However, samples in this group also display sub-atmospheric $^{40}Ar/^{36}Ar$ ratio values that cannot be explained by kinetic mass fraction alone. One possible suggestion for this phenomenon may be the repeated fracturing and healing process reported in obsidians, however this requires further investigation beyond the realms of this study.

Further discussion of the apparent ages presented in this chapter will be presented within a wider palaeoclimatic context in the following chapter 6 in conjuction with the detailed field observations presented in chapter 4. A palaeoclimatic history of Öræfajökull region throughout the mid to late Pleistocene will be also be proposed.

Chapter 6
Palaeoclimatic variability during the volcanic evolution of Öræfajökull

6.1. Introduction

The topographic relief of Iceland owes as much to glacial activity as it does to volcanism. Due to a combination of competing glacial and volcanic processes, Iceland features some of the best preserved records of Pliocene and Pleistocene terrestrial glacial cycles in the northern hemisphere, recording over 20 glaciations over the last 5 million years (Geirsdottir et al., 2007).

Subaerial lava flows erupted during warmer interglacial periods protect the interbedded glacial sediments that would otherwise have poor preservation potential while subglacially erupted palagonatised hyaloclastites are very resistant to erosion making them excellent indicators of palaeoclimatic conditions.

Successive episodes of glacial erosion remove evidence of previous glacial cycles, therefore terrestrial evidence of glaciations are best preserved in areas where constructional regimes outweigh erosional regimes. A good example of this can be found in the Vestfirdi peninsula, north west Iceland, which is an area dominated by glacially carved U-shaped valleys but where no Pliocene or Pleistocene glacial deposits have been recorded. No constructional volcanic activity has occurred in this area of the north west for 6 My and consequently the dominant erosive regime has stripped away all evidence of individual glacial cycles (Geirsdottir et al., 2007).

The dating of interglacial lava flows can provide age constraints for the intercalated glacial horizons (Eiriksson, 1985; Helgasson and Duncan, 2001). In addition, characteristic subglacial and intraglacial landforms such as tuyas and tindars can provide information about ice-sheet thicknesses during the time of eruption and K/Ar and /or $^{40}Ar/^{39}Ar$ dating methods and field observations have been successfully

System	Series	Stage	Age (ka)	MIS boundary	LR04 Age (ka)
QUATERNARY	Holocene		0 - 11.7		
	Pleistocene	Late	11.7 to 126	1/2	14
				2/3	29
				3/4	57
				4/5	71
				5.1(peak)	82
				5.2(peak)	87
				5.3(peak)	96
				5.4(peak)	109
				5.5(peak)	123
		Mid	126 to 781	5/6	130
				6/7	191
				7/8	243
				8/9	300
				9/10	337
				10/11	374
				11/12	424
				12/13	478
				13/14	533
				14/15	563
				15/16	621
				16/17	676
				17/18	712
				18/19	761
		Early	781 to 2.58 Ma	19/20	790

Fig. 6.1. A timeline of the Quaternary and boundaries of the marine interval stages based upon Lisieki and Raymo's LR04 benthic stack. (LR04 Data provided by Lisiecki : http://lorraine-lisiecki.com/LR04_MISboundaries.txt).

combined to calculate minimum ice-sheet thicknesses during particular glacial intervals throughout Iceland (McGarvie et al., 2006, MaGarvie et al.2007, Guillou et al., 2009, Flude et al., 2010) providing insight into the timings of glacial advances and retreats throughout the mid to late Pleistocene.

This approach has been adopted to propose a timeline for the evolution of Öræfajökull volcano and to discuss the regional palaeoclimatic variability during its evolution by combining the $^{40}Ar/^{39}Ar$ ages of subglacially and subaerially emplaced

lavas from the Goðafjall / Hrútsfjall and Vatnafjall areas with detailed field observations, the findings of which are presented in this chapter.

6.2. The glacial history of south east Iceland

Data from marine ice cores indicate that the northern hemisphere began to move steadily towards a cooler climate between 10 to 5 Ma with full-scale glaciations commencing during the mid-Pliocene from around 3.6 Ma (Lisiecki and Raymo, 2005, Geirsdóttir et al., 2007, Sarnthein et al., 2009, Ravelo, 2010) (fig. 6.1).

The oldest glacial deposits recorded in Iceland are located at Skaftafell in the south east of Iceland and have been dated at 4.6 – 4.7 Ma (Helgason and Duncan, 2001). The deposits have a limited extent and are believed to be due to small-scale localised glaciations. Further evidence of similar small-scale glaciations, dated between 3 and 4 Ma, is located in Fljótsdalur, in east Iceland (Geirsdottir and Eiriksson, 1996) which suggests that glaciation initiated in the south east to eastern regions before radiating outward in a northerly and westerly direction.

A change in regional glacial intensity took place around 2.75 Ma (MIS G6) with the onset of full terrestrial glaciation by MIS G4. This is corroborated by marine palaeoclimatic processes which show a large increase in ice rafted debris found in northern hemisphere drilling cores at MIS G4 to 6 (Kleiven et al., 2002, Ravelo, 2010) (Fig. 6.2).

The oldest evidence of subglacial volcanism is a basaltic hyaloclastite ridge in south east Iceland that has been dated at 2.8 Ma (Helgason and Duncan, 2001), which correlates with the onset of intensified glaciation across the northern hemisphere (fig. 6.3).

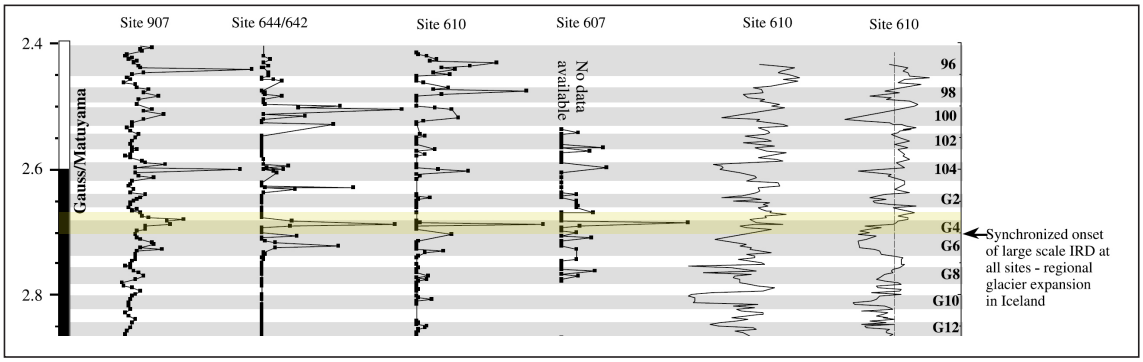

Fig. 6.2. After Kleiven et al., 2002: Ice rafted debris present in a number of cores show a peak at around 2.75 Ma.

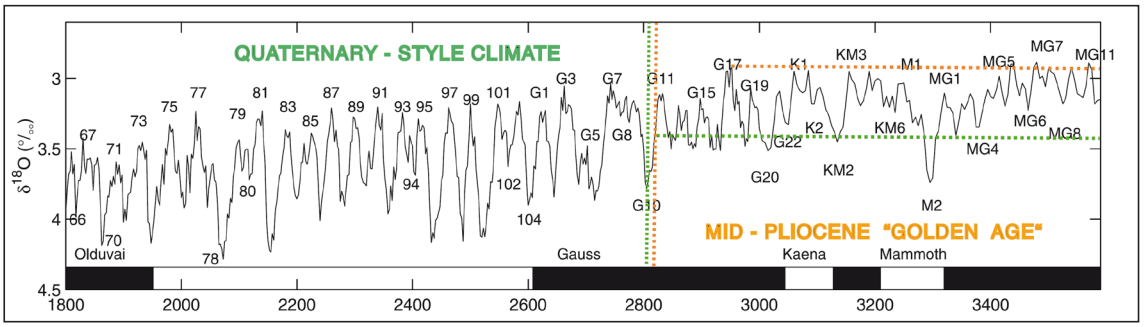

Fig. 6.3. After Sarnthein et al 2009: Transition from the mid-Pliocene "Golden Age" (2.9–3.4‰) to Quaternary-style climates near 3.0–2.8 Ma (based upon LR04 benthic stack (Lisiecki and Raymo, 2005)).

Helgason and Duncan (2001) proposed that the increase in topographic relief in the south east during this period led to the channelling of ice and the initiation of glacially carved valleys (fig. 6.4) triggering ice sheet expansion from the south east to the rest of Iceland some time between 2.7 to 2 Ma with the oldest recorded glacial deposits in the north and west of Iceland dated to 2.5 Ma (Geirsdottir and Eiriksson, 1996).

A build up in local topographic relief at Skaftafell to around an elevation of 600 m from 2.8 to 0.8 Ma is attributed to an increase in subglacial volcanism aided by a lack of subsidence due to the area's location away from the influence of the active spreading ridge.

A further increase in glacial intensity in the northern hemisphere occurred around 1 – 0.8 Ma and is recognised in both marine and terrestrial records (Helgason & Duncan, 2001; Lisiecki & Raymo, 2005; Geirsdottir and Eiriksson, 1996).

Topographic relief in the south east again increased dramatically from 0.8 Ma to the present day as glacial intensity coupled with in an increase in subglacial

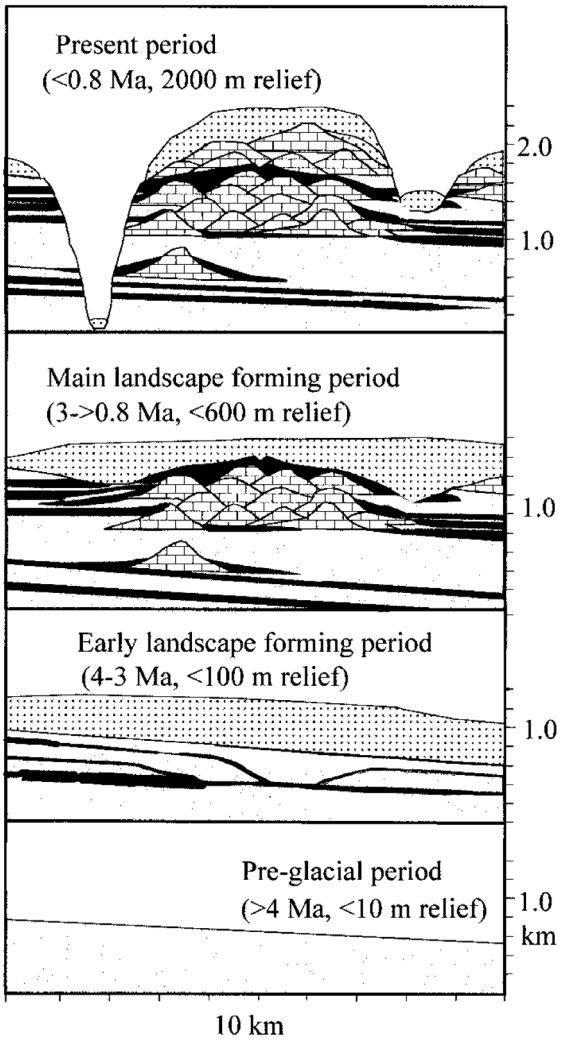

Fig. 6.4. After Helgasson and Duncan, 2001: Development of topographic relief in Skaftafell area of south east Iceland.

volcanism at Öræfajökull built up an edifice over 2000 m in height. This increase in overall elevation enabled a permanent ice sheet to be established in the area throughout the mid to late Pleistocene (Helgason & Duncan, 2001).

During the Weichselian (MIS 4-2) Iceland was fully glaciated with an ice sheet extending beyond the current coastline by a distance between 50 – 120 km off the shelf edge (Hubbard et al., 2007).

After the last glacial maximum (21 - 18 ka), deglaciation initiated in the north west of Iceland and advanced toward the south east at around 15 ka in a step-wise manner (Geirsdottir and Eiriksson, 1996; Ingólfsson et al, 1997, 2010). There is evidence to suggest that an extended ice cap remained in the south east well into the Holocene even though the rest of Iceland was relatively ice-free. During the glacial re-advance of the Younger Dryas (12.7 -11.5 ka) coastal areas to the north of Höfn in south east Iceland were ice-free but south of Höfn the ice sheet extended well beyond the coast out on to the shelf (fig. 6.5) (Norddahl and Einarsson, 2001,

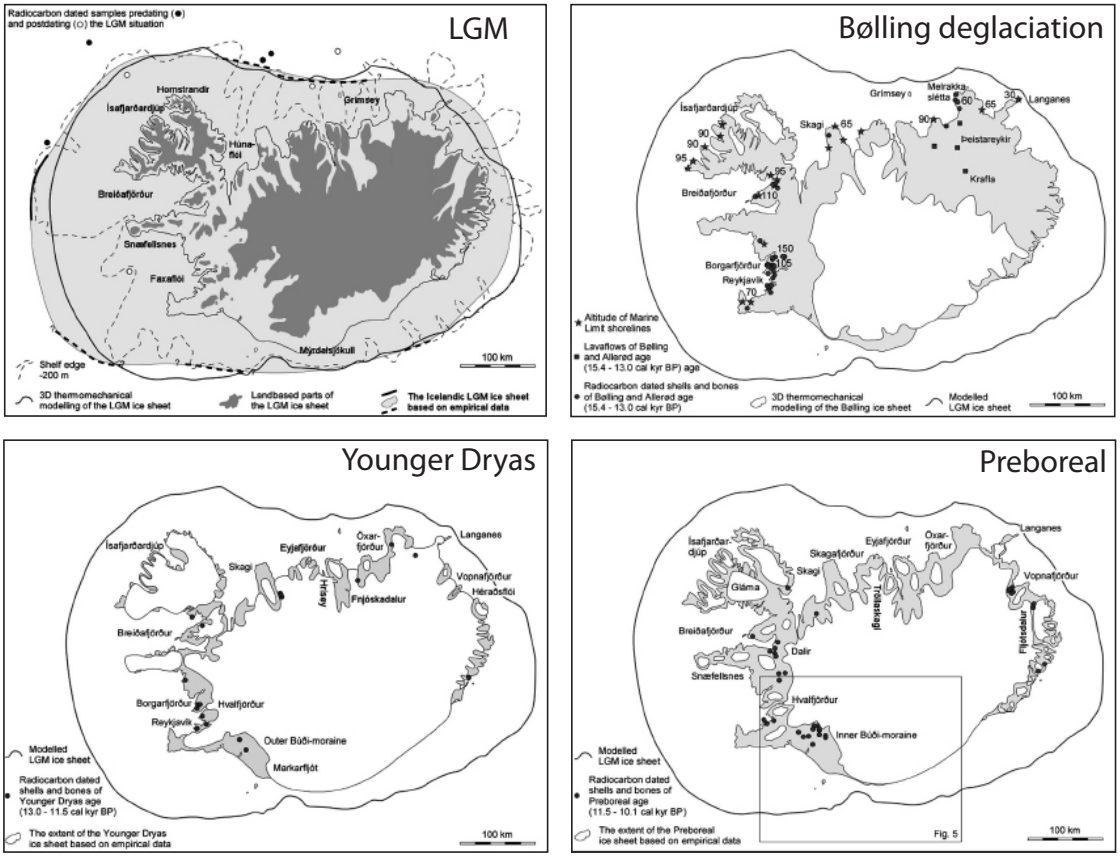

Fig. 6.5. After Ingolfsson et al, 2010: Advance and retreat of the ice sheet from the LGM to the early Holocene. Data suggests that the ice cap extended down to the south east coast even during the Bølling deglaciation.

Fig. 6.6. Satellite image of Iceland, acquired by the Moderate Resolution Imaging Spectroradiometer (MODIS) on NASA's Terra satellite on January 28, 2004. The island is almost completely covered in snow and ice, obscuring the permanent glaciers and icecaps that exist year-round. Credit: Jeff Schmaltz, MODIS Rapid Response Team, NASA/GSFC (Source: http://veimages.gsfc.nasa.gov/6605/Iceland.A2004028.1355.250m.jpg).

Ingólfsson et al, 2010).

A further glacial advance took place during the early Preboreal (11.5 – 10.1 ka) (Geirsdottir et al., 2000) but by 8 ka glacial cover across Iceland had retreated to present day levels (Ingólfsson et al., 1997, 2010). There is evidence to support a permanent ice cap at Vatnajokull throughout the Holocene and also evidence that the south eastern and southern coastal outlet glaciers were still present around the time of the Holocene Thermal Maximum (Rose et al., 1997; Kirkbride etal, 2006).

During the present warm interglacial climate, approximately 11% of Iceland is covered by glacial ice (Einarsson and Albertsson, 1988) with the largest glacier, Vatnajökull, covering an area of 8300 km^2 in the south east. Alpine-style valley glaciers are present along the south to south eastern margin of Vatnajökull from the Skaftafell region to Hornafjorður in the east. During the winter months the entire island can be covered in snow and ice (fig. 6.6).

As the recent subglacial eruptions of Grimsvötn (2011) and Eyjafjallajökull

(2010) demonstrate, subglacial and intraglacial eruptions can and do occur during interglacial periods. At least 50 % of historical eruptions have occurred under glaciers (Larsen et al., 2002) therefore subglacially produced prehistoric volcanic landforms may produce $^{40}Ar/^{39}Ar$ ages that correspond to both glacial and interglacial periods and this must be taken into account when trying to reconstruct eruptive palaeoenvironments.

6.3. The evolution of Goðafjall and Hrútsfjall, Öræfajökull

As discussed in section 6.2, in the neighbouring region of Skaftafell glacial processes outweighed volcanic processes during the mid to late Pleistocene (<0.8 Ma), leading to the formation of topographic relief with over 1200 m difference in height from valley floor to ridge summit (Helgason & Duncan 2001). In contrast, the main bulk of the volcanic edifice of Öræfajökull (2010 m) was constructed throughout the mid to late Pleistocene and the majority of its exposed south-facing flanks comprise mafic subglacial hyaloclastites overlain by younger subaerial lava flows (Prestvik, 1985) (fig. 6.7).

The timing of these constructive subglacial eruptions are poorly constrained as no attempt has been made to determine the age of the units due to difficulties arising with the dating of young (< 1 Ma), low-K basalts via the K-Ar and $^{40}Ar/^{39}Ar$ methods, although all the units are normally magnetised and therefore younger than 780 ka.

A small number of silicic outcrops are situated along the southern flanks of the edifice and their higher K content makes them more suitable for $^{40}Ar/^{39}Ar$ dating.

Two dominant silicic units from Goðafjall and Hrútsfjall have been dated as part of this study. By combining field observations of characteristic subglacial and subaerial landforms with $^{40}Ar/^{39}Ar$ ages of the silicic units, an evolutionary timeline and palaeoclimatic variability of the Goðafjall and Hrútsfjall area of Öræfajökull is proposed.

A further silicic sample from the nearby Vatnafjall ridge (fig. 6.7) has also been dated. The ridge was initially mapped by Stevenson et al. (2006) and the date of the unit will be discussed within the context of Stevenson's et al. interpretation in sec-

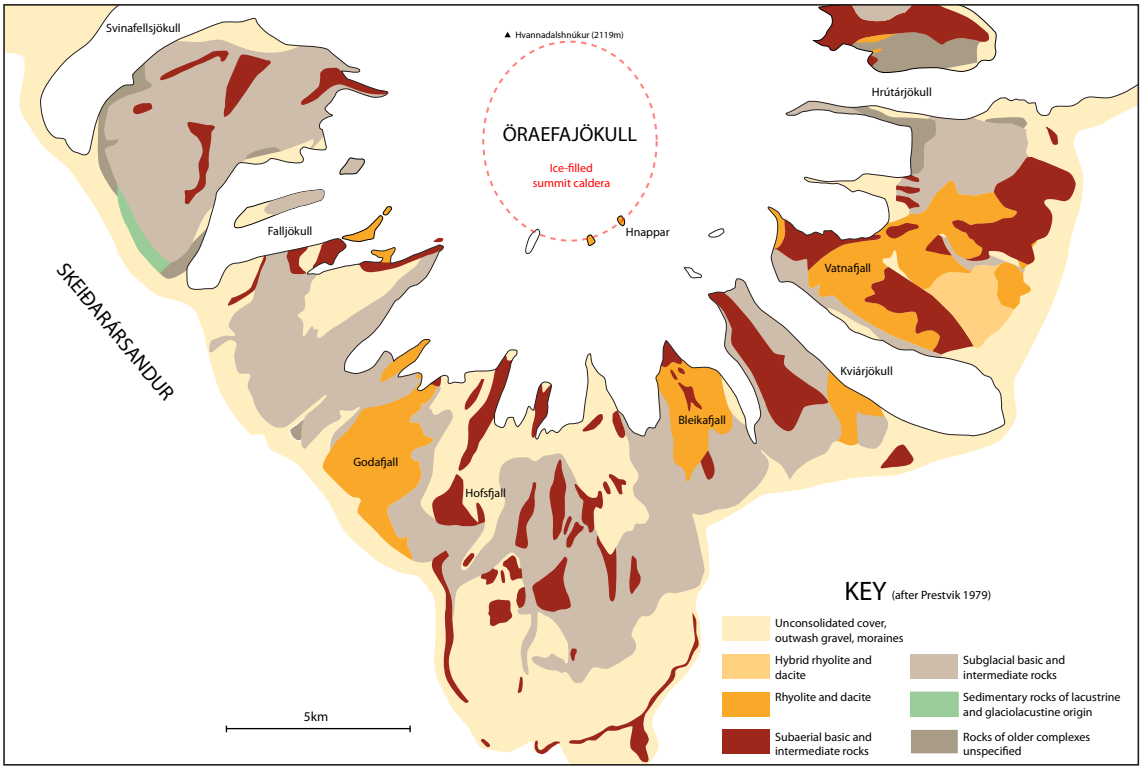

Fig. 6.7: Geological map of Öræfajökull based on Prestvik (1979).

tion 6.4.

To briefly recap on the volcanic stratigraphy of the Goðafjall area (fig. 6.8), the basement basalt complex (lithofacies A) is overlain by two main rhyolitic groups (lithofacies C and L) that have been identified by a combination of chemostratigraphy (chapter 3) and conventional field mapping (chapter 4). The Group One rhyolites outcrop lower in the stratigraphy, and although they have undergone substantial erosion, collectively the units exhibit evidence to support a subaerial emplacement environment.

The Group One rhyolites are stratigraphically overlain by the Group Two rhyolites, which, in comparison, display a wide range of morphologies that support a subglacial emplacement environment. Both of the rhyolite groups show evidence of post-emplacement glacial erosion.

Around the edge of the HVG Valley the Group Two rhyolites are unconformably overlain by a glacial diamicton followed by sub-horizontal mafic lavas which show evidence of glacial erosion on their upper surface. Further south towards the mouth of the valley another discontinuous glacial diamict is present towards the top of the sequence. The sequence is capped by layer of stratified tuff (lithofacies Q)

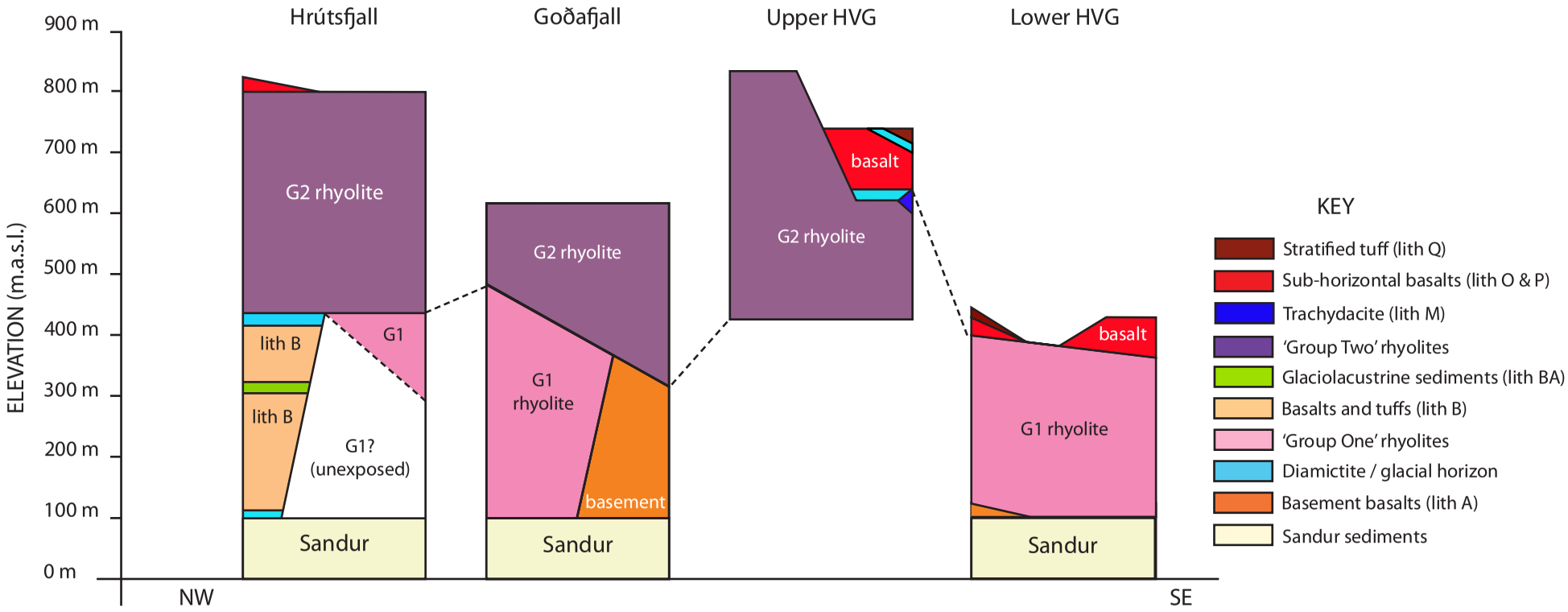

Fig. 6.8. Schematic diagram indicating distribution and thickness of main units across the field area.

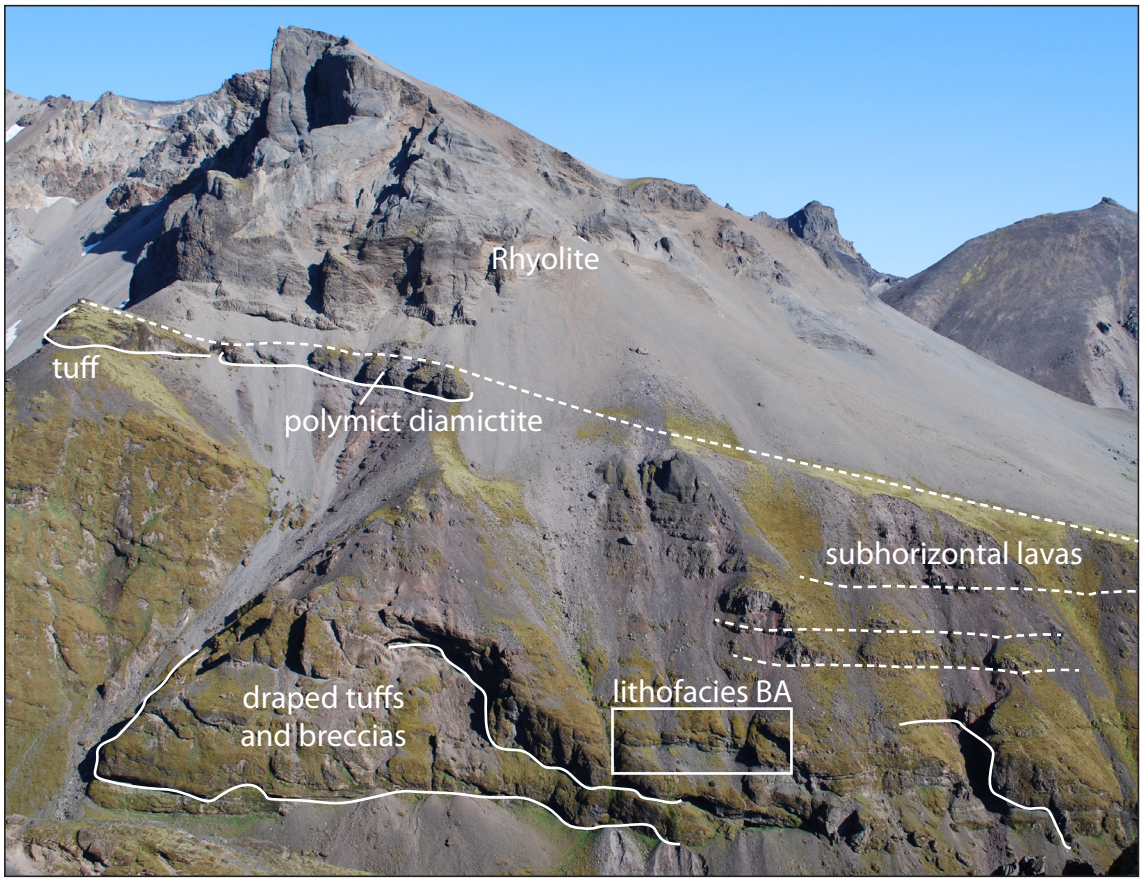

Fig. 6.9. Lower Hrútsfjall lithofacies B and BA underlie Group Two rhyolites with evidence of at least two glaciations prior to Group Two rhyolite emplacement.

originating from a near-by tuff cone, Hofsfjall, situated to the east of the field area.

In contrast Hrútsfjall ridge is bound to the north west by the glacially-incised Kota valley where the current difference in height from valley floor to the top of the basalt exposure, Vedrastapi (lithofacies O) at the ridge summit is 700 m.

The Group Two rhyolites (lithofacies L) cap the upper 300 m of the Hrútsfjall ridge, which is unconformably overlain by a discontinuous unit of fragmental basalt and lavas, forming the Veðrastapi tower, toward the head of the valley.

The layered succession of mafic lavas, hyaloclastites and sedimentary facies (lithofacies B and BA) (fig. 6.9) that make up the lower eastern valley wall show evidence of at least three episodes of glaciation that occurred prior to the emplacement of the Group Two rhyolites that are not represented in the Goðafjall section.

Throughout the combined Goðafjall and Hrútsfjall sequence there is evidence for at least five glaciations in total.

The Group One rhyolites were emplaced subaerially and yield a $^{40}Ar/^{39}Ar$ age of 0.204 ± 0.023 Ma which places the timing of eruption, from 227 to 181 k, within

MIS 7. (fig. 6.10). There is no evidence of a glacial horizon between the Group One and Group Two rhyolites which suggests that the eruptions took place in adjacent interglacial and glacial periods. This is corroborated by $^{40}Ar/^{39}Ar$ age of the Group Two rhyolites of 0.116 ± 0.018 Ma, which implies eruption from 134 to 98 k covering a period from the waning stages of MIS 6 to the onset of Eemian interglacial warm substage C (MIS 5c).

Evidence from the Vostock ice cores (Petit et al., 1999) suggests that MIS 6 was slightly colder than the last Weichselian ice age (MIS 4-2). The ice sheet extended over a greater area and sea level dropped at least 10 m lower (130 m below present) than MIS 2 levels (Lambeck et al., 2002). There is also evidence to suggest a 'Younger Dryas' type cooling event after the onset of warming during the early Eemian intergacial between 135 k and 126 k (Esat et al., 1999, Seidenkrantz et al., 1996). If similar deglaciation conditions toward the end of MIS 2 also apply to the end of MIS 6 then it is likely that this area of south east Iceland retained a thick ice sheet well into the Eemian interglacial, with continual ice cover through to the Weichselian.

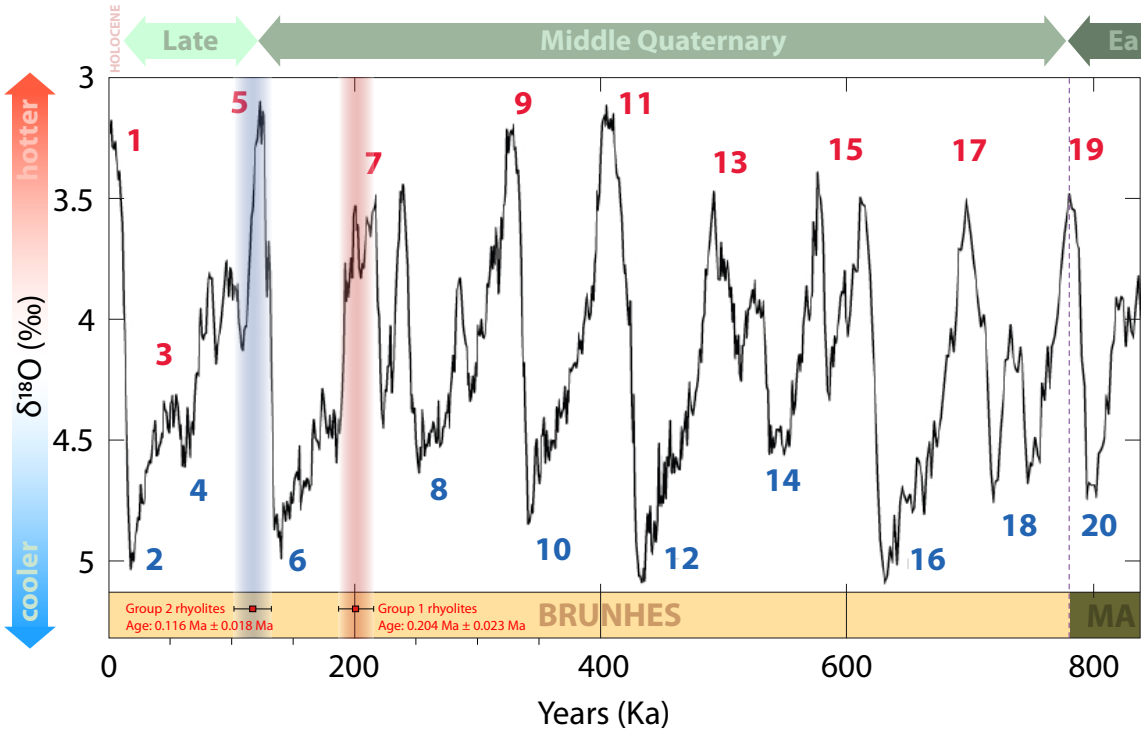

Adapted from: Lisiecki, L. E., and M. E. Raymo (2005), A Pliocene-Pleistocene stack of 57 globally distributed benthic d18O records, Paleoceanography, 20, PA1003, doi:10.1029/2004PA001071

Fig. 6.10. Eruption ages of Group One and Two rhyolites overlain on stacked benthic oxygen isotope record LR04 (modified from Lisiecki and Raymo, 2005). Numbers reperesent Marine interval stages (blue: glacial; red: interglacial).

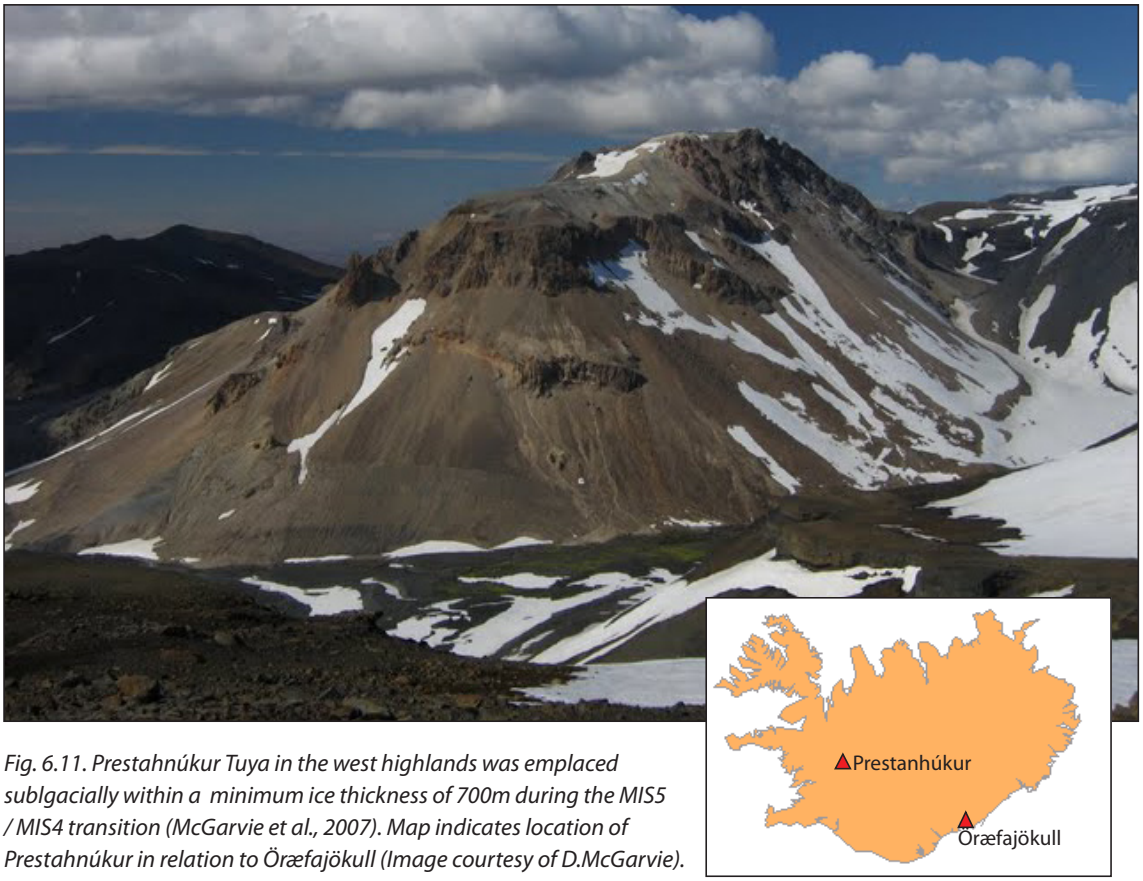

Fig. 6.11. Prestahnúkur Tuya in the west highlands was emplaced sublgacially within a minimum ice thickness of 700m during the MIS5 / MIS4 transition (McGarvie et al., 2007). Map indicates location of Prestahnúkur in relation to Öræfajökull (Image courtesy of D.McGarvie).

Group two rhyolites show evidence of ice confinement on the north-west facing flank of Hrútsfjall which suggests the presence of a well-established, thick valley fill glacier in the present Kota river valley built up over successive glacial periods, marked by the presence of glacial horizons, prior to the MIS 6/5 transition (fig.6.9).

No significant emergent lithofacies have been located anywhere within the Group Two rhyolites suggesting that its eruption was fully subglacial. Evidence of any emergent lithofacies may have been removed by subsequent glacial advance as there is field evidence of two further glacial advances after emplacement of this group, but it is worth noting that flow-top features have been preserved in the older underlying Group One rhyolites.

In comparison McGarvie et al. (1997) dated the Prestahnúkur tuya situated in the west highlands of Iceland (fig. 6.11) to 89 ± 24 k which implies eruption at some stage during the interglacial/glacial transition period of 5d to 5a. This interglacial transition has been linked with rapid temperature fluctuations and a rapid build up of land based ice during colder stadials. As Prestahnúkur is a fully subglacial edifice at least 700 m of ice is estimated to have been present at its eruption during this pe-

riod. Prestahnúkur is situated more than 250 km west of the of the main glacial ice divide (ID1) which is estimated to run across the centre of the present day Vatnajokull Glacier in a SW – NE direction (Einarsson and Albertsson, 1988; Bourgeois et al., 1998)(fig. 6.12), therefore it is reasonable to assume that ice thicknesses at Öræfajökull, less than 50 km from the ice divide, were at least as thick as those at Prestahnúkur and less susceptible to rapid fluctuations seen further away from the centre of the ice sheet.

During the Weichselian ice surfaces at the ice divide have been estimated at 1500 – 2000 m (Einarsson and Albertsson, 1988, Bourgeois et al., 1998) (fig. 6.12). Öræfajökull's position close to the ice divide implies a substantial ice thickness across the surrounding south eastern region. During the Weichselian there is no evidence of any subglacial eruption in the Goðafjall area, therefore it is assumed that erosive processes dominated throughout this glacial period. Glacial erosion removed large quantities of the Group two rhyolites, carving out the cirque formation (fig. 6.13) and defining the two ridges of Goðafjall and Hrútsfell.

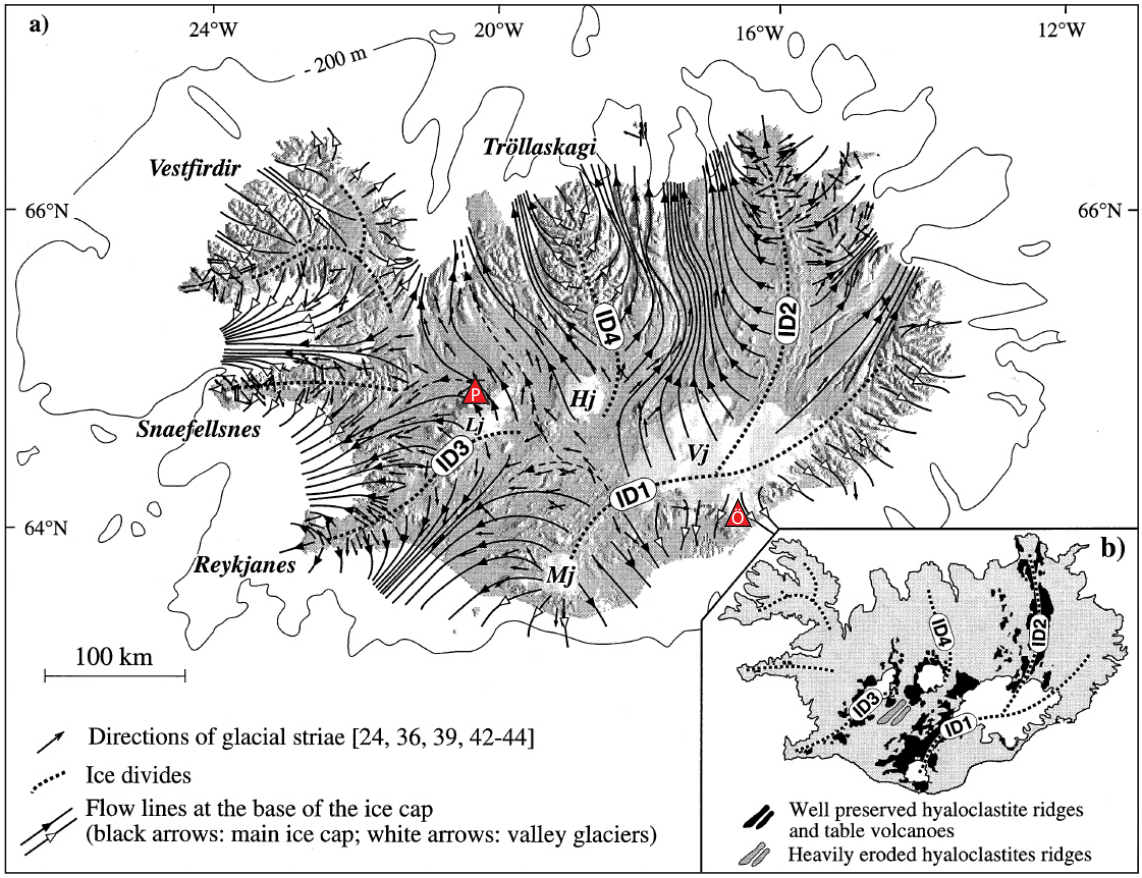

Fig. 6.12. After Bourgeois et al, 1998: Location of the ice divides during the LGM as implied by glacial striae combined with morphological features. The main long-lived ice divide is ID1. Red Traingles indicate location of Prestahnúkur and Öræfajökull.

A glacial diamicton, horizon which may be a marker for MIS 4-2, is situated unconformably above the Group Two rhyolites in the upper HVG valley and has been preserved due to the overlying subhorizontal basalts sheets (lithofacies O). The basalts were emplaced while the diamicton was still unconsolidated into a subaerial but semi-wet environment which may be representative of the post-MIS 2 deglaciation. It is proposed that during this time valley glaciers and some thin ice cover will have remained but upper elevations may have been relatively free of thick ice or ice-free.

Striations on the upper surfaces of the basalts indicate a later glacial advance with valley-fill ice increasing to at least 800 m in elevation. During the Younger Dryas the ice sheet advanced past the current coastline in this region (Norddahl and Einarsson, 2001) therefore it is reasonable to assume ice thicknesses to at least 800 m.a.s.l. in the Goðafjall area with ice filling the HVG and Kotá valleys. During this period the trachydacite ice-contact lobes were intruded into the basalts on the eastern wall of the HVG valley, where they came into contact with the valley fill glacier at the ice-bedrock interface partially melting the ice and forming radially columnar jointed lobes.

Fig. 6.13. View south east from Hrútsfjall down the HVG valley into the glacially carved cirque above Goðafjall ridge (right).

Fig. 6.14. View to south towards Hofsfjall tuff cone to the east of the Hvalvörðugil Valley. The tuff cone summit is 750 m.a.s.l.

A smaller discontinuous glacial horizon separating channel-fill hyaloclastites from stratified tuffs (lithofacies Q) may represent the last glacial advance of the early Holocene which has been dated to the early Preboreal between 11.5 to 10.1 ka (Hjartarsson & Ingolfsson, 1988; Geirsdottir, 2000). The stratified tuff deposits (lithofacies Q) are associated with a very well-preserved tuff cone located at Hosfjall approximately 1.8 km to the east of the HVG valley at an elevation of 600 m (fig. 6.14). The edifice has undergone very little glacial erosion and is therefore likely to have been emplaced during this final glacial surge during the Preboreal. Thin ice of at least 100 m in thickness and capable of allowing water to pond at the vent must have been present at an elevation of 600 m (above current sea level) in order for the Hosfjall tuff cone to form.

Figures 6.15 shows the of the proposed evolution of the Godafjall and Hrutsfjall ridge area of Öræfajökull depicted in 12 stages.

6.4. Vatnafjall ridge, Öræfajökull

Vatnafjall ridge (fig. 6.16a & b) is situated approximately 40 km to the east of the Goðafjall area and has been mapped in detail by Stevenson et al. (2006) and shows strong evidence of interaction with varying thicknesses of ice throughout its evolution (fig. 6.17).

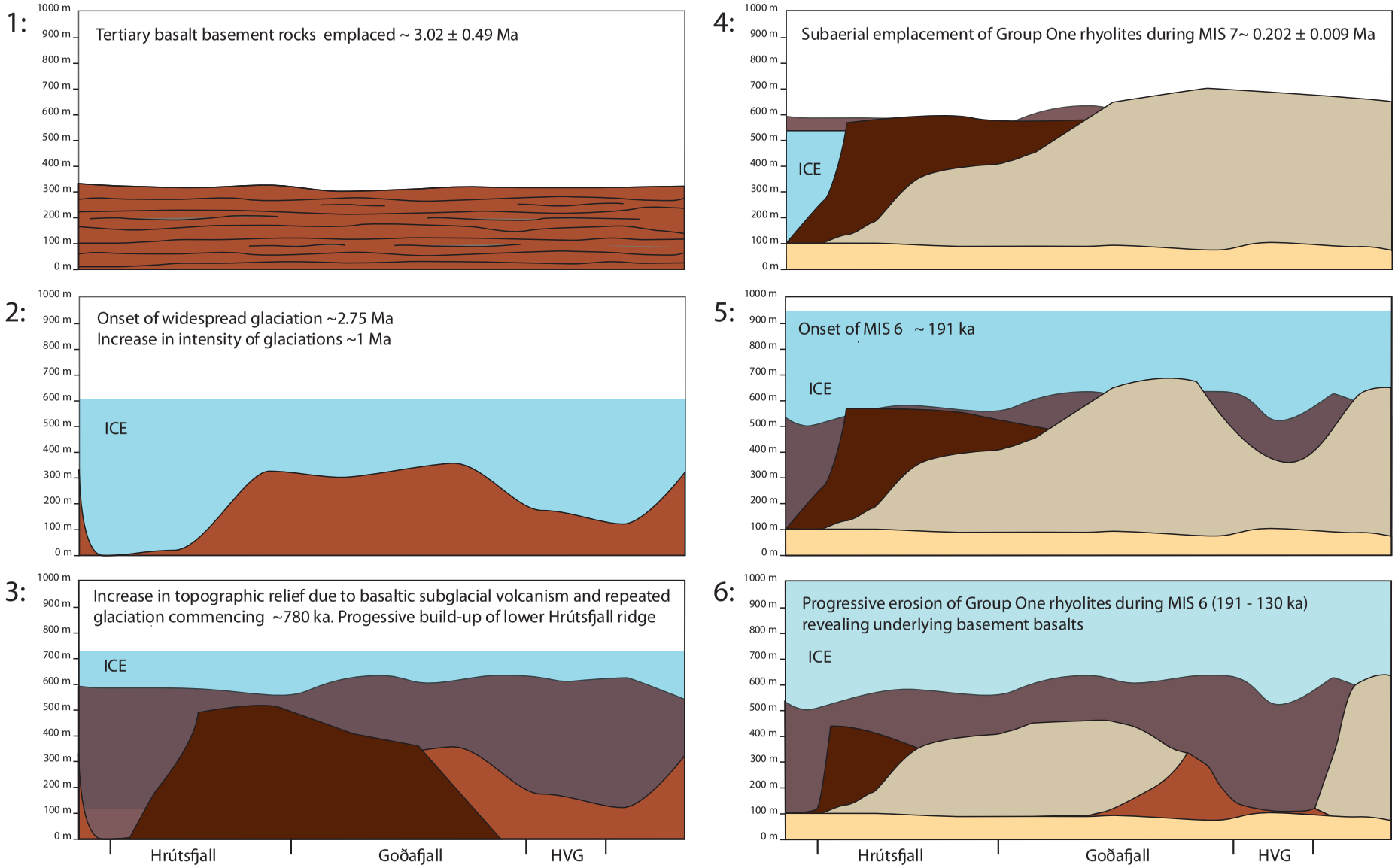

Fig. 6.15. Proposed timeline for the development of Goðafjall and Hrútsfjall ridges.

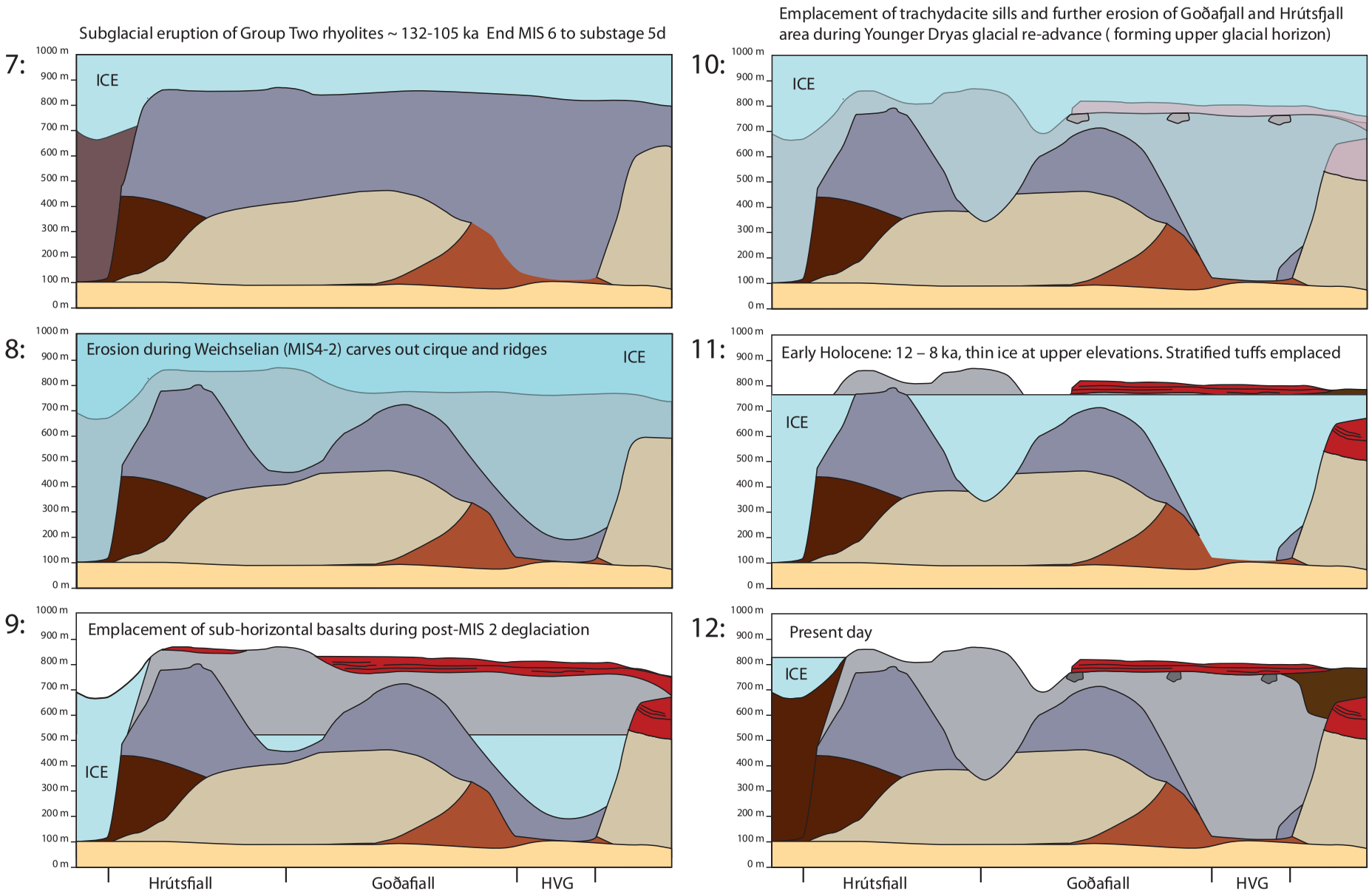
7:
Subglacial eruption of Group Two rhyolites ~ 132-105 ka End MIS 6 to substage 5d
ICE
8:
Erosion during Weichselian (MIS4-2) carves out cirque and ridges
ICE
9:
Emplacement of sub-horizontal basalts during post-MIS 2 deglaciation
ICE
10:
Emplacement of trachydacite sills and further erosion of Goðafjall and Hrútsfjall area during Younger Dryas glacial re-advance (forming upper glacial horizon)
ICE
11:
Early Holocene: 12 – 8 ka, thin ice at upper elevations. Stratified tuffs emplaced
ICE
12:
Present day
ICE
1000 m
900 m
800 m
700 m
600 m
500 m
400 m
300 m
200 m
100 m
0 m
Hrútsfiall
Goðafiall
HVG

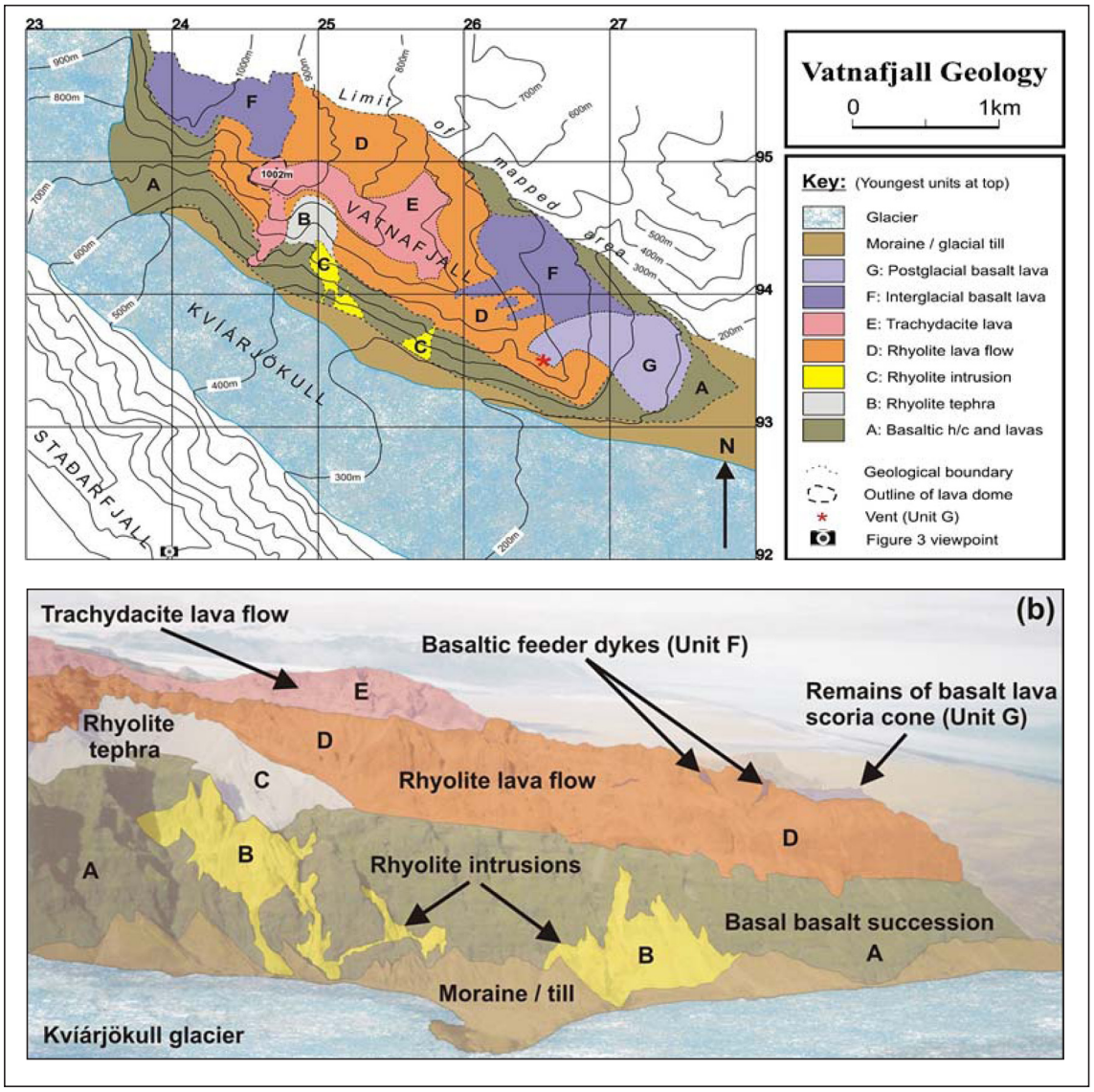

Fig.6.16. After Stevenson et al., 2006: A: Geolocial map of Vatnafjall ridge. B: field interpretation of Vatnafjall ridge

Samples of the upper trachydacite unit (Unit E: fig. 6.16b) have been dated using the $^{40}Ar/^{39}Ar$ technique in order to apply an absolute time constraint to the ridge construction.

Unit caps the ridge from an elevation of 700 to 1000 m.a.s.l. and shows strong evidence to suggest confinement by ice on its south western slope, adjacent to the Kviárjökull glacier valley, while its upper brecciated surface shows evidence of sub-aerial emplacement with some minor water interaction.

Unit E yields a $^{40}Ar/^{39}Ar$ age of 0.095 ± 0.007 Ma which implies emplacement from 112 ka to 88 k within the glacial /interglacial transition period of MIS 5d cold stage to 5d warm stage.

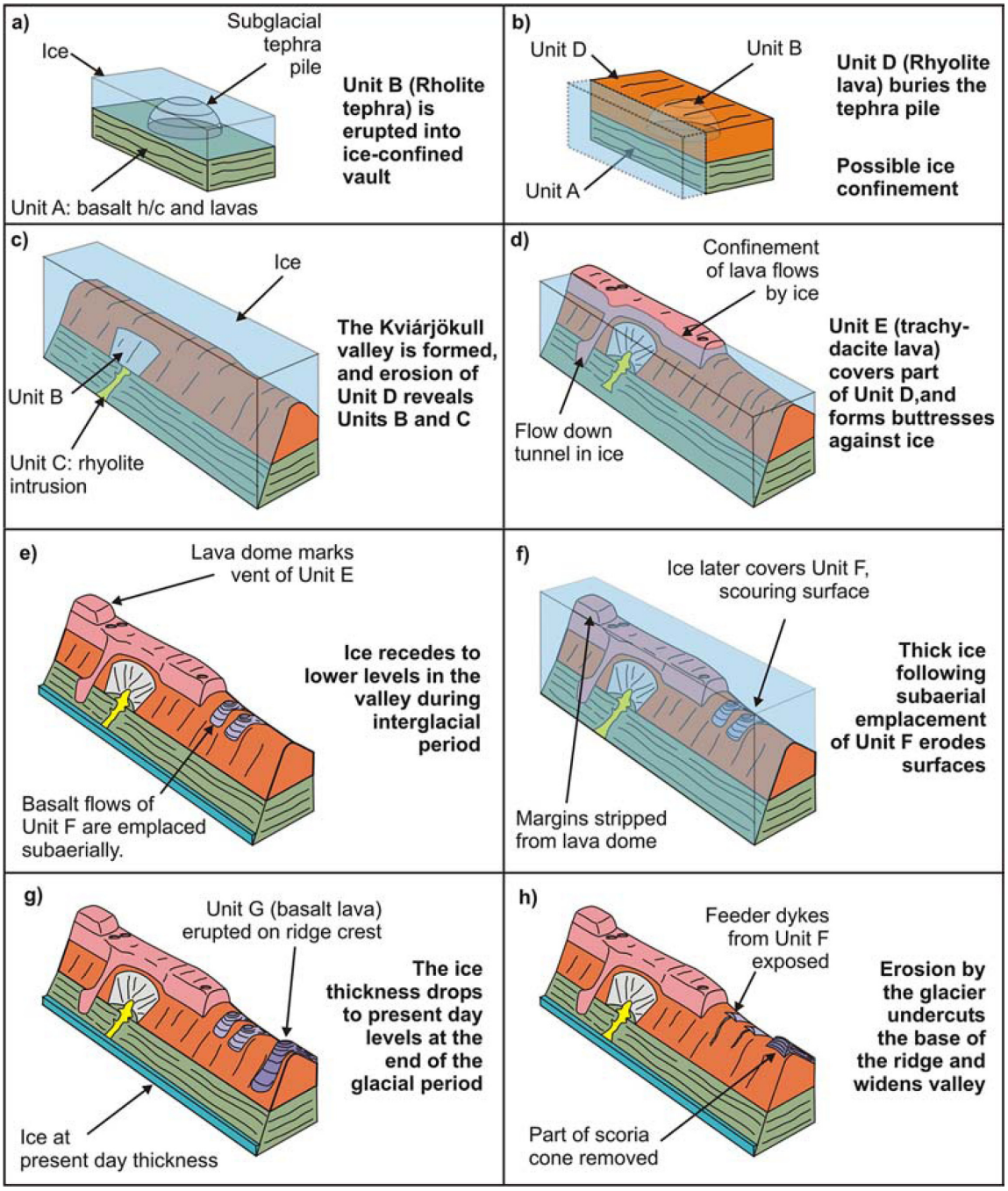

Fig. 6.17. After Stevenson et al. 2006: Evolution of Vatnafjall ridge and corresponding ice thicknesses

As previously discussed in section 6.3, MIS 5 has been described as a period of rapid temperature fluctuation and rapid land-based ice accumulation during the onset of colder stages. Vatnafjall Unit E was deposited within a similar timeframe to the Goðafjall Group Two rhyolites, which appear to have been emplaced wholly subglacially but with definite evidence for ice confinement on their glacierward side. It is worth noting that Vatnafjall unit E was emplaced at least 300 m higher in elevation than the Goðafjall Group Two rhyolites, therefore while the overall regional ice

Goðafjall and Hvalvörðugil Valley evolution timeline					
LITHOFACIES	CHEMOSTRAT GROUP	ROCK TYPE DESCRIPTION	PALAEOENVIRONMENT	$^{40}Ar/^{39}Ar$ AGE	MARINE INTERVAL STAGE (LR04 stack)
Q	mafic	hyolaoclastite tuff	subaqueous / glacial		MIS 2 to Holocene
GLACIAL UNCONFORMITY (Diamict)					MIS 2 to Holocene
N	trachydacite	columnar jointed lavas: sill	subglacial		MIS 4 to 2
GLACIAL UNCONFORMITY (Diamict)					MIS 4 to 2
P	mafic	channel fill hyaloclastite	subaerial – ice-marginal / water interaction		MIS 5
OB	mafic	oxidised lavas	subaerial		MIS 5
M		cross-bedded sandstone	subaerial fluvial		MIS 5
OA	mafic	lavas with diamict apopheses	ice-marginal / snow contact		MIS 6 / 5d
GLACIAL UNCONFORMITY (Diamicton)					MIS 6 / 5d cold substage
L	'Group Two' rhyolite	columnar jointed lavas	subglacial	0.116 ± 0.014 Ma	MIS 6 / 5 transition to cold substage 5d
K		dyke			
J		lapilli tuffs and breccias	evidence of both phreatomagmatic and volatile-driven explosivity – subglacially confined		
I					
H					
G					
GAP IN STRATIGRAPHY (?)					
F	'Group One' rhyolite	platy rhyolite lobes and breccias	subaerial – dry with minor water interaction	0.202 ± 0.009 Ma	MIS 7
E					
D					
C			subaerial – possible fluvial		
GAP IN STRATIGRAPHY – onset of large scale glaciation circa. 2.75 Ma (Kleiven et al., 2002)					
A	basalt	basement basalt complex	subaerial interglacial	3.02 ± 0.49 Ma	MIS G21

Table 6.1. Summary of development in the Goðafjall area.

cover may have been similar at an approximate minimum of 700 m, the localised ice thickness at Goðafjall may have been enough to sustain a wholly subglacial emplacement environment for the Group Two rhyolites.

Overall the unit E eruption ages and the physical evidence further support the presence of a well-developed and permanent ice sheet in the south east of Iceland, even during interglacial periods, as first proposed by Helgason and Duncan (2001).

6.5. Summary

A summary of the main stages of development are listed in table 6.1. At present the errors on the $^{40}Ar/^{39}Ar$ eruption ages mean that the eruption dates of individual silicic units cannot be tied solely to one glacial period with accuracy. Evaluation of

the eruption ages in combination with detailed field observation provides evidence to support the presence of a permanent and dynamic ice sheet in the south east of Iceland which developed throughout the mid to late Quaternary and is consistent with the findings of previous workers in neighbouring areas (Helgason and Duncan, 2001; Stevenson et al., 2006).

The ice sheet itself has developed alongside the evolution of Öræfajökull Volcano during the mid to late Pleistocene, with permanent ice and thick valley-fill glaciers remaining during transitional and interglacial periods, especially toward the later stages of the Pleistocene (MIS 6 onwards) and possibly well into the early Holocene.

Chapter 7
Concluding remarks and recommendations for further research

At the onset of this research project, two main aims were established:

1: To investigate the temporal and physical evolution of Öræfajökull volcano by compiling a detailed multi-disciplinary analysis of the Goðafjall and Hrútsfjall region, located on the volcano's exposed southern flank.

2. To reconstruct the local palaoenvironment of the Oraefi region of south east Iceland and investigate the changes in palaeo-environment that took place throughout the evolution of Öræfajökull volcano.

Both of these aims were investigated by combining the results of three areas of study: detailed field observation, major and trace element geochemistry and radiometric dating.

To the extent that these aims were met, this chapter presents a summary of the main conclusions derived from this body of research. The findings are presented in the order of the chapters they were first introduced:

1. The application of chemostratigaphy has been utilised succesfully to identify two geochemically distinct types of rhyolitic lava in the Goðafjall and Hrútsfjall area of Öræfajökull.

2. The $^{40}Ar/^{39}Ar$ dating technique has been utilised succesfully to provide eruption age constrains on the basement complex (3.02 ± 0.5 My) prior to the build up of the main volcanic edifice.

3. Age contraints have also been determined for two young (<1 Ma) rhyolite lava flows in the Goðafjall and Hrútsfjall area with ages of 0.204 ± 0.02 My and 0.116 ± 0.02 My. A further age constraint has been determined for one trachydacite lava flow in the Vatnafjall area of Öræfajökull with an age of 0.095 ± 0.01 My.

4. The combination of detailed field observations with $^{40}Ar/^{39}Ar$ eruption ages of the lavas has enabled age constraints to be applied to the phyiscal evolution of the Goðafjall and Hrútsfjall region.

5. Lava flow eruption ages and field evidence support the presence of a permanent but dynamic ice sheet in the south east of Iceland throughout mid to late Pleistocene during the evolution of Öræfajökull that has completely covered the developing edifice during the last two major episodes of glaciation in the northern hemisphere.

6. Prior to the onset of MIS 6, the Goðafjall area was free of thick ice at lower elevations, however during the advance of MIS 6 and the well into the MIS 5 transition the ice sheet advanced over the Goðafjall and Hrútsfjall area to a minimum thickness of 800 m.a.s.l.

7. Evidence supports the presence of a long-lived valley-fill glacier in the Kotá valley which was established prior to MIS 7 and which retreats to a valley head location, similar to that of present-day, during warmer stages.

8. Glacial erosion has been a major contributing factor to the topographic developement of the Goðafjall and Hrútsfjall area of Öræfajökull. Unconsolidated silicic volcanic products and capping lavas are easily removed by advancing ice leading to an increase in local topographic relief and defining the current-day ridges of Goðafjall and Hrútsfjall.

Recommendations for further research

Some areas for further investigation, which may help to impove and build upon the findings of this reseach project, have been listed below:

1. Investigation into the origin of the fractionated argon source would be helpful in further refining the $^{40}Ar/^{39}Ar$ dating technique as it applies to young Icelandic rhyolites. One future experiment to investigate the role of Soret diffusion in this phenomena would be the measurement of $^{40}Ar/^{36}Ar$ ratios in unirradiated sections of a columar joint from the column edge to the centre in order to establish whether $^{40}Ar/^{36}Ar$ ratios increase towards the centre of the column, where less atmospheric exchange will have occured during cooling.

2. A more detailed volcanological study of the unconsolidated tuffs (lithofacies G, H, I, J and L) may improve current understanding of the early stages of subglacial eruptions at stratovolcanoes. The traditional 'subaerial' and 'subaqueous' interpretations of tephra flow and fall deposits are difficult to apply to early-erupted subglacial products where lateral dispersion of tephra is limited, enabling more mixing to occur. To date, in-depth studies of early-erupted products of subglacial eruptions have been limted to tuyas where edifice build-up occurs via one prolonged eruption (Stevenson et al,. 2011) which makes them relatively easier to constrain and interpret.

3. Further detailed investigation of the north face of the lower Kotá valley (lithofacies B and BA) may provide more insight into the occurence of successive glaciations in the Goðafjall and Hrútsfjall area prior to MIS 7.

4. A more complete temporal evolution of Öræfajökull may be established by the $^{40}Ar/^{39}Ar$ dating of the other silicic centres located on the south facing flanks of the edifice (fig. 7.1).

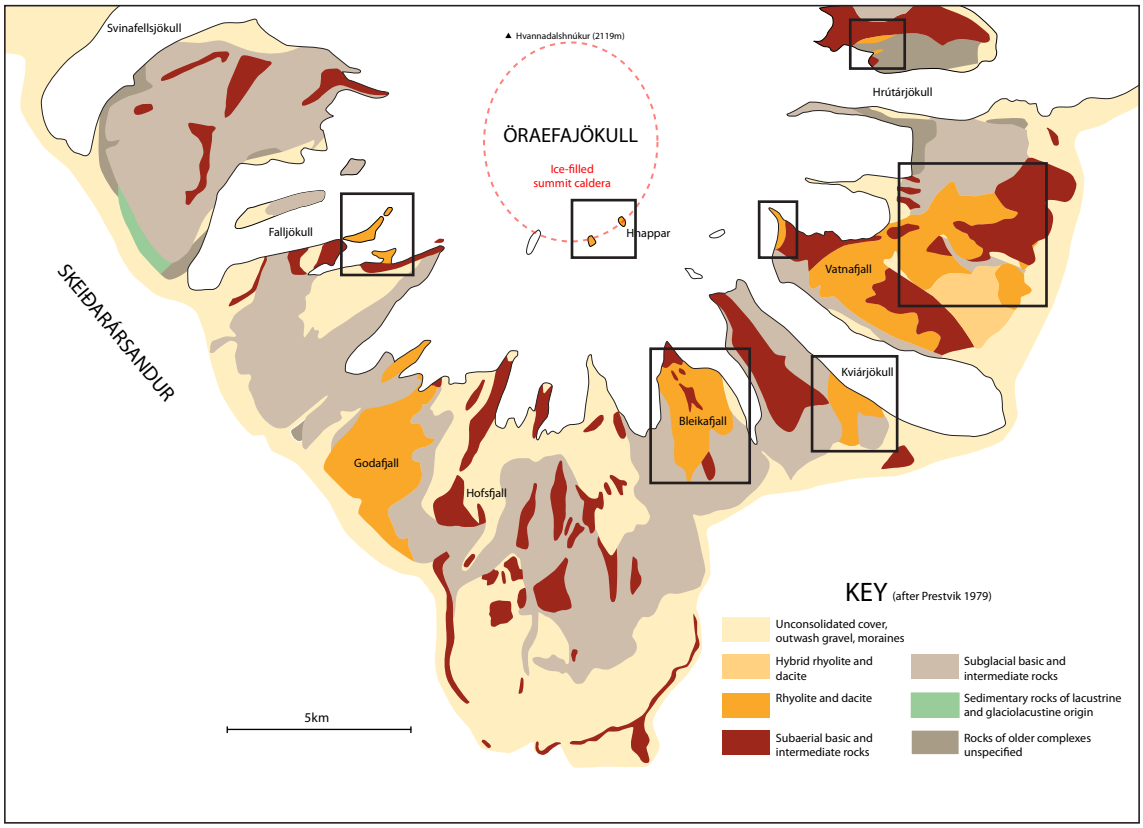

Fig. 7.1. Geological map of Oraefajokull. Black boxes indaticate other rhyolitic areas that have not yet been dated.

5. Geochemical investigation of the exposed rhyolitic nunataks (fig. 7.1) around the ege of the summit crater would also help to establish whether a relationship exists between the summit rhyolites and those exposed on the lower flanks. This would help to clarify whether all of the silicic lavas exposed on the lower flanks are true flank eruptions or whether some are central vent eruptions that have flowed some distance from the crater.

References

ALLEN, C. C. (1980) Icelandic subglacial volcanism: thermal and physical studies. Journal of Geology, 88, 108-117.

ALLEN, C. C., JERCINOVIC, M.J., ALLEN, J.S.B. (1982) Subglacial Volcanism in North-Central British Columbia and Iceland. Journal of Geology, 90, 699-715.

ANDERSON, S. W. & FINK, J. H. (1992) Crease structures: Indicators of emplacement rates and surface stress regimes of lava flows. Geological Society of America Bulletin, 104, 615-625.

ANDREWS, J. T., HARDARDOTTIR, J., HELGADO´ TTIR, G., JENNINGS, A. E., GEIRSDOTTIR, A., SVEINBJORNSDOTTIR, A. E., SCHOOLFIELD, S., KRISTJANSDOTTIR, G. B., SMITH, L. M., THORS, K. & SYVITSKI, J. P. M. (2000) The N and W Iceland shelf: insights into last glacial maximum ice extent and deglaciation based on acoustic stratigraphy and basal radiocarbon AMS dates. Quaternary Science Reviews, 19.

ALLEN, R. M., NOLET, G., MORGAN, W. J., VOGFJÖRD, K., NETTLES, M., EKSTRÖM, G., BERGSSON, B. H., ERLENDSSON, P., FOULGER, G. R., JAKOBSDÓTTIR, S., JULIAN, B. R., PRITCHARD, M., RAGNARSSON, S. & STEFÁNSSON, R. (2002) Plume-driven plumbing and crustal formation in Iceland. J. Geophys. Res., 107, 2163.

BALLENTINE, C.J., BARFORD, D.N. (2000) The origin of air-like noble gas in MORB and OIB. Earth Planet. Sci. Lett. 180, 39–48.

BJARNASON, I. T. & SCHMELING, H. (2009) The lithosphere and asthenosphere of the Iceland hotspot from surface waves. Geophysical Journal International, 178, 394-418.

BJORNSSON, H. & EINARSSON, P. (1990) Volcanoes beneath Vatnajokull, Iceland: Evidence from radio-echo sounding, earthquakes and Jolkulhaups. Jokull, 40, 147 - 168.

BONNISCHEN, B. & KUAFFMAN, D.F. (1987) Physical features of rhyolite flows in the Snake River Plain volcanic province, south-western Idaho. In: J.H. Fink (editor), The emplaceement of silicic domes and lava flows. Geological Society of America Special Paper, 119-145.

BOULTON, G. S., JARVIS, J. & THORS, K. (1988) Dispersal of glacially derived sediment over part of the continental shelf of south Iceland and the geometry of the resultant sediment bodies. Marine Geology, 83, 193–223.

BOURGEOIS, O., DAUTEUIL, O. & VAN VLIET-LANOË, B. (1998) Pleistocene subglacial volcanism in Iceland: tectonic implications. Earth and Planetary Science Letters, 164, 165-178.

BRADLEY, R. S. (1999) Paleoclimatology : reconstructing climates of the Quaternary, San Diego, Calif. ; London Harcourt/Academic Press 1999.

BROWN, F. H., REID, C. & NEGASH, A. (2009) Possible isotopic fractionation of argon in source obsidians and archeological artifacts from Kulkuletti, Ethiopia. Journal of Archaeological Science, 36, 2119-2124.

BURNARD, P., HARRISON, D. (2005) Argon isotope constraints on modification of oxygen isotopes in Iceland Basalts by surficial processes. Chemical Geology 216, 143– 156

CABRERA, A., WEINBERG, R. F., WRIGHT, H. M. N., ZLOTNIK, S. & CAS, R. A. F. (2011) Melt fracturing and healing: A mechanism for degassing and origin of silicic obsidian. Geology, 39, 67-70.

CARMICHAEL, I. S. E. (1964) The Petrology of Thingmuli, a Tertiary Volcano in Eastern Iceland. J. Petrology, 5, 435-460.

CARRIVICK, J. L., RUSSELL, A. J., RUSHMER, E. L., TWEED, F. S., MARREN, P. M., DEEMING, H. & LOWE, O. J. (2009) Geomorphological evidence towards a de-glacial control on volcanism. Earth Surface Processes and Landforms, 34, 1164-1178.

CASTRO, J. M. & CASHMAN, K. V. (1999) Constraints on rheology of obsidian lavas based on mesoscopic folds. Journal of Structural Geology, 21, 807-819.

CERLING, T. E., BROWN, F. H. & BOWMAN, J. R. (1985) Low-temperature alteration of volcanic glass: Hydration, Na, K, 18O and Ar mobility. Chemical Geology: Isotope Geoscience section, 52, 281-293.

CHARLIER, B. L. A., WILSON, C. J. N., LOWENSTERN, J. B., BLAKE, S., VAN CALSTEREN, P. W. & DAVIDSON, J. P. (2005) Magma Generation at a Large, Hyperactive Silicic Volcano (Taupo, New Zealand) Revealed by U/Th and U/Pb Systematics in Zircons. Journal of Petrology, 46, 3-32.

CHERNIAK, D. J. (2010) Cation Diffusion in Feldspars. Reviews in mineralogy and geochemistry, 72, 691-733.

CHERNIAK, D. J. & WATSON, E. B. (1994) A study of strontium diffusion in plagioclase using Rutherford backscattering spectroscopy. Geochimica et Cosmochimica Acta, 58, 5179-5190.

CLAY, P. L. (2010) Ar/Ar dating of young volcanic rocks. Department of Earth and Environmental Sciences. PhD thesis, the Open University, 278 pp.

DEMETS, C., GORDON, R. G., ANGUS, D. F., STEIN, S., (1994) Effect of Recent Revisions to the Geomagnetic Reversal Time Scale on Estimates of Current Plate Motions. Geophysical Research Letters, 21: 2191-2194

DENTON, J. S., TUFFEN, H., GILBERT, J. S., ODLING, N (2009) The hydration and alteration of perlite and rhyolite. Journal of the Geological Society of London, 166, 895-904.

DIXON, J. E., FILIBERTO, J. R., MOORE, J. G. & HICKSON, C. J. (2002) Volatiles in basaltic glasses from a subglacial volcano in northern British Columbia (Canada): implications for ice sheet thickness and mantle volatiles. Geological Society, London, Special Publications, 202, 255-271.

DONER, L. (2003) Late-Holocene paleoenvironments of northwest Iceland from lake sediments. Palaeogeography Palaeoclimatology Palaeoecology, 193, 535-560.

EDWARDS, EDWARDS, B., RUSSELL, RUSSELL, J., ANDERSON & ANDERSON, R. (2002) Subglacial, phonolitic volcanism at Hoodoo Mountain volcano, northern Canadian Cordillera. Bulletin of Volcanology, 64, 254-272.

EDWARDS, B. R. & RUSSELL, J. K. (2002) Glacial influences and eruptive products of Hoodoo Mountain volcano, Canada. IN SMELLIE, J. L. C., M.G (ED.) . LONDON, (Ed.) Volcano-Ice interaction on Earth and Mars. London, Geological Society

EDWARDS, B. R., SKILLING, I. P., CAMERON, B., HAYNES, C., LLOYD, A. & HUNGERFORD, J. H. D. (2009) Evolution of an englacial volcanic ridge: Pillow Ridge tindar, Mount Edziza volcanic complex, NCVP, British Columbia, Canada. Journal of Volcanology and Geothermal Research, 185, 251-275.

EINARSSON, T. & ALBERTSSON, K. J. (1988) The Glacial History of Iceland During the Past Three Million Years. Philosophical Transactions of the Royal Society of London. Series B, Biological Sciences, 318, 637-644.

ESAT, T. M., MCCULLOCH, M. T., CHAPPELL, J., PILLANS, B. & OMURA, A. (1999) Rapid Fluctuations in Sea Level Recorded at Huon Peninsula During the Penultimate Deglaciation. Science, 283, 197-201.

ESSER, R. P., MCINTOSH, W. C., HEIZLER, M. T. & KYLE, P. R. (1997) Excess argon in melt inclusions in zero-age anorthoclase feldspar from Mt. Erebus, Antarctica, as revealed by the 40Ar39Ar method. Geochimica et Cosmochimica Acta, 61, 3789-3801.

FISHER, R. V. A. S., H.U. (1984) Pyroclastic rocks, Springer-Verlag.

FINK, J. H. (1983) Structure and emplacement of a rhyolitic obsidian flow: Little Glass Mountain, Medicine Lake Highland, northern California. Geological Society of America Bulletin, 94, 362-380.

FINK, J. H. & ANDERSON, S. W. (2000) Lava domes and Coulees. Encyclopaedia of volcanoes, 307-319.

FINK, J. H., ANDERSON, S. W. & MANLEY, C. R. (1992) Textural constraints on effusive silicic volcanism: Beyond the permeable foam model. Journal of Geophysical Research, 97, 9073-9083.

FINK, J. H. & MANLEY, C. R. (1987)Origin of pumiceous and glassy textures in rhyolite flows and domes. In: J.H. Fink (editor), The emplaceement of silicic domes and lava flows. Geological Society of America Special Paper, 77-89.

FLUDE, S. (2005) Rhyolite volcanism in Iceland: Timing and timescales of Eruptions. PhD thesis, University of Manchester, 257 pp.

FLUDE, S., BURGESS, R., MCGARVIE, D.W. (2008) Silicic volcanism at Ljósufjöll, Iceland: Insights into evolution and eruptive history from Ar–Ar dating. Journal of Volcanology and Geothermal Research, 169, 154-175.

FLUDE, S., MCGARVIE, D., BURGESS, R. & TINDLE, A. (2010) Rhyolites at Kerlingarfjöll, Iceland: the evolution and lifespan of silicic central volcanoes. Bulletin of Volcanology, 72, 523-538.

FOLAND, K. A., FLEMING, T. H., HEIMANN, A. & ELLIOT, D. H. (1993) Potassium-argon dating of fine-grained basalts with massive Ar loss: Application of the 40Ar39Ar technique to plagioclase and glass from the Kirkpatrick Basalt, Antarctica. Chemical Geology, 107, 173-190.

FOULGER, G. R. (2002) Plumes, or plate tectonic processes? Astronomy & Geophysics, 43, 6.19-6.24.

FRIDLEIFSSON, I. B. (1973) Petrology and structure of the Esja Quaternary volcanic region, southwest Iceland,. Oxford.

FULLER, R.E.(1931) The aqueous chilling of basaltic lava on the Columbia River Plateau: American Journal of Science, v. 21, p. 281-300.

GALE, N. H., MOORBATH, S., SIMONS, J. & WALKER, G. P. L. (1966) KAr ages of acid intrusive rocks from Iceland. Earth and Planetary Science Letters, 1, 284-288.

GATHORNE-HARDY, F. J., ERLENDSSON, E., LANGDON, P. G. & EDWARDS, K. J. (2009) Lake sediment evidence for late Holocene climate change and landscape erosion in western Iceland. Journal of Paleolimnology, 42, 413-426.

GEIRSDOTTIR, A. & EIRIKSSON, J. (1996) A review of studies of the earliest glaciation of Iceland. Terra Nova, 8, 400-414.

GEIRSDOTTIR, A., HARDARDOTTIR, J. & SVEINBJORNSDOTTIR, Ã. E. (2000) Glacial extent and catastrophic meltwater events during the deglaciation of Southern Iceland. Quaternary Science Reviews, 19, 1749-1761.

GEIRSDÓTTIR, A., MILLER, G.H., ANDREWS, J.T. (2007) Glaciation, erosion, and landscape evolution of Iceland. Journal of geodynamics, 43, 170.

GEIRSDÓTTIR, Á., MILLER, G., THORDARSON, T. & ÓLAFSDÓTTIR, K. (2009) A 2000 year record of climate variations reconstructed from Haukadalsvatn, West Iceland. Journal of Paleolimnology, 41, 95-115.

GIBBARD, P. L. A. C., KIM, M (2008) Global chronostratigraphical correlation table forthe last 2.7 million years. Episodes, 31, 243-247.

GONNERMANN, H. M. & MANGA, M. (2003) Explosive volcanism may not be an inevitable consequence of magma fragmentation. Nature, 426, 432-435.

GOTO, Y. & TSUCHIYA, N. (2004) Morphology and growth style of a Miocene submarine dacite lava dome at Atsumi, northeast Japan. Journal of Volcanology and Geothermal Research, 134, 255-275.

GRÖNVOLD, K. P. D. T. (1972) Structural and petrochemical studies in the. Kerlingarfjöll region, central Iceland. Oxford.

GUDMUNDSSON, M. T., PALSSON, F., BJORNSSON, H. & HOGNADOTTIR, T. (2002) The hyaloclastite ridge formed in the subglacial 1996 eruption in Gjalp, Vatnajokull, Iceland: present day shape and future preservation. Volcano-Ice Interaction on Earth & Mars, Special Publication, Geological Society 319-336.

GUDMUNDSSON, M. T., SIGMUNDSSON, F. & BJORNSSON, H. (1997) Ice-volcano interaction of the 1996 Gjalp subglacial eruption, Vatnajokull, Iceland. Nature, 389, 954-957.

GUILLOU, H., VAN VLIET-LANOË, B., GUMUNDSSON, A. & NOMADE, S. (2010) New unspiked K-Ar ages of Quaternary sub-glacial and sub-aerial volcanic activity in Iceland. Quaternary Geochronology.

GUNNARSSON, B., MARSH, B. D. & TAYLOR, H. P. (1998) Generation of Icelandic rhyolites: silicic lavas from the Torfajökull central volcano. Journal of Volcanology and Geothermal Research, 83, 1-45.

HALL, K. (1982) Rapid deglaciation as an initiator of volcanic activity: An hypothesis. Earth Surface Processes and Landforms, 7, 45-51.

HARDARSON, B. S., FITTON, J. G., ELLAM, R. M. & PRINGLE, M. S. (1997) Rift relocation - a geochemical and geochronological investigation of a palaeo-rift in northwest Iceland. Earth and Planetary Science Letters, 153, 181-196.

HARDS, V. L., KEMPTON, P. D., THOMPSON, R. N. & GREENWOOD, P. B. (2000) The magmatic evolution of the Snæfell volcano; an example of volcanism during incipient rifting in Iceland? Journal of Volcanology and Geothermal Research, 99, 97-121.

HEIKEN, G. & WOHLETZ, K. (1985) Volcanic Ash, Berkeley, University of California Press.

HELGASON, J. & DUNCAN, R. A. (2001) Glacial-interglacial history of the Skaftafell region, southeast Iceland, 0-5 Ma. Geology, 29, 179-182.

HELGASON, J. (2007) Bedrock Geology of Skaftafell. Reykjavik, Gutenberg Hf.
HOLBROOK, W. S., LARSEN, H. C., KORENAGA, J., DAHL-JENSEN, T., REID, I. D., KELEMEN, P. B., HOPPER, J. R., KENT, G. M., LIZARRALDE, D., BERNSTEIN, S. & DETRICK, R. S. (2001) Mantle thermal structure and active upwelling during continental breakup in the North Atlantic. Earth and Planetary Science Letters, 190, 251-266.

HJARTARSON, A. & INGOLFSSON, O. (1988) Preboreal glaciation of Southern Iceland. Jökull, 38, 1–13.

HORA, J., SINGER, B., JICHA, B., BEARD, B., JOHNSON, C. & DE SILVA, S. (2010) Volcanic biotite-sanidine Ar-40/Ar-39 age discordances reflect Ar partitioning and pre-eruption closure in biotite. Geology, 38, 923-926.

HÖSKULDSSON, A. & SPARKS, R. S. J. (1997) Thermodynamics and fluid dynamics of effusive subglacial eruptions. Bulletin of Volcanology, 59, 219-230.

HÖSKULDSSON, A., SPARKS, R. & CARROLL, M. (2006) Constraints on the dynamics of subglacial basalt eruptions from geological and geochemical observations at Kverkfjöll, NE-Iceland. Bulletin of Volcanology, 68, 689-701.

HUBBARD, A., SUGDEN, D., DUGMORE, A., NORDDAHL, H. & PETURSSON, H. R. G. (2006) A modelling insight into the Icelandic Last Glacial Maximum ice sheet. Quaternary Science Reviews, 25, 2283-2296.

INGÓLFSSON, Ó., BJÖRCK, S., HAFLIDASON, H. & RUNDGREN, M. (1997) Glacial and climatic events in iceland reflecting regional north atlantic climatic shifts during the Pleistocene-Holocene transition. Quaternary Science Reviews, 16, 1135-1144.

INGÓLFSSON, Ó., NORDDAHL, H., SCHOMACKER, A. (2010) Deglaciation and Holocene Glacial History of Iceland. Developments in Quaternary Sciences, Volume 13, chapter 4, 51-69Elesevier

JOHNSON, D.M., HOOPER P.R., & CONREY, R.M., (1999) XRF Analysis of Rocks and Minerals for Major and Trace Elements on a Single Low Dilution Li-tetraborate Fused Bead. Advances in X-ray Analysis, vol 41, 843-867.

JONASSON, K. (2007) Silicic volcanism in Iceland: Composition and distribution within the active volcanic zones. Journal of Geodynamics, 43, 101-117.

JONES, J. G. (1969) Intraglacial volcanoes of the Laugarvatn region, southwest Iceland I. Quarterley Journal of the Geological Society of London, 124 (1969), 197–211.

JONES, J. G. (1970) Intraglacial volcanoes of the Laugarvatn region, southwest Iceland II. Journal of Geology, 78, 127-140.

KANEOKA, I., 1980. Rare-gas isotopes and mass fractionation – an indicator or gas transport into or from a magma. Earth and Planetary Science Letters 48, 284–292.

KANEOKA, I. (1994) The effect of water on noble gas signatures of volcanic materials. IN MATSUDA, J. (Ed.) Noble Gas Geochemistry and Cosmochemistry. Terra Scientific.

KELMAN, M. C., RUSSELL, J.K., AND HICKSON, C.K. (2002) Effusive intermediate glaciovolcanism in the Garibaldi volcanic belt, southwestern British Columbia, Canada. IN CHAPMAN, J. L. S. A. M. G. (Ed.) Volcano–ice Interaction on Earth and Mars. Geological Society, London.

KELLEY, S. (2002) Excess argon in K-Ar and Ar-Ar geochronology. Chemical Geology, 188, 1-22.

KETTLEBOROUGH, C. F. (1972) Transient laminar free convection between heated and vertical plates including entrance effects. . International Journal of Heat and Mass Transfer, 15, pp. 883-896.

KEYS, H. (2007) Lahars of Ruapehu Volcano, New Zealand: risk mitigation. Annals of Glaciology, 45, 155-162.

KILGOUR, G., MANVILLE, V., DELLA PASQUA, F., GRAETTINGER, A., HODGSON, K. A. & JOLLY, G. E. (2010) The 25 September 2007 eruption of Mount Ruapehu, New Zealand: Directed ballistics, surtseyan jets, and ice-slurry lahars. Journal of Volcanology and Geothermal Research, 191, 1-14.

KIRKBRIDE, M. P., DUGMORE, A. J. & BRAZIER, V. (2006) Radiocarbon dating of mid-Holocene megaflood deposits in the Jokulsa a Fjollum, north Iceland. The Holocene, 16, 605-609.

KJARTANSSON, G. (1943) Arnesingasaga. Arnesingafelagid, Reykjavik, 268 pp.

KLEIVEN, H., JANSEN, E., FRONVAL, T. & SMITH, T. M. (2002) Intensification of Northern Hemisphere glaciations in the circum Atlantic region (3.5-2.4 Ma) - ice-rafted detritus evidence. Palaeogeography, Palaeoclimatology, Palaeoecology, 184, 213-223.

KLEIVEN, H., JANSEN, E., FRONVAL, T. & SMITH, T. M. (2002) Intensification of Northern Hemisphere glaciations in the circum Atlantic region (3.5-2.4 Ma) - ice-rafted detritus evidence. Palaeogeography, Palaeoclimatology, Palaeoecology, 184, 213-223.

KRUMMENACHER, D. (1970) Isotopic composition of argon in modern surface volcanic rocks. Earth and Planetary Science Letters, 8, 109-117.

KOBAYASHI, N., SHIBATA, A. & YAMAMOTO, I. (1996) Numerical solution of argon 36-38-40 concetration profiles within thermal diffusion columns. Journal of Nuclear Science and Technology, 33, pp.781-786.

LACASSE, C. & GARBE-SCHÖNBERG, C. D. (2001) Explosive silicic volcanism in Iceland and the Jan Mayen area during the last 6 Ma: sources and timing of major eruptions. Journal of Volcanology and Geothermal Research, 107, 113-147.

LACASSE, C., SIGURDSSON, H., CAREY, S., JÓHANNESSON, H., THOMAS, L. & ROGERS, N. (2007) Bimodal volcanism at the Katla subglacial caldera, Iceland: insight into the geochemistry and petrogenesis of rhyolitic magmas. Bulletin of Volcanology, 69, 373-399.

LAMBECK, K., ESAT, T. M. & POTTER, E.-K. (2002) Links between climate and sea levels for the past three million years. Nature, 419, 199-206.

LANPHERE, M., CHAMPION, D., MELLUSO, L., MORRA, V., PERROTTA, A., SCARPATI, C., TEDESCO, D. & CALVERT, A. (2007) 40Ar/39Ar ages of the AD 79 eruption of Vesuvius, Italy. Bulletin of Volcanology, 69, 259-263.

LARSEN, G., EIRIKSSON, J., KNUDSEN, K. L. & HEINEMEIER, J. (2002) Correlation of late Holocene terrestrial and marine tephra markers, north Iceland: implications for reservoir age changes. Polar Research, 21, 283-290.

LEE, J.-Y., MARTI, K., SEVERINGHAUS, J. P., KAWAMURA, K., YOO, H.-S., LEE, J. B. & KIM, J. S. (2006) A redetermination of the isotopic abundances of atmospheric Ar. Geochimica et Cosmochimica Acta, 70, 4507-4512.

LEMASURIER, W. E. (2002) Achitecture and evolution of hydrovolcanic deltas in Marie Byrd Land, Antarctica. IN SMELLIE, J. L. C., M.G (Ed.) Volcano-Ice interaction on Earth and Mars. London, Geological Society

LESCINSKY, D. T. & FINK, J. H. (2000) Lava and ice interaction at stratovolcanoes: Use of characteristic features to determine past glacial extents and future volcanic hazards. J. Geophys. Res., 105(B10), 23,711–23,726.

LESCINSKY, D. T. & SISSON, T. W. (1998) Ridge-forming, ice-bounded lava flows at Mount Rainier, Washington. Geology, 26, 351-354.

LISIECKI, L. E. & RAYMO, M. E. (2005) A Pliocene-Pleistocene stack of 57 globally distributed benthic Î´18O records. Paleoceanography, 20.

LOUGHLIN, S. C. (2002) Facies analyis of proximal subglacial and proglacial volcaniclastic successions at the Eyjafjallajokull central volcano, southern Iceland. Volcano-Ice Interaction on Earth & Mars, Geological Society, London, 149-178.
LOWE, D. R., WILLIAMS, S. N., LEIGH, H., CONNORT, C. B., GEMMELL, J. B. & STOIBER, R. E. (1986) Lahars initiated by the 13 November 1985 eruption of Nevado del Ruiz, Colombia. Nature, 324, 51-53.

LUDWIG, K.R., 2003 Using Isoplot/Ex, Version 3.00: A geochronological toolkit for Microsoft Excel. Berkeley Geochronology Center Special Publication.

MACDONALD, R., D. W. MCGARVIE, H. PINKERTON, R. L. SMITH, AND Z. A. PALACZ (1990) Petrogenetic evolution of the Torfajoekull volcanic complex, Iceland; 1, Relationship between the magma types. Journal of Petrology:, 31(2), 429-459.

MACLENNAN, J., JULL, M., MCKENZIE, D., SLATER, L. & GRÖNVOLD, K. (2002) The link between volcanism and deglaciation in Iceland. Geochem. Geophys. Geosyst., 3, 1062.

MANLEY, C. R. (1996) In situ formation of welded-tuff like textures in the carapace of a voluminous silicic lava flow, Owyhee County, SW Idaho. Bulletin of Volcanology, 57, 672-686.

MANLEY, C. R. & FINK, J. H. (1987) Internal textures of rhyolite flows as revealed by research drilling. Geology, 15, 549-552.

MARSH, B. D., GUNNARSSON, B., CONGDON, R. & CARMODY, R. (1991) Hawaiian basalt and Icelandic rhyolite: Indicators of differentiation and partial melting. Geologische Rundschau, 80, 481-510.

MARTI, J., SORIANO, C. & DINGWELL, D. B. (1999) Tube pumices as strain markers of the ductile-brittle transition during magma fragmentation. Nature, 402, 650-653.

MARTIN, E. & SIGMARSSON, O. (2007) Crustal thermal state and origin of silicic magma in Iceland: the case of Torfajökull, Ljósufjöll and Snæfellsjökull volcanoes. Contributions to Mineralogy and Petrology, 153, 593-605.

MARTIN, E., MARTIN, H. & SIGMARSSON, O. (2008) Could Iceland be a modern analogue for the Earth's early continental crust? Terra Nova, 20, 463-468.

MARTIN, E. & SIGMARSSON, O. (2010) Thirteen million years of silicic magma production in Iceland: Links between petrogenesis and tectonic settings. Lithos, 116, 129-144.

MATSUMOTO, A., KOBAYASHI, T. (1995) K–Ar age-determination of late Quaternary volcanic rocks using the mass fractionation correction procedure – application to the younger Ontake volcano, Central Japan. Chemical Geology 125, 123–135.

MATTHEWS, W. H. (1951) The Table, a flat-topped volcano in southern British Columbia. Am J Sci, 249, 830-841.

MATTHEWS, W. H. (1947) 'Tuyas', Flat-topped volcanoes in Northern British Columbia. Am. Jour. Sci, 245, 560-570.

MCDOUGALL, I. & HARRISON, M. T. (1999) Geochonology and Thermochronology by the 40Ar/39Ar Method. pp.267.

MCDOUGALL, I., SAEMUNDSSON, K., JOHANNESSON, H., WATKINS, N. D. & KRISTJANSSON, L. (1977) EXTENSION OF GEOMAGNETIC POLARITY TIME SCALE TO 6.5 MY - K-AR DATING, GEOLOGICAL AND PALEOMAGNETIC STUDY OF A 3,500-M LAVA SUCCESSION IN WESTERN ICELAND. Geological Society of America Bulletin, 88, 1-15.

MCGARVIE, D. W. (1984) Torfajokull: A volcano dominated by magma mixing. Geology, 12, 685-688.

MCGARVIE, D. W., MACDONALD, R., PINKERTON, H. & SMITH, R. L. (1990) Petrogenetic Evolution of the Torfajokull Volcanic Complex, Iceland II. The Role of Magma Mixing. Journal of Petrology, 31, 461-481.

MCGARVIE, D. W., BURGESS, R., TINDLE, A. G. & TUFFEN, H. (2006) Pleistocene rhyolitic volcanism at Torfajokull, Iceland: eruption ages, glaciovolcansim and geochemical evolution. Jokull, 56, 57-75.

MCGARVIE, D. W., STEVENSON, J. A., BURGESS, R.; TUFFEN, H.; TINDLE, A.G. (2007) Volcanoice interactions at Prestahnukur, Iceland: rhyolite eruption during the last interglacialglacial transition. Annals of Glaciology, 45, 38-47.

MCGARVIE, D. (2009) Rhyolitic volcano-ice interactions in Iceland. Journal of Volcanology and Geothermal Research, 185, 367-389.

MEE, K., TUFFEN, H. & GILBERT, J. (2006) Snow-contact volcanic facies and their use in determining past eruptive environments at Nevados de Chillán volcano, Chile. Bulletin of Volcanology, 68, 363-376.

MERRIHUE, C. & TURNER, G. (1966) Potassium-Argon dating by activation with fast neutrons. J. Geophys. Res., 71, 2852-2857.

MIHALFFY, P., STEINBERGER, B. & SCHMELING, H. (2008) The effect of the large-scale mantle flow field on the Iceland hotspot track. Tectonophysics, 447, 5-18.

MITCHELL, J. G. (1968) The method for potassium-argon age determination. Geochimica et Cosmochimica Acta, 32, 781-790.

MITTELSTAEDT, E., ITO, G. & VAN HUNEN, J. (2011) Repeat ridge jumps associated with plume-ridge interaction, melt transport, and ridge migration. Journal of Geophysical Research-Solid Earth, 116, 20.

MORGAN, L. E., RENNE, P. R., TAYLOR, R. E. & WOLDEGABRIEL, G. (2009) Archaeological age constraints from extrusion ages of obsidian: Examples from the Middle Awash, Ethiopia. Quaternary Geochronology, 4, 193-203.

NIELSEN, N. (1937) A volcano under an ice-cap. Vatnajökull, Iceland, 1934-36. The Geographical Journal, 90.

NOMADE, S., RENNE, P. R., VOGEL, N., DEINO, A. L., SHARP, W. D., BECKER, T. A., JAOUNI, A. R. & MUNDIL, R. (2005) Alder Creek sanidine (ACs-2): A Quaternary Ar-40/Ar-39 dating standard tied to the Cobb Mountain geomagnetic event. Chemical Geology, 218, 315-338.

NORDDAHL, H. & EINARSSON, T. (2001) Concurrent changes of relative sea-level and glacier extent at the Weichselian-Holocene boundary in Berufjordur, Eastern Iceland. Quaternary Science Reviews, 20, 1607-1622.

OSKARSSON, N., STEINTHORSSON, S. & SIGVALDASON, G. E. (1985) Iceland Geochemical Anomaly: Origin, Volcanotectonics, Chemical Fractionation and Isotope Evolution of the Crust. J. Geophys. Res., 90.

OZAWA, A., TAGAMI, T., KAMATA, H. (2006) Argon isotopic composition of some Hawaiian historical lavas. Chemical Geology 226, 66–72.

PETIT, J. R., JOUZEL, J., RAYNAUD, D., BARKOV, N. I., BARNOLA, J. M., BASILE, I., BENDER, M., CHAPPELLAZ, J., DAVIS, M., DELAYGUE, G., DELMOTTE, M., KOTLYAKOV, V. M., LEGRAND, M., LIPENKOV, V. Y., LORIUS, C., PEPIN, L., RITZ, C., SALTZMAN, E. & STIEVENARD, M. (1999) Climate and atmospheric history of the past 420,000 years from the Vostok ice core, Antarctica. Nature, 399, 429-436.

PRESTVIK, T. (1979) Geology of the Öræfi District, S.E. Iceland. 79 01, Nordic Volcanological Institute, Reykjavik

PRESTVIK, T. (1980) Petrology of hybrid intermediate and silicic rocks from Öræfajökull, southeast Iceland. Geologiska Foereningan i Stockholm. Foerhandlingar, 101, 299-307

PRESTVIK, T. (1982) Petrography, chemical characteristics and nomenclature of Öræfajökull rocks. Jökull, 32, 69-76.

PRESTVIK, T. (1985) Petrology of Quaternary volcanic rocks from Öræfi, southeast Iceland. Rep. Dept. Geol. Univ. Trondheim (Norway), 21, 81.

PRESTVIK, T., GOLDBERG, S., KARLSSON, H. & GRÖNVOLD, K. (2001) Anomalous strontium and lead isotope signatures in the off-rift Öræfajökull central volcano in south-east Iceland : Evidence for enriched endmember(s) of the Iceland mantle plume? Earth and Planetary Science Letters, 190, 211-220.

RAVELO, A. C. (2010) Palaeoclimate: Warmth and glaciation. Nature Geosci, 3, 672-674.

RENNE, P. R., SHARP, W. D., DEINO, A. L., ORSI, G. & CIVETTA, L. (1997) 40Ar/39Ar Dating into the Historical Realm: Calibration Against Pliny the Younger. Science, 277, 1279-1280.

ROSE, J., WHITEMAN, C.A., LEE, J., BRANCH, N.P., HARKNESS, D.D., WALDEN, J. (1997) Mid- and late-Holocene vegetation, surface weathering and glaciation, Fjallsjökull, southeast Iceland. The Holocene, vol. 7, 4: pp. 457-471.

RUZIÉ, L. & MOREIRA, M. (2010) Magma degassing process during Plinian eruptions. Journal of Volcanology and Geothermal Research, 192, 142-150.

SAEMUNDSSON, K. (1972) Notes on the geology of the Torfajökull central volcano. Natturufraedingnum, 42, pp. 81–99.

SAEMUNDSSON, K., KRISTJANSSON, L., MCDOUGALL, I. & WATKINS, N. D. (1980) k-ar dating, geological and paleomagnetic study of a 5-km lava succession in northern iceland. journal of geophysical research, 85, 3628-3646.

SARNTHEIN, M., BARTOLI, G., PRANGE, M., SCHMITTNER, A., SCHNEIDER, B., WEINELT, M., ANDERSEN, N. & GARBE-SCHÖNBERG, D. (2009) Mid-Pliocene shifts in ocean overturning circulation and the onset of Quaternary-style climates. Clim. Past, 5.

SCHOPKA, H. H., GUDMUNDSSON, M. T. & TUFFEN, H. (2006) The formation of Helgafell, southwest Iceland, a monogenetic subglacial hyaloclastite ridge: Sedimentology, hydrology and volcano-ice interaction. Journal of Volcanology and Geothermal Research, 152, 359-377

SEIDENKRANTZ, M.-S., BORNMALM, L., JOHNSEN, S. J., KNUDSEN, K. L., KUIJPERS, A., LAURITZEN, S.-E., LEROY, S. A. G., MERGEAL, I., SCHWEGER, C. & VAN VLIET-LANOË, B. (1996) Two-step deglaciation at the oxygen isotope stage 6/5E transition: The Zeifen-Kattegat climate oscillation. Quaternary Science Reviews, 15, 63-75.

SIGMUNDSSON, F. (1991) Post-glacial rebound and asthenosphere viscosity in Iceland. Geophysical Research Letters, 18, 1131-1134.

SKILLING, I. P. (1994) Evolution of an englacial volcano: Brown Bluff, Antarctica. Bulletin of Volcanology, 56, 573-591.

SKILLING, I. P. (2002) Basaltic pahoehoe lava-fed deltas: large-scale characteristics, clast generation, emplacement processes and environmental discrimination. IN CHAPMAN, J. L. S. M. G. (Ed.) Volcano-Ice interaction on Earth and Mars. The Geological Society.

SMELLIE, J. L. (2001a) Lithofacies architecture and construction of volcanoes erutped in englacial lakes: Icefall Nunatak, Mount Murphy, eastern Marie Byrd Land, Antarctica. Antarctica. Spec. Publs. int. Ass. Sediment, 30, 9-34.

SMELLIE, J. L. (2008) Basaltic subglacial sheet-like sequences: Evidence for two types with different implications for the inferred thickness of associated ice. Earth-Science Reviews, 88, 60-88.

SMELLIE, J. L., HOLE, M. J., NELL. P.A.R. (1993) Late Miocene valley-confined subglacial volcanism in northern Alexander Island, Antarctic Peninsula. Bulletin of Volcanology, 55, Number 4, 273-288

SMELLIE, J. L. & SKILLING, I. P. (1994) Products of subglacial volcanic eruptions under different ice thicknesses: two examples from Antarctica. Sedimentary Geology, 91, 115-129.

SMELLIE, J. L. & HOLE, M. J. (1997) Products and processes in Pliocene–Recent, subaqueous to emergent volcanism in the Antarctic Peninsula: examples of englacial Surtseyan volcano construction. Bulletin of Volcanology, 58, 628-646.

SMELLIE, J. L., MCINTOSH, W. C. & ESSER, R. (2006) Eruptive environment of volcanism on Brabant Island: Evidence for thin wet-based ice in northern Antarctic Peninsula during the Late Quaternary. Palaeogeography, Palaeoclimatology, Palaeoecology, 231, 233-252.

SMELLIE, J.L., ROCCHI, S. & ARMIENTI, P (2011) Late Miocene volcanic sequences in northern Victoria Land, Antarctica: products of glaciovolcanic eruptions under different thermal regimes. Bulletin of Volcanology, 73, 1-25.

SMITH, J. V. & HOUSTON, E. C. (1994) Folds produced by gravity spreading of a banded rhyolite flow. Journal of Volcanology & Geothermal Research, 63, 89-94.

STEIGER, R. H. & JÃ¤GER, E. (1977) Subcommission on geochronology: Convention on the use of decay constants in geo- and cosmochronology. Earth and Planetary Science Letters, 36, 359-362.

STEVENSON, J. (2004) Volcano - ice interaction at Oraefajokull and Kerlingarfjoll, Iceland. PhD thesis, Earth Sciences. Lancaster, the Open University, 330 pp.

STEVENSON, J., MCGARVIE, D., SMELLIE, J. & GILBERT, J. (2006) Subglacial and ice-contact volcanism at the Öræfajökull stratovolcano, Iceland. Bulletin of Volcanology, 68, 737-752.

STEVENSON, J. A., SMELLIE, J. L., MCGARVIE, D. W., GILBERT, J. S. & CAMERON, B. I. (2009) Subglacial intermediate volcanism at Kerlingarfjöll, Iceland: Magma-water interactions beneath thick ice. Journal of Volcanology and Geothermal Research, 185, 337-351.

STEVENSON, J. A., GILBERT, J. S., MCGARVIE, D. W. & SMELLIE, J. L. (2011) Explosive rhyolite tuya formation: classic examples from Kerlingarfjöll, Iceland. Quaternary Science Reviews, 30, 192-209.

SUMINO, H., IKEHATA, K., SHIMIZU, A., NAGAO, K. & NAKADA, S. (2008) Magmatic processes of Unzen volcano revealed by excess argon distribution in zero-age plagioclase phenocrysts. Journal of Volcanology and Geothermal Research, 175, 189-207.

SVENSSON, A., NIELSEN, S. W., KIPFSTUHL, S., JOHNSEN, S. J., STEFFENSEN, J. P., BIGLER, M., RUTH, U. & ROTHLISBERGER, R. (2005) Visual stratigraphy of the North Greenland Ice Core Project (NorthGRIP) ice core during the last glacial period. Journal of Geophysical Research, 110, D02108.

THORARINSSON, S. (1958) The Öræfajökull Eruption of 1362. Acta Naturalia Islandica, II (2).

THORDARSSON, T., & HOSKULDSSON, A. (2002) Iceland, Terra Publishing.

TORSVIK, T. H., MOSAR, J. & EIDE, E. A. (2001) Cretaceous–Tertiary geodynamics: a North Atlantic exercise. Geophysical Journal International, 146, 850-866.

TUFFEN, H. (2001) Subglacial Rhyolite Volcanism at Torfajökull, Iceland. Environmental Science. Lancaster.

TUFFEN, H., GILBERT, J. & MCGARVIE, D. (2001) Products of an effusive subglacial rhyolite eruption: Bláhnúkur, Torfajökull, Iceland. Bulletin of Volcanology, 63, 179-190.

TUFFEN, H., MCGARVIE, D. W., GILBERT, J. & PINKERTON, H. (2002b) Physical volcanology of a subglacial to emergent rhyolitic tuya ar Raudufossafjoll, Torfajokull, Iceland. IN SMELLIE, J. L. & CHAPMAN, M. G. (Eds.) Volcano-Ice Interaction on Earth and Mars. London, Geological Society Special Publication No.202.

TUFFEN, H., PINKERTON, H., MCGARVIE, D. W. & GILBERT, J. S. (2002a-b) Melting of the glacier base during a small-volume subglacial rhyolite eruption: evidence from Bláhnúkur, Iceland. Sedimentary Geology, 149, 183-198.

TUFFEN, H., DINGWELL, D. B. & PINKERTON, H. (2003) Repeated fracture and healing of silicic magma generate flow banding and earthquakes? Geology, 31, 1089-1092.

TUFFEN, H., MCGARVIE, D., PINKERTON, H., GILBERT, J. & BROOKER, R. (2008) An explosive–intrusive subglacial rhyolite eruption at Dalakvísl, Torfajökull, Iceland. Bulletin of Volcanology, 70, 841-860.

TUFFEN, H., OWEN, J. & DENTON, J. (2010) Magma degassing during subglacial eruptions and its use to reconstruct palaeo-ice thicknesses. Earth-Science Reviews, 99, 1-18.

TURNER, G. (1971) Argon 40-argon 39 dating: the optimization of irradiation parameters. Earth and Planetary Science Letters, 10, 227-234.

UDAGAWA, S., KITAGAWA, H., GUDMUNDSSON, A., HIROI, O., KOYAGUCHI, T., TANAKA, H., KRISTJANSSON, L. AND KONO, M. (1999) Age and magnetism of lavas in Jökuldalur area, Eastern Iceland: Gilsá event revisited. Physics of the Earth and Planetary Interiors 115, 147-171.

VOIGHT, B. (1990) The 1985 Nevado del Ruiz volcano catastrophe: anatomy and retrospection. Journal of Volcanology and Geothermal Research, 44, 349-386.

VOGEL, N., NOMADE, S., NEGASH, A. & RENNE, P. R. (2006) Forensic 40Ar/39Ar dating: a provenance study of Middle Stone Age obsidian artifacts from Ethiopia. Journal of Archaeological Science, 33, 1749-1765.

WALKER, G. P. L. (1960) Zeolite Zones and Dike Distribution in Relation to the Structure of the Basalts of Eastern Iceland. The Journal of Geology, 68, 515-528.

WAYTHOMAS, C. F. (2010) Glacier Destruction and Lahar Generation during the 2009 Eruption of Redoubt Volcano, Alaska. American Geophysical Union, Fall Meeting 2010.

WHITE, R. S. (1997) Rift - plume interaction in the North Atlantic. Philosophical Transactions of the Royal Society of London. Series A:
Mathematical, Physical and Engineering Sciences, 355, 319-339.

WILSON, L. & HEAD, J. W. (2002) Heat transfer and melting in subglacial basaltic volcanic eruptions: implications for volcanic deposit morphology and meltwater volumes. IN CHAPMAN, J. L. S. A. M. G. (Ed.) Volcano–Ice Interaction on Earth and Mars, Geol. Soc. Lond., Spec. Publ. vol. 202 (2002). London, Geol. Soc.

WILSON, C. J. N. (1980) The role of fluidization in the emplacement of pyroclastic claws: An experimental approach. Journal of Volcanology and Geothermal Research, 8, 231-249.

YAMAMOTO, I., BABA, T. & KANAGAWA, A. (1987) Measurement of sperative characteristics of thermal diffusion columns for argon isotope separation. Journal of Nuclear Science and Technology, 24, pp. 565-572.

YAMAMOTO, I., KANOH, K. & KANAGAWA, A. (1986) Effect of changes in feed rate and cut on circulating flow within thermal diffusion columns for isotope separation. Journal of Nuclear Science and Technology, 23, pp.896-904.

Appendix 1

Rock sample inventory

Sample	Rock type	collected	Area collected	map grid reference	elevation
OR03	rhyolite	2007	Goðafell West	0414133/7090557	
OR06	basalt	2007	HVG Valley Basement basalts	0414894/7089991	160m
OR08	rhyolite	2007	HVG Valley		
OR09	rhyolite	2007	Goðafjall East lower lobes		
OR10	obsidian	2007	Goðafjall Col	0415090/7090650	463m
OR12	rhyolite	2007	HVG entrance R.H.S	0414722/0789834	138m
OR13	rhyolite	2007	Goðafell East	0415826/7090585	431m
OR18	rhyolite	2007	Hrutsfjall Dyke		
OR20	basalt	2007	Godafjall A		
OR23	pumice	2007	Hrutsfjall	0415399/7091161	
OR30	rhyolite	2007	Upper Hrutsfall / Vedrastapi	0416366/7091414	754m
OR38	rhyolite	2007	Goðafjall West	0415068/7090428	356m
OR44	rhyolite	2007	Goðafjall West summit	0414877/7090666	558m
OR46	rhyolite	2007	Goðafjall West	0414765/7090380	445m
OR49	rhyolite	2007	Hrutsfjall	0414914/7091661	433m
OR50	rhyolite	2007	HVG valley R.H.S	0415460/7090131	247m
OR54	rhyolite	2007	Cirque / HVG valley R.H.S	0415952/7090190	414m
OR55	intermediate	2007	HVG valley R.H.S	0416169/7090313	541m
OR58	rhyolite	2007			
OR59	rhyolite	2007	Kotarjokull N	0414770/7093573	806m
OR62	obsidian	2007	Rotarfjall	0415204/7092426	610m
OR100	rhyolite	30.05.08	Goðafjall W on way to col. Possible 'Scab'	0415060/7090562	415m
OR101	obsidan	30.05.08	Block removed from pumice ash breccia at top of col	0415158/7090725	481m
OR102	rhyolite	30.05.08	OR102 & 103 taken together from layered unit at top of col	0415155/7090743	483m
OR103	obsidian	30.05.08		0415155/7090743	483m
OR104	rhyolite		Patchy exposure on front of Goðafjall West	0414702/7090669	500m
OR105	basement	30.05.08	Basement rocks with zeolites from exposure on Goðafjall West	0415147/7090312	
OR106	glassy rhyolite	31.05.08	Base of flow at Hrutsfjall	0414863/7091616	426m
OR107	glassy rhyolite	01.06.08	Slaga north. REPLACED BY OR317		

OR108		01.06.08	Slaga north. Tillite horizon under basalt flow at top of valley	0414280/7092492	393m
OR109		01.06.08	Slaga north. Tillite horizon under basalt flow at top of valley	0414280/7092492	393m
OR110	basalt	01.06.08	Slaga north. Basalt columar joints on top of turret	0414295/7092406	405m
OR111	glassy rhyolite	01.06.08	Slaga north. Rhyolite exposed on north face of turret below basalts	0414312/7092358	377m
OR112	glassy intermediate	01.06.08	Slaga south. Lava lobes flowing downslope into valley	0414433/7092062	
OR113	sedimentary	01.06.08	Slaga south. Layered sedimentary structure below hyaloclastite	0414277/7091962	330m
OR114	glassy vesicular	01.06.08	Slaga south. Lobe with feldspar phenocrysts. Possible intrusion	0414088/7091629	239m
OR115	pumice	02.06.08	pumice ash breccia exposure on HGV south face	0414989/7089780	
OR116	basalt	06.06.08	Slaga north. Basalt exposure on top of north slope	0413143/7091660	
OR117	basalt	06.06.08	Slaga north. Basalt intrusions - contact with 'A'	0413094/7091501	148m
OR130	glassy rhyolite	03.06.08	N.E of Hruts. West of col above Batman plain	0415435/7091379	
OR131	microcryst. rhyolite	03.06.08	N.E of Hruts.	0415667/7091506	
OR132	obsidian	03.06.08	N.E of Hruts. lobe margin on ridge crest	0415881/7091602	
OR133	obsidian	03.06.08	N.E of Hruts. margin of lobe on top of large buttress	0415997/7091846	
OR134	basalt	03.06.08	N.E of Hruts. flow lobe	0416263/7092052	
OR135	bomb exterior	03.06.08	N.E of Hruts.	0410846/7091454	
OR136	pumice	03.06.08	N.E of Hruts.	0410846/7091454	
OR137	microcryst. rhyolite	05.06.08	Kvisker. Front of large buttress	0428976/7094418	
OR138	glassy rhyolite	05.06.08	Kvisker.	0428976/7094418	
OR139	glassy rhyolite	05.06.08	Kvisker. Farthest point upstream	0427740/7093777	
OR140			Stadharfjall.	RB & DM collected	
OR141			Stadharfjall.	RB & DM collected	
OR142			Stadharfjall.	RB & DM collected	
OR143			Stadharfjall.	RB & DM collected	
OR144			Stadharfjall.	RB & DM collected	
OR145			Stadharfjall.	RB & DM collected	
OR146			Stadharfjall.	RB & DM collected	
OR147			Stadharfjall.	RB & DM collected	
OR148			Stadharfjall.	RB & DM collected	
OR150	glassy rhyolite	07.06.08	Valley above Höf.	0415836/7088905	264m

OR151	rhyolite	08.06.08	Kotárjoküll N.E (Dave collected)		
OR152	rhyolite	09.06.08	Slaga south (river level)	0413663/7090903	151m
OR153	obsidian	09.06.08	Goð W	0414223/7091024	220m
OR154	glassy rhyolite	10.06.08	Kristinartindar	0405973/7105878	943m
OR155	microcryst. rhyolite	10.06.08	Kristinartindar	0405973/7105878	943m
OR160	rhyolite		HVG roadside	0415411/7089586	420m
0R161	microcryst. rhyolite	11.06.08	HVG	0415599/7089852	
OR162	rhyolite	11.06.08	HVG	0415117/7089866	242m
OR163	basalt scoria	12.06.08	Sandfell	0414655/7094697	963m
OR164	rhyolite	12.06.08	Sandfell	0414623/7094977	975m
OR165	microcryst. rhyolite	12.06.08	Sandfell		
OR166	obsidian	12.06.08	Sandfell		
OR167	brecciated rhyolite	12.06.08	Sandfell	0414510/7095170	
OR168	rhyolite	12.06.08	Sandfell (lower exposure)	0413067/7093493	497m
OR200	rhyolite	15.06.08	HVG entrance	0414855/7089690	
OR201	ash	16.06.08	HVG roadside	0414872/7089568	133m
OR202	obsidian	16.06.08	HVG	0415260/7089580	289m
OR203	rhyolite	17.06.08	HVG	0415200/7089941	223m
OR204	dyke	17.06.08	HVG		244m
OR205	dyke	17.06.08	HVG		
OR206		17.06.08	HVG		
OR207	rhyolite	17.06.08	HVG	0415404/7089953	302m
OR208	microcryst. rhyolite	18.06.08	HVG valley top	0416163/7091040	
OR209		18.06.08	HVG valley top	0416177/7090996	581m
OR210	basalt	18.06.08	HVG valley top	0416192/7090992	
OR211	glassy rhyolite	18.06.08	HVG valley top	0416399/7091204	642m
OR212	glassy rhyolite	18.06.08	HVG valley top	0416455/7091398	691m
OR213	glassy rhyolite	18.06.08	HVG valley top	0416447/7091520	732m
OR214	ash	18.06.08	HVG valley top	0416084/7091097	553m
OR215	rhyolite	19.06.08	Hrùtsfjall	0414717/7091323	329m

OR216	rhyolite	19.06.08	Hrùtsfjall	0414715/7091218	408m
OR217	vesicular rhyolite	19.06.08	Hrùtsfjall	0414794/7091202	393m
OR218	rhyolite	19.06.08	Hrùtsfjall	0414809/7091182	384m
OR219	glassy rhyolite	19.06.08	Hrùtsfell (end of field book 1)	0414858/7091200	407m
OR220	rhyolite	25.06.08	Riverbank exposure below Goðafjall West (field book 2)	0413685/7090944	130m
OR221	obsidian	25.06.08	Riverbank exposure below Goðafjall West	0413728/7090958	130m
OR222	vesicular basalt	25.06.08	Riverbank exposure below Goðafjall West	0414050/7091187	154m
OR223	intermediate	26.06.08	Cube jointed exposure below Goðafell West	0414011/7090975	
OR224	rhyolite	26.06.08	Goðafjall West Cliffs	0414244/7090673	259m
OR225	rhyolite	26.06.08	Goðafjall West Cliffs	0414117/7090520	156m
OR226	rhyolite	26.06.08	Goðafjall West Cliffs	0414257/7090243	149m
OR227	basalt	26.06.08	Goðafjall West	0414718/7090070	
OR228	rhyolite	27.06.08	Goðafjall West	0114648/7090208	277m
OR229	rhyolite breccia	27.06.08	Goðafjall West	0414647/7090247	300m
OR230	obsidian	27.06.08	Goðafjall West	0414762/7090215	288m
OR231	orange breccia	27.06.08	Goðafjall West	0414799/7090276	317m
OR232	rhyolite	27.06.08	Goðafjall West	0414862/7090249	349m
OR233	rhyolite	27.06.08	Goðafjall West	0415015/7090371	358m
OR234	ash breccia	27.06.08	Goðafjall West	0415058/7090325	319m
OR235	obsidian (?)	27.06.08	Goðafjall West	0415019/7090378	
OR236	ash breccia	30.06.08	HVG Cirque	0415862/7090883	474m
OR237	glassy rhyolite	30.06.08	HVG Cirque	0415984/7090935	520m
OR238	basalt	30.06.08	Top	0416337/7090861	707m
OR239	basalt	30.06.08	Top	0416501/7091243	731m
OR240	ash breccia	30.06.08	Top	0416446/7091735	
OR241	rhyolite	30.06.08	Top	0416053/7091922	812m
OR242	basalt	30.06.08	Veðrastapi (base)	0415971/7091737	803m
OR243	rhyolite	30.06.08	Veðrastapi (base)	0415931/7091667	776m
OR244	rhyolite	30.06.08	Veðrastapi (base)	0415883/7091609	738m
OR245	rhyolite	30.06.08	HVG corrie	0415818/7091420	640m

OR246	basalt	03.07.08	Goðafjall East	0415302/7090284	
OR247	rhyolite	03.07.08	Goðafjall East	0415279/7090302	
OR248	glassy rhyolite	03.07.08	Goðafjall East	0415263/7090309	
OR249	rhyolite	03.07.08	Goðafjall West	0415067/7090579	427m
OR250	rhyolite	03.07.08	Goðafjall West	0414968/7090656	510m
OR251	rhyolite	03.07.08	Goðafjall West	0414974/7090705	537m
OR252	glassy rhyolite	03.07.08	Goðafjall West	0414836/7090836	484m
OR253	grey frothy rhyolite	03.07.08	Goðafjall West	0414927/7090524	463m
OR254	glassy rhyolite	03.07.08	Goðafjall West	0414961/7090501	441m
OR255	glassy rhyolite	03.07.08	Goðafjall West	0414943/7090519	458m
OR256	brecciated rhyolite	03.07.08	Goðafjall West	0414935/7090437	432m
OR257	rhyolite	03.07.08	Goðafjall West	0415000/7090423	391m
OR258	rhyolite	07.07.08	HVG	0415452/7090132	241m
OR259	rhyolite	07.07.08	Goðafjall East	0415599/7090471	384m
OR260	rhyolite	07.07.08	Goðafjall East	0415579/7090396	
OR261	obsidian	07.07.08	Goðafjall East	0415388/7090144	230m
OR262	platy rhyolite	08.07.08	Goðafjall West / Hrùtsfjall	0414224/7090911	
OR263	platy rhyolite	08.07.08	Goðafjall West / Hrùtsfjall	0414502/7090996	
OR264	rhyolite	08.07.08	Goðafjall West / Hrùtsfjall	0414706/7091056	
OR265	rhyolite	08.07.08	Goðafjall West / Hrùtsfjall	0414706/7091056	
OR266	rhyolite	08.07.08	Hrùtsfjall	0415171/7091120	453m
OR267	obsidian	08.07.08	Hrùtsfjall	0415231/7091064	475m
OR268	rhyolite	08.07.08	Hrùtsfjall	0415289/7091149	513m
OR269	rhyolite	09.07.08	HVG (upper)	0415955/7090870	508m
OR270	platy rhyolite	09.07.08	HVG (upper)	0416023/7090795	521m
OR280	obsidian	10.07.08	HVG (lower)	0415708/7089911	424m
OR281	trachydacite??	10.07.08	HVG (mid)	0415801/7089985	
OR282	rhyolite	10.07.08	HVG (mid)	0415897/7090088	410m
OR290	scab	13.07.08	Goðafjall West	0414499/7090857	346m
OR291	platy rhyolite	13.07.08	Goðafjall West	0414468/7090708	

OR292	platy rhyolite	13.07.08	Goðafjall West	0414511/7090450	269m
OR293	obsidian	13.07.08	Goðafell West. Dull obsidian band above cliffs		
OR294	rhyolite	14.07.08	Goðafell East		
OR295	rhyolite	14.07.08	Hrùtsfell side of cirque		
OR296	basalt	15.07.08	Hof	0415726/7089298	
OR297	rhyolite	15.07.08	Hof		
OR298	vesicular rhyolite	15.07.08	Hof		
OR299	obsidian	15.07.08	Hof	0415710/7089205	351m
OR300	rhyolite dyke	26.08.08	Hrùtsfjall	0414719/7091057	325m
OR301	glassy rhyolite	27.08.08	Hrùtsfjall	0415413/7091177	518m
OR302	pumice	27.08.08	Hrùtsfjall	0415413/7091177	
OR303	matrix	27.08.08	Hrùtsfjall	0415413/7091177	
OR304	pumice	27.08.08	Hrùtsfjall	0415413/7091177	
OR305	matrix	27.08.08	Hrùtsfjall	0415413/7091177	
OR306	matrix	27.08.08	Hrùtsfjall	0415413/7091177	
OR307	pumice	27.08.08	Hrùtsfjall	0415413/7091177	
OR308	obsidian	27.08.08	Hrùtsfjall	0415413/7091177	
OR309	matrix	27.08.08	Hrùtsfjall	0415413/7091177	508m
OR310	pumice	29.08.08	HVG roadside		
OR311	obsidian	29.08.08	HVG	0415523/7089865	404m
OR312	rhyolite	29.08.08	HVG	0415523/7089865	404m
OR313	obsidian	30.08.08	Slaga	0413837/7091913	233m
OR314	rhyolite	30.08.08	Slaga	0413837/7091913	
OR315	pumice	30.08.08	Slaga	0413837/7091913	
OR316	rhyolite	30.08.08	Slaga		
OR317	rhyolite	30.08.08	Slaga	0414254/7092106	382m
OR318	trachydacite	30.08.08	Slaga		
OR319	obsidian	31.08.08	HVG fluvial		
OR320	pumice	31.08.08	HVG fluvial		
OR321	sandstone matrix	31.08.08	HVG fluvial		

OR322	trachydacite	31.08.08	HVG top	0416107/7090920	
OR323	ash	01.09.08	Hrùtsfjall		
OR324	pumice	01.09.08	Hrùtsfjall		
OR325	pumice	01.09.08	Hrùtsfjall		
OR326	ash	01.09.08	Hrùtsfjall		
OR327	vitreous grey unit	01.09.08	Hrùtsfjall		
OR328	pumice	01.09.08	Hrùtsfjall	0414626/7091079	338m
OR329	glassy rhyolite	02.09.08	Veðrastapi - ridge	0415857/7091582	725m
OR330	perlitised obsidian	03.09.08	Col		
OR331	mud matrix	03.09.08	Col		
OR400	rhyolite	18.06.09	Scab' slope-draping outcrop on Godafell West		
OR401	rhyolite	18.06.09	Scab' slope-draping outcrop on Godafell West		
OR402	rhyolite	18.06.09	Goðafjall West	0414627/7090689	447m
OR403	rhyolite	18.06.09	Goðafjall West	0414684/7090442	441m
OR404	rhyolite	21.06.09	Hrùtsfjall	0414914/7090893	564m
OR405	rhyolite	21.06.09	Hrùtsfjall	0415277/7091400	653m
OR406	rhyolite	21.06.09	Hrùtsfjall		
OR407		21.06.09	Hrùtsfjall		
OR408	sandstone		Hrùtsfjall		
tuff 01	tuff cone		Hofsfjall		
tuff 02	tuff cone		Hofsfjall		
OR500	obsidian	18.07.09	Col		
OR501	unconsoldated	18.07.09	Col		
OR502	unconsoldated	18.07.09	Col		
OR505	obsidian breccia	19.07.09	HVG valley	0415241/7090094	
OR506	unconsolidated		Hrùtsfjall	415391/7091415	653m
OR507	sandstone		Slaga	0414598/7091880	207m
OR508	mafic (basalt?)		Hof		
OR509	basalt		Col (dug out from obsidan pods)		
OR510	obsidian /rhyolite	01.08.09	Col (dug out from obsidan pods)		

OR511	pumice ash breccia	01.08.09	Hrùtsfjall double chilled lobes	0415315/7091655	452m
OR512	pumice	01.08.09	Hrùtsfjall double chilled lobes	0415315/7091655	452m
OR513	pumice	01.08.09	Hrùtsfjall double chilled lobes	0415315/7091655	452m

Appendix 2
XRF errors and uncertainties

A2.1. Error calculations: major and trace element geochemistry

Prior to preparation for XRF analysis, in order to prevent contamination, the samples were examined by hand in order to remove as much weathering and surface alteration as possible and milled in two stages firstly with a tungsten carbide mill followed by an agate mill. The mills were washed, rinsed and thoroughly dried between each sample.

Instrumental error was calculated from Panalytical internal standards which are run alongside each of the four sample batches.

A further control on internal accuracy was carried out on sample OR213 – a Group Two rhyolite – by pressing four identical pellets and running simultaneous major and trace element analysis (table A2.1 and A2.2). The standard deviation for each element was converted into a percentage, the value of which was applied as error bars above and below the measured value of each sample analysed (figs. A2.1 - 2).

	OR213a	OR213b	OR213c	OR213d	mean	std dev	% std dev
SiO2	72.43	72.40	72.37	72.40	72.40	0.02	0.03
Al2O3	13.35	13.41	13.38	13.41	13.39	0.03	0.20
Fe2O3	2.75	2.73	2.71	2.70	2.72	0.02	0.86
MgO	0.12	0.15	0.14	0.11	0.13	0.02	15.46
CaO	0.92	0.90	0.91	0.91	0.91	0.01	1.14
Na2O	4.50	4.53	4.53	4.56	4.53	0.02	0.54
K2O	3.97	3.99	3.96	3.92	3.96	0.03	0.71
P2O5	0.02	0.02	0.02	0.02	0.02	0.00	2.57
Ti	0.12	0.12	0.12	0.12	0.12	0.00	1.63
Mn	0.06	0.06	0.06	0.06	0.06	0.00	2.53

Table A2.1: Major element internal accuracy based on sample OR213

	or213a	or213b	or213c	or213d	mean	STD dev	% STD dev
Sc	3.10	2.90	1.90	1.90	2.45	0.64	26.14
V	2.10	1.80	2.30	3.00	2.30	0.51	22.17
Cr	2.30	1.10	4.30	1.00	2.18	1.53	70.57
Co	19.20	18.50	18.70	19.50	18.98	0.46	2.41
Ni	1.60	1.60	1.60	1.40	1.55	0.10	6.45
Cu	6.80	6.10	6.10	6.10	6.28	0.35	5.58
Zn	98.50	98.70	98.90	97.10	98.30	0.82	0.83
Ga	25.70	26.00	26.30	25.40	25.85	0.39	1.50
Rb	94.00	94.50	94.60	93.10	94.05	0.69	0.73
Sr	47.20	47.30	47.30	46.50	47.08	0.39	0.82
Y	84.40	84.70	84.80	83.40	84.33	0.64	0.76
Zr	457.30	460.50	459.90	453.60	457.83	3.14	0.69
Nb	71.50	72.00	72.00	71.10	71.65	0.44	0.61
Mo	4.50	4.40	4.70	4.50	4.53	0.13	2.78
Ba	684.00	689.20	692.20	683.90	687.33	4.09	0.59
La	79.80	87.10	85.30	83.60	83.95	3.11	3.71
Ce	173.00	169.20	164.70	164.50	167.85	4.06	2.42
Nd	65.00	65.30	65.50	65.40	65.30	0.22	0.33
Sm	15.40	17.20	12.70	19.10	16.10	2.72	16.92
Yb	6.90	6.30	6.70	7.10	6.75	0.34	5.06
Pb	6.60	6.60	6.70	6.90	6.70	0.14	2.11
Th	13.20	13.10	14.00	13.70	13.50	0.42	3.14
U	3.60	3.60	3.10	3.80	3.53	0.30	8.47

Table A2.2: Trace element internal accuracy based on sample OR213

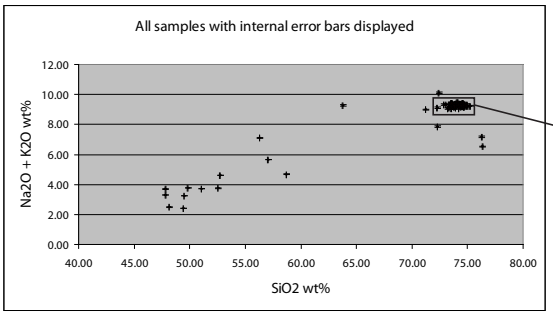

Fig. A2.1: Standard deviation of OR213 reproducibility added as error bars to all samples

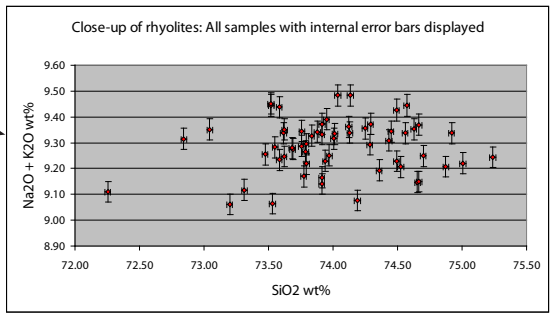

Fig. A2.2: Close-up of rhyolite cluster from Figure A3.1

A2.2. Tema mill contamination test

In order to test for tungsten carbide contamination through the use of the tema mill at the Univeristy of Manchester, two sets of pellets were prepared for two previoulsy analysed samples with powders prepared on agate mills at the open university (Stevenson, 2005).

The results below (table A2.3) indicate that Co and W contamination has occured, while the other key trace elements in this study have undergone little or no contamination.

	Sample	Co	Zn	Sr	Y	Zr	Nb	W
NEW	JS244a	96.90	94.00	62.50	73.70	436.20	63.00	792.50
OLD	JS244	2.80	88.90	57.00	73.60	435.80	62.90	3.60
NEW	JS202a	72.00	144.30	50.30	96.50	523.20	81.70	845.50
OLD	JS202	1.80	139.40	62.90	95.70	517.60	79.70	4.10

Appendix 3

Unormalised Major element data

Sample no.	OR03	OR12	OR38	OR150	OR200	OR202	OR221	OR228	OR230
location	0414119/	0414722/	0415068/	0415836/	0414855/	0415260/	0413728/	0114648/	0414762/
SiO2	73.43	73.64	73.46	73.60	73.38	73.02	73.18	73.52	73.40
Al2O3	12.99	12.90	12.97	12.96	12.75	12.97	12.82	12.94	12.96
Fe2O3	2.24	2.46	2.52	2.70	2.68	2.70	3.00	2.54	2.64
MgO	0.09	0.05	0.04	0.01	0.01	0.06	0.01	BDL	0.01
CaO	0.71	0.69	0.53	0.82	0.73	0.81	0.84	0.71	0.74
Na2O	5.30	5.20	5.28	5.16	5.09	5.09	4.96	5.35	5.23
K2O	3.95	3.91	3.91	4.13	4.15	4.11	4.43	4.07	4.09
P2O5	0.01	0.01	0.01	0.01	0.01	0.01	0.01	0.01	0.01
Ti	0.10	0.11	0.11	0.12	0.11	0.12	0.13	0.10	0.10
Mn	0.07	0.07	0.06	0.07	0.07	0.06	0.08	0.07	0.07
otal (no LOI) wt %	**98.90**	**99.03**	**98.89**	**99.57**	**98.98**	**98.95**	**99.45**	**99.30**	**99.25**
LOI total	0.75	0.66	0.81	0.00	0.72	0.67	0.27	0.30	0.36

Sample no.	or08	or09	or10	or13	or44	or49	or54	or106	or132 (a)
location	0415166/	0415166/	0415156/	0415826/	0414877/	0414914/	0415952/	0414863/	0415881/
SiO2	72.38	72.61	72.10	72.48	72.56	72.58	72.23	72.91	73.01
Al2O3	12.97	12.92	12.86	12.89	13.07	12.97	13.02	12.95	12.97
Fe2O3	2.58	2.61	2.70	2.50	2.50	2.55	2.56	2.77	2.75
MgO	0.12	0.08	0.16	0.07	0.07	0.09	0.11	0.07	0.08
CaO	0.84	0.88	0.89	0.84	0.83	0.87	0.81	0.89	0.89
Na2O	5.01	5.08	5.11	5.12	5.16	5.18	5.12	5.08	5.13
K2O	3.99	3.99	3.94	3.93	3.95	3.96	3.98	4.17	4.25
P2O5	0.03	0.02	0.02	0.02	0.02	0.02	0.02	0.02	0.02
Ti	0.13	0.13	0.14	0.12	0.12	0.12	0.12	0.12	0.13
Mn	0.07	0.07	0.07	0.06	0.06	0.06	0.06	0.07	0.07
otal (no LOI) wt %	**98.11**	**98.39**	**97.98**	**98.02**	**98.34**	**98.41**	**98.02**	**99.04**	**99.30**
LOI total	1.30	1.17	1.26	1.34	1.17	1.15	1.18	0.57	0.36

Sample no.	or04 (dyke)	OR406	or115 (ash)	or162	or236 (ash)	or151 (kotar)	or154	or164	or165
location	0414707/	Vesicular rhy. Top	0414989/	0415117/	0415862/	0415836/	Kristinartindar	0414623/	0414623/
SiO2	71.02	68.08	70.55	73.79	69.55	72.01	71.45	73.16	72.87
Al2O3	13.11	14.27	12.86	12.80	13.02	13.18	13.01	13.26	13.04
Fe2O3	2.59	3.13	2.74	2.48	4.50	3.87	3.05	2.43	2.75
MgO	0.26	0.15	0.18	0.01	0.12	0.01	0.06	0.09	0.16
CaO	0.92	0.89	0.91	0.58	1.31	1.22	0.89	0.95	1.01
Na2O	6.24	3.13	4.80	5.04	5.57	5.58	5.47	5.21	4.85
K2O	3.67	4.28	3.97	4.00	3.21	3.50	3.67	4.19	4.33
P2O5	0.04	0.02	0.02	0.00	0.03	0.02	0.00	0.02	0.02
Ti	0.16	0.15	0.13	0.10	0.23	0.17	0.11	0.14	0.07
Mn	0.06	0.08	0.07	0.03	0.11	0.10	0.09	0.05	0.07
otal (no LOI) wt %	**98.08**	**94.18**	**96.23**	**98.83**	**97.64**	**99.66**	**97.82**	**99.51**	**99.18**
LOI total	2.83	4.78	3.61	0.95	2.21	0.13	1.68	0.13	0.35

Sample no.	**OR255**	**OR263**	**OR280**	**OR293**	**or224**	**or226**	**or250**	**or160**	**or207**
location	0414943/								
SiO2	73.27	72.83	72.42	72.56	74.34	74.18	73.99	74.16	74.26
Al2O3	12.94	12.20	12.04	12.36	12.34	13.20	13.25	12.72	12.73
Fe2O3	2.69	2.62	2.73	2.53	2.51	2.24	2.33	2.48	2.40
MgO	0.01	0.02	0.05	0.02	0.09	0.03	0.05	0.05	0.03
CaO	0.80	0.76	0.80	0.73	0.50	0.38	0.35	0.58	0.43
Na2O	5.12	4.93	4.88	5.10	5.05	5.23	5.00	5.10	4.97
K2O	4.15	4.00	4.09	3.97	4.22	4.16	4.14	4.19	4.16
P2O5	0.01	0.02	0.02	0.02	0.02	0.02	0.02	0.03	0.03
Ti	0.12	0.11	0.12	0.11	0.11	0.10	0.10	0.10	0.12
Mn	0.07	0.07	0.07	0.08	0.05	0.05	0.05	0.05	0.05
otal (no LOI) wt %	**99.18**	**97.56**	**97.21**	**97.48**	**99.23**	**99.59**	**99.28**	**99.47**	**99.18**
LOI total	0.64	0.41	0.53	0.51	0.33	0.41	0.70	0.28	0.57

Sample no.	**or133**	**or211**	**or212**	**or219**	**or247**	**OR301a**	**or23**	**or213d**	**or241**
location	0415997/	0416399/	0416455/	0414858/	0415279/		0415399/		
SiO2	73.05	72.90	72.41	73.09	72.98	72.19	68.70	72.89	73.75
Al2O3	13.07	13.00	12.94	13.03	12.96	12.74	12.35	12.49	13.14
Fe2O3	2.58	2.73	2.57	2.72	2.84	2.63	2.79	2.71	2.48
MgO	0.10	0.08	0.01	0.09	0.08	0.10	0.02	0.11	0.13
CaO	0.92	0.93	0.88	0.86	0.89	0.85	0.90	0.91	0.76
Na2O	5.01	4.95	4.90	5.05	4.90	4.91	4.77	4.92	4.91
K2O	4.26	4.25	4.05	4.15	4.26	4.04	3.70	4.26	4.31
P2O5	0.02	0.01	0.02	0.02	0.02	0.02	0.01	0.02	0.03
Ti	0.13	0.19	0.12	0.13	0.13	0.13	0.11	0.12	0.13
Mn	0.06	0.07	0.06	0.06	0.07	0.06	0.08	0.05	0.05
otal (no LOI) wt %	**99.21**	**99.12**	**97.97**	**99.20**	**99.13**	**97.67**	**93.42**	**98.49**	**99.70**
LOI total	0.35	0.58	1.74	0.43	0.56	0.74	6.84	1.13	0.27

Sample no.	**or166**	**or146**	**OR139**	**OR316**	**or297**	**or161**	**0r203**	**or262**	**or46**
location	0414623/	Stadharfjall	**kvisker**	**Slaga**					0414759/
SiO2	73.17	71.85	71.72	73.29	73.72	74.00	73.45	74.41	73.08
Al2O3	12.95	13.17	13.19	13.06	13.24	12.85	11.69	12.36	13.25
Fe2O3	2.71	2.80	2.70	2.48	2.52	2.47	2.68	2.44	2.28
MgO	0.11	0.22	0.20	0.15	0.06	0.07	0.05	0.10	0.09
CaO	0.74	1.14	1.03	0.89	0.41	0.70	0.56	0.57	0.73
Na2O	5.17	4.90	4.69	5.04	5.07	5.14	5.02	5.08	5.28
K2O	4.07	4.29	4.18	4.24	4.25	4.20	4.00	4.07	3.99
P2O5	0.00	0.04	0.02	0.03	0.04	0.02	0.01	0.02	0.02
Ti	0.11	0.18	0.17	0.13	0.11	0.10	0.10	0.10	0.10
Mn	0.07	0.06	0.06	0.05	0.05	0.05	0.05	0.05	0.06
otal (no LOI) wt %	**99.10**	**98.64**	**97.97**	**99.36**	**99.46**	**99.61**	**97.62**	**99.20**	**98.87**
LOI total	0.49	1.04	0.48	0.55	0.57	0.21	1.56	0.35	0.37

Sample no.	**OR400**	**or399**	**or290**	**or401**	**OR402**
location					
SiO2	72.60	73.78	74.19	74.03	73.50
Al2O3	12.82	12.91	12.69	12.48	12.69
Fe2O3	2.53	2.53	2.46	2.56	2.23
MgO	0.05	0.11	0.09	0.07	0.03
CaO	0.73	0.58	0.53	0.59	0.60
Na2O	5.21	5.20	5.19	5.11	5.23
K2O	3.95	4.24	4.00	4.26	4.00
P2O5	0.02	0.02	0.01	0.02	0.02
Ti	0.11	0.10	0.10	0.10	0.10
Mn	0.07	0.05	0.05	0.05	0.06
otal (no LOI) wt %	**98.09**	**99.52**	**99.32**	**99.28**	**98.44**
LOI total	0.06	0.33	0.38	0.36	0.24

Sample no.	**or304**	**or306**	**or308**	**OR403**	**OR218**
location					
SiO2	67.70	68.13	73.44	73.13	73.18
Al2O3	10.93	10.97	12.65	12.42	12.51
Fe2O3	2.54	2.80	2.71	2.55	2.36
MgO	0.17	0.26	0.12	0.03	0.03
CaO	0.86	1.01	0.89	0.73	0.62
Na2O	2.83	2.56	4.14	5.15	5.24
K2O	3.54	3.27	4.85	4.03	3.93
P2O5	0.02	0.02	0.02	0.02	0.02
Ti	0.11	0.14	0.12	0.11	0.11
Mn	0.05	0.05	0.05	0.07	0.05
otal (no LOI) wt %	**88.75**	**89.24**	**98.98**	**98.23**	**98.07**
LOI total	8.26	7.80	0.57	0.27	0.44

Appendix 4

Supplementary statistical data: Dendrograms

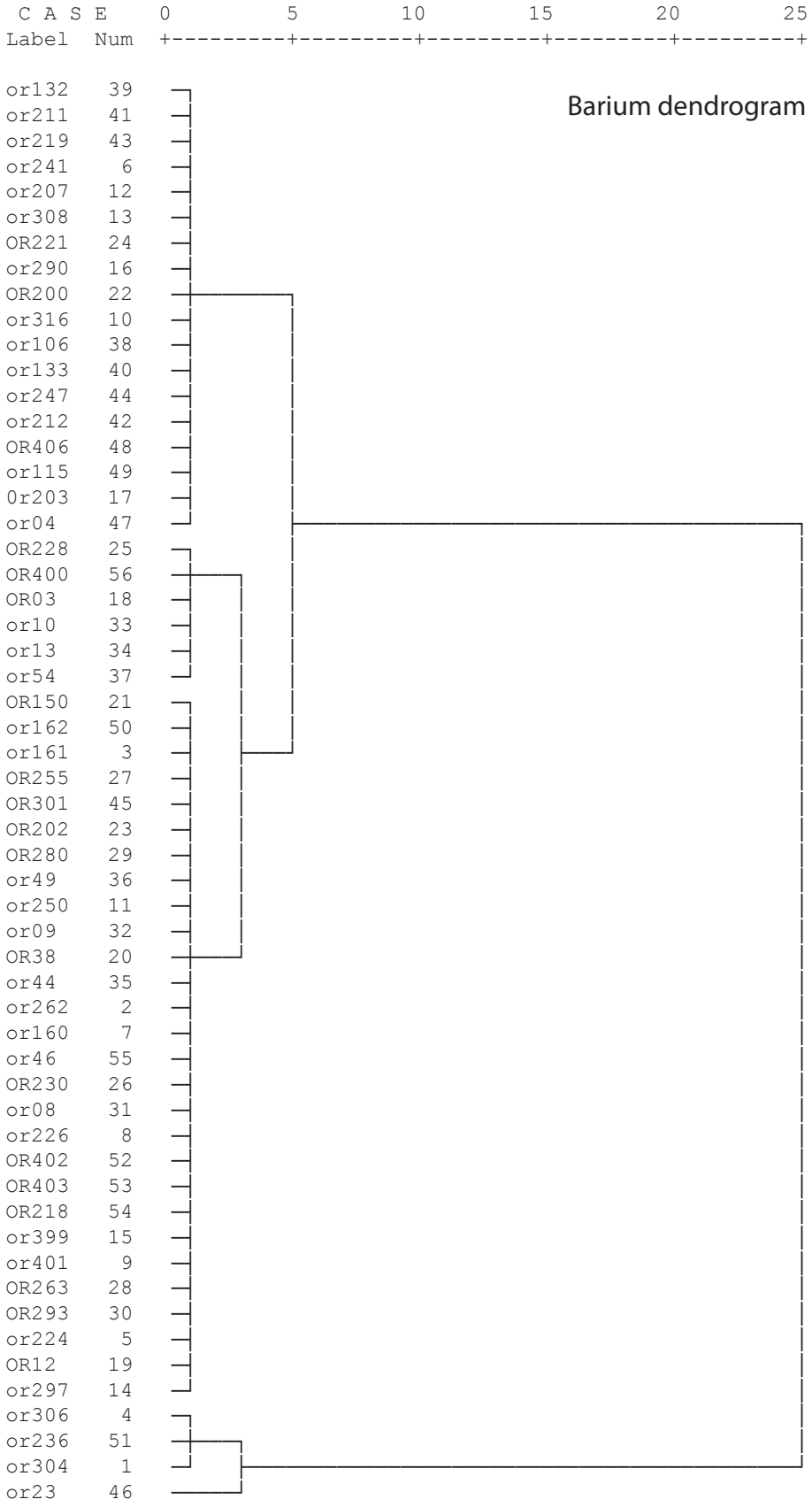

Barium dendrogram

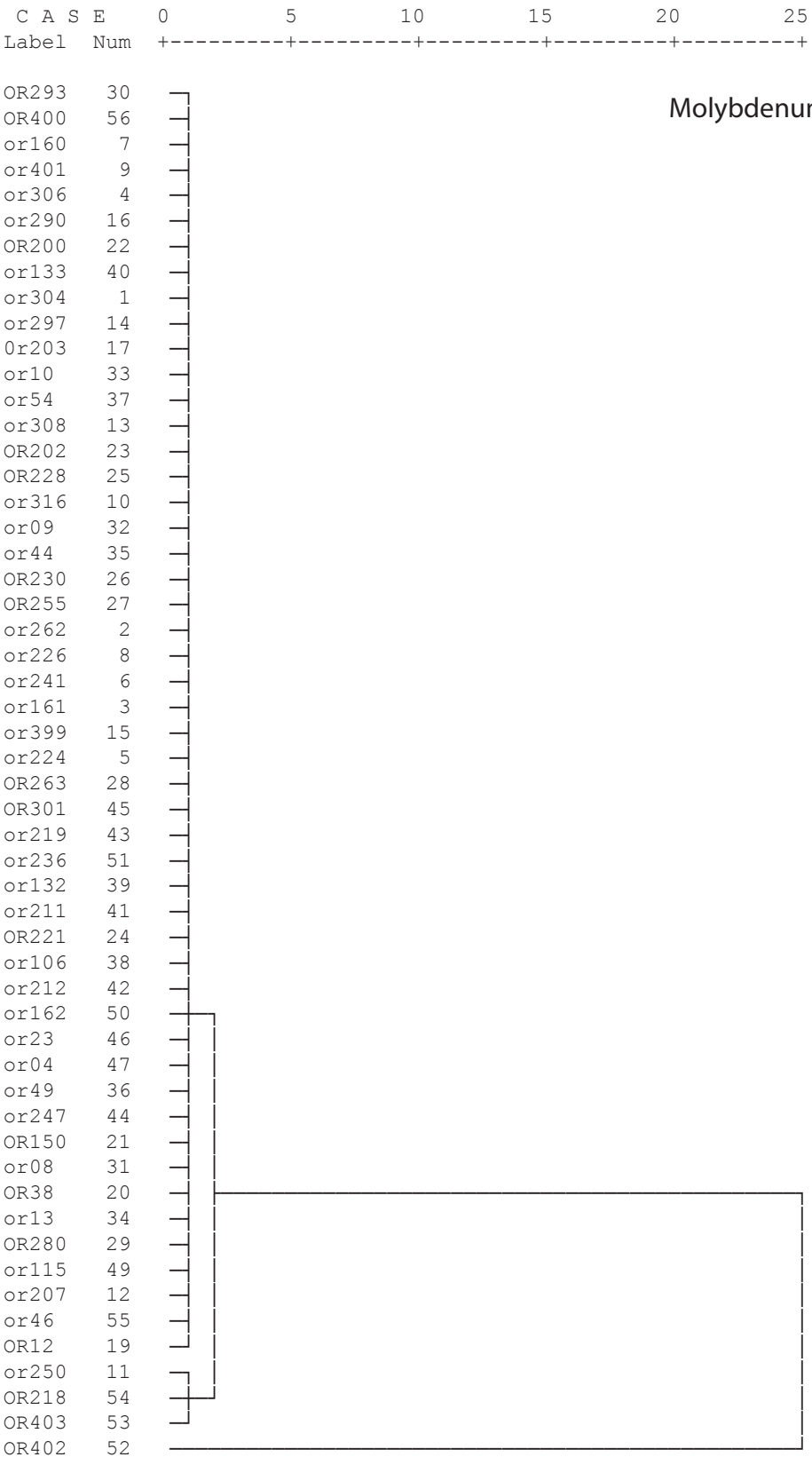

Molybdenum dendrogram

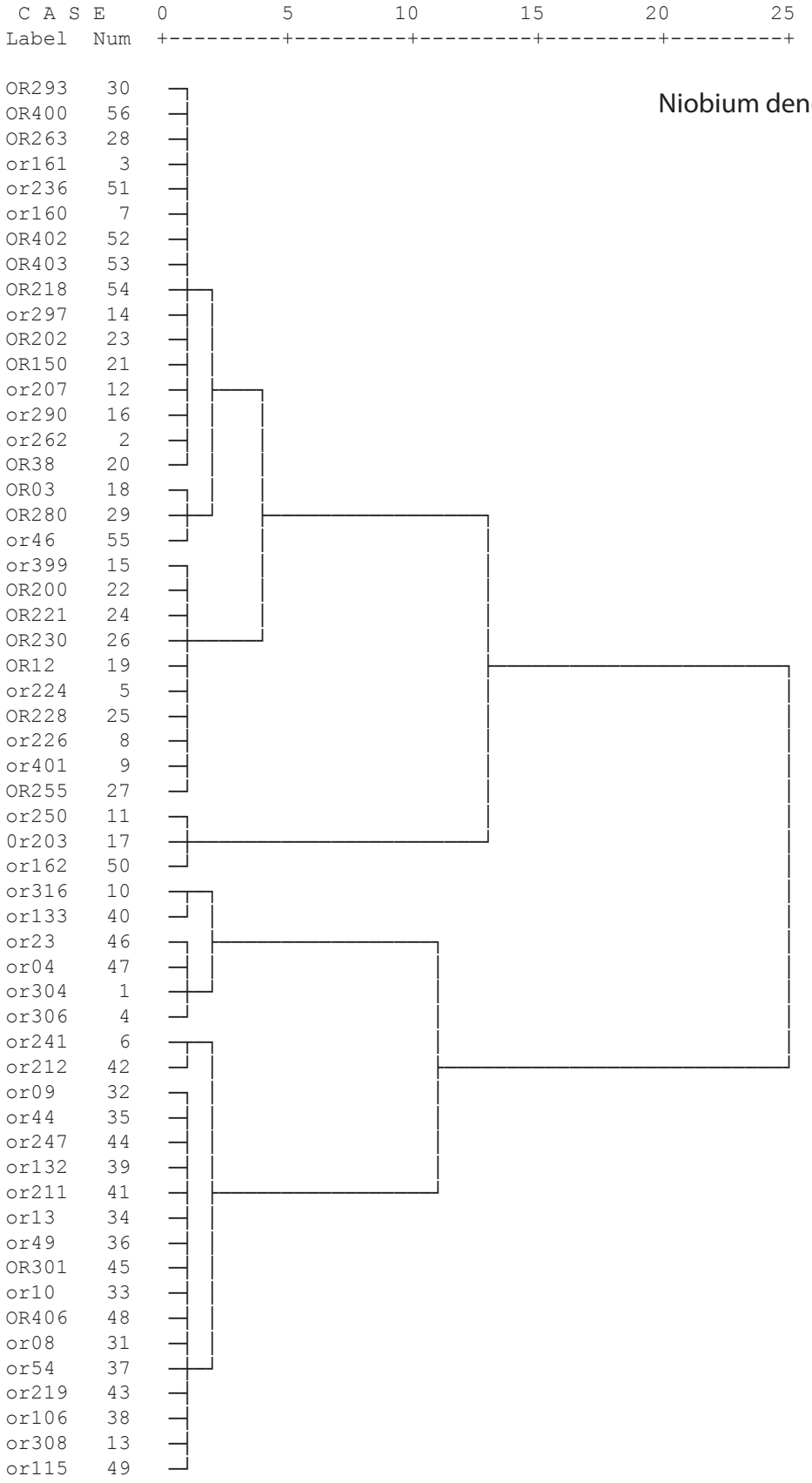

Niobium dendrogram

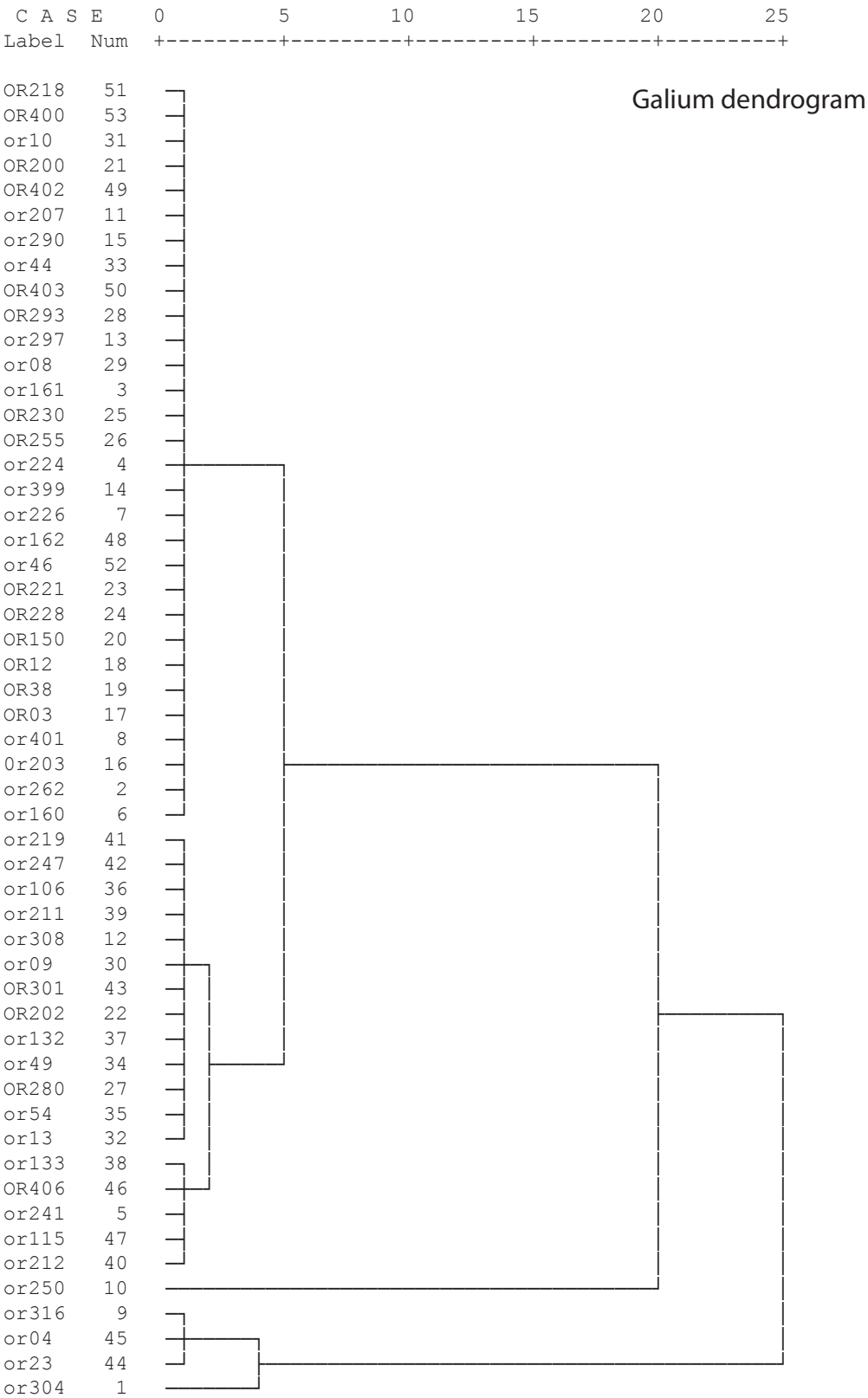

Galium dendrogram

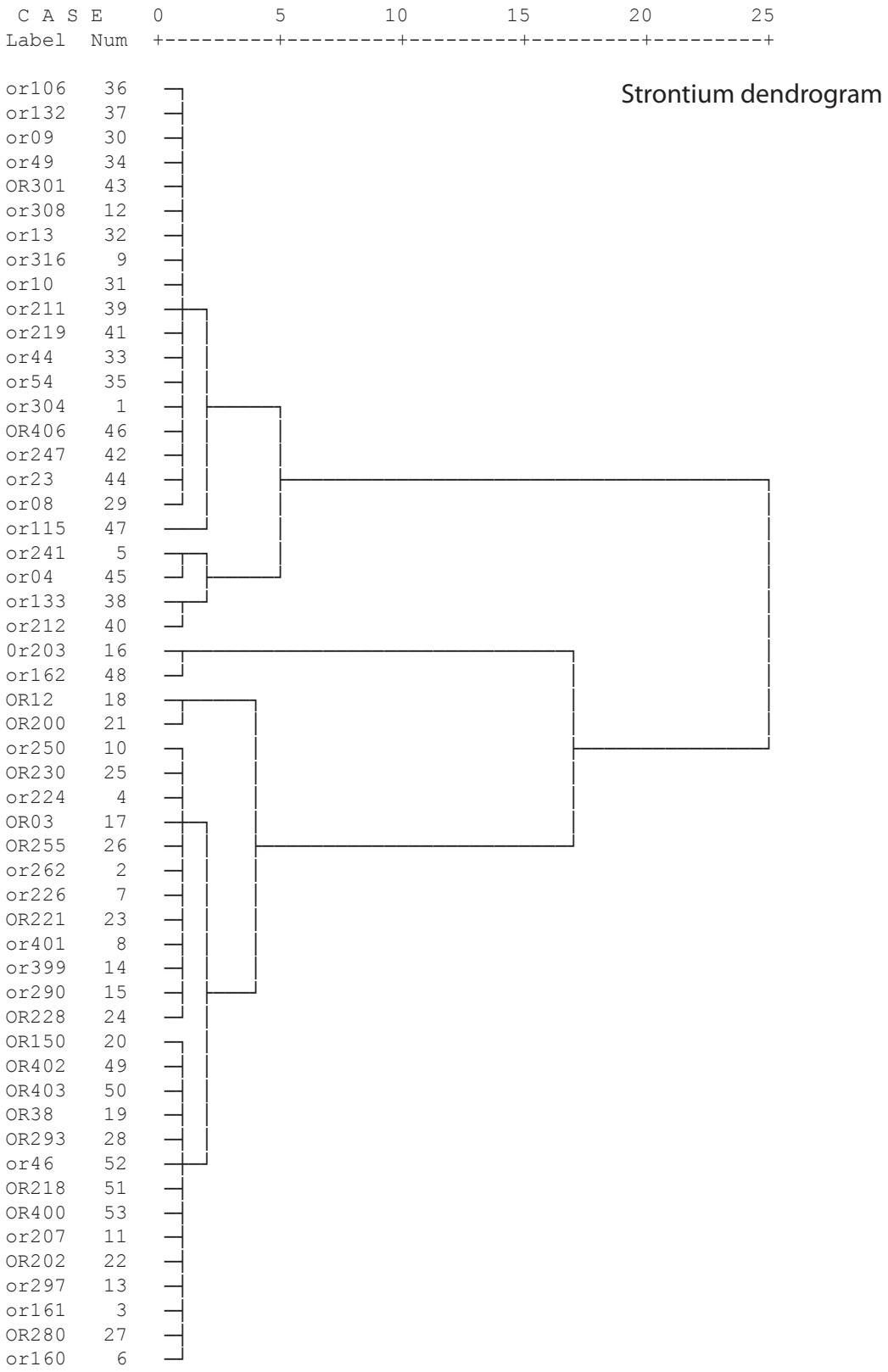

Strontium dendrogram

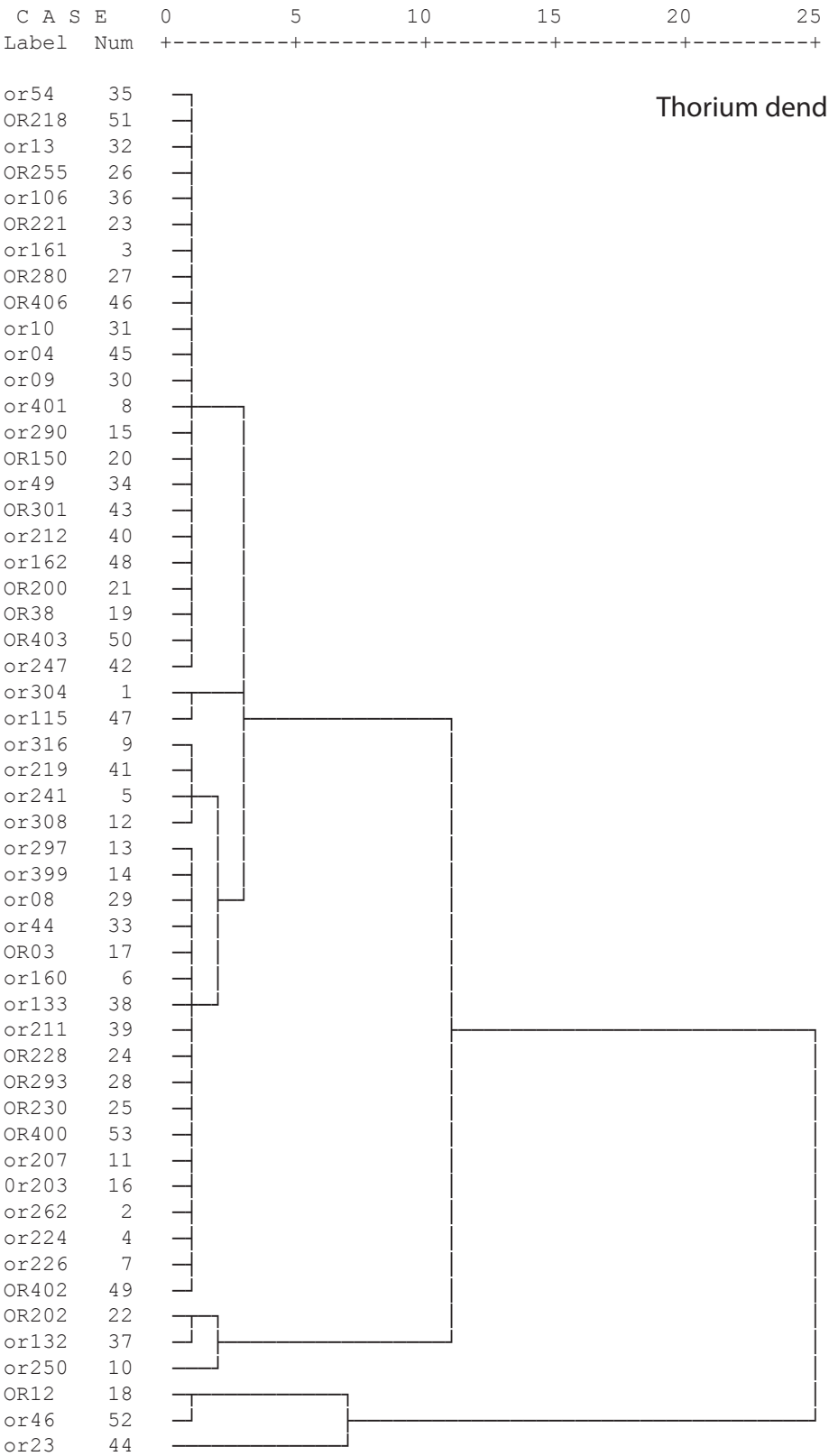

Thorium dendrogram

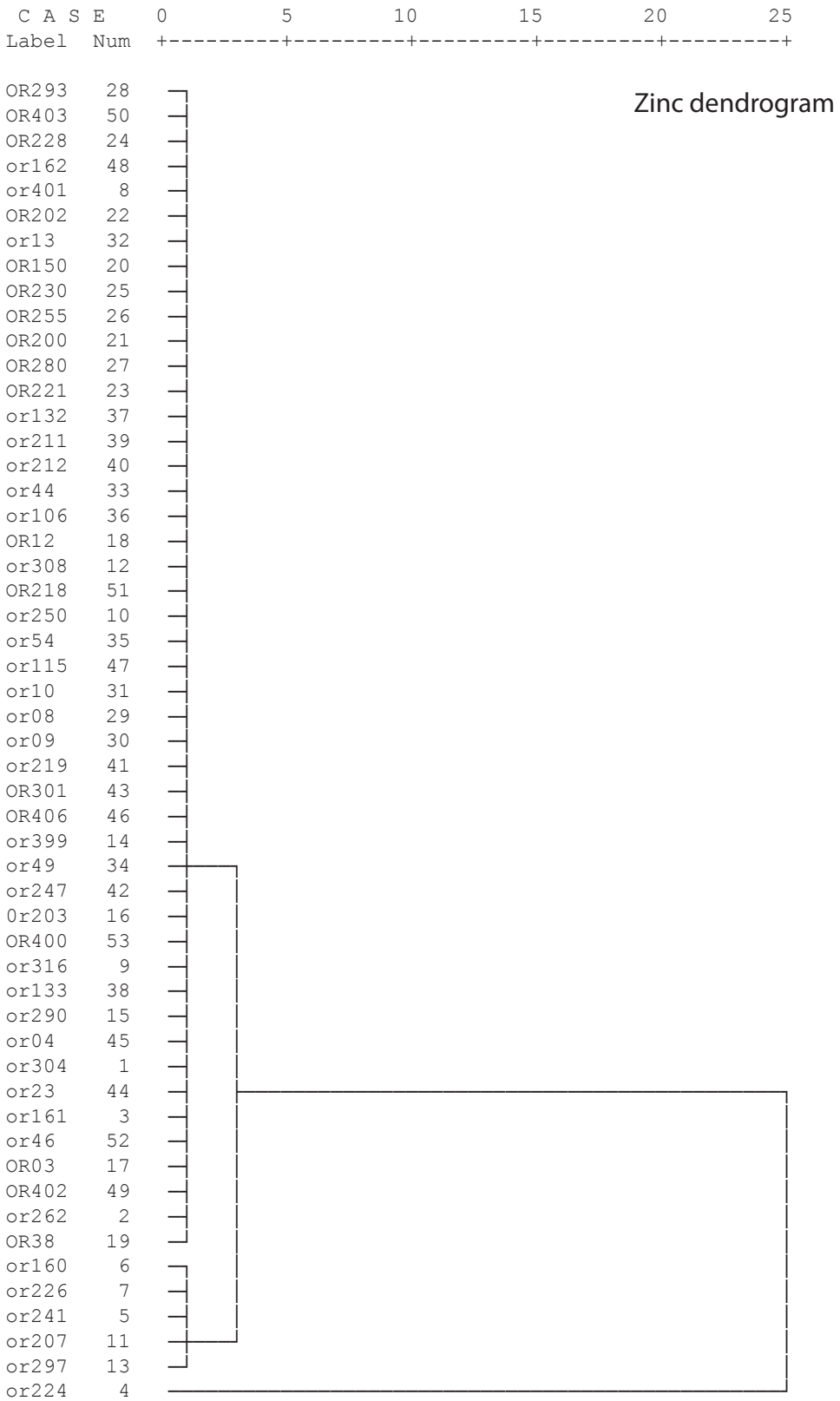

Zinc dendrogram

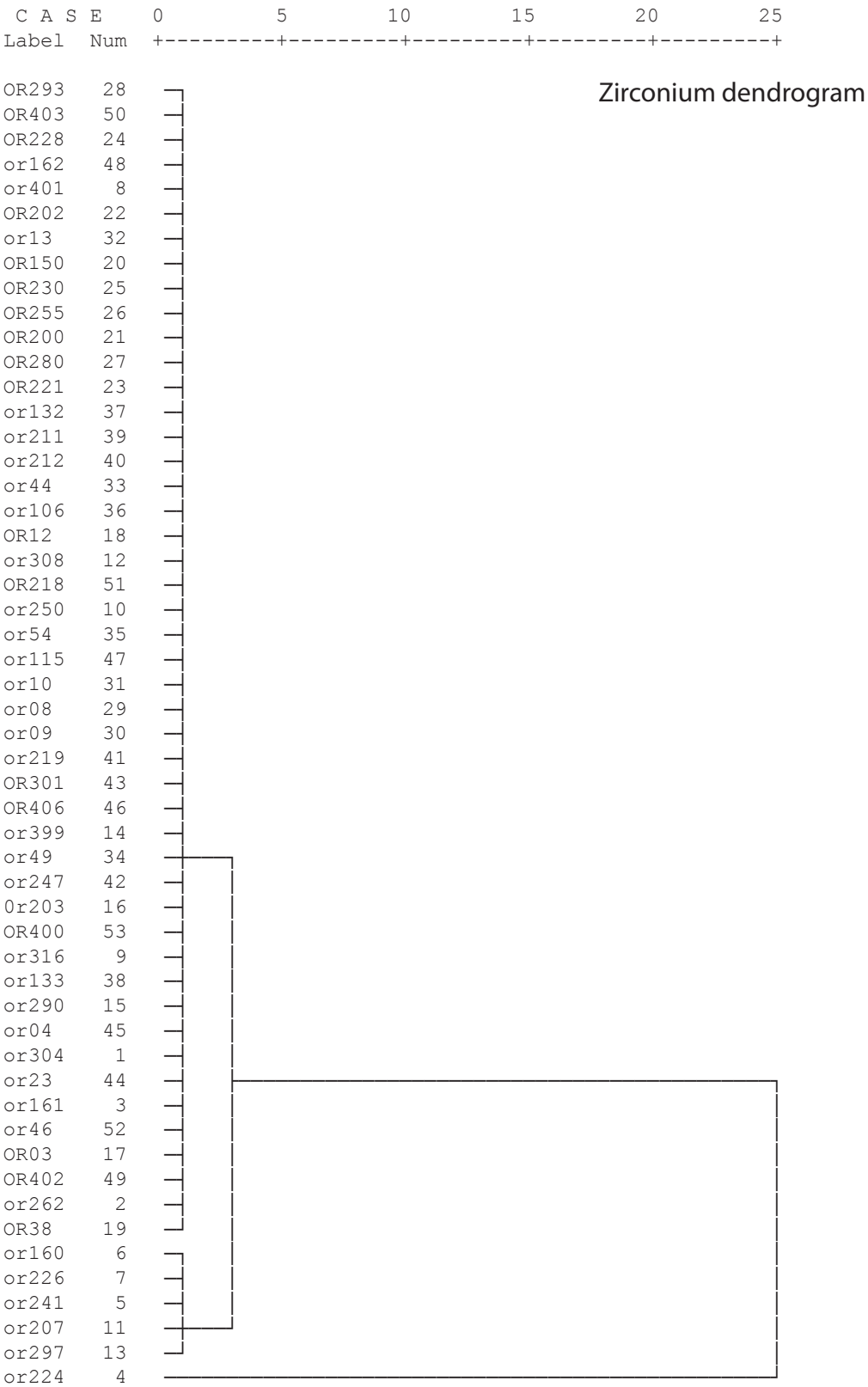

Zirconium dendrogram

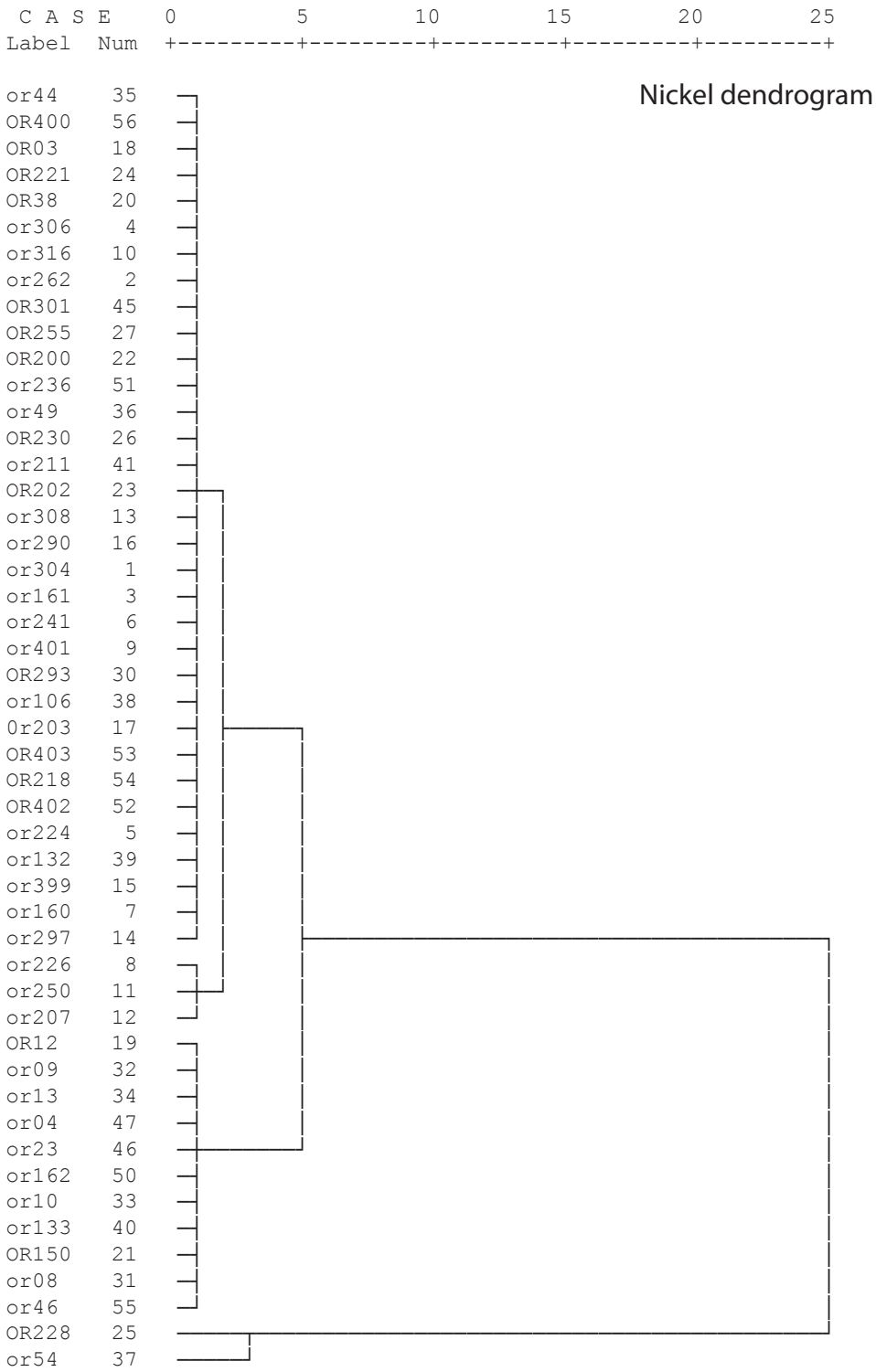

Nickel dendrogram

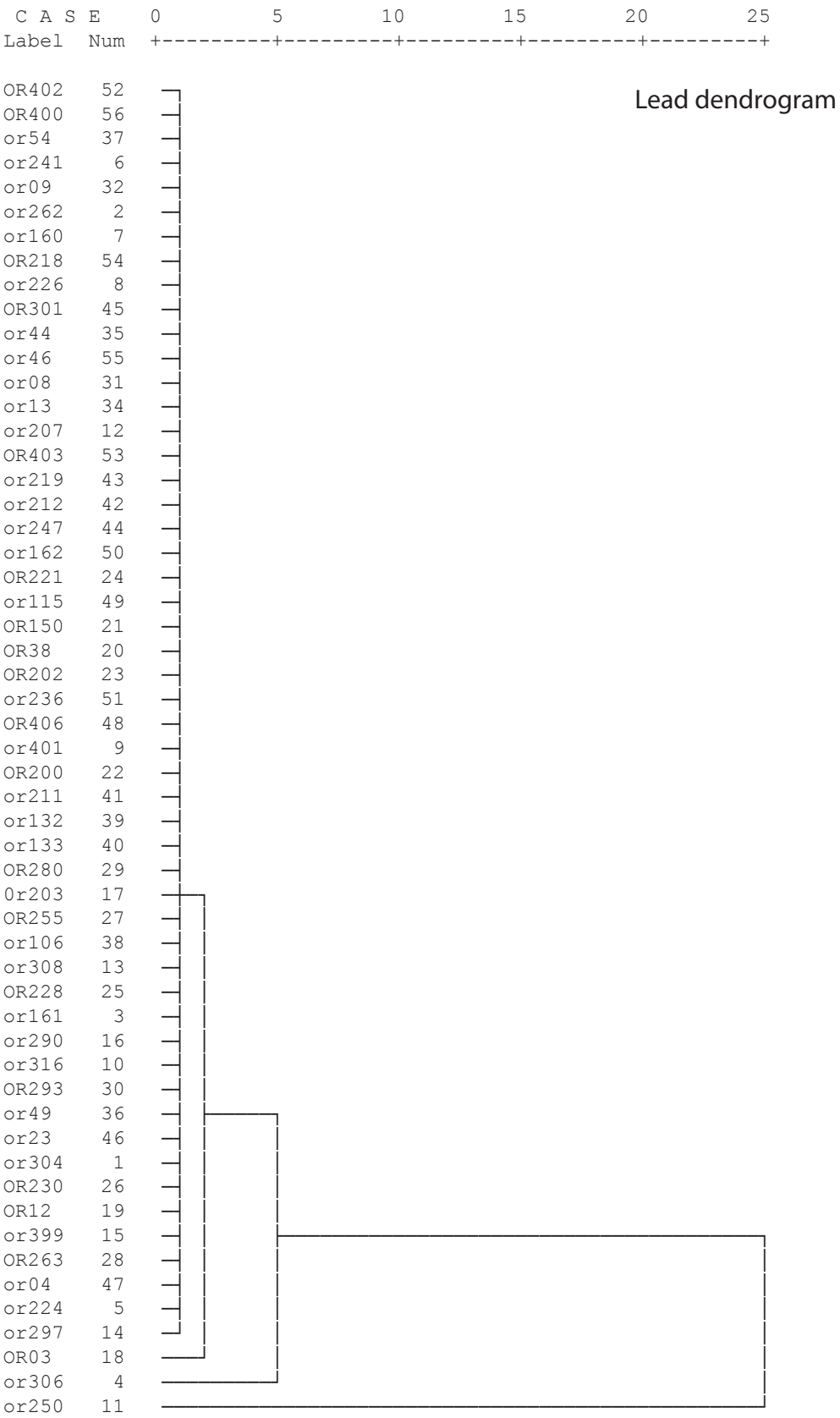

Lead dendrogram

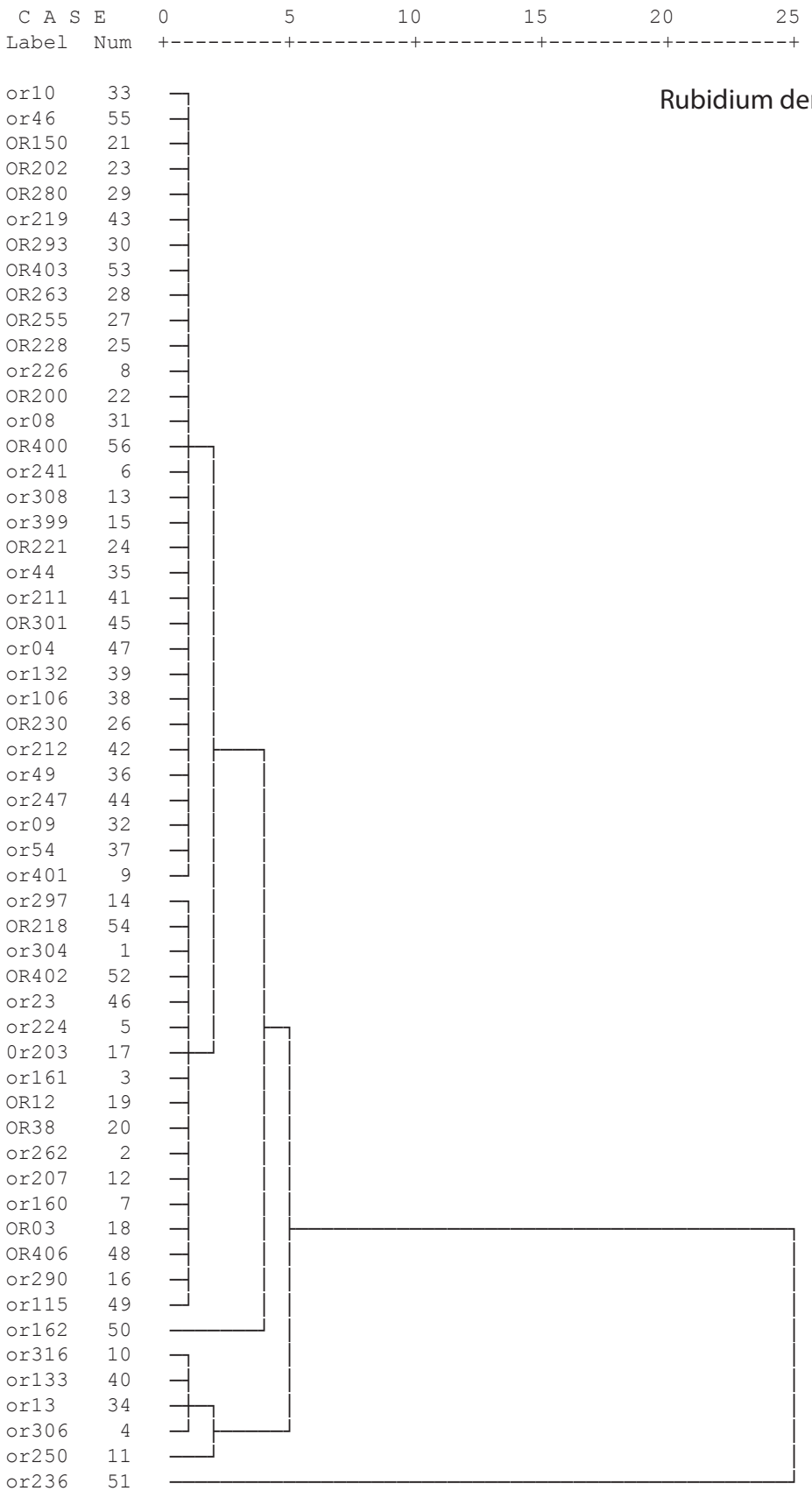

Rubidium dendrogram

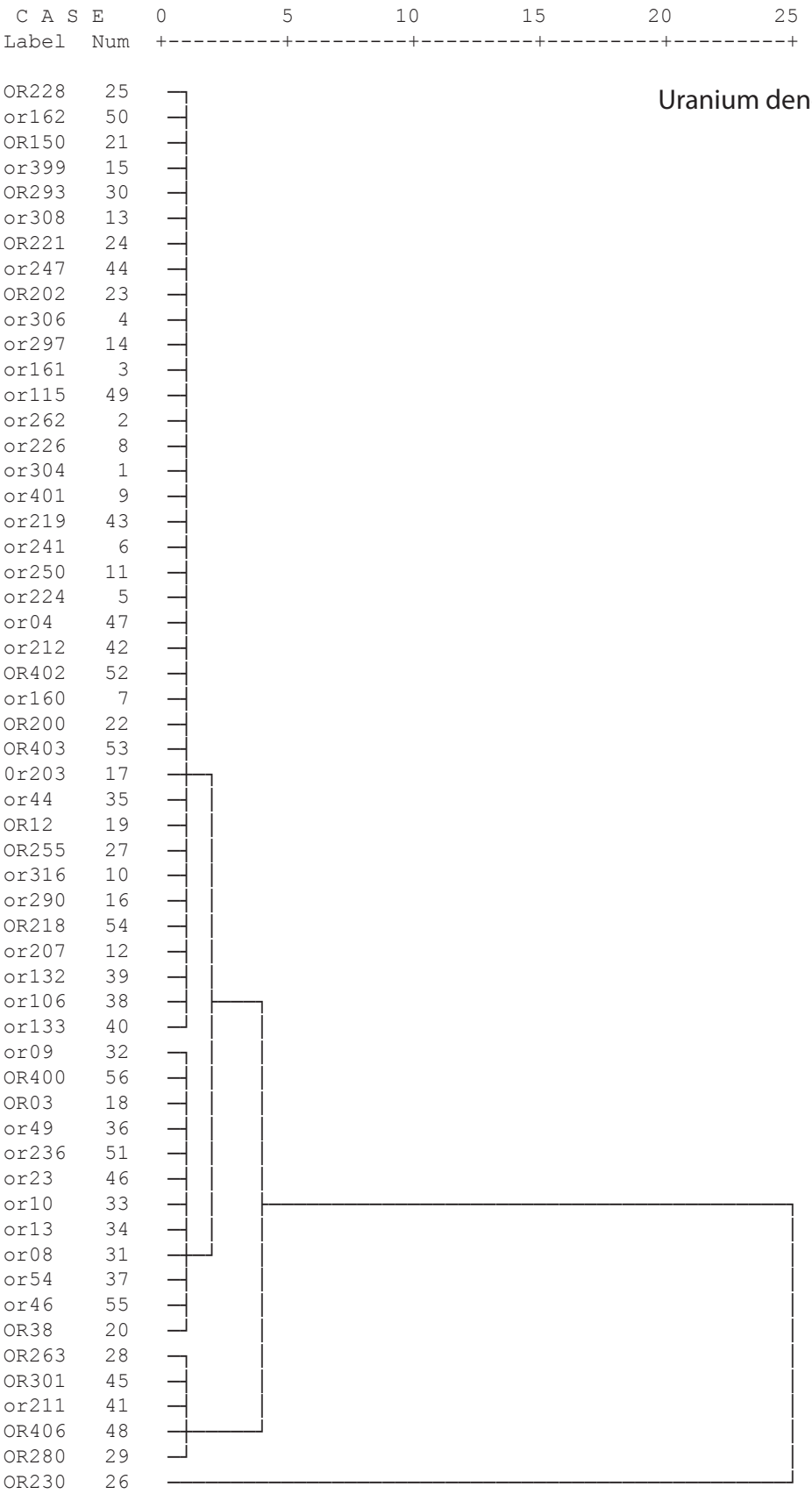

Uranium dendrogram

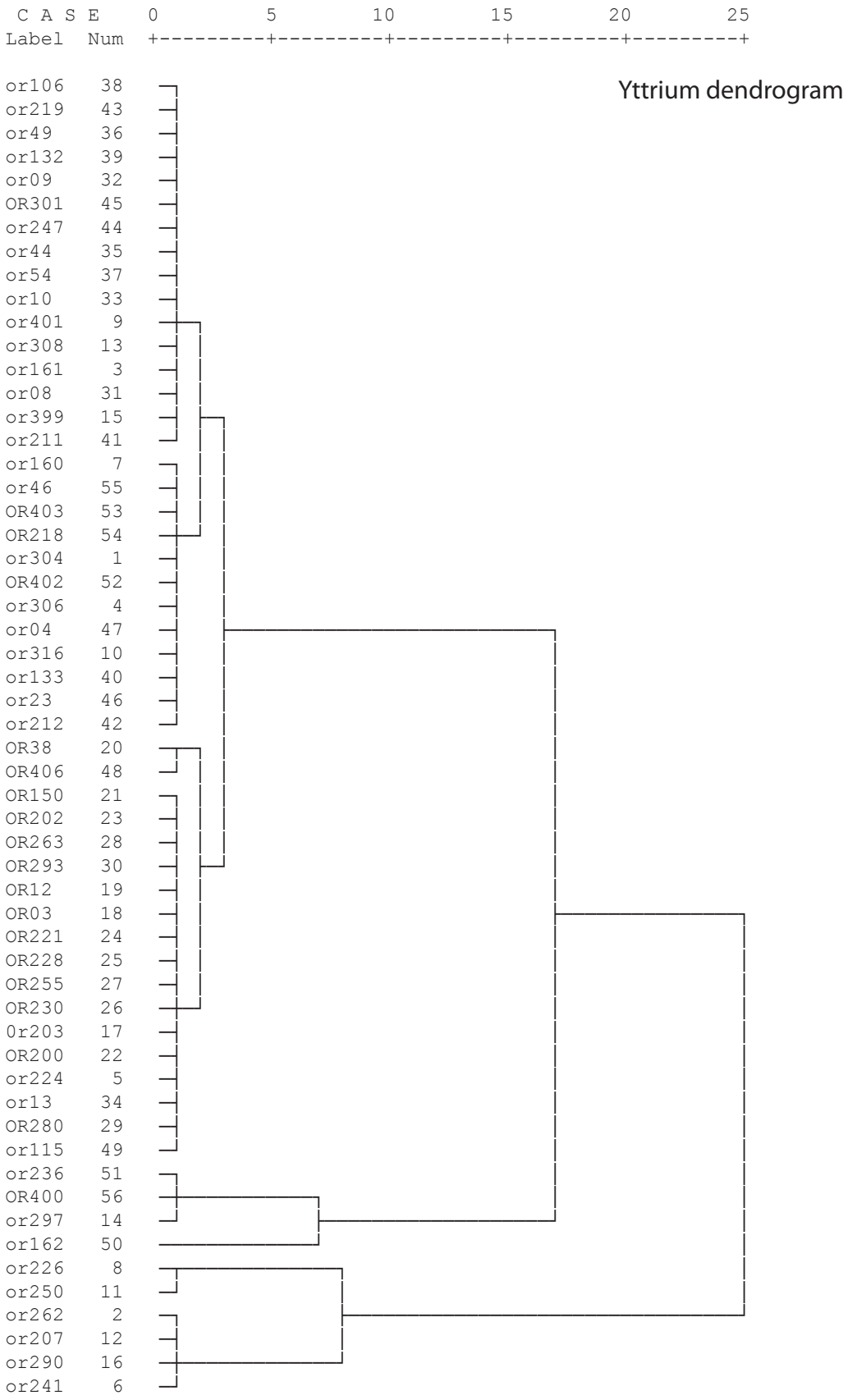

Yttrium dendrogram

Appendix 5

Microprobe data: OR44 and OR228

OR44	Oxide percentage										
Label	**SiO2**	**TiO2**	**Al2O3**	**Cr2O3**	**MgO**	**CaO**	**MnO**	**FeO**	**Na2O**	**K2O**	**Total**
Feldspar 1:											
OR44_Crystal1_1	61.97	0.03	22.96	0.00	0.00	4.67	0.02	0.33	8.07	0.84	98.88
OR44_Crystal1_2	62.99	0.03	23.11	0.00	0.01	4.46	0.00	0.33	8.38	0.87	100.17
OR44_Crystal1_3	62.67	0.05	22.99	0.00	0.00	4.37	0.00	0.31	8.26	0.89	99.54
OR44_Crystal1_4	63.23	0.02	22.81	0.00	0.02	4.34	0.00	0.31	8.43	0.89	100.03
OR44_Crystal1_5	63.15	0.01	22.72	0.00	0.02	4.32	0.00	0.30	8.40	0.86	99.77
Feldspar 2:											
OR44_Crystal2_1	59.78	0.04	25.13	0.00	0.00	6.82	0.00	0.31	7.35	0.53	99.96
OR44_Crystal2_2	60.03	0.06	25.14	0.00	0.02	6.80	0.01	0.29	7.43	0.48	100.25
OR44_Crystal2_3	61.19	0.02	24.40	0.01	0.03	5.67	0.00	0.32	7.71	0.62	99.96
OR44_Crystal2_4	60.58	0.04	24.52	0.00	0.01	6.37	0.00	0.30	7.62	0.55	99.98
OR44_Crystal2_5	63.03	0.00	22.73	0.00	0.00	4.33	0.00	0.30	8.37	0.89	99.66
Feldspar 3:											
OR44_Crystal4_1	63.38	0.01	22.51	0.01	0.02	3.95	0.00	0.34	8.76	0.96	99.94
OR44_Crystal4_2	62.98	0.04	22.91	0.00	0.00	4.24	0.02	0.34	8.65	0.88	100.05
OR44_Crystal4_3	63.99	0.06	21.76	0.01	0.01	3.35	0.01	0.35	8.88	1.13	99.55
OR44_Crystal4_4	61.82	0.06	22.87	0.00	0.01	4.59	0.01	0.31	8.42	0.82	98.89
OR44_Crystal4_5	62.71	0.06	23.10	0.00	0.00	4.32	0.00	0.34	8.45	0.91	99.88
Feldspar 4:											
OR44_Crystal5_1	62.94	0.03	22.92	0.00	0.00	4.44	0.01	0.29	8.70	0.89	100.22
OR44_Crystal5_2	63.15	0.03	23.13	0.01	0.02	4.41	0.01	0.31	8.58	0.88	100.52
OR44_Crystal5_3	62.92	0.00	23.09	0.00	0.01	4.40	0.01	0.34	8.44	0.87	100.07
OR44_Crystal5_4	63.58	0.01	22.90	0.00	0.00	3.94	0.00	0.37	8.57	0.98	100.36
OR44_Crystal5_5	59.30	0.01	21.35	0.00	0.01	4.20	0.02	0.32	8.76	0.90	94.87
Pyroxene 1:											
OR44_Crystal3_1	50.99	0.17	0.71	0.00	9.68	20.19	0.82	16.90	0.37	0.00	99.83
OR44_Crystal3_2	50.58	0.18	0.59	0.00	9.25	19.36	0.99	18.46	0.40	0.00	99.80
OR44_Crystal3_3	51.14	0.20	0.68	0.01	9.67	20.12	0.80	17.22	0.40	0.00	100.25
OR44_Crystal3_4	51.27	0.24	0.63	0.00	9.60	19.92	0.83	17.17	0.39	0.02	100.07
OR44_Crystal3_5	51.20	0.21	0.63	0.00	9.67	20.37	0.86	16.79	0.36	0.00	100.11
Pyroxene 2:											
OR44_cryst1a_1	50.43	0.17	0.63	0.02	9.94	20.30	0.84	16.93	0.37	0.00	99.61
OR44_cryst1a_2	50.23	0.24	0.63	0.03	9.84	19.83	0.78	17.13	0.36	0.01	99.08
Feldspar 5:											
OR44_cryst2a_1	62.93	0.03	22.71	0.00	0.01	4.53	0.00	0.29	8.70	0.87	100.08
OR44_cryst2a_2	63.15	0.03	22.63	0.00	0.02	4.30	0.00	0.32	9.01	0.91	100.37
Feldspar 6:											
OR44_cryst3a_1	61.01	0.00	24.69	0.01	0.03	6.55	0.00	0.29	7.65	0.57	100.80
OR44_cryst3a_2	61.79	0.06	24.05	0.01	0.01	6.02	0.00	0.28	7.98	0.59	100.77
Feldspar 7:											
OR44_cryst4a_1	62.52	0.00	22.33	0.00	0.00	4.26	0.00	0.30	8.91	0.87	99.18
OR44_cryst4a_2	63.12	0.02	22.50	0.00	0.03	4.23	0.07	0.30	8.76	0.92	99.95
Pyroxene 3:											
OR44_cryst5a_1	50.28	0.18	0.82	0.02	9.73	19.01	0.96	18.14	0.46	0.00	99.59
OR44_cryst5a_2	50.83	0.21	0.68	0.01	9.83	19.72	0.76	17.00	0.47	0.01	99.52

OR44 (cont.)	Oxide percentage										
Label	**SiO2**	**TiO2**	**Al2O3**	**Cr2O3**	**MgO**	**CaO**	**MnO**	**FeO**	**Na2O**	**K2O**	**Total**
Opaques:											
OR44_Opaque_1_1	0.18	12.38	1.22	0.03	0.58	0.00	0.72	80.21	0.08	0.02	95.41
OR44_Opaque_1_2	0.15	12.81	1.26	0.03	0.68	0.01	0.77	79.74	0.01	0.00	95.46
OR44_Opaque_1_3	0.18	12.44	1.19	0.03	0.60	0.02	0.73	80.00	0.02	0.02	95.21
Microphenocrysts:											
OR44_Micro1	65.93	0.01	20.62	0.00	0.00	1.74	0.00	0.40	8.40	2.64	99.74
OR44_Micro2	65.36	0.04	21.55	0.00	0.03	2.62	0.01	0.46	8.20	1.62	99.91
OR44_Micro3	66.15	0.05	21.18	0.00	0.00	1.97	0.00	0.32	8.59	2.44	100.69
OR44_Micro4	68.60	0.09	17.72	0.01	0.02	1.37	0.02	1.01	6.83	2.76	98.42
OR44_Micro5	74.06	0.11	15.07	0.00	0.01	0.83	0.00	1.11	4.85	3.27	99.32
OR44_Micro6	70.35	0.07	16.68	0.00	0.04	1.41	0.07	0.98	7.47	2.85	99.90
OR44_Micro7	68.47	0.08	18.74	0.00	0.02	1.45	0.03	0.59	8.21	2.62	100.21
OR44_Micro8	68.26	0.06	17.90	0.00	0.00	1.79	0.00	0.68	7.75	2.45	98.89
OR44_Micro9	48.55	0.41	1.33	0.01	6.75	17.33	1.06	22.47	0.41	0.08	98.40
Glass matirx:											
OR44_Ground1	77.18	0.17	12.12	0.00	0.01	0.32	0.02	1.48	2.26	4.55	98.11
OR44_Ground2	75.98	0.16	13.11	0.00	0.01	0.51	0.03	1.41	3.43	4.17	98.81
OR44_Ground3	76.50	0.16	12.26	0.00	0.01	0.37	0.02	1.55	2.59	4.16	97.62
OR44_Ground4	76.06	0.23	11.63	0.02	0.03	0.36	0.07	1.78	3.91	4.76	98.85
OR44_Ground5	72.53	0.35	13.47	0.01	0.02	0.65	0.09	3.04	5.33	4.12	99.60

OR228	Oxide percent										
Label	**SiO2**	**TiO2**	**Al2O3**	**Cr2O3**	**MgO**	**CaO**	**MnO**	**FeO**	**Na2O**	**K2O**	**Total**
Feldspar 1:											
OR228_Crystal1_1	63.78	0.04	21.98	0.00	0.00	3.66	0.00	0.29	8.96	1.21	99.92
OR228_Crystal1_2	63.67	0.00	22.10	0.01	0.00	3.47	0.00	0.28	8.71	1.26	99.50
OR228_Crystal1_3	63.75	0.01	22.35	0.00	0.00	3.60	0.02	0.26	8.79	1.16	99.94
OR228_Crystal1_4	64.53	0.01	22.54	0.01	0.01	3.80	0.00	0.32	8.70	1.02	100.94
OR228_Crystal1_5	63.92	0.00	22.16	0.01	0.01	3.42	0.00	0.29	8.78	1.07	99.65
OR228_Crystal1_6	63.76	0.00	22.28	0.00	0.02	3.79	0.00	0.30	8.74	0.93	99.81
OR228_Crystal1_7	64.17	0.05	22.31	0.00	0.00	3.56	0.01	0.31	8.88	0.97	100.25
OR228_Crystal1_8	64.57	0.02	22.05	0.00	0.02	3.31	0.00	0.27	8.96	1.09	100.28
Feldspar 2:											
OR228_Crystal2_1	62.79	0.03	21.44	0.00	0.02	3.37	0.00	0.25	9.24	1.25	98.39
OR228_Crystal2_2	63.86	0.03	22.10	0.00	0.01	3.71	0.00	0.30	8.70	1.04	99.74
OR228_Crystal2_3	63.95	0.06	22.30	0.01	0.01	3.53	0.00	0.27	8.79	0.99	99.90
OR228_Crystal2_4	63.64	0.04	22.29	0.01	0.00	3.46	0.00	0.26	8.68	1.17	99.56
Misc. phenocrysts:											
OR228_Opaque1	0.11	13.95	0.60	0.02	0.21	0.02	0.80	79.84	0.04	0.01	95.59
OR228_Opaque2	29.56	0.07	0.00	0.00	4.86	0.32	4.11	60.15	0.04	0.02	99.12
OR228_Opaque3	98.63	0.05	1.03	0.00	0.00	0.00	0.01	0.40	0.28	0.16	100.54
OR228_Opaque4	29.16	0.02	0.02	0.01	3.53	0.37	3.17	63.10	0.02	0.01	99.39
Microphenocrysts:											
OR228_Micro1	97.71	0.08	1.32	0.00	0.00	0.01	0.01	0.02	0.30	0.21	99.65
OR228_Micro2	98.18	0.04	0.75	0.00	0.00	0.00	0.01	0.05	0.19	0.12	99.34
OR228_Micro3	67.01	0.12	14.86	0.00	0.05	0.71	0.04	1.66	6.99	4.05	95.48
OR228_Micro4	96.51	0.07	2.59	0.00	0.00	0.01	0.00	0.14	0.59	0.45	100.36
Glass matrix:											
OR228_Matrix1	66.95	0.05	18.27	0.00	0.00	0.21	0.00	0.45	6.46	6.89	99.28
OR228_Matrix2	64.39	0.04	19.90	0.01	0.00	1.35	0.01	0.34	9.16	3.72	98.91
OR228_Matrix3	65.88	0.04	19.79	0.00	0.01	1.12	0.00	0.33	7.81	4.25	99.22
OR228_Matrix4	75.38	0.04	13.83	0.01	0.02	0.30	0.00	0.47	5.39	4.11	99.53

Appendix 6
$^{40}Ar/^{39}Ar$ data

OR12 Extraction	lamp (W)	Irradiance ($Wm^{-2} \times 10^5$)	36Ar (cc)	±36Ar (cc)	38Ar* (cc)	±38Ar* (cc)	39Ar (cc)	±39Ar (cc)	40Ar (cc)	±40Ar (cc)	40Ar/39Ar	±40Ar/39Ar	**Age (Ma)**	**± Age (Ma)**	%r 40Ar*	40Ar/36Ar	±40Ar/36Ar	38Ar/39Ar	±38Ar/39Ar
OR12-2																			
OR12-2-01	0.51	0.26	1.42E-13	6.01E-14	1.13E-13	1.42E-13	1.27E-11	7.65E-13	4.19E-11	2.87E-11	3.29	2.26	**0.35**	**0.244**	0	296	238.4	0.01	0.0112
OR12-2-02	0.73	0.37	3.26E-14	7.99E-14	8.55E-15	6.31E-14	6.79E-12	2.96E-13	1.44E-11	1.33E-12	2.12	0.22	**0.23**	**0.023**	100	na	na	0.00	0.0093
OR12-2-03	1.00	0.51	-1.89E-14	5.05E-14	-2.50E-14	6.11E-14	5.32E-12	1.11E-13	1.03E-11	7.87E-13	1.93	0.15	**0.21**	**0.017**	100	na	na	0.00	-0.0115
OR12-2-04	1.30	0.66	4.17E-14	1.13E-13	-3.67E-14	1.68E-13	2.91E-12	1.09E-13	5.29E-12	6.63E-13	1.82	0.24	**0.20**	**0.026**	100	na	na	-0.01	-0.0577
OR12-2-05	3.65	1.86	-3.64E-15	6.98E-14	2.43E-14	5.79E-14	7.28E-12	3.41E-13	1.07E-11	1.11E-12	1.47	0.17	**0.16**	**0.018**	100	na	na	0.00	0.0079
OR12-2-06	5.50	2.80	3.13E-14	5.65E-14	-3.29E-14	4.91E-14	3.23E-12	5.67E-14	7.36E-12	7.11E-13	2.28	0.22	**0.25**	**0.024**	100	na	na	-0.01	-0.0152
OR12-2-07	8.90	4.53	-6.72E-14	1.05E-13	-1.19E-13	6.30E-14	1.55E-12	9.84E-14	6.94E-12	6.82E-13	4.47	0.52	**0.48**	**0.056**	100	na	na	-0.08	-0.0409
OR12-3																			
OR12-3-01	0.51	0.26	1.38E-13	9.88E-14	-1.58E-14	8.75E-14	1.06E-11	4.60E-13	1.92E-11	1.48E-12	1.81	0.16	**0.19**	**0.017**	100	na	na	0.00	-0.0082
OR12-3-02	0.73	0.37	-4.77E-14	1.32E-13	-1.22E-13	2.36E-13	9.11E-12	1.68E-13	1.36E-11	1.29E-12	1.49	0.14	**0.16**	**0.016**	100	na	na	-0.01	-0.0259
OR12-3-03	1.00	0.51	8.36E-14	5.93E-14	-5.59E-15	8.20E-14	5.05E-12	1.02E-13	9.99E-12	6.88E-13	1.98	0.14	**0.21**	**0.015**	100	na	na	0.00	-0.0162
OR12-3-04	1.30	0.66	4.65E-14	5.83E-14	-7.14E-14	5.48E-14	3.19E-12	9.74E-14	6.33E-12	4.13E-13	1.99	0.14	**0.21**	**0.015**	100	na	na	-0.02	-0.0172
OR12-3-05	3.65	1.86	7.32E-14	6.75E-14	1.49E-14	4.48E-14	8.31E-12	1.14E-13	1.57E-11	5.81E-13	1.88	0.07	**0.20**	**0.008**	100	na	na	0.00	0.0054
OR12-3-06	5.50	2.80	9.74E-14	6.36E-14	1.27E-14	9.19E-14	2.52E-12	1.87E-13	6.45E-12	3.98E-13	2.56	0.25	**0.28**	**0.027**	100	na	na	0.01	0.0365
OR12-3-07	8.90	4.53	6.20E-14	9.71E-14	-1.65E-14	5.16E-14	1.56E-12	1.08E-13	8.85E-12	6.41E-13	5.67	0.57	**0.61**	**0.061**	100	na	na	-0.01	-0.0331
OR12-4																			
OR12-4-01	0.51	0.26	2.83E-13	5.86E-14	1.14E-14	7.11E-14	1.93E-12	4.00E-14	7.48E-11	2.19E-12	38.81	1.39	**4.18**	**0.150**	0	265	55.4	0.01	0.0369
OR12-4-02	0.73	0.37	2.97E-13	2.38E-14	5.30E-14	1.10E-13	1.58E-11	8.13E-13	1.14E-10	1.11E-12	7.24	0.38	**0.78**	**0.041**	23	386	31.1	0.00	0.0070
OR12-4-03	1.00	0.51	1.98E-13	5.16E-14	8.37E-14	4.39E-14	5.89E-12	2.31E-13	2.77E-11	3.11E-12	4.71	0.56	**0.51**	**0.060**	0	140	39.7	0.01	0.0075
OR12-4-04	1.30	0.66	2.76E-13	4.99E-14	1.96E-14	4.10E-14	9.96E-12	4.02E-13	7.98E-11	1.16E-12	8.01	0.34	**0.86**	**0.037**	0	290	52.6	0.00	0.0041
OR12-4-05	3.65	1.86	1.05E-13	5.26E-14	2.19E-14	3.84E-14	2.94E-12	1.74E-13	2.63E-11	1.24E-12	8.96	0.68	**0.97**	**0.073**	0	249	124.8	0.01	0.0131
OR12-4-06	5.50	2.80	7.20E-14	4.02E-14	-6.56E-14	8.00E-14	1.00E-12	3.30E-14	1.53E-11	1.23E-12	15.20	1.32	**1.64**	**0.142**	0	212	119.6	-0.07	-0.0797
OR12-5																			
OR12-5-01	0.51	0.26	5.05E-13	1.62E-13	4.06E-13	9.45E-14	1.24E-11	5.65E-13	2.36E-10	3.04E-12	19.06	0.90	**2.05**	**0.097**	37	468	150.7	0.03	0.0078
OR12-5-02	0.73	0.37	1.81E-13	2.71E-14	1.69E-13	3.75E-14	#REF!	#REF!	#REF!	#REF!	7.99	0.19	**0.86**	**0.02**	26	398	59.9	0.02	0.0042
OR12-5-03	1.00	0.51	-2.08E-14	1.28E-13	4.26E-14	2.05E-13	4.57E-12	2.28E-13	2.07E-11	1.85E-12	4.53	0.46	**0.49**	**0.050**	100	na	na	0.01	0.0448
OR12-5-04	1.30	0.66	8.14E-14	5.34E-14	1.18E-14	6.23E-14	3.01E-12	1.21E-13	1.72E-11	6.38E-13	5.71	0.31	**0.62**	**0.034**	100	na	na	0.00	0.0207
OR12-5-05	3.65	1.86	2.84E-13	3.26E-14	5.49E-14	2.29E-14	7.77E-12	2.32E-13	4.98E-11	3.21E-12	6.41	0.46	**0.69**	**0.049**	0	175	23.0	0.01	0.0030
OR12-5-06	5.50	2.80	1.80E-13	5.34E-14	1.58E-13	2.84E-14	2.91E-12	8.82E-14	3.35E-11	1.31E-12	11.53	0.57	**1.24**	**0.061**	0	187	56.0	0.05	0.0099
or12-5-07	8.90	4.53	-4.63E-15	1.06E-13	1.16E-13	4.08E-14	8.36E-13	4.84E-14	1.45E-11	6.28E-13	17.37	1.26	**1.87**	**0.135**	100	na	na	0.14	0.0495
OR12-6																			
OR12-6-01	0.51	0.26	4.76E-13	1.20E-13	4.97E-13	3.54E-13	1.67E-11	2.01E-12	2.27E-10	9.62E-12	13.56	1.73	**1.46**	**0.186**	38	476	122.2	0.03	0.0215
OR12-6-02	0.73	0.37	-3.79E-15	1.38E-13	3.60E-14	6.06E-14	6.78E-12	1.39E-13	1.17E-11	1.81E-12	1.72	0.27	**0.19**	**0.029**	100	na	na	0.01	0.0090
OR12-6-03	1.00	0.51	4.84E-15	6.24E-14	5.64E-14	4.45E-14	4.71E-12	1.06E-13	5.21E-12	1.18E-12	1.11	0.25	**0.12**	**0.027**	100	na	na	0.01	0.0095
OR12-6-04	1.30	0.66	-4.77E-15	9.33E-14	6.60E-14	5.16E-14	3.16E-12	1.04E-13	1.57E-12	7.28E-13	0.50	0.23	**0.05**	**0.025**	100	na	na	0.02	0.0163
OR12-6-05	3.65	1.86	6.43E-14	5.10E-14	1.55E-14	7.69E-14	7.49E-12	1.86E-13	3.58E-11	6.12E-13	4.78	0.14	**0.52**	**0.016**	100	na	na	0.00	0.0103
OR12-6-06	5.50	2.80	8.93E-14	6.89E-14	-3.92E-14	4.42E-14	2.11E-12	1.10E-13	1.17E-11	1.68E-12	5.57	0.85	**0.60**	**0.092**	100	na	na	-0.02	-0.0210
OR12-6-07	8.90	4.53	-1.79E-14	6.10E-14	-5.29E-14	4.16E-14	8.28E-13	9.49E-14	4.07E-12	7.08E-13	4.92	1.02	**0.53**	**0.110**	100	na	na	-0.06	-0.0508

OR06: *Extraction*	*irradiance* ($Wm^{-2} \times 10^{5}$)	36Ar (cc)	±36Ar (cc)	38Ar* (cc)	±38Ar* (cc)	39Ar (cc)	±39Ar (cc)	40Ar (cc)	±40Ar (cc)	40Ar* (cc)	±40Ar* (cc)	*40Ar*/39Ar*	*±40Ar*/39Ar*
OR06-9													
OR06-9-01	0.26	6.62E-14	4.15E-14	3.54E-14	2.55E-14	-8.62E-14	1.06E-13	6.74E-12	2.75E-12	-1.28E-11	5.36E-13	148.86	234.49
OR06-9-02	0.66	7.39E-13	2.16E-13	1.26E-13	1.90E-13	2.42E-12	4.51E-13	1.47E-10	2.30E-11	-7.17E-11	1.25E-12	-29.67	-28.62
OR06-9-03	2.01	2.16E-12	2.64E-13	6.56E-13	2.16E-13	9.89E-12	1.06E-12	2.16E-10	2.30E-11	-4.24E-10	1.39E-12	-42.83	-9.41
OR06-9-04	2.01	5.75E-13	1.17E-13	5.22E-14	3.86E-14	2.80E-12	1.77E-13	2.24E-10	3.82E-12	5.42E-11	8.94E-13	19.38	12.53
OR06-9-05	2.01	1.73E-13	8.23E-14	2.52E-14	3.57E-14	6.98E-13	1.06E-13	4.79E-11	2.92E-12	-3.22E-12	7.49E-13	-4.62	-35.10
OR06-8													
OR06-8-02	0.66	1.098E-13	1.327E-13	2.046E-13	6.606E-14	1.55E-12	9.865E-14	9.525E-11	4.379E-12	6.28E-11	9.512E-13	40.51	25.59
OR06-8-03	0.92	1.914E-13	1.241E-13	-2.36E-14	4.167E-14	1.682E-12	1.562E-13	1.219E-10	1.76E-12	6.537E-11	9.175E-13	38.87	22.12
OR06-8-04	1.25	4.164E-13	6.184E-14	-7.27E-14	6.23E-14	1.791E-12	9.727E-14	1.58E-10	1.662E-12	3.493E-11	6.484E-13	19.50	10.30
OR06-8-05	1.58	3.284E-13	8.24E-14	7.708E-14	6.477E-14	2.039E-12	1.179E-13	1.667E-10	2.92E-12	6.966E-11	7.505E-13	34.16	12.19
OR06-8-06	1.86	4.28E-13	9.853E-14	4.266E-14	1.098E-13	2.293E-12	1.198E-13	1.887E-10	6.84E-13	6.223E-11	8.174E-13	27.14	12.78
OR06-8-07	2.01	2.946E-13	5.888E-14	-9.24E-15	5.824E-14	1.491E-12	1.071E-13	1.215E-10	1.206E-12	3.45E-11	6.321E-13	23.14	11.81
OR06-9-08	2.04	1.722E-13	5.927E-14	-8.95E-15	3.424E-14	8.416E-13	5.624E-14	6.091E-11	1.609E-12	1.003E-11	6.344E-13	11.92	20.91
OR06-8-09	2.75	4.052E-13	5.488E-14	4.365E-14	4.65E-14	1.749E-12	5.67E-14	1.537E-10	2.264E-12	3.393E-11	6.125E-13	19.40	9.38
OR06-7													
OR06-7-02	0.92	3.218E-13	6.433E-14	1.293E-13	4.917E-14	1.782E-12	2.09E-13	1.17E-10	3.349E-12	2.185E-11	6.648E-13	12.26	10.93
OR06-7-03	1.25	2.546E-13	6.076E-14	7.438E-14	4.836E-14	1.306E-12	1.053E-13	1.029E-10	2.031E-12	2.766E-11	6.433E-13	21.18	13.94
OR06-7-04	1.58	3.147E-13	9.467E-14	3.977E-14	5.557E-14	1.705E-12	7.847E-14	1.323E-10	1.533E-12	3.928E-11	8.011E-13	23.03	16.46
OR06-7-05	1.86	3.223E-13	1.715E-13	-2.16E-14	7.02E-14	1.522E-12	8.506E-14	1.301E-10	2.127E-12	3.482E-11	1.078E-12	22.88	33.36
OR06-7-06	2.01	3.646E-13	1.347E-13	-1.65E-14	4.797E-14	1.627E-12	1.927E-13	1.499E-10	4.495E-12	4.213E-11	9.579E-13	25.89	24.81
OR06-7-07	2.04	1.295E-13	7.989E-14	2.195E-15	4.5E-14	7.166E-13	2.459E-13	6.409E-11	1.682E-12	2.583E-11	7.361E-13	36.05	35.27
OR06-7-08	2.75	1.084E-13	6.824E-14	8.778E-15	2.602E-14	5.313E-13	7.52E-14	4.305E-11	1.239E-12	1.102E-11	6.8E-13	20.74	38.14

OR06 cont: *Extraction*	***Age (Ma)***	***± Age (Ma)***	*%40Ar**	*40Ar/36Ar*	*±40Ar/36Ar*	*39Ar/40Ar*	*±39Ar/40Ar*	*38Ar/39Ar*	*±38Ar/39Ar*
OR06-9-01	19.50	30.55	0	102	76.10	-0.01	-0.02	-0.411	-0.59
OR06-9-02	nd		0	199	65.80	0.02	0.00	0.052	0.08
OR06-9-03	nd		0	100	16.15	0.05	0.01	0.066	0.02
OR06-9-04	2.55	1.65	24	390	79.84	0.01	0.00	0.019	0.01
OR06-9-05	nd		0	277	132.73	0.01	0.00	0.036	0.05
OR06-8									
OR06-8-02	5.33	3.36	66	867	1048.94	0.02	0.00	0.132	0.04
OR06-8-03	5.11	2.91	54	637	412.99	0.01	0.00	-0.014	-0.02
OR06-8-04	2.57	1.35	22	379	56.48	0.01	0.00	-0.041	-0.03
OR06-8-05	4.49	1.60	42	508	127.65	0.01	0.00	0.038	0.03
OR06-8-06	3.57	1.68	33	441	101.51	0.01	0.00	0.019	0.05
OR06-8-07	3.04	1.55	28	413	82.57	0.01	0.00	-0.006	-0.04
OR06-9-08	1.57	2.75	16	354	122.12	0.01	0.00	-0.011	-0.04
OR06-8-09	2.55	1.23	22	379	51.66	0.01	0.00	0.025	0.03
OR06-7									
OR06-7-02	1.61	1.44	19	363	73.39	0.02	0.00	0.073	0.03
OR06-7-03	2.79	1.83	27	404	96.77	0.01	0.00	0.057	0.04
OR06-7-04	3.03	2.16	30	420	126.54	0.01	0.00	0.023	0.03
OR06-7-05	3.01	4.39	27	404	214.81	0.01	0.00	-0.014	-0.05
OR06-7-06	3.41	3.26	28	411	152.40	0.01	0.00	-0.010	-0.03
OR06-7-07	4.74	4.63	40	495	305.74	0.01	0.00	0.003	0.06
OR06-7-08	2.73	5.02	26	397	250.22	0.01	0.00	0.017	0.05

INITIAL LASER SET-UP TEST RUNS:

Extraction	*lamp (W)*	*irradiance (Wm^{-2} x 10^5)*	*36Ar (cc)*	*±36Ar (cc)*	*38Ar* (cc)*	*±38Ar* (cc)*	*39Ar (cc)*	*±39Ar (cc)*	*40Ar (cc)*	*±40Ar (cc)*	***40Ar/39Ar***	*± error*	***Age (Ma)***	***± error***	*%rad 40Ar*	*40Ar/36Ar*	*±40Ar/36Ar*	*38Ar/39Ar*	*±38Ar/39Ar*
OR44																			
OR44obs2-1	6.80	3.46	2.75E-13	1.02E-13	8.52E-14	8.58E-14	2.94E-11	9.42E-13	1.15E-10	2.92E-12	**3.92**	0.16	**0.52**	**0.021**	29	419	155.9	0.0029	0.0029
OR44obs2-2	15.90	8.10	3.30E-13	1.02E-13	1.04E-13	9.29E-14	4.30E-11	5.99E-13	1.18E-10	3.25E-12	**2.74**	0.08	**0.36**	**0.011**	17	357	110.6	0.0024	0.0022
OR44obs2-3	15.90	8.10	2.17E-13	7.57E-14	3.56E-14	8.35E-14	1.24E-11	1.99E-13	3.34E-11	2.95E-12	**2.70**	0.24	**0.36**	**0.032**	0	154	55.2	0.0029	0.0068
OR44obs2-4	15.90	8.10	5.38E-14	7.62E-14	1.08E-13	1.08E-13	1.18E-11	2.19E-13	1.80E-11	3.20E-12	**1.52**	0.27	**0.20**	**0.036**	12	334	476.2	0.0092	0.0092
OR44obs3-1	6.80	3.46	1.49E-13	7.12E-14	1.76E-13	8.23E-14	2.62E-11	2.40E-13	6.09E-11	2.91E-12	**2.33**	0.11	**0.31**	**0.015**	28	408	195.6	0.0067	0.0031
OR44obs3-2	15.90	8.10	5.30E-14	1.36E-13	1.93E-13	9.25E-14	3.09E-11	3.62E-13	5.63E-11	3.04E-12	**1.82**	0.10	**0.24**	**0.013**	72	1063	2724.5	0.0062	0.0030
OR44obs3-3	15.90	8.10	-1.69E-13	1.12E-13	-3.30E-14	8.88E-14	5.75E-12	1.39E-13	9.02E-12	2.97E-12	**1.57**	0.52	**0.21**	**0.068**	100	n/a	n/a	-0.0057	-0.0154
OR44obs4-1	6.80	3.46	8.46E-14	3.45E-13	-6.45E-15	3.17E-13	3.69E-12	3.67E-12	1.95E-11	6.93E-11	**5.27**	19.48	**0.69**	**2.564**	0	230	1244.5	-0.0017	-0.0859
OR44obs4-2	15.90	8.10	4.39E-13	1.40E-13	2.52E-13	9.23E-14	4.15E-11	6.29E-13	1.87E-10	4.18E-12	**4.51**	0.12	**0.59**	**0.016**	31	427	136.3	0.0061	0.0022
OR44obs4-3	15.90	8.10	1.33E-13	7.20E-14	3.19E-13	1.03E-13	2.08E-11	4.21E-13	4.23E-11	3.67E-12	**2.03**	0.18	**0.27**	**0.024**	7	319	175.6	0.0153	0.0050
OR440bs4-4	15.90	8.10	8.16E-14	7.18E-14	1.47E-13	1.12E-13	9.90E-12	1.23E-13	9.77E-12	2.95E-12	**0.99**	0.30	**0.13**	**0.039**	100	n/a	n/a	0.0148	0.0113
OR54																			
OR54obs2-1	0.51	0.26	1.11E-13	9.23E-14	2.91E-13	7.17E-14	1.62E-12	1.61E-13	9.32E-12	5.14E-12	**5.76**	3.22	**0.76**	**0.424**	-252	84	83.5	0.1799	0.0477
OR54obs2-2	4.00	2.04	6.08E-13	1.53E-13	1.73E-12	5.14E-13	4.55E-11	2.70E-12	6.95E-11	1.02E-10	**1.53**	2.24	**0.20**	**0.295**	-159	114	169.8	0.0380	0.0115
OR54obs2-3	5.40	2.75	1.94E-13	1.42E-13	1.02E-12	3.26E-13	4.86E-11	2.06E-12	6.88E-11	4.20E-11	**1.42**	0.87	**0.19**	**0.114**	17	355	338.2	0.0211	0.0068
OR54obs3-1	0.51	0.26	4.55E-14	5.90E-14	4.28E-14	5.31E-14	2.88E-13	8.74E-14	4.09E-12	2.54E-12	**14.21**	9.82	**1.87**	**1.292**	-229	90	129.3	0.1488	0.1900
OR54obs3-2	2.45	1.25	3.17E-13	1.04E-13	3.13E-13	1.92E-13	3.91E-11	4.60E-13	5.39E-11	5.30E-12	**1.38**	0.14	**0.18**	**0.018**	-74	170	58.1	0.0080	0.0049
OR54obs3-3	4.00	2.04	2.46E-14	6.87E-14	1.63E-13	5.30E-14	1.16E-11	3.18E-13	1.52E-11	4.67E-12	**1.32**	0.41	**0.17**	**0.053**	52	618	1732.4	0.0141	0.0046
OR54obs3-4	5.50	2.80	1.40E-13	7.34E-14	3.02E-13	8.05E-14	3.91E-11	7.61E-13	3.75E-11	7.74E-12	**0.96**	0.20	**0.13**	**0.026**	-10	268	151.2	0.0077	0.0021
OR10																			
OR10obs1-1	0.51	0.26	3.24E-14	8.78E-14	7.43E-14	7.88E-14	8.76E-13	9.66E-14	9.32E-12	2.43E-12	**10.64**	3.01	**1.40**	**0.396**	-3	288	783.8	0.0848	0.0904
OR10obs1-3	2.45	1.25	3.36E-13	2.50E-13	4.79E-14	9.52E-14	1.73E-11	3.39E-13	8.32E-11	2.37E-12	**4.80**	0.17	**0.63**	**0.022**	-19	248	184.3	0.0028	0.0055
OR10obs1-4	4.00	2.04	7.41E-13	8.40E-14	3.54E-13	5.25E-14	3.95E-11	6.27E-13	2.26E-10	1.32E-11	**5.72**	0.35	**0.75**	**0.046**	3	305	38.9	0.0090	0.0013
OR10obs1-5	5.50	2.80	-9.75E-14	1.12E-13	-6.50E-14	9.19E-14	-3.46E-13	9.74E-14	8.27E-11	1.85E-12	**-238.93**	-67.46	**-31.74**	**9.041**	135	-849	-979.3	0.1877	0.2706
OR10obs2-1	0.51	0.26	2.25E-14	7.40E-14	2.23E-14	7.44E-14	2.18E-13	1.13E-13	2.73E-12	1.53E-12	**12.55**	9.59	**1.65**	**1.262**	-143	121	405.6	0.1027	0.3461
OR10obs2-2	2.45	1.25	7.01E-13	7.16E-14	2.22E-13	1.37E-13	2.86E-11	7.12E-13	1.83E-10	3.67E-12	**6.40**	0.20	**0.84**	**0.027**	-13	261	27.2	0.0078	0.0048
OR10obs2-3	4.00	2.04	4.66E-13	1.43E-13	2.97E-13	9.53E-14	2.08E-11	5.30E-13	1.48E-10	6.90E-12	**7.11**	0.38	**0.94**	**0.050**	7	318	98.4	0.0143	0.0046
OR10obs2-4	5.50	2.80	5.48E-13	7.83E-14	1.61E-13	8.69E-14	2.09E-11	3.83E-13	1.63E-10	6.04E-12	**7.80**	0.32	**1.03**	**0.042**	0	297	43.8	0.0077	0.0042
OR10obs2-5	7.60	3.87	4.56E-13	7.26E-14	1.54E-13	8.36E-14	2.93E-11	1.11E-12	1.28E-10	2.15E-12	**4.37**	0.18	**0.58**	**0.024**	-5	281	45.1	0.0053	0.0029
OR10obs2-6	7.60	3.87	3.55E-13	9.69E-14	-2.83E-14	1.37E-13	1.95E-11	1.94E-13	1.12E-10	2.86E-12	**5.77**	0.16	**0.76**	**0.021**	7	317	86.8	-0.0015	-0.0070
OR10obs3-1	0.51	0.26	3.73E-14	7.24E-14	7.06E-14	5.99E-14	5.70E-13	6.06E-14	2.83E-12	1.54E-12	**4.96**	2.76	**0.65**	**0.364**	-290	76	152.9	0.1239	0.1059
OR10obs3-2	2.45	1.25	1.38E-13	1.50E-13	1.22E-13	1.20E-13	1.63E-11	4.09E-13	6.27E-11	4.02E-12	**3.85**	0.26	**0.51**	**0.035**	35	454	492.2	0.0075	0.0074
OR10obs3-3	4.00	2.04	1.52E-13	8.53E-14	3.11E-14	1.26E-13	9.32E-12	3.56E-13	2.85E-11	3.96E-12	**3.06**	0.44	**0.40**	**0.058**	-57	188	108.4	0.0033	0.0135
OR10obs3-4	5.50	2.80	5.98E-13	6.76E-14	2.38E-13	1.01E-13	3.57E-11	9.31E-13	1.68E-10	5.85E-12	**4.69**	0.20	**0.62**	**0.027**	-5	280	33.1	0.0067	0.0028
OR10obs3-5	7.60	3.87	3.23E-13	6.08E-14	1.64E-13	6.45E-14	1.88E-11	2.57E-13	1.01E-10	2.71E-12	**5.38**	0.16	**0.71**	**0.021**	6	314	59.8	0.0087	0.0034
OR10obs3-6	7.60	3.87	5.16E-13	8.11E-14	1.18E-13	7.98E-14	1.31E-11	1.50E-13	1.61E-10	2.95E-12	**12.30**	0.27	**1.62**	**0.035**	5	311	49.3	0.0090	0.0061

OR150		irradiance																
Extraction	*lamp(W)*	*(Wm^{-2} x 10^5)*	*36Ar (cc)*	*±36Ar (cc)*	*38Ar* (cc)*	*±38Ar* (cc)*	*39Ar (cc)*	*±39Ar (cc)*	*40Ar (cc)*	*±40Ar (cc)*	*40Ar/39Ar*	*± error*	***Age (Ma)***	***± error***	*%rad 40Ar*	*40Ar/36Ar*	*±40Ar/36Ar*	*38Ar/39Ar*	*±38Ar/39Ar*
OR150-1																			
OR150-1-01	1.30	0.66	3.83E-13	3.64E-14	1.57E-14	9.91E-14	3.62E-12	7.43E-14	1.12E-10	4.68E-13	30.97	0.65	**3.34**	**0.070**	0	293	28.0	0.0043	0.0274
OR150-1-02	1.80	0.92	1.70E-13	3.53E-14	3.05E-14	2.94E-14	2.69E-12	8.52E-14	5.53E-11	2.78E-13	20.55	0.66	**2.22**	**0.071**	9	326	67.9	0.0113	0.0109
OR150-1-03	2.45	1.25	8.73E-13	5.34E-14	3.25E-15	2.67E-14	4.05E-12	2.64E-13	2.43E-10	8.71E-12	59.89	4.45	**6.45**	**0.478**	0	278	19.7	0.0008	0.0066
OR150-1-04	3.10	1.58	1.40E-12	6.50E-14	3.14E-14	3.07E-14	7.62E-12	9.03E-14	3.88E-10	3.30E-12	50.94	0.74	**5.49**	**0.080**	0	278	13.1	0.0041	0.0040
OR150-1-05	3.10	1.58	3.76E-13	2.72E-14	1.80E-14	2.98E-14	3.89E-12	7.11E-14	1.02E-10	1.39E-12	26.18	0.60	**2.82**	**0.064**	0	271	19.9	0.0046	0.0077
OR150-1-06	3.10	1.58	1.05E-13	3.48E-14	2.82E-14	4.15E-14	2.57E-12	9.38E-14	3.94E-11	4.30E-13	15.34	0.58	**1.65**	**0.063**	21	376	124.7	0.0110	0.0162
OR150-1-07	3.65	1.86	5.74E-13	2.80E-14	-3.63E-14	7.65E-14	6.49E-12	1.47E-13	1.31E-10	9.26E-13	20.14	0.48	**2.17**	**0.051**	0	228	11.2	-0.0056	-0.0118
OR150-1-08	3.95	2.01	5.80E-13	3.35E-14	1.87E-14	1.85E-14	9.38E-12	1.15E-13	1.65E-10	4.56E-13	17.58	0.22	**1.90**	**0.024**	0	284	16.4	0.0020	0.0020
OR150-1-09	4.00	2.04	2.85E-13	4.22E-14	7.63E-14	3.69E-14	6.39E-12	7.97E-14	8.82E-11	7.22E-13	13.81	0.21	**1.49**	**0.022**	5	310	45.9	0.0119	0.0058
OR150-1-10	4.00	2.04	8.09E-14	4.15E-14	7.16E-15	1.60E-14	3.12E-12	7.04E-14	3.92E-11	9.27E-13	12.57	0.41	**1.36**	**0.044**	39	485	249.1	0.0023	0.0051
OR150-1-11	5.40	2.75	3.37E-13	2.12E-14	1.37E-14	1.50E-14	5.21E-12	1.37E-13	8.44E-11	5.30E-13	16.21	0.44	**1.75**	**0.047**	0	251	15.9	0.0026	0.0029
OR150-1-12	7.60	3.87	2.78E-13	6.20E-14	6.28E-14	3.46E-14	4.96E-12	1.41E-13	8.37E-11	6.38E-13	16.88	0.50	**1.82**	**0.054**	2	301	67.3	0.0127	0.0070
OR150-1-13	13.30	6.77	3.00E-13	3.07E-14	5.79E-14	2.41E-14	4.28E-12	7.75E-14	8.98E-11	5.67E-13	20.99	0.40	**2.26**	**0.043**	1	299	30.7	0.0135	0.0056
OR150-1-14	13.90	7.08	6.93E-14	5.14E-14	1.70E-14	5.37E-14	1.36E-12	6.11E-14	3.03E-11	2.53E-13	22.29	1.02	**2.40**	**0.110**	32	437	324.0	0.0125	0.0395

OR202		irradiance																	
Extraction	*lamp (W)*	*(Wm^{-2} x 10^5)*	*36Ar (cc)*	*±36Ar (cc)*	*38Ar* (cc)*	*±38Ar* (cc)*	*39Ar (cc)*	*±39Ar (cc)*	*40Ar (cc)*	*±40Ar (cc)*	*40Ar/39Ar*	*± error*	***Age (Ma)***	***± error***	*%rad 40Ar*	*40Ar/36Ar*	*±40Ar/36Ar*	*38Ar/39Ar*	*±38Ar/39Ar*
OR202-1																			
OR202-1-02	1.3	0.66	1.64E-12	7.08E-14	8.94E-14	4.85E-14	7.93E-12	1.38E-13	4.96E-10	4.30E-12	62.62	1.22	**6.74**	**0.131**	2	302	13.3	0.0113	0.0061
OR202-1-03	1.3	0.66	5.93E-13	1.33E-13	-6.40E-14	5.95E-14	4.55E-12	7.79E-14	1.91E-10	3.41E-12	42.05	1.04	**4.53**	**0.112**	8	323	72.4	-0.0141	-0.0131
OR202-1-04	1.8	0.92	1.16E-12	4.90E-14	-4.05E-14	1.04E-13	8.20E-12	3.32E-13	3.68E-10	4.80E-12	44.82	1.90	**4.83**	**0.205**	7	318	14.1	-0.0049	-0.0127
OR202-1-05	2.45	1.25	1.31E-12	7.89E-14	3.15E-14	7.39E-14	1.12E-11	1.21E-13	3.35E-10	1.38E-11	29.86	1.27	**3.22**	**0.137**	0	255	18.6	0.0028	0.0066
OR202-1-06	3.10	1.58	4.20E-13	7.73E-14	-5.93E-14	6.29E-14	5.63E-12	7.55E-14	1.31E-10	1.97E-12	23.25	0.47	**2.51**	**0.050**	5	312	57.5	-0.0105	-0.0112
OR202-1-07	3.65	1.86	1.72E-13	4.77E-14	-1.01E-13	8.43E-14	2.97E-12	9.04E-14	5.80E-11	1.20E-12	19.52	0.72	**2.10**	**0.077**	12	337	93.5	-0.0341	-0.0284
OR202-1-08	3.95	2.01	2.35E-14	7.91E-14	8.22E-15	9.44E-14	1.42E-12	1.29E-13	2.80E-11	1.13E-12	19.76	1.97	**2.13**	**0.213**	100	n/a	n/a	0.0058	0.0667
OR202-1-09	5.40	2.75	1.83E-13	5.75E-14	2.10E-15	6.74E-14	1.72E-12	9.30E-14	3.43E-11	9.99E-13	19.92	1.22	**2.15**	**0.132**	0	188	59.4	0.0012	0.0391

OR221		irradiance																	
Extraction	*lamp(W)*	*(Wm^{-2} x 10^5)*	*36Ar (cc)*	*±36Ar (cc)*	*38Ar* (cc)*	*±38Ar* (cc)*	*39Ar (cc)*	*±39Ar (cc)*	*40Ar (cc)*	*±40Ar (cc)*	*40Ar/39Ar*	*± error*	***Age (Ma)***	***± error***	*%rad 40Ar*	*40Ar/36Ar*	*±40Ar/36Ar*	*38Ar/39Ar*	*±38Ar/39Ar*
OR221-1																			
OR221-1-01	1.3	0.66	1.84E-13	2.67E-14	3.03E-14	2.86E-14	2.14E-12	5.70E-14	4.99E-11	7.63E-13	23.37	0.72	**2.52**	**0.077**	0	272.0	39.8	0.0142	0.0134
OR221-1-02	1.8	0.92	1.74E-13	2.76E-14	2.07E-14	4.00E-14	2.32E-12	9.71E-14	4.07E-11	6.62E-13	17.54	0.79	**1.89**	**0.085**	0	234.1	37.3	0.0089	0.0173
OR221-1-03	2.45	1.25	2.81E-13	2.77E-14	1.60E-14	3.66E-14	4.03E-12	1.11E-13	6.95E-11	1.18E-12	17.25	0.56	**1.86**	**0.060**	0	247.3	24.7	0.0040	0.0091
OR221-1-04	3.1	1.58	7.11E-13	3.73E-14	4.43E-14	3.34E-14	8.81E-12	2.74E-13	1.96E-10	2.19E-12	22.27	0.73	**2.40**	**0.079**	0	275.8	14.8	0.0050	0.0038
OR221-1-05	3.65	1.86	7.85E-13	3.39E-14	3.86E-14	4.77E-14	1.14E-11	6.92E-14	2.05E-10	1.88E-12	17.89	0.20	**1.93**	**0.021**	0	260.9	11.5	0.0034	0.0042
OR221-1-06	3.95	2.01	1.02E-12	4.55E-14	3.74E-14	3.06E-14	1.46E-11	1.71E-13	2.95E-10	1.14E-12	20.25	0.25	**2.18**	**0.027**	0	288.1	12.9	0.0026	0.0021
OR221-1-07	4	2.04	5.96E-13	5.39E-14	5.91E-14	3.64E-14	8.45E-12	2.05E-13	1.94E-10	1.88E-12	22.95	0.60	**2.47**	**0.065**	9	325.7	29.7	0.0070	0.0043
OR221-1-08	5.4	2.75	5.99E-13	3.73E-14	8.69E-15	3.46E-14	6.48E-12	1.23E-13	1.44E-10	9.05E-12	22.27	1.46	**2.40**	**0.157**	0	240.8	21.3	0.0013	0.0053
OR221-1-09	7.6	3.87	3.40E-13	5.17E-14	1.99E-14	2.83E-14	3.49E-12	7.00E-14	9.08E-11	8.77E-13	26.04	0.58	**2.81**	**0.062**	0	267.1	40.7	0.0057	0.0081
OR221-1-10	8.9	4.53	1.99E-13	4.88E-14	1.36E-14	2.78E-14	2.38E-12	6.85E-14	6.21E-11	9.69E-13	26.13	0.86	**2.82**	**0.092**	5	311.6	76.3	0.0057	0.0117
or221-1-11	13.3	6.77	5.12E-13	3.68E-14	5.90E-15	2.71E-14	2.68E-12	5.59E-14	1.58E-10	6.86E-13	58.77	1.25	**6.33**	**0.135**	4	307.9	22.2	0.0022	0.0101

OR39		irradiance											36Ar Correction applied		36Ar Correction applied		36Ar Correction not applied		36Ar Correction not applied						
traction Nam	lamp (W)	(Wm⁻² x 10⁵)	36Ar (cc)	±36Ar (cc)	38Ar* (cc)	±38Ar* (cc)	39Ar (cc)	±39Ar (cc)	40Ar (cc)	±40Ar (cc)	40Ar* (cc)	±40Ar* (cc)	40Ar*/39Ar	±40Ar*/39Ar	**Age (Ma)**	**± Age (Ma)**	40Ar/39Ar	± error	**Age (Ma)**	**± error**	%rad 40Ar	40Ar/36Ar	±40Ar/36Ar	38Ar/39Ar	±38Ar/39Ar
OR39																									
OR39-1																									
OR39-1-01	15amp	#VALUE!	2.85E-12	2.69E-13	1.35E-12	5.18E-13	9.50E-11	4.21E-12	6.11E-10	7.31E-10	-2.31E-10	4.10E-12	-2.35	20.43	**-0.31**	**0.309**	6.44	7.70	**0.85**	**1.014**	0	215	257.3	0.0143	0.0055
OR39-1-02	2.50	1.27	2.84E-12	5.53E-14	-3.01E-13	1.67E-13	4.57E-11	2.57E-12	6.81E-10	5.40E-11	-1.58E-10	1.24E-12	-3.29	5.39	**-0.43**	**0.433**	14.89	1.45	**1.96**	**0.190**	0	240	22.1	-0.0066	-0.0037
OR39-2																									
OR39-2-01	1.30	0.66	2.87E-12	1.28E-13	2.01E-12	1.82E-12	9.70E-11	6.56E-12	7.39E-10	1.38E-09	-1.08E-10	5.62E-12	-1.04	97.78	**-0.14**	**0.136**	7.63	14.24	**1.00**	**1.875**	0	258	485.5	0.0207	0.0188
OR39-2-02	2.50	1.27	2.36E-13	3.18E-14	-8.48E-14	1.32E-13	5.69E-12	1.36E-13	4.23E-11	9.52E-13	-2.73E-11	4.66E-13	-4.70	2.58	**-0.62**	**0.618**	7.44	0.24	**0.98**	**0.032**	0	180	34.0	-0.0149	-0.0232
OR39-2-03	13.30	6.77	2.20E-12	3.65E-14	1.05E-15	9.38E-14	2.61E-11	4.98E-13	6.52E-10	7.07E-12	4.63E-13	5.43E-13	0.23	695.20	**0.03**	**0.030**	25.00	0.55	**3.29**	**0.072**	0	296	8.4	0.0000	0.0036
OR39-2-04	13.30	6.77	3.50E-13	5.03E-14	1.17E-13	8.51E-14	2.90E-12	2.13E-13	1.31E-10	1.77E-12	2.73E-11	5.85E-13	9.74	24.91	**1.28**	**1.278**	45.11	3.37	**5.93**	**0.442**	21	374	118.1	0.0403	0.0295
OR39-3																									
OR39-3-01	1.30	0.66	2.73E-12	5.12E-14	5.99E-13	6.48E-14	9.54E-11	8.36E-13	8.21E-10	5.38E-11	1.49E-11	1.13E-12	0.23	32.32	**0.03**	**0.030**	8.60	0.57	**1.13**	**0.075**	2	301	23.4	0.0063	0.0007
OR39-3-02	2.50	1.27	6.51E-13	5.04E-14	-2.24E-14	8.69E-14	1.04E-11	2.47E-13	2.08E-10	2.48E-12	1.60E-11	5.88E-13	1.69	18.91	**0.22**	**0.223**	20.02	0.53	**2.63**	**0.070**	8	320	54.7	-0.0022	-0.0084
OR39-3-03	13.30	6.77	1.21E-12	4.54E-14	8.17E-14	5.93E-14	8.20E-12	2.16E-13	3.58E-10	3.95E-12	-6.64E-13	5.66E-13	0.29	918.94	**0.04**	**0.038**	43.61	1.25	**5.73**	**0.164**	0	295	22.2	0.0100	0.0072
OR39-3-04	13.30	6.77	7.26E-13	4.28E-14	1.08E-13	9.37E-14	2.84E-12	2.23E-13	1.37E-10	1.26E-11	-7.75E-11	6.41E-13	-26.67	11.77	**-3.52**	**3.500**	48.30	5.85	**6.35**	**0.768**	6	189	27.1	0.0380	0.0331
OR39-4																									
OR39-4-01	3.95	2.01	1.94E-12	4.00E-14	3.49E-13	1.98E-13	6.96E-11	5.23E-13	5.55E-10	2.19E-11	-1.70E-11	7.54E-13	-0.18	11.61	**-0.02**	**0.023**	7.97	0.32	**1.05**	**0.042**	0	287	15.3	0.0050	0.0028
OR39-4-02	5.40	2.75	1.63E-12	3.49E-14	1.40E-13	8.98E-14	2.58E-11	3.21E-13	4.70E-10	4.35E-12	-1.01E-11	5.06E-13	-0.23	20.20	**-0.03**	**0.031**	18.24	0.28	**2.40**	**0.037**	0	289	9.8	0.0054	0.0035
OR39-4-03	8.90	4.53	1.22E-12	3.10E-14	5.48E-14	6.30E-14	1.20E-11	4.75E-14	3.84E-10	3.53E-12	2.47E-11	4.74E-13	2.31	12.70	**0.30**	**0.304**	31.99	0.32	**4.21**	**0.042**	6	316	11.3	0.0046	0.0053
OR39-4-04	13.30	6.77	5.09E-13	3.36E-14	8.28E-14	7.86E-14	4.27E-12	1.55E-13	1.55E-10	3.89E-12	5.17E-12	4.94E-13	1.51	75.14	**0.20**	**0.198**	36.42	1.61	**4.79**	**0.211**	3	306	30.7	0.0194	0.0184

OR255		irradiance																	
Extraction	lamp (W)	(Wm⁻² x 10⁵)	36Ar (cc)	±36Ar (cc)	38Ar* (cc)	±38Ar* (cc)	39Ar (cc)	±39Ar (cc)	40Ar (cc)	±40Ar (cc)	40Ar/39Ar	± error	**Age (Ma)**	**± error**	%rad 40Ar	40Ar/36Ar	±40Ar/36Ar	38Ar/39Ar	±38Ar/39Ar
OR255-1																			
OR255-1-01	0.51	0.26	4.97E-14	4.98E-14	4.14E-14	4.16E-14	7.93E-13	8.23E-14	1.63E-11	1.23E-12	20.54	2.63	**2.21**	**0.284**	10	328	329.2	0.0522	0.0527
OR255-1-02	1	0.51	5.21E-14	3.36E-14	-2.57E-14	5.93E-14	1.82E-12	1.07E-13	1.95E-11	7.35E-13	10.72	0.75	**1.16**	**0.081**	21	374	241.8	-0.0141	-0.0326
OR255-1-03	2.45	1.25	5.00E-13	4.56E-14	1.49E-13	5.07E-14	1.53E-11	1.94E-13	1.63E-10	9.52E-13	10.64	0.15	**1.15**	**0.016**	9	326	29.8	0.0097	0.0033
OR255-1-04	3.65	1.86	6.09E-14	5.68E-14	-1.69E-14	5.09E-14	9.81E-12	1.87E-13	2.06E-11	8.85E-13	2.10	0.10	**0.23**	**0.011**	100	n/a	n/a	-0.0017	-0.0052
OR255-1-05	4.8	2.44	9.33E-15	3.88E-14	4.99E-14	7.82E-14	4.65E-12	8.57E-14	1.40E-11	7.88E-13	3.00	0.18	**0.32**	**0.019**	100	n/a	n/a	0.0107	0.0168
OR255-1-06	5.85	2.98	9.45E-14	3.25E-14	5.63E-15	5.78E-14	2.40E-12	9.19E-14	1.77E-11	8.31E-13	7.41	0.45	**0.80**	**0.048**	0	188	65.1	0.0023	0.0241
OR255-1-07	8.9	4.53	1.73E-13	7.04E-14	8.53E-14	8.14E-14	2.47E-12	1.19E-13	4.19E-11	1.02E-12	16.99	0.92	**1.83**	**0.099**	0	243	99.1	0.0346	0.0330

OR280		irradiance																	
Extraction	lamp (W)	(Wm⁻² x 10⁵)	36Ar (cc)	±36Ar (cc)	38Ar* (cc)	±38Ar* (cc)	39Ar (cc)	±39Ar (cc)	40Ar (cc)	±40Ar (cc)	40Ar/39Ar	± error	**Age (Ma)**	**± error**	%rad 40Ar	40Ar/36Ar	38Ar/39Ar	±38Ar/39Ar
OR280-1																		
OR280-1-01	1.3	0.66	2.73E-13	4.29E-14	7.12E-15	3.78E-14	2.38E-12	1.07E-13	7.82E-11	6.61E-13	32.92	1.50	**3.55**	**0.162**	0	286.3	0.0030	0.0006
OR280-1-02	1.3	0.66	8.24E-14	2.85E-14	-4.50E-15	2.50E-14	1.73E-12	1.10E-13	1.89E-11	5.36E-13	10.92	0.76	**1.18**	**0.082**	0	229.0	-0.0026	-0.0005
OR280-1-03	2.45	1.25	1.96E-13	5.07E-14	4.60E-14	2.70E-14	3.38E-12	9.38E-14	6.40E-11	7.22E-13	18.96	0.57	**2.04**	**0.061**	9	326.4	0.0136	0.0232
OR280-1-04	3.1	1.58	2.18E-13	4.26E-14	3.74E-14	2.88E-14	6.23E-12	1.54E-13	6.33E-11	9.69E-13	10.15	0.30	**1.09**	**0.032**	0	289.7	0.0060	0.0078
OR280-1-05	3.65	1.86	5.13E-13	4.73E-14	3.55E-14	3.06E-14	4.73E-12	1.15E-13	1.45E-10	8.72E-13	30.70	0.77	**3.31**	**0.083**	0	283.0	0.0075	0.0087
OR280-1-06	3.95	2.01	1.73E-12	3.96E-14	2.40E-13	4.64E-14	2.10E-11	1.28E-13	5.28E-10	1.18E-11	25.15	0.58	**2.71**	**0.063**	3	304.7	0.0114	0.0592
OR280-1-07	4	2.04	6.58E-13	1.69E-14	4.07E-14	3.36E-14	9.61E-12	2.25E-13	1.95E-10	1.55E-12	20.31	0.50	**2.19**	**0.054**	0	296.3	0.0042	0.0051
OR280-1-08	5.4	2.75	4.23E-13	1.72E-14	5.17E-14	2.46E-14	7.21E-12	1.25E-13	1.22E-10	1.01E-12	16.96	0.32	**1.83**	**0.035**	0	289.2	0.0072	0.0151
OR280-1-09	7.05	3.59	9.86E-13	3.39E-14	-3.02E-15	3.62E-14	4.43E-12	1.38E-13	2.91E-10	4.64E-12	65.73	2.29	**7.08**	**0.246**	0	295.6	-0.0007	-0.0001

OR44 Extraction	lamp (W)	irradiance (Wm^{-2} x 10^5)	36Ar (cc)	±36Ar (cc)	38Ar* (cc)	±38Ar* (cc)	39Ar (cc)	±39Ar (cc)	40Ar (cc)	±40Ar (cc)	40Ar/39Ar	± error	**Age (Ma)**	**± error**	% 40Ar*	40Ar/36Ar	±40Ar/36Ar	38Ar/39Ar	±38Ar/39Ar
OR44-4																			
OR44-4-01	1.30	0.66	3.35E-15	4.38E-14	5.52E-14	4.36E-14	2.66E-12	9.66E-14	2.08E-11	1.31E-12	7.84	0.57	**1.03**	**0.075**	100	n/a	n/a	0.0208	0.0263
OR44-4-02	1.80	0.92	1.92E-14	4.52E-14	3.22E-14	2.78E-14	2.72E-12	6.20E-14	1.06E-11	1.24E-12	3.90	0.46	**0.51**	**0.061**	100	n/a	n/a	0.0118	0.0137
OR44-4-03	2.45	1.25	1.65E-15	5.89E-14	-2.87E-15	2.19E-14	3.02E-12	6.80E-14	8.85E-12	9.57E-13	2.93	0.32	**0.39**	**0.043**	100	n/a	n/a	-0.0010	-0.0001
OR44-4-04	3.10	1.58	-4.55E-14	4.84E-14	3.83E-14	2.67E-14	4.49E-12	7.10E-14	1.04E-11	9.27E-13	2.31	0.21	**0.30**	**0.028**	100	n/a	n/a	0.0085	0.0122
OR44-4-05	3.65	1.86	-3.15E-14	4.34E-14	6.03E-14	5.71E-14	9.07E-12	1.21E-13	2.08E-11	1.22E-12	2.30	0.14	**0.30**	**0.018**	100	n/a	n/a	0.0066	0.0070
OR44-4-06	3.95	2.01	-6.30E-15	3.64E-14	1.74E-14	4.02E-14	3.65E-12	6.73E-14	6.34E-12	9.82E-13	1.74	0.27	**0.23**	**0.036**	100	n/a	n/a	0.0048	0.0021
OR44-4-07	4.00	2.04	-3.05E-15	4.14E-14	4.74E-15	2.34E-14	5.23E-12	1.33E-13	6.52E-12	1.13E-12	1.25	0.22	**0.16**	**0.029**	100	n/a	n/a	0.0009	0.0002
OR44-4-08	5.40	2.75	8.43E-14	1.65E-13	3.84E-15	3.70E-14	7.03E-12	1.82E-13	1.24E-11	1.22E-12	1.77	0.18	**0.23**	**0.024**	100	n/a	n/a	0.0005	0.0001
OR44-4-09	7.06	3.60	3.47E-14	5.54E-14	1.35E-14	3.89E-14	4.68E-12	7.15E-14	4.35E-12	9.46E-13	0.93	0.20	**0.12**	**0.027**	100	n/a	n/a	0.0029	0.0010
OR44-5																			
OR44-5-01	1.30	0.66	8.33E-14	4.04E-14	2.06E-14	1.98E-14	3.08E-12	5.55E-14	2.52E-11	1.13E-12	8.17	0.39	**1.08**	**0.052**	2	302	147.2	0.0067	0.0070
OR44-5-02	1.80	0.92	4.74E-14	4.65E-14	4.80E-15	2.87E-14	3.27E-12	1.06E-13	1.32E-11	1.08E-12	4.03	0.35	**0.53**	**0.047**	0	278	273.3	0.0015	0.0002
OR44-5-03	2.45	1.25	4.43E-14	6.58E-14	3.65E-14	4.04E-14	5.74E-12	1.18E-13	1.79E-11	7.37E-13	3.11	0.14	**0.41**	**0.019**	100	n/a	n/a	0.0064	0.0058
OR44-5-04	3.10	1.58	4.64E-14	7.00E-14	3.65E-14	3.82E-14	4.70E-12	1.61E-13	1.04E-11	6.14E-13	2.20	0.15	**0.29**	**0.020**	100	n/a	n/a	0.0078	0.0074
OR44-5-05	3.65	1.86	5.83E-14	3.48E-14	6.30E-14	2.65E-14	7.61E-12	1.45E-13	1.56E-11	8.27E-13	2.05	0.12	**0.27**	**0.015**	100	n/a	n/a	0.0083	0.0197
OR44-5-06	3.95	2.01	-3.39E-15	3.53E-14	7.88E-14	3.69E-14	8.25E-12	8.79E-14	9.89E-12	7.55E-13	1.20	0.09	**0.16**	**0.012**	100	n/a	n/a	0.0096	0.0204
OR44-5-07	4.00	2.04	-2.68E-14	5.12E-14	2.54E-14	2.03E-13	5.49E-12	9.23E-14	8.13E-12	8.28E-13	1.48	0.15	**0.20**	**0.020**	100	n/a	n/a	0.0046	0.0006
OR44-5-08	5.40	2.75	2.42E-14	3.42E-14	9.17E-14	2.56E-14	8.84E-12	2.63E-13	9.43E-12	1.76E-12	1.07	0.20	**0.14**	**0.027**	100	n/a	n/a	0.0104	0.0371
OR44-5-09	7.06	3.60	9.90E-15	3.82E-14	4.72E-14	2.08E-14	8.55E-12	8.77E-14	9.59E-12	6.83E-13	1.12	0.08	**0.15**	**0.011**	100	n/a	n/a	0.0055	0.0125
OR44-5-10	8.9	4.53	2.97E-14	4.37E-14	-3.02E-17	3.95E-14	5.58E-12	1.05E-13	6.42E-12	1.03E-12	1.15	0.19	**0.15**	**0.024**	100	n/a	n/a	0.0000	0.0000
OR44-6																			
OR44-6-01	1.30	0.66	1.24E-13	2.66E-14	-1.23E-14	2.70E-14	3.21E-12	8.75E-14	2.72E-11	4.51E-13	8.49	0.27	**1.12**	**0.036**	0	220	47.5	-0.0038	-0.0018
OR44-6-02	1.80	0.92	9.51E-14	4.15E-14	-2.58E-14	1.88E-14	5.27E-12	1.47E-13	2.00E-11	3.00E-13	3.79	0.12	**0.50**	**0.016**	0	210	91.7	-0.0049	-0.0067
OR44-6-03	2.45	1.25	1.61E-14	7.61E-14	6.03E-14	4.67E-14	3.58E-12	6.62E-14	8.94E-12	7.32E-13	2.50	0.21	**0.33**	**0.028**	100	n/a	n/a	0.0169	0.0218
OR44-6-04	3.10	1.58	5.39E-14	2.38E-14	2.40E-14	2.39E-14	5.51E-12	8.81E-14	1.31E-11	8.08E-13	2.38	0.15	**0.31**	**0.020**	100	n/a	n/a	0.0044	0.0044
OR44-6-05	3.65	1.86	1.11E-14	2.54E-14	7.30E-14	3.69E-14	6.56E-12	4.32E-13	1.05E-11	5.36E-13	1.60	0.13	**0.21**	**0.018**	100	n/a	n/a	0.0111	0.0220
OR44-6-06	3.95	2.01	2.61E-14	1.71E-14	5.20E-14	5.28E-14	7.11E-12	3.91E-14	1.75E-11	3.49E-13	2.47	0.05	**0.32**	**0.007**	100	n/a	n/a	0.0073	0.0072
OR44-6-07	4.00	2.04	2.92E-14	1.84E-14	4.02E-14	3.92E-14	5.28E-12	1.06E-13	1.15E-11	4.47E-13	2.17	0.10	**0.29**	**0.013**	100	n/a	n/a	0.0076	0.0078
OR44-6-08	5.40	2.75	1.13E-13	3.38E-14	4.61E-14	2.87E-14	6.72E-12	1.43E-13	2.44E-11	4.41E-13	3.63	0.10	**0.48**	**0.013**	0	215	64.1	0.0069	0.0110

n/a: 40/36Ar ratio cannot be calculated for aliquots that do not release 36Ar
% 40Ar* is assumed to be 100 when 36Ar is not released

OR49	irradiance																	
Extraction	*(Wm $^{-2}$x 10 ^{5})*	*36Ar (cc)*	*±36Ar (cc)*	*38Ar* (cc)*	*±38Ar* (cc)*	*39Ar (cc)*	*±39Ar (cc)*	*40Ar (cc)*	*±40Ar (cc)*	*40Ar/39Ar*	*± error*	***Age (Ma)***	***± error***	*%rad 40Ar*	*40Ar/36Ar*	*±40Ar/36Ar*	*38Ar/39Ar*	*±38Ar/39Ar*
OR49-2																		
OR49-2-01	0.66	1.67E-13	6.84E-14	6.83E-14	6.39E-14	3.89E-12	9.10E-14	5.78E-11	1.99E-12	14.87	0.62	**1.96**	**0.081**	15	347	83.1	0.0176	0.0164
OR49-2-02	0.92	1.82E-13	1.04E-13	4.14E-14	8.68E-14	6.51E-12	2.95E-13	1.25E-11	2.88E-12	1.93	0.45	**0.25**	**0.059**	0	69	24.4	0.0064	0.0133
OR49-2-03	1.25	3.21E-13	1.94E-13	2.16E-13	8.51E-14	1.77E-11	3.37E-13	3.62E-11	2.39E-12	2.04	0.14	**0.27**	**0.018**	0	113	24.6	0.0122	0.0048
OR49-2-04	1.58	3.03E-13	1.08E-13	2.52E-16	1.88E-13	1.61E-11	4.72E-13	7.53E-11	5.12E-12	4.68	0.35	**0.62**	**0.046**	0	249	44.2	0.0000	0.0117
OR49-2-05	1.86	2.40E-13	1.17E-13	1.27E-13	1.65E-13	2.16E-11	2.45E-13	3.29E-11	3.22E-12	1.52	0.15	**0.20**	**0.020**	0	137	32.6	0.0059	0.0076
OR49-2-06	2.01	3.09E-13	1.20E-13	1.68E-13	1.17E-13	6.77E-12	2.41E-13	4.27E-11	2.31E-12	6.30	0.41	**0.83**	**0.054**	0	138	24.7	0.0249	0.0173
OR49-2-07	2.04	1.37E-13	6.43E-14	1.24E-13	1.48E-13	1.18E-11	3.16E-13	4.23E-12	3.37E-12	0.36	0.29	**0.05**	**0.038**	100	n/a	n/a	0.0105	0.0125
OR49-2-08	2.75	4.17E-14	6.82E-14	1.08E-13	8.92E-14	9.38E-12	1.68E-13	1.03E-11	1.48E-12	1.09	0.16	**0.14**	**0.021**	100	n/a	n/a	0.0116	0.0095
OR49-2-09	3.59	-1.43E-14	7.50E-14	4.81E-14	5.21E-14	5.71E-12	2.52E-13	7.69E-12	1.53E-12	1.35	0.28	**0.18**	**0.036**	100	n/a	n/a	0.0084	0.0091
OR49-2-10	4.53	5.24E-14	8.22E-14	1.13E-14	5.36E-14	3.14E-12	7.43E-14	2.53E-12	1.50E-12	0.80	0.48	**0.11**	**0.063**	100	n/a	n/a	0.0036	0.0171
OR49-1																		
OR49-1-01	0.66	3.44E-13	8.63E-14	1.50E-13	4.74E-14	6.26E-12	8.20E-14	8.33E-11	3.00E-12	13.31	0.51	**1.75**	**0.067**	0	242	32.5	0.0240	0.0076
OR49-1-02	0.92	1.95E-13	6.38E-14	1.02E-13	1.15E-13	7.20E-12	1.82E-13	1.78E-11	2.45E-12	2.47	0.35	**0.33**	**0.046**	0	92	22.0	0.0142	0.0160
OR49-1-03	1.25	-2.09E-14	3.75E-14	8.44E-14	3.74E-14	9.75E-12	5.20E-13	8.50E-12	3.58E-12	0.87	0.37	**0.11**	**0.049**	100	n/a	n/a	0.0087	0.0039
OR49-1-04	1.58	-2.06E-14	1.04E-13	4.61E-13	9.56E-14	3.35E-11	3.78E-13	6.96E-12	8.54E-12	0.21	0.25	**0.03**	**0.034**	100	n/a	n/a	0.0137	0.0029
OR49-1-05	1.86	5.59E-14	2.70E-13	4.61E-13	2.53E-13	2.99E-11	3.29E-13	3.93E-11	8.07E-12	1.31	0.27	**0.17**	**0.036**	58	710	1019.2	0.0154	0.0085
OR49-1-06	2.01	1.25E-13	6.81E-14	6.68E-14	1.31E-13	1.32E-11	4.61E-13	1.80E-11	1.96E-12	1.36	0.16	**0.18**	**0.021**	0	144	48.4	0.0051	0.0099
OR49-1-07	2.04	1.08E-13	1.07E-13	1.28E-13	8.35E-14	1.11E-11	2.15E-13	6.54E-12	2.01E-12	0.59	0.18	**0.08**	**0.024**	0	61	33.5	0.0115	0.0075
OR49-1-08	2.75	1.03E-13	1.13E-13	1.14E-13	1.09E-13	7.89E-12	5.14E-13	1.89E-11	2.25E-12	2.40	0.33	**0.32**	**0.043**	0	183	92.9	0.0145	0.0139
OR49-1-09	3.59	-4.15E-14	6.27E-14	5.04E-14	3.87E-14	3.89E-12	1.34E-13	3.52E-12	1.97E-12	0.91	0.51	**0.12**	**0.067**	100	n/a	n/a	0.0130	0.0100
OR49-1-10	4.53	4.80E-15	3.56E-14	2.79E-14	3.44E-14	2.78E-12	9.77E-14	6.89E-12	2.01E-12	2.48	0.73	**0.33**	**0.096**	100	n/a	n/a	0.0100	0.0124
OR49-3																		
OR49-3-01	0.66	1.43E-13	1.36E-13	8.53E-14	4.71E-14	5.16E-12	2.36E-13	6.95E-11	2.01E-12	13.48	0.73	**1.77**	**0.096**	39	487	190.4	0.0165	0.0092
OR49-3-02	0.92	2.29E-13	8.51E-14	1.12E-13	7.18E-14	8.14E-12	4.01E-13	2.96E-11	2.62E-12	3.63	0.37	**0.48**	**0.049**	0	129	27.3	0.0137	0.0088
OR49-3-03	1.25	6.52E-14	5.34E-14	1.13E-13	8.54E-14	1.48E-11	1.94E-13	2.98E-11	7.00E-13	2.01	0.05	**0.26**	**0.007**	35	458	246.2	0.0076	0.0058
OR49-3-04	1.58	1.60E-13	6.93E-14	2.07E-13	1.90E-13	2.23E-11	6.20E-13	3.91E-11	1.78E-12	1.75	0.09	**0.23**	**0.012**	0	245	62.1	0.0093	0.0085
OR49-3-05	1.86	5.98E-14	9.22E-14	4.57E-13	1.05E-13	3.20E-11	3.49E-13	4.75E-11	1.16E-11	1.49	0.36	**0.20**	**0.048**	100	n/a	n/a	0.0143	0.0033
OR49-3-06	2.01	1.72E-13	9.28E-14	2.87E-13	2.99E-13	2.60E-11	4.97E-13	2.84E-11	7.99E-12	1.09	0.31	**0.14**	**0.041**	0	166	64.6	0.0110	0.0115
OR49-3-07	2.04	7.74E-14	6.84E-14	5.44E-14	4.60E-14	5.95E-12	3.09E-13	7.02E-12	1.38E-12	1.18	0.24	**0.16**	**0.032**	0	91	49.8	0.0091	0.0078
OR49-3-08	2.75	3.96E-14	6.76E-14	7.18E-15	8.40E-14	5.33E-12	2.81E-13	1.16E-11	3.97E-12	2.17	0.75	**0.29**	**0.099**	100	n/a	n/a	0.0013	0.0158
OR49-3-09	3.59	3.38E-14	8.05E-14	9.29E-14	6.49E-14	3.45E-12	1.07E-13	5.26E-12	1.23E-12	1.53	0.36	**0.20**	**0.048**	100	n/a	n/a	0.0269	0.0188
OR49-3-10	4.53	-2.90E-14	1.09E-13	5.79E-14	4.04E-14	1.56E-12	7.39E-14	4.04E-12	6.79E-13	2.59	0.45	**0.34**	**0.060**	100	n/a	n/a	0.0371	0.0259

OR49-4																		
OR49-4-01	0.66	3.04E-13	5.82E-14	1.15E-13	4.45E-14	4.46E-12	2.57E-13	8.00E-11	1.14E-12	17.96	1.07	**2.36**	**0.140**	0	264	31.9	0.0259	0.0101
OR49-4-02	0.92	6.08E-14	4.60E-14	3.32E-14	3.80E-14	4.99E-12	1.11E-13	2.12E-11	1.63E-12	4.25	0.34	**0.56**	**0.045**	15	349	188.2	0.0067	0.0076
OR49-4-03	1.25	5.69E-14	4.84E-14	2.81E-13	1.07E-13	1.73E-11	5.15E-13	2.15E-11	1.97E-12	1.24	0.12	**0.16**	**0.016**	22	380	226.2	0.0163	0.0062
OR49-4-04	1.58	5.74E-14	1.18E-13	1.94E-13	1.21E-13	2.20E-11	2.46E-13	3.76E-11	4.20E-12	1.71	0.19	**0.22**	**0.025**	55	657	602.6	0.0088	0.0055
OR49-4-05	1.86	1.21E-13	6.51E-14	1.75E-13	5.51E-14	8.04E-12	1.23E-13	1.23E-11	2.03E-12	1.53	0.25	**0.20**	**0.033**	0	102	36.5	0.0217	0.0069
OR49-4-06	2.01	-9.76E-15	3.63E-14	2.40E-13	6.70E-14	1.92E-11	4.79E-13	2.47E-11	3.05E-12	1.28	0.16	**0.17**	**0.021**	100	n/a	n/a	0.0125	0.0035
OR49-4-07	2.04	2.98E-13	8.14E-14	2.06E-13	3.27E-14	1.57E-11	2.56E-13	3.75E-11	6.34E-12	2.40	0.41	**0.32**	**0.054**	0	126	28.1	0.0131	0.0021
OR49-4-08	2.75	1.01E-13	6.99E-14	1.10E-13	1.15E-13	1.05E-11	3.01E-13	1.46E-11	3.03E-12	1.39	0.29	**0.18**	**0.038**	0	144	64.3	0.0105	0.0110
OR49-4-09	3.59	1.24E-13	4.23E-14	1.59E-13	6.51E-14	8.80E-12	1.19E-13	8.27E-12	1.54E-12	0.94	0.18	**0.12**	**0.023**	0	67	20.9	0.0181	0.0074
OR49-4-10	4.53	1.10E-13	2.94E-14	1.25E-13	5.42E-14	4.01E-12	2.05E-13	4.00E-12	6.10E-13	1.00	0.16	**0.13**	**0.021**	0	36	10.2	0.0313	0.0136

OR49	irradiance																	
Extraction	*(Wm^{-2}x 10^{5})*	*36Ar (cc)*	*±36Ar (cc)*	*38Ar* (cc)*	*±38Ar* (cc)*	*39Ar (cc)*	*±39Ar (cc)*	*40Ar (cc)*	*±40Ar (cc)*	*40Ar/39Ar*	*± error*	***Age (Ma)***	***± error***	*%rad 40Ar*	*40Ar/36Ar*	*±40Ar/36Ar*	*38Ar/39Ar*	*±38Ar/39Ar*
OR49-5																		
OR49-5-01	0.66	3.23E-13	4.79E-14	1.20E-13	5.69E-14	5.49E-12	1.03E-13	6.70E-11	1.56E-12	12.20	0.36	**1.61**	**0.048**	0	208	21.9	0.0219	0.0104
OR49-5-02	0.92	-1.04E-15	4.17E-14	1.88E-14	1.16E-13	4.26E-12	8.89E-14	2.00E-11	1.62E-12	4.69	0.39	**0.62**	**0.052**	100	n/a	n/a	0.0044	0.0272
OR49-5-03	1.25	1.62E-13	2.98E-14	1.94E-14	1.38E-13	1.18E-11	2.68E-13	1.77E-11	1.01E-12	1.50	0.09	**0.20**	**0.012**	0	110	18.8	0.0016	0.0117
OR49-5-04	1.58	2.04E-13	8.21E-14	2.59E-13	6.64E-14	2.55E-11	3.67E-13	2.59E-11	4.98E-12	1.02	0.20	**0.13**	**0.026**	0	128	36.6	0.0102	0.0026
OR49-5-05	1.86	3.52E-13	5.17E-14	2.22E-13	1.15E-13	3.82E-11	4.08E-13	3.49E-11	9.65E-12	0.91	0.25	**0.12**	**0.033**	0	99	29.1	0.0058	0.0030
OR49-5-06	2.01	4.47E-13	4.62E-14	1.91E-13	1.76E-13	2.40E-11	3.97E-13	8.36E-11	9.26E-12	3.48	0.39	**0.46**	**0.051**	0	187	24.8	0.0080	0.0073
OR49-5-07	2.04	1.20E-13	3.91E-14	9.74E-14	3.18E-14	7.04E-12	1.17E-13	2.94E-11	1.51E-12	4.18	0.23	**0.55**	**0.030**	0	246	62.7	0.0138	0.0045
OR49-5-08	2.75	1.27E-13	3.34E-14	1.16E-14	8.31E-14	1.35E-11	2.62E-13	4.95E-11	2.69E-12	3.68	0.21	**0.48**	**0.028**	24	390	87.6	0.0009	0.0062
OR49-5-09	3.59	7.04E-14	6.13E-14	1.00E-13	4.22E-14	5.94E-12	1.96E-13	7.06E-12	6.19E-13	1.19	0.11	**0.16**	**0.015**	0	100	54.3	0.0169	0.0071
OR49-5-10	4.53	1.22E-13	4.43E-14	3.12E-14	4.66E-14	3.18E-12	9.82E-14	1.09E-11	9.79E-13	3.42	0.33	**0.45**	**0.043**	0	89	24.5	0.0098	0.0147
OR49-6																		
OR49-6-01	0.66	5.51E-13	8.24E-14	1.88E-13	9.31E-14	6.16E-12	3.91E-13	1.36E-10	1.11E-11	22.05	2.28	**2.90**	**0.300**	0	247	28.1	0.0304	0.0152
OR49-6-02	0.92	4.33E-13	1.75E-13	6.83E-14	1.13E-13	6.78E-12	2.00E-13	1.23E-10	3.01E-12	18.08	0.69	**2.38**	**0.091**	0	283	42.0	0.0101	0.0166
OR49-6-03	1.25	2.76E-13	4.31E-14	1.22E-13	5.12E-14	1.56E-11	3.01E-13	6.59E-11	5.25E-12	4.21	0.35	**0.55**	**0.045**	0	239	33.2	0.0078	0.0033
OR49-6-04	1.58	8.96E-14	4.22E-14	3.51E-13	6.05E-14	2.70E-11	3.78E-13	4.61E-11	2.79E-12	1.71	0.11	**0.22**	**0.014**	43	517	183.0	0.0130	0.0022
OR49-6-05	1.86	2.38E-13	6.92E-14	3.94E-13	6.41E-14	3.11E-11	4.62E-13	5.83E-11	6.26E-12	1.88	0.20	**0.25**	**0.027**	0	246	48.9	0.0127	0.0021
OR49-6-06	2.01	2.01E-13	5.61E-14	1.58E-13	7.79E-14	2.00E-11	5.21E-13	4.86E-11	2.47E-12	2.43	0.14	**0.32**	**0.018**	0	241	44.7	0.0079	0.0039
OR49-6-07	2.04	8.32E-14	5.05E-14	1.34E-14	3.86E-14	1.14E-11	2.14E-13	2.14E-11	2.07E-12	1.88	0.19	**0.25**	**0.024**	0	257	108.1	0.0012	0.0034
OR49-6-08	2.75	8.32E-14	5.05E-14	1.34E-14	3.86E-14	1.14E-11	2.14E-13	2.14E-11	2.07E-12	1.88	0.19	**0.25**	**0.024**	0	257	108.1	0.0012	0.0034
OR49-6-09	3.59	4.47E-14	2.69E-14	4.46E-14	3.44E-14	4.84E-12	1.92E-13	1.52E-11	8.70E-13	3.14	0.22	**0.41**	**0.029**	0	341	190.4	0.0092	0.0071
OR49-6-10	4.53	9.85E-14	3.48E-14	5.39E-14	4.26E-14	3.97E-12	6.75E-14	8.62E-12	7.88E-13	2.17	0.20	**0.29**	**0.027**	0	88	26.3	0.0136	0.0107

n/a: 40/36Ar ratio cannot be calculated for aliquots that do not release 36Ar
% 40Ar* is assumed to be 100 when 36Ar is not released

OR54 Extraction	lamp(W)	irradiance (Wm^{-2} x 10^5)	36Ar (cc)	±36Ar (cc)	38Ar* (cc)	±38Ar* (cc)	39Ar (cc)	±39Ar (cc)	40Ar (cc)	±40Ar (cc)	40Ar/39Ar	± error	**Age (Ma)**	**± error**	%rad 40Ar	40Ar/36Ar	±40Ar/36Ar	38Ar/39Ar	±38Ar/39Ar
OR54-1																			
OR54-1-01	1.30	0.66	-7.45E-14	8.51E-14	-3.29E-15	5.15E-14	5.37E-12	1.32E-13	1.64E-11	1.75E-12	3.06	0.33	**0.40**	**0.044**	100	n/a	n/a	-0.000613	-0.0096
OR54-1-02	1.80	0.92	1.14E-15	5.84E-14	-1.64E-14	1.44E-13	8.17E-12	1.04E-13	7.74E-12	1.50E-12	0.95	0.18	**0.12**	**0.024**	100	n/a	n/a	-0.002001	-0.0176
OR54-1-03	2.45	1.25	-4.59E-14	9.50E-14	1.71E-13	8.72E-14	2.03E-11	3.63E-13	5.32E-12	5.58E-12	0.26	0.27	**0.03**	**0.036**	100	n/a	n/a	0.0084124	0.0043
OR54-1-04	3.10	1.58	-5.55E-14	7.00E-14	7.58E-14	6.87E-14	1.66E-11	2.07E-13	1.11E-11	5.10E-12	0.67	0.31	**0.09**	**0.040**	100	n/a	n/a	0.0045678	0.0041
OR54-1-05	3.65	1.86	3.72E-14	6.50E-14	1.66E-14	3.56E-14	1.12E-11	2.68E-13	1.07E-11	2.57E-12	0.95	0.23	**0.13**	**0.031**	100	n/a	n/a	0.0014866	0.0032
OR54-1-06	3.95	2.01	8.75E-14	6.72E-14	3.73E-14	1.08E-13	1.25E-11	2.11E-13	1.18E-11	1.77E-12	0.95	0.14	**0.12**	**0.019**	100	n/a	n/a	0.0029786	0.0086
OR54-1-07	4.00	2.04	1.79E-14	5.66E-14	3.35E-14	4.92E-14	2.76E-12	1.82E-13	4.51E-12	1.57E-12	1.63	0.58	**0.21**	**0.076**	100	n/a	n/a	0.0121394	0.0178
OR54-1-08	5.40	2.75	4.79E-14	5.50E-14	3.47E-14	4.08E-14	4.22E-12	1.48E-13	5.05E-12	1.57E-12	1.20	0.37	**0.16**	**0.049**	100	n/a	n/a	0.0082261	0.0097
OR54-1-09	7.06	3.60	9.75E-15	6.17E-14	1.12E-14	2.73E-14	3.33E-12	1.01E-13	1.46E-12	1.34E-12	0.44	0.40	**0.06**	**0.053**	100	n/a	n/a	0.0033545	0.0082
OR54-2																			
OR54-2-01	1.30	0.66	1.30E-13	4.48E-14	1.87E-15	3.22E-14	3.46E-12	1.71E-13	3.42E-11	1.67E-12	9.91	0.69	**1.30**	**0.090**	100	n/a	n/a	0.0005415	0.0093
OR54-2-02	1.80	0.92	1.95E-14	7.79E-14	1.21E-13	8.19E-14	1.01E-11	9.82E-14	8.35E-12	1.77E-12	0.83	0.18	**0.11**	**0.023**	100	n/a	n/a	0.0119883	0.0081
OR54-2-03	2.45	1.25	1.12E-13	6.05E-14	9.95E-14	1.20E-13	1.44E-11	4.43E-13	2.23E-11	1.03E-11	1.55	0.72	**0.20**	**0.095**	100	n/a	n/a	0.0069296	0.0084
OR54-2-04	3.10	1.58	2.45E-13	1.34E-13	1.88E-13	1.00E-13	1.33E-11	3.38E-13	2.38E-11	8.71E-12	1.79	0.66	**0.24**	**0.086**	100	n/a	n/a	0.0141346	0.0075
OR54-2-05	3.65	1.86	4.16E-14	6.60E-14	1.82E-13	9.62E-14	1.34E-11	2.34E-13	1.55E-11	3.77E-12	1.16	0.28	**0.15**	**0.037**	100	n/a	n/a	0.013548	0.0072
OR54-2-06	3.95	2.01	8.10E-16	4.86E-14	2.89E-14	1.05E-13	1.28E-11	3.84E-13	9.91E-12	1.89E-12	0.78	0.15	**0.10**	**0.020**	100	n/a	n/a	0.0022683	0.0082
OR54-2-07	4.00	2.04	-1.47E-14	4.82E-14	8.39E-14	4.16E-14	6.61E-12	1.63E-13	5.79E-12	2.02E-12	0.88	0.31	**0.12**	**0.040**	100	n/a	n/a	0.0126829	0.0063
OR54-2-08	5.40	2.75	-9.23E-14	8.50E-14	9.79E-14	3.83E-14	7.07E-12	1.35E-13	7.37E-12	2.01E-12	1.04	0.29	**0.14**	**0.038**	100	n/a	n/a	0.0138377	0.0054
OR54-2-09	7.06	3.60	4.22E-14	6.89E-14	5.54E-15	5.36E-14	3.23E-12	9.58E-14	2.05E-12	1.65E-12	0.63	0.51	**0.08**	**0.067**	100	n/a	n/a	0.0017122	0.0166
OR54-3																			
OR54-3-01	1.30	0.66	1.35E-13	2.16E-14	3.54E-14	4.59E-14	5.43E-12	1.19E-13	2.83E-11	8.15E-13	5.21	0.19	**0.69**	**0.025**	100	n/a	n/a	0.0065227	0.0085
OR54-3-02	1.80	0.92	2.89E-15	4.57E-14	1.69E-13	5.30E-14	1.36E-11	1.59E-13	1.49E-11	8.74E-13	1.10	0.07	**0.14**	**0.009**	100	n/a	n/a	0.0123884	0.0039
OR54-3-03	2.45	1.25	7.35E-14	4.03E-14	1.35E-13	2.65E-14	1.26E-11	2.33E-13	6.88E-12	2.15E-12	0.54	0.17	**0.07**	**0.022**	100	n/a	n/a	0.0106728	0.0021
OR54-3-04	3.10	1.58	1.43E-15	5.32E-14	1.05E-13	6.51E-14	1.19E-11	2.38E-13	7.20E-12	1.77E-12	0.60	0.15	**0.08**	**0.020**	100	n/a	n/a	0.0087839	0.0055
OR54-3-05	3.65	1.86	-1.40E-13	1.86E-13	3.62E-13	1.11E-13	2.65E-11	4.67E-13	2.81E-11	5.72E-12	1.06	0.22	**0.14**	**0.029**	100	n/a	n/a	0.0136566	0.0042
OR54-3-06	3.95	2.01	2.65E-14	3.44E-14	3.97E-14	4.81E-14	6.75E-12	7.57E-14	6.84E-12	4.42E-13	1.01	0.07	**0.13**	**0.009**	100	n/a	n/a	0.0058775	0.0071
OR54-3-07	4.00	2.04	4.06E-14	2.73E-14	1.90E-15	3.61E-14	2.80E-12	1.06E-13	2.14E-12	4.43E-13	0.76	0.16	**0.10**	**0.021**	100	n/a	n/a	0.0006778	0.0129
OR54-3-08	5.40	2.75	-2.95E-14	3.40E-14	4.30E-14	2.86E-14	7.80E-12	1.37E-13	5.48E-12	9.41E-13	0.70	0.12	**0.09**	**0.016**	100	n/a	n/a	0.0055107	0.0037
OR54-3-09	7.06	3.60	2.13E-14	3.43E-14	2.84E-14	2.47E-14	2.04E-12	6.49E-14	1.78E-12	5.52E-13	0.87	0.27	**0.11**	**0.036**	100	n/a	n/a	0.0139236	0.0121

n/a: 40/36Ar ratio cannot be calculated for aliquots that do not release 36Ar
% 40Ar* is assumed to be 100 when 36Ar is not released

OR55 Extraction	Lamp (W)	Irradiance ($Wm^{-2} \times 10^5$)	36Ar (cc)	±36Ar (cc)	38Ar* (cc)	±38Ar* (cc)	39Ar (cc)	±39Ar (cc)	40Ar (cc)	±40Ar (cc)	40Ar/39Ar	± error	**Age (Ma)**	**± error**	%rad 40Ar	40Ar/36Ar	±40Ar/36Ar	38Ar/39Ar	±38Ar/39Ar
OR55-09																			
OR55-9-01	1.30	0.66	2.29E-13	3.33E-14	4.91E-14	2.80E-14	3.21E-12	6.11E-14	5.51E-11	4.96E-13	17.14	0.36	**2.26**	**0.047**	0	241	51.0	0.0153	0.0268
OR55-9-02	1.80	0.92	4.11E-14	3.32E-14	1.83E-14	3.49E-14	3.37E-12	4.21E-14	1.86E-11	5.13E-13	5.52	0.17	**0.73**	**0.022**	35	453	531.2	0.0054	0.0029
OR55-9-03	2.45	1.25	1.05E-13	3.31E-14	2.65E-14	4.56E-14	4.94E-12	1.25E-13	3.23E-11	3.55E-13	6.54	0.18	**0.86**	**0.024**	4	307	140.1	0.0054	0.0031
OR55-9-04	3.10	1.58	3.78E-13	7.48E-14	3.16E-14	6.51E-14	8.69E-12	1.29E-13	4.12E-11	7.40E-13	4.74	0.11	**0.62**	**0.015**	0	212	70.5	0.0036	0.0018
OR55-9-05	3.65	1.86	1.84E-13	4.20E-14	7.42E-14	4.24E-14	9.33E-12	5.33E-13	3.01E-11	1.17E-12	3.23	0.22	**0.42**	**0.029**	0	164	69.2	0.0080	0.0139
OR55-9-06	3.95	2.01	1.07E-14	3.73E-14	3.10E-14	7.15E-14	7.10E-12	1.24E-13	1.94E-11	3.07E-13	2.73	0.06	**0.36**	**0.008**	100	n/a	n/a	0.0044	0.0019
OR55-9-07	4.00	2.04	4.22E-14	3.31E-14	3.03E-15	2.28E-14	2.94E-12	4.19E-14	7.47E-12	5.17E-13	2.54	0.18	**0.33**	**0.024**	0	177	201.1	0.0010	0.0001
OR55-9-08	5.40	2.75	4.36E-14	3.65E-14	-1.34E-14	9.39E-14	2.17E-12	1.24E-13	5.15E-12	3.38E-13	2.38	0.21	**0.31**	**0.027**	0	118	157.9	-0.0062	-0.0010
OR55-9-09	7.06	3.60	7.81E-14	3.47E-14	8.09E-14	3.23E-14	4.48E-12	4.80E-14	1.11E-11	3.26E-13	2.49	0.08	**0.33**	**0.010**	0	142	95.7	0.0181	0.0453
OR55-9-10	8.9	4.53	9.97E-14	4.60E-14	1.27E-13	3.03E-14	4.37E-12	1.12E-13	1.29E-11	2.71E-13	2.95	0.10	**0.39**	**0.013**	0	129	119.5	0.0291	0.1218
OR55-08																			
OR55-8-01	1.30	0.66	1.38E-13	3.56E-14	1.86E-14	3.33E-14	2.41E-12	6.92E-14	3.30E-11	1.91E-13	13.68	0.40	**1.80**	**0.053**	0	238	95.8	0.0077	0.0043
OR55-8-02	1.80	0.92	1.81E-14	2.60E-14	2.26E-14	2.47E-14	2.54E-12	7.49E-14	1.75E-11	5.37E-13	6.88	0.29	**0.91**	**0.039**	100	n/a	n/a	0.0089	0.0082
OR55-8-03	2.45	1.25	1.95E-13	2.94E-14	-6.22E-14	4.23E-14	3.20E-12	1.22E-13	4.31E-11	9.34E-13	13.46	0.59	**1.77**	**0.078**	0	221	43.3	-0.0194	-0.0286
OR55-8-04	3.10	1.58	1.82E-13	4.31E-14	5.72E-14	5.24E-14	5.78E-12	1.49E-13	5.41E-11	9.66E-13	9.36	0.29	**1.23**	**0.039**	1	298	132.8	0.0099	0.0108
OR55-8-05	3.65	1.86	2.73E-14	3.85E-14	4.28E-14	7.10E-14	6.96E-12	1.70E-13	2.51E-11	2.92E-13	3.60	0.10	**0.47**	**0.013**	100	n/a	n/a	0.0061	0.0037
OR55-8-06	3.95	2.01	8.67E-14	2.71E-14	2.84E-14	3.30E-14	3.94E-12	2.39E-13	1.31E-11	2.88E-13	3.34	0.22	**0.44**	**0.028**	0	152	56.1	0.0072	0.0062
OR55-8-07	4.00	2.04	1.02E-13	2.36E-14	3.25E-14	2.47E-14	7.87E-12	1.76E-13	2.77E-11	5.85E-13	3.52	0.11	**0.46**	**0.014**	0	271	64.7	0.0041	0.0054
OR55-8-08	5.40	2.75	7.93E-14	2.63E-14	8.49E-14	2.60E-14	5.73E-12	8.17E-14	2.25E-11	4.30E-13	3.93	0.09	**0.52**	**0.012**	0	283	107.9	0.0148	0.0484
OR55-8-09	7.06	3.60	2.59E-13	3.26E-14	1.25E-13	2.06E-14	8.97E-12	1.09E-13	4.37E-11	5.43E-13	0.64	0.64	**0.64**	**0.64**	0	169	30.3	0.0140	0.0846
OR55-8-10	8.9	4.53	1.17E-13	3.27E-14	1.82E-13	2.42E-14	4.26E-12	5.84E-14	9.65E-12	3.49E-13	0.30	0.30	**0.30**	**0.30**	0	82	32.9	0.0426	0.3199
55 unirradiated																			
OR55-UN-02	1.30	0.66	2.61E-14	3.97E-14	-2.81E-16	3.08E-14			1.08E-11	3.09E-13						n/a	n/a		
OR55-UN-03	1.80	0.92	-8.95E-14	7.79E-14	3.29E-14	3.54E-14			1.44E-11	2.06E-13						n/a	n/a		
OR55-UN-04	2.45	1.25	1.49E-13	9.32E-14	-6.56E-14	6.61E-14			2.64E-11	5.97E-13						177	110.7		
55-UN-05(5	3.10	1.58	1.63E-14	1.09E-13	5.31E-14	4.25E-14			1.88E-11	5.50E-13						n/a	n/a		
55-UN-05(5	3.65	1.86	3.09E-13	1.04E-13	-1.80E-15	6.63E-14			3.27E-11	1.95E-12						106	36.1		
OR55-UN-06	3.95	2.01	2.29E-13	4.79E-14	-3.54E-15	4.89E-14			3.68E-11	3.42E-13						161	33.7		
OR55-UN-07	4.00	2.04	1.25E-13	4.65E-14	3.62E-15	3.66E-14			1.51E-11	5.70E-13						121	45.2		
OR55-UN-08	5.40	2.75	1.05E-13	6.07E-14	7.62E-14	3.85E-14			1.53E-11	4.39E-13						145	83.7		
OR55-UN-09	7.06	3.60	1.59E-13	7.27E-14	9.05E-14	3.36E-14			1.70E-11	1.18E-12						107	49.2		
OR55-UN-10	8.9	4.53	9.04E-14	5.36E-14	4.41E-14	3.81E-14			1.12E-11	2.09E-13						124	73.4		

OR293 *Extraction*	*lamp(W)*	*irradiance ($Wm^{-2} \times 10^5$)*	*36Ar (cc)*	*±36Ar (cc)*	*38Ar* (cc)*	*±38Ar* (cc)*	*39Ar (cc)*	*±39Ar (cc)*	*40Ar (cc)*	*±40Ar (cc)*	*40Ar/39Ar*	*± error*	***Age (Ma)***	***± error***	*%rad 40Ar*	*40Ar/36Ar*	*±40Ar/36Ar*	*38Ar/39Ar*	*±38Ar/39Ar*
OR293-1																			
OR293-1-01	1.30	0.66	8.01E-14	5.35E-14	7.56E-14	3.38E-14	1.69E-12	1.58E-13	2.27E-11	8.27E-12	13.44	5.05	**1.45**	**0.544**	100	n/a	n/a	0.0447	0.0204
OR293-1-02	1.80	0.92	1.19E-15	7.48E-14	-5.14E-15	5.84E-14	2.98E-12	1.52E-13	8.92E-12	9.61E-13	3.00	0.36	**0.32**	**0.039**	100	n/a	n/a	-0.0017	-0.0196
OR293-1-03	2.45	1.25	6.78E-14	8.72E-14	-2.45E-15	4.48E-14	3.77E-12	1.48E-13	2.41E-11	7.89E-13	6.38	0.33	**0.69**	**0.035**	100	n/a	n/a	-0.0007	-0.0119
OR293-1-04	3.10	1.58	-2.15E-14	4.12E-14	5.68E-14	4.57E-14	6.95E-12	1.58E-13	1.12E-11	2.12E-12	1.61	0.31	**0.17**	**0.033**	100	n/a	n/a	0.0082	0.0066
OR293-1-05	3.65	1.86	1.11E-13	1.15E-13	1.54E-13	5.02E-14	1.72E-11	4.04E-13	3.40E-11	1.30E-11	1.97	0.75	**0.21**	**0.081**	100	n/a	n/a	0.0089	0.0029
OR293-1-06	3.95	2.01	8.81E-14	6.27E-14	1.05E-13	6.04E-14	1.34E-11	3.32E-13	1.49E-11	5.53E-12	1.11	0.41	**0.12**	**0.044**	100	n/a	n/a	0.0078	0.0045
OR293-1-07	4.00	1.86	-4.99E-14	5.20E-14	5.63E-14	4.10E-14	6.86E-12	3.40E-13	6.98E-12	1.25E-12	1.02	0.19	**0.11**	**0.020**	100	n/a	n/a	0.0082	0.0060
OR293-1-08	5.40	2.01	1.22E-16	5.07E-14	2.80E-14	3.97E-14	7.29E-12	2.33E-13	6.96E-12	8.10E-13	0.95	0.12	**0.10**	**0.012**	100	n/a	n/a	0.0038	0.0054
OR293-1-09	7.60	2.04	3.64E-15	4.38E-14	4.98E-15	4.02E-14	2.76E-12	1.37E-13	2.94E-12	6.71E-13	1.06	0.25	**0.11**	**0.027**	100	n/a	n/a	0.0018	0.0146
OR293-2																			
OR293-2-01	1.30	0.66	5.32E-13	6.92E-14	3.04E-13	6.52E-14	6.01E-12	9.27E-13	8.95E-11	1.31E-10	14.90	21.89	**1.61**	**2.360**	0	168.2	246.8	0.0506	0.0134
OR293-2-02	1.30	0.66	9.04E-14	3.41E-14	1.74E-14	5.24E-14	1.84E-12	1.24E-13	6.88E-12	8.64E-13	3.74	0.53	**0.40**	**0.057**	100	n/a	n/a	0.0095	0.0285
OR293-2-03	1.80	0.92	5.39E-14	3.23E-14	-1.33E-14	4.91E-14	2.19E-12	1.16E-13	6.35E-12	4.03E-13	2.90	0.24	**0.31**	**0.026**	100	n/a	n/a	-0.0061	-0.0224
OR293-2-04	2.45	1.25	1.75E-13	1.93E-13	-1.87E-14	7.49E-14	3.77E-12	1.03E-13	9.78E-12	5.87E-13	2.59	0.17	**0.28**	**0.018**	100	n/a	n/a	-0.0049	-0.0198
OR293-2-05	3.10	1.58	1.44E-13	3.58E-14	2.60E-14	4.57E-14	7.60E-12	1.78E-13	3.70E-11	9.47E-13	4.86	0.17	**0.52**	**0.018**	100	n/a	n/a	0.0034	0.0060
OR293-2-06	3.65	1.86	4.22E-15	3.46E-14	2.59E-14	4.19E-14	1.42E-11	2.65E-13	1.77E-11	1.61E-12	1.24	0.12	**0.13**	**0.012**	100	n/a	n/a	0.0018	0.0030
OR293-2-07	3.95	2.01	6.09E-16	3.47E-14	1.15E-13	4.83E-14	1.40E-11	1.41E-13	1.24E-11	8.78E-13	0.89	0.06	**0.10**	**0.007**	100	n/a	n/a	0.0082	0.0034
OR293-2-08	4.00	1.86	5.39E-14	3.22E-14	-2.99E-15	4.37E-14	5.24E-12	1.16E-13	5.25E-12	7.89E-13	1.00	0.15	**0.11**	**0.016**	100	n/a	n/a	-0.0006	-0.0083
OR293-2-09	5.40	2.01	3.46E-14	3.45E-14	-3.96E-14	5.03E-14	7.40E-12	1.93E-13	9.11E-12	7.35E-13	1.23	0.10	**0.13**	**0.011**	100	n/a	n/a	-0.0054	-0.0068
OR293-2-10	7.60	2.04	4.17E-14	3.31E-14	3.28E-14	4.99E-14	3.86E-12	1.25E-13	4.44E-12	8.27E-13	1.15	0.22	**0.12**	**0.023**	100	n/a	n/a	0.0085	0.0129
OR293-3																			
O293-3-01	1.30	0.66	1.51E-13	1.84E-14	7.21E-14	3.51E-14	3.60E-12	7.33E-14	3.19E-11	6.14E-12	8.85	1.71	**0.95**	**0.185**	0	210.8	48.0	0.0200	0.0098
O293-3-02	1.30	0.66	2.55E-14	6.43E-14	2.44E-14	2.86E-14	1.15E-12	1.08E-13	7.50E-12	3.49E-13	6.52	0.68	**0.70**	**0.074**	100	n/a	n/a	0.0212	0.0249
O293-3-03	1.80	0.92	8.69E-15	6.06E-14	3.18E-14	2.32E-14	2.50E-12	2.88E-14	1.02E-11	3.14E-13	4.09	0.13	**0.44**	**0.014**	100	n/a	n/a	0.0127	0.0093
O293-3-04	2.45	1.25	4.76E-14	4.13E-14	4.33E-14	1.52E-14	4.18E-12	1.08E-13	1.44E-11	3.01E-13	3.45	0.11	**0.37**	**0.012**	100	n/a	n/a	0.0104	0.0037
O293-3-05	3.10	1.58	4.08E-14	2.05E-14	8.81E-14	4.15E-14	6.86E-12	9.59E-14	1.43E-11	5.88E-13	2.09	0.09	**0.23**	**0.010**	100	n/a	n/a	0.0128	0.0061
O293-3-06	3.65	1.86	1.68E-14	2.86E-14	1.52E-13	1.94E-14	1.53E-11	4.78E-13	2.10E-11	8.83E-13	1.37	0.07	**0.15**	**0.008**	100	n/a	n/a	0.0099	0.0013
O293-3-07	3.95	2.01	1.69E-14	4.73E-14	8.06E-14	3.95E-14	1.23E-11	1.06E-13	3.35E-11	2.62E-13	2.73	0.03	**0.29**	**0.003**	100	n/a	n/a	0.0066	0.0032
O293-3-08	4.00	1.86	8.65E-15	8.26E-14	3.99E-14	2.91E-14	7.65E-12	1.08E-13	1.12E-11	3.73E-13	1.46	0.05	**0.16**	**0.006**	100	n/a	n/a	0.0052	0.0038
O293-3-09	5.40	2.01	1.13E-13	1.80E-14	2.40E-14	2.27E-14	7.69E-12	5.16E-14	2.56E-11	6.40E-13	3.33	0.09	**0.36**	**0.009**	100	n/a	n/a	0.0031	0.0030
O293-3-10	7.60	2.04	6.33E-14	2.52E-14	7.64E-14	2.89E-14	2.66E-12	6.16E-14	1.95E-11	3.89E-13	7.32	0.22	**0.79**	**0.024**	4	306.7	6.1	0.0287	0.0109

JS203 Extraction	lamp	irradiance (Wm^{-2} x 10^5)	36Ar (cc)	±36Ar (cc)	38Ar* (cc)	±38Ar* (cc)	39Ar (cc)	±39Ar (cc)	40Ar (cc)	±40Ar (cc)	40Ar/39Ar	± error	Age (Ma)	± error	%rad 40Ar	40Ar/36Ar	±40Ar/36Ar	38Ar/39Ar	±38Ar/39Ar
JS203-1																			
1-04 (from 5	3.10	1.58	-1.90E-14	4.47E-14	7.58E-14	3.73E-14	8.06E-12	1.49E-13	1.60E-11	8.70E-13	1.99	0.11	0.26	0.015	100	n/a	n/a	0.0094	0.0046
JS203-1-05	3.65	1.86	1.53E-13	3.68E-14	3.08E-14	3.51E-14	1.05E-11	1.92E-13	3.55E-11	7.92E-13	3.39	0.10	0.45	0.013	0	232	44	0.0029	0.0034
JS203-1-06	3.95	2.01	7.67E-14	3.31E-14	8.75E-14	3.08E-14	9.08E-12	1.74E-13	2.12E-11	1.38E-12	2.33	0.16	0.31	0.021	0	277	101	0.0096	0.0034
JS203-1-07	4.00	2.04	2.19E-14	3.39E-14	4.26E-15	3.88E-14	6.47E-12	1.06E-13	2.11E-11	7.03E-13	3.27	0.12	0.43	0.016	100	n/a	n/a	0.0007	0.0060
JS203-1-08	5.40	2.75	-3.40E-15	3.52E-14	1.13E-13	4.16E-14	8.84E-12	1.48E-13	8.52E-12	8.29E-13	0.96	0.10	0.13	0.013	100	n/a	n/a	0.0128	0.0047
JS203-1-09	7.60	3.87	5.95E-14	3.93E-14	7.27E-14	3.29E-14	3.83E-12	1.37E-13	1.15E-11	7.74E-13	3.01	0.23	0.40	0.030	100	n/a	n/a	0.0190	0.0086
JS203-2																			
JS203-2-01	2.45	1.25	-4.47E-14	3.62E-14	1.08E-13	4.86E-14	4.81E-12	7.01E-13	8.68E-12	7.08E-13	1.80	0.30	0.24	0.040	100	n/a	n/a	0.0225	0.0106
JS203-2-02	3.10	1.58	-3.18E-14	4.30E-14	5.48E-14	3.55E-14	5.15E-12	1.45E-13	8.12E-12	7.98E-13	1.58	0.16	0.21	0.021	100	n/a	n/a	0.0106	0.0069
JS203-2-03	3.65	1.86	-1.08E-13	3.82E-14	8.27E-14	1.76E-13	9.02E-12	2.71E-13	7.81E-12	7.48E-13	0.87	0.09	0.11	0.011	100	n/a	n/a	0.0092	0.0195
JS203-2-04	3.95	2.01	1.82E-14	4.56E-14	7.12E-14	2.68E-14	1.14E-11	1.50E-13	9.06E-12	6.87E-13	0.80	0.06	0.11	0.008	100	n/a	n/a	0.0063	0.0024
JS203-2-05	4.00	2.04	6.33E-15	4.11E-14	3.00E-14	5.69E-14	5.09E-12	1.81E-13	4.58E-12	7.91E-13	0.90	0.16	0.12	0.021	100	n/a	n/a	0.0059	0.0112
JS203-2-06	5.40	2.75	4.37E-14	4.82E-14	5.75E-14	5.37E-14	9.37E-12	1.55E-13	7.85E-12	8.46E-13	0.84	0.09	0.11	0.012	100	n/a	n/a	0.0061	0.0057
JS203-3																			
JS203-3-01	2.45	1.25	5.62E-14	4.09E-14	9.66E-15	3.62E-14	6.27E-12	1.42E-13	1.35E-11	7.01E-13	2.16	0.12	0.28	0.016	100	n/a	n/a	0.0015	0.0058
JS203-3-02	3.10	1.58	-4.17E-14	9.54E-14	5.12E-14	4.03E-14	6.59E-12	2.03E-13	6.98E-12	4.43E-13	1.06	0.07	0.14	0.010	100	n/a	n/a	0.0078	0.0061
JS203-3-03	3.65	1.86	1.61E-14	4.19E-14	7.11E-14	5.41E-14	1.03E-11	2.03E-13	7.14E-12	4.71E-13	0.69	0.05	0.09	0.006	100	n/a	n/a	0.0069	0.0052
JS203-3-04	3.95	2.01	7.67E-15	3.68E-14	6.54E-14	3.98E-14	8.04E-12	1.36E-13	4.33E-12	8.27E-13	0.54	0.10	0.07	0.014	100	n/a	n/a	0.0081	0.0049
JS203-3-05	4.00	2.04	-1.63E-14	4.16E-14	-1.98E-14	6.37E-14	5.51E-12	1.03E-13	3.65E-12	4.12E-13	0.66	0.08	0.09	0.010	100	n/a	n/a	-0.0036	-0.0116
JS203-3-06	5.40	2.75	-6.94E-14	3.98E-14	6.77E-14	3.04E-14	6.24E-12	3.40E-13	2.64E-12	1.51E-12	0.42	0.24	0.06	0.032	100	n/a	n/a	0.0108	0.0049
JS203-3-07	7.60	3.87	2.01E-15	3.56E-14	3.76E-14	5.05E-14	4.15E-12	1.60E-13	1.99E-12	4.36E-13	0.48	0.11	0.06	0.014	100	n/a	n/a	0.0091	0.0122

JS226		irradiance																	
Extraction	*lamp (W)*	*(Wm^{-2} x 10^5)*	*36Ar (cc)*	*±36Ar (cc)*	*38Ar* (cc)*	*±38Ar* (cc)*	*39Ar (cc)*	*±39Ar (cc)*	*40Ar (cc)*	*±40Ar (cc)*	*40Ar/39Ar*	*± error*	***Age (Ma)***	***± error***	*%rad 40Ar*	*40Ar/36Ar*	*±40Ar/36Ar*	*38Ar/39Ar*	*±38Ar/39Ar*
JS226-1																			
JS226-1-02	3.10	1.58	-2.31E-15	4.03E-14	5.44E-14	3.51E-14	3.19E-12	1.02E-13	6.50E-12	4.14E-13	2.04	0.15	**0.27**	**0.019**	100	n/a	n/a	0.0171	0.0110
JS226-1-03	3.65	1.86	-2.01E-14	3.57E-14	5.64E-14	4.09E-14	6.36E-12	2.94E-13	6.17E-12	3.57E-13	0.97	0.07	**0.13**	**0.009**	100	n/a	n/a	0.0089	0.0065
JS226-1-05	3.95	2.01	-2.97E-14	2.69E-14	9.18E-14	3.50E-14	9.66E-12	3.33E-13	7.47E-12	6.71E-13	0.77	0.07	**0.10**	**0.010**	100	n/a	n/a	0.0095	0.0036
JS226-1-06	4.00	2.04	-4.92E-14	4.18E-14	1.74E-14	3.08E-14	4.65E-12	2.78E-13	2.08E-12	4.73E-13	0.45	0.11	**0.06**	**0.014**	100	n/a	n/a	0.0037	0.0066
JS226-2																			
JS226-2-01	2.45	1.25	1.24E-14	2.93E-14	4.51E-14	3.02E-14	3.99E-12	1.18E-13	1.16E-11	5.61E-13	2.91	0.16	**0.38**	**0.022**	100	n/a	n/a	0.0113	0.0076
JS226-2-02	3.10	1.58	-1.09E-14	3.81E-14	2.52E-14	5.09E-14	6.07E-12	1.84E-13	6.39E-12	9.57E-13	1.05	0.16	**0.14**	**0.021**	100	n/a	n/a	0.0042	0.0084
JS226-2-03	3.65	1.86	2.88E-14	2.98E-14	8.06E-14	2.80E-14	1.05E-11	3.21E-13	1.19E-11	6.31E-13	1.14	0.07	**0.15**	**0.009**	100	n/a	n/a	0.0077	0.0027
JS226-2-04	3.95	2.01	1.34E-13	5.87E-14	7.25E-14	3.44E-14	1.07E-11	1.46E-13	1.10E-11	5.64E-13	1.03	0.05	**0.13**	**0.007**	100	n/a	n/a	0.0068	0.0032
JS226-2-05	4.00	2.04	6.95E-14	4.01E-14	2.43E-14	4.63E-14	6.75E-12	1.57E-13	8.91E-12	6.01E-13	1.32	0.09	**0.17**	**0.012**	100	n/a	n/a	0.0036	0.0069
JS226-2-06	5.40	2.75	-2.65E-14	2.59E-14	5.29E-14	6.65E-14	9.13E-12	1.57E-13	8.00E-12	5.53E-13	0.88	0.06	**0.12**	**0.008**	100	n/a	n/a	0.0058	0.0073
JS226-2-07	7.60	3.87	4.12E-14	3.01E-14	4.12E-14	4.93E-14	5.13E-12	1.77E-13	3.71E-12	8.30E-13	0.72	0.16	**0.10**	**0.022**	100	n/a	n/a	0.0080	0.0096
JS226-2-08	8.90	4.53	3.19E-14	2.80E-14	8.26E-15	3.17E-14	3.21E-12	1.06E-13	3.10E-12	5.21E-13	0.96	0.17	**0.13**	**0.022**	100	n/a	n/a	0.0026	0.0099
JS226-3																			
JS226-3-01	2.45	1.25	7.48E-15	3.53E-14	5.38E-14	3.08E-14	2.07E-12	2.91E-13	2.97E-12	4.17E-13	1.43	0.28	**0.19**	**0.038**	100	n/a	n/a	0.0260	0.0153
JS226-3-02	3.10	1.58	-2.82E-14	2.75E-14	4.51E-14	3.95E-14	3.84E-12	1.31E-13	4.84E-12	5.84E-13	1.26	0.16	**0.17**	**0.021**	100	n/a	n/a	0.0118	0.0103
JS226-3-03	3.65	1.86	4.15E-15	2.59E-14	4.27E-14	5.34E-14	7.46E-12	1.24E-13	7.21E-12	5.00E-13	0.97	0.07	**0.13**	**0.009**	100	n/a	n/a	0.0057	0.0072
JS226-3-04	3.95	2.01	6.08E-14	2.80E-14	4.35E-14	3.74E-14	1.25E-11	1.87E-13	9.97E-12	4.74E-13	0.80	0.04	**0.11**	**0.005**	100	n/a	n/a	0.0035	0.0030
JS226-3-05	4.00	2.04	1.15E-14	2.55E-14	3.87E-14	3.60E-14	7.80E-12	1.26E-13	6.01E-12	5.40E-13	0.77	0.07	**0.10**	**0.009**	100	n/a	n/a	0.0050	0.0046
JS226-3-06	5.40	2.75	-2.11E-14	2.73E-14	8.04E-14	2.54E-14	8.33E-12	5.10E-13	4.54E-12	5.04E-13	0.54	0.07	**0.07**	**0.009**	100	n/a	n/a	0.0097	0.0031

GOÐAFJALL & HVG VALLEY

- mor — glacial moraine deposits
- R — LITHOFACIES R: fluvially reworked tuff cone deposits (or PDCs)
- O — LITHOFACIES O: subaerial basalts, breccias and tuffs
- diam — DIAMICTON: glacial unconformity
- N — LITHOFACIES N: Intermediate lobes
- L — LITHOFACIES L: flowbanded columnar-jointed rhyolite
- H — LITHOFACIES H: mLT - pumice rich breccia
- G — LITHOFACIES G: mLT - pumice rich breccia
- F — LITHOFACIES F: slope draping breccia
- E — LITHOFACIES E: aphyric rhyolite breccia
- D — LITHOFACIES D: aphyric rhyolite
- C — LITHOFACIES C: columnar jointed rhyolite
- A — LITHOFACIES A: basement basalt

HRÚTSFJALL

- mor — glacial moraine deposits
- O — LITHOFACIES O: subaerial basalt and breccia
- L — LITHOFACIES L: flowbanded columnar-jointed rhyolite
- J — LITHOFACIES J: mLT - massive pumice breccia
- I — LITHOFACIES I: dsLT - lapilli tuff
- H — LITHOFACIES H: mLT - pumice rich breccia
- D — LITHOFACIES D: aphyric rhyolite
- tb — mafic tuff breccia / hyaloclastites
- con — Conglomerates (fluvial)
- B3 — polymict diamictite
- B2 — slope draped tuff and lavas
- B1 — bedded sedimentary units
- till — glacial diamict / till

LITHOFACIES B and BA

SLAGA

- Sk — tuff breccia / hyaloclastite
- Sj — fine grained laminated unit
- Si — mafic sheet lavas
- Sg — intermediate lobes
- Sf — polymict diamict
- Se — mafic sheet lavas and tuff breccias / hyaloclastites
- Sd — basalt lavas
- Sc — glassy flow banded rhyolite
- Sb — Diamictite (glacial unconformity)
- B1 — LITHOFACIES BA: bedded sedimentary unit
- Sa — pillow breccia
- A — LITHOFACIES A: basement basalts

ROTARFJALL

- Rb — rhyolite (ridge bound flow)
- Ra — Subaerial and subglacial basalts

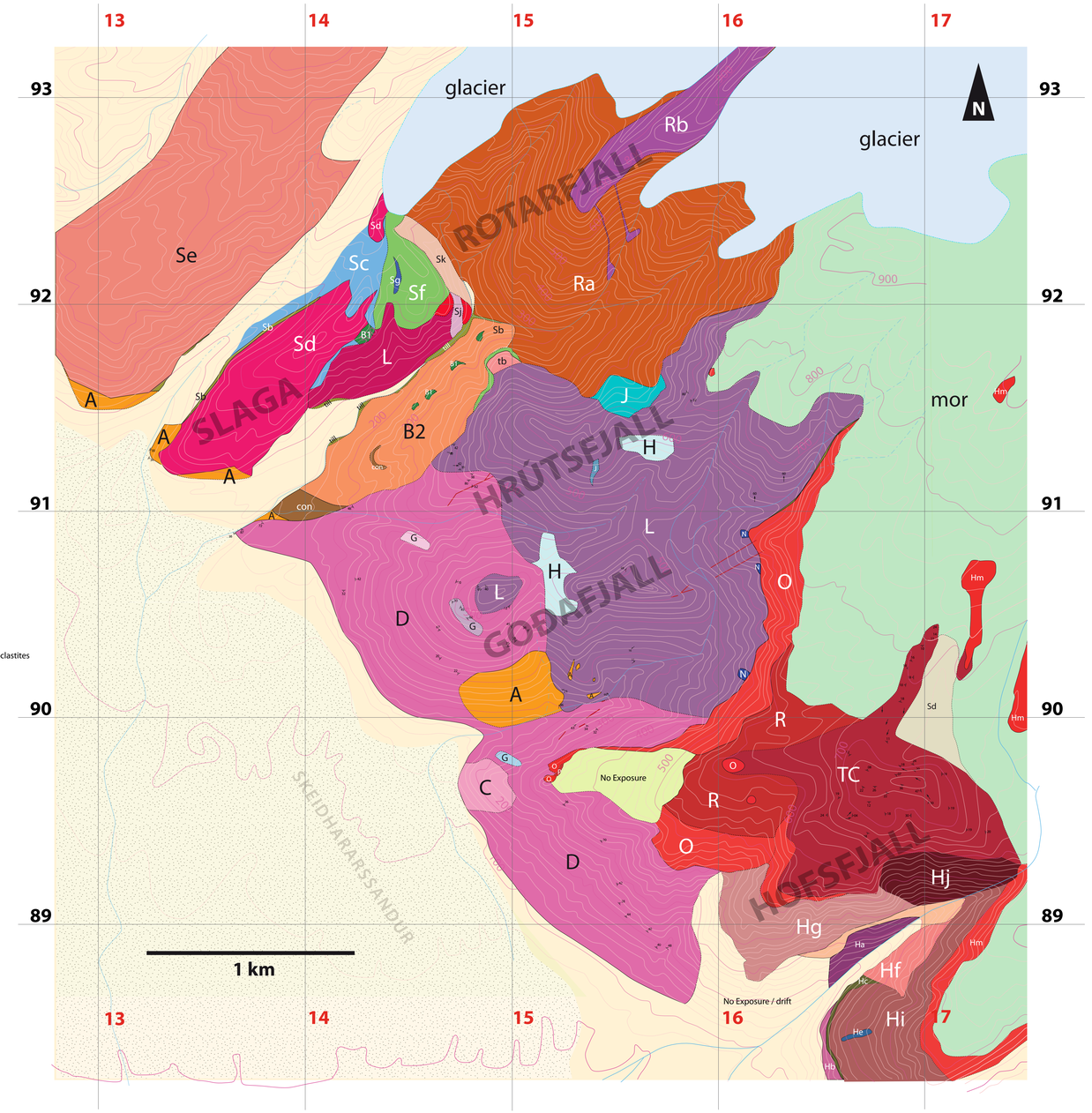

HOFSFJALL

- mor — glacial moraine deposits
- Sd — unconsolidated rhyolite tephra
- Hm — subaerial basalt lavas
- TC — tuff cone deposits (LGM 21 Ka)
- Hj — fragmental/ breccia - chaotic unit (observed via binoculars)
- Hi — massive tuff breccia / hyaloclastite & lava intrusions
- Hg — stratified unit (observed via binoculars)
- Hf — stratified lapilli tuff
- He — pillow basalts
- Hd — finely laminated lapilli tuff
- Hc — glacial diamict
- Hb — subaerial basalt lavas
- Ha — porphyritic vesicular basaltic andesite

KEY:

- 500m
- CONTACT
- DYKE
- INFERRED CONTACT
- UNCONFORMITY
- 20 — PLATE STRIKE & DIP
- 60 — COLUMN ORIENTATION AND PLUNGE